MICHIGAN STATE UNIVERSITY LIBRARIES
3 1293 01407 5935
LIBRARY
Michigan State
University

THESIS
4

This is to certify that the

dissertation entitled

SPECTRAL CALIBRATION AND KINEMATIC PROPERTIES
OF THE
FIELD HORIZONTAL BRANCH STARS

presented by

Ronald J. Wilhelm

has been accepted towards fulfillment
of the requirements for

Ph.D. degree in Physics

Dr. Timothy Beers
Major professor

Date 5/3/93

MSU is an Affirmative Action/Equal Opportunity Institution O-12771

PLACE IN RETURN BOX to remove this checkout from your record.
TO AVOID FINES return on or before date due.

DATE DUE	DATE DUE	DATE DUE
MAY 06 2000		
MAY 03 2002		

MSU is An Affirmative Action/Equal Opportunity Institution

c:\circ\datedue.pm3-p.1

SPECTRAL CALIBRATION AND KINEMATIC PROPERTIES OF THE FIELD HORIZONTAL BRANCH STARS

By

Ronald Joseph Wilhelm

A DISSERTATION

Submitted to

Michigan State University

in partial fulfillment of the requirements

for the degree of

DOCTOR OF PHILOSOPHY

Department of Physics and Astronomy

1995

ABSTRACT

SPECTRAL CALIBRATION AND KINEMATIC PROPERTIES OF THE FIELD HORIZONTAL BRANCH STARS

By

Ronald J. Wilhelm

An understanding of the kinematic properties of the Galactic halo is an essential component to the ultimate understanding of the Galactic formation history. The blue field horizontal branch stars (FHB) are excellent stellar probes with which to explore these properties. The FHB stars are both intrinsically luminous, which allows kinematic exploration beyond the confines of the local solar neighborhood, and numerous, which is important for good statistical results. In the past, however, isolating a pure sample of FHB stars from their main sequence, A-star, counterparts has proven to be a difficult and highly uncertain task leaving the FHB kinematic results open to skepticism. This dissertation explores the kinematic properties of an FHB sample identified through the use of a new spectral calibration technique.

Medium resolution (1-2 Å) spectroscopic and UBV photometric observations have been completed for 1213 FHB and main sequence A-type stars (FHB/A) drawn from the candidates in the HK objective prism surveys of Beers *et al.*. A new spectral calibration was developed using synthetic spectra and colors to calculate the physical parameters for the program stars. The corresponding parameter uncertainties of $\sigma T_{eff} = \pm 250$ K, σlog g= ± 0.25, and σ[Fe/H]= ± 0.30, are sufficient to push the stellar class misidentifications below 10%.

A statistical kinematic analysis of the FHB stars indicates the halo is composed of at least two components. The dominant component is flattened with a vertical velocity dispersion of $\sim$ 70 km/s and has a mild pro-grade systemic rotation of $\sim$ 20 km/sec. The second appears to have a more isotropic velocity ellipsoid and a systemic counter-rotation of ~ -90 km/s. The kinematics of the metal-poor main sequence A-stars (BMP) indicate an isotropic velocity ellipsoid of $\sim$ 90 km/s and a systemic rotation of $\sim$ 90 km/s. These values are different from either the halo or thick-disk populations.

The kinematic evidence from the FHB stars strongly suggests that the outer halo of the Galaxy formed from accretion of discrete fragments while the inner halo kinematics are consistent with a contracted origin. The BMP kinematics are consistent with an origin from one or more delayed accretion events.

For Jennifer and Olivia, the center of *my* universe.

ACKNOWLEDGEMENTS

I would like to begin by thanking my thesis advisor, Dr. Timothy C. Beers. About three years ago Tim sketched out a possible thesis topic that held the insurance of many new and exciting advances in the understanding of A-type stars in particular and the Galactic halo in general. The vast amount of topics presented in this thesis stand as testimony to the scientific depth of the research project which he had envisioned. On a professional level I want to thank Tim for his infectious excitement of astronomical pursuits, for guidance onto the correct paths through the enormous number of research obstacles, and for giving me the freedom to pursue and develop my own lines-of-reasoning. On a personal level I am indebted to Tim for his kind understanding of the conflicts that occasionally arise between research and family life.

I would also like to thank my many collaborators, without whom this project would not have been possible. Namely, Richard Gray, Jeff Pier, Jesper Sommer-Larson, Andy Layden, Chris Flynn, George Preston, and Steve Shectman. I would also like to thank my thesis committee: Horace Smith, Ed Loh, Jack Bass, S.D. Mahanti, and Suzanne Hawley. Thanks also to Nancy Silbermann for the use of her 486 PC in the computation of a large number of synthetic spectra.

I also wish to acknowledge a debt of gratitude to my entire family for encouragement of my astronomical pursuits over the years. In particular, I would like to thank Mom and Dad, my mother-in-law, Regina Sundberg and my father-in-law,

TABLE OF CONTENTS

INTRODUCTION 1

1.1 Preface 1

1.2 The Milky Way Galaxy 3

1.3 In *Mode* and *Measure* 5

1.4 Formation Models 11

1.5 Previous Surveys 13

1.6 The Field Horizontal Branch and Main Sequence A-type Stars 16

1.7 FHB stars as Kinematic Tracers 19

PROGRAM STAR OBSERVATIONS AND REDUCTIONS 26

2.1 The Sample 26

2.2 UBV Photometric Observations 26

2.3 Spectral Observations 27

2.4 Spectral Extractions 32

2.5 Radial Velocity Determination 35

SPECTRAL CALIBRATION 43

3.1 Introduction 43

3.2 Parameter Calibration 45

3.2.1 The Observables 45

3.2.1.1 The Balmer Lines 45

3.2.1.2 The (U-B) Colors 47

3.2.1.3 The (B-V) Colors 48
3.2.1.4 The CaII K Line 49
3.2.2 The Calibration Grid 49
3.2.3 Observable Dependencies 52
3.3 Assignment of Stellar Physical Parameters 60
3.3.1 The Grid Comparison Technique 60
3.3.2 Secondary Abundance Indicator 63
3.4 Standard Star Results 66
3.4.1 Physical Parameter Comparisons 71
3.4.2 Separation of FHB/A Stars 75
3.4.3 The Ca and Fe Indicators 77
3.5 Low Signal-to-Noise Analysis 85
3.5.1 Line Widths 86
3.5.2 Effects on the Derived Parameters 92
3.5.3 Misidentifications 106
3.5.4 Abundance Comparisons for the Globular BHB stars 106
THE FHB AND A-STAR PROPERTIES 113
4.1 Program Star Calibration 113
4.1.1 Internal Accuracy in the Program Stars 114
4.1.2 Stellar Class Separation 120
4.1.2.1 Am Contamination 126
4.1.2.2 RR Lyrae Contamination 127
4.1.2.3 A-type Giants 132
4.1.2.4 Log g Uncertainty 133
4.1.3 The [Ca/Fe] Analysis 135
4.1.3.1 The [Ca/Fe] Ratios 137

4.1.3.2 Blended Interstellar CaII K 144
4.1.3.3 Concluding Remarks on [Ca/Fe] 148
4.2 Characteristics of the FHB Sample 148
4.2.1 Bias and Selection Effects 148
4.2.2 The Metallicity Distribution Function (MDF) 153
4.2.3 Abundance Gradients 155
4.2.3.1 Radial Abundance Gradient 157
4.2.3.2 Vertical Abundance Gradient 162
4.2.4 The 2nd Parameter Effect 167

KINEMATICS OF THE FHB STARS 173
5.1 The Distribution of Velocities 173
5.2 Sample Velocities as a Function of $|Z|$ and [Fe/H] 176
5.3 The Systemic Rotational Velocity 181
5.3.1 V_{rot} Assuming Constant Angular Velocity 181
5.3.2 V_{rot} Assuming Constant Rotational Velocity 185
5.3.3 The Velocity Ellipsoid 189
5.3.4 Comparison to Other Published Results 194
5.4 The Binned Data Results 196
5.5 The Vertical Velocity Distribution 201
5.6 The Halo Kinematics 207
5.7 The Metal-Weak Thick Disk (MWTD) 216
5.8 Systemic Rotational Properties (Revisited) 224
5.9 Concluding Remarks 230

KINEMATICS OF THE A-STAR SAMPLE 232
6.1 The Sample Properties 232

6.2 A-star Kinematics 236
6.2.1 Binned Solutions 236
6.2.2 The Vertical Velocity Dispersion 239
6.3 Population I Kinematics 243
6.4 The BMP Sample 245
6.4.1 BMP Kinematics 247
6.4.2 Mixture Analysis 253
6.4.3 The Low Metallicity, Zero Rotation Sample 256
6.4.4 Contaminates (Revisited) 260
6.4.5 Conclusions for BMP Sample 261
CONCLUSION 263
7.1 Summary of Results 263
7.2 Possible Scenarios for Galactic Formation 265
7.3 Future Work 270

APPENDICES

Appendix A Spectral Calibration Grid 273
Appendix B Program FHB/A Results 301
BIBLIOGRAPHY 346

LIST OF TABLES

Table 3.1 Standard Star Results 69

Table 3.2 Standard Star External Accuracy 72

Table 3.3 Standard Star Internal Accuracy 72

Table 3.4 Standard Template Comparison Results 78

Table 3.5 Globular BHB Results 108

Table 4.1 [Ca/Fe] Ratios 138

Table 5.1 Kinematic Solutions for FHB Sample 184

Table 5.2 Previously Published Halo Kinematic Results 195

Table 5.3 Halo Kinematics 215

Table 5.4 KMM Analysis for Rotation Direction 215

Table 6.1 Pop. I Systemic Rotation 244

Table 6.2 Kinematic Solutions for the BMP Sample 248

Table A.1 Spectral Calibration Grid 273

Table A.2 Observable Weightings 297

Table B.1 The FHB Sample 301

Table B.2 The A-star Sample 320

Table B.3 The FHB/A Sample 336

Table B.4 The Am Candidates 342

LIST OF FIGURES

Figure 1.1 Observational Sketches by Rosse and Herschel 2

Figure 1.2 ELS Plot of Angular Momentum as a Function of δ(U -B) 7

Figure 1.3 Zinn Plot of Spatial and Abundance Distribution of Globular Clusters 8

Figure 1.4 Plot of Distribution of Galactic Coordinates for the FHB/A Sample 18

Figure 1.5 Color-Magnitude Diagram of Glaobular Cluster M 3 20

Figure 2.1a Characteristic Spectra from Observations at ESO 28

Figure 2.1b Characteristic Spectra from Observations at KPNO 29

Figure 2.1c Characteristic Spectra from Observations at Lowell 31

Figure 2.2 Plots of Various IRAF Extraction Stages 33

Figure 2.3 Plot of Cross-Correlation Peak from FXCOR 37

Figure 2.4 Comparison of Derived and Published Radial Velocities for Standard Stars 40

Figure 2.5 Scatter in Radial Velocity Determination for Program stars with Mulitiple Observations 41

Figure 3.1 Temperature Dependence of Hδ Balmer Line 46

Figure 3.2 3-D Plot of T_{eff} - Log g Dependency of UBV Colors and Balmer Line Witdths 53

Figure 3.3 2-D Plot of T_{eff} - Log g Dependency of UBV Colors and Balmer Line Witdths 54

Figure 3.4 T_{eff} - [Fe/H] Dependency of W_k 56

Figure 3.5 Log g Dependency of W_k 57

Figure 3.6 New Calibration Comparison of W_k - (B-V) to that of Pier 59

Figure 3.7 Observable Matches to the Calibration Grid 62

Figure 3.8 Metallic Regions Used in Tamplate Comparison Technique 65

Figure 3.9 Template Match to CaII K line 67

Figure 3.10 Template Match to Metallic Line Regions 68

Figure 3.11 External Accuracy of Physical Parameters for the Standard Stars 74

Figure 3.12 Separation of the Standard Stars 76

Figure 3.13 Comparison of [Ca/H] and [Fe/H] to that of AP 81

Figure 3.14 Comparison of Derived [Ca/Fe] ratio to that of AP 82

Figure 3.15 [Ca/Fe] for All FHB Standard Stars 84

Figure 3.16 Comparison of Noisy Synthetic Spectra to Real Low S/N Spectra 87

Figure 3.17 Noise Induced Scatter in Hδ $D_{0.2}$ 88

Figure 3.18 Normalized Fractional Scatter in Hδ $D_{0.2}$ 90

Figure 3.19 Noise Induced Scatter in W_k 91

Figure 3.20 Noise Induced Scatter in T_{eff} 93

Figure 3.21 Bubble Plot of Residual in $D_{0.2}$ 95

Figure 3.22 Noise Induced Scatter in Log g 96

Figure 3.23 Bubble Plot of Residuals in $D_{0.2}$ and T_{eff} 98

Figure 3.24 Noise Induced Scatter in [Fe/H] 99

Figure 3.25 Bubble Plot of Residuals in W_k and T_{eff} 101

Figure 3.26 Scatter in [Fe/H] from CTA and MTA 102

Figure 3.27 Scatter in Physical Parameters with UBV Uncertainty Included 105

Figure 3.28 Estimate of Class Misidentification for Noisy Synthetic Spectra 107

Figure 3.29 Scatter in [Fe/H] for Globular Cluster BHB Stars 110

Figure 3.30 [Ca/Fe] Ratio for Globular Cluster BHB Stars 111

Figure 4.1 Internal Scatter in the Program Physical Parameters for All Stars with Multiple Measures 115
Figure 4.2 Internal Scatter in the Program Physical Parameters for ESO/KPNO Stars with Multiple Measures 117
Figure 4.3 Internal Scatter in the Program Physical Parameters for Lowell Stars with Multiple Measures 118
Figure 4.4 Internal Scatter in [Fe/H] split at T_{eff} = 8000 K 119
Figure 4.5 Histogram of Am Candidates Compared to Published Distribution 121
Figure 4.6 Comparison of Am Candidates to Am and FHB Standard Stars 122
Figure 4.7a Separtation of Program FHB and A-type Stars 124
Figure 4.7b Plot of [Fe/H] - T_{eff} for FHB and A-type Stars 125
Figure 4.8 (B-V) - T_{eff} Plot used to Identify RR Lyrae Candidates 129
Figure 4.9 Histogram of Excess Stars in the A-star Sample 131
Figure 4.10 Correlations of Abundance Indicators for the Program Stars 136
Figure 4.11 [Ca/Fe] Ratios for the Various Studied Samples 139
Figure 4.12 [Ca/Fe] Ratios as a function of T_{eff} 141
Figure 4.13 Effects of Interstellar CaII at Low $|Z|$ Heights 145
Figure 4.14 Effects of Interstellar CaII Toward the Galactic Center 146
Figure 4.15 Removal of the Wheeler *et al* Trend in the FHB Stars 149
Figure 4.16 Decrease in Distance as a Function of (B-V) for FHB Sample 151
Figure 4.17 Normalized Residual Plot of Decreasing Distance as a Function of (B-V) 152
Figure 4.18 Distrbution of Metallicities for the FHB Sample 154
Figure 4.19 Grid Edge Effects From Scatter in Calculated [Fe/H] Values 156
Figure 4.20 Gradient in Metallicity as a Function of Galactocentric Distance 158
Figure 4.21 Result of Selection Effects in the Inner Halo FHB Sample 159

Figure 4.22 Binned Abundance Results as a Function of R 161

Figure 4.23 Gradient in Metallicity as a Function of Vertical Height 164

Figure 4.24 Gradient in Metallicity for Polar Cap Region 166

Figure 4.25 FHB Sample Plotted with Age Models from Lee 168

Figure 4.26 FHB Sub-samples Showing Age Effects with Increasing
Galactocentric Distance 171

Figure 5.1 Histogram of Velocities for the FHB Sample 174

Figure 5.2 Histogram of Velocities in the Galactic Cardinal Directions 177

Figure 5.3 FHB Velocities as a Function of Vertical Height and [Fe/H] 178

Figure 5.3e FHB Metallicity as a Function of $|Z|$ 180

Figure 5.4 Systemic Rotational Velocity for FHB Sample
Assuming Solid Body Rotation 182

Figure 5.5 Systemic Rotational Velocity Split in $|Z|$ and R 186

Figure 5.6 Systemic Rotational Velocity for FHB Sample
Assuming Constant Rotational Velocity 190

Figure 5.7 Systemic Rotational Velocity Split in $|Z|$ and R 191

Figure 5.8 Continously Binned Frenk and White Solutions for FHB Sample 198

Figure 5.9 Continously Binned Woolley Velocity Ellipsoid Dispersions
for FHB Sample 199

Figure 5.10 Estimated W velocities as a Function of $|Z|$ and [Fe/H] 202

Figure 5.11 Plot Showing Increase in W Velocity Dispersion
as a Function of [Fe/H] 203

Figure 5.12 Histogram of W Velocities for FHB Sub-samples 204

Figure 5.13 Single and Double Gaussian Fit to Polar Cap Region 206

Figure 5.14 Change in Systemic Rotation of Halo Sample as a Function of $|Z|$ 209

Figure 5.15 Plot of Counter-Rotation FHB Sample 211

Figure 5.16 Histogram of Rotation Direction Sample Split in [Fe/H] 214

Figure 5.17 Systemic Rotation for Halo Sample Split at $|Z| = 3$ kpc 218

Figure 5.18 Single and Double Gaussian Fit to the Galactic Center Region 219

Figure 5.19 Projected Rotational Velocities for FHB Rotational Direction 221

Figure 5.20 Histogram of Various Splits in Rotation Sample 223

Figure 5.21 Single Gaussian Fits to the Galactic Rotation Sample 228

Figure 5.22 Double Gaussian Fits to the Galactic Rotation Sample 229

Figure 6.1 Spatial and Abundance Distribution for A-star Sample 233

Figure 6.2 Comparison of Metallicity Distribution for A-star and FHB Samples 235

Figure 6.3 V_{lsr} as a Function of [Fe/H] and $|Z|$ 237

Figure 6.4 Continuously Binned Systemic Rotation Solutions 238

Figure 6.5 Non-continuously Binned Rotation and Dispersion Solutions 240

Figure 6.5b Non-continuously Binned Woolley Solutions 241

Figure 6.6 W Velocities for Polar Cap Region 242

Figure 6.7 Abundance Comparison for PBS and Program BMP stars 246

Figure 6.8 Systemic Rotational Velocities for A-stars split in [Fe/H] 250

Figure 6.9 Histogram of Rotational Direction Velocities for BMP stars 251

Figure 6.10 Single and Double Gaussian Fit for BMP stars with $-0.75 >$ [Fe/H] > -2.2 252

Figure 6.11 Single and Double Gaussian Fit for BMP stars with $-1.0 >$ [Fe/H] > -2.2 254

Figure 6.12 Single and Double Gaussian Fit for BMP stars with [Fe/H]< -1.0 255

Figure 6.13 Log g - T_{eff} Plot for A-Stars with [Fe/H]< -2.2 257

CHAPTER 1

INTRODUCTION

1.1 Preface

When Nicolaus Copernicus published De Revolutionibus Orbin Coelestium in 1543 the fundamental notion of a geocentric cosmos was forever destroyed. What followed were the monumental advances in physics and astronomy by the likes of Kepler, Galileo, and Newton. A new classical picture of a clockwork universe governed by the force of gravity and described in terms of energy and angular momentum soon emerged and with it the tools for the mathematical modeling of astronomical systems and interactions.

An example of the use of such models can be seen in the seldom referenced work of Alexander (1852). Borrowing from the observations of Sir John Herschel and Lord Rosse (Figure 1.1), and the nebular hypothesis for the solar system's formation by Laplace, Alexander attempted to explain the physical appearance of the various "nebulae" and star clusters in terms of angular momentum conservation and radiative cooling. Although his unification schemes were dealt a serious blow as improved observations (through the use of larger telescopes and photographic plates) shed new "light" on these objects, in his work the precursor of our modern ideas of early galactic evolution can be clearly seen. The origin of flattened spiral nebula as a result of dissipational collapse and later rotational support of the collapsing gas cloud, is still a pervasive theme in contemporary theories of galaxy formation. Alexander's hypothesis that the stellar component in globular star clusters

Fig 1.1: Observational sketches of various nebulae by Herschel and Rosse from the paper by Alexander

preserve the original spherical distribution of the gas is the central assumption in all modern kinematic surveys which rely on stellar tracers to explore the galactic formation history. The evocation of a merger hypothesis, where two components fall into dynamic equilibrium about a common center of mass, used by Alexander in an attempt to explain the existence of barred spiral galaxies, today has gained wide spread acceptance in many modern theories of giant elliptical galaxy formation. The work by Alexander, and others of his day, helped to lay the ground work for the unification of physical theory and astronomical observations which still resonates through much of our modern understanding of Galactic evolution.

In astronomy, as in all of science, the merit of a phenomenological theory is gauged by the wealth of supporting observations. As so eloquently pointed out by Alexander himself:

"*Now it is quite supposable that an explanation may be altogether adequate in mode, while such may be the state of our knowledge, or such may be the very greatness of the quantities concerned, or both, that it may as yet be impracticable to show distinctly how far any given explanation of the phenomena may be adequate in measure; though we may arrive at a reasonable probability that such is the fact.*"

These words, which were a foreshadowing in the case of the majority of the results in Alexander's paper, also serves as a starting point for this dissertation research, as we strive for an explanation of Galactic halo formation which is adequate in both *mode* and *measure*.

1.2 The Milky Way Galaxy

The Milky Way Galaxy is a spiral galaxy. The vast majority of the stellar and non-stellar (gas and dust) components reside in either the spatially flattened distribution that is designated the disk of the Galaxy, or in the central spheroidal

region known as the Galactic bulge. The disk (hereafter "thin disk") is very thin ($\sim$ 200 pc) and extends radially to distances of $\sim$ 25 kpc. Historically the stellar component of the thin disk has been labeled as population I and is characterized by both young and older stars with metal contents similar to that of the sun. Also, the Pop. I stars are on nearly circular orbits about the Galactic center and move with a rapid systemic rotational velocity of $\sim$ 220 km/s. As would be expected from the thin nature of the disk, there is not a large range of velocities perpendicular to the disk. In fact the total spread in velocities, or velocity dispersion, is $\sim$ 20 km/s. The bulge of the Galaxy has very little gas content and thus is comprised mainly of old stars. The metal abundance of the stars, however, varies from low-metallicity to values substantially higher than solar.

A third component to the Galaxy is the halo. The halo is an approximately spherical distribution of stars that extends to distances of $\sim$ 30 kpc from the Galactic center. In all, the halo represents $\sim$ 1% of the stellar content of the Galaxy. It is made up of ancient stars whose origin date back to the formation time of the Galaxy itself. These stars are found in both globular star clusters ($\sim$ 1% of the halo) and individually in the field. There is only a small amount of gas content in the halo and it is therefore not considered a site of active star formation. The stars that make up the halo have been traditionally labeled population II and have a metal content that ranges from one-tenth that of solar down to at least one-thousandth of solar. Unlike the Pop. I stars the halo shows virtually no systemic rotation and the velocity dispersions are quite large ($\sim$ 100 km/s). It is assumed that these stars have maintained the kinematic signature of the gas from which they formed and it is therefore suggested that the distribution of matter in the early Galaxy was significantly different then what is observed today.

There is also a possible fourth component to the Galaxy that has become known as the thick-disk. The stellar component of the thick-disk has metal abundance and kinematic properties that are between the extremes of the thin disk and halo, but more closely resemble the thin disk in nature. The vertical scale height of the thick-disk in the Galactic vicinity of the Sun is $\sim$ 1-2 kpc. It is generally more metal-weak than the thin disk, extending to values $\sim$ one-tenth of solar and has a systemic rotation which lags the thin disk by $\sim$ 25 km/s. It also has a larger vertical velocity dispersion, $\sim$ 45 km/s, which is expected from the larger scale height. It remains unclear if the thick-disk is actually a discrete component of the Galaxy or part of a continuous evolutionary transition phase between two components.

By probing the characteristics of these various components and their associations with one another, it is possible to begin to assemble the chain of events that have led from the earliest formation time of the Galaxy to the distribution of matter we observe today.

1.3 In *Mode* and *Measure*

Our modern understanding of the formation and early evolution of the Milky Way Galaxy began with the landmark work of Eggen, Lynden-Bell, and Sandage (1962) (hereafter ELS). Their observations of stars with high proper motions indicated a decrease in orbital ellipticity and a decrease in ultraviolet excess (increase in metal abundance) as a function of decreasing height above the Galactic plane. Taken together these findings suggested the Galaxy had formed from a slowly rotating protogalactic cloud which spun-up as a result of angular momentum conservation during a free-fall collapse time. Through the duration of the rapid collapse, it was imagined that metallic self-enrichment of the Galactic interstellar medium occurred as the first generation of massive stars underwent supernova explosions.

The correlation of angular momentum to ultraviolet excess is clearly seen in figure 6 of ELS, reproduced here in figure 1.2.

This monolithic picture of the evolution of the galactic halo met serious objection with the findings of Searle and Zinn (1978) and Zinn (1985) that the galactic globular cluster system, which spatially overlaps the halo field population, could be best described as a two component system. One component showed nearly zero systemic rotation, a large line of sight velocity dispersion, and was spatially spherical in extent. The other exhibited a large systemic rotational velocity, small line of sight velocity dispersion and was spatially disk-like in extent (figure 1.3a from Zinn 1985). When separate analysis of the two populations, split at an abundance of [Fe/H] = -0.8, was carried out, it showed an outer halo component with little or no sign of an abundance gradient in either galactocentric distance (R) (figure 1.3b), or height above the plane (Z). These findings led to the postulation of a halo formed from discrete sub-units, each with its own particular kinematic and chemical history.

With the battle lines drawn it was left to halo field surveys to unravel the conflicting results. The discovery by Gilmore and Reid (1983) of the existence of a thick disk and halo component in the field stars lent some credence to the proposed formation model of Searle and Zinn. The existence of a thick disk in the Milky Way was not only the field analogy of the disk globular clusters but also suggested that the results of ELS were in part due to a mixture of thick disk and halo kinematics. The extensive high-proper-motion surveys of field sub-dwarf stars by Norris and Ryan (1989) and Carney, Latham and Laird (1990) confirmed the existence of a thick disk component but were unable to clearly discern if the transition between the halo and thick disk was continuous (ELS model) or discrete (SZ model).

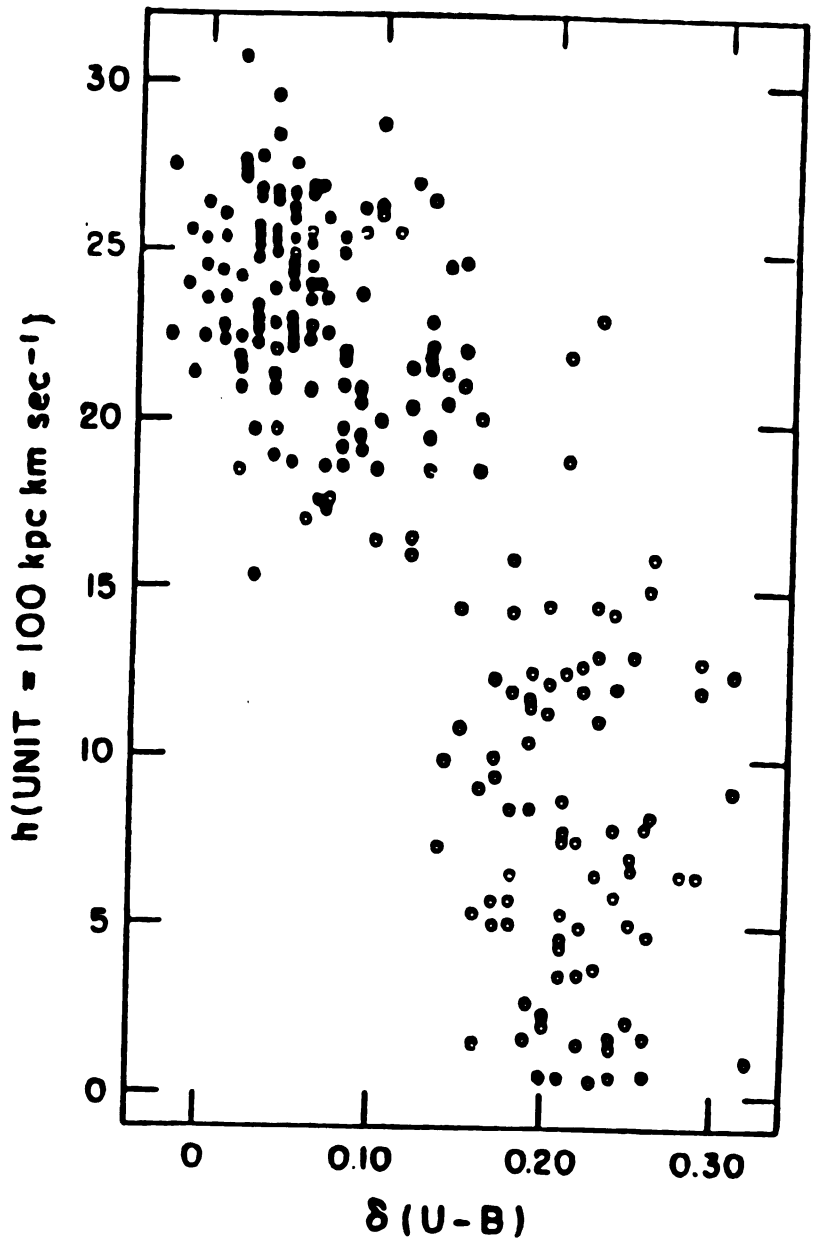

Fig 1.2: ELS plot of angular momentum as a function of ultraviolet excess for high velocity subdwarfs

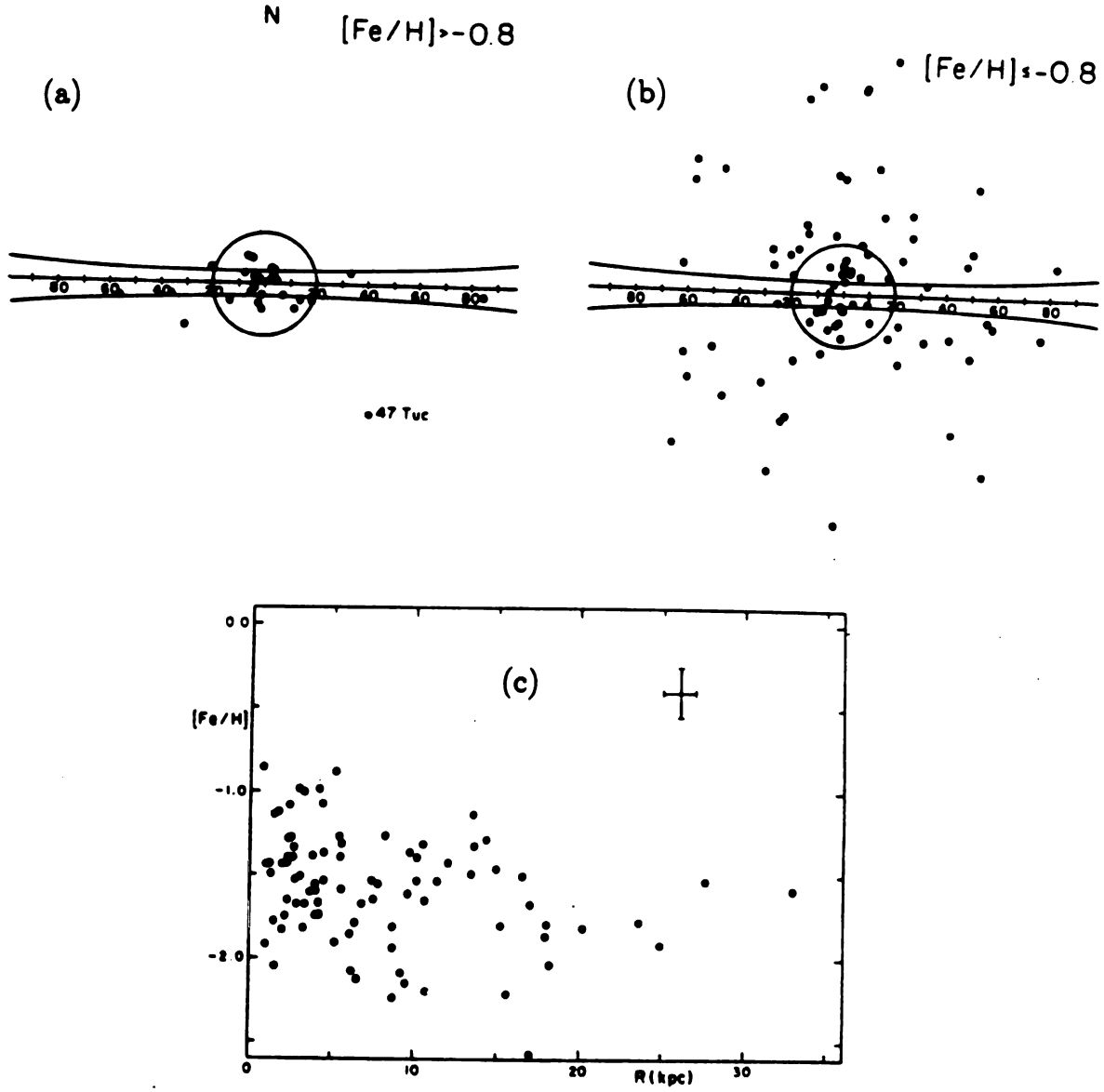

Fig 1.3: Zinn plot of globular cluster spatial distribution for (a) the clusters with [Fe/H]> −0.8 and (b) the clusters with [Fe/H]< −0.8. Figure (c) is a plot of abundance as a function of galactocentric distance (R).

The inclusion of results from other halo studies served to further polarize the formation picture. Rodgers and Paltoglou (1984) discovered a subset of halo globular clusters that appeared to be in retro-grade orbits. Rodgers, Harding and Sadler (1981) and Lance (1988) identified mildly metal poor A-type stars in the galactic halo, with relatively young ages that strongly supported an accretion origin. The findings of Pier (1984) and Sommer-Larsen and Zhen (1990), that the halo field horizontal branch stars inside the solar circle were radially anisotropic in their velocity ellipsoid, argued for a contracting halo model in the inner halo but an accreted origin for the FHB stars outside the solar circle. In conjunction with this, the findings of Preston, Beers and Shectman (1991) of a color shift in their FHB sample from the inner halo to the outer halo suggested an older inner halo and younger (possibly accreted) outer halo. The discovery of a metal-poor component of the thick disk by Norris, Bessell, and Pickles (1985), Morrison, Flynn and Freeman (1990) and Morrison (1993) further added to the debate, since an apparent larger scale height of the metal-poor component argued for a dissipational collapse, at least in the inner halo.

In the past several years, new investigations and reanalysis of older ones have led to a hybrid model in which both ELS and SZ scenarios play a role. In his thesis, Majewski (1992) undertook a proper motion survey in the direction of the North Galactic Pole. Because this was a magnitude limited survey, it suffered from neither kinematic nor metallicity biases. His findings indicated the existence of a flattened stellar component which dominated the sample to a height of 5 kpcs. Above 5 kpcs the stellar distribution was more spherical and, oddly, in counter-rotation. These results led him to the conclusion that the galactic halo was made up of only two components. One, a flattened pro-grade rotating component, which has an

increasing systemic rotation as a function of decreasing height above the plane, and the other, a spherical component which is in counter-rotation, and only dominates at a Z-height above 5 kpc. In such a two-component model the flattened component encompasses both the "old" zero-rotation halo, metal weak thick disk, and normal thick disk by assuming the change in kinematics between each is continuous and a result of "spin-up" as envisioned by ELS. The spherical component is then due to accretion of discrete sub-units, which at later times fell into dynamical equilibrium with the Galaxy.

In concurrence with this perspective, a reanalysis of the Carney, Latham, and Laird sample by Norris (1994) shows only a two-component halo model, contracted and accreted, to be simultaneously consistent with the rotational velocities and cardinal velocity dispersion solutions. Using newly-calculated models for horizontal branch morphology, Zinn (1993) found the halo globulars clusters to be composed of an "older" and "younger" population. The older halo population exhibits a flattened distribution and mildly pro-grade rotation, while the younger halo globulars exhibit a spherical distribution and possible counter-rotation. In addition to this, the older halo globulars and disk globulars may form a continuous population, exhibiting the effects of Galactic spin-up. Taken together these results seem to indicate the two-component hybrid ELS/SZ model can explain the events that led to the formation and early evolution of the galaxy we see today. Caveats, however, still remain.

With the exclusion of the thick-disk component at the lower Z heights, ($|Z| < 1$ kpc) there is little or no evidence of an abundance gradient as a function of Z, as may result from a dissipational collapse. There is also conflicting evidence that "spin-up" of the flattened component has occurred. Recent kinematic findings by Beers and Sommer-Larsen (1995), using a sample of nearly 2000 metal-poor stars selected

without kinematic bias, suggest that the metal-weak component is consistent with thick-disk kinematics and shows virtually no sign of dissipational collapse. They speculate these results are more consistent with dynamical heating of an old disk population by a merger event in the early stages of Galaxy formation.

Evidence for Galactic mergers are not without precedence. Along with the findings of Rodgers, Harding, and Sadler (1981), and Lance (1988), mentioned earlier, Preston, Beers and Shectman (1994) have identified a large population of metal-poor main sequence A-type stars (hereafter BMP) with kinematics distinct from either the thick-disk or halo populations. These stars, which have ages too young to have formed contemporarily with the bulk of the halo globulars, are believed to have originated in one or more dwarf galaxies which have now merged with the Galaxy. The first direct evidence of just such an accretion event was the discovery of the Sagittarius dwarf spheroidal by Ibata, Gilmore, and Irwin (1994). This galaxy, which is 16 kpc from the Galactic center, shows clear signs of tidal disruption and is expected to merge with the Galaxy in the not too distant future. Possible remnants of similar mergers can be found in the ever growing number of moving group candidates discovered in the past few years. (Eggen 1987; Sommer-Larson & Christensen 1987; Doinidis & Beers 1989; Croswell et al. 1991; Arnold & Gilmore 1992; Majewski 1992; Poveda et al. 1992; Cote et al. 1993; Majewski, Munn & Hawley 1994) Although the growing evidence for prolonged accretion events does not rule out the ELS portion of the hybrid model, it does indicate that accretion may have played an important role in the formation history of the local halo.

1.4 Formation Models

In terms of the most recent observational advances, we now explore three possible scenarios for the formation of the Galactic halo.

(i) The ELS/SZ Hybrid Model

In this picture the inner portions of the Galactic halo first underwent an ELS-type of collapse. As stars condensed out of the dissipational gas, they froze in time the memory of the gas kinematics from which they formed. This process led to a stellar component which dominates the inner regions of the Galactic halo and which exhibits an increase in rotational velocity and decrease in velocity dispersion as a function of height above the Galactic plane. Furthermore, the stellar population exhibits a gradient in abundance due to self-enrichment of the interstellar medium. This continuous component contains the previously recognized old halo, thick-disk with metal-weak tail, and thin-disk components. Sprinkled throughout the dominating flattened component is a more spherical component, which shows no clear dependency of rotation or abundance on Z height, and dominates only above Z = 5 kpc. Since this accreted component did not take part in the original contraction it can have a net counter-rotation.

(ii) Accreted Halo with Dynamically heated Thick Disk

In this scenario, the bulge and disk of the Galaxy formed from either dissipational collapse or mergers of smaller stellar systems. The halo then formed, as prescribed by SZ, through the accretion and subsequent disruption of discrete subunits falling into dynamical equilibrium with the already formed Galaxy. The energy from such accretion events serve to dynamically heat the old-disk population, causing it to "puff-up", and thus form a thick disk. With time the gas left in the thick disk falls back into the thin disk configuration as observed today. In this picture, the previously identified metal-weak tail of the thick disk could be the result of an earlier accretion event, when the interstellar medium contained less metal rich gas, or is simply the remnants of an accreted/disrupted metal-poor population. In such

a chaotic model of halo formation, we would expect to see no trends of rotation or abundance with increasing Z height and a thick disk which is kinematicly discrete from the halo.

(iii) An Even Mixture of (i) & (ii)

Implicit in the ELS/SZ hybrid model is the assumption that the accreted populations amount to very weak "noise" in the very strong "signal" of contraction. If in reality, both the ELS and SZ models have contributed equally to the stellar components of the old halo and thick disk, then the problem becomes quite formidable. The contracted component of the hybrid model becomes littered with a large stellar component from disrupted satellites still possessing the unique kinematic signature of their parent system. The portion of the thick disk which formed as a part of the continuous collapse would also be contaminated by the dynamically heated component which could possibly erase any kinematic or metallic trends that were previously present, and also add confusion to the question of whether the halo and thick disk are continuous or discrete. As mentioned earlier, the evidence for recent accretion events is strong. If these events, however, amount to only a small fraction of the total stellar population of the halo/thick disk, then the signatures of an ELS collapse should still be present above the accreted noise. Likewise, if moving groups or streams dominate the stellar component then they too should be recognizable against the flat continuum signature of a weaker contracted component.

1.5 Previous Surveys

As can be surmised from the previous section, a great many surveys of the stellar components in the thick disk and halo have been carried out in the past. The shortcomings of each type of survey has left many questions concerning Galactic halo formation.

(i) The Globular Star Clusters

The globular clusters are a global sample of halo objects which suffer little from observational incompleteness. The main shortcoming of the globular clusters as halo tracers is their relatively small number. Since the vast majority of globulars lie at large distances from the sun, very few have full space motion solutions. Therefore, kinematic analysis of the system relies on statistical analysis of the radial (or line-of-sight) velocities. As with any statistical analysis, meaningful results depend on having a large number of objects. This necessarily prohibits the subdivision of the globular system to probe small scale variations in the kinematics.

A secondary concern is whether the globular clusters can be used to represent the characteristics of the halo field population. Approximately 1% of the halo stellar component is in the form of globular clusters. There is strong evidence that the metallicity distribution function for the globulars and fields stars is quite different. There is also mounting evidence that many elemental ratios in globular cluster stars differ from those in the field. These lines of evidence suggest that the formation histories of the globular clusters may be different than the field stars and brings into question whether the clusters and field form a single population.

(ii) The Halo field Stars

The primary difficulty in studying the halo field stars is finding such stars amidst the overwhelming number of Pop I stars associated with the thin disk of the Galaxy. Magnitude-limited surveys typically explore a very small region of the sky, observing all stars that fall within the given solid angle. This type of survey is unbiased and complete to within each spectral type's limiting magnitude. Proper motions and/or radial velocities are then found for all stars in the sample. This method is potentially superior to all others in constraining the kinematic properties of the

field population. The observational requirements, however, are quite formidable. The number of stars, even in a small search area, is very large, and the majority are associated with the Pop. I component. To make photometric and spectroscopic observations deep into the halo component requires an enormous amount of time on a large telescope. Such surveys are also typically constrained to the galactic polar regions, since at lower galactic latitudes the disk star contamination greatly increases. Because of these difficulties, magnitude-limited surveys give kinematic results for only the halo population near the solar circle.

Because of the disk star contamination, halo surveys are usually carried out on stars that have a high potential for being members of the Galactic halo. Halo candidates are culled from the overall sample by identifying some halo characteristic which is presented by the given star. One such characteristic is a high proper motion, which is determined from photographic plates taken at different epochs. (It should be noted that halo stars typically have small Galactic space motions, but large motions when observed at the Local Standard of Rest, which itself is moving at 220 km/sec about the galactic center.) The use of proper motions in conjunction with line-of-sight velocities, computed from spectral observations, allow the full space motions for the sample to be found. This removes the ambiguity inherent in samples (such as the globular clusters) that have only radial velocities determined. Samples of halo stars that are found by this method, however, suffer from primarily two shortcomings. First, the sample is kinematically biased against finding halo stars that have small proper motions. This bias is particularly problematic when the kinematics of the sample is what is being explored. It is especially difficult to clearly characterize the kinematic properties of the thick disk and halo populations since some percentage of the lower proper motion stars are missing from the sample.

The second major problem arises from the local nature of the sample. For accurate proper motions to be determined at all, it is necessary that the stars not be too distant. In general, proper motion samples extend to only several hundred parsecs from the sun. This not only means that changes in the nature of the halo outside of this range are not directly detected, but also that contamination from the thick-disk (especially the metal-poor tail) is considerable.

Through the analysis of low-dispersion, objective-prism spectroscopy, stars of low metal abundance (which are not typically found in the thin disk population) can be identified. Such a sample has the advantage of not being kinematically biased, but does deselect halo population stars which are metal rich. Follow-up spectroscopic observations at higher resolution allow the determination of radial velocities. By selecting stars that are intrinsically luminous, such as giants, RR Lyrae variables, or horizontal branch stars, it is possible to study in more detail the Galactic kinematic properties beyond the immediate solar neighborhood. The disadvantage of such a survey has historically been the lack of proper motions at the distance of the luminous stars. This means, as with the globular clusters, the kinematic analysis must be statistical, using only the radial velocities. Meaningful solutions, then, can only be determined from a large sample of stars. In the past such surveys have concentrated on a particular Galactic direction. The directions are typically chosen so that the stellar radial velocities and velocity dispersions sample mainly a given component of the Galactic coordinate system. Such surveys have the advantage of being relatively complete but the disadvantage of being unable to give a simultaneous global solution for the systemic rotation and velocity ellipsoid.

1.6 The Field Horizontal Branch and Main Sequence A-type Stars

The ongoing HK interference-filter/objective-prism surveys of Beers, Preston,

and Shectman (1985,1988) in the South Galactic Hemisphere (SGH) and Beers, Wilhelm, Doinidis, and Mattson (1995) in the North Galactic Hemisphere (NGH) have been very successful in identifying low abundance stars in the thick disk and halo of the Galaxy. The primary purpose of these surveys is to use the low resolution prism plate spectra to identify extremely metal poor candidates by virtue of their weak CaII K line. The majority of these candidates are either main sequence turn-off stars or giants. Since the initiation of the survey the number of stars with abundance below -3.0 has increased by a factor of ten. The HK survey has also been very successful in identifying hot stars in the halo of the galaxy, by virtue of their weak or non-existent CaII K lines but broad H ϵ (indicating a "hot" star) features. The vast majority of these stars ($\sim$ 80%) are classified as field horizontal branch or main sequence A-type stars (FHB/A). The rest are generally hotter stars, such as white dwarfs or sub-dwarf O and B stars. To date, the FHB/A candidates number 4400 in the SGH and 4200 in the NGH, with an estimated total of 12,000 candidates expected by the survey's completion in the next year.

This dissertation work is a part of a continuing program to study the kinematic properties of the FHB and A-type stars in the halo and thick disk of the Galaxy. A follow-up observing program has been underway for several years now to acquire broadband UBV photometric and medium resolution, low-signal-to-noise (S/N) spectroscopic observations. At present the total number of FHB/A candidates with complete follow-up information is 1213. Figure 1.4 is a plot of the Galactic longitude, l, and Galactic latitude, b, for all FHB/A star candidates with complete follow-up observations. This includes fields in all three cardinal directions, (Galactic center, rotation and anti-rotation directions, and north and south polar cap regions) as well as, many directions in between. Unlike earlier spectroscopic

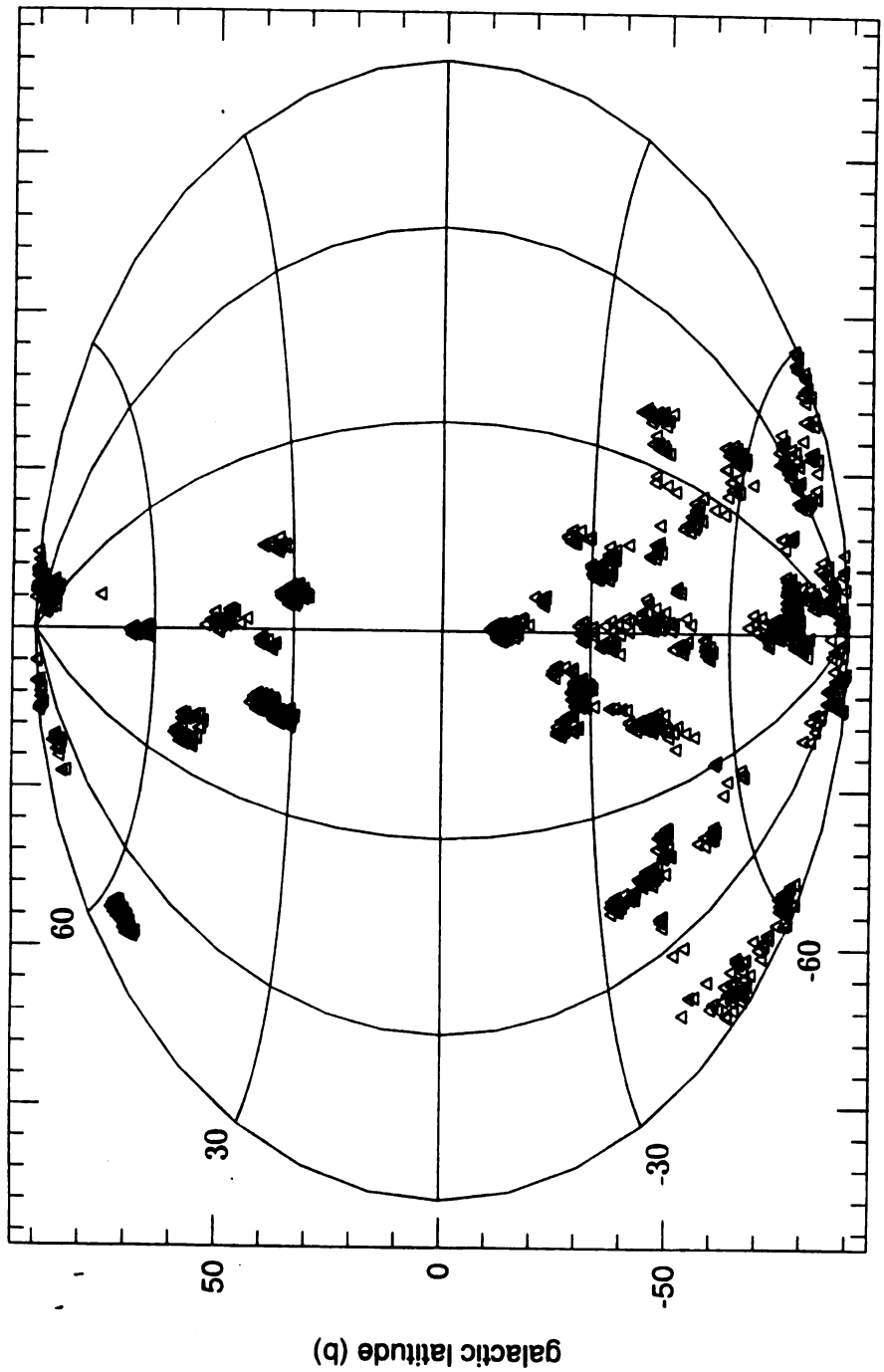

Fig 1.4: A plot of the distribution of galactic coordinates for the entire program FHB/A sample.

surveys that have concentrated on a single cardinal direction, this sample is large enough in number and sky coverage to allow good statistical solutions for both the systemic rotational velocity and the velocity ellipsoid.

1.7 FHB Stars as Kinematic Tracers

Horizontal branch stars are evolved stars which have exhausted their core hydrogen supply, traversed up the giant branch and finally settled onto a "second" main sequence were core helium is converted to carbon and oxygen and the overlying shell of hydrogen is converted to helium. The higher energy output associated with this phase results in relatively high temperatures and a somewhat larger radial extent then main sequence stars of similar spectral type. The typically quoted mass for the horizontal branch stars is $\sim 0.6\ M_{\odot}$, which, combined with a large radius, yields surface gravities values that are ~ 10 times less than found in main sequence stars.

Figure 1.5 is a plot of a color-magnitude diagram for the globular cluster M 3, with the horizontal branch (HB) stars labeled. These stars are usually identified in accord with their position on the HB, where blue HB are those stars hotter than the instability strip, red HB are cooler then the instability strip and the RR Lyrae variables found within the instability strip. The majority of the program FHB stars lie in the color range of $0.0 < (B - V) < 0.4$, which associates them with the blue HB and bluer edge of the instability strip.

As with all kinematic population tracers, the FHB stars have both favorable and unfavorable characteristics, which must be weighed in determining their value to this aspect of Galactic research. We will begin with a discussion of the positive aspects.

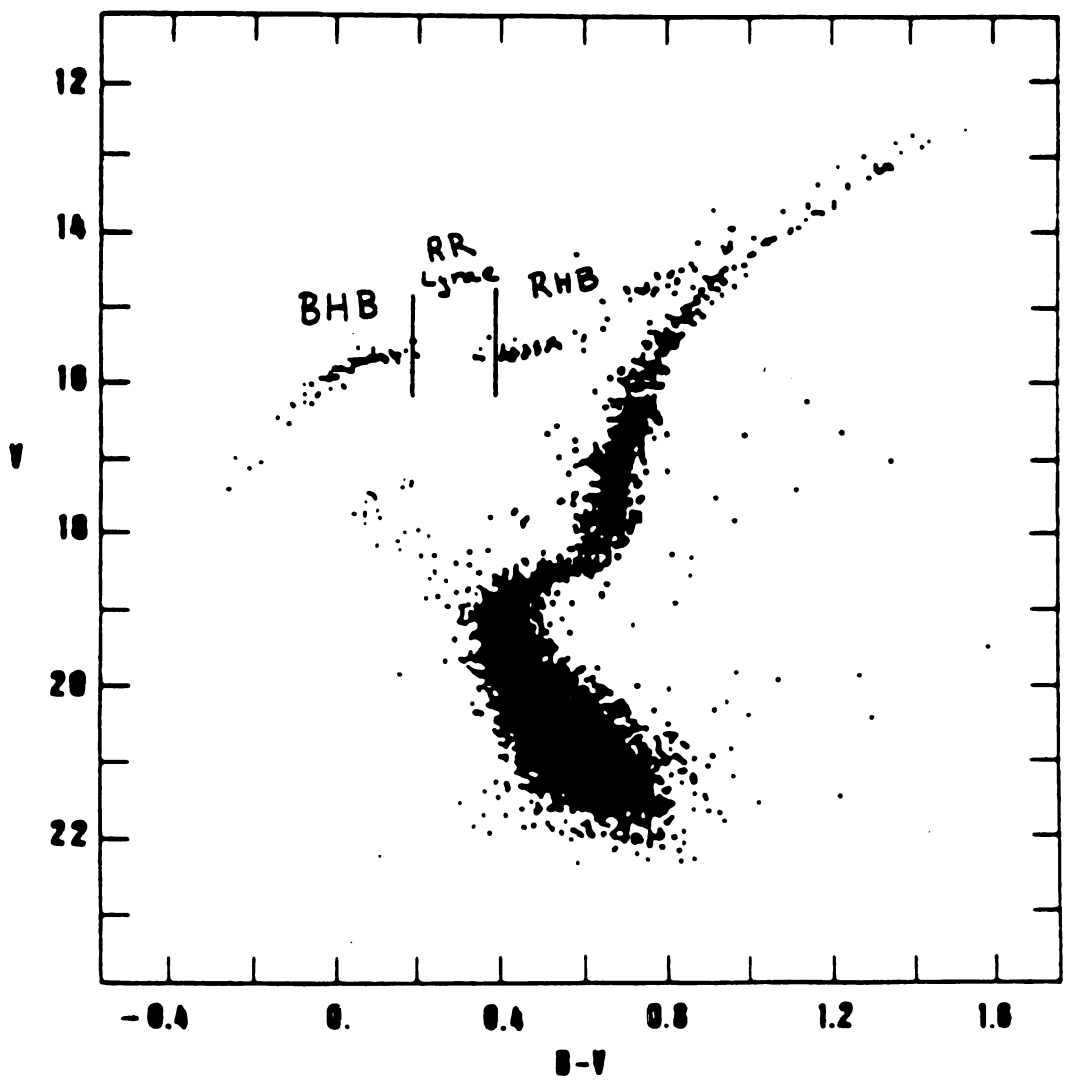

Fig 1.5: Color-magnitude diagram of the globular cluster M 3

P1) Ease of Identification – On an objective prism plate the FHB/A star candidates are easy to identify, owing to the very broad nature of the hydrogen Balmer lines, which persists from early F-type to late B-type stars. Actually separating the FHB and main sequence A stars is not easy, as discussed in C1.

P2) Intrinsic Luminosity – The horizontal branch stars are intrinsically bright stars. Their absolute magnitude exceeds that of the main sequence turn-off stars by anywhere from 2 to 3 magnitudes. This amounts to an increase of a factor of 5 to 7.5 in distance. Such an increase allows the probing of the more distant halo, free from thick-disk or contracted-halo contamination. It also allows for a more global examination of such characteristics as abundance gradients and kinematical differences with respect to position in the Galaxy.

P3) Nearly Constant Absolute Magnitude – Horizontal branch stars get their name from their nearly constant absolute magnitude across a large range of color (or temperature). The flatness of this relation means errors in the photometric colors translate into small errors in the distance determination. This is unlike the strong dependence of absolute magnitude on color, seen in both the main sequence and giant branch stars, where even small errors in color can translate into large errors in estimated distance. This feature of the horizontal branch stars will become increasingly more important as proper motion surveys, of which the largest source of uncertainty is the distance, encompass more and more FHB stars.

P4) Relatively Large Numbers – The RR Lyrae variable stars have been used very effectively in the past as a tracer population of the Galactic halo. This is primarily due to the fact that variability allows for unambiguous identification, rendering a pure sample. Because stars pass rapidly through the instability strip, however, the actual number of RR Lyrae variables is significantly smaller than the

rest of the horizontal branch stars. Preston, Beers, and Shectman (1991) find the space density of blue horizontal branch stars in the solar neighborhood to exceed the number of RR-Lyrae variables by a factor of 6. This means the FHB stars offer a much larger sample with which to carry out a kinematic study.

P5) HB Morphology as an Age Indicator – The position of a star on the horizontal branch is a complicated function of several parameters. Generally accepted as the dominating parameter (1st parameter) is a star's metal abundance, which causes a shift to bluer colors as a function of decreasing [Fe/H]. The currently recognized 2nd parameter is age, which tends to shift even metal-poor stars back toward redder colors. A shift toward redder colors as a function of galactic distance was identified in the FHB sample of Preston, Beers, and Shectman (1991). This shift was attributed to a decrease in age as galactocentric distance increased, suggesting the outer portions of the galaxy are younger then the inner regions. The ability to carry out such a differential age analysis in the field shows that the FHB stars are potentially powerful diagnostic tools of Galactic formation.

C1) Distinguishing the FHB and Main Sequence Stars – A-type stars are easily identified by their broad hydrogen balmer line features, however, both the FHB stars and main sequence A-type stars exhibit this characteristic. Intrinsic differences in stellar surface gravity can be used as a separation diagnostic for stars later then spectral type B8. This technique depends on careful calibration of the observables to the key stellar physical parameters, Teff, log g, and [Fe/H], making it a nontrivial task to compile a pure FHB sample.

C2) Difficulty in Assigning [Fe/H] – The blue FHB stars are both metal-deficient and hot. Because of this, the metallic features are very weak and abundance measurements at modest resolution must be carried out primarily using the CaII K

line. The strength of the CaII K line can be affected by contamination from the interstellar CaII K line and also from stellar diffusion mechanisms which act in this temperature range. Therefore, getting precise abundance measurements is difficult and can only be achieved through careful analysis of the CaII K line, coupled with a secondary metallic abundance indicator.

C3) HB morphology - The interesting aspects of HB morphology which were listed in P5 can also add confusion when interpreting results. Since the color of a FHB star depends on abundance, and the absolute magnitude for stars blueward of (B-V) = 0.2 depends on color, a survey's magnitude limit can potentially bias the investigation of abundance trends with distance. Similarly, great care must be taken when investigating color shifts (age differences) as a function of distance, since the magnitude limit will serve to remove bluer stars in a similar fashion as the 2nd parameter effect.

1.8 The Thesis Project

This thesis project has been undertaken with two primary goals in mind. The first is to develop a calibration technique that will improve our ability to assign class identifications of either FHB or main sequence A-type to the mixture of FHB/A candidates. This is crucial to the kinematic analysis because a large percentage of class misidentifications will result in a mixture of populations thus causing erroneous kinematic results. As part of the new calibration procedure we also hope to improve the precision of the metallicity determinations which are important to the understanding of variations in kinematic characteristics.

The second goal is to make use of the FHB intrinsic luminosity and large numbers to investigate the kinematics of the inner and outer halo and to search for evidence of a metal-weak component of the thick disk (MWTD). This is expected

to yield new and interesting results because the FHB stars lie beyond the immediate solar neighborhood, breaking the boundary within which most kinematic surveys are confined. In conjunction with the FHB analysis, the kinematics of the metal-poor main sequence A-stars will be examined to see if their unique kinematic signature remains when the sample size is increased. Both the FHB and A-star kinematic analysis is expected to be able to address the question of satellite accretion in the Galactic halo.

This thesis can be separated into several phases of research, each of which are essential to the understanding of the kinematics of the FHB and main sequence A-type stars. The first phase deals with the follow-up, photometric and spectroscopic observations of the candidate FHB/A stars. The collaborative observing effort by Dr. T. Beers, Dr. J. Pier, Dr. J. Sommer-Larson, Dr. C. Flynn, Dr. A. Layden, Dr. G. Preston, Dr. S. Shectman and myself have yielded the 1213 FHB/A candidate with complete follow-up observations that make up the program sample for this thesis. In the past 3 years my efforts to the follow-up program have included a total of 8 observing runs of which 5 were spectroscopic and 3 photometric. I have also been solely responsible for the spectroscopic data reductions of the program stars.

The second phase is to secure a "pure" sample of FHB and main sequence A-type stars. This is achieved through the use of a new spectral calibration that allows the FHB and A-type stars to be separated by virtue of their inherent differences in surface gravity. Also, the new calibration allows more precise metal abundance determinations than were possible in the past.

The third phase is to characterize the results for the program stars in an attempt to understand the physical parameter uncertainties, the amount of class misidentification, and metal abundance trends as a function of Galactic position.

Finally, a statistical kinematic analysis is carried out on both the FHB and main sequence A-stars, making use of the known quantities of star position and line-of-sight velocity. This analysis yields important kinematic quantities such as the systemic rotational velocity and velocity dispersion.

Each research phase is presented by chapter. Chapter 2 begins with a discussion of the follow-up observational program for the FHB/A star candidates. This is accompanied by a summary of the spectroscopic reduction techniques and finally the techniques used to determine line-of-sight velocities. Chapter 3 deals with the development of the new spectral calibration technique which is used to assign physical parameters and to separate the FHB and main sequence stars. Detailed analysis of the effects of low S/N spectroscopy on the calculated physical parameters is also discussed. Chapter 4 explores the effectiveness of the calibration technique for the program stars and concludes with a discussion of the abundance characteristics of the FHB sample. The kinematic properties of the FHB and main sequence A-stars are investigated in detail in Chapters 5 and 6, respectively. Chapter 7 begins with a summary of the results from this thesis, followed by a discussion of how these results add to our understanding of Galactic halo formation.

CHAPTER 2

PROGRAM STAR OBSERVATIONS AND REDUCTIONS

2.1 The Sample

The FHB/A star candidates with complete broadband UBV photometric and medium resolution spectroscopic observations number 1213. This sample is a subset of stars that were selected from the southern galactic candidate lists of Beers, Preston, and Shectman (1985,1988) and the northern galactic list of Beers, Wilhelm, Doinidis and Mattson (1995), and have been given the classification of either, "A" (for stars with weak CaII K lines and broad Hϵ), or "AB" (if no CaII K line is discernible). From follow-up observations of these stars we estimate that 80% are bonifide FHB/A stars. The rest are a variety of stellar types which include white dwarfs, O and B subdwarfs, and later-type stars that were misidentified. As shown in figure 1.4, the sample includes both galactic hemispheres with stars from all three cardinal directions represented.

2.2 UBV Photometric Observations

The majority of the broadband UBV photometry for the program FHB/A stars has been drawn from the published results of Preston, Shectman and Beers (1991) and Doinidis and Beers (1990). This sample has also been supplemented by further photoelectric observations of Preston (1994) and CCD observations by Layden (1995).

From standard star observations the internal errors in the photometry are esti-

mated to be $\sigma_V = \pm 0.015$, $\sigma_{(B-V)} = \pm 0.009$, and $\sigma_{(U-B)} = \pm 0.012$. Extinction and reddening corrections have been found for each field by measuring the color excess from the shift in the color-color relation of the FHB stars (Preston *et al.* (1991)) and/or adopting the E(B - V) values from the maps of Burstein and Heiles (1992). The final uncertainty in the UBV colors, due to internal errors and errors in the adopted reddening corrections, is estimated to be no greater than ± 0.03 mag.

2.3 Spectroscopic Observations

The spectroscopic observations have been made using the ESO (1.5 m), KPNO (2.1 m) and Perkins (72 inch) Telescopes.

A total of 5 observing runs were completed using the 1.5 m telescope at the European Southern Observatories between September 1992 and September 1994. The Boller and Chivens spectrograph was used in conjunction with a FA2K CCD chip. The grating used was 900 lines/mm (2nd order), resulting in a dispersion of $\sim$ 0.65 Å/pixel and spectral resolution of $\sim$ 1.8 Å. The wavelength coverage was from 3575 - 4900 Å. The integration times for program objects ranged from 3-5 minutes, for the brightest stars, up to 45 minutes for objects fainter than magnitude B = 15. Typical ESO spectra of a program FHB and a main sequence A-star are shown in figure 2.1a.

A total of 3 observing runs were completed using the 2.1 m telescope at Kitt Peak National Observatories between February 1993 and August 1993. For all runs the GoldCam spectrograph equipped with a Ford CCD chip was used. A 900 line/mm grating (in 2nd order) was also used throughout, giving a dispersion of $\sim$ 0.65 Å/pixel and resolution of $\sim$ 1.8 Å. The wavelength coverage was from 3700 - 5000 Å, allowing access to the CaII K line, Hδ, Hγ, Hβ and several higher order Balmer lines. Typical integration times were 3 - 5 minutes for the brightest stars

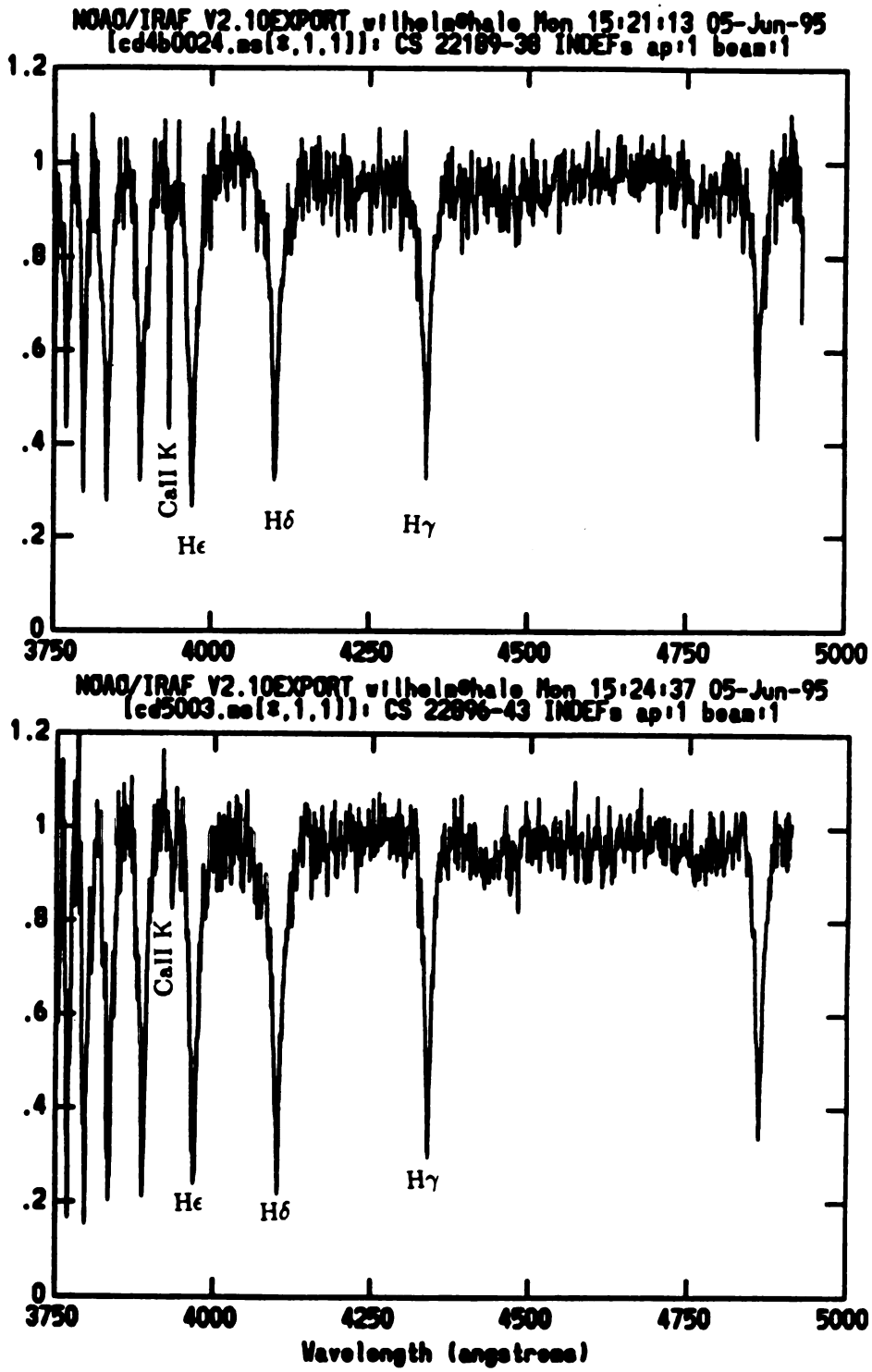

Fig 2.1a: Plots of two characteristic program spectra taken with the ESO 1.5 meter telescope. An FHB star is shown at the top and a main sequence A-type star is on the bottom.

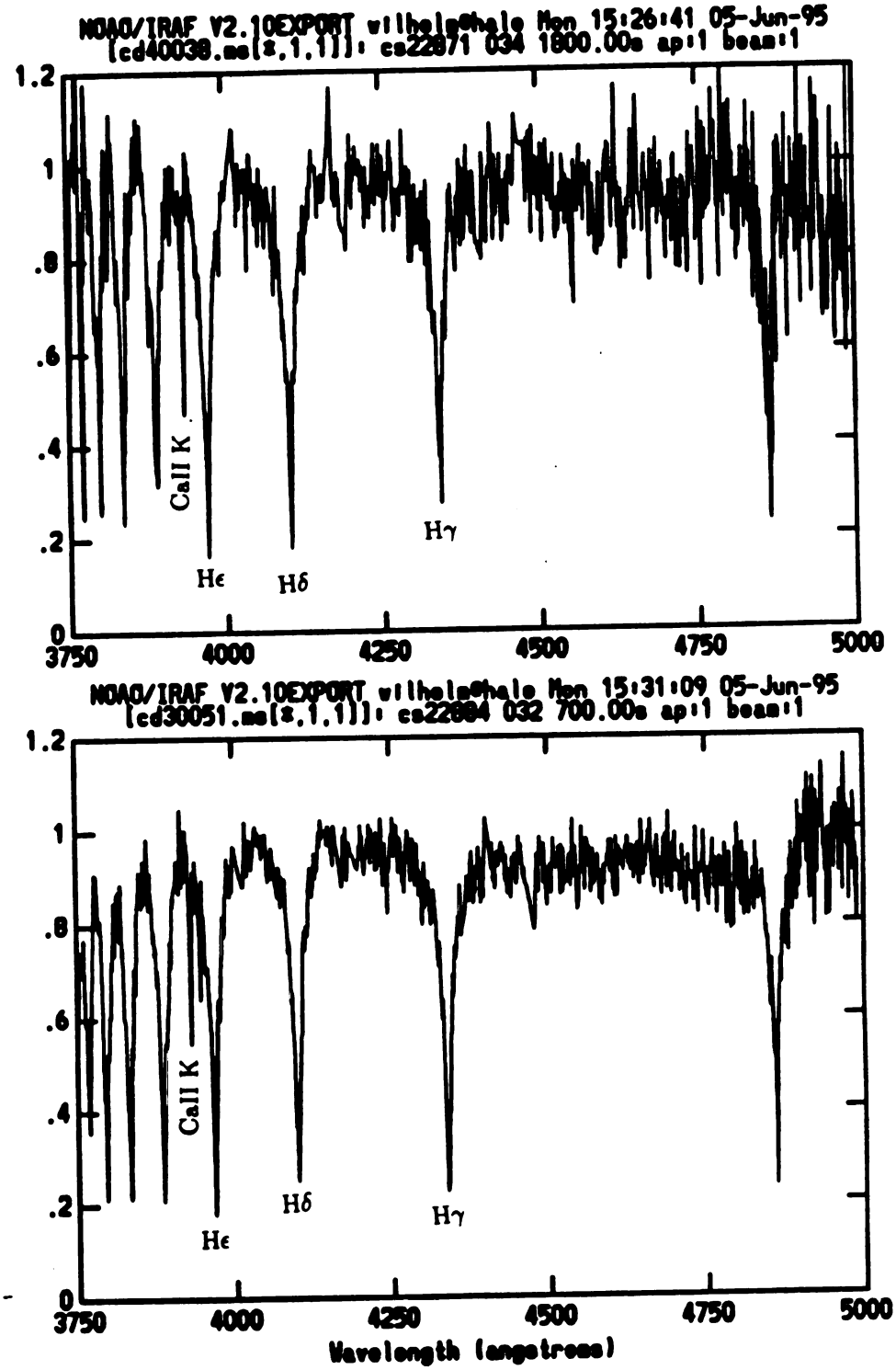

Fig 2.1b: Plots of two characteristic program spectra taken with the KPNO 2.1 meter telescope. An FHB star is shown at the top and a main sequence A-type star is on the bottom.

(B $\sim$ 12 mag) and 20 - 30 minutes for the faintest (B $\sim$ 15 mag). Typical KPNO spectra of a program FHB and a main sequence A-star are shown in figure 2.1b.

Finally, a total of 5 observing runs were completed using the 72 inch Perkins telescope at Lowell Observatories between August 1992 and July 1993. The instrument was a Boller and Chivens spectrograph equipped with a Tek 512 CCD detector. Again, a diffraction grating of 900 line/mm was used throughout, giving a dispersion of 0.97 Å/pixel and spectral resolution of $\sim$ 2.9 Å. Because of the rapid decline in the chip's quantum efficiency in the ultraviolet, the wavelength coverage was from 3970 - 4490 Å. This coverage included the Hδ and Hγ lines but did not include the CaII K line. Typical integration times ranged from 3 - 30 minutes. Typical Lowell spectra of a program FHB and a main sequence A-star are shown in figure 2.1c.

The same general observing scheme was implemented in all spectroscopic runs. Each night's observations began with a series of zero integration bias frames ($\sim$ 10) and a series of 5 minute dome flats ($\sim$ 5). The integration times for the program objects were adjusted so as to achieve a minimum of 100 ADUs at the CaII K line (3932 Å). For objects where the integration time was too short an additional spectrum was taken so that the combined spectrum met the 100 count criteria. A 90 second spectrum of the comparison arc lamp was taken for every one to two stellar spectra, depending on the integration time and amount of telescope movement between corresponding objects. This allowed flexure effects to be minimized when computing the wavelength calibration. Finally, throughout the night several radial-velocity standard stars were observed at high S/N to check for night-to-night and run-to-run zero-point shifts in the derived radial velocities.

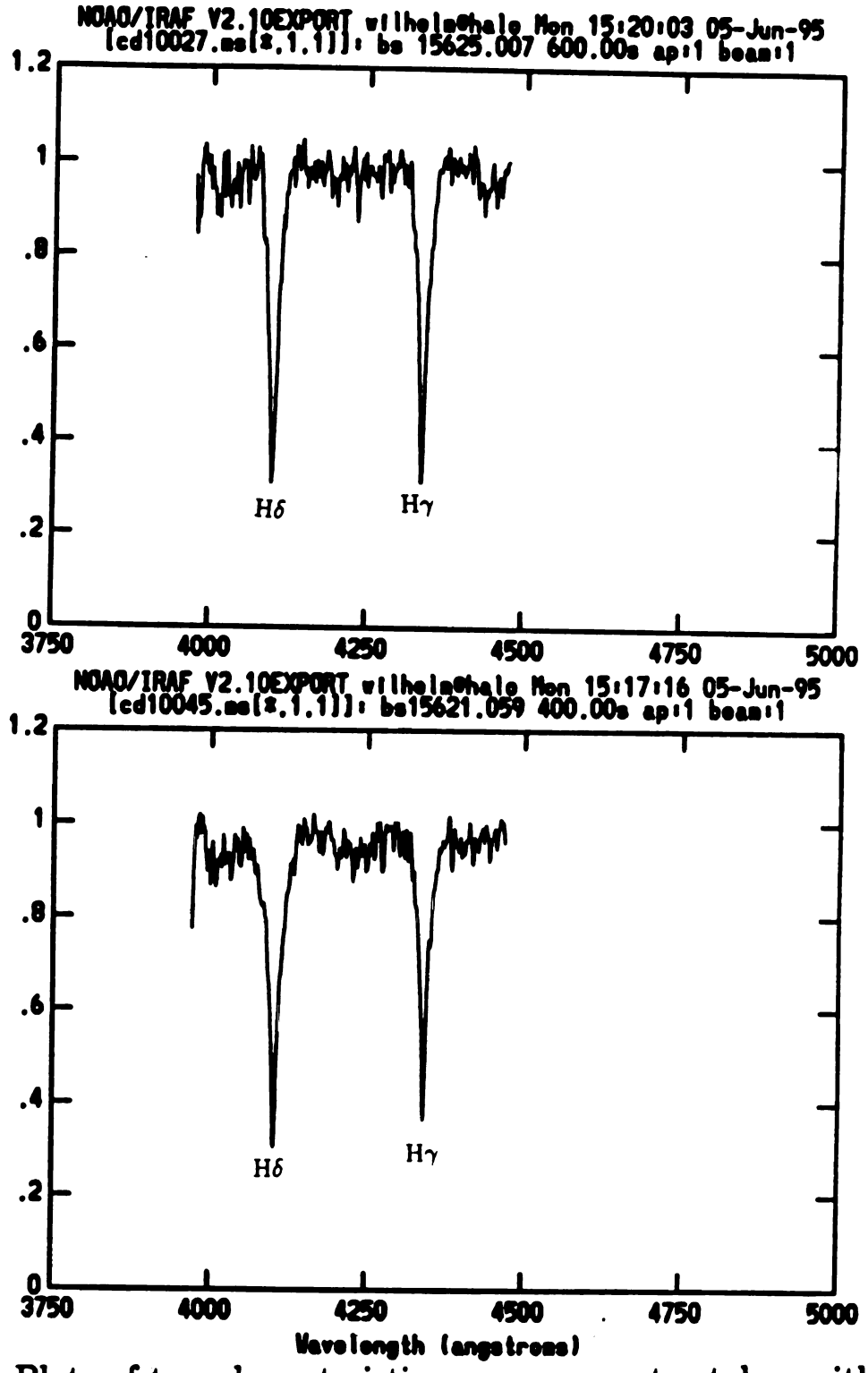

Fig 2.1c: Plots of two characteristic program spectra taken with the Lowell 1.8 meter telescope. An FHB star is shown at the top and a main sequence A-type star is on the bottom.

2.4 Spectral Extractions

All CCD spectral reductions and extractions were carried out using the Image Reduction and Analysis Facility (IRAF) on a Sun Sparc2 workstation. The procedure followed was virtually the same for the entire data set. First the bias frames for each night were combined using the task ZEROCOMBINE. This master bias frame was used to set the overall pedestal level for each night. Individual variations in this level from frame to frame are then set by the bias level of the overscan region on each image. Using the task CCDPROC, the bias level was subtracted from the dome flat images and images were trimmed to preserve only the data portion of the frame. The flats were then combined using FLATCOMBINE and normalized using the task RESPONSE. The object spectra and corresponding comparison arc spectra were then processed using CCDPROC. This amounted to trimming the image, subtracting the bias level, and flat field dividing to remove the multiplicative pixel-to-pixel gain variations on the chip.

The interactive task, APALL, was next used to extract the spectral data from each science frame. Figures 2.2 a-d show the various APALL displays for a typical program star. For all the spectral reductions an optimal extraction technique was used. Optimal extraction makes use of the known noise characteristics of the detector to set the weight of the mathematical extraction to the inverse of the statistical noise. This weighting is particularly useful when the spectrum is of low S/N, as is the case with the majority of our program objects.

When APALL is run, a graphical display indicates the position of the spectral and background windows, which can be interactively repositioned or resized in accord with each particular spectrum (Fig 2.2a-b). Initially the size of the extraction window was set to 10 pixels. To subtract the background sky level, two windows,

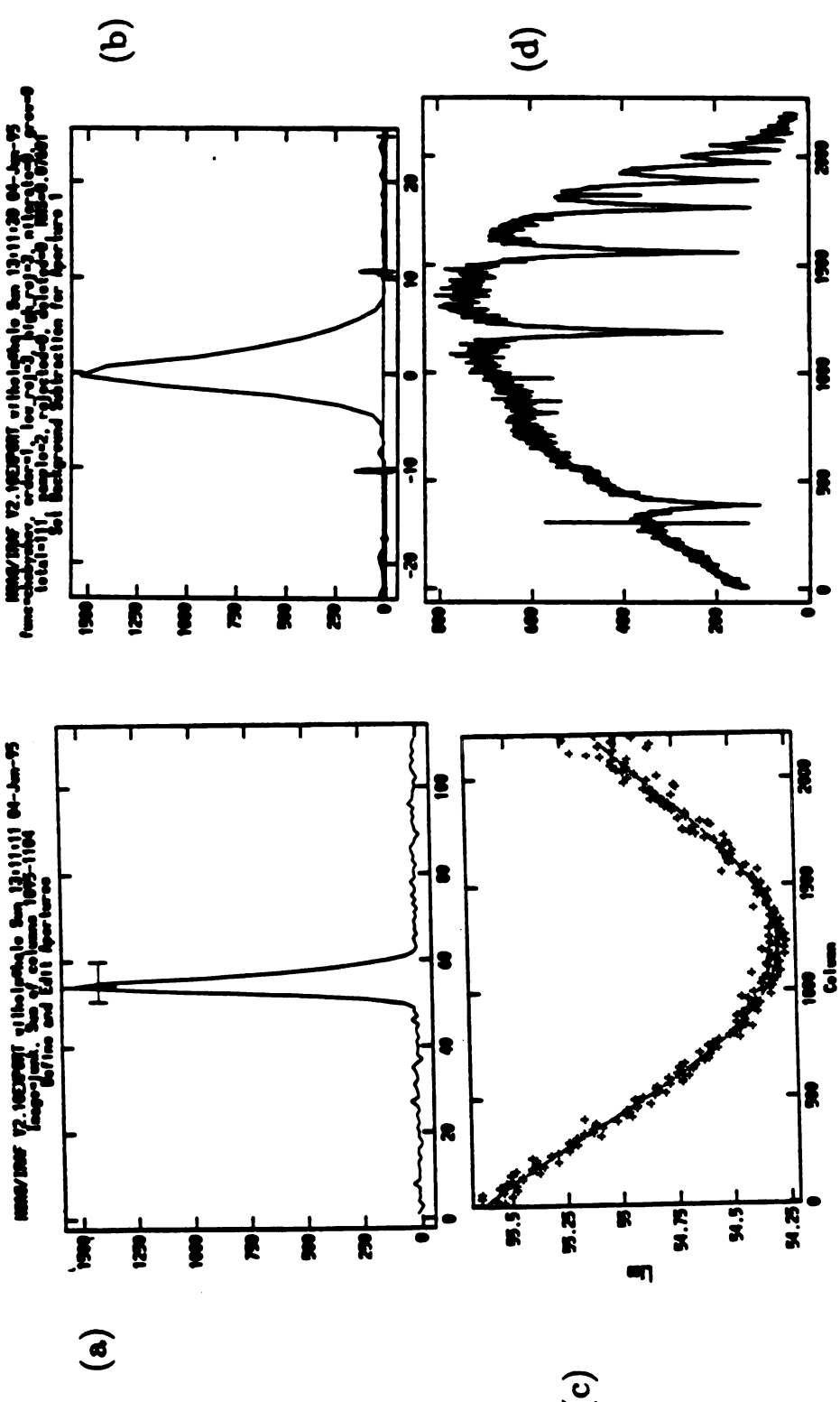

Fig 2.2: Plots of the various stages of spectral extraction. (a) shows the spectral extraction window, (b) the sky backround windows, (c) the spectral trace, (d) the final extracted spectrum.

30 pixels wide were positioned on either side of the spectral window. Upon leaving this display the interpolated value of the background level at the position of the spectrum is subtracted from the image. Next the spectral trace across the CCD is fit with a polynomial to insure the spectral window remains centered on the spectrum along the entire length of the image (Fig 2.2c). Once the trace fit is determined the spectrum is extracted by adding up the pixel values for each row within the extraction window. The result is a one-dimensional spectrum with a single intensity value for every pixel value along the dispersion direction in the image (Fig 2.2d). The corresponding comparison arc is then extracted using the identical windowing and trace parameters as were used for the object spectral extraction.

At this point the dispersion solution for the spectra were determined. To do this, the emission features in each HeNeAr comparison arc were identified and given the appropriate wavelength value using the task IDENTIFY. A starting wavelength and dispersion solution was then determined by fitting a chebyshev function to the data. The order of the function was then adjusted to remove large scale variations in the solution, and excessively deviant points were removed from the fit. In general, the final RMS scatter in the wavelength derived from the fit compared to the known line position was less than ± 0.02 Å. This scatter amounts to an uncertainty in radial velocity for the program spectra of approximately 1.5 km/sec. Finally, the task DISPCOR was run on the program spectra and using the starting wavelengths and dispersion solutions from the corresponding comparison spectra, a wavelength solution was determined for each.

As a final step in the reduction procedure, the continuum of the object spectra were normalized using the task CONTINUUM. The continuum was fit using a higher order cubic spline. The order varied between 7 and 19, depending on the stellar

spectral type. For A-type stars, the order was generally at the lower limit to avoid fitting the broad wings of the hydrogen Balmer lines.

2.5 Radial Velocity Determination

Two separate methods were carried out to determine the radial velocities for the program stars. The first is a line averaging technique (LAT) developed by Beers (Beers *et al* (1985)). The procedure identifies the minimum of the prominent absorption lines using a Gaussian-derivative convolution technique as described by Schneider and Young (1980). For the ESO and KPNO stars a velocity was determined for the Balmer lines from Hγ to H10 and the CaII K line. The blend of Hϵ/CaII H was not used since the line minimum result depends on the relative strengths of the two lines. Lines which suffered the most from low signal-to-noise or large asymmetries were removed from the initial average velocity determination and a standard deviation for the individual line velocities was computed. To further remove lines with erroneous velocity determinations, the initial standard deviation was used to trim any individual line velocity which was more than 2σ from the average. A final average velocity was then computed using the velocity determinations for the remaining lines. Typically, the average velocity was determined from 4 - 6 lines. In the case of the Lowell spectroscopy, only the Hδ and Hγ lines were used due to the smaller wavelength coverage.

Radial velocities were also calculated using the Fourier cross-correlation technique, FXCOR, in IRAF. FXCOR passes the Fourier transform of a given template spectrum through the transformed object spectrum and locates the peak in the correlation function which corresponds to the optimal overlap of the absorption features in the two spectra. The relative wavelength shift between the template and object spectra, defined by the peak, allows calculation of the object's line-of-sight velocity

(V_{los}).

Ten velocity template spectra were used for the FHB/A sample. These templates were generated from the synthetic spectra originally created for the spectral calibration of the Balmer and CaII K lines (see Chapter 3). To encompass the large changes in the Balmer and CaII K line widths, 5 temperatures (T_{eff} = 6000, 6500, 7500, 8500, and 9500), and 2 metal abundances ([Fe/H] = 0.0, -2.0) were used. Because the spectral features for the synthetic templates are centered on their laboratory wavelengths, each template has zero velocity. The object spectra were rebinned before the analysis to precisely match the 0.7 Å/pixel dispersion of the template spectra, and the starting wavelength was trimmed to correspond to the starting wavelength of the templates at 3900 Å

Before the actual correlation was carried out, the object spectra were Fourier filtered, using a Welch function, to restrict the range of frequencies. The high frequency cutoff was set to a wavenumber of 10,000 in order to remove the higher frequency variations due to noise. Generally, the low frequency cut-off is used to remove the slowly changing variations in the continuum level. For the FHB/A stars it was also important to set this parameter to remove the effects of the large Balmer line wings. If the low frequency cut-off is set too low, then the Balmer line profile completely dominates the correlation peak. If it is set too high, the Balmer lines are removed completely from the correlation and the size of the peak is determined only from the much weaker metallic lines. Through experimentation, it was found that the optimal low frequency cut-off occurred at a wavenumber of 30. This value allows the cores of the Balmer lines to be included, but prevents the full profile from dominating the signal.

Figure 2.3 is a plot of the cross-correlation peak for a typical FHB/A program

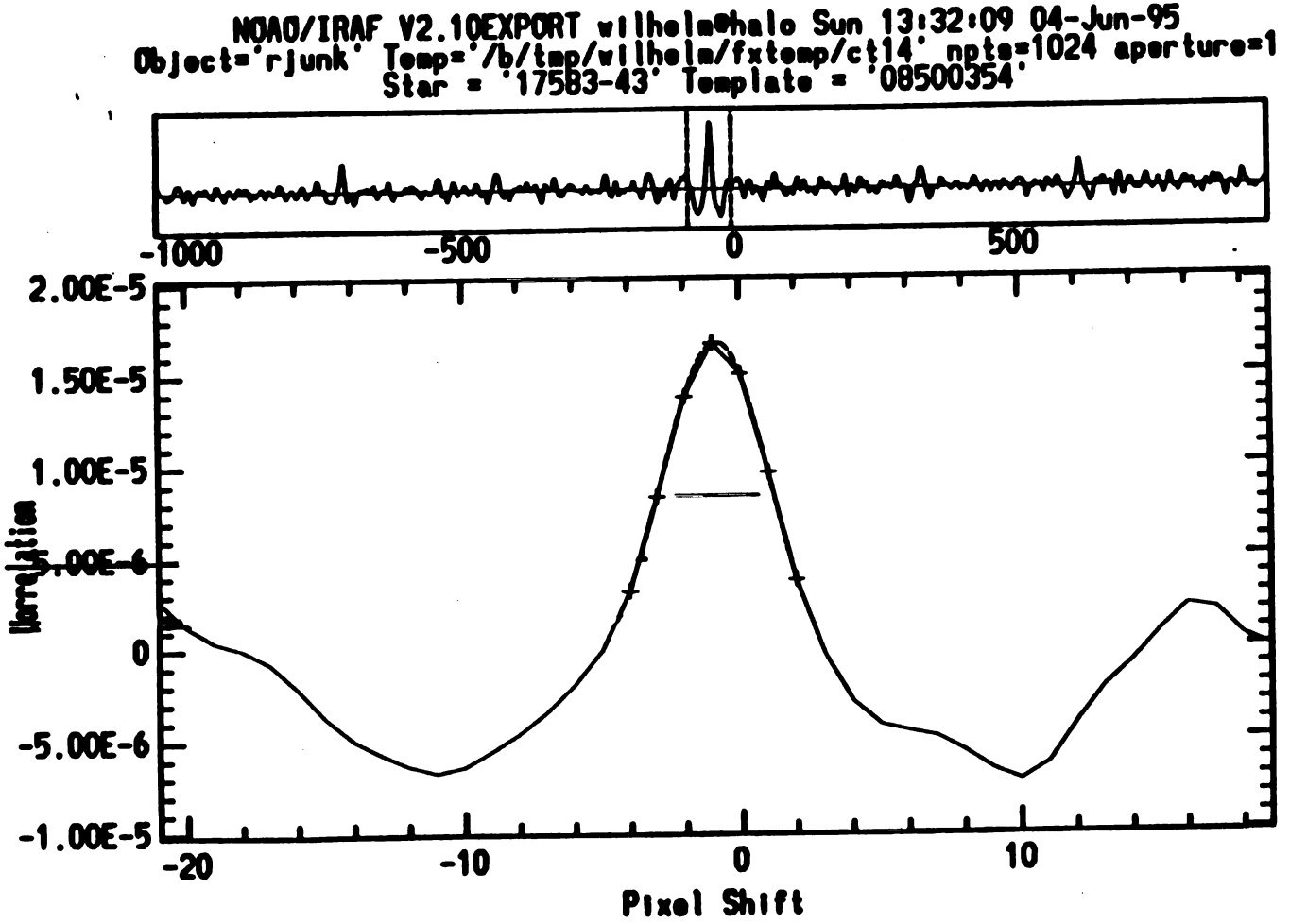

Fig 2.3: Cross-correlation peak from FXCOR.

star. A parabola is fit to the correlation function in order to precisely compute the location of the peak. The output from this procedure gives the computed velocity from the relative wavelength shift, as well as, an estimate of the uncertainty, found using the method by Tonry and Davis (1979). This uncertainty is computed by taking into account both the peak height and the antisymmetric noise. When running FXCOR on a program object, we do not attempt to preselect an appropriate template for a given star. Rather, all ten templates are used for each object spectrum and the optimal match, determined by the Tonry and Davis uncertainty, is selected as the best V_{los} for the star.

To compute a final velocity for the program stars the velocities from the LAT and from FXCOR were compared. When the velocities differed by less than $\sim$ 12 km/s, which was the case for the vast majority of the program spectra, the two values were simply averaged. If larger deviations occurred then each procedure was examined more closely to try to identify which of the two values was in error. In a few cases, the S/N was sufficiently low, and the deviations still small enough ($<$ 20 km/s) that a decision to average the values was made. For a small number of cases where more deviant values were found, the velocity was "checked by hand" to identify the best value to use.

The final velocity, thus computed, is a geocentric velocity and is a combination of the stellar V_{los} and the various peculiar motions of the earth and sun. To convert this velocity to a heliocentric V_{los}, the IRAF task, RVCORRECT was run for each of the program spectra. RVCORRECT calculates the amount of velocity correction needed to take into account the rotational velocity of the earth, its orbital velocity about the sun, the earth's velocity relative to the earth-moon epicenter and earth-sun epicenter. This calculation depends on each object's sky coordinates, the time

of observation, the date of the observation and the location of the given observatory. When this correction is applied we arrive at the final heliocentric V_{los} for the star.

Figure 2.4a is a plot of the difference between the observed and published radial velocities for all standard star taken at the three observatories. The circles, triangles and squares represent the ESO, KPNO, and Lowell standards, respectively. The total distribution is approximately centered on zero, with no strong indication of a zero-point shift between observatories. The overall the median difference value is ±6.6 km/s. Each individual observatory has a very similar scatter of 7.5, 6.5, and 6.0 km/s, for ESO, KPNO, and Lowell. This indicates the velocities in the high S/N standards have a 1σ precision of at least ±10 km/s. As a final check of the external accuracy, we examine the scatter for the frequently observed standard HD 161817 (27 observations). The median difference is ±9.1 km/s with an average difference consistent with zero-velocity shift.

Because the actual program spectra are of low S/N we would like to test the internal differences for those stars with multiple velocity measurements. Figures 2.5a-c are plots showing the correspondence between two separate measurements for each star. Figure 2.5a is a plot of all stars, with no distinction made between any of the three observatories. The scatter appears to be rather small with no extreme departures from the y = x line. We calculate the amount of scatter by finding the median difference value and multiplying it by the standard deviation correction factor, 0.8862, from Pearson and Stephens (see section 3.5.4). The estimated internal scatter for all stars with multiple measurements is $\sigma = 9.3$ km/s.

Figure 2.5b is a plot of stars only taken at KPNO and ESO. There are not enough stars with spectra taken at both observatories to make a direct comparison between KPNO and ESO velocities. Therefore, we simply plot the stars that were

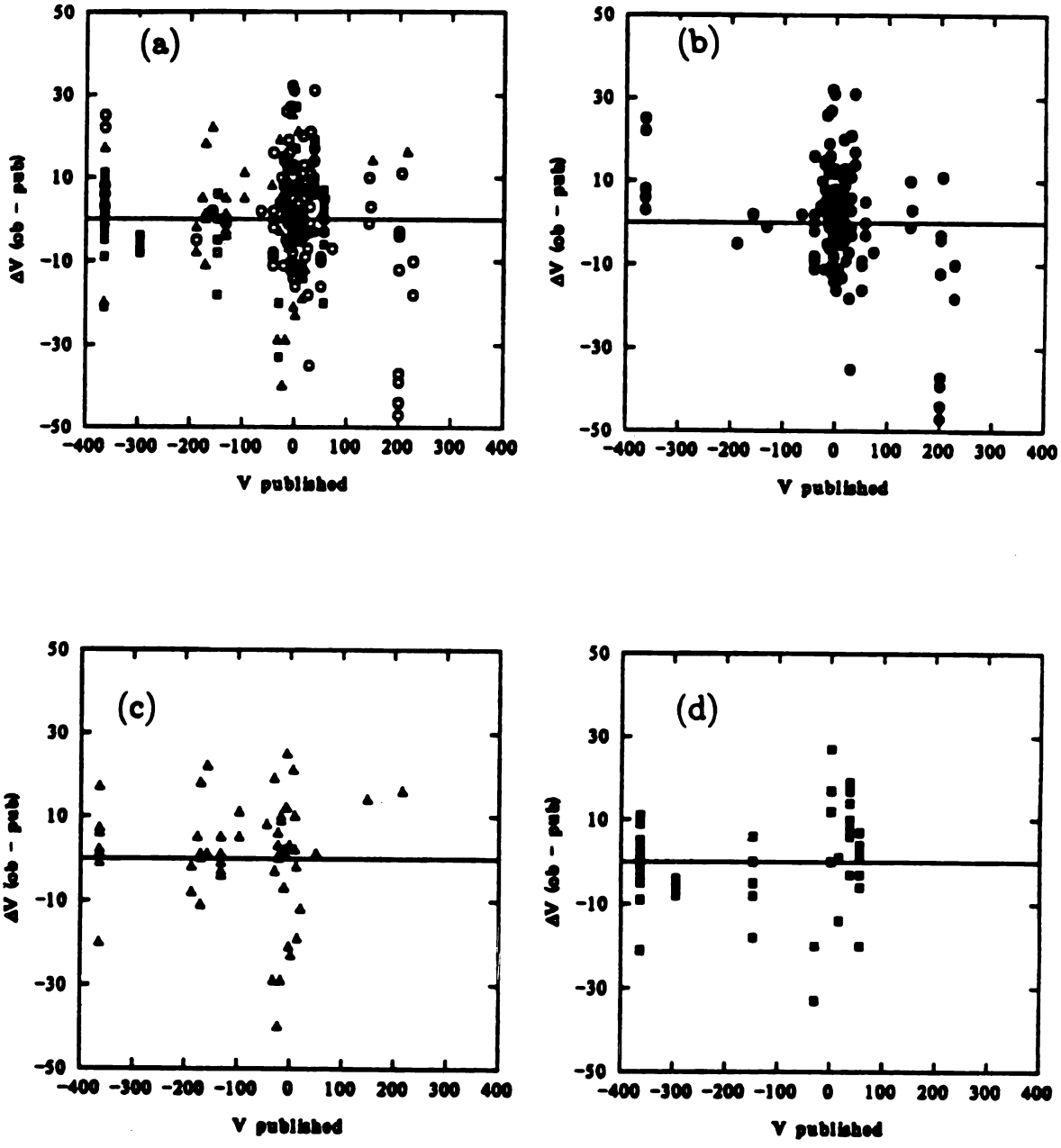

Fig 2.4: Plots the difference between the derived velocities and the published values for the standards stars. Circles, triangles and squares represent ESO, KPNO, and Lowell data, respectively.

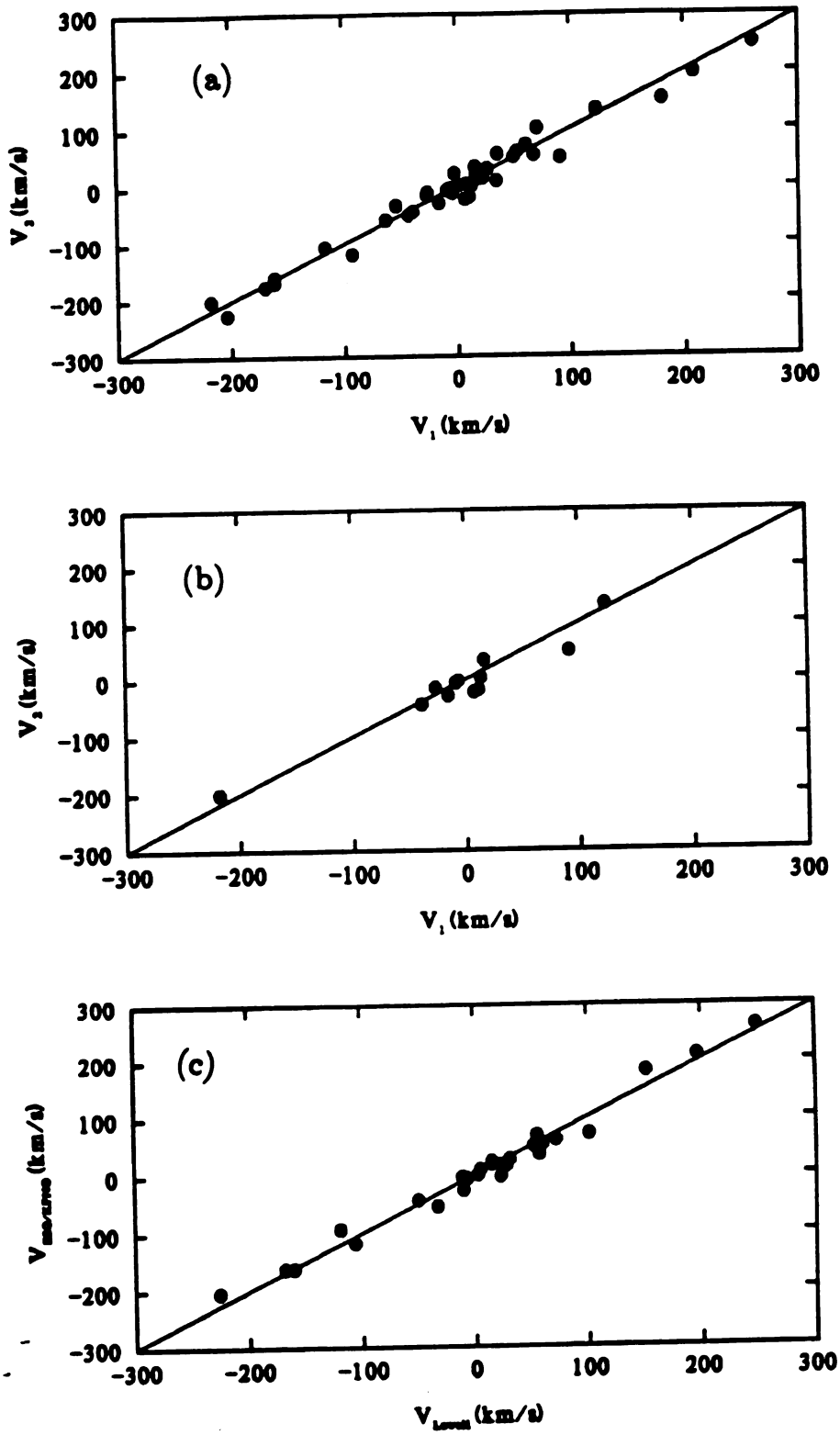

Fig 2.5 The scatter in velocities for program stars with multiple measurements. Figure (a) shows all stars, figure (b) the ESO and KPNO stars, and figure (c) the ESO/KPNO velocites compared with velocites from the Lowell stars.

taken at either and compute a scatter of σ = 10.6 km/s. Finally, Figure 2.5c is a plot of the stars observed at either KPNO or ESO as a function of the velocity computed from the Lowell data. The correlation is very good with no evidence of a systematic trend in the velocities. The average difference for all the stars is $< \Delta V >= 0.4 \pm 2.8$ km/s, with an internal scatter of $\sigma = 8.4$ km/s. We therefore conclude that there is no clear systematic errors in the velocities of the program objects and that the consistency between any two velocity measures from any of the three observatories is better than 10 km/s.

CHAPTER 3

SPECTRAL CALIBRATION

3.1 Introduction

As mentioned in the Introduction, the task of isolating a pure sample of FHB stars is formidable, since their luminosity and temperature overlap with the main sequence A stars at a spectral type of B8. If the A stars were constrained only to thin disk, Population I stars, then the isolation of a pure FHB sample could be achieved by virtue of metallicity or kinematics alone. However, the findings of Rodgers *et al.* (1981) and Lance (1988) of a metal weak ([Fe/H]~ -0.5) main-sequence A star population, along with the identification of Preston, Beers, and Shectman (1994) of a blue metal poor ([Fe/H]< -1.0) population (BMP) with main sequence surface gravities, prevents the use of metal abundance as a separation criteria. The findings of Morrison, Flynn, and Freeman (1990) and Beers and Sommer-Larson (1995) of a metal-poor tail associated with the thick disk renders a kinematic criteria equally inappropriate. This is especially true since the BMP stars exhibit kinematic properties intermediate between thick disk and halo. Although it has been shown by Peterson(1983) and Green and Morrison (1993) that the rotational diagnostic, vsin(i), is potentially an effective way to separate the FHB and main sequence populations, obtaining the required high resolution spectroscopy for a large number of faint stars is not practical. Therefore, the most effective and practically obtainable method for separating the FHB and main sequence A-type stars is by virtue of their differing surface gravities for those stars later than B8.

In the past, surveys by Pier(1983) and Flynn and Sommer-Larsen (1988) have made use of the Balmer line widths and broadband photometric colors to isolate the lower surface gravity FHB stars from their higher surface gravity counterparts. The calibration of these observables has been based on the findings of Pier, using synthetic spectra from Manduca and Bell (1978). Many other authors have used the CaII K equivalent width calibrations from Pier to assign crude stellar metallicities. These existing spectral calibrations are now over a dozen years old and are based on a crude grid spacing which corresponds to a restricted number of physical parameters. Though of obvious importance to future study of both FHB and A star populations, to date we know of no published calibration of the spectral line strengths for the complete range of T_{eff}, log g, and [Fe/H] that corresponds to the FHB/A stars.

Since our intention is to separate the FHB/A star populations by exploiting their inherent differences in surface gravity, it was necessary to construct a calibration grid for the stellar physical parameters in terms of the available observational parameters. This grid includes the UBV colors, as well as the Hδ, Hγ line widths and CaII K equivalent widths. In conjunction with the calibration grid, a technique for finding the physical parameters which best optimizes the dependencies of the observables has been developed.

In section 2 of this chapter a full grid of spectral line widths, broadband photometric colors and corresponding physical parameters is presented along with a discussion of how each observable depends on the model parameters. In section 3 a technique for separating the FHB/A stars is discussed and in section 4 the effectiveness of the technique is examined using observations of standard stars. Also indepth analysis of the Ca and Fe abundances of some of the standards is discussed along

with a technique for identifying metallic-line (Am) stars. Section 5 examines the effects that low signal-to-noise spectra (S/N) and photometric uncertainties have on the separation technique and the assignment of metal abundances.

3.2 Parameter Calibration

3.2.1 The Observables

3.2.1.1 The Balmer Lines

The Balmer line widths undergo enormous change as the stellar spectral type moves from early F to late B. Figure 3.1 is a plot of Hδ for the F0V star HD 220647, the A4V star τ^3 ERI, and the A0V star HD 105388. These changes can be understood as a combination of line broadening effects and changes in the continuous absorption opacity, each of which can dominate as the physical conditions in the atmosphere of the star change. The dominant effect to the Balmer lines is Stark broadening. As the surface temperature of a star increases many elemental species become either singly or doubly ionized. In contrast the hydrogen atoms in A-type stars are generally not ionized due to their relatively high excitation energies. Interactions between the neutral hydrogen and the neighboring ions cause sufficient perturbations in the hydrogen energy levels to broaden the energy region over which the hydrogen atom can absorb incident photons. The result is an increase in the breadth of the Balmer lines as a function of increasing temperature and series number. This trend begins to reverse for spectral types earlier than A0 due to ionization of neutral hydrogen at higher temperatures.

The second broadening effect that is of interest for early F and A-type stars is pressure broadening. For the range of spectral types of interest here, the effects of pressure on the line width change with increasing temperature. In the range from 6000 - 8000 K, H- is still a major source of continuum opacity. H- absorption is

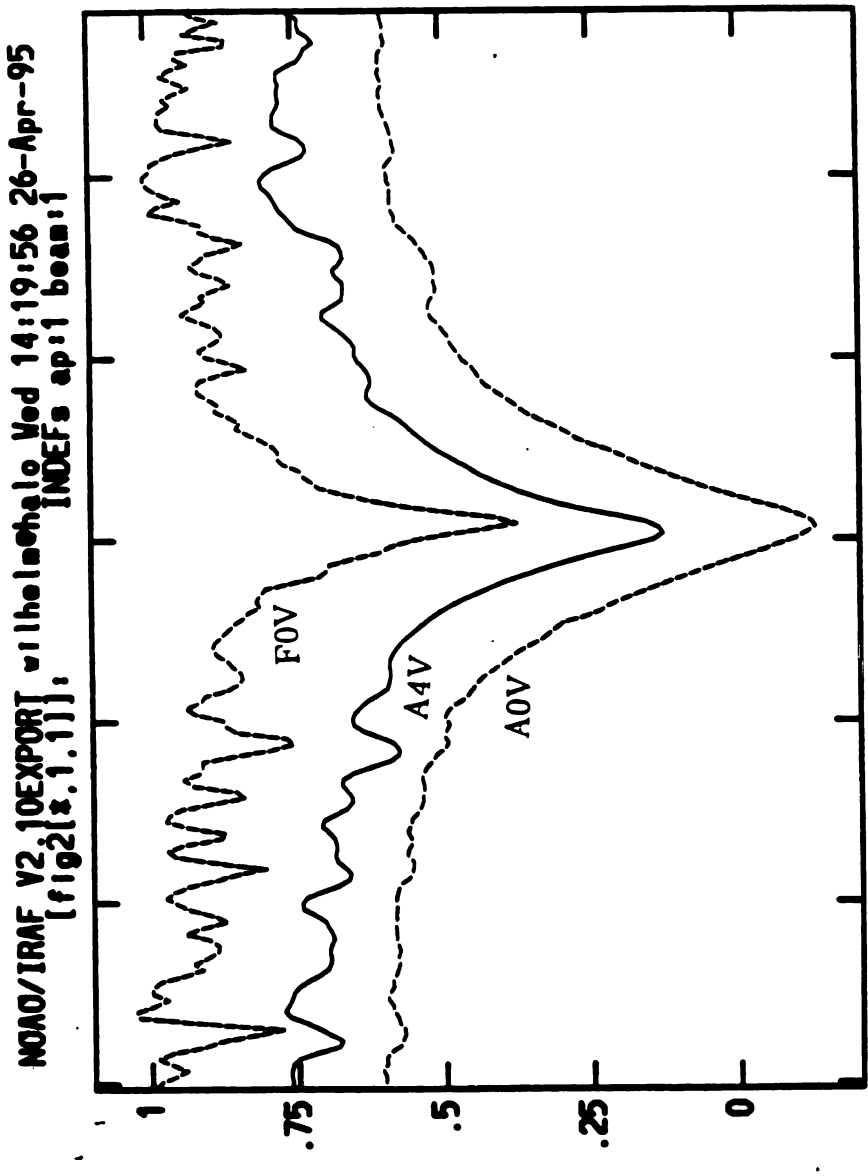

Fig 3.1: Temperature dependence of the Hδ Balmer line width

a function of pressure since a higher pressure increases the number of neighboring free electrons. Therefore, decreasing pressure causes a decrease in the continuum opacity of the H- ion and an increase in the geometric depth of the photosphere. The result is a larger number of neutral hydrogen line absorbers causing an increase in line strength with decreasing pressure. As the temperature approaches 8000K, the extent of H- ionization is such that it is no longer a prominent component of continuum opacity and neutral hydrogen becomes the dominant continuous absorber at higher temperatures. To first order, the neutral hydrogen continuum opacity does not depend on pressure since it does not have to capture an extra neighboring electron. For temperatures of approximately 8000 - 10,000K the hydrogen line widths increase with increasing pressure due to the larger number of ion collisions with the line absorbers.

3.2.1.2 (U-B) Colors

The Johnson UBV system is comprised of three broad-band filters each with a transmission band-pass of $\sim$ 900 Å. The U band is centered at 3500 Å and thus measures the strength of the Balmer discontinuity. The B band is centered at 4300 Å, and is mildly effected by the strengths of $H\beta$, $H\gamma$, $H\delta$, and $H\epsilon$ in the FHB/A stars. As mentioned above, in the temperature range of 6000-8000 K, H- is a prominent continuous absorber and thus the Balmer line strength increases as the pressure decreases. As the Balmer lines grow in strength the steepness of the Balmer discontinuity increases and the flux in the U band-pass decreases. Therefore at a given temperature, lower surface gravity (lower pressure) stars, such as FHB stars, have larger values of (U-B) than do higher gravity main sequence A stars. This effect causes (U-B) to be a strong function of pressure in this temperature range. However, unlike the Balmer lines, the (U-B) color is also a function of the

star's metallicity. Many metal lines reside in the ultraviolet and thus contribute to the decrease in flux in the U band. Because of this effect there is an inherent ambiguity in the use of (U-B) as a pressure indicator. Although the flux in the U band for a solar metallicity main sequence A star is greater than a FHB star of similar metal abundance and temperature, a metal poor FHB star can have a similar flux due to the deblanketing of the metal lines in the ultraviolet. Therefore, (U-B) can only be used as an unambiguous surface gravity indicator for the FHB/A stars if an independent measure of a given star's metallicity can be made.

For temperatures in the range of 8000-10,000 K, the steepness of the Balmer discontinuity begins to decrease for low surface gravity stars and increase for high surface gravity stars as neutral hydrogen becomes the dominant source of continuum opacity. This turn-around in the steepness of the Balmer discontinuity causes the derived pressure values from the (U-B) colors to become degenerate. Thus, the usefulness of (U-B) as a surface gravity indicator in this temperature range is limited.

3.2.1.3 The (B-V) Colors

The Johnson V filter is centered at 5500 Å. When used in conjunction with the B filter the corresponding (B-V) color is a strong function of temperature for most of the temperature range of the FHB/A stars. This is due simply to the difference in the continuum level in the two band-passes. What makes (B-V) a better indicator of temperature then the (U-B) color is its relatively small dependence on surface gravity and metallicity. Because of the inclusion of Hβ, Hγ, Hδ and Hϵ in the B band, there is a mild dependency on surface gravity but much smaller than that of the Balmer discontinuity in the U band. Also, there is some sensitivity to metal abundance, again due to metal lines in the B band, but the relatively few lines

compared to the ultraviolet cause this effect to be small, especially for stars with [Fe/H]< -0.5.

3.2.1.4 The CaII K Line

In general the equivalent width of the CaII K line is dependent on temperature and the number of absorbers (abundance), while the line wings can also depend on electron and gas pressure (log g). The width of the CaII K line increases as a function of temperature, reaches a peak, and then decreases in strength at hotter temperatures. This effect is due to the increase in the number of excitation photons with temperature, up to the peak spectral line strength. At higher temperatures, ionization results in a decrease in line width. Because of the enormous range in CaII K line strengths for our program stars, the effects of changing the number of line absorbers varies. For the hotter, metal-poor stars, the amount of change in CaII equivalent width is set by the line depth, making the width linearly proportional of the number of absorbers. However, for the cooler, solar abundance stars, where the CaII K line saturates, the change in equivalent width is governed by the line wings, resulting in a line width which is proportional to the square root of the number of absorbers.

3.2.2 The Calibration Grid

We have computed a total of 833 synthetic spectra using the Atlas9 Kurucz model atmospheres (Kurucz 1992) and the spectral-synthesis routine SPECTRUM (written by R. Gray). SPECTRUM uses the fully blanketed Kurucz model atmospheres as input, utilizing the mass depth points and run of temperature and pressure for all 64 levels. SPECTRUM then iteratively solves 7 nonlinear differential equations to find the electron number density and number densities of H, He, C, N, O, their ions and relevant diatomic molecules. Next, reference opacities and

optical depths are calculated at each level in the atmosphere. Finally, using each elemental abundance, SPECTRUM computes the opacity and optical depth of the line and continuum to find the normalized residual intensity at each spectral point.

The parameter space coverage of the 833 synthetic spectra is from 6000 $\leq$ T_{eff} $\leq$ 10000 K, in increments of 250 K; 2.0 $\leq$log g$\leq$ 5.0 in increments of 0.5; and 0.0 $\geq$[Fe/H]$\geq$ -3.0, in increments of 0.5 dex. The spectra were smoothed using a Gaussian filter to a resolution of approximately 2 Å. The $H\delta$ and $H\gamma$ lines were fit with a Voigt profile and both the equivalent width and $D_{0.2}$ width (width at 20% of the local continuum level) were calculated. The local continuum level was found by calculating the average continuum in two windows of width 10 Å, located at the extremes of the Balmer line regions. The effects of other absorption features in the wings were removed by replacing the largest deviant values with the average continuum value. This procedure was then iterated until changes in the continuum level were less then 5%. The local continuum was then defined as the height the Voigt profile reached at a distance of 50 Å from the absorption line center. This distance is beyond the wings of all but the very broadest Balmer lines. The CaII K line was also fit with a Voigt profile and the equivalent width (W_k) was calculated. Because of the large variation of CaII K line widths over the entire parameter space, and close proximity of the CaII H/Hϵ line, a windowing technique was used which allowed the Voigt profile to extend to a width of 10 Å, 20 Å, or 28 Å, depending on the size of the CaII K line.

A compiled list for the line widths and UBV colors for all combinations of the physical parameters can be found in Table A.1 in the appendix. Columns 1 - 3 are the values of T_{eff}, log g, and [Fe/H] from each of the input Kurucz model atmospheres. Columns 4 - 5 are the calculated (B-V) and (U-B) values from the

Kurucz color calibrations. Column 6 is the equivalent width of the CaII K line and columns 7 - 10 are the equivalent widths and $D_{0.2}$ widths for $H\delta$ and $H\gamma$, respectively.

Since our goal is to use the CaII K line strength as an indicator of each star's overall metal abundance, [Fe/H], the calcium abundance was adjusted in the line list before the synthetic spectra were computed. The amount of this adjustment is in keeping with the results of Wheeler *et al.* (1989), which show that the α elements in later type stars are overabundant relative to iron as a function of decreasing [Fe/H]. We can express this relation as:

$$[\mathrm{Ca/Fe}] = -0.012 - 0.332[\mathrm{Fe/H}] - 0.060[\mathrm{Fe/H}]^2 \qquad (3-1)$$

where [Ca/Fe] is the amount of correction to the [Ca/H] abundance used in the computation of the synthetic spectra. It is debatable whether the trend found by Wheeler *et al.* can be applied to stars as early as A-type. Recent abundance results published by Adelman and Philip (1994) for eight FHB stars show no such trend in their [Ca/Fe] ratios. In fact, two stars show Ca to be underabundant by as much as 1.0 dex. This may be accredited to diffusion processes acting in the stellar envelopes at the blue end of the horizontal branch (Michaud *et al.* 1983). Also, from observations of old open clusters, Thogersen *et al.* (1993) have argued that Mg abundance is a function of cluster age and not iron abundance. Further discussion concerning trends in [Ca/Fe] for our calibration can be found in section 3.4.3 and Chapter 4. If desired the [Ca/Fe] relation can be used to recapture the original [Ca/H] abundance once the metal abundance for a star is found.

3.2.3 Observable Dependencies

To determine the physical parameters for an FHB or A-type star it is important to understand how the calibrated observables depend on each of these parameters. This information allows the optimal observable to be chosen for a given parameter, as well as indicating the range over which the observable remains an effective indicator. Figure 3.2a is a 3-dimensional plot of (B-V) as a function of both T_{eff} and log g at [Fe/H] = 0.0, while figure 3.3a is the same plot collapsed into 2-dimensions to enhance the log g dependency. Both plots clearly shows (B-V) to be a strong function of T_{eff} over the entire range of the grid. The log g dependency is less noticeable but can be seen as a larger curvature in the plot at log g values of 2.0 and less so at 5.0. Similar analysis indicates that (B-V) is only mildly dependent on metal abundance at the lowest temperatures and virtually insensitive at the highest temperatures.

Figures 3.2b-c and 3.3b-c show the values of (U-B) and $D_{0.2}$ from the $H\delta$ line, as a function of T_{eff} and log g, respectively. Of primary interest is how well each of these observables function as a surface gravity indicator. Figure 3.2b shows that there is a substantial difference in the (U-B) color between the values of log g = 2.0 and log g = 5.0 in the temperature range of 6000 - 8000 K. Sensitivity to log g is first lost at the low surface gravity end at a $T_{eff} \sim 7500$ K. This trend continues until nearly all log g sensitivity is lost at $\sim$ 8000 K. At higher temperatures the (U-B) values become degenerate in log g as the continuum opacity shifts from H-dominance to that of neutral hydrogen. The converse is true of the $D_{0.2}$ plots. Here we see sensitivity to surface gravity beginning for log g = 2.0 at around 7500 K. This sensitivity proceeds to higher log g values and at $\sim$ 8500 K is as strong surface gravity indicator for all log g values. At temperatures cooler than 8000 K, $D_{0.2}$ is

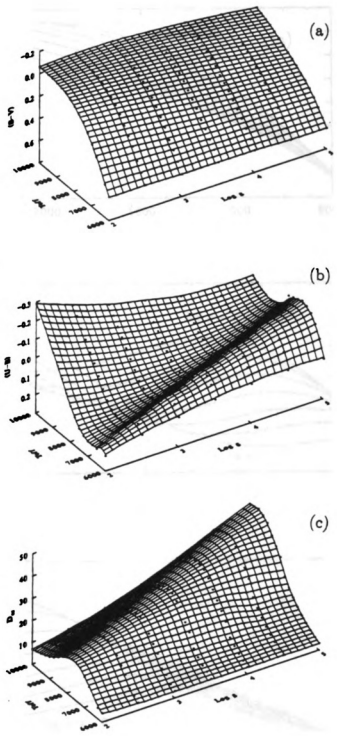

Fig 3.2: T_{eff} - Log g dependency of the UBV broadband colors and Balmer line width

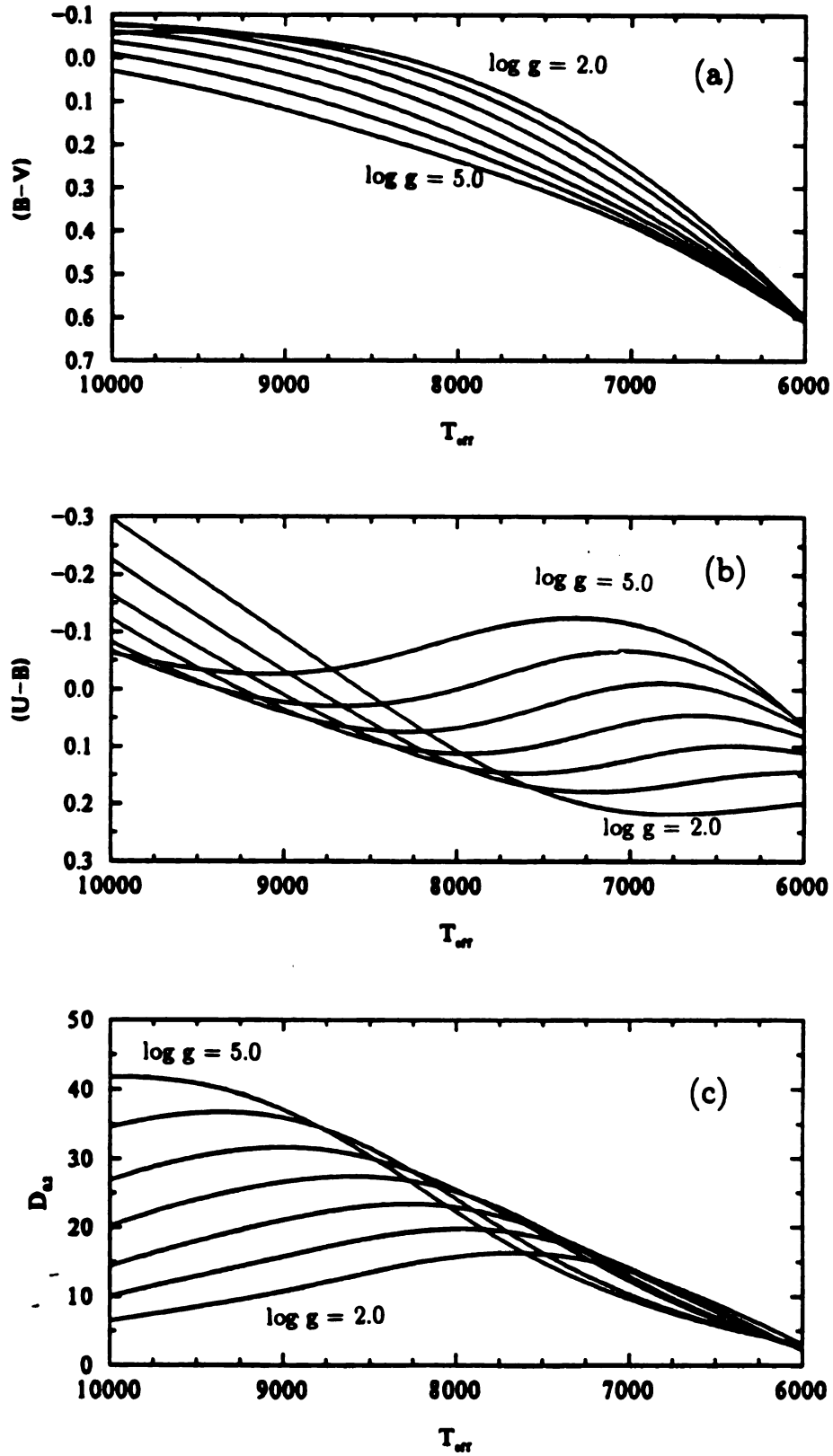

Fig 3.3: Same as Fig 3.2 but collapsed into 2-dimensions

a strong function of T_{eff}. What is immediately apparent from figures 3.2 and 3.3 is that neither the (U-B) colors nor $D_{0.2}$ line widths can be used as a surface gravity indicator for the entire range of T_{eff} values. In the past, investigators using only $D_{0.2}$ to constrain the surface gravity were forced to limit their samples to (B-V) values blueward of 0.2 ($\sim$ 8000 K). If, however, the broadband U magnitudes are available then it is possible to derive reliable log g values by shifting the surface gravity indicator from (U-B) at cooler T_{eff} values, to $D_{0.2}$ for the hotter stars. In such a scheme the (B-V) colors can be used as the primary T_{eff} indicator with either (U-B) or $D_{0.2}$ as a good secondary T_{eff} indicator depending on the temperature of the star. The details of this technique are discussed in the following section.

Finally, we investigate the functional dependence of the CaII K line equivalent width (W_k) on the stellar physical parameters. Figure 3.4a is a 3-D plot of W_k as a function of T_{eff} and [Fe/H] for a log g value of 3.5. Figure 3.4b is the same plot again collapsed into 2 dimensions and with W_k shown as a function of temperature. As was expected, we see that W_k is a strong function of both T_{eff} and [Fe/H] for most of the grid values. Since the energy level associated with the CaII K transition becomes depopulated at the highest temperatures, sensitivity for the most metal deficient cases begins to be lost at around 9000 K. All sensitivity to both T_{eff} and [Fe/H] is lost when the temperature reaches 10,000 K.

Perhaps not too surprising is the fact that W_k is also somewhat dependent on surface gravity, especially in cooler, high abundance stars where the line wings become large. Figures 3.5a-c show this dependency for a metal abundance of solar, -1.0, and -2.0 dex, respectively. From these plots it appears that the largest log g dependency is constrained to $T_{eff} < 8000$ and [Fe/H] ≥ -1.0 dex. Although for the

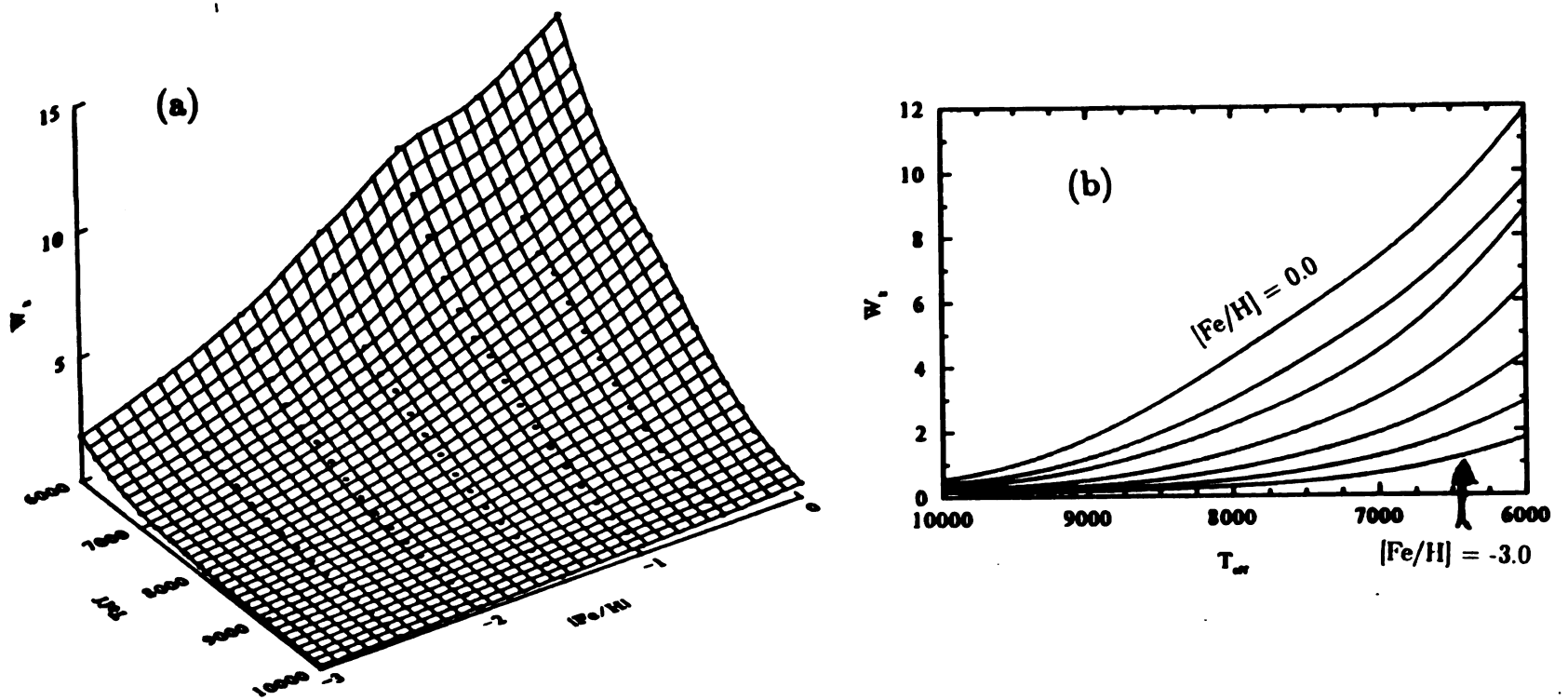

Fig 3.4: T_{eff} - [Fe/H] dependency of the CaII K line equivalent width

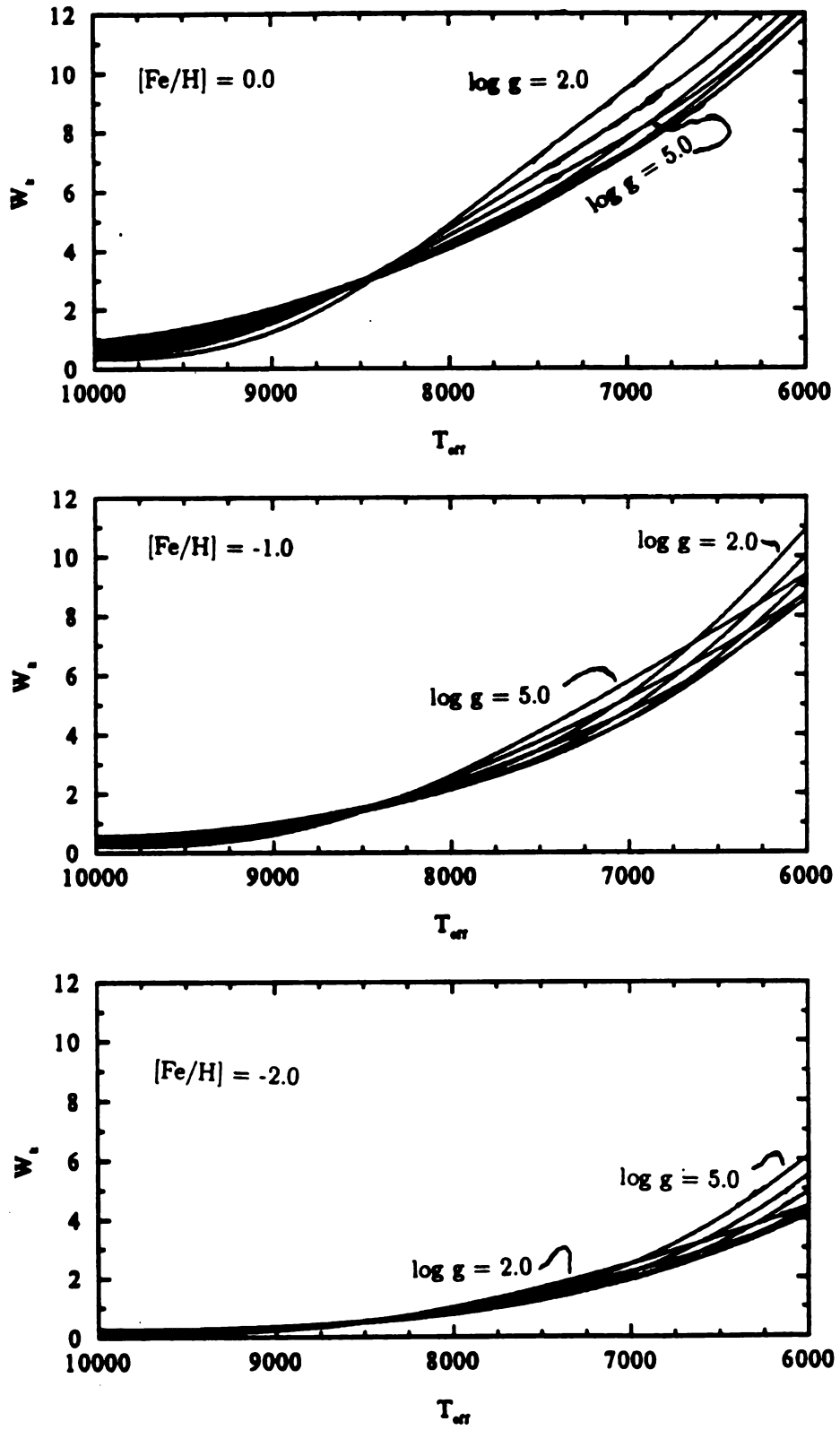

Fig 3.5: The Log g dependency of W_k for for [Fe/H] = 0.0, -1.0, and -2.0, respectively.

majority of our program stars this W_k dependency is not a major concern, it is of interest to see how log g affects the abundances determined from a W_k, (B-V) plot, which in the past has been customarily used to estimate [Fe/H]. Figure 3.6a is a plot from Pier (1983) of his derived abundance calibration as a function of (B-V) colors. Also plotted are the program stars from his sample. The envelopes of constant abundance values ([Fe/H] = -0.5, -1.0, and -2.0) are bounded by a range in log g values that correspond to his program stars. It can be seen that there is minimal overlap between these envelopes for Pier's cruder grid spacing. Figure 3.6b is the same plot but now using the W_k values from the new calibration grid. The upper envelope is for an abundance of [Fe/H] = -0.5 with a range of log g from 2.0 to 4.5. The lower envelopes have [Fe/H] = -1.0, and -2.0. We see a rather large overlap at in the higher abundance envelopes due to the log g dependency of both W_k and (B-V). This large overlap is also seen in figure 3.6c where the [Fe/H] = -1.5 envelope is included. It is clear from these plots that accurate metallicities can only be determined if log g values for the stars are known. Even if high surface gravity main sequence stars are separated from the lower surface gravity FHB stars the overlap is such that errors as large as ± 0.5 dex would still be present. In section 3.4 it is shown that abundances as precise as ± 0.23 dex can be found for the high S/N spectra of standard stars using the new grid calibrations. Such precision can only be achieved, however, by taking into account the log g dependency of the CaII K line.

It can be concluded from the observable dependency plots that it is possible to constrain the surface gravity over the majority of the T_{eff} range. In the region of T_{eff} > 8000 K the Balmer line widths are very sensitive to changes in log g and can be used quite effectively as a surface gravity indicator, providing the scatter in

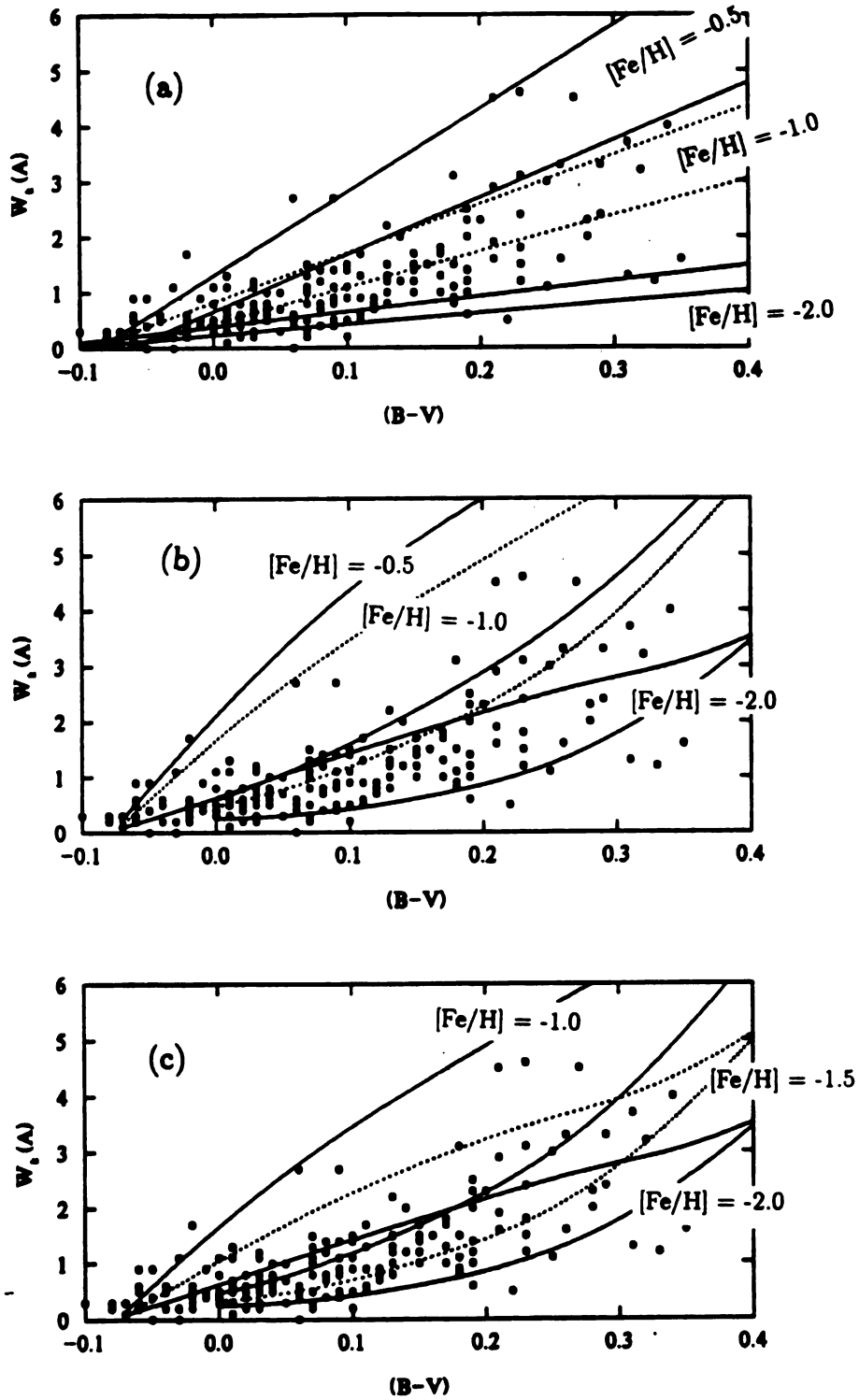

Fig 3.6: Comparison of the Pier W_k - (B-V) relation with that of the new calibration. Envelopes of constant abundance show significant overlap due to Log g effects.

the derived line widths from low S/N spectroscopy is kept small compared to the width separation in the calibration grid. Likewise, the (U-B) colors are shown to be a function of log g for T_{eff} < 8000 K. However, since (U-B) also depends on metallicity, stellar abundances must be calculated in order to completely remove ambiguity between FHB and A star colors. For a small transition region near 8000 K neither $D_{0.2}$ or (U-B) are strong surface gravity indicators, since there is some degeneracy in both parameters.

To use the observables as effectively as possible we have quantified the dependency of each with respect to the physical parameters. Ideally, the value of the partial derivative at each grid point, (833 points), for all combinations of observables (3) and physical parameters (3) could be calculated. However, this gives an enormous number of slopes, (3 x 3 x 833 = 7997) and probably would add little to the observable characterization. Therefore, changes in the observable dependencies were characterized by calculating the slope for the largest applicable regions in the T_{eff} - log g plane and across all metallicities. Table A.2 lists the results of the dependency calibration. Columns 1 and 2 are the model parameters T_{eff} and log g. Columns 3-8 are the normalized fractional weights for the 3 observables as a function of the two physical parameters. These weighting factors were determined directly from the scaled slopes in the dependency plots. In section 3, a technique is presented which uses these weighting factors to help predict the stellar physical parameters.

3.3 Assignment of Stellar Physical Parameters

3.3.1 The Grid Comparison Technique

Using the calibration grid it is now possible to assign T_{eff} and log g values to the FHB and main-sequence A-type stars. A comparison technique has been developed

which assigns stellar physical parameters by searching for all possible matches to the grid observables, in the T_{eff} - log g plane, within the estimated observable uncertainties.

In section 3.5, a detailed analysis of the effects of low S/N on the derived line widths is presented. The results indicate that for a S/N = 14 the scatter in the $H\delta$ line width, $D_{0.2}$, is $\sim$ 6% of the true width. The scatter in $D_{0.2}$ for $H\gamma$ is generally larger, especially in later stars where the G-band affects the fitting of the continuum, and is only used to help constrain the initial estimate of T_{eff} and log g. The photometry suffers from small internal uncertainties and uncertainties in the adopted reddening values that amount to a scatter of about $\pm$ 0.03 in each of the colors. W_k has been excluded as a T_{eff}, log g indicator since it is also a strong function of metallicity.

Figure 3.7a is an example of all possible matches in T_{eff} and log g, for the prototypical FHB star HD 161817 and the main sequence A star HD 201601. Although there are many possible matches for an individual observable there is a clearly recognizable region in which most or all of the observables overlap. It is immediately apparent that the overlap regions indicate HD 161817 is a low surface gravity star while HD 201601 has a surface gravity indicative of a main sequence star.

To quantify the true overlap region, we first assign each observable/grid point match in T_{eff} and log g the appropriate value from the weighting calibration. At grid points where two or more observables overlap the value of the grid point is the sum of the weight for each. Since it is not always the case that all observables overlap at one specific grid point, the value at each grid point is added to the sum of the eight surrounding points and a value for the immediate region is determined. Quadratic interpolation is then performed within the region of maximal overlap and

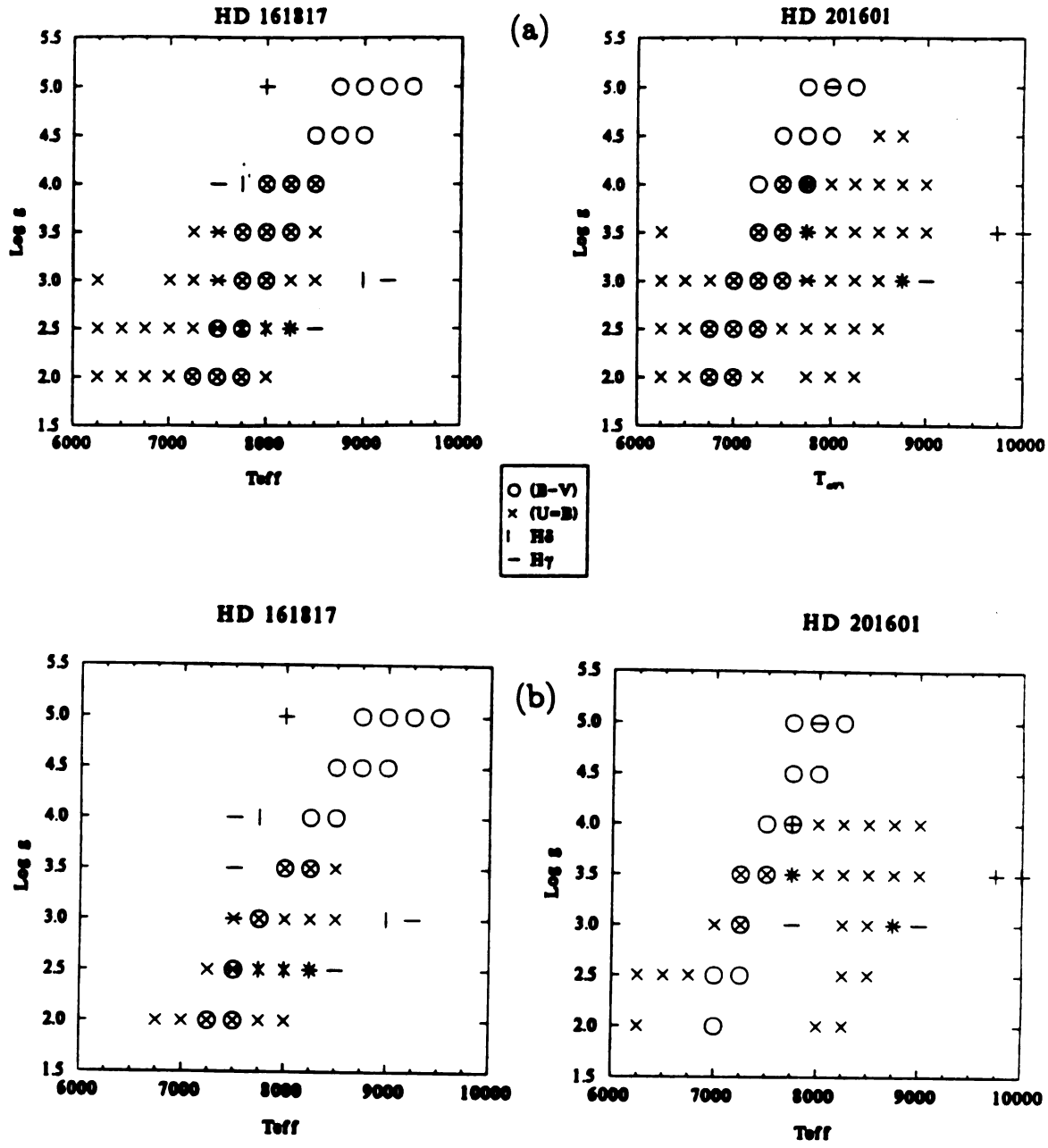

Fig 3.7: Observable matches to the calibration grid for two standard stars: (a) shows the initial matches and (b) the matches after intitial abundance correction.

initial values of T_{eff} and log g are found.

The observed parameter, W_k, serves as our primary metal abundance indicator. We have presumed that a monotonic relation between [Ca/Fe] and [Fe/H] exists for the stars under consideration, and that the strength of CaII K is indicative. The procedure finds the best grid match for W_k at the initial values of T_{eff} and log g. This match gives an estimate of the metal abundance, parameterized by [Fe/H].

The color matches are then constrained by the initial value of [Fe/H], and a new overlap region in the T_{eff}, log g plane is found (Figure 3.7b). To insure the overlap region is consistent with the actual observed parameters a simultaneous fit to all the observables at a given T_{eff} and log g is calculated and divided by the regional weighted value at that point. This division prevents a severely deviant observable from "dragging" the solution too far from the identified overlap region. The minimum of this calculation gives the new T_{eff} and log g values. The process is iterated one more time and the final values of T_{eff}, log g and [Fe/H] are found.

3.3.2 Secondary Abundance Indicator

A number of concerns arise when using only the CaII K line equivalent width as an estimator of the overall metal abundance [Fe/H]. First, abnormalities in a star's calcium abundance could have drastic effects on the derived value of [Fe/H]. This is most pronounced in the peculiar and metallic-line A stars where calcium can be underabundant by 1-2 dex. A second concern is whether calcium faithfully tracks the iron abundance as the stellar metallicity decreases. As discussed in section 3.2.2 we have adopted the Wheeler *et al.* relation for [Ca/Fe] as a function of [Fe/H] in computing the synthetic spectra. New evidence suggests this may not be the case for all FHB stars and that a simple relation between Ca and Fe may not exist at all. Third, the stellar CaII K line can be blended with the interstellar Ca line causing

an erroneously high abundance to be calculated. This could be a problem for our program FHB stars in the direction of the Galactic center where the interstellar calcium line can rival and even exceed the strength of the stellar line in metal-poor stars (Beers 1990, Morrison 1994). Finally, for the hottest stars in our sample the effects of low S/N become important. At about 8500K the CaII K line has shrunk to a point where it is hard to distinguish from the noise and at higher temperatures the line fit is dominated by the noise. This causes large scatter in the derived abundance at these temperatures. (See section 3.5)

Carney *et al.* (1987) have shown that metallicites as accurate as ±0.15 dex can be determined for subdwarfs using a synthetic template correlation technique to find the best χ^2 fit to high resolution, low-S/N spectroscopy. Following their lead we have attempted to use a similar technique for our earlier stars at moderate resolution to derive abundances from the CaII K line and the metallic lines in the regions from 4175 Å- 4310 Å and 4360 - 4500 Å. The metallic lines from these regions can be seen in figure 3.8, which is a spectrum of the FHB star HD 161817. It should be noted that the metallic regions include the Ca I line at 4227 Å and the Mg II line at 4480 Å. These were included to help tie down the abundance solution in the hotter and more metal-poor stars. Investigations, using high-S/N FHB standards, indicate that $\sim$ 80% of the total equivalent width in these regions come from the various neutral and singly ionized iron lines, with Ca and Mg contributing $\sim$ 15%. Therefore the abundance from these regions is more closely identified as an actual metal ($\sim$iron) abundance.

Our procedure compares the program spectra to templates constructed from the previously calculated synthetic spectra. The synthetic spectra were originally smoothed to 1.9 Å resolution, approximately matching the observed data. The

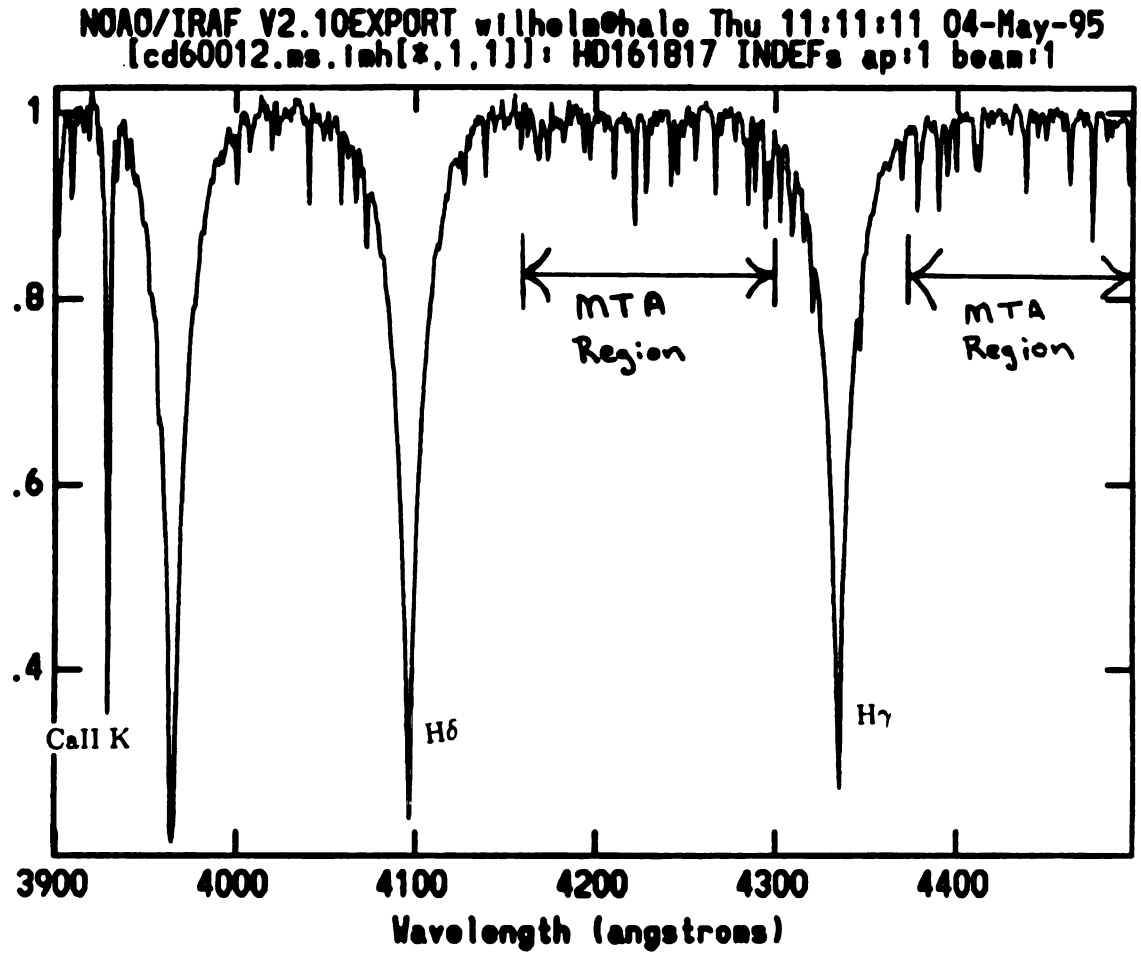

Fig 3.8: Spectrum of HD 161817 with metallic regions indicated.

templates are first prepared with wavelength solutions recalculated to precisely match each individual program spectrum by linearly interpolating the normalized intensity values from the bracketing pixels. Then the synthetic spectra are shifted to match the observed radial velocity of the program star. Generally, 28 synthetic templates are matched to each observed spectrum. This covers the 7 abundances at each of the four grid points that surround the T_{eff} and log g values found from the grid comparison technique. The χ^2 fit for each template match is found, and the abundance is quadratically interpolated at each grid point to find the metal abundance that corresponds to the minimum χ^2 value. The four resulting abundance values are then linearly interpolated in T_{eff} and log g to find the abundance at the input temperature and surface gravity. Figures 3.9 and 3.10 show the template fits to the CaII K line and one of the metallic line regions for HD 161817, at the abundance values of [Fe/H] = -1.0, -1.5 and -2.0, respectively. The best match to the observed CaII K line is clearly the [Fe/H] = -1.5 template while the best abundance value for the metallic region is between the [Fe/H] = -1.0 and -1.5 dex templates.æ

3.4 Standard Star Results

Over the past two years a large number of standard star observations have been accumulated, most of which have doubled as radial velocity standards for our program stars. The standard stars that have been classified as FHB or A type by previous studies number 81. Altogether, 21 of these stars have been identified as FHB from the high- dispersion studies of Adelman and Philip (1994), Green and Morrison (1993), and the photometric study of high velocity stars by Stetson (1991). The A stars include "normal" main-sequence stars of solar abundance, A III giants, peculiar and metallic-line A stars, λ Bootis stars, and population II halo blue stragglers. Table 3.1 is a list of all the standard stars used in this

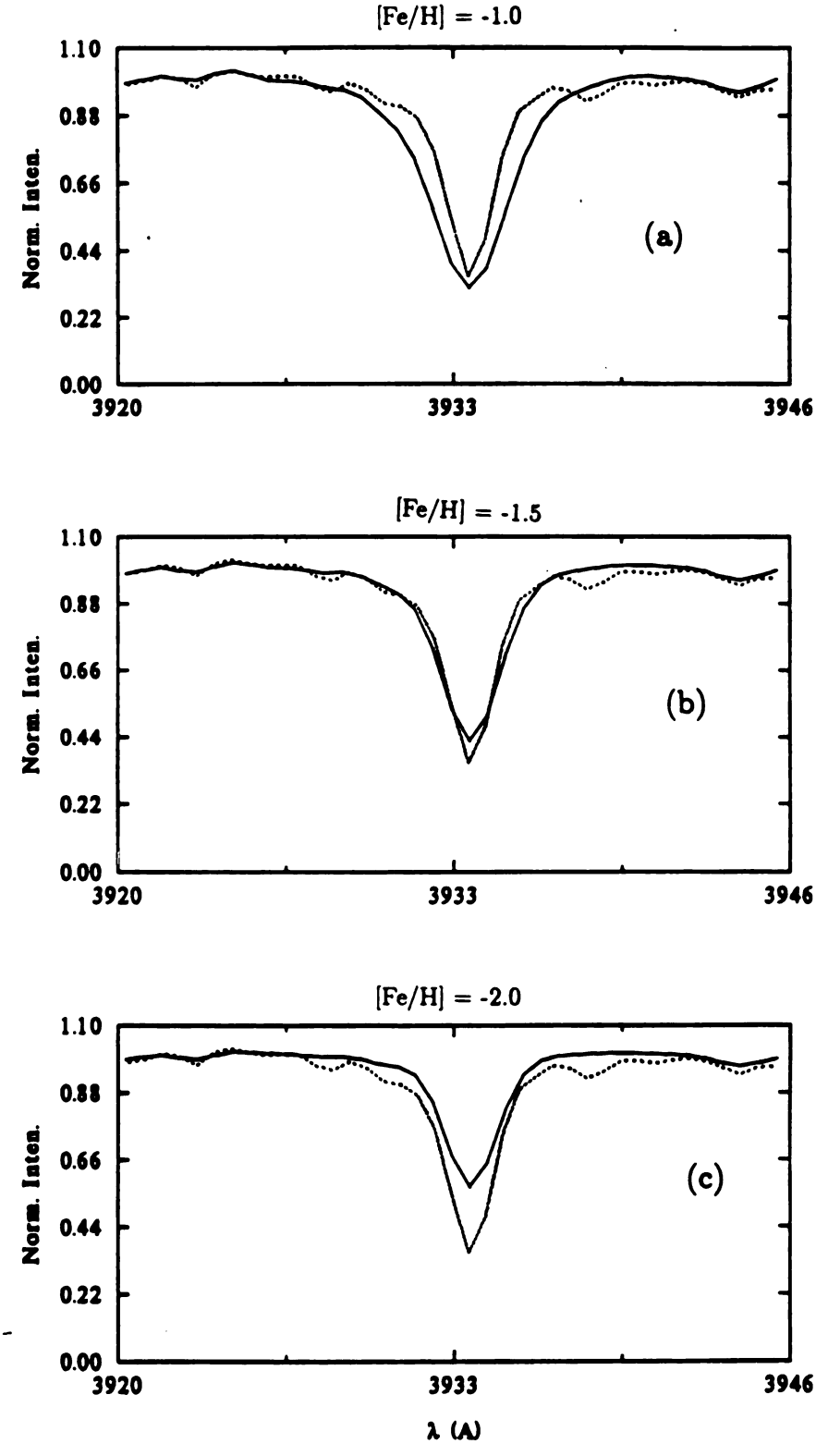

Fig 3.9: Template match to CaII K line for HD 161817. The solid lines show the templates with [Fe/H] = -1.0, -1.5, and -2.0.

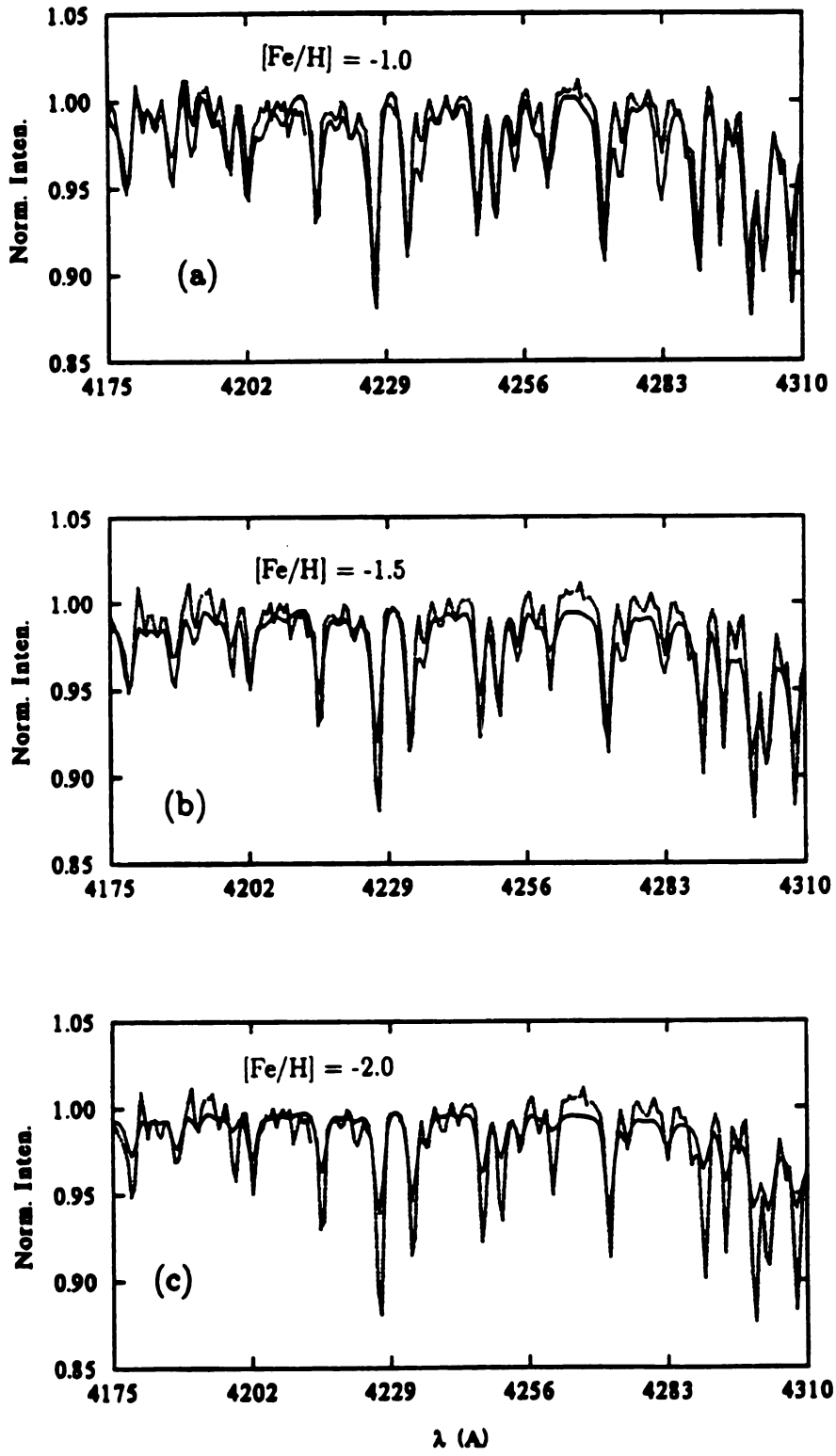

Fig 3.10: Template match to one of the metallic regions in HD 161817. The solid lines show the templates with [Fe/H] = -1.0, -1.5, and -2.0.

Table 3.1. Standard Star Results.

Star (1)	Obser (2)	$(B-V)_o$ (3)	$(U-B)_o$ (4)	T_{eff} (5)	Log g (6)	[Fe/H] (7)	Class (8)	Spec Type (9)	Notes (10)
HD 11257	1	0.29	-0.06	7447	4.5	0.0	1	F2Vw	
HD 188041	2	0.14	0.04	7765	4.2	0.0	1	AVp var	S
HD 189849	1	0.07	0.07	8618	3.0	0.0	5	A4III	
HD 193432	2	-0.07	-0.11	9738	3.4	-0.4	1	B9IV	
HD 201601	3	0.23	0.07	7695	4.0	0.0	1	F0p	S
HD 209625	2	0.21	0.14	7502	3.0	-0.8	3	A5m	
HD 214994	1	-0.03	-0.02	9266	3.5	0.0	1	A1IV	S
HD 140283	1	0.40	-0.26	6329	4.5	-2.2	1	SdF3	
HD 2421	1	0.01	-0.03	9222	3.5	0.0	1	A2Vs	
HD 2628	1	0.24	0.08	7287	3.3	0.0	1	A7III	S
HD 5797	1	0.03	0.03	8375	2.5	-2.8	3	Am	
HD 114330	1	-0.02	-0.01	9440	3.5	0.0	1	A1V	S
HD 192640	1	0.04	0.00	9163	3.5	0.0	4	A2V	
HD 195725	1	0.06	0.06	8567	3.0	0.0	5	A7IIIp	
HD 182564	1	-0.01	0.04	9016	3.5	0.0	1	A2IIIs	S
HD 104957	1	0.25	0.03	7229	3.0	-1.1	3	Am(carbon)	
HD 193182	1	-0.20	-0.19	7763	3.8	-2.0	5	Ap(shell)	
HD 21931	1	-0.06	-0.22	9692	3.3	-1.2	1	B9V	
HD 24000	1	0.29	0.20	7753	4.0	-1.2	1	A0V	
HD 117624	1	0.24	0.14	7239	2.6	-1.7	5	A2	
HD 319	2	0.14	0.06	7996	3.6	-1.3	4	A1V(λBoo)	
HD 6340	1	0.08	0.03	8660	4.0	0.0	1	A1V	
HD 8716	1	0.23	0.10	7495	3.5	0.0	1	A7V	*
HD 11413	1	0.15	0.03	8008	4.0	-1.5	4	A1V(λBoo)	*
HD 11490	3	0.28	0.09	7202	3.2	-0.3	1	F0V	*
HD 13232	1	0.28	0.12	7280	2.8	-3.0	3	Am	
HD 18735	4	0.00	-0.02	9575	4.0	0.0	1	A0V	*
HD 20010	7	0.58	0.08	6212	3.3	-0.8	1	F8IV	
HD 14252	1	0.01	0.03	8967	3.5	0.0	1	A2V	
HD 24450	1	0.36	-0.06	6998	3.9	0.0	1	F3V	
HD 36017	3	0.14	0.03	7579	3.8	0.0	4	A3(λBoo)	
HD 39655	6	0.35	-0.07	7072	4.2	-0.3	1	F2V	*
HD 68452	1	0.06	0.05	8918	3.5	-1.1	1	A1V	*
HD 105388	2	-0.02	0.02	9363	4.0	-1.1	4	A0V	
HD 113083	2	0.49	-0.15	6000	4.0	-1.5	1	F9V	
HD 142703	6	0.17	-0.13	7697	4.5	-1.4	4	A2Ib/II(λBoo)	*
HD 154694	7	0.43	-0.05	6630	3.6	-0.3	1	F8	*
HD 160043	10	0.44	-0.03	6463	3.3	-0.7	1	F6V	
HD 193256	1	0.11	0.05	7997	3.3	-0.5	4	A2IV(λBoo)	*
HD 193281	1	0.13	0.08	8209	3.8	-0.6	4	(λBoo)	*

Table 3.1. (continued)

Star (1)	Obser (2)	$(B-V)_o$ (3)	$(U-B)_o$ (4)	T_{eff} (5)	Log g (6)	[Fe/H] (7)	Class (8)	Spec Type (9)	Notes (10)
HD 201187	7	0.43	-0.10	6576	3.8	-0.7	1	F3V	*
HD 204041	1	0.14	0.04	8021	3.9	-1.6	4	A1IV(λBoo)	
HD 219436	5	0.08	0.06	8522	3.6	-0.1	1	A1V	*
HD 220647	2	0.28	0.03	8235	4.5	0.0	1	F0V	*
HD 224964	3	0.10	0.04	8617	4.0	0.0	1	A3V	*
G 64-12	1	0.38	-0.23	6743	4.4	-3.0	1	F0	
BD -4 3208	3	0.38	-0.21	6554	3.8	-2.0	1	A7	
BD-15 2546	1	0.41	-0.24	6599	4.4	-1.8	1	SdF6	
HD 8554	1	0.30	-0.10	7260	4.0	-1.1	6	...	*
1 - ERI	1	0.48	0.00	6258	2.4	-1.1	1	F5V	
HD 13588	1	0.18	0.13	7779	3.3	-1.5	3	Am	
13 - ERI	1	0.09	0.23	7750	2.0	-1.0	3	A5m	
HD 135549	1	0.30	-0.18	7250	5.0	-0.8	6	...	*
HD 142575	1	0.37	-0.01	6741	3.1	-0.9	6	...	
HD 155898	1	0.25	-0.06	7536	4.5	0.0	6	...	*
HD 217602	1	0.16	0.09	7045	2.3	-2.4	3	Am	
HD 224927	1	0.31	-0.12	7280	4.4	-0.5	6	...	*
42 - ERI	1	0.08	0.08	8505	3.6	-0.5	1	A2V	
88 - TAU	1	0.18	0.11	7774	3.5	-0.5	3	A5m	
TAU3 - ERI	1	0.16	0.08	8074	3.9	0.0	1	A4V	
HD 4850	1	0.07	0.12	8243	3.0	-1.6	2	...	
HD 13780	1	0.12	0.13	7758	3.0	-1.7	2	...	*
HD 16456	1	0.22	0.03	7484	3.5	-1.5	2	...	*
HD 31943	1	0.14	0.16	7541	2.5	-1.8	2	...	*
HD 139961	1	-0.01	0.09	9216	3.5	-0.9	2	...	
HD 176387	1	0.02	-0.02	8736	2.5	-1.5	2	...	*
HD 180903	1	0.13	0.04	7745	3.4	-1.5	2	...	*
HD 161817	13	0.13	0.11	7542	2.6	-1.8	2	A2	S
HD 109995	6	0.05	0.13	8220	3.0	-2.0	2	A0V	S
HD 14829	3	0.01	0.05	9035	3.4	-1.9	2	A0	
HD 130095	4	-0.01	0.03	9128	3.3	-2.1	2	A0V	S
HD 2857	4	0.13	0.21	7613	2.6	-1.7	2	A2	S
HD 86986	3	0.11	0.14	7990	3.0	-2.0	2	A1V	S
HD 167105	4	0.02	0.05	9225	3.5	-1.2	2	A0	S
HD 74721	1	0.01	0.12	8297	3.0	-2.1	2	A0V	
HD 177880	2	-0.01	0.05	8741	3.0	-2.5	2	B9IV	
HD 202759	2	0.21	0.09	7463	3.1	-2.3	2	A0III	*
HD 203563	1	0.00	0.04	9040	3.0	0.0	2	A0	*
HD 93329	1	0.08	0.10	8173	3.0	-1.9	2	A0	*
HD 87112	1	-0.04	-0.04	9567	3.5	-1.6	2	A0	*
HD 87047	1	0.08	0.16	7820	2.8	-1.7	2	A0	*

investigation. Columns 1 and 2 are the star name and number of observations for each star. Columns 3 and 4 are the adopted dereddened UBV colors. Columns 5-7 are the derived physical parameters from the calibration technique. Column 8 lists the published class identification, where main sequence A stars are (1), FHB stars (2), Am stars (3), λ Bootis stars (4), and Ap stars (5). Column 9 is the published spectral type identification as listed in the SIMBAD database. Column 10 denotes the stars used as external standards with an (S); an asterisk indicates that no broadband photometry was available and the colors were derived from Stromgren photometry using comparisons to the Kurucz colors.

3.4.1 Physical Parameter Comparisons

Before testing the ability of the grid comparison technique to separate the FHB/A stars, we first want to quantify how well the procedure can reproduce the physical parameters. Twelve stars were chosen from Table 3.1 to serve as physical parameter standards. To be selected, a star must have multiple high dispersion analyses with a small enough scatter in the physical parameters so that a confident value can be assigned. The overall scatter in the published values for the 12 stars is $\sigma(T_{eff}) = \pm$ 109 K, (σlog g) = $\pm$ 0.23, and σ([Fe/H]) = $\pm$ 0.19 dex.

The observed spectra were fit with Voigt profiles in the identical way as the synthetic spectra (see Section 3.2.2). The grid comparison technique was then run using the colors and line widths as input and T_{eff}, log g, and [Fe/H] values found. Table 3.2 list the published values, the calculated values and the difference (calculated - published) for each star. For those stars where multiple spectra were taken, the calculated parameters are the average for all observations. From these values we find the external accuracy, characterized by the mean and standard deviation of the mean in the difference values, to be $\Delta(T_{eff}) = 35 \pm 74$ K, Δ(log g) = -0.05

Table 3.2. Standard Star External Accuracy.

Star (1)	T_{eff} (2)	Calc. Log g (3)	[Fe/H] (4)	T_{eff} (5)	Publ. Log g (6)	[Fe/H] (7)	ΔT_{eff} (8)	Diff. ΔLog g (9)	Δ[Fe/H] (10)
HD 2628	7287	3.3	0.0	7400	3.6	-0.1	-113	-0.3	0.1
HD 114330	9440	3.5	0.0	9510	3.6	0.0	-70	-0.1	0.0
HD 182564	9016	3.5	0.0	9000	3.5	0.0	16	0.0	0.0
HD 188041	7765	4.2	0.0	8000	4.0	0.1	-235	0.2	-0.1
HD 201601	7695	4.0	0.0	7750	3.7	0.0	-55	0.3	0.0
HD 214994	9266	3.5	0.0	9500	3.6	0.2	-234	-0.1	-0.2
HD 2857	7613	2.6	-1.7	7636	2.9	-1.5	-23	-0.3	-0.2
HD 86986	7990	3.0	-2.0	7800	3.1	-1.8	190	-0.1	-0.2
HD 109995	8220	3.0	-2.0	8150	3.3	-1.9	70	-0.1	-0.2
HD 130095	9128	3.3	-2.1	9250	3.4	-2.0	-122	-0.1	-0.1
HD 161817	7542	2.6	-1.8	7225	2.8	-1.6	317	-0.2	-0.2
HD 167105	9225	3.5	-1.2	8550	3.3	-1.8	675	0.2	0.6

Table 3.3. Standard Star Internal Accuracy.

Star (1)	σT_{eff} (K) (2)	A-type σLog g (3)	σ[Fe/H] (4)	Star (5)	σT_{eff} (K) (6)	FHB σLog g (7)	σ[Fe/H] (8)
HD 18735	± 97	± 0.04	± 0.00	HD 2857	± 44	± 0.05	± 0.10
HD 20010	± 78	± 0.50	± 0.20	HD 109995	± 25	± 0.08	± 0.05
HD 39655	± 36	± 0.11	± 0.86	HD 130095	± 251	± 0.23	± 0.11
HD 142703	± 7	± 0.02	± 0.05	HD 161817	± 44	± 0.05	± 0.10
HD 154694	± 132	± 0.63	± 0.19	HD 167105	± 21	± 0.02	± 0.20
HD 160043	± 89	± 0.54	± 0.31				
HD 219436	± 0	± 0.00	± 0.19				

$\pm$ 0.05, and Δ([Fe/H]) = -0.04 $\pm$ 0.07. This indicates that there are no systematic errors within the stated uncertainty. The 1 σ scatter in the data values shows the precision in the parameter determinations to be $\sigma(T_{eff})$ = $\pm$ 257 K, σ(log g) = $\pm$ 0.19, and σ([Fe/H]) = $\pm$ 0.23. The somewhat large value for the T_{eff} scatter is inflated by the large discrepancy in the determination for HD 167105. If this star is excluded then σT_{eff} = $\pm$ 168 K.

Figures 3.11 a-c are plots of the difference values as a function of each physical parameter for all the stars in Table 3.1 with published high dispersion analysis. Filled circles represent FHB stars and open circles the "normal" main sequence A stars. Open triangles, stars, and squares represent A peculiar (Ap), Am, and λ Bootis stars, respectively. With the exclusion of the more abnormal A-type stars, the scatter in all three parameters is relatively small. Most importantly, there appears to be very little evidence of systematic errors across the sampled parameter regions.

It is also informative to test the internal consistency of our procedure. Table 3.3 lists the internal scatter in the calculated parameters for those stars with 4 or more observations. Overall, the scatter is $\sigma(T_{eff})$ = $\pm$69 K, σ(log g) = $\pm$0.19, and σ([Fe/H]) = $\pm$0.21. For most of the stars the internal scatter in all three parameters is quite small. The exception are the three stars with T_{eff} < 7000 K, where the internal scatter in log g is $\sim$ 0.55. These stars, HD 20010, HD 160043, and HD 154694 are identified in the SIMBAD database as normal main sequence stars and so are not expected to be variables. Instead, the anomalously large scatter is probably due to insensitivity in the surface gravity indicator. In this temperature range log g is determined almost completely from the (U-B) colors. Since the input colors were kept constant for a each star, the large variations in log g are only due to errors

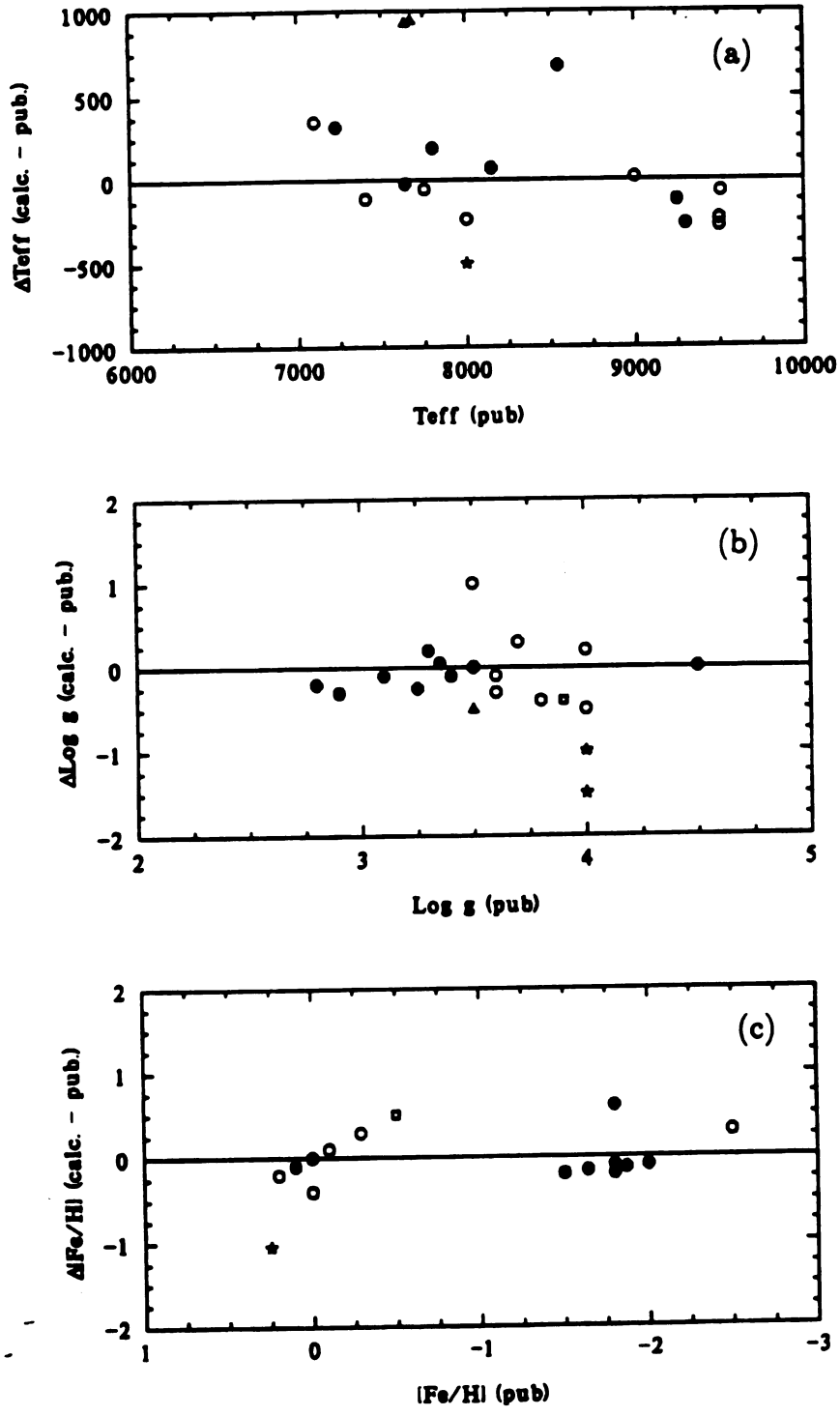

Fig 3.11: External accuracy of the three physical parameters for the standard stars. Normal main sequence A-stars, FHB, Am, Ap, and λ Boo stars are represented by open circles, filled circles, stars, triangles, and squares, respectively.

in T_{eff} brought about by small uncertainties in the line widths from the high S/N spectra. If we return to the observable dependency plots in figures 3.2, 3.3, and 3.4, we see that for main sequence surface gravities and temperatures below 6500 K the dependency of (U-B) is relatively weak and that scatter in T_{eff} as small as 100 K can change the log g determination by ~0.5. This evidence coupled with the results for low S/N spectra in section 3.5, suggest that the uncertainty in log g is somewhat larger at the extreme cool end of the grid.

3.4.2 Separation of FHB/A Stars

We next use the calculated stellar parameters for the entire sample of standard stars from Table 3.1 in order test the ability of the procedure to separate the FHB and other A-type stars. Figure 3.12 shows the placement of these stars in the log g, T_{eff} plane. The horizontal solid line, at log g = 3.5, is the nominal cut-off for a main sequence star in this temperature range. The horizontal dashed line at log g = 3.26 reflects the uncertainty in log g from the standard parameter comparisons. The sloping solid line is the theoretical ZAHB line from Sweigart (1987), for stars with a helium abundance of Y = 0.25. In general, stars on the horizontal branch move to lower surface gravities as they evolve, making this line the upper limit for log g at a given T_{eff}. The sloping dashed line is again the uncertainty of 0.24 dex in log g. From these lines we expect unambiguous separation of the two populations for $T_{eff} < 7500$ K. Temperatures below 9000 K should separate reasonably well since the majority of FHB stars will not be on the ZAHB. For the majority of the stars above 9000 K the two populations are no longer separable in log g.

As before, the filled circles in Figure 3.12a are the FHB stars, while the variety of open symbols represent the other various A-type stars. The two populations separate quite well for $T_{eff} < 9000$ K with the exception of the Am and some Ap

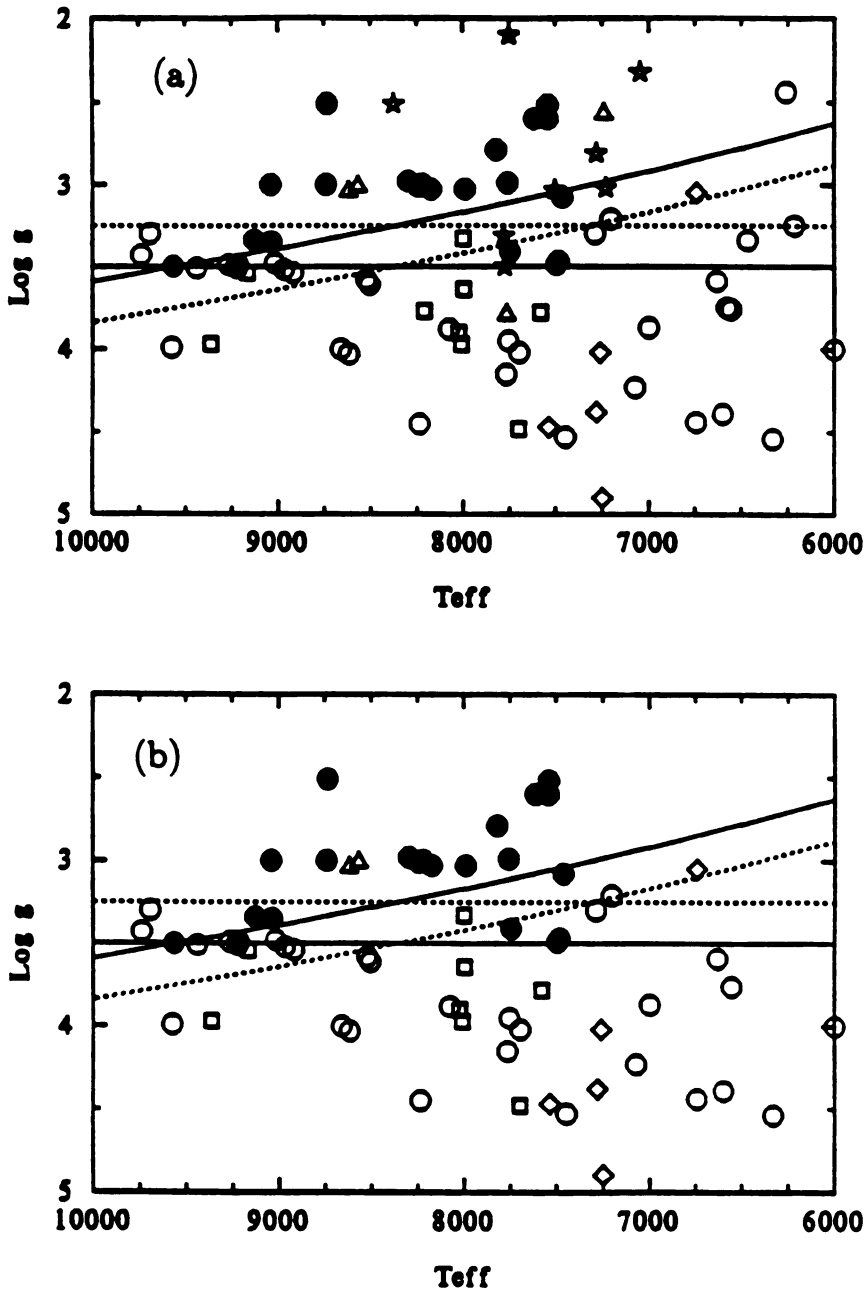

Fig 3.12: Separation of the standard stars. The horizontal solid line is the cut-off for main sequence surface gravity and the sloping solid line is the theoretical zero-age horizontal branch isochrone from Sweigart. Dotted lines indicate the uncertainty in Log g. Figure (b) is the same as figure (a) but with Am stars identified from the template comparison technique removed.

stars. These stars will be identified using the technique described below. Two stars (HD 16456 and HD 180903) classified as FHB by Stetson appear in our plot to be main-sequence A stars. The broadband colors for these stars, however, were estimated using available Stromgren photometry with rather uncertain results in the (B-V) and (U-B) transformations and therefore may be FHB stars. Another exception is the blue straggler candidate, HD 142575 (also from Stetson), which appears to have a surface gravity consistent with an FHB star. If HD 142575 is an FHB star, then the derived abundance of [Fe/H] = -0.9 would indicate that it may be a member of the thick disk on the blue edge of the instability strip. For T_{eff} < 9000 K, full agreement has been found with the identifications of FHB and A stars from Green and Morrison, who used a vsin(i) criteria. As expected, both populations overlap at T_{eff} > 9000 K and can not be separated using this plot. If we now exclude the two Stetson FHB stars and the Ap and Am stars, but include the Stetson blue straggler candidate, we find only 3 misidentifications, all of which occur at temperatures less than 7250 K. This gives a misidentification rate of 4% for the standard stars.

3.4.3 The Ca and Fe Indicators

As discussed in section 3.3.2, the standard stars were analyzed using the template comparison technique to derive abundances from the CaII K line and two regions of metallic lines. The template abundance results for all the standards are presented in columns (5), and (6) of Table 3.4 with their corresponding T_{eff}, log g, and [Fe/H] (columns (2), (3), and (4)) values from the grid comparison technique. The agreement in derived [Fe/H] is excellent for most standard stars. The exceptions are the Am stars and a few Ap stars. The large difference between the metallicity derived from the metallic line regions and that of the CaII K line is due

Table 3.4. Standard Template Comparison Results

Star (1)	T_{eff} (2)	Log g (3)	$[Fe/H]_{W_k}$ (4)	$[Fe/H]_{CTA}$ (5)	$[Fe/H]_{MTA}$ (6)	C_c (7)	C_p (8)	MisID (9)
HD 11257	7447	4.5	0.0	-0.1	0.0	A	A	
HD 188041	7765	4.2	0.0	0.0	0.0	A	A	
HD 189849	8618	3.0	0.0	0.0	0.0	FHB	Ap	(X)
HD 193432	9738	3.4	-0.4	-0.7	-0.5	FHB/A	A	
HD 201601	7695	4.0	0.0	0.0	0.0	A	A	
HD 209625	7502	3.0	-0.8	-0.9	0.0	Am	Am	
HD 214994	9266	3.5	0.0	-0.4	0.0	FHB/A	A	
HD 140283	6329	4.5	-2.2	-2.2	-2.0	A	A	
HD 2421	9222	3.5	0.0	-0.1	-0.4	FHB/A	A	
HD 2628	7287	3.3	0.0	-0.5	0.0	A	A	
HD 5797	8375	2.5	-2.8	-2.5	0.0	Am	Am	
HD 114330	9440	3.5	0.0	-0.1	0.0	FHB/A	A	
HD 192640	9163	3.5	0.0	-0.3	-1.3	FHB/A	λB[illegible]	
HD 195725	8567	3.0	0.0	0.0	0.0	FHB	[illegible]	
HD 182564	9016	3.5	0.0	0.0	0.0	FHB/A	A	
HD 104957	7229	3.0	-1.1	-1.2	-0.4	Am	Am	
HD 193182	7763	3.8	-2.0	-2.0	-0.5	Am	Ap	
HD 21931	9692	3.3	-1.2	-1.5	-2.8	FHB/A	A	
HD 24000	7753	4.0	-1.2	-1.6	-1.4	A	A	
HD 117624	7239	2.6	-1.7	-1.7	0.0	Am	Ap	
HD 319	7996	3.6	-1.3	-1.8	-0.8	A	λBoo	
HD 6340	8660	4.0	0.0	-0.6	0.0	A	A	
HD 8716	7495	3.5	0.0	-0.5	0.0	A	A	
HD 11413	8008	4.0	-1.5	-2.2	-3.0	A	λBoo	
HD 11490	7202	3.2	-0.3	-0.8	-0.2	FHB/A	A	
HD 13232	7280	2.8	-3.0	-2.1	0.0	Am	Am	
HD 18735	9575	4.0	0.0	-0.4	-0.6	A	A	
HD 20010	6212	3.3	-0.8	-1.0	-0.1	Am	A	(X)
HD 14252	8967	3.5	0.0	-0.1	0.0	FHB/A	A	
HD 24450	6998	3.9	0.0	-0.3	0.0	A	A	
HD 36017	7579	3.8	0.0	-0.5	-0.3	A	λBoo	
HD 39655	7072	4.2	-0.3	-0.5	0.0	A	A	
HD 68452	8918	3.5	-1.1	-1.3	-0.7	FHB/A	A	
HD 105388	9363	4.0	-1.1	-1.8	-0.8	A	λBoo	
HD 113083	6000	4.0	-1.5	-1.3	-2.3	A	A	
HD 142703	7697	4.5	-1.4	-1.8	-1.2	A	λBoo	
HD 154694	6630	3.6	-0.3	-0.4	0.0	A	A	
HD 160043	6463	3.3	-0.7	-0.8	-0.2	Am	A	(X)
HD 193256	7997	3.3	-0.5	-0.9	-1.2	FHB/A	λBoo	
HD 193281	8209	3.8	-0.6	-1.0	-0.5	A	λBoo	

Table 3.4. (continued)

Star (1)	T_{eff} (2)	Log g (3)	$[Fe/H]_{W_k}$ (4)	$[Fe/H]_{CTA}$ (5)	$[Fe/H]_{MTA}$ (6)	C_c (7)	C_p (8)	MisID (9)
HD 201187	6576.	3.8	-0.7	-0.7	-0.2	A	A	
HD 204041	8021	3.9	-1.6	-2.1	-1.1	A	λBoo	
HD 219436	8522	3.6	-0.1	-0.7	-0.3	A	A	
HD 220647	8235	4.5	0.0	-0.8	0.0	A	A	
HD 224964	8617	4.0	0.0	-0.2	0.0	A	A	
G 64-12	6743	4.4	-3.0	-3.0	-3.0	A	A	
BD -4 3208	6554	3.8	-2.0	-2.2	-2.1	A	A	
BD-15 2546	6599	4.4	-1.8	-1.9	-3.0	A	A	
HD 8554	7260	4.0	-1.1	-1.5	-1.1	A	BS	
1 - ERI	6258	2.4	-1.1	-0.9	0.0	Am	A	(X)
HD 13588	7779	3.3	-1.5	-1.5	0.0	Am	Am	
13 - ERI	7750	2.0	-1.0	-1.2	0.0	Am	Am	
HD 135549	7250	5.0	-0.8	-1.2	-0.7	A	BS	
HD 142575	6741	3.1	-0.9	-1.1	-0.7	FHB	BS	(X)
HD 155898	7536	4.5	0.0	-0.6	0.0	A	BS	
HD 217602	7045	2.3	-2.4	-2.2	0.0	Am	Am	
HD 224927	7280	4.4	-0.5	-1.0	-0.6	A	BS	
42 - ERI	8505	3.6	-0.5	-0.9	-1.0	A	A	
88 - TAU	7774	3.5	-0.5	-0.9	0.0	Am	Am	
TAU3 - ERI	8074	3.9	0.0	-0.7	-0.5	A	A	
HD 4850	8243	3.0	-1.6	-1.7	-1.1	FHB	FHB	
HD 13780	7758	3.0	-1.7	-2.0	-1.4	FHB	FHB	
HD 16456	7484	3.5	-1.5	-1.8	-1.2	A	FHB	(X)*
HD 31943	7541	2.5	-1.8	-1.6	-0.8	FHB	FHB	
HD 139961	9216	3.5	-0.9	-1.3	-1.1	FHB/A	FHB	
HD 176387	8736	2.5	-1.5	-1.5	-2.2	FHB	FHB	
HD 180903	7745	3.4	-1.5	-1.6	-1.0	A	FHB	(X)*
HD 161817	7542	2.6	-1.8	-1.8	-1.3	FHB	FHB	
HD 109995	8220	3.0	-2.0	-2.3	-1.8	FHB	FHB	
HD 14829	9035	3.4	-1.9	-2.7	-2.1	FHB/A	FHB	
HD 130095	9128	3.3	-2.1	-2.9	-2.0	FHB/A	FHB	
HD 2857	7613	2.6	-1.7	-1.8	-1.5	FHB	FHB	
HD 86986	7990	3.0	-2.0	-2.2	-1.8	FHB	FHB	
HD 167105	9225	3.5	-1.2	-1.8	-1.6	FHB/A	FHB	
HD 74721	8297	3.0	-2.1	-2.4	-1.5	FHB	FHB	
HD 117880	8741	3.0	-2.5	-2.8	-1.7	FHB	FHB	
HD 202759	7463	3.1	-2.3	-2.4	-2.1	FHB	FHB	
HD 203563	9040	3.0	0.0	0.0	0.0	FHB	FHB	
HD 93329	8173	3.0	-1.9	-1.8	-1.4	FHB	FHB	
HD 87112	9567	3.5	-1.6	-2.6	-1.1	FHB/A	FHB	
HD 87047	7820	2.8	-1.7	-2.6	-2.5	FHB	FHB	

to the underabundance of Ca and/or overabundance of Fe in these stars. We select as possible Am candidates those stars with $[Fe/H]_{Fe} \geq -0.50$ and $[Fe/H]_{Ca} \leq -1.0$. Using this criteria, we find excellent agreement between our identified candidates and those stars with published Am classifications. The final stellar classification can be found in columns (7) and (8) of Table 3.4, where C_c is our classification and C_p is the published classification. Column (9) notes the misclassified stars with an (X); an asterisk indicating the broadband colors were transformed from Stromgren photometry. Figure 3.12b shows the T_{eff} - log g plot with the Am stars identified from the template comparison technique removed. It will be shown in Chapter 4, that this technique is also very effective in Am classification of program objects, even at low S/N.

At this point we wish to carefully examine the iron abundance derived from the template comparison technique and explore our ability to predict [Ca/Fe] ratios in the FHB stars. Of the 21 FHB standard stars for which we have spectroscopy, 7 are in common with the published high dispersion analysis of Adelman and Philip (1994 hereafter AP). Figure 3.13a is a plot of our derived iron abundance compared to that found by AP. The scatter about the line with slope = 1 is very small (± 0.11), but there appears to be a small systematic difference of 0.09 dex. For comparison purposes we apply a zero-point shift of $[Fe/H]_{Fe} = 0.09$, in order to bring both data sets onto the same abundance scale. The result of correcting our $[Fe/H]_{Fe}$ can be seen in Figure 3.13b. As prescribed in section 3.2.2, we next remove the Wheeler *et al.* correction that was originally applied to the calcium abundance. This gives the [Ca/H] value for each star. Figures 3.13 c-d show the calculated [Ca/H] values from W_k and the template comparison technique plotted against the derived [Ca/H] from AP.

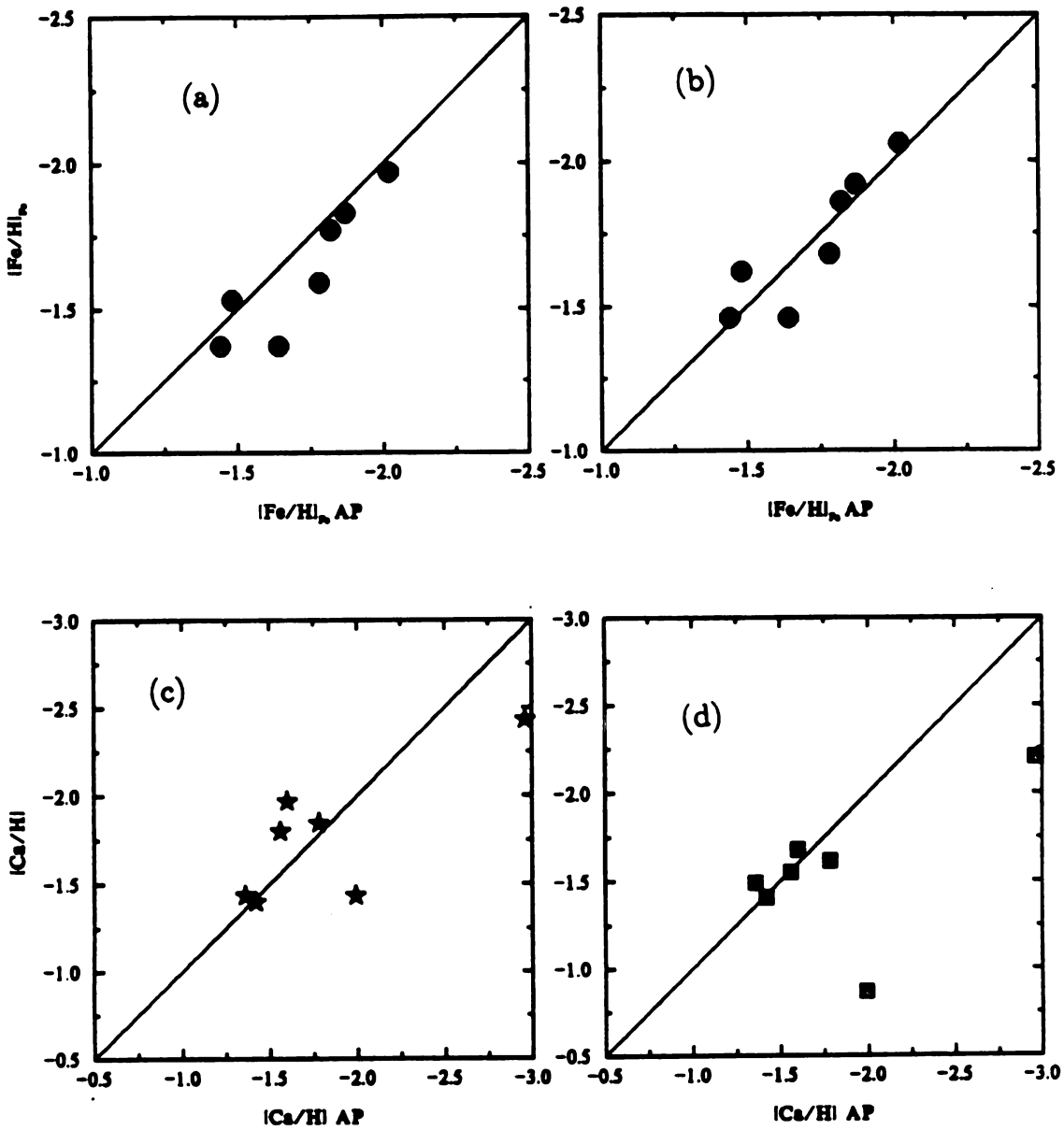

Fig 3.13: Comparison of the three abundance indicators to the published values of Adelman and Philip (1994). Figures (a), (c) and (d) compare the abundance from the metallic-line regions, the CaII K template fit, and the CaII K equivalent width, respectively. Figure (b) is the same as figure (a) but with a zero-point shift of-0.09 dex.

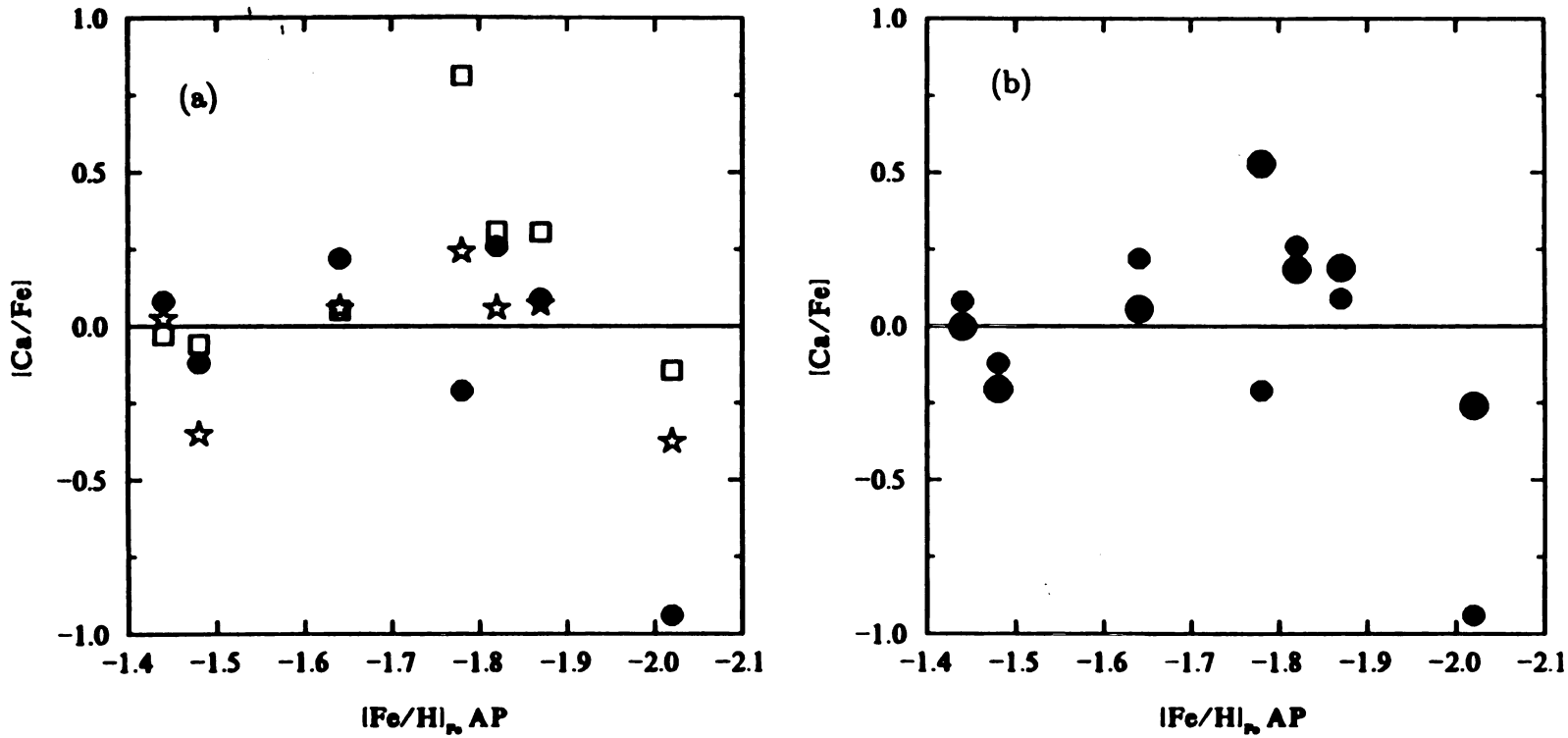

Fig 3.14: Comparison of the derived [Ca/Fe] ratio to the published values of Adelman and Philip (AP). In figure (a) the squares and stars represent the [Ca/Fe] values using the CaII K equivalent width and template comparison, respectively. The filled circles are the AP values. Figure (b) uses the average calcium abundance and is represented by the larger circles.

Figure 3.14a is a plot of the [Ca/Fe] ratio as a function of [Fe/H] from AP. The results from AP are shown as filled circles, our [Ca/Fe] values using the W_k calcium determination is shown as squares, and the calcium template match is represented by stars. Figure 3.14b is the same plot but with the W_k and template values averaged to reduce the error in the Ca abundance. We are encouraged by the overall agreement in both plots, which suggests that at high S/N our procedure is able to reproduce, in general, abundance results found from high dispersion data. Two notable departures are for the stars HD 167105 and HD 130095. AP has found [Ca/Fe] = -0.21 and [Ca/Fe] = -0.93 for each of these stars, respectively. In both cases our procedure finds calcium abundances that are larger than those found by AP. In the case of HD 130095, this difference is undoubtly due to grid edge effects, since removing the Wheeler shift to retrieve the calcium abundance also shifts the grid edge to -2.55, making it impossible to achieve a [Ca/Fe] value less than -0.53 for this star. HD 167105 is probably discrepant due to the fact that our procedure gives a T_{eff} value that is ~700 K hotter than that found by AP. The higher temperature would predict a weaker CaII K line at a given abundance, resulting in a high calcium abundance determination. Because the CaII K line is more temperature sensitive than the iron lines the higher temperature gives a larger [Ca/Fe] ratio.

As the next step in this investigation, the [Ca/Fe] ratios were calculated for all 21 standard FHB stars. Figures 3.15a-b show the results using both the W_k and Ca template abundances. The curving line is a locally weighted robost smoothing algorithm (LOWESS) meant to illustrate the trend in the data. There appears to be no strong evidence for Ca overabundance in the total sample. To contrast this result, figure 3.15c-d is a plot of [Fe/H] calculated from the calcium lines, using the Wheeler *et al.* relation. From this figure there is clearly an underabundance

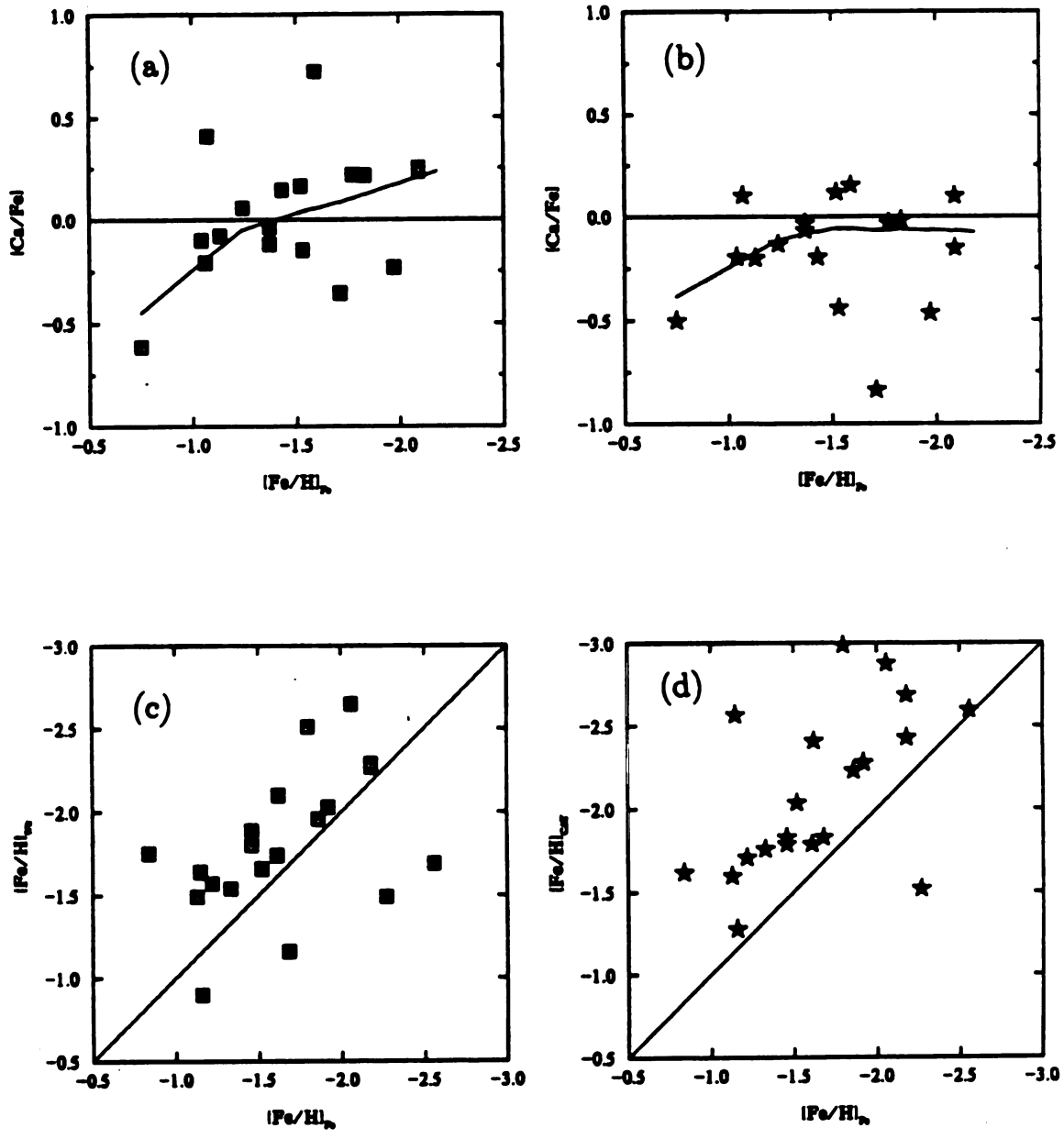

Fig 3.15: The [Ca/Fe] ratio for all 21 FHB standard stars are shown in the top plots, where figures (a) and (b) use the Ca abundance from W_k and CTA, respectively. Figures (c) and (d) show the comparison in the derived [Fe/H] from the three abundance indicators.

relative to [Fe/H] from the metallic line regions. It seems certain that if a trend exists in the [Ca/Fe] ratios for this sample, then it is not consistent with the findings of Wheeler *et al.* If the scatter seen in figures 3.15a-b is not real but instead due to uncertainties in the derived parameters, then on average [Ca/Fe] is approximately zero for the 21 FHB standards. If, on the other hand, at least some of the scatter is real, then our data suggests there is no clear trend of [Ca/Fe] as a function of [Fe/H] in the FHB stars, in agreement with the findings of AP. Real scatter could be the result of primordial differences in the [Ca/Fe] ratio, but is more likely due to diffusion effects, as seen in the slowly rotating Am stars. The diffusion hypothesis is particularly appealing since slow stellar rotation is also observed for the FHB stars.

Whether or not the scatter in the FHB [Ca/Fe] ratio is real, it appears that in the mean, Ca is not significantly overabundant compared to Fe in the FHB stars. This is in agreement with the recent findings of Gray and Corbally (1995) for their sample of HB stars in several globular clusters. This result will be investigated further in Chapter 4.

3.5 Low Signal-to-Noise Analysis

In the previous section it was shown that accurate stellar physical parameters can be derived using the new calibration grid, and that these parameters are of sufficient accuracy to effectively separate the FHB and A-type populations. The standard stars used, however, have spectra of relatively high S/N. The program stars for which this technique was devised have available spectroscopy of nonuniform S/N with values between 10 and 20. It is of interest at this point to attempt to quantify how much affect low S/N has on the final parameter values. The chief concern is the ability to calculate reliable values for $D_{0.2}$, because the separation technique depends critically on the position of overlap between the photometric indices and

$D_{0.2}$ line width in the log g - T_{eff} plane. Kinman *et al.* (1994) have compared the $D_{0.2}$ widths they derive for FHB/A stars that are in common with Sommer-Larson *et al.* (1989), who measured $D_{0.2}$ from lower S/N spectra (100 counts at CaII K). In their paper, Kinman *et al.* show that a large amount of scatter exists between the two data sets and interprets this as the Sommer-Larson group's inability to measure precise $D_{0.2}$ widths from low S/N spectra. In this section we address this concern by presenting a detailed analysis of the effects of low S/N on the derived physical parameters, as well as, analysis of a smoothing technique used to improve this precision.

3.5.1 Line Widths

Gaussian noise was added to the synthetic spectra that were originally computed for the grid calibrations. The two values of signal-to-noise chosen, S/N = 10 and S/N = 14, reflect the minimum and typical S/N values for our data set. As an illustration, Figure 3.16a shows the synthetic spectrum for T_{eff} = 8000, log g = 3.0, and [Fe/H] = -1.5. Figure 3.16b is a plot of the same spectrum but with Gaussian noise of S/N = 10 added. For comparison the spectrum of II-90, a BHB star in the globular cluster M10 with similar S/N, is shown in figure 3.16c.

Figures 3.17a and 3.17c show the effect low S/N has on the measured $D_{0.2}$ width of the Hδ line. These plots are the difference values between $D_{0.2}$ for infinite S/N spectra and S/N = 10 and S/N = 14, respectively. Along with the large amount of scatter, we see a great number of values that are significantly in error. The asymmetric trend of higher $D_{0.2}$ widths for the low S/N data is an artifact of the Voigt fitting routine. In order to reach the true continuum level for the cooler stars and the stars of higher metal abundance, it was necessary to remove metal lines in the local continuum by smoothing out those pixel values that have greater than

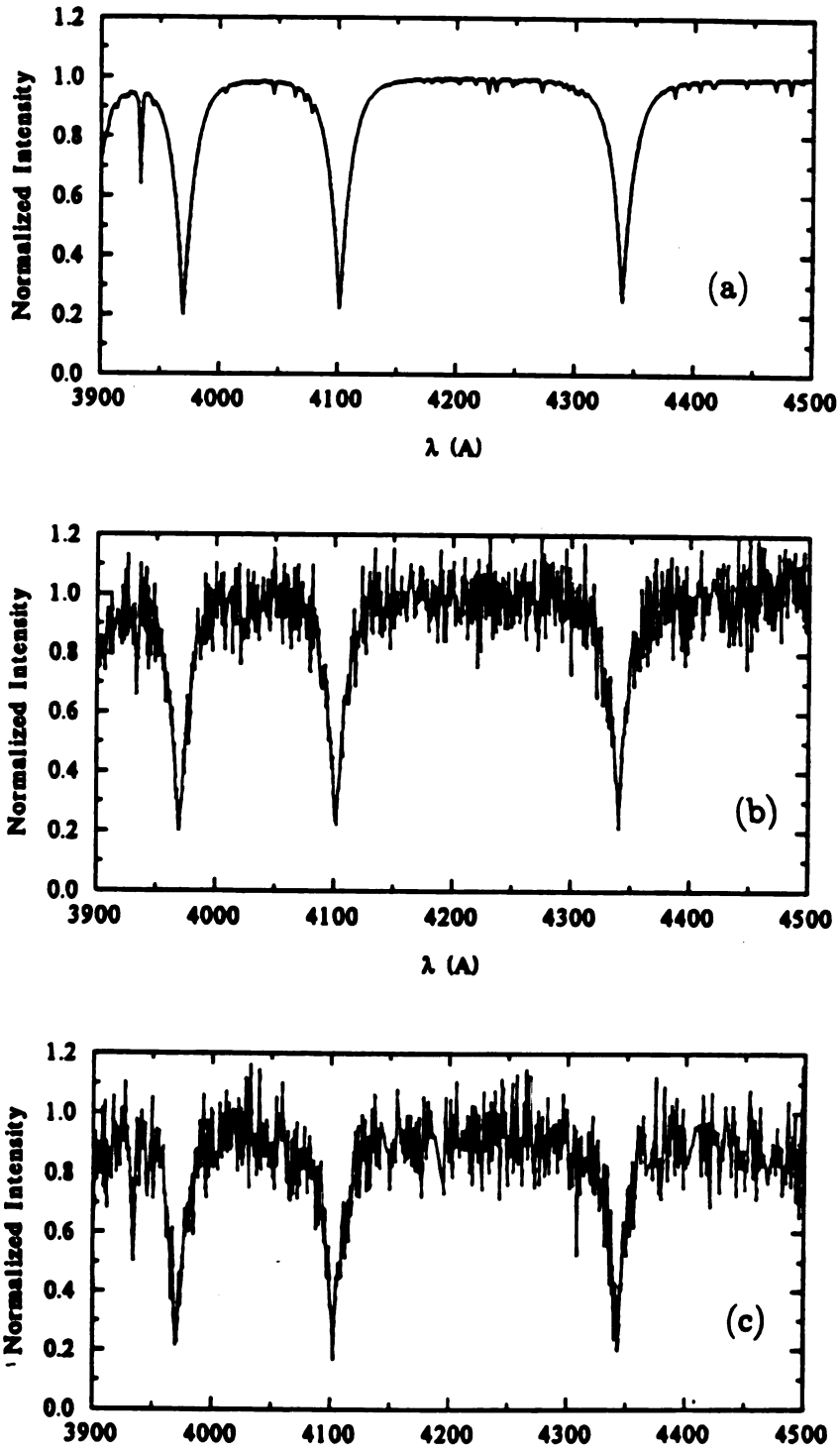

Fig 3.16: Comparison of a noisy synthetic spectrum (S/N = 10) to real low-S/N data. Figure (a) is a normal synthetic spectrum, (b) the same spectrum but with Gaussian noise added, and (c) a spectrum of II-90 in M10.

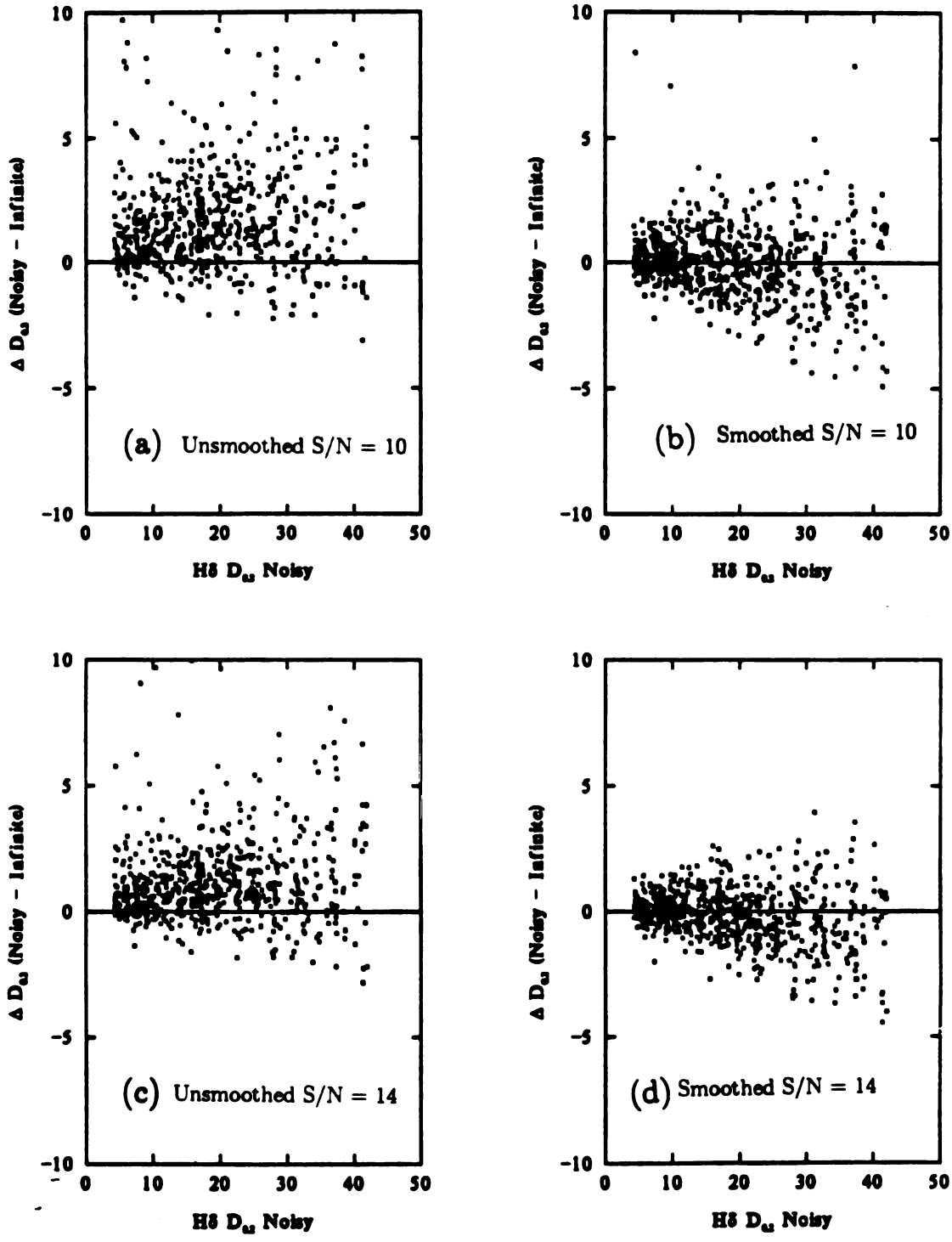

Fig 3.17: Noise induced scatter in Hδ for unsmoothed and smoothed cases.

1σ standard deviation below the average continuum mean. This process, however, asymmetrically smooths the noise when the S/N values become sufficiently low by also trimming the lower portions of the continuum noise. The result is to force the average continuum level up and increase the $D_{0.2}$ values.

To better constrain the continuum level the same noisy synthetic spectra were smoothed using a smoothing routine by Hayden (1987). The Hayden routine deconvolves the noise spectrum from the ideal spectrum by removing variations that are too rapid to be correlated with the instrument response function. This procedure optimally removes the root n noise while minimally broadening the spectral features. Also, as an attempt to rectify the asymmetrical trimming problem, deviant values were trimmed both above and below the average local continuum level. Figures 3.17b and 3.17d are plots of the smoothed $D_{0.2}$ widths compared to the infinite S/N widths. It is immediately evident that the significantly erroneous values have been removed. The scatter about the zero line has also been reduced.

Figures 3.18a-d are the same plots but with the difference values expressed as a more meaningful fractional difference. The fractional difference was computed by dividing the difference value by the actual $D_{0.2}$ width for the infinite S/N spectrum. This shows that the relative error in $D_{0.2}$ is smallest for the broadest lines, as would be expected. The 1σ scatter for the unsmoothed data is found to be 26% and 12% for S/N = 10 and 14. The combination of the Hayden smoothing and improved continuum placement has greatly reduced the scatter for the smoothed data which has variations of only 10% and 6% for S/N = 10 and 14.

Figures 3.19a-d are plots of the fractional differences in the CaII K line equivalent width for low S/N values. As with $D_{0.2}$, the smoothing routine has helped to reduce the scatter in W_k. The standard deviation constrained to $W_k > 1.0$ Åfor

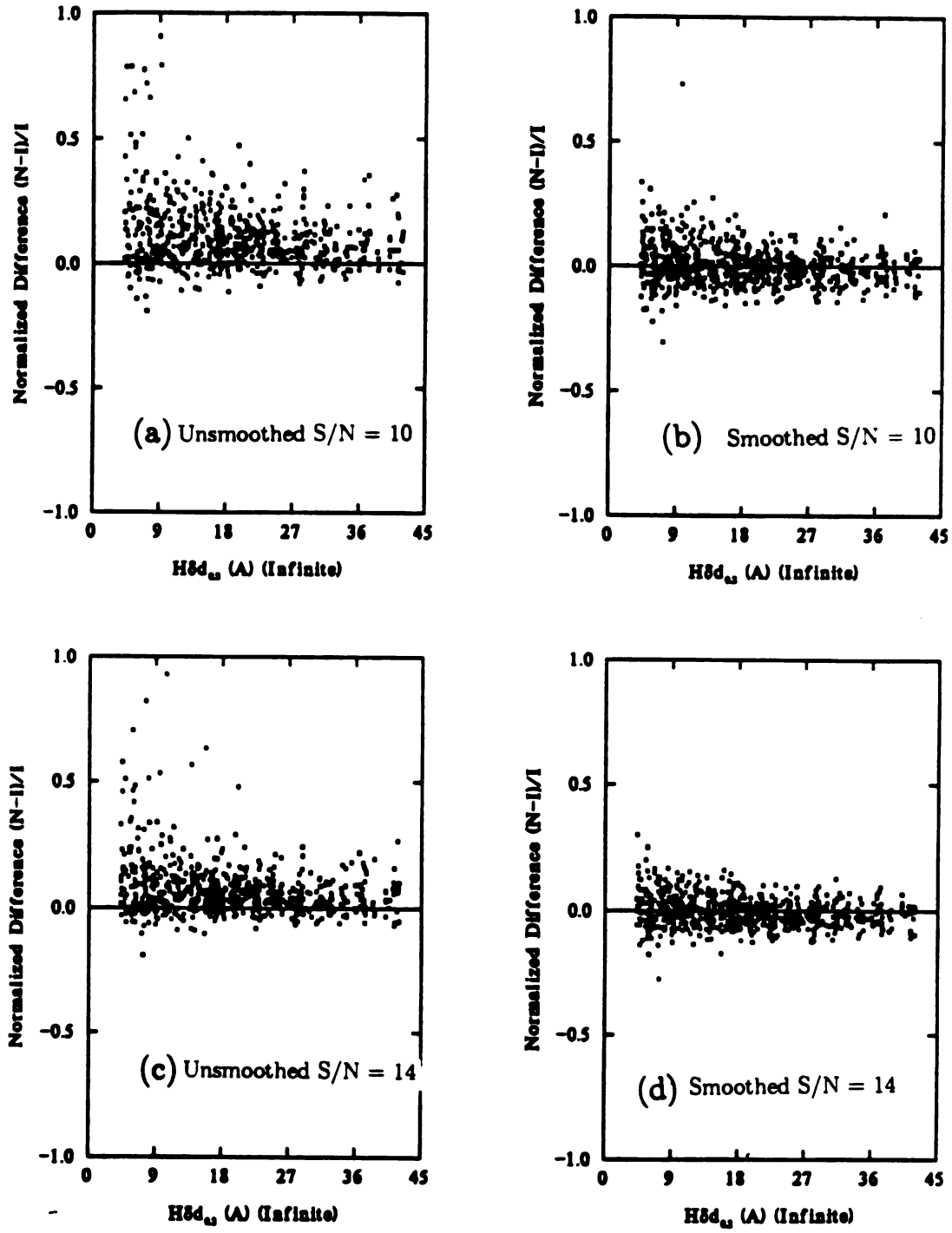

Fig 3.18: Same as Fig 3.17, but plotted in terms of the normalized fractional difference.

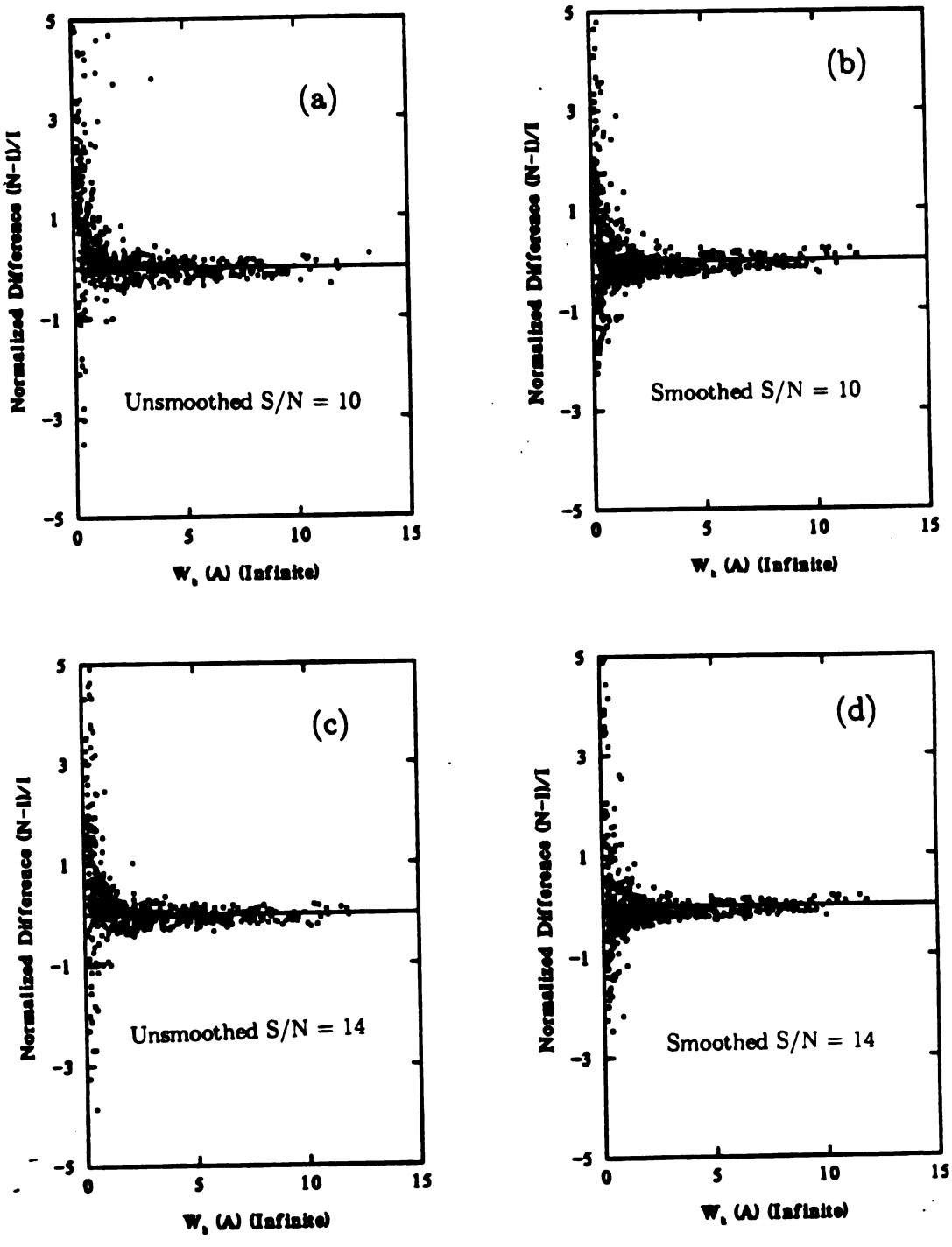

Fig 3.19: Noise induced scatter in W_k for the unsmoothed and smoothed cases.

S/N = 10 has decreased from 99% to 44% for the smoothed data while a decrease from 40% to 18% has been achieved by smoothing of the S/N = 14 data. Although the smoothing has decreased the scatter in the larger W_k measurements, for values of $W_k < 1.0$ Å the scatter due to noise still amounts to errors of several hundred percent in the extremely deviant cases. In this region, the noise has become nearly as big as the CaII K line itself resulting in a Voigt fit to the line that is noise dominated. As will be shown in the following sections, the metal abundance determination becomes very uncertain at small values of W_k primarily due to this effect.

3.5.2 Effects on the Derived Parameters

With an understanding of how S/N affects the derivation of the line parameters we next consider the effect these uncertainties have on the estimation of the physical parameters. The values for the line widths found in the previous section are used as input values for the calibration comparison technique. The uncertainty in the line widths, found from the standard deviation computed in the last section, is set to ± 6% of $D_{0.2}$ and 30% for W_k. Since, we first wish to quantify the effects of low S/N spectra, the exact values for the photometric colors that correspond to each input synthetic spectrum were used.

Figures 3.20a-d show the effects on the estimated value of T_{eff} for the noisy and smoothed spectra at each value of S/N. The difference in the derived T_{eff} value and the value from the input model atmospheres were calculated and averaged for each temperature. The error bars indicate the 1σ standard deviation of the individual data points from the average (Note: Not the standard deviation of the mean). In all the plots, the derived T_{eff} values are systematically too high. Removal of the asymmetric scatter in $D_{0.2}$ for the smoothed data has clearly helped this situation.

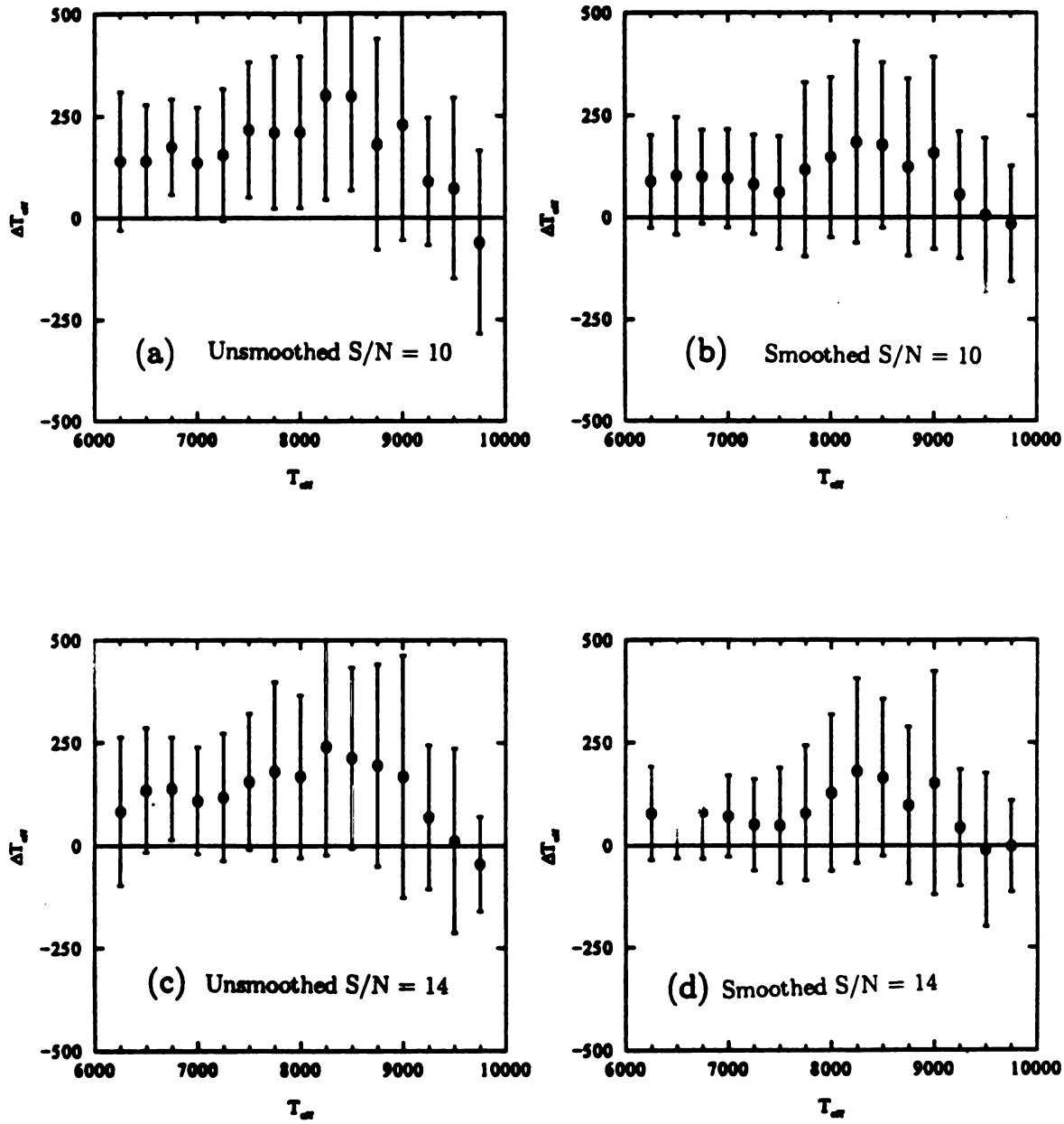

Fig 3.20: Noise induced scatter in T_{eff} for the unsmoothed and smoothed cases. (Note: The error bars indicated 1σ scatter and NOT standard deviation of the mean)

For the smoothed data the temperatures are on average ~70 K to high. Since there is no apparent systematic problem with the smoothed $D_{0.2}$ values this is probably an artifact of the weighted calibration technique.

We expect that the scatter in T_{eff} is a combination of the weighting scheme employed and errors in the line widths due to low S/N. Below 8000 K the temperature is driven by the (B-V) colors and $D_{0.2}$. The scatter in this range is in part due to the asymmetric scatter found for $D_{0.2}$ in the last section. Supporting this conclusion is the decrease in the deviation for the smoothed data in this range. The peak just beyond 8000 K is due to an inherent problem with the dependency weighted technique. In the transition region, $8250 \leq T_{eff} \leq 8500$ the physical parameters are less constrained than anywhere on the grid. In this range $D_{0.2}$ begins the change from a T_{eff} indicator to a log g indicator, while (U-B) has just lost its log g dependency. Since none of the observables strongly constrain log g in this range and (B-V) alone constrains T_{eff}, small errors in $D_{0.2}$ can allow the identified overlap region to jump as much as 500 K in T_{eff}, usually to higher temperatures where $D_{0.2}$ carries the most weight.

To better investigate these two effects, we examine the errors in T_{eff} caused by the $D_{0.2}$ residuals. Figures 3.21a-b are bubble plots of ΔT_{eff} as a function of T_{eff} with the symbol size representing the residual in the corresponding $D_{0.2}$ width. Figure 3.21a-b shows the results for the unsmoothed and smoothed spectra with S/N = 14. As expected, for $T_{eff} < 8000$ K the large residuals in $D_{0.2}$ have caused large errors in T_{eff} for the unsmoothed data, which are greatly reduced in the smoothed data. Also, we see in the region of $8000 < T_{eff} < 9000$, the largest errors in T_{eff} do not seem to be correlated to the residuals in $D_{0.2}$. This is the area where the T_{eff} is not as strongly constrained.

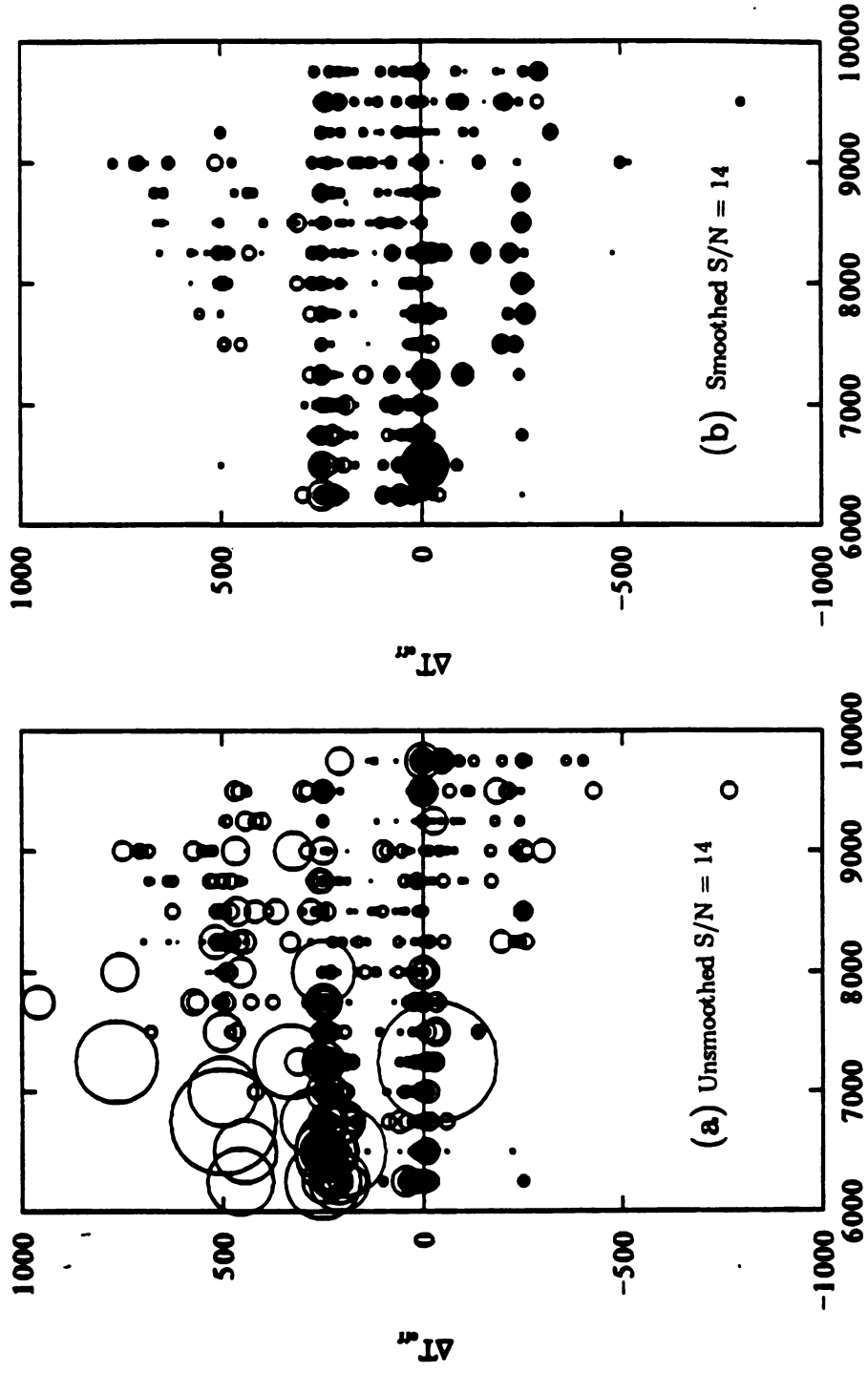

Fig 3.21: Bubble plot showing the effects of errors in $D_{0.2}$ on the derived T_{eff}.

Bubble size is correlated to residual in $D_{0.2}$.

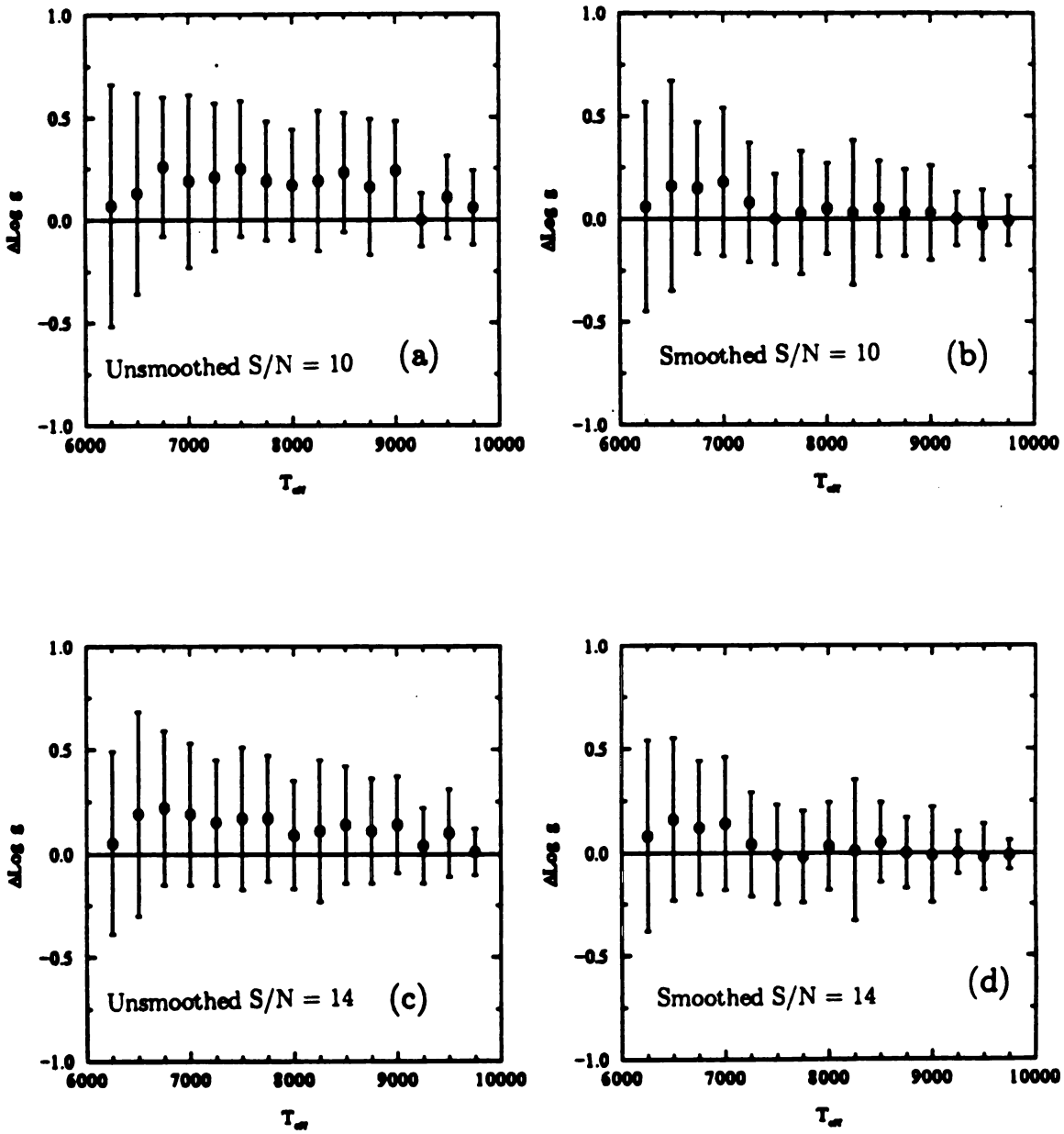

Fig 3.22: Noise induced scatter in Log g for the unsmoothed and smoothed cases.

Figure 3.22a-d is a series of plots showing the effects on log g. Systematically, the log g values remain quite accurate throughout. The scatter is also very low especially for $T_{eff} \geq 8000$ K where $D_{0.2}$ takes over as the primary surface gravity indicator. The problem of the systematically high T_{eff} values do not effect this outcome since $D_{0.2}$ is virtually temperature independent in the range of 8000 - 9000 K. For $T_{eff} < 8000$ K uncertainties in $D_{0.2}$ can influence the temperature and thus indirectly affect the log g determination. This shows up as the smaller scatter in log g for the smoothed data solutions. At the lowest temperatures the large uncertainties in log g are primarily due to degeneracy in (U-B) for some metallicities, meaning small errors in $D_{0.2}$ and W_k can affect the assigned log g.

Figures 3.23a-d are again residual plots for the S/N = 14 spectra. Figures 3.23a-b show Δ log g as a function of T_{eff} with the $D_{0.2}$ residuals represented by the symbol size. At lower temperatures, large $D_{0.2}$ residuals help to drive the errors in log g as can be seen in the smaller residuals and scatter in log g for the smoothed data. For $T_{eff} > 8000$ the errors in log g and the residuals are both quite small. Figures 3.23c-d are the same plots but with the residuals representing the errors in T_{eff}. For $T_{eff} < 8000$ we again see the errors in log g correlated to the errors in temperature. This isn't surprising since the $D_{0.2}$ and T_{eff} residuals are not independent. For the higher temperatures the relatively large T_{eff} residuals appear to have only a small effect on the scatter in log g.

Finally, figures 3.24a-d shows the affects on the derived metal abundance. Again, systematically the metal abundance remains accurate. A slight hump in the range $8250 \leq T_{eff} \leq 8500$ K can be seen in most of the plots and is undoubtedly due to the error in T_{eff}. For $T_{eff} < 8000$ K the uncertainties are driven mainly by uncertainty in the local continuum. This is why the higher S/N plots show less

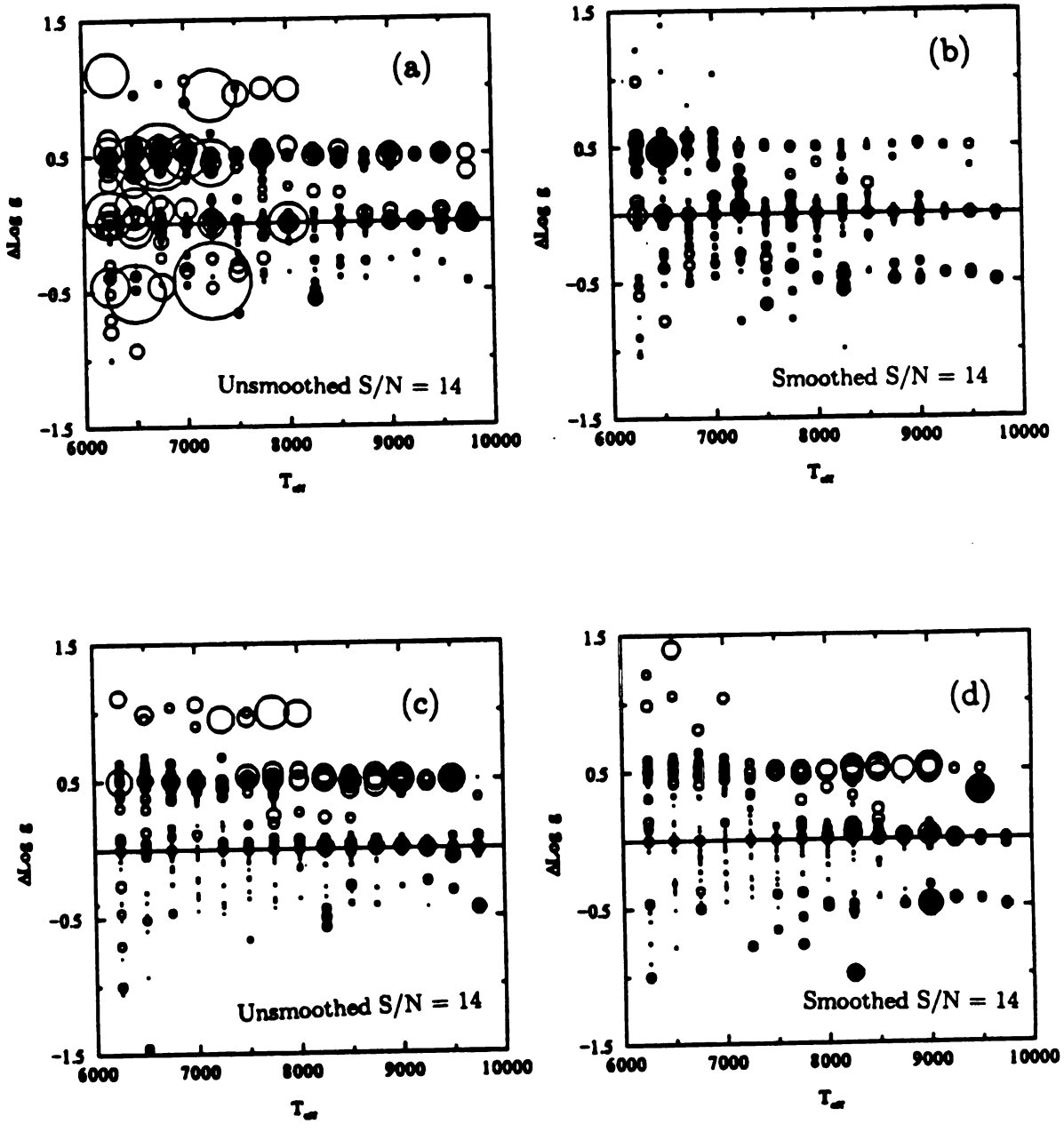

Fig 3.23: Bubble plot showing the effects of errors in $D_{0.2}$, (a,b), and T_{eff}, (c,d), on the derived log g.

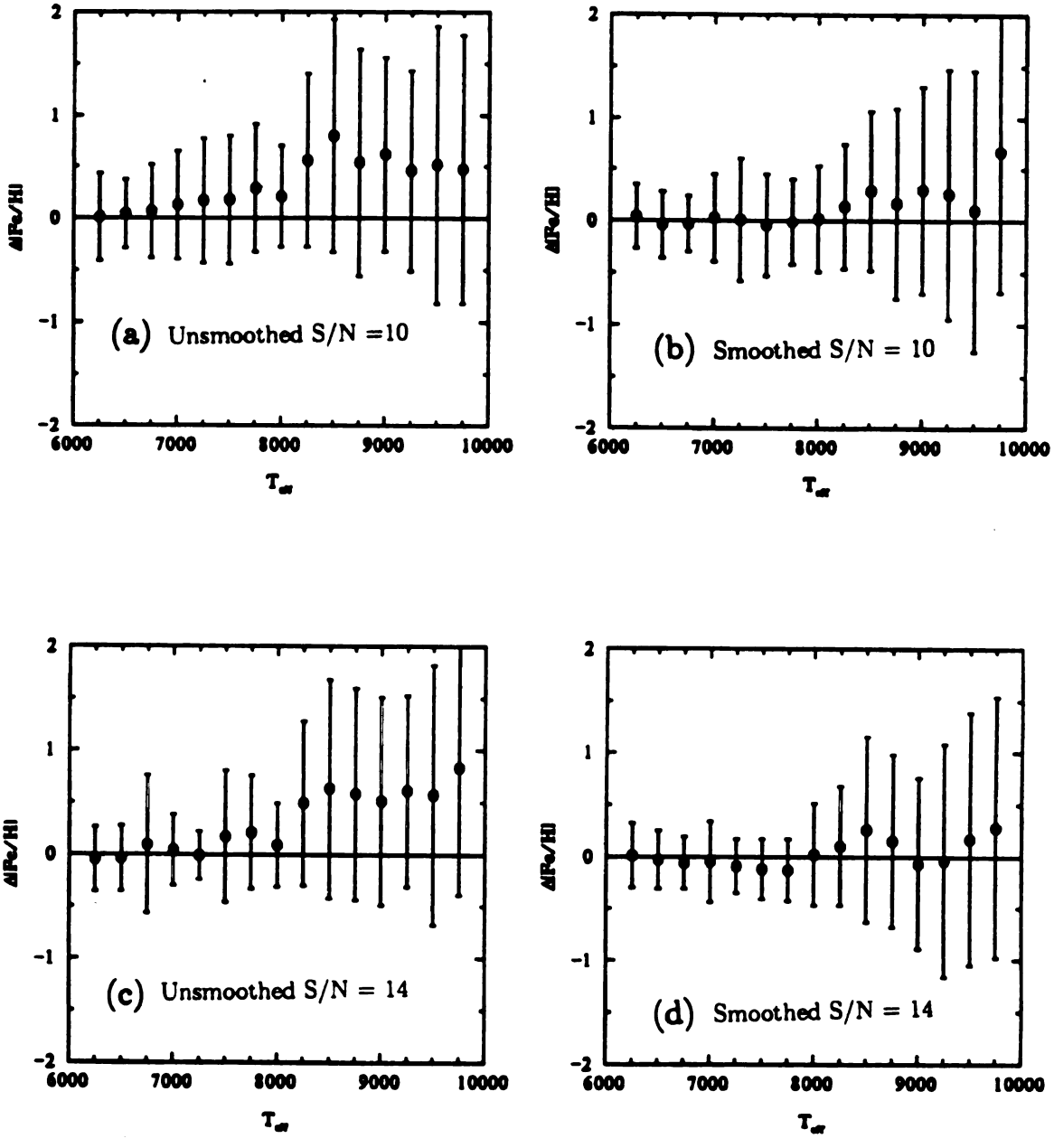

Fig 3.24: Noise induced scatter in [Fe/H] for the unsmoothed and smoothed cases.

scatter in this region and why the smoothed data show less scatter then the corresponding unsmoothed data. Above 8000 K the uncertainty in [Fe/H] becomes quite large. We will show in the next section that uncertainties in T_{eff} probably have little to do with this outcome. Instead, as was found from the S/N analysis of W_k, the noise dominated Voigt fit causes large uncertainty in W_k and thus large uncertainty in [Fe/H].

Figures 3.25a-b are bubble plots with the residual in W_k representing the symbol size. It is clear that the largest residuals in W_k occur at the higher temperatures and are correlated to the largest errors in [Fe/H]. Figures 3.25c-d are the same plots but with the symbol size representing the residuals in T_{eff}. Now the largest residuals occur in the range of $8000 < T_{eff} < 9000$ and are clearly related to the T_{eff} errors from the grid comparison technique. The large scatter associated with the noise domination of W_k has caused errors in [Fe/H] that are unsatisfactory at higher temperatures. We therefore attempt to improve the precision in [Fe/H] by investigating secondary abundance indicators.

As discussed in the standard star section, a template comparison technique has been developed to calculate metal abundance from the CaII K line and metallic-lined regions that include mainly iron lines. Since the derived χ^2 fit is the result of fitting the entire line profile the resultant [Fe/H] value is more resistant to noise effects than is the equivalent width from a functional fit. To first order the template fitting routine is independent of the S/N since the noise detracts from the overall goodness- of-fit but not the identification of the χ^2 minimum. Figures 3.26a-b show the results for the CaII K template fit and the fit to the metallic regions for the S/N = 14, smoothed spectra. We see in both plots that the overall abundance determination is much better, especially at the high temperature end. The overall

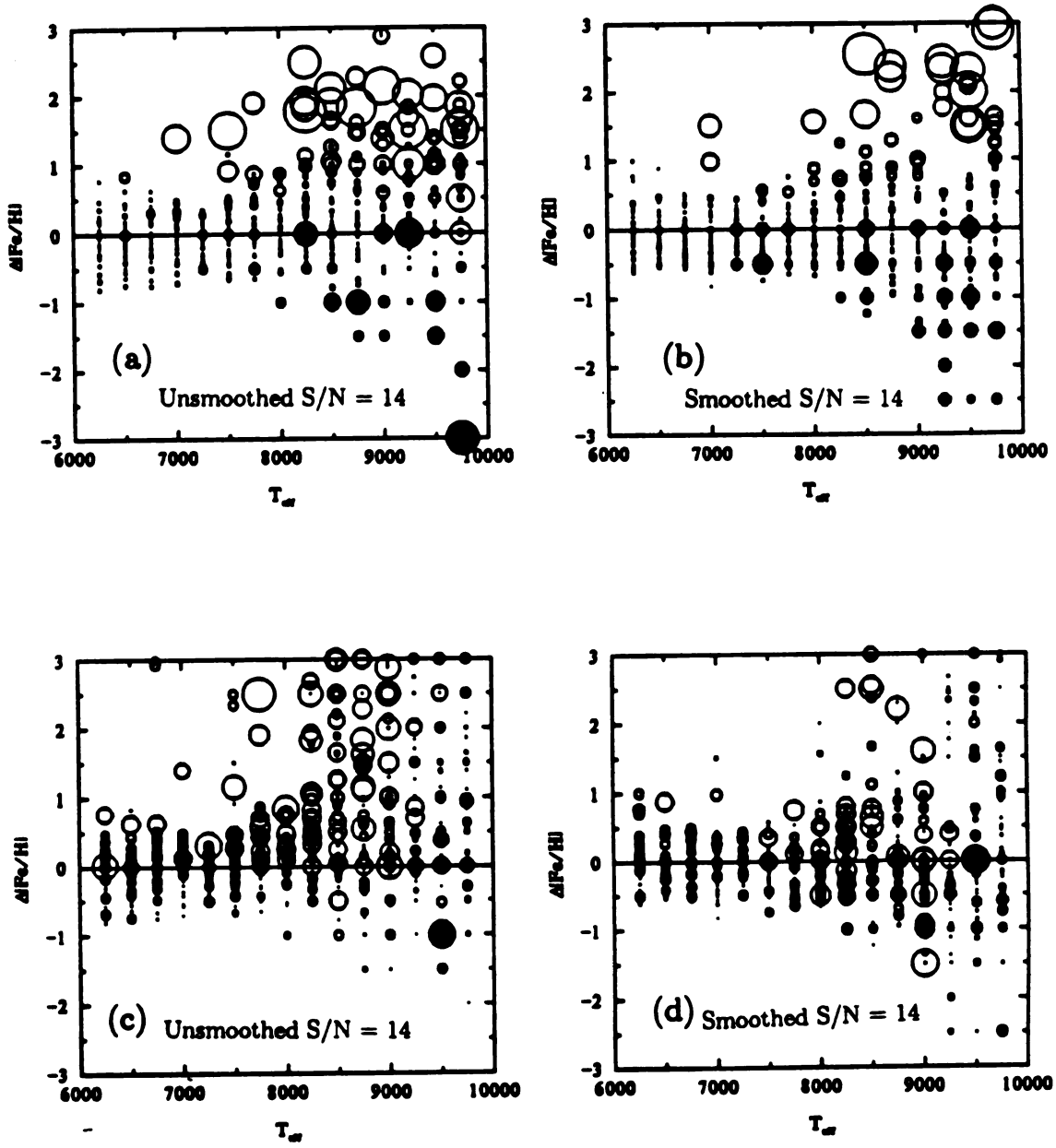

Fig 3.25: Bubble plot showing the effects of errors in W_k, (a,b), and T_{eff}, (c,d), on the derived [Fe/H].

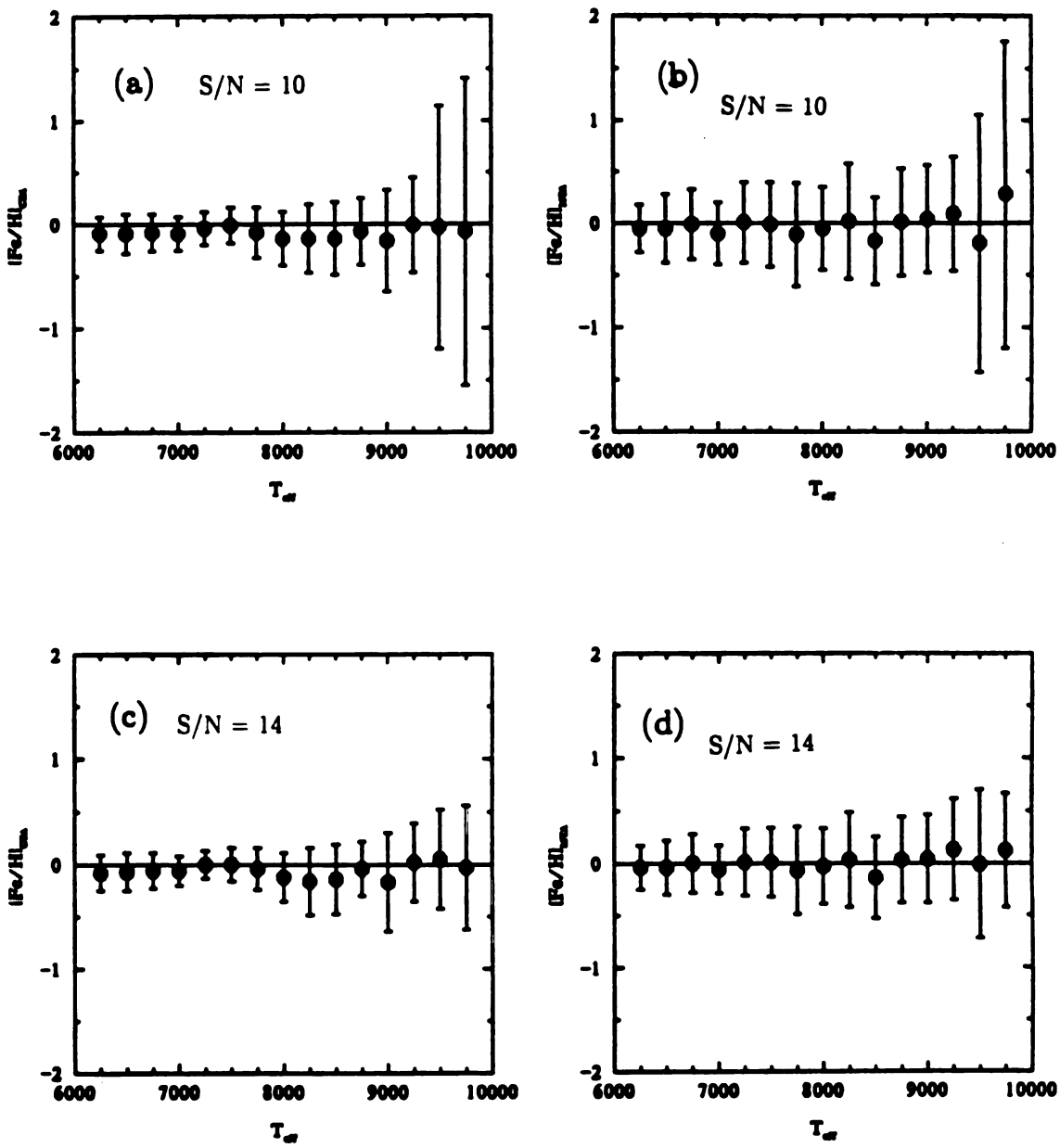

Fig 3.26: The scatter in the CTA and MTA abundances at S/N = 10 and 14.

scatter in the Ca template comparison is quite small and only becomes large for $T_{\rm eff} > 9500$ K. Though overall the metallic line fit shows more scatter, it still remains quite effective at high temperatures. From plots of the Ca comparison it is also clear that the errors in $T_{\rm eff}$ are not the dominate cause of the large uncertainties found in the $W_{\rm k}$ derived abundances, since the same input $T_{\rm eff}$ and log g were used for both. There is a small increase in the scatter for the Ca template comparison at $T_{\rm eff} = 8250$ and 8500 K. But this increase amounts to a scatter of only ~ 0.2 dex.

The template comparison results would seem to indicate that this method is superior to the $W_{\rm k}$ grid comparison technique. However, there are two hidden sources of error. The first is error due to the continuum placement. As the S/N becomes low it is increasingly difficult to define the level of the continuum. When normalizing the continuum it is also difficult to keep low frequency continuum fluctuations from occurring. Since the template comparison finds the difference in the normalized flux values at each pixel across the range, either effect can cause errors to arise in the derived metal abundance. To help the situation the average flux value for the noisy continuum is found and the template continuum is corrected to match this level. However, the continuum fluctuations are not corrected and can still be a source of error. This effect is not seen in the previous analysis since, presumably the underlying continuum in the noisy synthetic spectra still precisely match that of the infinite S/N spectra. Another source of error is the stellar radial velocity. In order for the template to match the observed spectrum it is necessary to take into account the shift in the spectral features due to the doppler effect. Although at medium resolution spectral features are broadened to a point where small scale errors in the radial velocity have little effect, if an error of greater than 30 km/sec is made the effect becomes significant and results in an abundance underestimate,

since the observed and template spectral features do not match up. This is also not seen in the previous analysis since both spectra have zero velocity.

Because of these hidden uncertainties in the template comparison technique, the W_k grid comparison is still used as our primary abundance indicator for setting the values of T_{eff} and log g. However, before determining the final abundance the values from W_k, the Ca template comparison, and the metallic region, are compared and the two most consistent values are averaged and a [Fe/H] value is found. We expect improved accuracy in the abundance determinations from this average because, the scatter in the template abundances that occur from uncertainties in the continuum placement and the radial velocities are not necessarily correlated with the S/N problems seen at high T_{eff} values in the W_k derived abundances.

The final step in this discussion is to add noise to the photometric colors in an attempt to mimic the true observable uncertainties. Gaussian noise with one sigma deviation of ± 0.03 was added to the color values from the calibration grid and together with the line widths from the noisy synthetic spectra were used as input for the grid calibration technique. The results can be found in figures 3.27a-d. As might be expected the overall scatter in T_{eff} has increased. The worst scatter is evident in the region where the observable dependency is the lowest. The overall scatter in T_{eff} still remains fairly good at ± 217 K. The log g determination also remains very good with only a slight increase in scatter for the lower temperatures where log g is determined primarily by (U-B). The overall scatter in log g is found to be ± 0.28. The overall scatter found in [Fe/H] derived from W_k remains nearly the same with [Fe/H] = ± 0.62. Figure 3.27d shows that the scatter in [Fe/H] using the averaging technique is about half this amount at ± 0.32 dex.

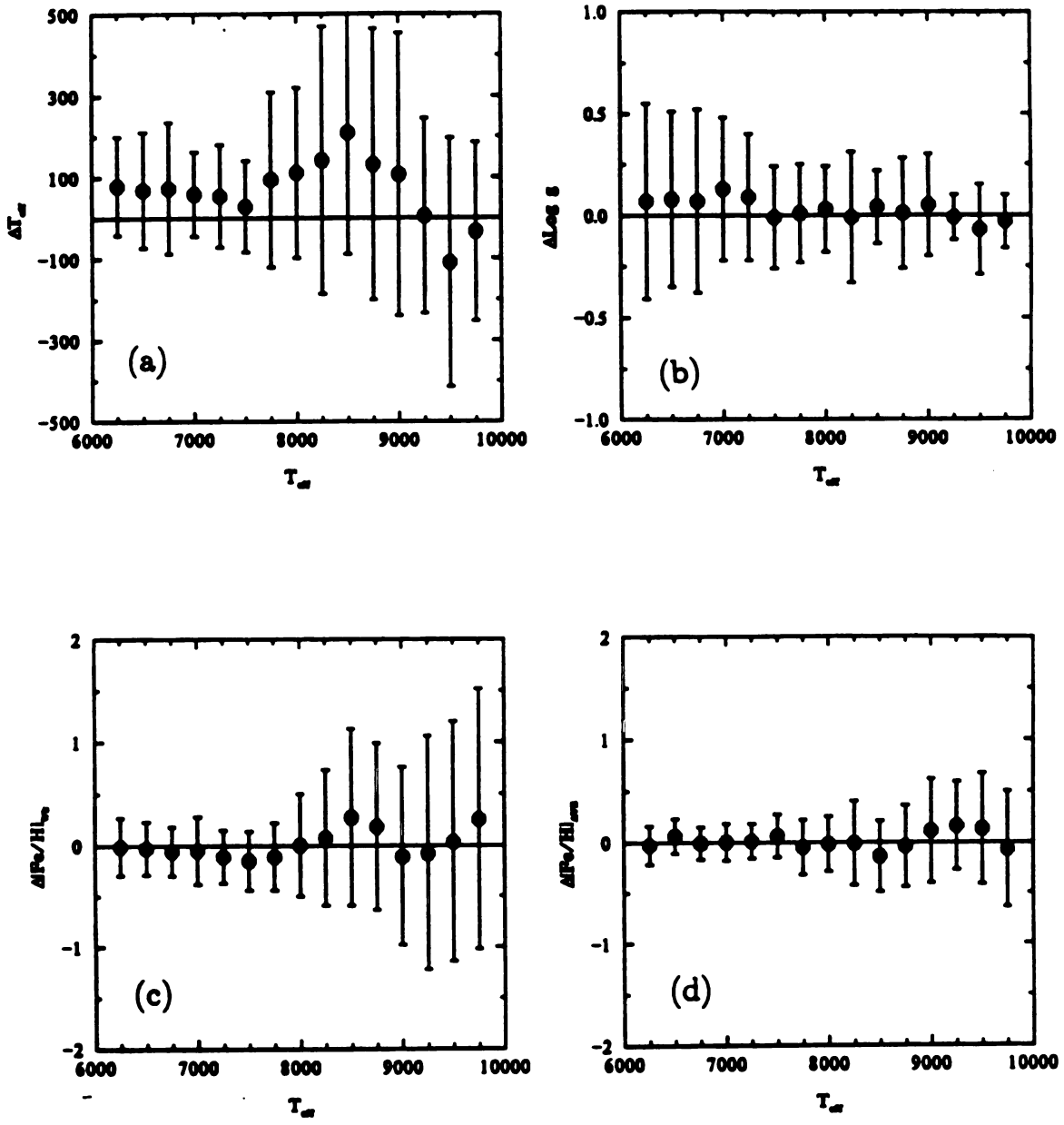

Fig 3.27: Scatter in the derived physical parameters taking into account both the low S/N spectroscopy and uncertainty in the UBV photometry. All figures using smoothed, S/N = 14 results.

3.5.3 Misidentifications

Using the last output values for T_{eff} and log g it is now possible to test the number of misidentifications that would have occurred had these been real program stars by comparing their positions on the log g-T_{eff} plot with the same stellar class limits as in section 4. We have assume an uncertainty in log g of ± 0.24, slightly lower than the overall value above, in order to match the smaller scatter found at $T_{eff} > 6750$ K. Figures 3.28a-b show the results at log g intervals that would be consistent with FHB and main sequence surface gravities. We find some misidentification has occurred in the temperatures cooler than 8000 K, but virtually no misidentifications at higher temperatures. If we assume the majority of FHB stars will lie in the range of $2.5 \leq \log g \leq 3.0$, then the total number of points, with input log g values consistent with FHB stars, is 210. The number that have been misidentified as main sequence stars is 17. This amounts to 8% of the total input FHB stars. Using the range $3.5 \leq \log g \leq 4.0$ to characterize the A-type stars we find misidentification in 10 test stars, giving a percentage 5%. Therefore, at S/N values and photometric uncertainties consistent with our typical program stars, we estimate class misidentification to be no more than 8%. This value is slightly higher than the 4% found from the standard star results, as might be expected. It is somewhat reassuring that all misidentification have occurred in the cooler temperatures, consistent with the standard star findings.

3.5.4 Abundance comparisons for the Globular BHB stars

Over the past two years we have made spectroscopic observations of 17 blue horizontal branch stars and 1 RR Lyrae variable. The S/N values for most of these stars are in the same range ($10 < S/N < 20$) as the program stars. T_{eff}, log g and [Fe/H] values were found for all the stars and the results are listed in Table

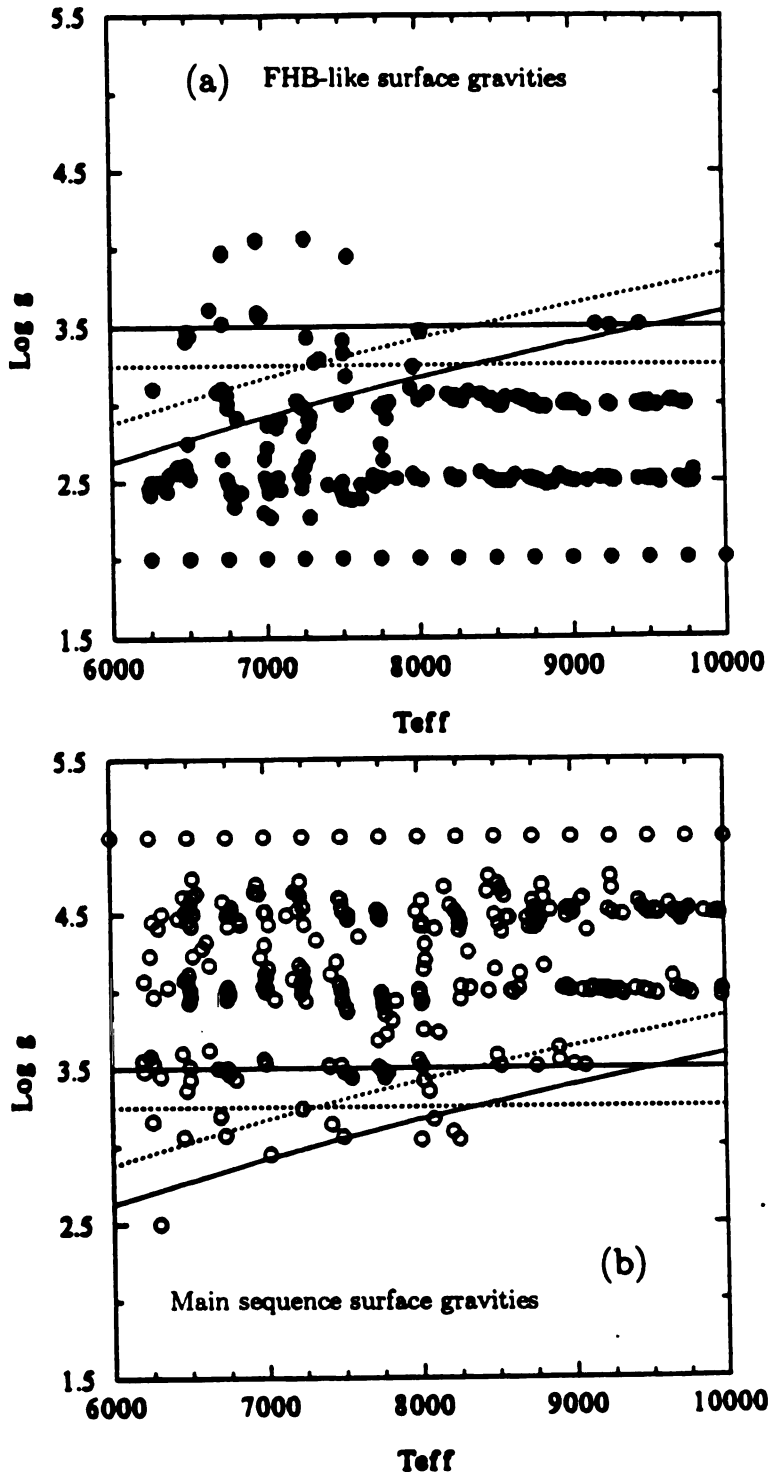

Fig 3.28: Estimate of class misidentification using values from the noisy synthetic observables.

Table 3.5. Globular BHB results.

Star (1)	T_{eff} (2)	Log g (3)	$[Fe/H]_{Ave}$ (4)	$[Fe/H]_{W_k}$ (5)	$[Fe/H]_{CTA}$ (6)	$[Fe/H]_{MTA}$ (7)	$\Delta[Fe/H]$ (8)
M 4 2602	7766	3.2	-1.4	-1.4	-1.5	-1.1	-0.1
M 4 2612	6763	2.5	-0.6	-0.7	-1.0	-0.5	0.7
M 4 2613	9084	3.5	-1.1	-1.1	-1.0	-1.6	0.2
M 4 2614	8031	3.4	-2.1	-2.1	-2.1	-1.2	-0.8
M 4 2616	7537	3.4	-1.3	-1.3	-1.3	-0.7	0.0
M 4 3633	8036	3.7	-1.2	-1.2	-1.2	-1.0	0.1
M 5 II-78	7507	2.5	-1.6	-1.6	-1.8	-1.7	-0.2
M 5 IV-20	8074	3.0	-1.8	-1.8	-1.9	-1.7	-0.4
M 10 II-90	7729	3.5	-1.9	-1.9	-1.6	-1.9	-0.3
M 13 J11	7476	2.6	-1.7	-1.6	-1.9	-1.2	-0.1
M 13 J52	8014	3.0	-2.2	-2.2	-3.0	-2.2	-0.6
M 22 1-31	7655	3.5	-1.7	-1.7	-1.6	-2.3	0.1
M 22 1-32	8227	3.9	-1.4	-0.9	-1.3	-1.4	0.4
M 22 1-38	7287	2.4	-1.7	-1.7	-1.7	-1.6	0.1
M 22 1-39	7754	3.0	-1.5	-1.3	-1.8	-3.0	0.2
M 92 IV-27	7750	3.4	-2.0	-1.9	-2.1	-2.0	0.2
M 92 VIII-30	8381	3.0	-2.1	-2.0	-2.2	-3.0	0.1
M 92 Bu468	8949	3.5	-1.5	-1.0	-1.6	-1.5	0.7

3.5. Columns 1-3 are the star name, Teff, and log g. Columns 4-7 are the derived abundances from the adopted average value, as discussed above, and each of the abundance indicators. Column 8 lists the difference between the average abundance and the cluster's published value.

For many of these stars, no U magnitude could be found in the literature, and the (U-B) color was estimated from the fiducial fit to the clusters color-color diagram. Because of this, there are expected to be large uncertainties and even systematic errors in the surface gravity values. Therefore, the values of log g that have been found offer little insight into the procedures ability to identify horizontal branch stars. Since the abundance determination depends only indirectly on a star's (U-B) color it is possible, however, to investigate our ability to predict metallicity at low S/N. This is especially important because it offers a chance to fully test the template comparison technique.

In the following analysis, two stars, M4 2612 and M4 2614, have been excluded. M4 2612 is our only RR Lyrae variable which was serendipitously on the slit during another observation. Though analyzed it has a lower S/N ($\sim$5) then is indicative of our program stars. M4 2614 has a close stellar neighbor that could not be separated, probably causing blending effects. Figures 3.29a-c are plots of the difference between the published and calculated [Fe/H] values, from each of the abundance indicators, for the BHB stars as a function of the published [Fe/H] values. The dashed lines indicate the 1σ scatter. It is evident that the metal abundances from the two calcium indicators suffer from the least amount of scatter ($\pm$0.46 for both), while the metallic line regions has slightly more ($\pm$0.54). For each abundance determination technique there are a few stars with relatively large errors in their metallicity determinations. However, seldom do any two techniques have severe departures for the same star.

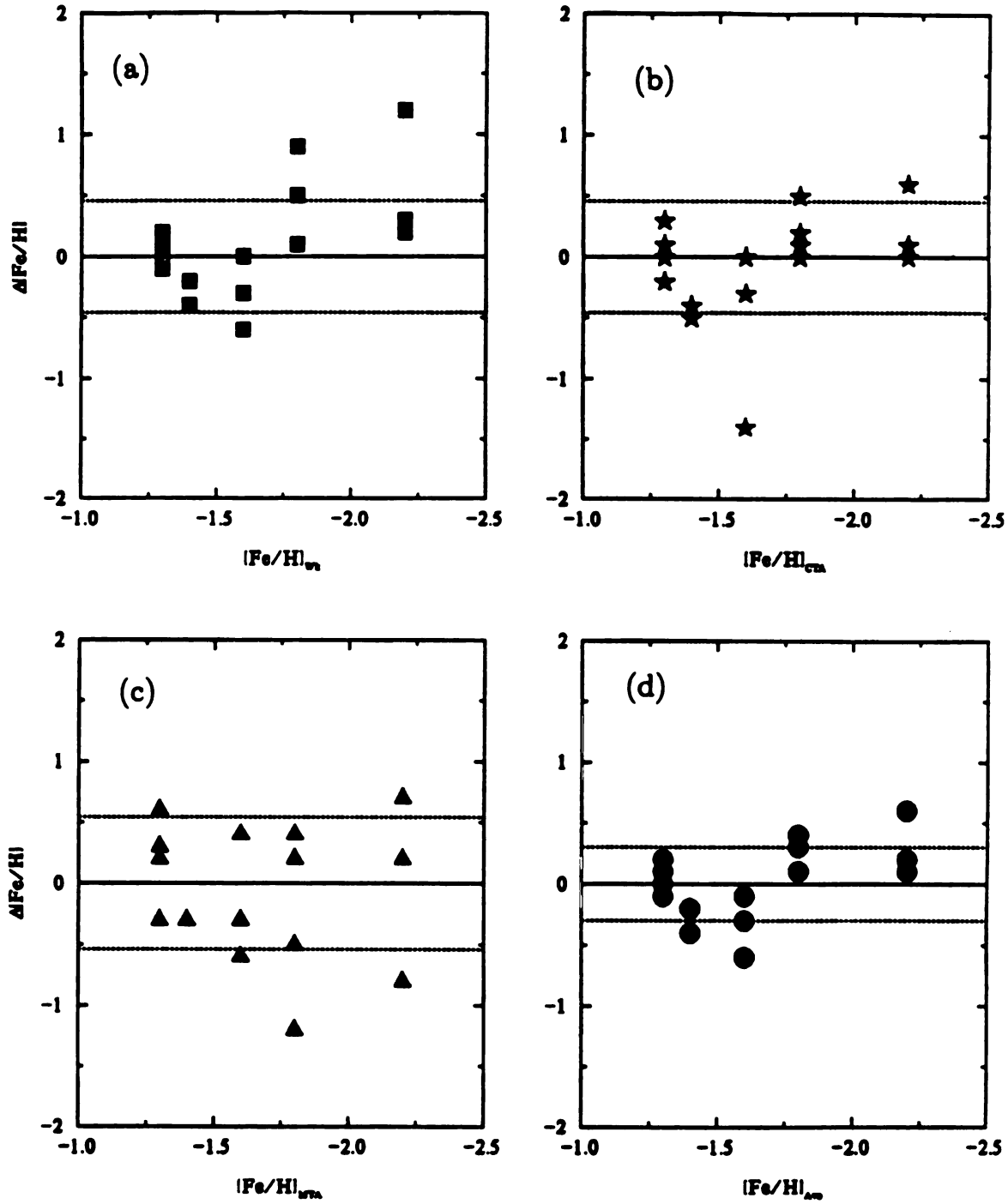

Fig 3.29: Scatter in the abundance indicators for the globular cluster BHB stars. Abundances from W_k (a), CTA (b), MTA (c), and Average (d) are shown. The dotted lines indicate the 1σ deviation.

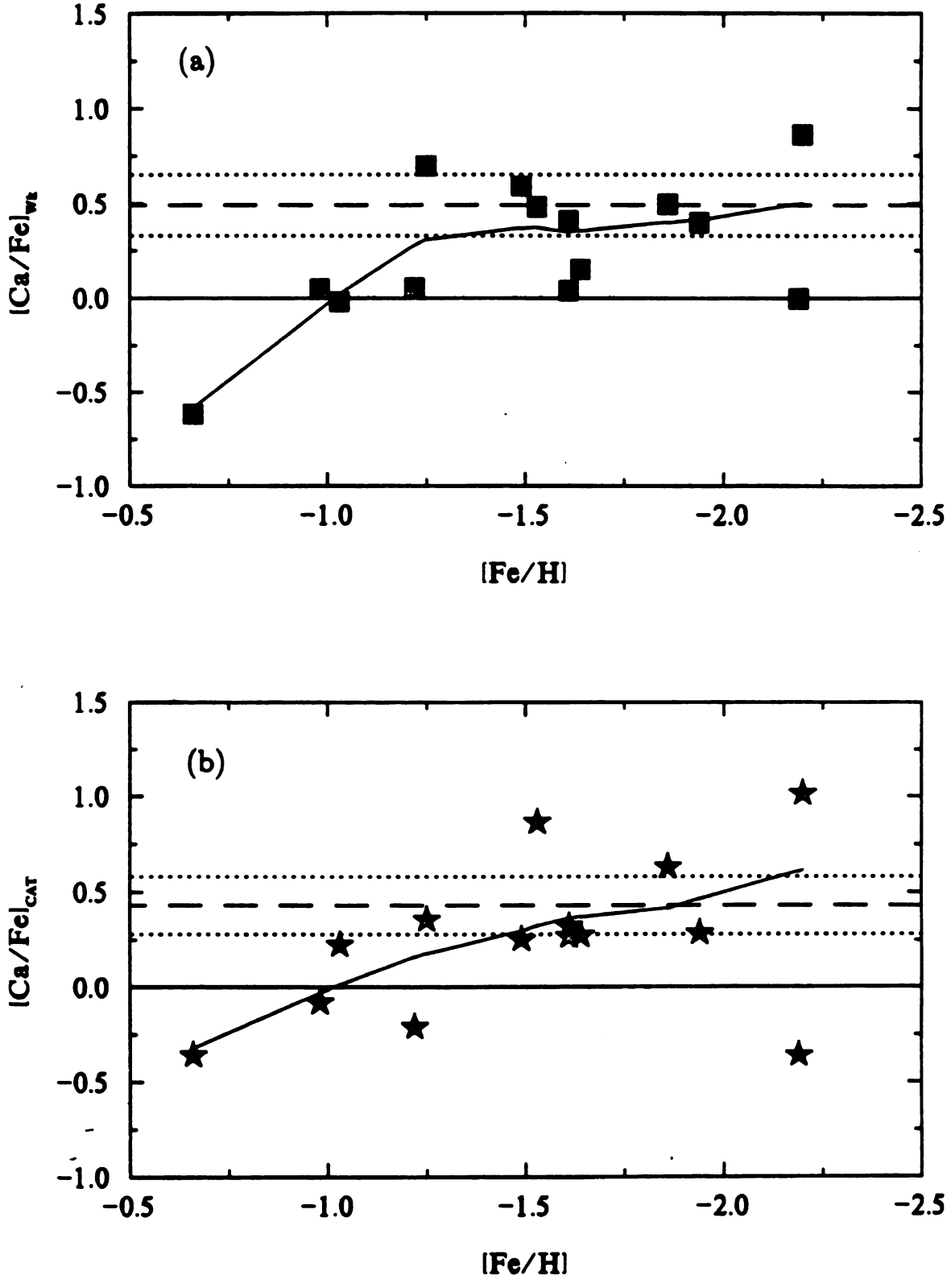

Fig 3.30: [Ca/Fe] ratios for the globular cluster BHB. Dashed line indicates average value and dotted line the error in the mean.

Figure 3.29d is the same plot but for [Fe/H] values determined from the averaging technique. We now see a tighter correlation with a one sigma scatter of ±0.31 dex. This is essentially identical to the scatter of ±0.32 found from the synthetic noise analysis.

As a final exercise, we investigate the derived [Ca/Fe] ratio for the sample BHB stars. Figures 3.30a-b show the calcium abundances derived from W_k and the Ca template respectively. In both cases we see a general trend of overabundance in Ca. The average and standard error is $\Delta[\mathrm{Ca/Fe}]_{W_k} = 0.49 \pm 0.16$ and $\Delta[\mathrm{Ca/Fe}]_{CTA} = 0.43 \pm 0.15$. Both values are statistically significant and consistent with the Wheeler et al. findings, as well as, other investigations for the globular cluster stars. This is, however, not consistent with our earlier [Ca/Fe] findings for the standard FHB stars.

CHAPTER 4

THE FHB AND A-STAR PROPERTIES

4.1 Program Star Calibration

The standard star analysis in Chapter 3 has allowed us to establish the external accuracy of the stellar physical parameters derived from both the calibration grid and template comparison techniques. We are now prepared to discuss the results for the program FHB/A candidates.

The spectral observations of the FHB/A sample with color information breaks down as follows: 656 stars taken at KPNO/ESO, 224 taken at Lowell Observatories, and 333 taken at Las Campanas as published in Beers et al. (1991). For the KPNO/ESO data the procedure for determining the stellar physical parameters was identical to that outlined in section 3.3 for the noisy synthetic spectra. For the Beers *et al.* data (hereafter, "hot star" data), stellar parameters were determined by adopting the CaII K line index and balmer line index, as published. Since the spectra themselves were not reanalyzed, no template comparison was run on these stars. A special technique was developed for the Lowell spectra, since the poor CCD response in the blue prohibited the acquisition of W_k for the CaII K line. This special procedure compared the colors and balmer line widths, found from voigt fits, to the calibration grid, but metal abundance was estimated using the template comparison of the metallic line regions. This procedure was then iterated to determine the physical parameters.

4.1.1 Internal Accuracy in the Program Stars

As a consistency check, we now begin with an analysis of the internal accuracy of the program sample, by examining the scatter in the derived physical parameter for the stars with multiple observations. Figures 4.1a-c are plots of T_{eff}, Log g, and [Fe/H], found for two separate spectral observations of each star. At this point no distinction has been made between the different observatories where the data were taken. The open triangles indicate the stars for which the identification Am was made. Large differences for the Am stars, especially in abundance, occur between the ESO/KPNO sample and the Lowell sample, since the Lowell stars have no CaII K observations and the abundances are only determined from the metallic line regions. Overall, the relationship between the derived parameters is fairly good. The increase in scatter for $T_{eff} > 8000$ K is in part due to an increase in uncertainty in [Fe/H] and in part due to the loss of a good T_{eff} indicator at the highest temperatures.

To quantify the scatter for two separate measurements we have used the median difference for the sample multiplied by the Pearson and Stephens factor of 0.8862 (see section 3.5.4) for n=2 observations. This prevents vastly deviant outliers from unduly influencing the result. Excluding the Am stars the internal accuracy for the remaining 47 stars is, $\sigma_{PS}T_{eff} = \pm 132$, σ_{PS}Logg $= \pm 0.19$, σ_{PS}[Fe/H] $= \pm 0.26$. As would be expected, the internal scatter is less then the estimates of the external accuracy from the low S/N synthetic spectral analysis.

As noted above, the spectra taken at Lowell Observatory and at ESO/KPNO are quite different. The Lowell data was taken at a lower resolution ($\simeq 2.5\mathring{A}$), and did not include the CaII K line. The ESO/KPNO data, however, are very similar and will be investigated first. Unfortunately, there are only four objects that have

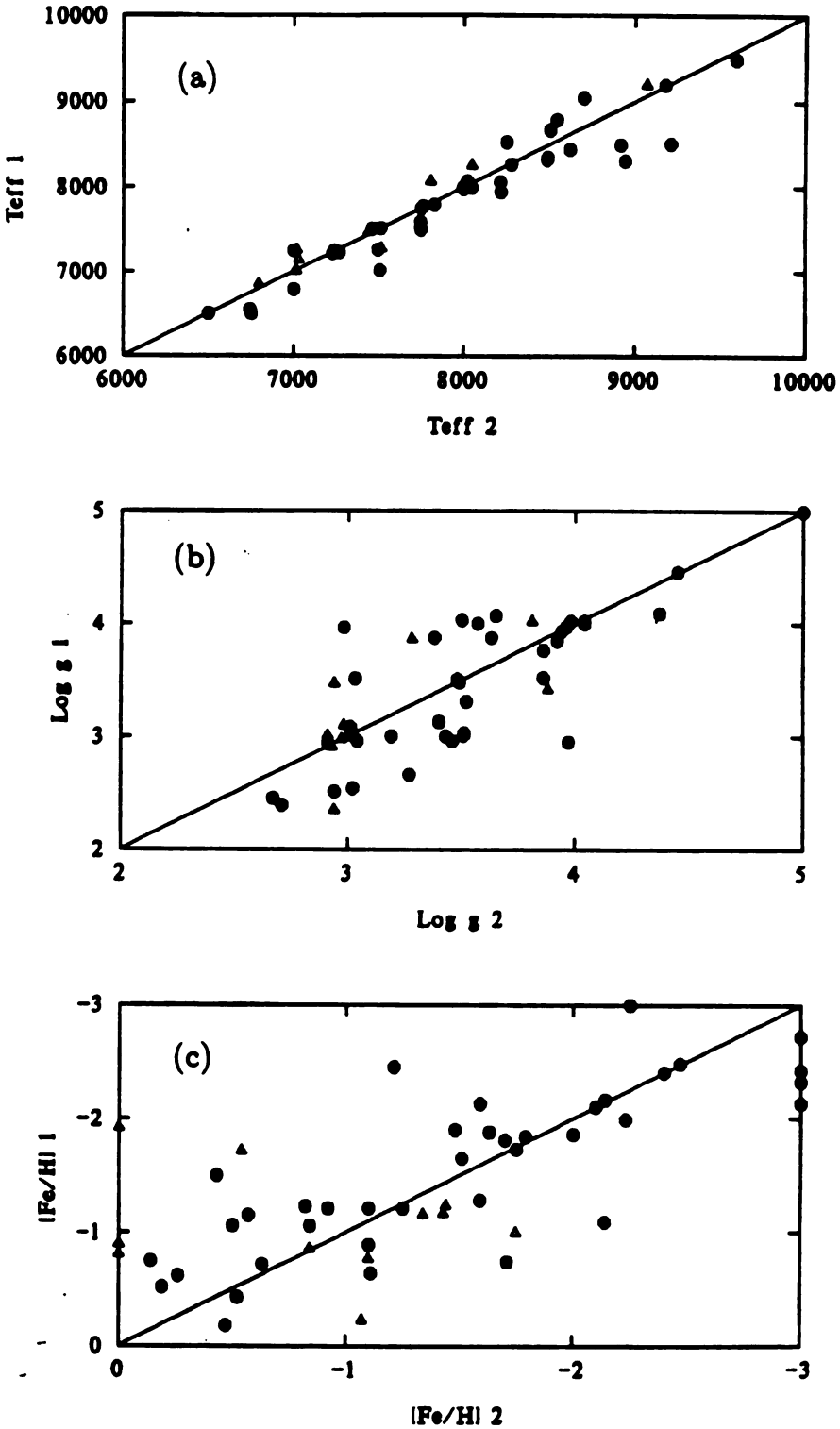

Fig 4.1: Internal scatter in calculated physical parameters for ALL program stars with multiple measures. Triangles indicate Am candidates.

been observed both at KPNO and at ESO. This number is too small to make any real comparison between the two samples. There are, however, a significant number of stars with multiple observations taken at either of the observatories. We therefore make no distinction between the observatories in the analysis, but instead use the combined sample to investigate the internal scatter.

Figures 4.2a-c show the results for multiple observations from the 17 stars from the ESO/KPNO sample. Again, the correspondence is one-to-one between the different observations, with an increase in T_{eff} scatter at the hotter end. Excluding the low-S/N stars the internal accuracy of the ESO/KPNO sample is; $\sigma_{PS}T_{eff} = \pm 132$,$\sigma_{PS}$Logg $= \pm 0.27$, and σ_{PS}[Fe/H] $= \pm 0.18$. Not surprisingly, the abundance values show a smaller scatter since the CaII K line was analyzed for the ESO/KPNO data.

We next investigate the accuracy of the Lowell physical parameters by comparing to the KPNO/ESO results. Figure 4.3a-c shows the results for T_{eff}, Log g, and [Fe/H]. The Lowell and ESO/KPNO results appear also to be in a one-to-one correspondence with a very small scatter in T_{eff}. The internal accuracy for this sample is; $\sigma_{PS}T_{eff} = \pm 69$, σ_{PS}Logg $= \pm 0.13$, and σ_{PS}[Fe/H] $= \pm 0.27$. The scatter in [Fe/H] for the Lowell data is slightly larger than the above ESO/KPNO scatter. To further examine this result, it is worthwhile to compare the Lowell [Fe/H] results to the metallic line regions for the ESO/KPNO data. This should remove any differences between the Ca and Fe abundances that may be physically present in the star. Figure 4.4a is a plot of this relationship with the Am stars now included. We see that the scatter has decreased to some extent. The internal accuracy of the abundance is now, σ_{PS}[Fe/H] $= \pm 0.15$, consistent with the ESO/KPNO results.

Finally, it is of interest to identify the cause of the most deviant [Fe/H] values.

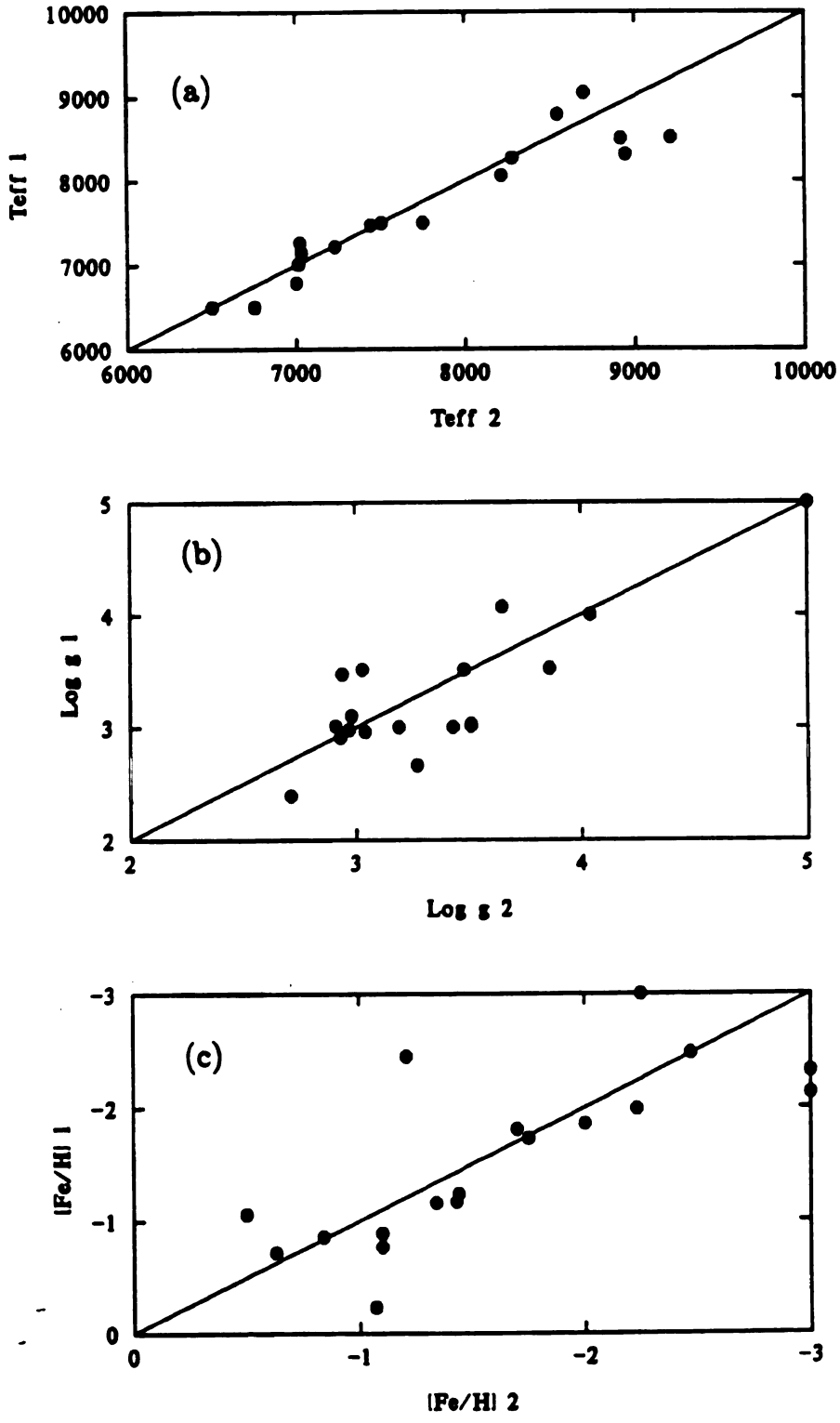

Fig 4.2: Same as Fig 4.1 but only showing ESO and KPNO stars. Am candidates are not plotted.

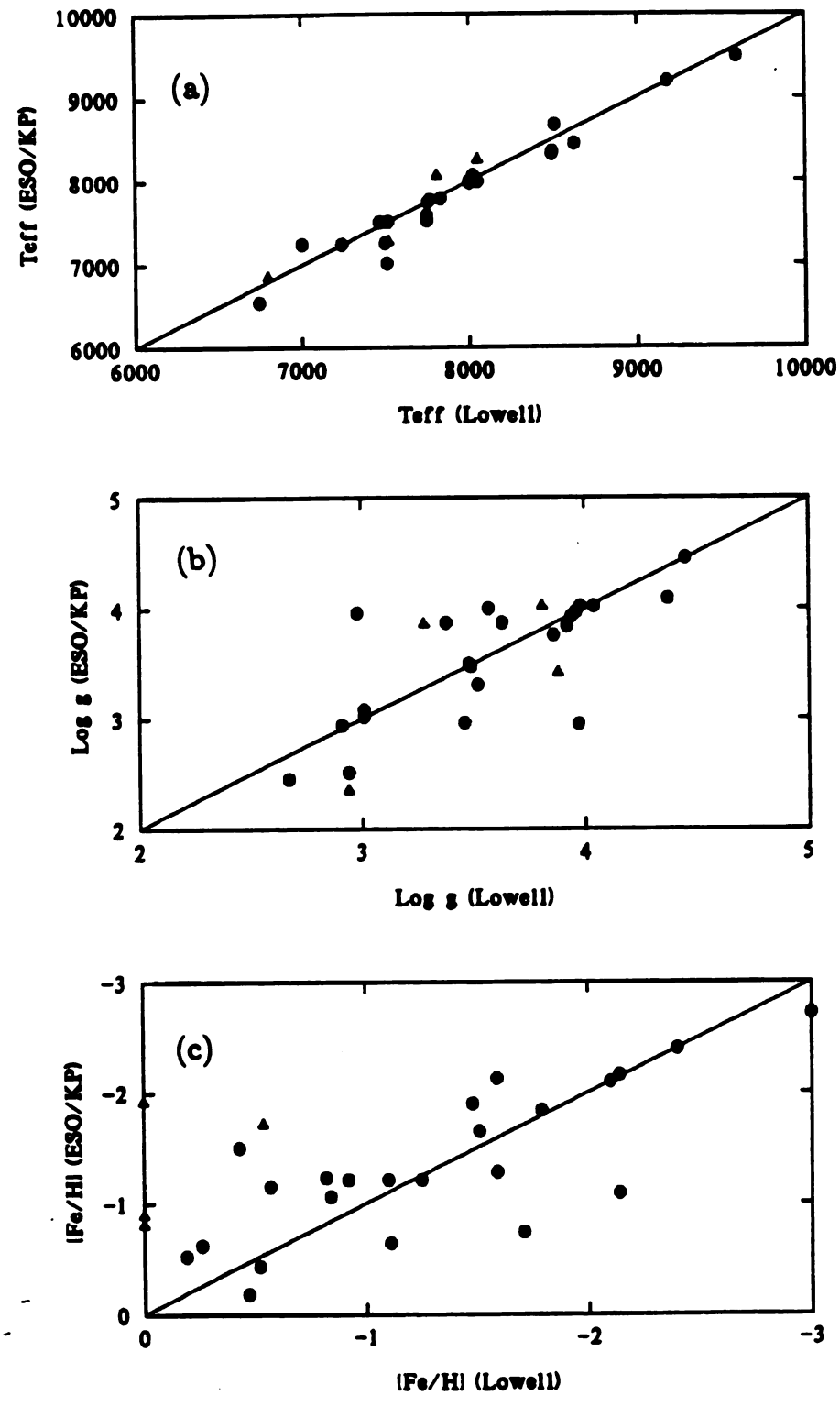

Fig 4.3: Same as Fig 4.1 but comparing results from ESO/KPNO to that of Lowell. Triangles indicate Am candidates.

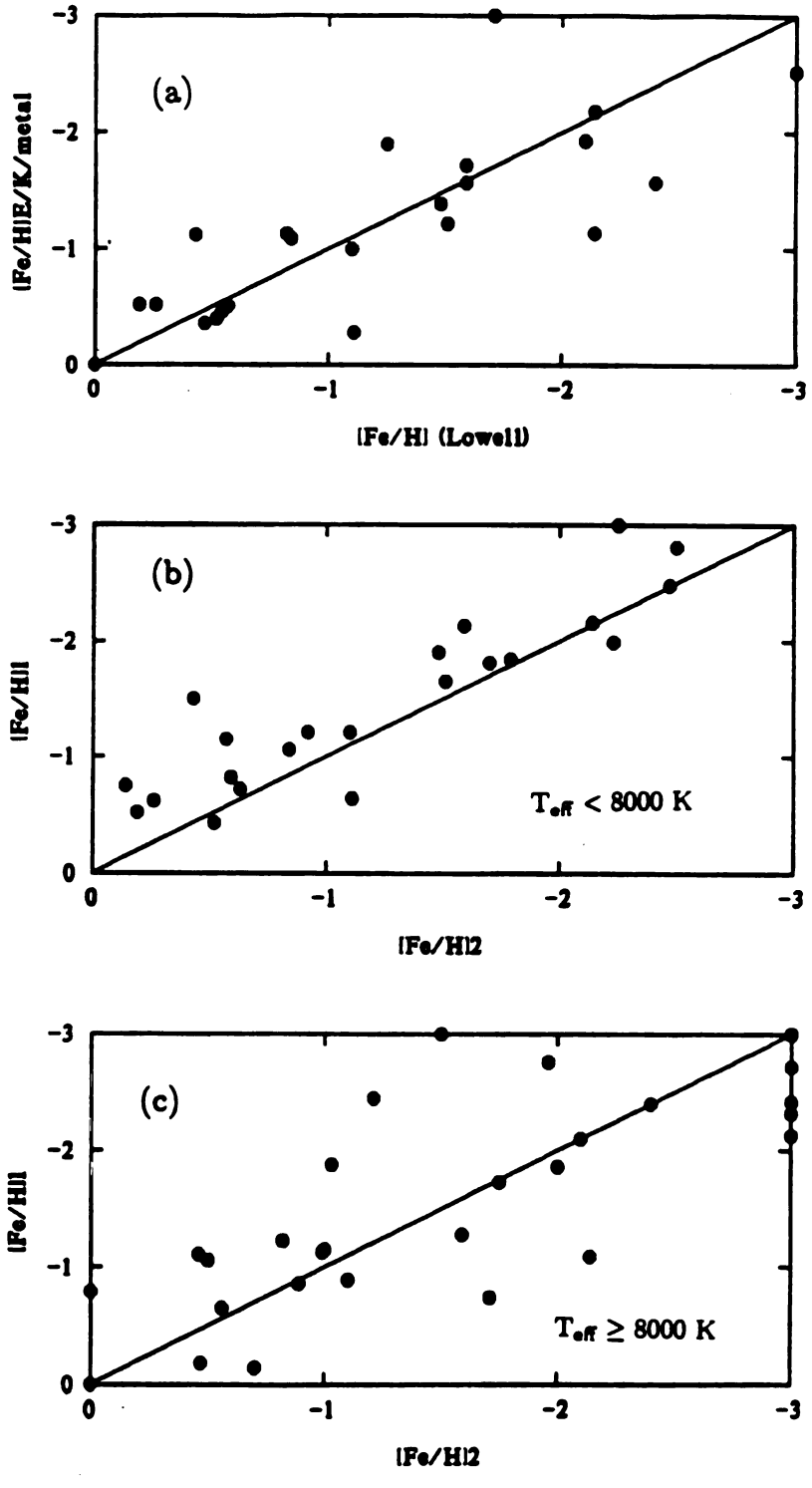

Fig 4.4: Top plot shows comparison of $[Fe/H]_{MTA}$ to that of Lowell. Middle and Bottom plots show abundances for sample split at T_{eff} = 8000 K.

It is expected that these will occur at higher temperatures where the CaII K line and metallic lines are the weakest and most strongly affected by low S/N. Figures 4.4b-c are plots of all the multiple observation stars split at T_{eff} = 8000 K. The scatter at cooler temperatures is substantially less with σ_{PS}[Fe/H] = $\pm$0.21, compared to $\pm$0.32 at the higher temperatures. The internal scatter for the hottest stars, however, is still small enough that meaningful abundances should be obtainable.

4.1.2 Stellar Class Separation

The procedure for Am star identification outlined in section 3.4.3 was carried out for the 656 spectra with template comparison results. Of these 82 were flagged as possible Am candidates. Figure 4.5 is a histogram of the temperature distribution of program Am candidates. The solid line overlay is the distribution of known Am stars from high dispersion analysis of Smith (1973). The peak temperature of the two distributions agree very well along with the qualitative shape of the high temperature end. The excess of program Am stars at the cool end of the distribution is not expected to be real since the Am phenomenon is generally not seen in F-type stars. Therefore, it seems likely that these stars are actually RR Lyrae variables with peculiar abundances due to errors in their assigned T_{eff} values.

To check the procedure's identification ability at low S/N, four Am candidates (which were identified from low S/N spectra) were re-observed at a S/N of $\sim$ 50. Figure 4.6 shows a plot of two of the high S/N spectra together with the known Am star HD 209625 and the FHB star HD 161817. All four stars have nearly the same T_{eff} values and all show similar CaII K line strengths. The abundance calculated from the CaII K lines show a range in values from $-1.0 <$ [Fe/H] < -2.0. The abundance, however, from the metallic lined region is solar for the Am candidates and HD 209625, while the metallic and CaII K abundances are consistent for HD

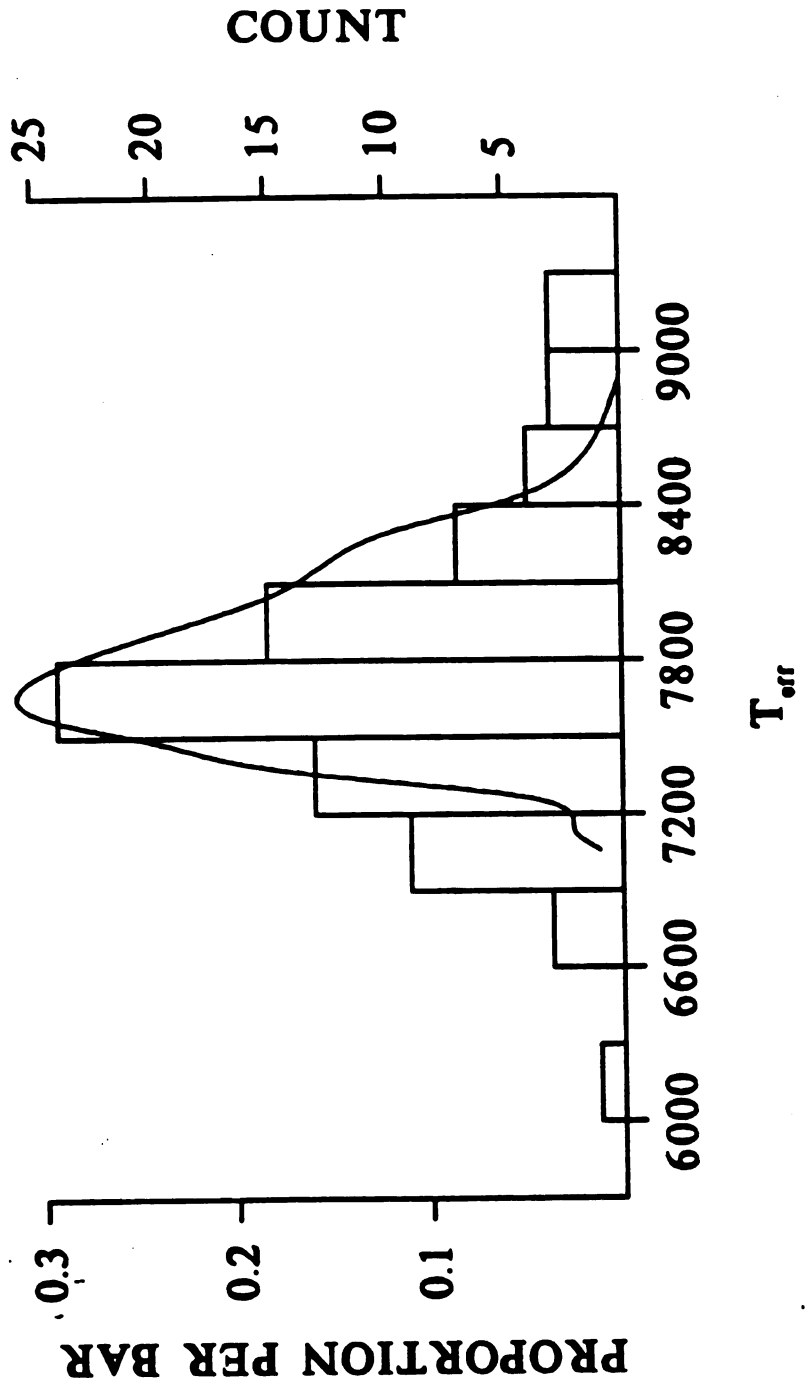

Fig 4.5: Histogram of Am candidates compared to published T_{eff} distribution.

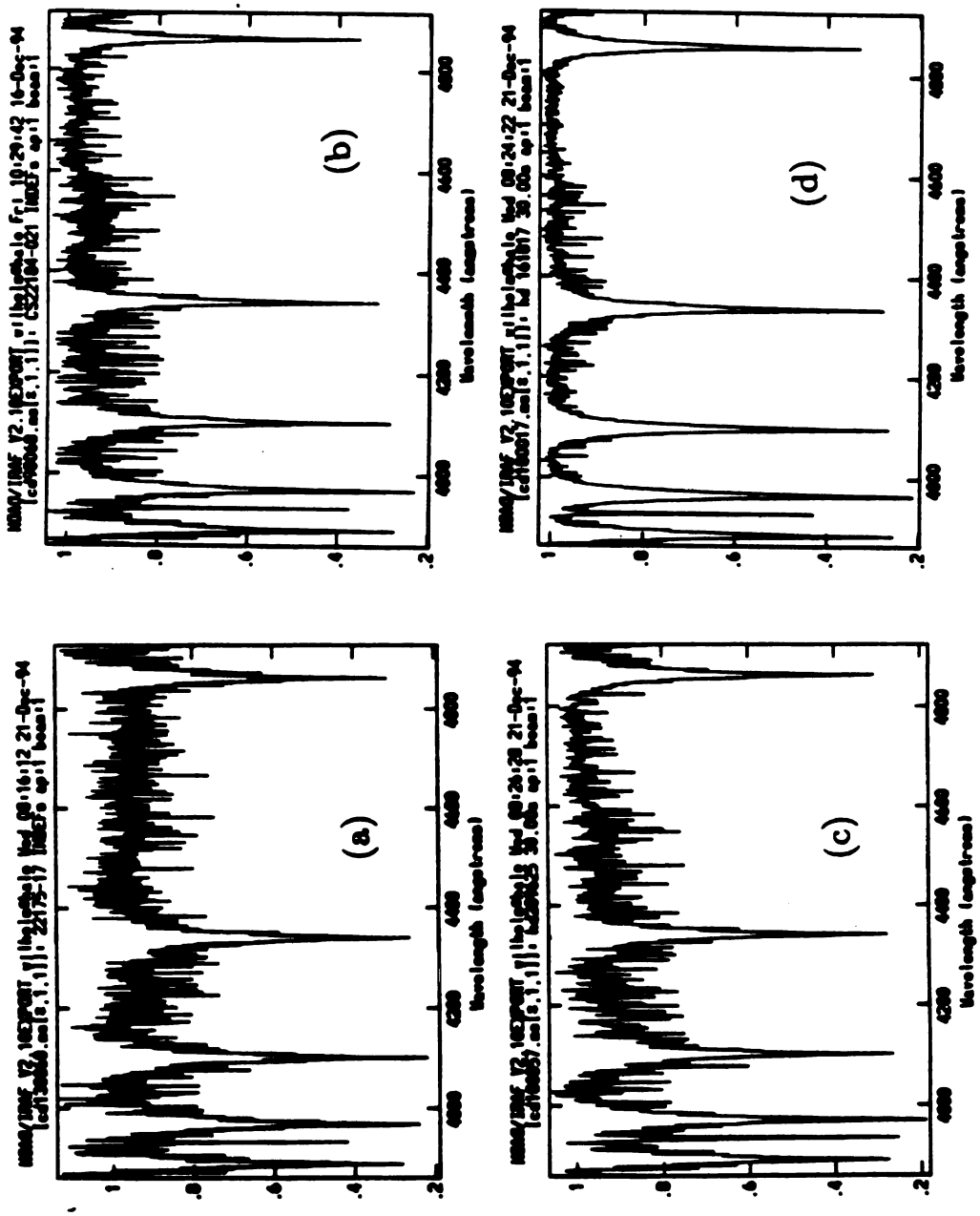

Fig 4.6: Comparison of program Am candidates (a,b) to standard Am star (c), HD 209625, and FIIB standard (d), HD 161817.

161817($\simeq -1.5$ dex). This result can be clearly seen in figure 4.6, where the presence of strong metallic lines in the Am candidates more closely resemble HD 209625 then HD 161817.

With the suspected Am stars removed from the sample, we next use the Log g - T_{eff} separation criteria to identify the FHB and main-sequence stars. Of the 1121 stars remaining in the sample, 564 are unambiguously identified as FHB, 448 as main sequence A-type stars, and 109 for which unambiguous class determination is not possible by this procedure. Figure 4.7a is a plot of this sample of stars showing the identified FHB, A, and FHB/A stars. Tables B.1, B.2, B.3, and B.4 contain all of the parameter results for the FHB, A-star, FHB/A, and Am candidate stars. These tables can be found in Appendix B.

Figures 4.7c-d are plots of [Fe/H] as a function of T_{eff} for the FHB and A-star samples, respectively. It is clear from these plots that the overall distribution of metallicities is quite different for the two samples. The FHB sample has much fewer metal-rich stars and many more metal-poor stars than the A-star sample. This is expected since the temperature of a star on the horizontal branch is correlated to its metallicity in the sense that hot FHB stars are generally metal-poor. No such physical constraint is present for the metal-rich A-stars, but the age-metallicity relationship limits the number of metal-poor main sequence A-stars that can still exist in the Galactic halo. The presence of these sample characteristics suggest that many of the program stars have been correctly identified. The differences in the distribution of metal abundances can, however, be potentially troublesome since even a modest percentage of misidentified stars from one sample can be a large percentage in the other. Although great care has been taken in isolating pure stellar types, we will now investigate several forms of contaminates that are expected to

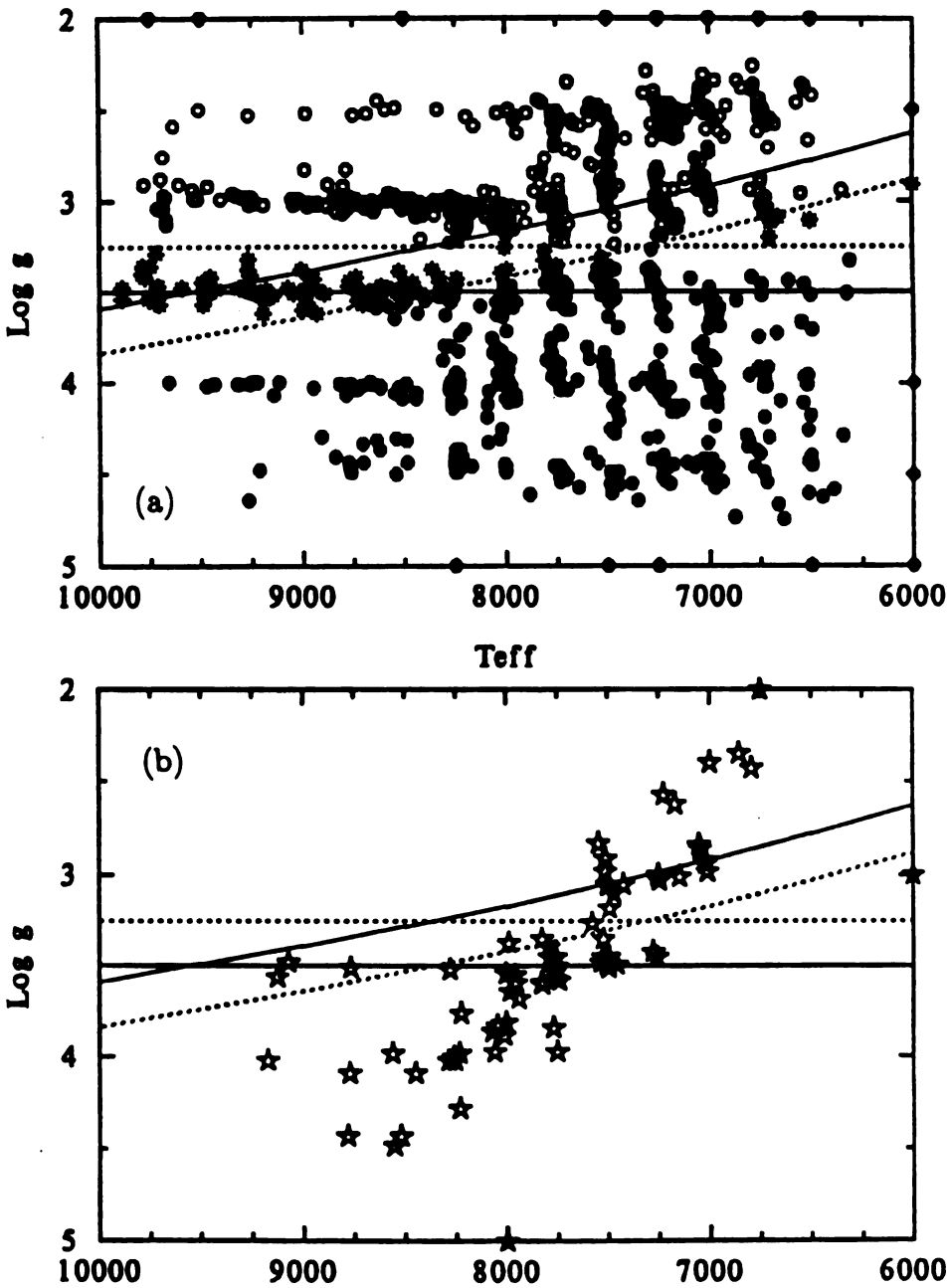

Fig 4.7A: Log g - Teff plot used to separate the program FHB/A stars into respective stellar class. The FHB, A, and FHB/A stars are represented in figure (a) as open circles, closed circles and asterisks. Figure (b) shows the distribution of all program Am candidates.

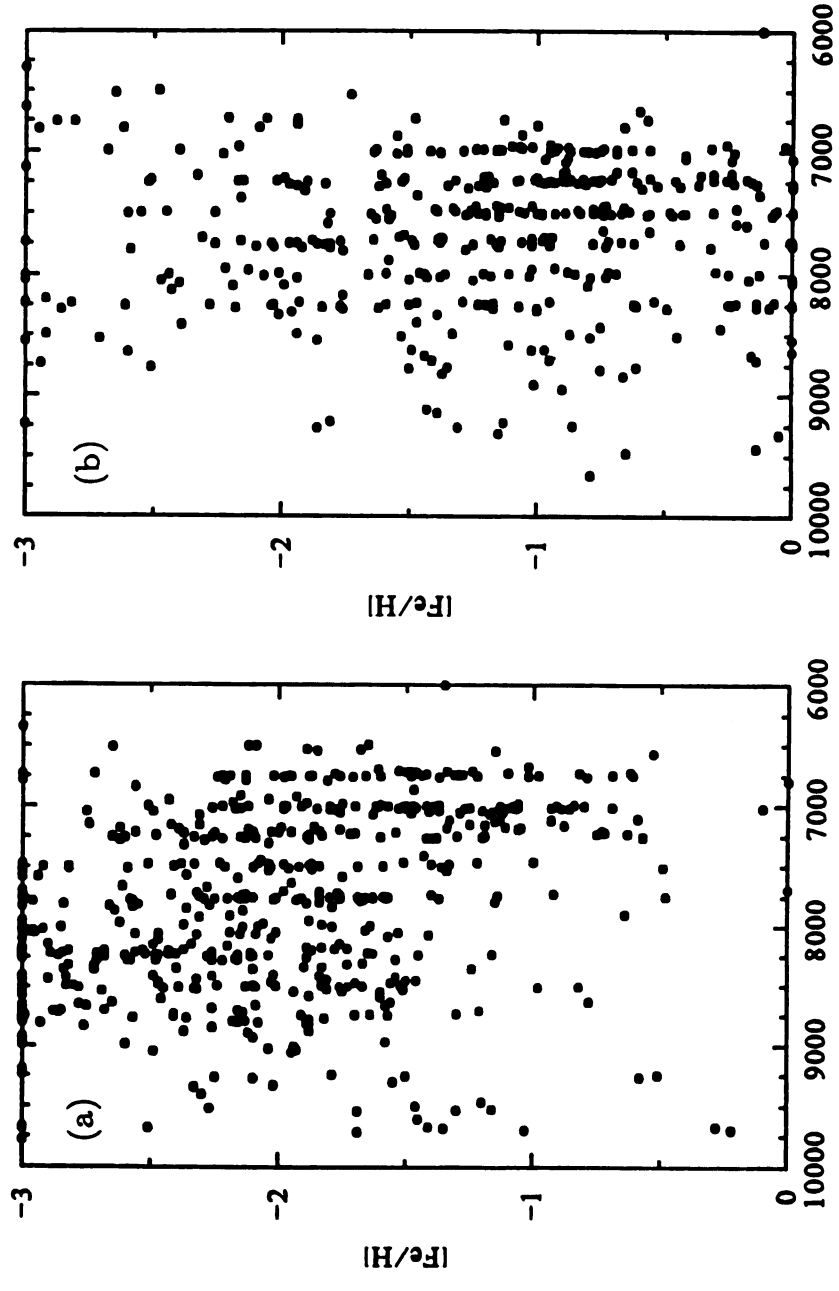

Fig 4.7B: [Fe/H] as a function of T_{eff} for the FHB (a), and A-star (b) sample.

still be present.

4.1.2.1 Am Contamination

The Am candidates have been removed from the sample of 656 stars with template comparison results available, but can not be identified in either the Lowell or "hot star" samples. We can, however, estimate the amount of contamination still present from the Am component. Figure 4.7b shows the Log g - T_{eff} plot for the Am candidates. We see in this plot a trend that begins with FHB-like surface gravities at cooler temperatures, and which changes over to main sequence surface gravities at higher T_{eff}. The transition region occurs around T_{eff} = 7750 K. This is exactly what is expected, since the Log g values cooler than this are driven primarily by the (U-B) colors (which suffer from metallic line blanketing) while the Log g values for the hotter stars are derived from the balmer line widths (which are virtually unaffected by line blanketing).

We would now like to estimate the amount of contamination still present in the FHB and A samples separately. Using the percentage of identified Am stars present in the KPNO/ESO sample, 12.5%, we can estimate the number of Am stars present in the Lowell/"hot star" sample to be 72. From figure 4.7b, we see that the percentage of Am candidates that would have been misidentified as FHB is 24%. Therefore, we expect that around 17 Am stars are still present in the final sample of 564 FHB stars. This amounts to less than 3% of the sample, and is probably insignificant. It should be noted that, of the three Am stars with both KPNO/ESO and Lowell observations, the Lowell data show these stars to be near solar abundance. Therefore, even if they had FHB surface gravities they would appear in the sample as peculiar stars, since FHB star with solar abundance are not expected to exist.

Although the Am stars are main-sequence A stars, estimating the contamination to the A sample is still important since some of these stars will be confused for blue metal-poor main sequence stars (BMP) which have values of [Fe/H] < -1.0. The BMP stars have very different kinematics compared to disk stars (Preston *et al.* 1994) and the inclusion of a significant number of Pop. I Am stars could affect this result. We estimate the percentage of Am stars that would have been misidentified as BMP (low abundance but main sequence Log g) to be 32%. The total number of A stars matching the BMP abundance criteria is 241 and the estimated remaining number of Am stars is 23. This means the percentage of misidentified BMP stars is nearly 10%. As mentioned above, however, the Lowell abundances, which are calculated from the metallic lines, are expected to return solar values for the Am stars. Also, the majority of the A-type stars from the "hot star" sample are at cooler temperatures where Am misidentification leads to FHB classification. Therefore, the true contamination is probably $< 5\%$, and is not expected to be significant.

4.1.2.2 RR Lyrae Contamination

In general the program stars have one photometric and one spectroscopic observation each. This means we have very limited information on stellar variability. There are, however, a large portion of FHB stars that have colors consistent with the RR Lyrae instability strip. Some percentage of the RR Lyrae stars in the sample are expected to have been photometrically observed at maximum "light". Because Log g in this temperature range is set by the (U-B) color, which is also at a maximum, it is expected that some of these stars have been misidentified as A-type.

Before testing for possible contamination, we estimate the equilibrium temperature at the blue edge of the instability strip, for the Kurucz color calibration. This was done by deriving temperatures for a number of known, bluer, RR Lyrae

stars with published UBV observations. The results indicate the blue edge of the instability strip to be $T_{eff} \sim 7050$ K. This value is somewhat less then the derived temperature of $T_{eff} = 7560$ K, for HD 161817, a FHB star that is known to lie near the blue edge of the instability strip (Kinman *et al* (1994)). At maximum light the majority of these stars fall in the temperature range of $7000 < T_{eff} < 7500$. In nearly all cases the surface gravity remains consistent with that of low surface gravity FHB stars. Finally, a constant CaII K equivalent width was assigned and the estimated abundance error due to the color change from minimum-to-maximum light was found to be ~ 0.6 dex.

We begin now by searching for evidence of program RR Lyrae stars by plotting the observed $(B\text{-}V)_o$ colors as a function of the derived T_{eff} values. T_{eff}, for the program stars in this color range, are determined by a weighted combination of $(B\text{-}V)_o$ colors and the D0.2 widths. If the spectroscopy and photometry were taken at a different phase in the RR Lyrae pulsation, then we would expect to see scatter in the (B-V) - T_{eff} relation. Figure 4.8a shows this relationship for the FHB sample. The bounding solid lines are the Kurucz model relations for Log g = 2.0, [Fe/H] = -3.0 and Log g = 3.5, [Fe/H] = 0.0. The majority of the stars that are scattered outside these limits have values of $T_{eff} < 7500$ K and represent good candidates for RR Lyrae variables. In contrast to this plot, figure 4.8b shows the same relation for the A-star sample. The solid lines are the extreme Kurucz model results of Log g = 3.5, [Fe/H] = -3.0 and Log g = 5.0, [Fe/H] = 0.0. The small number of scattered stars below $T_{eff} = 7500$, indicate that the FHB scatter is real and not an artifact of the calibration technique. The number of scattered RR lyrae candidates present in the A-sample is relatively small. Of the total number of 219 A-stars in this range only 16 are outside the model bounds, amounting to about 7% contamination or

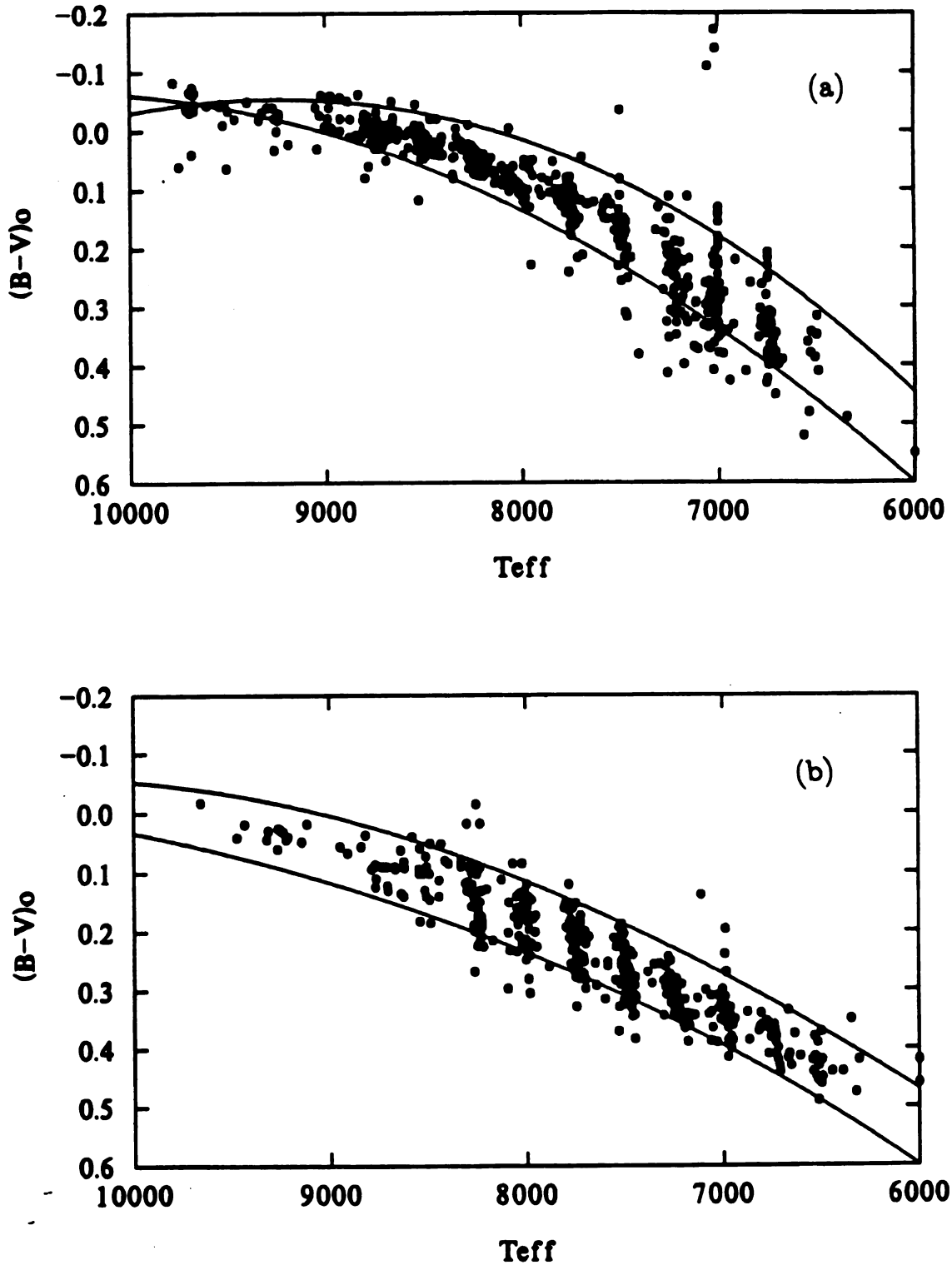

Fig 4.8: (B-V) - T_{eff} plot used to identify RR Lyrae candidates. Solid lines indicate the constraining physical parameters from the calibration grid. The FHB and A-star samples are shown in plots (a) and (b), respectively.

only $\sim$ 3% of the total A-sample.

This contamination percentage is calculated from the number of RR lyrae variables for which the spectroscopic and photometric observations were apparently taken out of phase. It does not, however, give an indication of the contamination when both observations are made at maximum light. To better quantify this number, we turn to figures 4.9a and 4.9b, which are histograms of abundance for the A-star sample, binned in 0.2 dex intervals, in the temperature range of $7000 \leq T_{eff} < 7500$, and $7500 < T_{eff} \leq 8000$ K, respectively. If we adopt as a working hypothesis that the percentage of stars from each abundance bin should be the same for both histograms if no contamination has occurred, then it is immediately recognizable that an excess exist in figure 4.9a near [Fe/H] = -1.0. Figure 4.9c is a plot of the difference in percentage (4.9a - 4.9b) as a function of [Fe/H]. The 1 σ scatter about the zero line is 2.6% and is denoted as dashed lines in the plot. The percentage difference in the bin at -1.0 dex seems to be significant at more than the 2σ level. There is also marginal excess near -0.3 dex and a marginal deficit in two bins near -2.0 dex. We estimate the total excess of A-stars, by calculating the percentage difference greater than 1 sigma, to be 5%. The number of A-stars represented in the two histograms is 248 bringing the number of misidentified RR Lyraes to 12 and making a total percentage of misidentified RR Lyrae stars in the A-star sample of 2.6%. In all likelihood, this is an underestimate of the actual RR Lyrae contamination, but it does indicate that a large amount of contamination is not likely.

From the analysis of program stars with multiple spectroscopic observations, there are 15 stars which have temperatures consistent with the instability strip. Of these, 6 show agreement as FHB stars, 5 as A-stars, and 4 that disagree on the

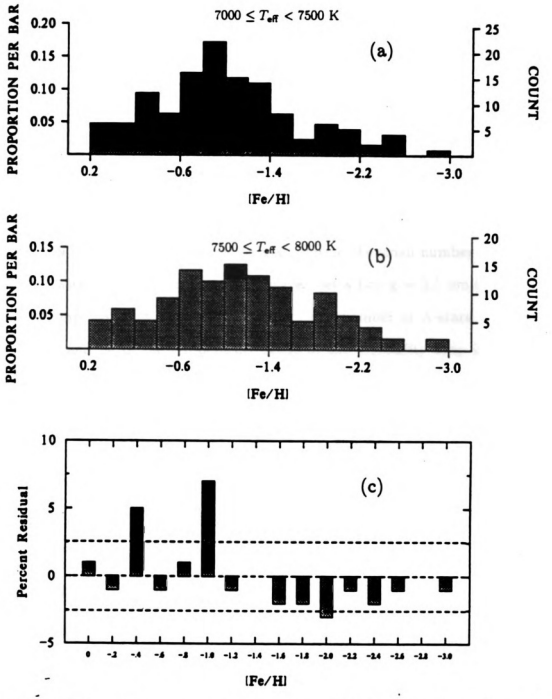

Fig 4.9: Evidence of excess number of stars from RR Lyrae contamination of A-star sample. Plot (c) shows the percentage difference between plots (a) and (b).

stellar class. The A-stars that show agreement, all have surface gravities near Log g = 4.0, making it more likely that the four stars showing disagreement are variables with observations at a different phase rather then misidentfications due to uncertainties in log g. If this is the case, then we might conclude that approximately 33% of the time the RR Lyrae's are misidentified. Since we find 226 FHB stars cooler than the blue edge of the instability strip, there should be 113 RR Lyrae stars which are misidentified. This amounts to 24% of the entire A-star sample. This enormous amount of contamination is not seen, however, in either the (B-V) - T_{eff} plot or figure 4.9 and is probably an overestimate due to the small number statistics. The objects with multiple measures do, however, set a Log g = 3.5 limit, for which we can attempt to identify A-star intruders. The number of A-stars that have Log g < 3.5, and lie in the temperature range of the instability strip is 27, or 6% of the total sample. This number, added to the 16 stars found from the (B-V) - T_{eff} relation, represents 9% of the A-star sample. If in fact this percentage is correct, the effect on the kinematics of the A-stars should be minimal, since the RR Lyrae thick disk and halo kinematics are not too different from the BMP and metal weak A-stars. Effects of this contamination will be examined, however, in the kinematic section.

4.1.2.3 A-type Giants

In their high-dispersion survey of local FHB stars, Morrison and Green (1993) discovered that a large percentage of stars that had been identified as FHB from Strömgren photometry were actually strong-lined A giants and supergiants. These stars, with Log g values between 2.5 and 3.5, are confused with FHB stars because their path in the Log g - T_{eff} plane tracks directly across the blue horizontal branch. Because the Log g values are indistinguishable, they can only be unambiguously

identified from high dispersion observations. We can, however, attempt to estimate their numbers in our FHB sample.

Our main concern is contamination to the FHB thick disk and metal-weak tail where inclusion of a low velocity dispersion A-giant population would have the strongest effect. Lance (1988) estimates the lifetime on of the A giant phase to be $\sim$ 10% of the total lifetime of the star. Since there are a total of 448 A-stars in our sample we estimate the number of giants to be near 45. Because over half of the A-star sample has [Fe/H]< -1.0, around 25 of these A-giants will have BMP progenitors. The other 20 should have strong disk-like kinematics. As an upper limit to the contamination present in the FHB subsample with [Fe/H] > -1.0, we estimate that 20 A-giants are present, amounting to 20% of the FHB thick disk population. Likewise the upper limit to the metal-weak tail contamination (taken to be $-1.0 \leq$ [Fe/H] ≤ -1.6) is $\sim$ 13%. Given the previously stated range of Log g values for the A-giants it would be expected that only half of these would actually make it though our FHB Log g criteria, making the estimated contamination closer to 10% and 6%, respectively. If this rather crude estimate is at all indicative of the true A-giant contamination, then the effect on the FHB kinematics is probably not significant.

4.1.3.4 Log g Uncertainty

Although each of the three previously mentioned stellar classes undoubtedly contribute to contamination of either sample, the main source of overall contamination is the uncertainty in the derived Log g values. From the analysis of 81 standard stars and low S/N synthetic spectra in sections 3.4.2 and 3.5.3 respectively, we have estimated this contamination to be $\sim$ 8%.

We can carry this analysis one step further by assuming all metal rich FHB

stars are actually misidentified main sequence A-stars. This is a good assumption since the (U-B) colors of the metal rich A-stars overlap with the metal poor FHB stars, and since we do not expect to find solar abundance FHB stars. The total number of FHB stars with abundances greater than -0.5 dex is 9. Comparing this number to the total number of stars with [Fe/H]> -0.5 from the A-star sample, 92, we find 9% of near solar abundance A-stars are misidentified. If we now make the conservative assumption that abundance has little effect on the stellar class identification, then we find overall that 47 A-stars have crept into the FHB sample. This is a contamination percentage of 8%. Happily, this is completely consistent with the previous findings from Chapter 3. We can of course help lower this result by trimming the near solar abundance FHB stars, and in so doing the percentage drops to 6.5%. This percentage is still high but not as significant to the kinematic results of the FHB stars, since the extremely different kinematics of the thin disk stars have now been removed. It should be noted that, of the 60 stars with multiple spectroscopic measures, 6 (10%) show disagreement in class identification. As mentioned earlier, 4 of these lie in the instability strip, resulting in 3% misidentification for the non-instability strip stars.

As a curiosity we can also examine the 14 stars in figure 4.7c that fall in the region of $T_{eff} > 7500$ K, and $-0.5 >$ [Fe/H] > -1.2. We expect to find virtually no blue FHB stars in this region since the current theories on HB morphology predict that hot FHB stars should be metal-poor. There are 6 FHB stars with near solar abundance and $T_{eff} > 7500$ K. Comparing this with the 51 stars in the same region of the A-star sample indicates 11% are misidentified. There are 78 identified A-stars with $T_{eff} > 7500$ and $-0.5 >$ [Fe/H] > -1.2. Assuming 8% misidentification, nine A-stars should inhabit this region of the FHB plot, making the percentage of

contamination 64%. Therefore, it seems very unlikely that many of the 14 stars in figure 4.7c are really FHB stars.

4.1.3 The [Ca/Fe] Analysis

In section 3.3.2, concerns were raised as to the effectiveness of using the CaII K line as an overall metallicity indicator for the program stars. Diffusion can affect the calcium abundance relative to iron and the interstellar CaII K line can be blended with the stellar line causing an excessively high abundance determination. Before launching into the abundance analysis of the program stars it is first necessary to examine the characteristics of the CaII K line as a metallicity indicator.

Figure 4.10a is a plot of [Fe/H], derived by W_k, as a function of the calcium template abundance (hereafter "CTA") for 656 program stars with template comparison results. The lowess fit to the data indicates that overall, the agreement is in nearly a one-to-one correspondence. In the mean, the CTA is underabundant by -0.14 ± 0.02 dex, and the overall standard deviation of ± 0.50 dex. There appears to be an inconsistency between the two methods for abundances greater than -1.0. This is due to an underabundance in the calcium template result, caused from an inability to properly constrain the continuum level when the absorption feature becomes very broad. Also evident is a large scatter at the lowest abundances. This is primarily due to the noise dominated CaII K line, controlling the voigt profile fit as described in section 3.5.1.

The calcium abundance was calculated by removing the Wheeler et al. [Ca/Fe] trend implemented in the synthetic spectral synthesis. To help improve the more deviant points, the [Ca/Fe] analysis is carried out using the mean of the Wk and CTA abundances. Figure 4.10c is a plot the average calcium abundances with respect to [Fe/H] derived from the metallic lined regions (MTA). The lowess fit

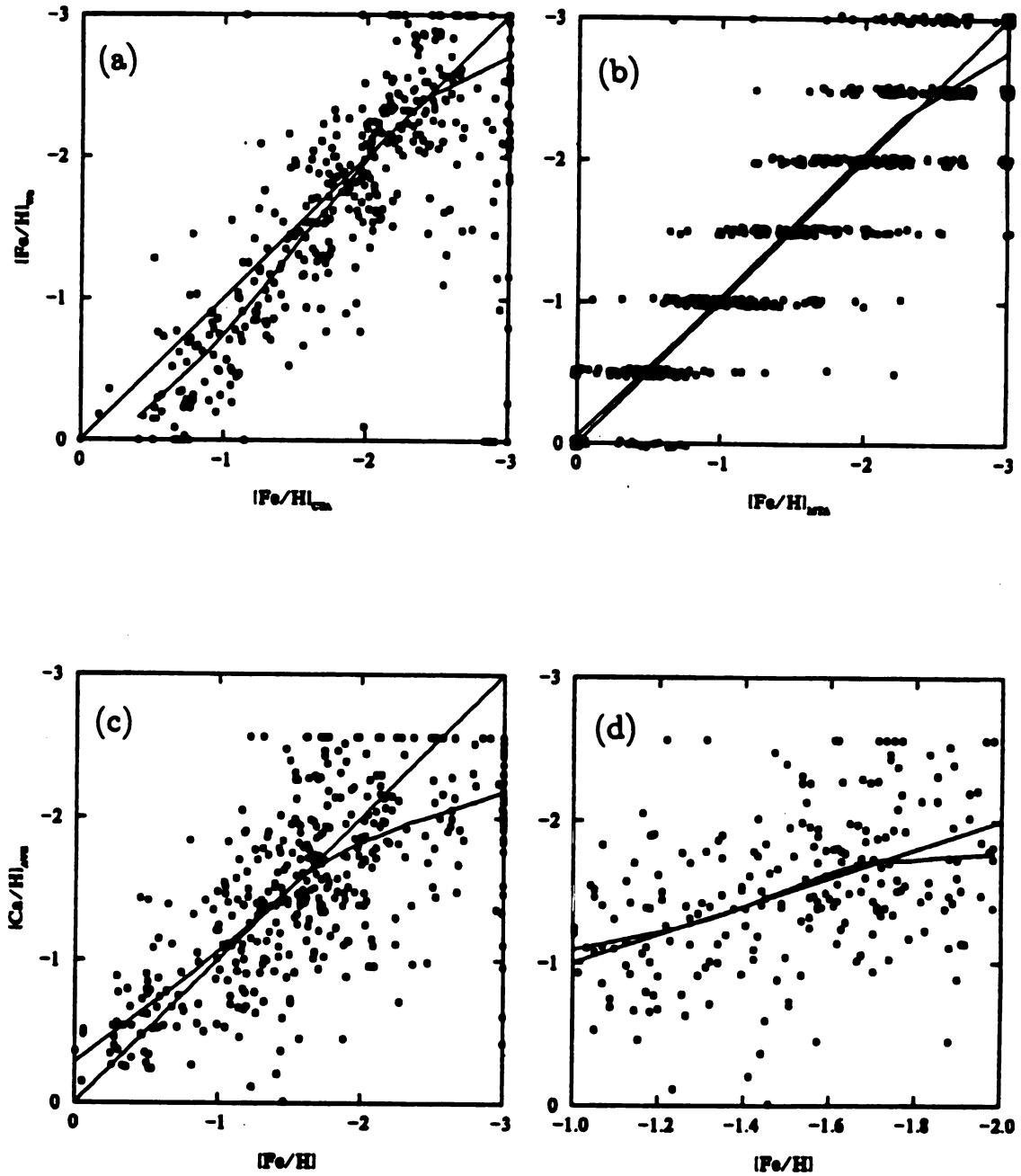

Fig 4.10: Correlations of the abundance indicators for the program stars. Plot (a) compares [Fe/H] from W_k and CTA. Plot (b) compares [Fe/H] calculated with MTA from noisy synthetic data. Plots (c) and (d) show the relationship between [Ca/H], averaged from W_k and CTA results, and [Fe/H] from MTA.

shows calcium underabundance at the high metallicity end, caused by the underabundance of CTA mentioned above, and overabundance at the low metallicity end. This calcium overabundance is largely due to asymmetric scatter at the grid edge ([Ca/H] = -2.55). Overall, calcium is overabundant by $0.14 \pm .03$ dex with a standard deviation of ± 0.56 dex. To help ensure that any [Ca/Fe] trends are not due to systematic effects in the derived MTA, figure 4.10b shows the relation between [Fe/H] from the atmospheric model and that of MTA derived from the noisy synthetic spectra. For clarity of presentation, the model abundances were "jittered" from their half dex interval values. The relationship shows the MTA is consistent with the model abundances for all but the lowest values, even though the scatter is ± 0.40 dex.

4.1.3.1 The [Ca/Fe] Ratios

In determining the [Ca/Fe] ratios for each stellar class of objects, we have constrained the [Fe/H] abundance to the range $-1.0 >$ [Fe/H] > -2.0. As shown in figure 4.10d, this removes most of the problems caused by the CTA and most of the grid edge effects. Figures 4.11a-f show the [Ca/Fe] ratios as a function of [Fe/H] for the noisy synthetic spectra, FHB standards, globular cluster BHB stars, all program stars, the program FHB sample, and the program A-star sample. A lowess fit to the data indicates that the two FHB samples show an overall [Ca/Fe] ratio that is in contrast to the other three samples. Although the scatter is somewhat large, the number of stars is sufficient to allow a meaningful interpretation of the mean value.

Table 4.1 lists the mean [Ca/Fe] values and the 1σ scatter for each stellar group. The noisy synthetic spectral analysis serves as a zero-point standard, as well as a powerful discriminate of the noise induced scatter. From the Wheeler et al. calcium abundance relation we expect the mean ratio value in this abundance range to be

Table 4.1 [Ca/Fe] Ratios.

Sample (1)	N (2)	$<$ [Ca/Fe] $>$ (3)	σ (4)	$<$ [Ca/Fe] $>_{cor}$ (5)	$\Delta <$ [Ca/Fe] $>$ (6)
Synthetic Spec.	190	0.241 ± 0.031	0.423	0.321 ± 0.031	0.029
Standard FHB	15	-0.088 ± 0.076	0.293	-0.008 ± 0.076	0.358
Globular BHB	11	0.246 ± 0.106	0.353	0.326 ± 0.106	0.024
Program All	238	0.011 ± 0.031	0.483	0.091 ± 0.031	0.319
Program FHB	160	-0.086 ± 0.039	0.497	-0.006 ± 0.039	0.356
Program A	87	0.172 ± 0.043	0.399	0.252 ± 0.043	0.098

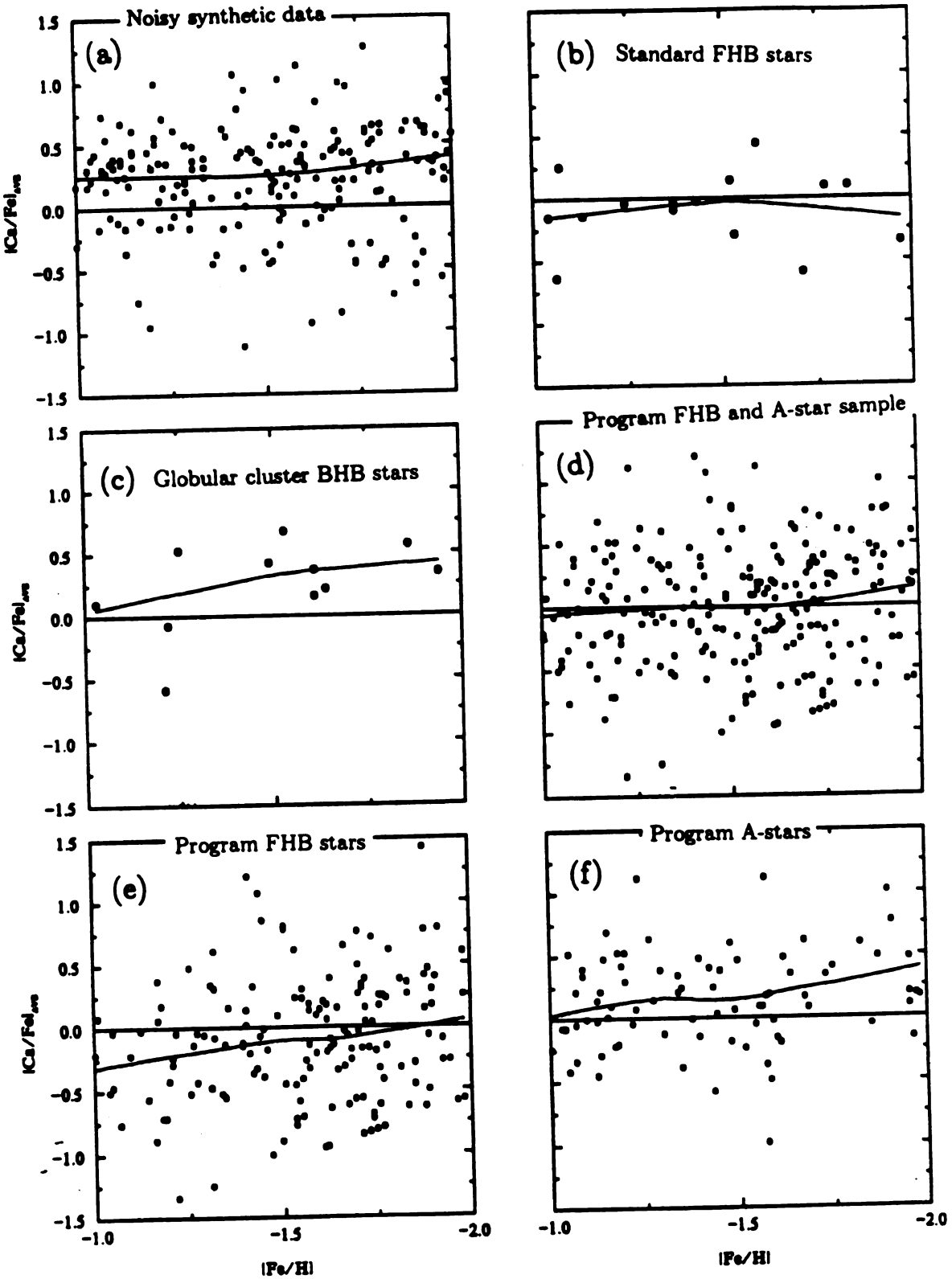

Fig 4.11: [Ca/Fe] ratios as a function of $[Fe/H]_{MTA}$ for various studied samples.

$< [Ca/Fe] > = 0.35$. Within the 1σ uncertainty, the synthetic spectral result is 0.08 dex too low, mostly due to the W_k abundance being systematically less than CTA by 0.1 dex. Correcting the other ratios by this zero-point shift, we find excellent agreement between the Wheeler et al. [Ca/Fe] value for the halo dwarfs and the values for the globular BHB and program A-type stars. The results for both the standard and program FHB stars remain very close to zero. It is also of interest that while the program A-star sample shows a 1σ scatter slightly less than expected from the synthetic analysis, the program FHB sample exhibits a scatter which is substantially higher than might be expected from noise alone.

A possible explanation for this larger scatter is the inclusion of RR Lyrae variables. As shown earlier, the temperature is more uncertain for these stars since the photometry and spectroscopy may have been taken at different pulsation phases. The effect of a temperature error on the CaII K line strength is greater (due to the strong temperature dependency of CaII K) than on the other metallic lines, and so may be the result of the higher [Ca/Fe] scatter. Contrary to this explanation, figure 4.12e, which is a plot of [Ca/Fe] as a function of T_{eff}, indicates very little scatter for the T_{eff} values which are consistent with the instability strip. Instead the largest scatter occurs for $T_{eff} > 7500$ K and is probably in part due to the weakened nature of the absorption features at higher T_{eff}. It is also interesting that the A-star sample (figure 4.12f) shows a dip in [Ca/Fe] at the same temperature that the number of Am candidates peak (figure 4.5). This could be an indication that some of the BMP stars exhibit very mild Am-type abundance characteristics, however, in the absence of higher S/N data this is very far from a foregone conclusion.

These results indicate a real difference in [Ca/Fe] ratio for the program FHB stars compared to the Wheeler dwarfs, program metal-poor A-stars, and possibly

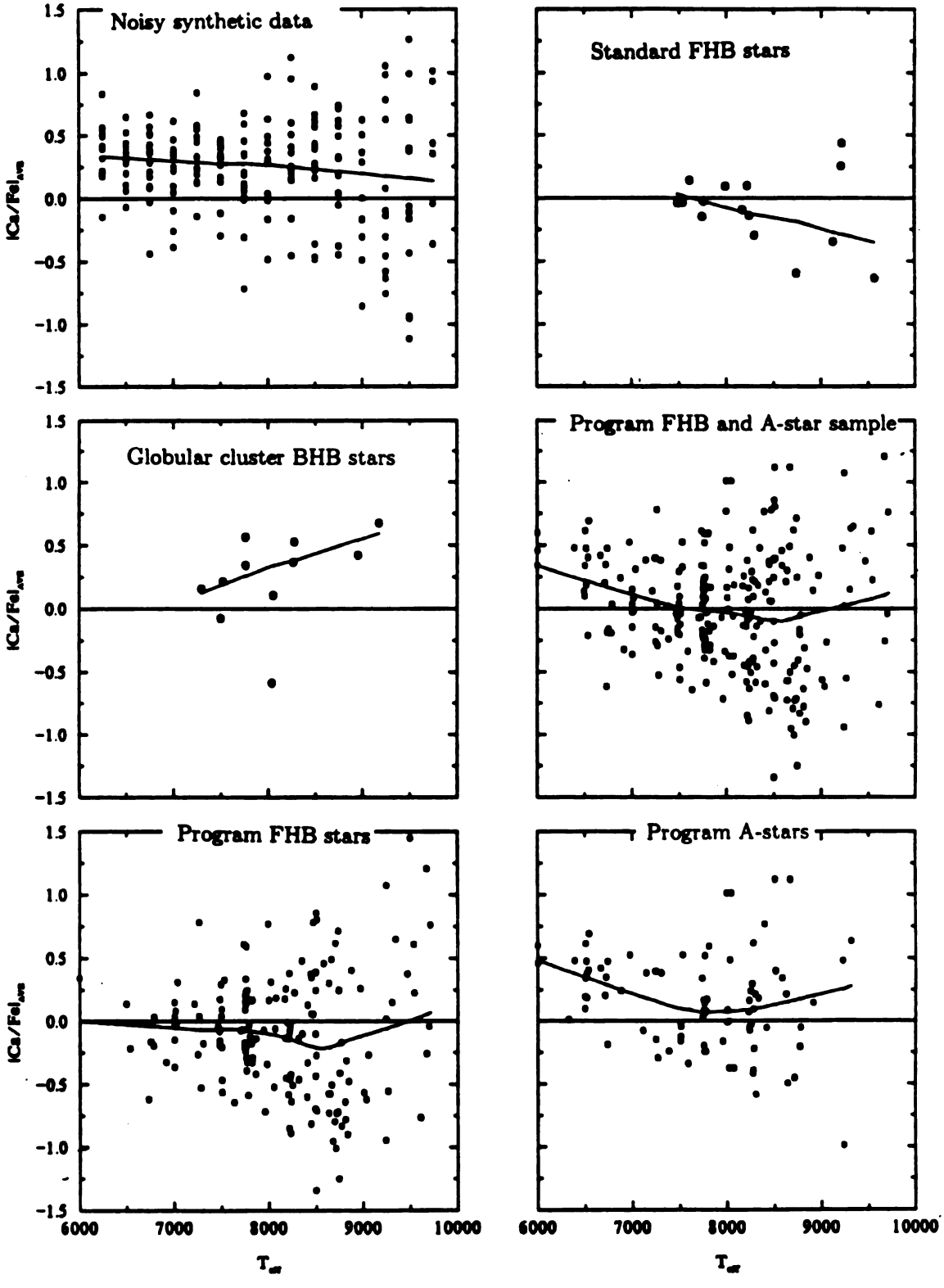

Fig 4.12: [Ca/Fe] ratios as a function of T_{eff} for various studied samples.

the globular horizontal branch stars. The discrepancy with respect to the globularBHB stars suggest that a primordial difference in the [Ca/Fe] ratio may be the correct interpretation of the result. The number of observed globular BHB stars is small, however, and most have only photographic (B-V) colors, making the difference between them and the FHB sample more questionable. Kodaira and Philip (1984) have in fact claimed an underabundance of Ca relative to Fe is observed in some of the globular BHB stars which they have observed at high-dispersion. This leads us to the conclusion that the effects seen in the FHB sample may be the Pop II analog of the diffusion effects that are at work in the main sequence Am stars. This diffusion process can occur when the radiative acceleration of Fe becomes larger than its gravitational acceleration causing the element to rise to the stellar surface, while the Ca, which has a smaller radiative acceleration sinks. The work of Michaud et al. (1983) has shown that the time for such a process to take place is shorter than the HB lifetime, especially for the hottest HB stars. Although this diffusion effect is not predicted from the Michaud et al. models for stars in the temperature range of the FHB sample, it is well with the uncertainties in their calculations, for diffusion to take place. An excellent test for diffusion effects would be to observe the FHB stars at high resolution and search for correlations between rotational velocity and temperature with respect to the observed [Ca/Fe] ratio, since it would be expected that very slowly rotating, hot FHB stars should suffer the most from diffusion.

Finally, we can speculate about the lack of evidence for strong diffusion effects in the metal-poor A-star sample. For diffusion to occur at all it is necessary for a star to have a slow stellar rotation. If this were not the case then correolis-type circulations in the outer envelope of the star would tend to mix materials and inhibit the diffusion effects. It is for this reason that metallic-line A-stars are nearly

always found in binaries, where tidal braking by the secondary component slows the A-star's rotational speed to the point where diffusion can occur.

In the abundance range, $-1.0 > [Fe/H] > -2.0$, which was analyzed in calculating the overall [Ca/Fe] ratio, the A-star sample is dominated by blue metal-poor main sequence stars (BMP). There is still considerable debate as to whether these stars are "normal" main sequence stars or field halo blue stragglers which have extended main sequence lifetimes through binary mass transfer or binary coalescence. In general it would be expected that the blue stragglers would have large rotational velocities from spin-up caused by orbital angular momentum transfer. This effect is in fact observed in many open cluster blue straggler stars. It has been found, however, that a large number of blue stragglers in the intermediate age open clusters ($\sim$ 1 Gyr old) have slow rotational velocities and a significant number show Am characteristics. At present it is not known if similar effects are operating in the older globular cluster blue stragglers, although Peterson has claimed no Am stars have been found in her sample of M 4 blue stragglers.

The overall lack of evidence for diffusion effects in the A-star sample would seem to indicate that the BMP stars do not belong to the class of slowly rotating blue stragglers. Unfortunately, differentiation between fast rotating blue stragglers and normal A-type stars is not possible from our [Ca/Fe] results. A stronger test will come when measurements of lithium (thought to be destroyed during a merger event) are finally carried for the BMP stars. A final note, however, should be made concerning the consistency between the Wheeler halo dwarfs and the A-star sample. If BMP stars are the stellar remnants of an accreted dwarf galaxy it is curious that their self-enrichment history so closely matches that of the galactic halo. For the globular cluster stars which have been investigated in high resolution

studies, the [Ca/Fe] ratios very closely match that of the Wheeler et al. trend. This result, coupled with the Peterson observations, indicate that the [Ca/Fe] ratio for the BMP's are consistent with the interpretation that the BMP stars are blue stragglers from disrupted globular clusters. There is, however, strong evidence that the dwarf spheroidal galaxies have metallicity distribution functions that, together, strongly resemble the Galactic halo (Suntzeff 1993). Such evidence hints at a halo field population that is made up of accreted dwarf galaxies. If other dwarf spheroidal elemental ratios, including [Ca/Fe], also resemble the galactic halo, then such a scenario is strengthened and the BMP results remain consistent with an accretion origin.

4.1.3.2 Blended Interstellar CaII K

We next wish to examine the effects of the interstellar CaII K component on the derived stellar abundance. Figures 4.13a and 4.13b are plots of the [Ca/Fe] abundance as a function of height above the galactic plane, for the FHB and A-star samples. Although the most metal deficient stars are potentially the best probes for the interstellar contamination (a weak stellar line has a larger percentage of interstellar contamination), the grid edge effect forces us to again examine the range of $-1.0 <$ [Fe/H] < -2.0. The plot of the FHB sample clearly shows an overabundance of calcium nearer the plane ($|Z| < 1.5$ kpc), where as the A-star sample shows no clear trend in $|Z|$ height. It is expected that the calcium overabundance in the FHB sample is due to contamination of the interstellar component. Since the A-stars extend to smaller distances than the FHB stars the amount of intervening material is probably smaller, leading to the difference between the samples.

To further probe the question of interstellar contamination, figure 4.14a shows the [Ca/Fe] values for the FHB stars with $|Z| < 1.5$ kpc as a function of sin(l). In

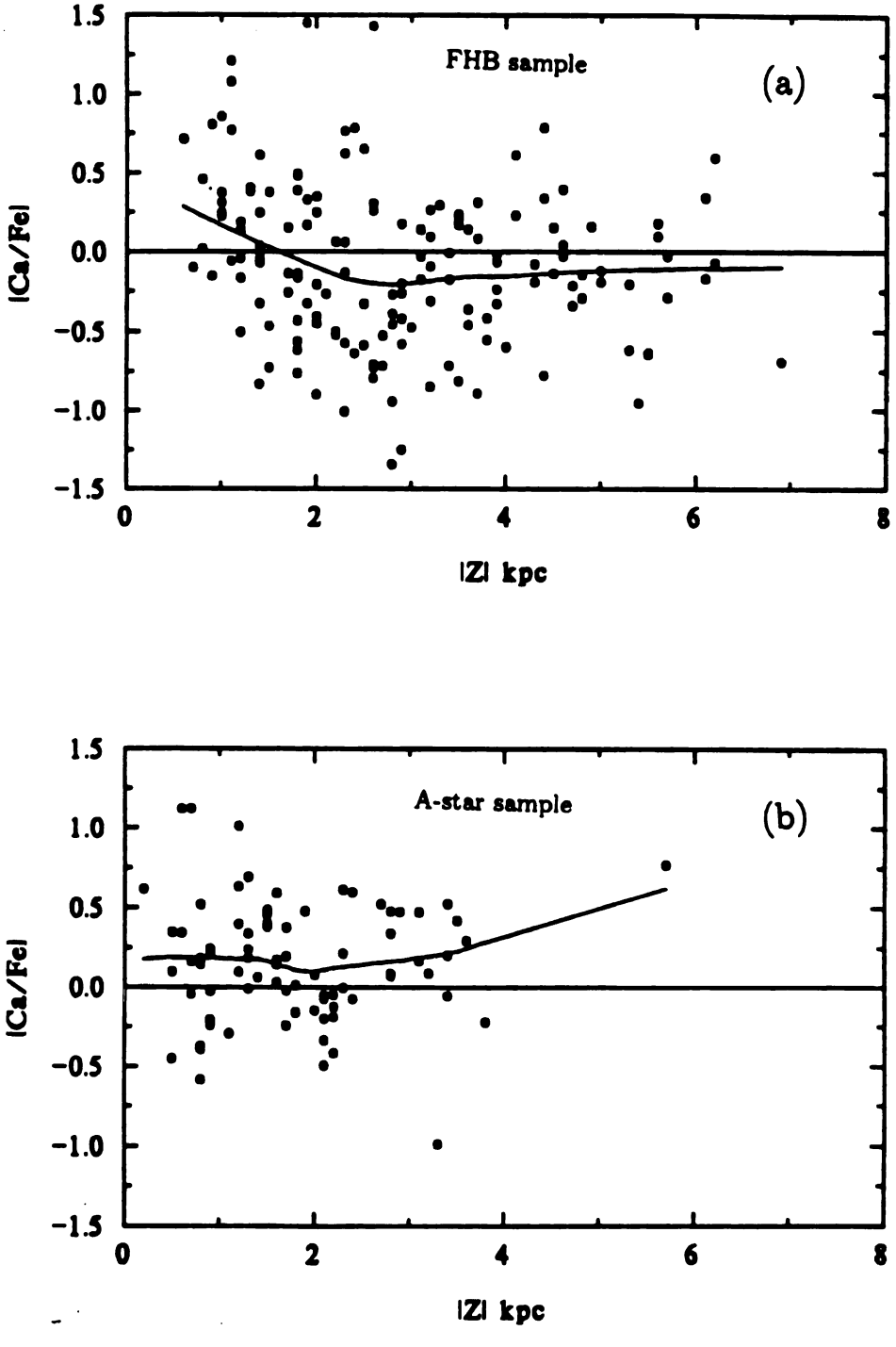

Fig 4.13: Effects of interstellar CaII at low $|Z|$ heights.

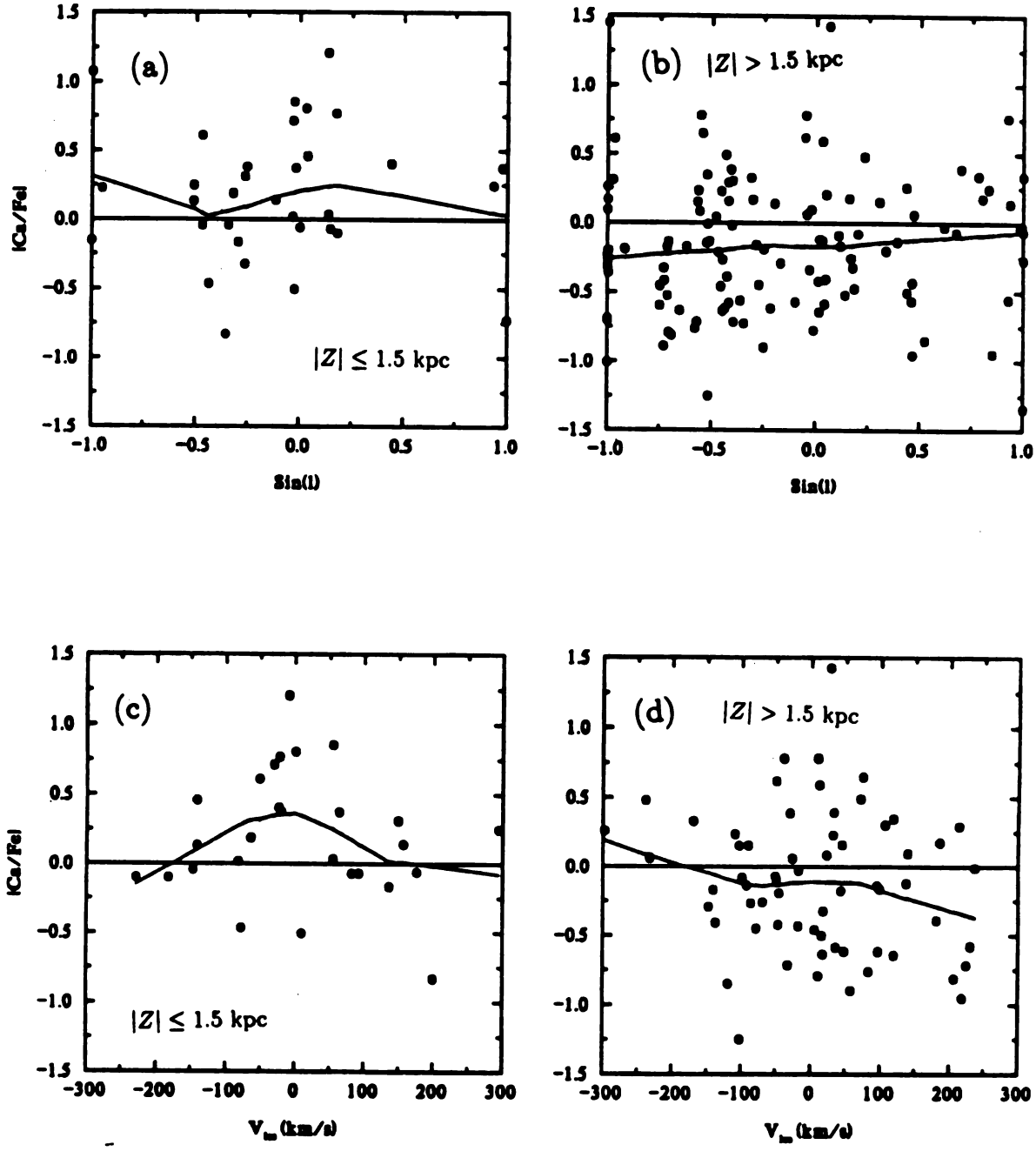

Fig 4.14: Effects of interstellar CaII toward the galactic center.

this plot, the stars in the direction of the galactic center have a value of sin(l) = 0. Although there are to few stars to identify a clear trend it does appear that the majority of stars with excessive calcium overabundance lie in the direction of the Galactic center. As a comparison, figure 4.14b shows the sin(l) dependency of [Ca/Fe] is not present in the FHB stars with $|Z| > 1.5$ kpc.

The interstellar CaII K component is a potential problem for our procedure, if it is blended with the stellar component. This occurs if the intervening gas cloud and a given star have nearly the same line-of-sight velocity. In the direction of the galactic center it is expected that the interstellar gas will have a small V_{los} since it is probably the case that the gas is in rotation with the galactic disk and thus has only a small radial velocity dispersion. The FHB stars, however, have a large range of V_{los} and we would expect the worst contamination to occur for the stars with small V_{los} values. Figure 4.14c shows the [Ca/Fe] as a function of the observed V_{los} for the FHB stars in the direction of the Galactic center and at $|Z| < 1.5$ kpc. As expected, the peak in [Ca/Fe] occurs near $V_{los} = 0$ km/sec. Again, for comparison figure 4.14d shows that the stars toward the Galactic center, but with $|Z| > 1.5$ kpc shows no trend in V_{los}.

If we take these indications to be the signature of contamination from the interstellar CaII K line, then in this abundance range the interstellar component contributes to an overabundance as large as 1.0 dex. It would be expected that this effect would be even larger for the more metal deficient star ([Fe/H] < -2.0). From the plots, however, it appears that only a small percentage of stars with |Z| < 1.5 kpcs are affected. This sample is only a small percentage of the total sample of FHB stars, so it is unlikely that the interstellar component will play a major role in the overall uncertainty of the FHB metallicities. The A-star sample appears to

be virtually unaffected by the interstellar line.

4.1.3.3 Concluding Remarks on [Ca/Fe]

It appears that the calcium abundances for the A-star sample are consistent with the implemented [Ca/Fe] trend from Wheeler et al. In the mean, the FHB sample however, shows virtually no overabundance of calcium, and thus the implementation of the Wheeler trend may have resulted in derived [Fe/H] values which are systematically too low. Figures 4.15a and 4.15b are plots of the derived [Fe/H] values and [Fe/H] with the Wheeler trend removed, as a function of T_{eff} for the FHB sample. Typically quoted abundance values for the transition of thick disk to halo population is approximately [Fe/H] = -1.0 dex. We see that the sample with the Wheeler trend removed is a much better representation of what is expected for this transition region and may indicate our metallicity scale is several tenths of a dex too low for the FHB stars. This question will be addressed again in the chapter on kinematics. For now, suffice it to say, the overall [Ca/Fe] ratio for the FHB sample appears to be near zero, and is expected to be mainly the result of diffusion mechanisms operating in these slowly rotating stars. The consistency found between the metal-poor A-stars and the Wheeler et al. halo dwarfs indicate that extensive diffusion is not operating in this sample. This conclusion makes it very unlikely that the BMP stars are slowly rotating halo blue stragglers. It is also expected that interstellar CaII K contamination plays only a minor role in the overall uncertainty of the derived program star abundances.

4.2 Characteristics of the FHB sample

4.2.1 Bias and Selection Effects

Before examining the spatial and abundance characteristics of the FHB stars, it is necessary to discuss the amount of incompleteness present in the sample. As

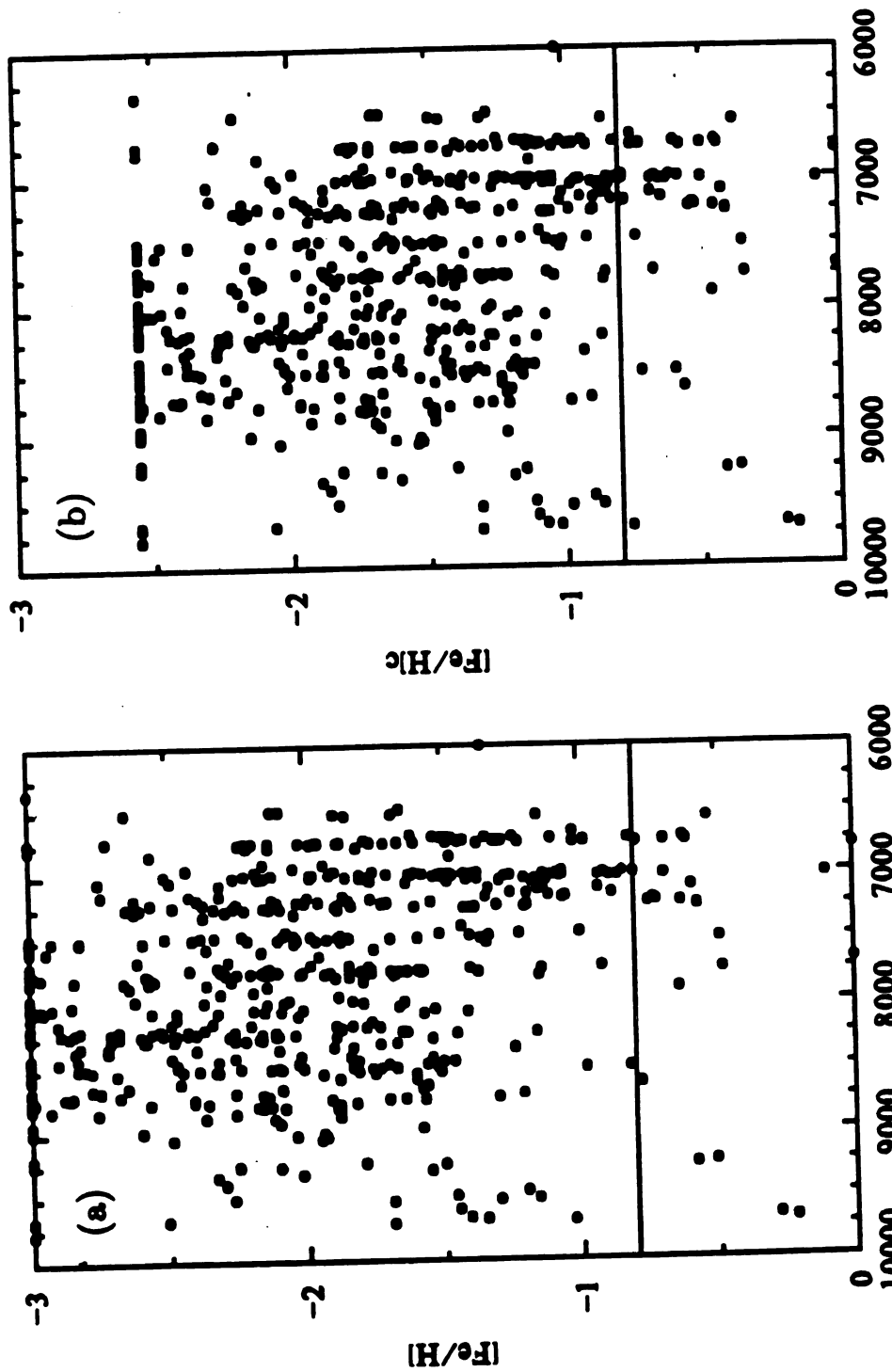

Fig 4.15: Removal of the Wheeler *et al.* trend in the FHB stars. Solid line indicates the generally accepted metallicity cut-off for the thick disk.

mentioned earlier, the FHB/A candidate sample is non-kinematically selected but is biased against inclusion of stars with strong CaII K features. The CaII K line has been shown to be both a strong function of temperature and metallicity. Therefore, the heaviest bias is expected to occur in the stars with cooler temperatures and higher metal abundance. The effect of this biasing is probably small for the majority of halo FHB stars, which extend to hotter temperatures due to their inherent lower abundances. Such is not the case for the more metal rich thick disk stars, which should be found only at the cooler end of the sample. This bias greatly limits the discussion of global abundance trends and kinematics of the thick disk and possibly the most metal rich halo populations.

Observational selection effects are also extremely troublesome to our investigation since oversampling any particular color range is tantamount to over selecting a particular abundance range. This problem will be overcome in the near future as the follow-up survey expands to all FHB candidates which have been identified in each of the fields. For the moment it is difficult to identify the selection criteria, employed in a given field, on a given night, of a given run, by any one of the various collaborative observers. This problem will become most evident as we investigate the possibility of abundance gradients with galactocentric distance and height above the plane. In most cases these selection effects force us, for now, to be content to identify potentially interesting results, which can be further investigated as the sample completeness is realized.

Finally, the limiting magnitude of the FHB sample is color dependent. This dependency arises from the fact that the horizontal branch is not in reality "horizontal", but decreases in absolute magnitude as the stars become bluer (hotter). This effect can be responsible for a shift in the sample to redder colors, and possibly

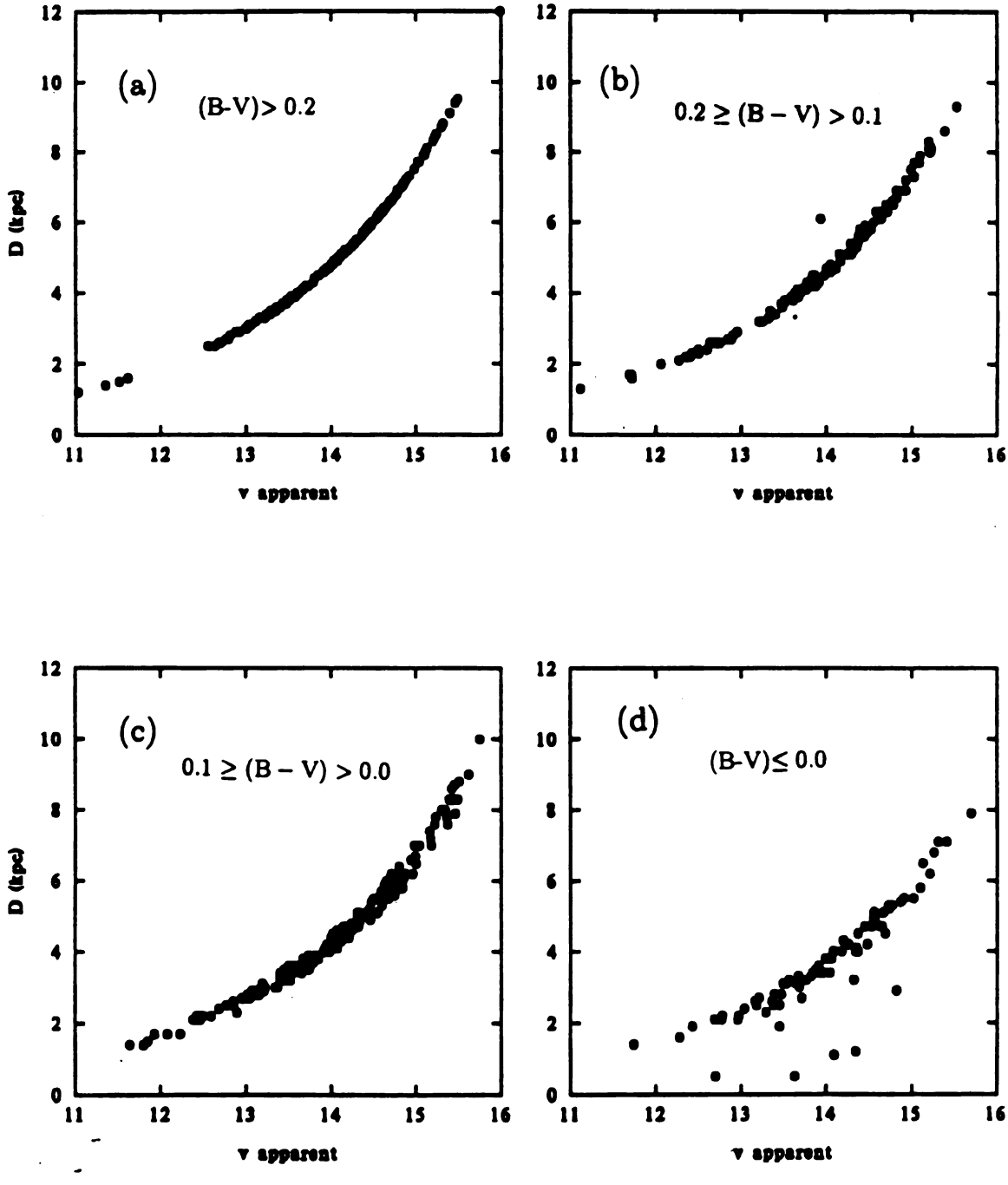

Fig 4.16: Decrease in sample distance as a function of apparent magnitude for the FHB stars.

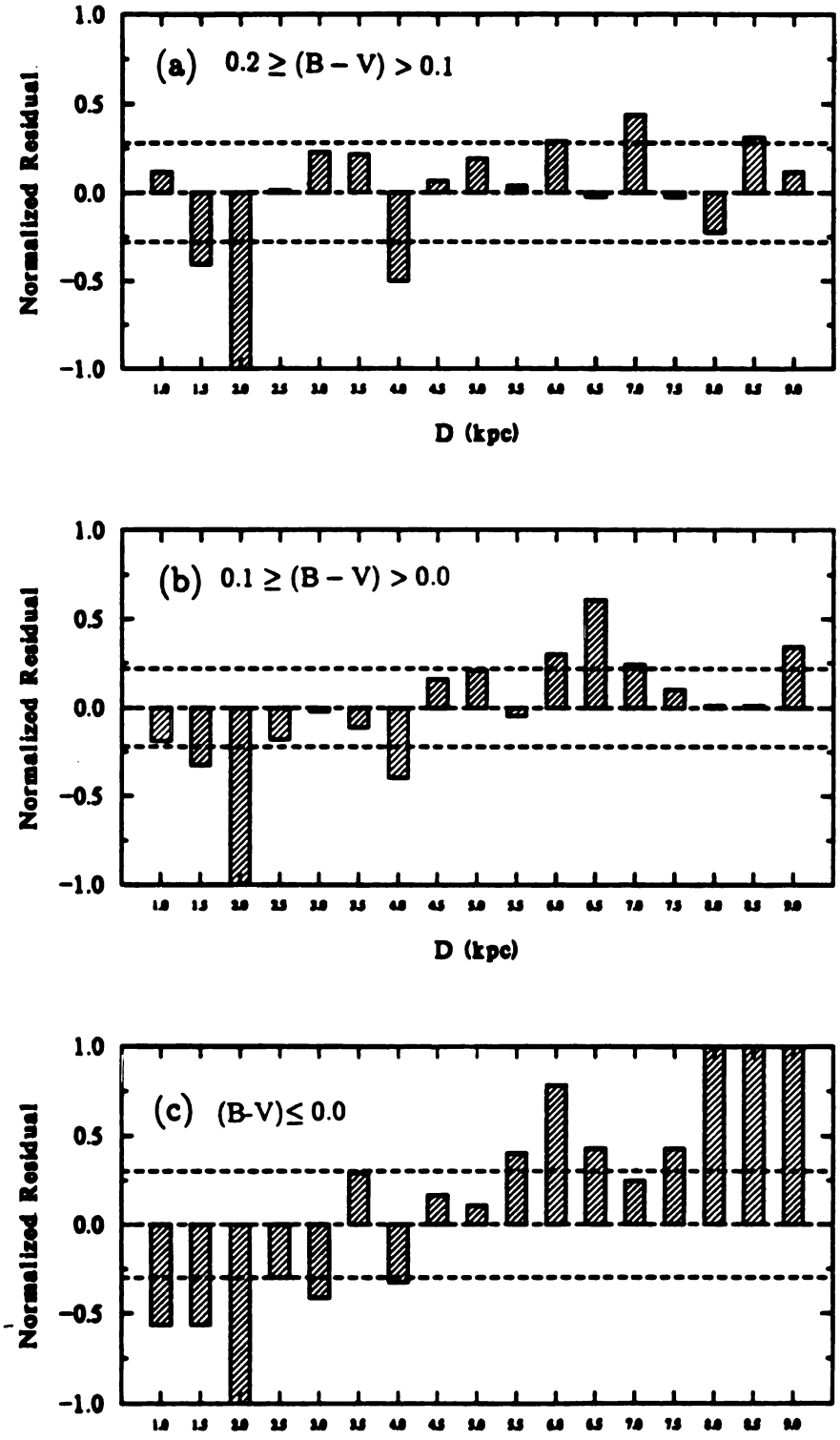

Fig 4.17: Noramalized residual plot calculated by comparing to the sample with (B-V)> 0.2. The bluest stars suffer the greatest decline in number with increasing distance.

higher abundances, as the distance limits of the sample are reached. Figures 4.16a-d show the effect of this limiting magnitude for four cuts in (B-V). There appears to be a continual decrease in distance as the stars become bluer, with the largest effect occurring for (B-V)< 0.0. To better quantify this effect figures 4.17a-c show the fractional normalized residuals as a function of distance for the 3 bluer samples from figure 4.16. This residual was calculated by first normalizing each sample and then comparing the fractional difference between the subsample with (B-V)> 0.2 and the other three samples. This was done assuming that the reddest subsample extended to the greatest distance. Plots (a) and (b) show no real signs of sample depletion at the largest distances. Plot (c), on the other hand, clearly shows a lack of stars in the beginning at $\sim$ 6 kpc. distant.

Therefore, care must be taken when interpreting abundance gradients and temperature shifts in the hottest stars (e.g. 2nd parameter effects) at the distance limit of the survey.

4.2.2 The Metallicity Distribution Function (MDF)

We begin the investigation of the abundance properties of the FHB sample by plotting a histogram of the MDF. It should be remembered that the previously-discussed incompleteness factors will have direct bearing on the number of observed FHB stars in a given region of the plot. This is especially true at the metal-rich end. Figure 4.18a is a plot of the derived abundance for the FHB sample, binned in 0.2 dex intervals. Unlike the findings of Laird *et al.* (1993) for their sample of local dwarfs, we find very few stars with abundance values less than [Fe/H] = -1.2. This is due to the metallicity bias in the sample, and the fact that hot, metal-rich FHB stars are not expected to exist. The peak in the MDF occurs at approximately [Fe/H] = -2.0. This is 0.4 dex lower than the peak found by Laird *et al.*

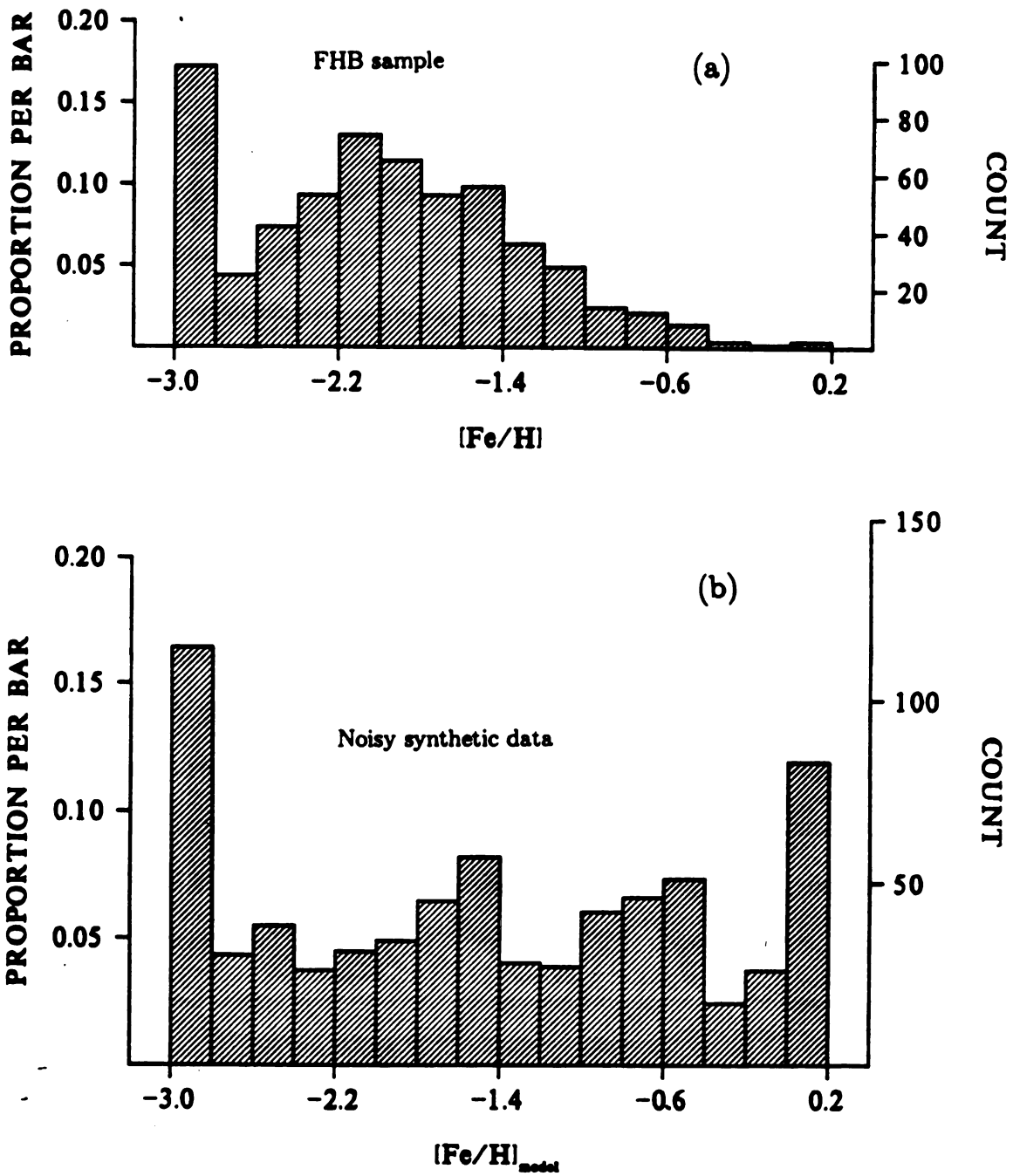

Fig 4.18: The MDF for the FHB stars. The bottom plot shows the distribution for the noisy synthetic spectra.

It is probably not a coincidence that this is very close to the amount of shift that would occur if the aforementioned Wheeler *et al.* trend was removed from the FHB sample.

In examining the MDF, it is particularly troubling that so many of the FHB stars have metallicities near [Fe/H] = -3.0, especially since the decline beyond the peak is qualitatively similar to the Laird it et al. MDF. It is expected that this effect is the result of large scatter at the metal-poor end of the distribution, which is asymmetrically bound by the edge of the calibration grid. We can test this assumption by once again returning to the noisy synthetic spectral analysis. Figure 4.18b is a histogram of the derived results for the noisy synthetic spectra, binned in intervals of 0.2 dex. We immediately see the same overpopulation for the lowest metallicity bin as was found for the FHB sample. Figures 4.19a-h show the breakdown of the derived synthetic results for a range in abundance of $-1.5 \geq$ [Fe/H] ≥ -3.0. The temperature is also split with $T_{eff} < 8000$ K shown on the left. We see that the vast majority of the metallicity values which are scattered into the lowest abundance bin are from the higher temperature low-metallicity spectra where the various absorption features are the weakest. From this we conclude that the vast majority of stars with abundances in the lowest histogram bin have actual abundances below [Fe/H] = -2.0 and that large scatter associated with this effect is confined to the hottest stars. Determination of the 1σ scatter in the noisy synthetic spectra for $-1.5 \geq$ [Fe/H] ≥ -3.0 shows only a ± 0.19 dex scatter for $T_{eff} < 8000$ K, while the scatter is ± 0.50 dex for $T_{eff} \geq 8000$ K.

4.2.3 Abundance Gradients

As mentioned in the Introduction, the existence of a halo abundance gradient with respect to galactocentric distance or height above the plane is a strong

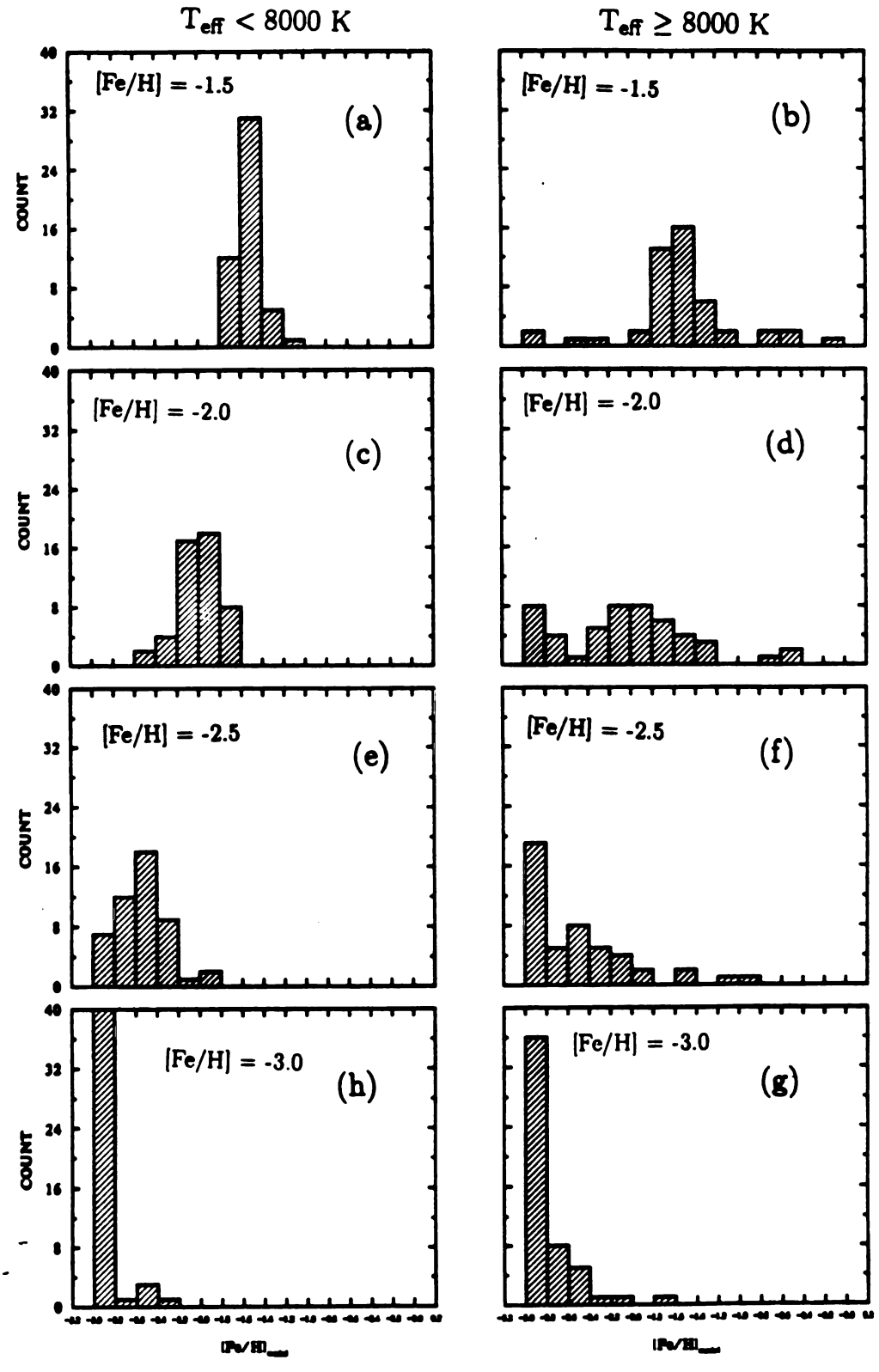

Fig 4.19: Grid edge effects from scatter in the calculated [Fe/H] values for the noisy synthetic data.

indication of self-enrichment of the halo during a dissipational collapse. Therefore, it is of great interest to see if such gradients exist. The FHB sample is potentially ideal for such an investigation, since the large spatial extent of the sample allows a broad baseline over which to identify abundance trends. At the moment our sample is incomplete and thus observational selection effects greatly inhibit our ability to constrain such results. It is still, however, a worthwhile endeavor to investigate the question of abundance gradients if for no other reason then to help characterize our current data set.

4.2.3.1 Radial Abundance Gradient

Results outside the solar circle (R > 8 kpc) for the globular clusters (Zinn 1985), field dwarfs (Carney *et al.* 1990) and RR Lyrae variables (Suntzeff *et al.* 1991) all show virtually no radial abundance gradient. Inside the solar circle, all 3 surveys show the existence of gradients on the order of -0.06 dex/kpc. These results indicate that the inner portions of the halo may have participated in a dissipational type collapse. Figure 4.20a is a plot of [Fe/H] as a function of galactocentric distance R, for the program FHB sample. A LOWESS fit to the data shows the general trend of decreasing abundance with increasing R to a distance of R = 8 kpc, after which the fit levels off. Although such a trend appears to confirm an abundance gradient inside the solar circle two points of caution are warranted.

First, we see a substantially larger number of stars with [Fe/H] > -1.2 in the inner halo sample. Although the LOWESS fit is resistant to outliers, their presence in the sample could still be in part responsible for the trend toward higher abundances in this portion of the plot. Also, it is expected that many of these stars are members of the thick disk population, and therefore should be removed when examining the possibility of a gradient in the halo. Figure 4.20b shows the

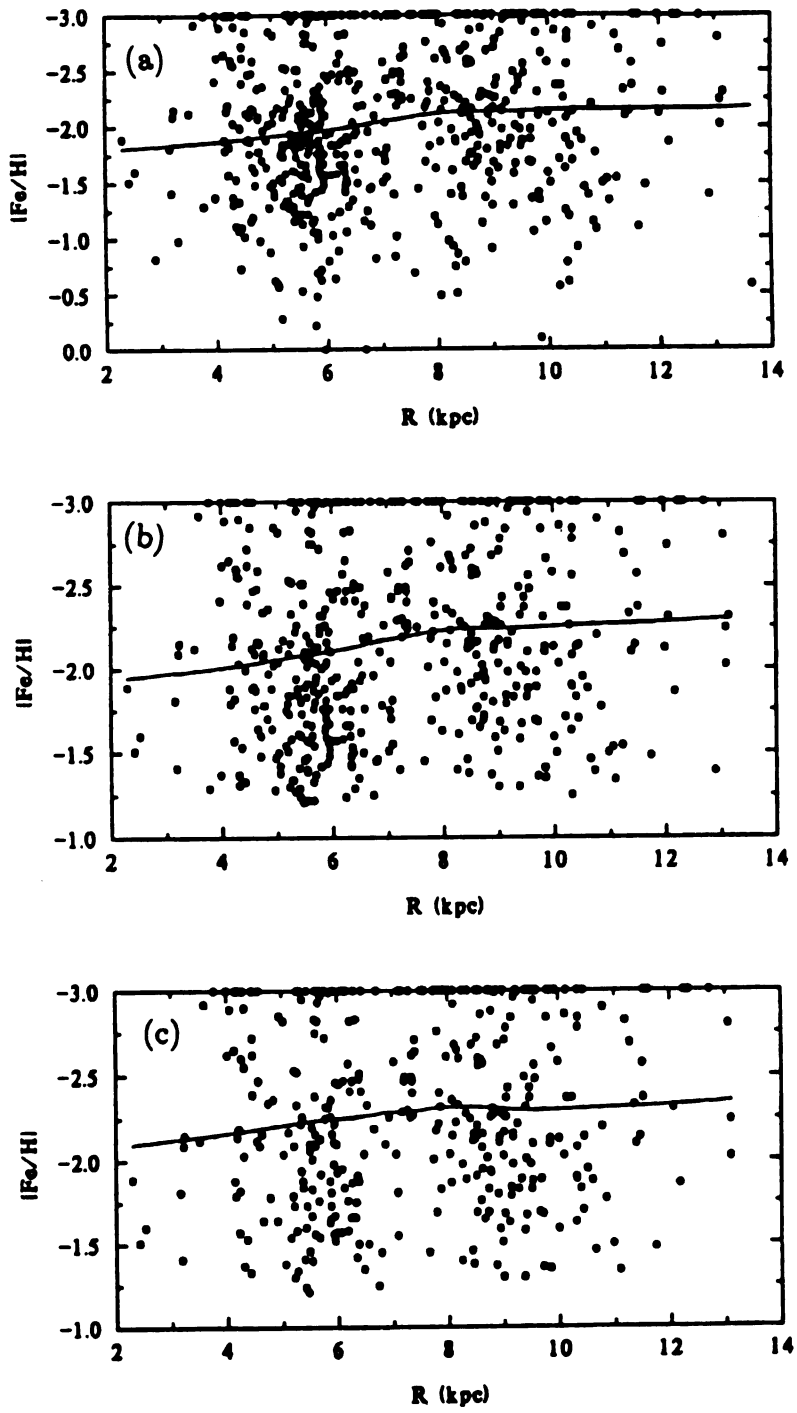

Fig 4.20: Gradient in metallicity as a function of Galactocentric distance (R). Plot (a) shows the entire FHB sample, plot (b) has stars with [Fe/H]> -1.2 removed, and plot (c) with the "hot star" sample removed. The curving line is a LOWESS fit to the data.

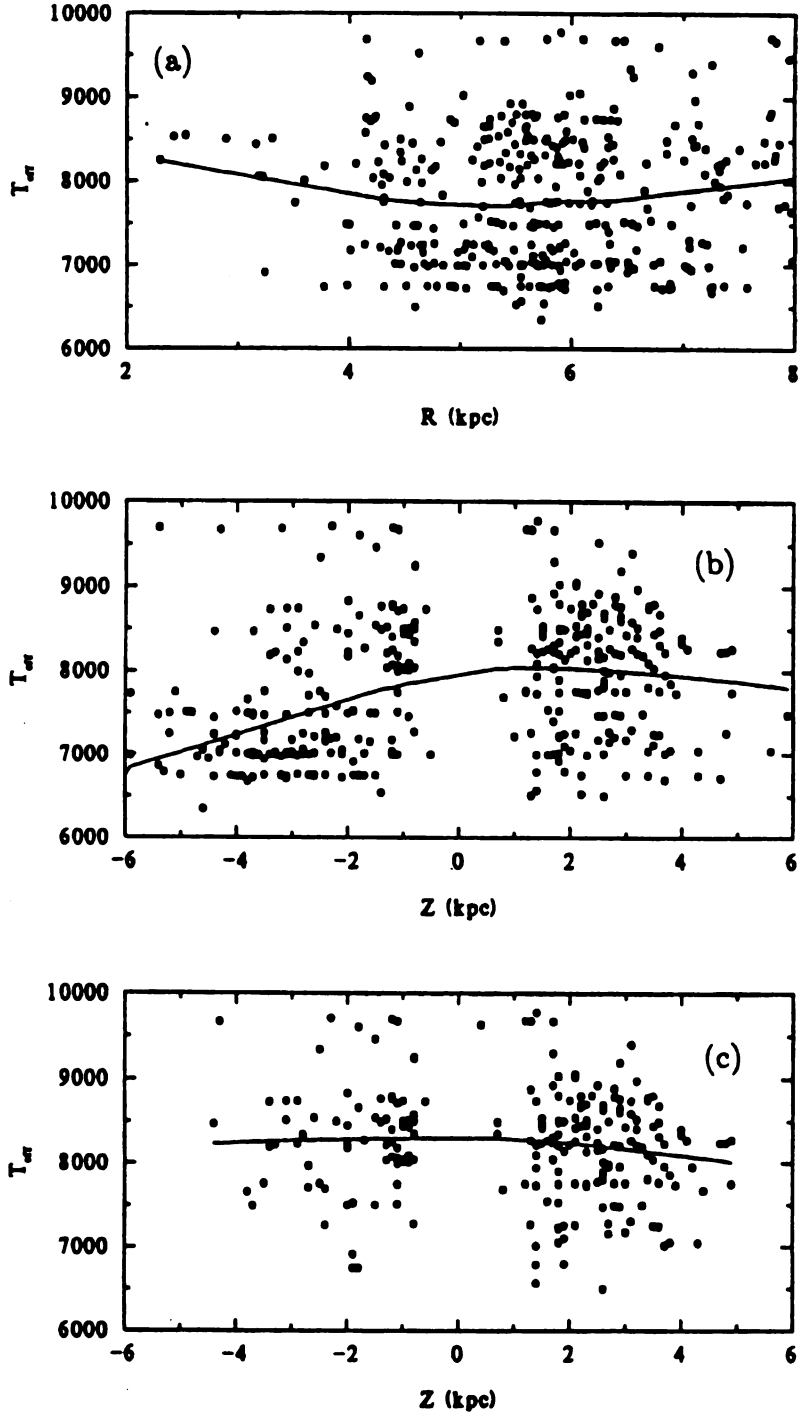

Fig 4.21: T_{eff} as a function of (R) and ($|Z|$) showing a difference in the selection criteria between the "hot star" and the more recently observed FHB samples. Plots (a) and (b) show an excess of cooler stars exists in regions dominated by the "hot star" sample. Plot (c) shows no excess when the "hot star" sample is removed.

LOWESS fit for the stars with [Fe/H] ≤ -1.2. As would be expected the overall fit has shifted to slightly lower abundances but the inner gradient still persists.

Though not evident in figure 4.20, a second point of concern is a decrease in T_{eff} near R = 5 kpc. Figure 4.21a is a plot of T_{eff} with respect to R, for the inner halo region, and shows a dip in temperature as would be expected for higher abundance FHB stars. Figure 4.21b is a plot of T_{eff} as a function of Z height out of the plane. We see clearly that the sample in the south Galactic hemisphere is overrepresented at cooler temperatures compared to the north Galactic sample. Upon first inspection this plot seems to indicate a substantial difference in HB morphology (possibly due to abundance) between the two hemispheres. It is more likely the case that this is an excellent example of observational selection effects. Many of the stars in this region of the south galactic hemisphere were drawn from the "hot star" sample. The observational follow-up selection criteria employed for this sample resulted in a larger number of cooler FHB stars than have been observed in the more recent observing runs. Figure 4.21c is a plot of the same region but with the "hot star" sample removed. This has greatly reduced the cooler star dominance in the south and strengthens the selection effect hypothesis.

With the "hot star" sample removed, figure 4.20c shows the plot of [Fe/H] as a function of R for the remaining sample of 411 FHB stars. The LOWESS fit indicates that the inner halo gradient has become shallower, but still exists with a slope of ~ -0.03 dex/kpc. The abundance gradient question is taken one step further by calculating the mean [Fe/H] value for four radial bins of ~100 stars each. Figure 4.22a shows the results for the binned data, where the sloping line is a least-squares fit to all four bins and the horizontal line is the fit excluding the inner most bin. For this bin it remains uncertain how much of a role other selection effects play, as

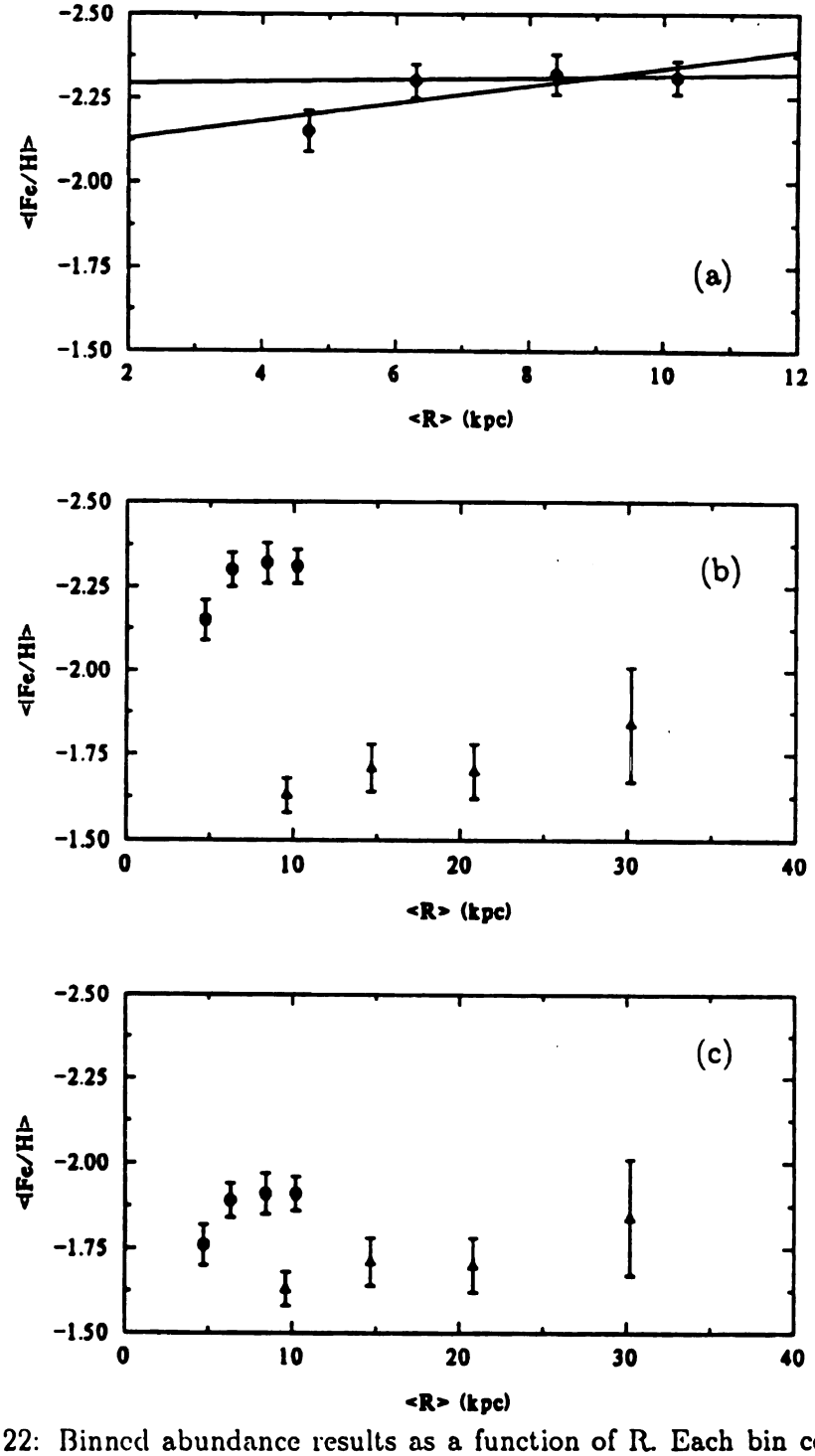

Fig 4.22: Binned abundance results as a function of R. Each bin contains $\sim$ 100 stars. In plot (a) the least-square fits to all the data points (sloping line) and the 3 most distant points (horizontal line) are shown. Plot (b) compares the FHB results (circles) to that of the Carney *et al* sample (triangles). Plot (c) is with the Wheeler *et al.* trend removed.

well as, the extent of interstellar CaII K contamination toward the Galactic center. From our data we conclude there is no significant radial abundance gradient beyond R = 6 kpc, and only a -0.02 dex/kpc gradient between the inner most bins.

Finally, we can use these results to test for systematic errors in our program star abundances. Figure 4.22b is a plot of our data compared to the results from the Carney *et al.* dwarf survey. The Carney group tested for abundance gradients by calculating the apogalacticon distance for their local high-velocity stars and used a kinematic criteria to constrain their halo sample. The plot clearly indicates a large difference in the mean abundances between the two samples. Even if we included the stars with [Fe/H] > -1.2 the derived mean values are still several tenths of a dex too low. Figure 4.22c is the same plot but with the previously debated Wheeler et al. trend removed. We see the samples differ now by only about 0.2 dex. This amount could be attributed to differences in halo selection criteria along with the propensity for our stars to migrate to the lowest abundances (see section 4.2.2). This adds to the evidence that the Wheeler trend may not be applicable to the FHB stars.

4.2.3.2 Vertical Abundance Gradient

There is no dispute that the average metal abundances decrease as a function of increasing distance out of the Galactic plane. The majority of this effect is due, however, to the presence of the relatively metal-rich thick- disk population. Excluding the thick disk, there has as yet, been no consensus on the existence of a Z abundance gradient in the halo itself. This is one of the primary pieces of evidence that precludes wide scale acceptance of the ELS/SZ hybrid model. The lack of a Z gradient does not disprove a contracted model interpretation of halo formation, but it does suggest that mergers may have played a major role in "shuffling the dex" of

abundance. Because of the importance of this question, we now examine the FHB data for evidence of a Z gradient.

We begin by searching for evidence of a $|Z|$ abundance gradient inside and outside the solar circle (R = 8 kpc). Because Z height is a function of the Galactocentric distance, R, the samples were instead split according to their R distance projected onto the galactic plane (U). The inner sample ranges from $4 < U < 8$ kpc, while the outer sample is from $8 < U < 12$ kpc. Figures 4.23a and 4.23e are plots of [Fe/H] as a function of $|Z|$ for each of these regions. As with the radial gradient analysis, the most metal rich stars, [Fe/H] > -1.2, have been excluded from the samples in an attempt to secure a pure halo sample. The LOWESS fit in figure 4.23a indicates a mild gradient throughout. This sample, however, includes the stars from the "hot star" sample, as discussed in the last section. Figure 4.23c is the same plot but with the "hot star" sample removed. There still remains a possible gradient below $|Z| = 3$ kpc, but the rest of the gradient has, for the most part, been removed. In contrast, the outer sample (figure 4.23e) indicates that no gradient exists for $|Z| < 4$ kpc. The apparent slope in the LOWESS fit beyond this point is very uncertain, and probably not real, since it is generated by only a few low metallicity stars.

Figures 4.23b, 4.23d and 4.23e are the binned mean values for the previous plots. Although the best linear fit to the data would indicate a |Z| gradient in figure 4.23b, $d[Fe/H]/d|Z| = -0.030 \pm 0.011$ dex/kpc, the majority of this signal disappears in figure 4.23d, where $d[Fe/H]/d|Z| = -0.022 \pm 0.012$ dex/kpc. The slope that does remain is the result of the lowest $|Z|$ height bin which is barely significant at the 1σ level. This small difference could easily be explained by incompleteness or contamination from BMP stars. Figure 4.23e is the binned plot for the outer sample, which indicates a gradient of $d[Fe/H]/d|Z| = -0.065 \pm 0.012$ dex/kpc. This

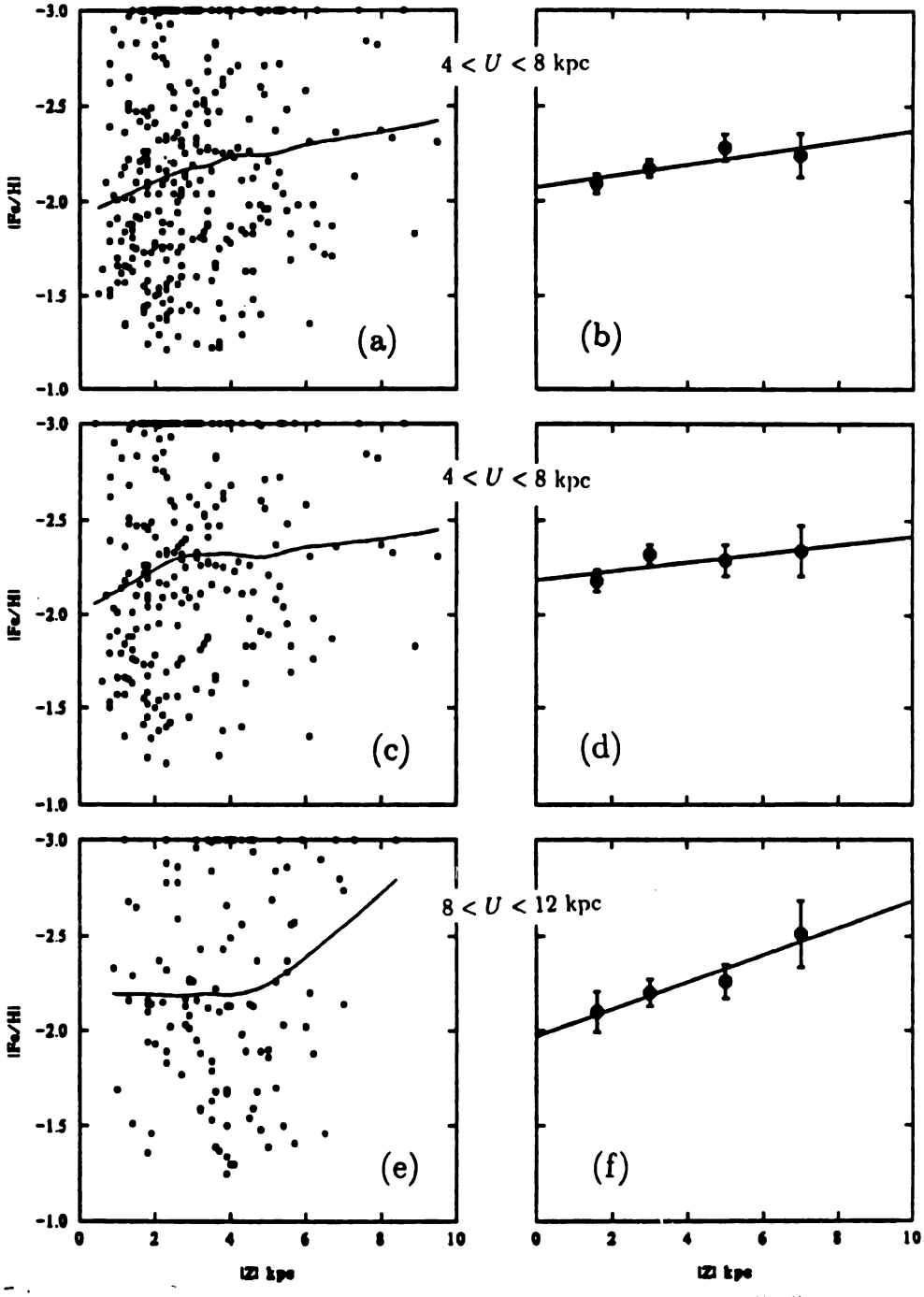

Fig 4.23: Gradient in metallicity as a function of vertical height ($|Z|$) for the inner and outer halo samples. Plots (a) and (b) show the inner halo region for all halo FHB stars while (c) and (d) have the "hot star" sample removed. Plots (e) and (f) represent the outer halo FHB sample.

slope arises completely from the inclusion of the highest $|Z|$ bin, which contains only 10 stars. Because there are so few stars in this bin, it is not possible to make strong claims about an actual change in the halo abundance distribution and we must conclude that there is not good evidence for an abundance gradient in the outer halo. It should be noted, however, that this lower metallicity does not arise from magnitude limit incompleteness since this effect operates in the opposite sense.

Next we examine the FHB sample in the direction of the polar caps ($|b| > 65$). Figure 4.24a is the corresponding plot of [Fe/H] with respect to |Z|. Again, we see no clear indication of an abundance gradient. This is also true for the binned data in figure 4.24b. It is unclear in this plot, however, which stars are passing through a given region of |Z| and which are at their maximum distance out of the plane. Without this knowledge, it is possible that a gradient could be smeared out by inclusion of low metallicity, high velocity, interlopers. We can constrain the maximum |Z| height by only considering the FHB stars with W velocities of $-30 <$ W < 30 km/sec. This helps to ensure that the stars will not travel significantly further out of the plane then where they are observed. Without full space motions, however, it is impossible to estimate the fraction of this sample which have large transverse velocities that could ultimately carry them far from the polar regions. Figure 4.24c is a plot of the binned polar cap region for the sample near their maximum |Z| height. Again, we see no clear dependency on abundance. The best linear fit to the data shows the existence of a slight gradient, however, it is not significant within the uncertainties of the mean.

Figure 4.24d is a plot of the $|Z|_{max}$ sample after removal of the Wheeler *et al.* abundance trend. Our data is represented by filled circles and for comparison, the Carney *et al.* data for halo dwarfs at $|Z|_{max}$ is shown as filled triangles with the

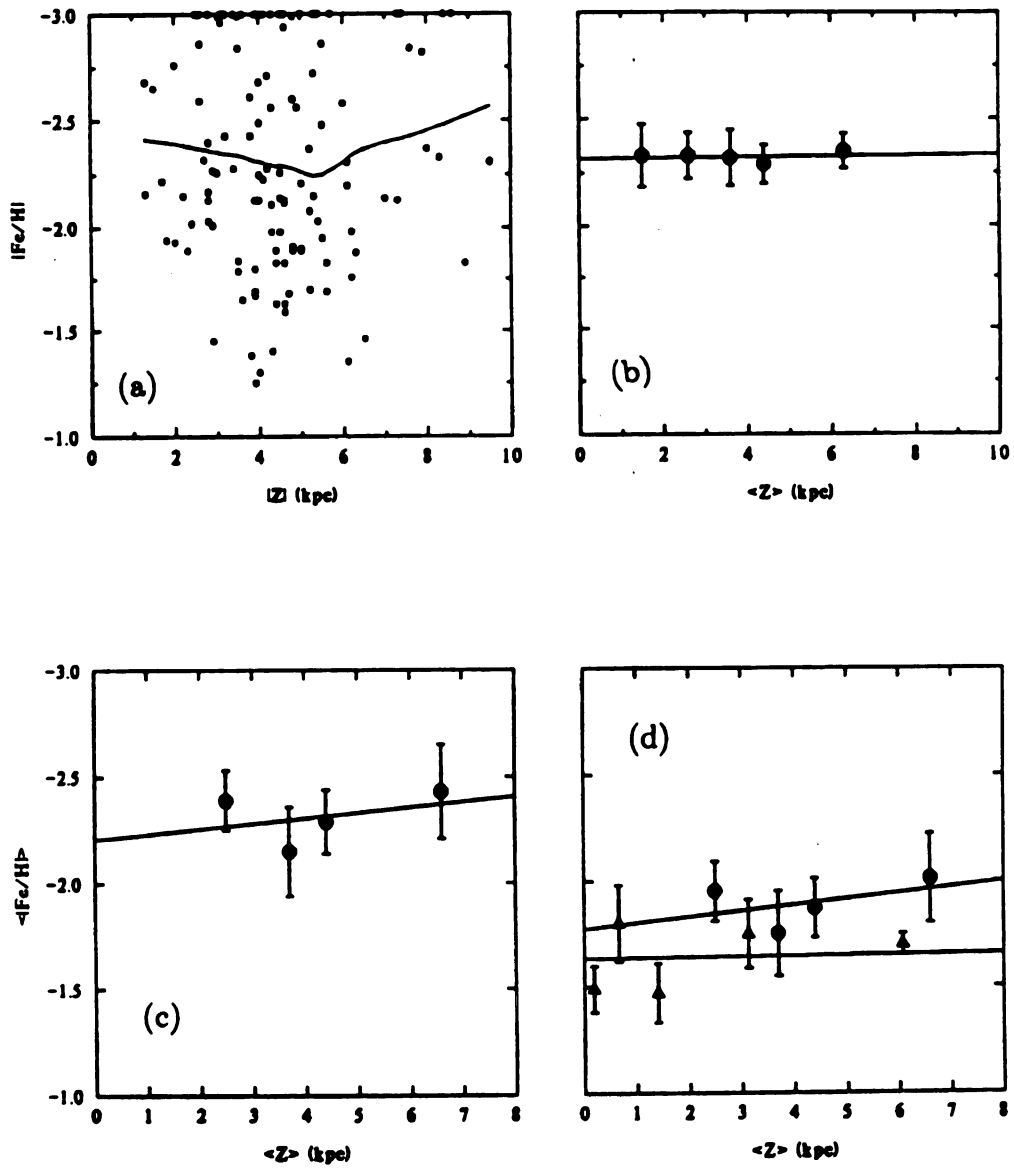

Fig 4.24: Gradient in metallicity as a function of vertical height ($|Z|$) for the polar cap regions. Plots (a) and (b) show all halo FHB stars. Plot (c) is the binned result for stars at a maximum $|Z|$ height. Plot (d) is a comparison to the Carney *et al.* sample with the Wheeler *et al.* trend removed from the FHB abundances. The sloping line is a least-square fit to the FHB sample the horizontal line is the fit the Carney *et al.* data.

lower line showing the fit to their data. It is very reassuring that within the uncertainties of both samples the external agreement in abundance is quite good. In fact, three of the five Carney bins shown are not significantly different from our abundance data.

We conclude from our data, that no significant |Z| abundance gradient exists in any of the regions explored. The good agreement with the Carney *et al.* results seem to indicate, that at least in the polar regions, incompleteness problems within our sample are minimal. The null abundance gradient result, though not totally compelling from our FHB sample, leads to serious questions concerning a collapsed component of the halo. If such a component exists, the corresponding abundance gradient has either been erased by mixing of the age-metallicity relationship, possibly from subsequent mergers of chemically distinct sub-units, or the collapse occured to rapidly for elemental recycling to occur.

4.2.4 The 2nd Parameter Effect

As discussed briefly in the Introduction, a star's temperature on the zero age horizontal branch is potentially a function of many different parameters. The so-called first parameter is metal abundance, which causes a shift in (B-V) toward bluer colors as metallicity decreases. It has been realized for some time that a second parameter is at work in some metal-poor globular clusters, which shifts the HB colors back towards the red. The primary candidate for this 2nd parameter effect is age. It has been shown by Lee (1993), that the metal-poor clusters which exhibit this effect are younger by several Gyrs, than the metal-poor non-second parameter clusters.

A similar 2nd parameter effect has been identified in the field by the investigations of Zinn (1986), Preston *et al.* (1991), Suntzeff *et al.* (1991) and Lee (1992).

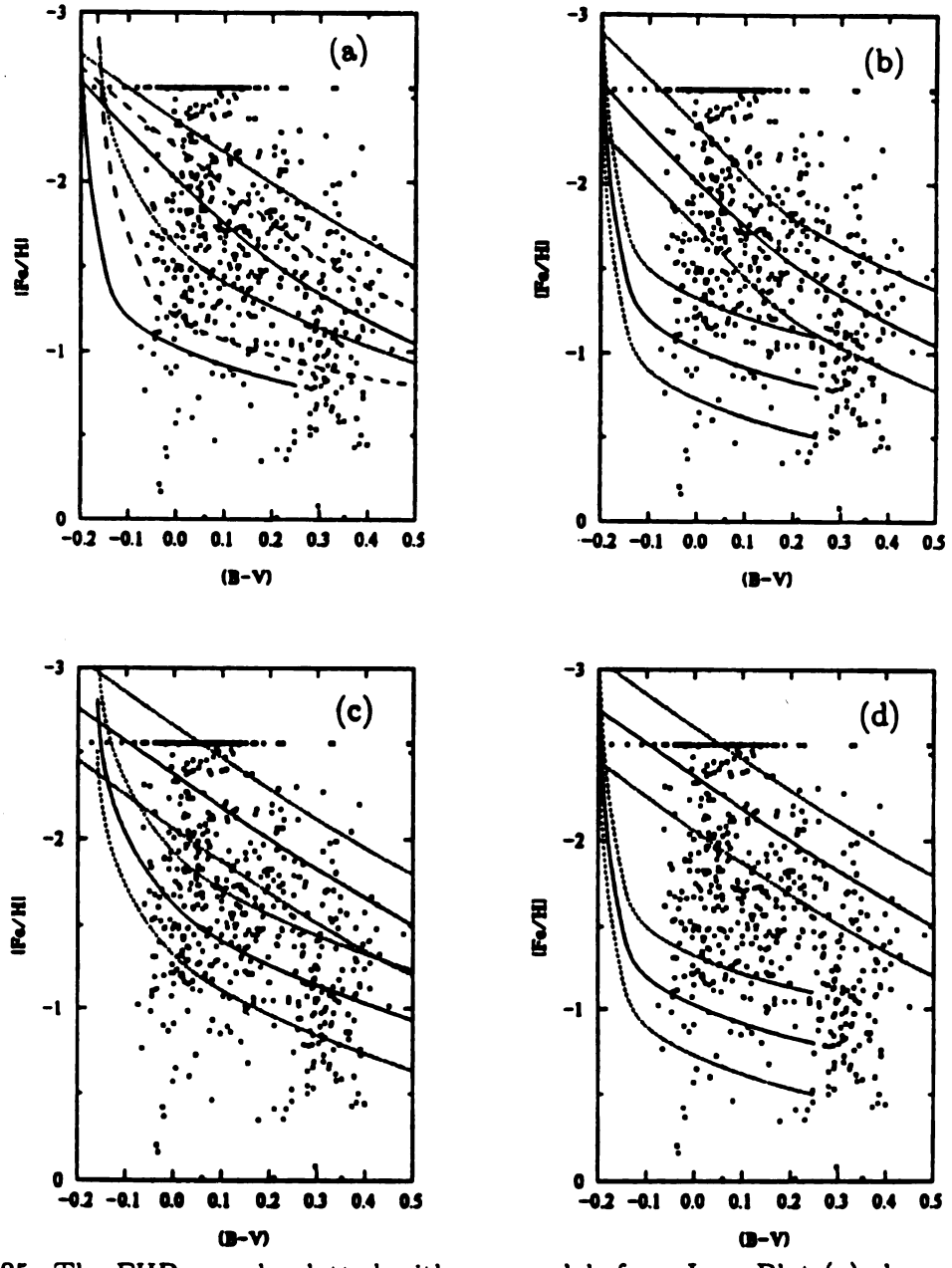

Fig 4.25: The FIIB sample plotted with age models from Lee. Plot (a) shows the oldest (solid lines), 1.3 Gyrs younger (dashed lines) and 3.3 Gyrs younger (dotted lines) models. Plots (b) and (c) are for the oldest and youngest models, respectively, with the uncertainty in [Fe/H] shown as dotted lines. Plot (d) shows the model fits using the oldest model for the blue edge and the youngest model for the red edge of the horizontal branch.

The results indicate that a shift to redder colors occurs as a function of increasing Galactocentric distance. If the interpretation of this effect is age, then it is strongly suggested that the galactic halo is older in the inner regions of the Galaxy and increasingly younger at greater distances. This places strong constraints on the timescale of Galactic halo formation.

To investigate the second parameter effect in our FHB sample we make use of the HB models by Lee *et al.* (1991,1993). Figure 4.25a is a plot of [Fe/H] values for the program FHB stars, as a function of $(B\text{-}V)_o$ color. The [Fe/H] values have been corrected to remove the Wheeler *et al.* [Ca/Fe] trend, so that the FHB stars and globular cluster stars are on a similar abundance scale. Plotted as solid lines are the model parameters for the blue and red edge of the horizontal branch assuming an age consistent with the oldest known globular star clusters. The dashed and dotted lines are the same but with the age decreased by 1.3 and 3.3 Gyrs, respectively. It is interesting to note that the older models for the blue edge of the HB match very well to the apparent cut-off in the FHB sample at higher abundances. However, it appears that the youngest model for the red edge is a better match to the cut-off at lower abundances.

Figures 4.25b and 4.25c are separate plots for the oldest and youngest models, where now the dotted lines indicate the estimated scatter in the derived abundances. We can now see that the oldest model (figure 4.25b) is a good match for the blue edge, within the uncertainties. As noted in the discussion on the MDF for the FHB sample, the scatter at the lowest metallicity values is greater then the average, especially for the hotter stars. Even so it is difficult to reconcile the red edge model with the observed data at cooler temperatures. It appears that the youngest model (figure 4.25c) remains a better fit to the data. This seems to be an indication that

there is indeed an age spread in the FHB sample.

For discussion purposes we construct figure 4.25d, using the oldest model to constrain the blue edge of the HB and the youngest (3.3 Gyrs younger) to constrain the red edge. Because the blue edge is at the highest abundance values, we must be concerned whether the sample metallicity bias has effected the result. This seems somewhat unlikely since it is expected that the bias will be the strongest for the cooler, metal-rich stars, which have the strongest CaII K features. As can be seen in the plot, there is no shortage of these stars. Therefore, it is expected that abundance biasing of the sample is not primarily responsible for the cut-off seen at higher temperatures. It is very interesting to note that the blue edge of the suspected thick disk stars also match well with the oldest model fit. If we had attempted to use a younger model for the blue edge, then the corresponding edge at [Fe/H] = -0.8 would be shifted much farther to the red (see figure 4.25a). With these considerations it appears that the blue edge of our sample is best constrained by the oldest Lee models. If this result is correct, it is also very suggestive that the thick disk is as old as the oldest halo stars in the sample. The red edge of the data also appears to be well constrained by the youngest Lee Models. The result that a younger population exists is independent of any bias or selection effects. This is true because the stars have been observed and no amount of incompleteness can remove them from the sample. A major concern is still the amount of scatter at the low metallicity end. Realistically it is possible that the intermediate age model could also fit the data within the expected scatter, but it remains unlikely that the coolest stars are consistent with the oldest model. A final concern is whether misidentified A-stars could have been included, filling in this region of the plot. This seems fairly unlikely since the number of stars redder then the oldest model is quite large, and

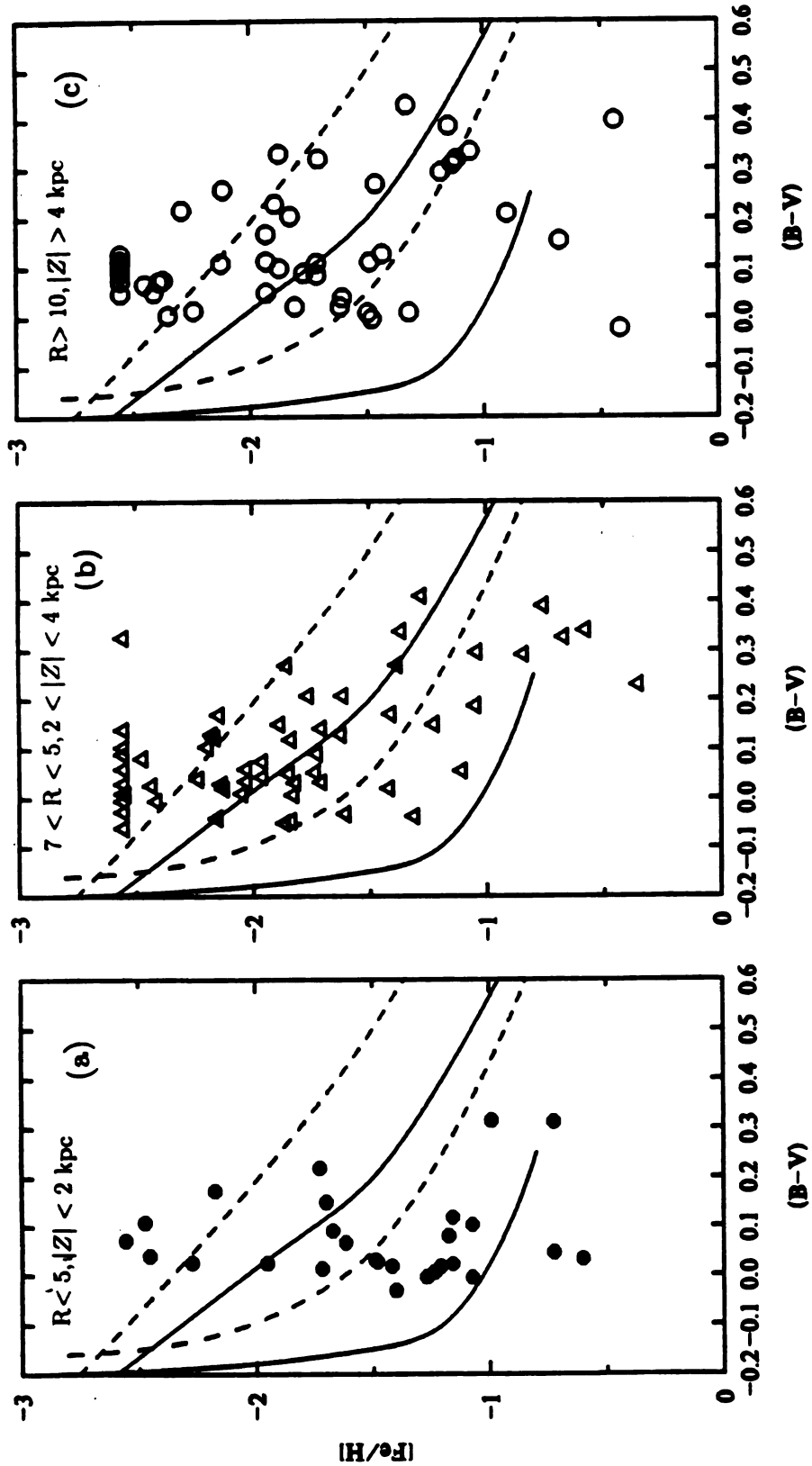

Fig 4.26: FHB sub-samples showing age effects with increasing Galactocentric distance. The solid constraining lines are from the oldest Lee models, the dashed lines are from the models which are 3.3 Gyrs younger.

the A-star sample has relatively few stars at the lowest abundances.

We conclude this section by investigating possible changes in age as a functionof spatial position. Figures 26a-c are plots of FHB subsamples with R< 5, $|Z| < 2$ kpc; $7 < R < 9$, $2 < |Z| < 4$ kpc; and R> 10, $|Z| > 4$ kpc, respectively. These samples were chosen to represent the extremes and average Galactocentric distance within the total FHB sample, in an attempt to enhance any age differences. The plots show a clear trend away from the oldest model as a function of increasing distance from the galactic center. In fact the most distant sample, figure 26c, is fit very well by the youngest Lee model. This result appears to confirm the previously published findings that the halo becomes younger as galactic distance increases, and suggests that the outer halo may have formed as a result of accretion of external stellar systems which exhibited delayed star formation.

MICHIGAN STATE UNIV.
3129301407

MICHIGAN STATE UNIVERSITY LIBRARIES
3 1293 01400 5916

THESIS
4

LIBRARY
Michigan State
University

PLACE IN RETURN BOX to remove this checkout from your record.
TO AVOID FINES return on or before date due.

DATE DUE	DATE DUE	DATE DUE
MAY 06 2000		
MAY 03 2002 04 19 02		

MSU Is An Affirmative Action/Equal Opportunity Institution
c:\circ\datedue.pm3-p.1

CHAPTER 5

KINEMATICS OF THE FHB STARS

5.1 The Distribution of Velocities

We now begin an exploration of the kinematic properties of the FHB sample. The overall scheme of this section is to explain the modeling tools used in the kinematic analysis and to employ them to both characterize the sample and identify areas which may hold interest.

Before beginning the kinematic investigation the previously calculated line-of-sight velocities were converted to velocities with respect to the Local Standard of Rest (LSR), in order to remove the effects of the solar motion. This was accomplished using the transformation equation:

$$V_{lsr} = V_{los} + 20([cos(l_o)cos(l_*) + sin(l_o)sin(l_*)][cos(b_o)cos(b_*) + sin(b_o)sin(b_*)]) \quad (5-1)$$

where l_o and b_o are the directional angles of the solar motion, given by $l_o = 57$ deg and $b_o = 22$ deg, and 20 (km/s) is the velocity of the sun with respect to the LSR. The values of l_* and b_* are the Galactic longitude and latitude for a given program star.

Figure 5.1a is a histogram of the velocity distribution for the entire FHB sample. The solid line is the best gaussian fit to the distribution. The plot indicates a

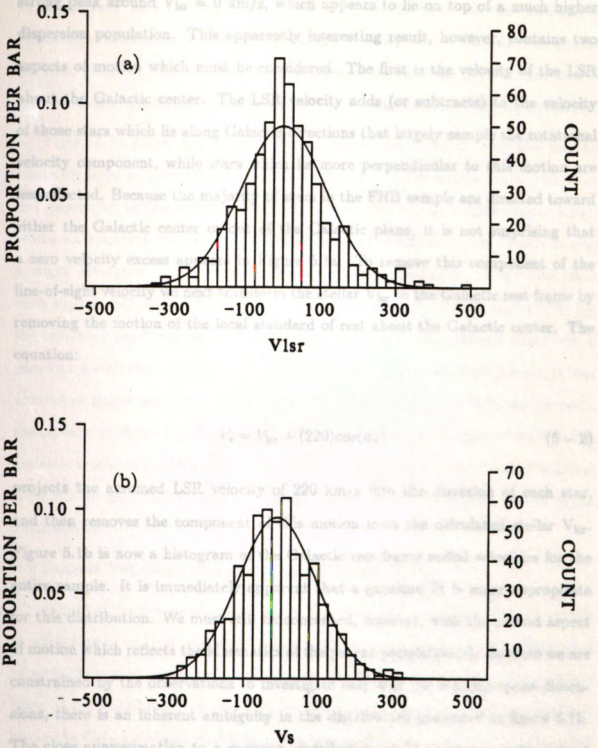

Fig 5.1 Histogram of velocities for the entire FHB sample

strong peak around $V_{lsr} = 0$ km/s, which appears to lie on top of a much higher dispersion population. This apparently interesting result, however, contains two aspects of motion which must be considered. The first is the velocity of the LSR about the Galactic center. The LSR velocity adds (or subtracts) to the velocity of those stars which lie along Galactic directions that largely sample the rotational velocity component, while stars which lie more perpendicular to this motion are less affected. Because the majority of stars in the FHB sample are directed toward either the Galactic center or out of the Galactic plane, it is not surprising that a zero velocity excess appears in Figure 5.1a. To remove this component of the line-of-sight velocity we next transform the stellar V_{lsr} to the Galactic rest frame by removing the motion of the local standard of rest about the Galactic center. The equation:

$$V_s = V_{lsr} + (220)cos(\alpha_*) \qquad (5-2)$$

projects the assumed LSR velocity of 220 km/s into the direction of each star, and then removes the component of this motion from the calculated stellar V_{lsr}. Figure 5.1b is now a histogram of the Galactic rest frame radial velocities for the entire sample. It is immediately apparent that a gaussian fit is more appropriate for this distribution. We must still be concerned, however, with the second aspect of motion which reflects the kinematics of the parent population(s). Because we are constrained by the observations to investigate only 4 of the 6 phase space dimensions, there is an inherent ambiguity in the distribution presented in figure 5.1b. The close approximation to a gaussian distribution could suggest a single parent population with nearly zero systemic rotation and which is isotropic in its velocity dispersions. From what we already know about the FHB sample and the kinematics

of the Galactic halo and thick disk, it is more likely the case that the distribution appears gaussian because it is dominated by a large number of stars in a particular Galactic direction. To test this assumption we now split the FHB sample into 3 groups, each of which predominately sample one of the cardinal Galactic directions.

Figure 5.2a shows an approximate gaussian distribution of velocities for the relatively large number of stars in the center and anti-center directions. This does not appear to be the case for the stars in the polar cap directions (figure 5.2b), where an apparent two-component distribution of velocities exists. There is also a slight difference in the gaussian width (velocity dispersion) for the two plots with σ_{GC} = 102 km/s and σ_{PC} = 93 km/s. Finally, figure 5.2c shows that for the relatively small number of stars in the rotation and anti-rotation directions, a gaussian distribution appears to be inappropriate. The velocity dispersion is also somewhat larger with σ_{Rot} = 112 km/s. It therefore appears that the gaussian distribution in figure 5.1b is predominantly due to the large number of stars in the Galactic center and polar regions. In the following sections more powerful statistical tools will be used to help in the investigation of the true kinematic nature of the FHB sample.

5.2 Sample Velocities as a Function of |Z| and [Fe/H]

As part of the sample characterization it is customary to plot the velocities both as a function of vertical height and metal abundance. This aids in the identification of multiple parent populations within a given sample. Figures 5.3a and 5.3b are plots of the distribution of velocities for the FHB sample as a function of height above the Galactic plane. Plot 5.3a, showing the velocities transformed to the local standard of rest, suggests the presence of an excess of stars with low dispersion ($|V_{lsr}| < 100$ km/s) that appear to be embedded in a higher dispersion population.

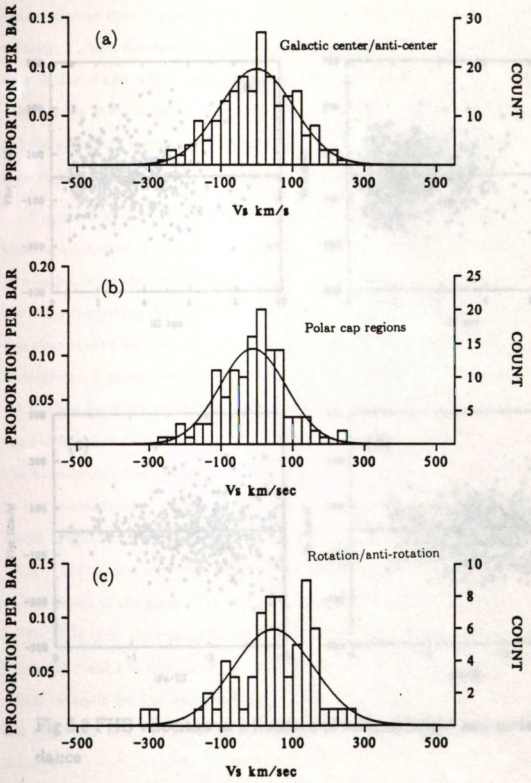

Fig 5.2 Histogram of velocities in the Galactic cardinal directions

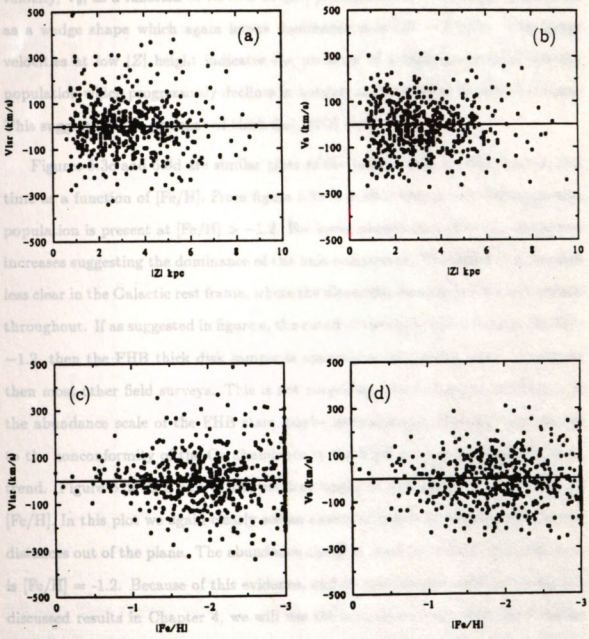

Fig 5.3 FHB velocities as a function of vertical height and metal abundance

This higher dispersion population begins to dominate the sample at vertical distances greater than 5 kpcs. Figure 5.3b, which now shows the Galactic rest frame velocity, V_s, as a function of vertical height, presents the low dispersion population as a wedge shape which again looses dominance near $|Z| = 5$ kpcs. The larger velocities at low $|Z|$ height indicates the presence of a higher rotational velocity population which progressively declines in number as the vertical distance increases. This suggests of the presence of thick disk FHB stars.

Figures 5.3c and 5.3d are similar plots of the sample velocity distribution, this time as a function of [Fe/H]. From figure 5.3c it is clear that a very low-dispersion population is present at [Fe/H] > -1.2. For lower-abundance values the dispersion increases suggesting the dominance of the halo component. This effect is somewhat less clear in the Galactic rest frame, where the dispersion remains relatively constant throughout. If as suggested in figure c, the cutoff of the thick disk occurs at [Fe/H]~ -1.2, then the FHB thick disk sample is approximately 0.4 dex more metal-poor then most other field surveys. This is not surprising, since as noted in Chapter 4, the abundance scale of the FHB stars maybe several tenths of a dex too low due to the nonconformity of the Ca abundance in the FHB stars to the Wheeler *et al.* trend. Figure 5.3e is a plot of the vertical height of the sample as a function of [Fe/H]. In this plot we again clearly see an excess of higher metallicity stars at low distances out of the plane. The abundance cutoff of these suspected thick disk stars is [Fe/H] = -1.2. Because of this evidence, and in conjunction with the previously discussed results in Chapter 4, we will use the abundance scale with the Wheeler trend removed for the remainder of the kinematic analysis. This removal shifts the thick disk cutoff to approximately [Fe/H] = -0.9 in good agreement with other surveys.

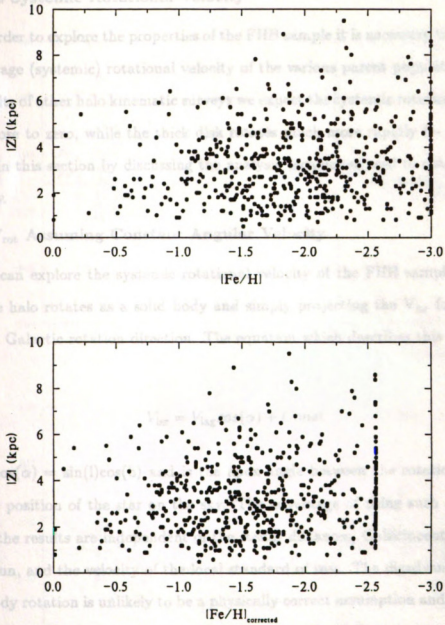

Fig 5.3e: Plots showing metallicity as a function of $|Z|$. The bottom plot is with the Wheeler *et al.* abundance trend removed and appears to be a better match to the suspected thick-disk stars.

5.3 The Systemic Rotational Velocity

In order to explore the properties of the FHB sample it is necessary to determine the average (systemic) rotational velocity of the various parent populations. From the results of other halo kinematic surveys we expect the systemic rotational velocity to be close to zero, while the thick disk rotates much more rapidly ($\sim$ 195 km/s). We begin this section by discussing the analysis techniques used to determine this property.

5.3.1 V_{rot} Assuming Constant Angular Velocity

We can explore the systemic rotational velocity of the FHB sample assuming that the halo rotates as a solid body and simply projecting the V_{lsr} for each star into the Galactic rotation direction. The equation which describes this model is:

$$V_{lsr} = V_{lag} cos(\alpha) + Const \qquad (5-3)$$

where $\cos(\alpha) = \sin(l)\cos(b)$ and is the apex angle between the rotation direction and the position of the star on the sky. The advantage of using such a technique is that the results are independent of the stellar distances, Galactocentric distance of the sun, and the velocity of the local standard of rest. The disadvantage is that solid body rotation is unlikely to be a physically correct assumption and is expected to break down for a sample at large distances from the Galactic center.

Figure 5.4a is a plot of the V_{lsr} as a function of $\cos(\alpha)$ for the entire FHB sample. In this plot, stars which rotate with the LSR will lie along the line of zero rotation because their apparent motion is comoving with the LSR. The overall apparent slope in the data is due to a systematic lag of the sample behind the LSR. The sloping line is a least squares fit to the data. The value of the slope, is

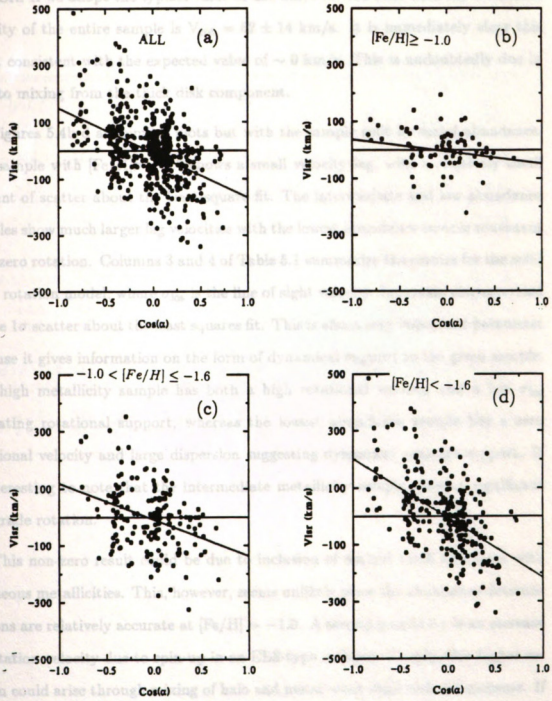

Fig 5.4 Rotational velocities for FHB subsamples split in [Fe/H] and assuming solid body rotation.

$V_{lag} = -158 \pm 14$ km/s indicating that the FHB sample lags considerably behind the LSR. If we adopt the typical value of 220 km/s for the LSR then the rotational velocity of the entire sample is $V_{rot} = 62 \pm 14$ km/s. It is immediately clear this is not consistent with the expected value of ~ 0 km/s. This is undoubtedly due in part to mixing from the thick disk component.

Figures 5.4b-d are similar plots but with the sample split by metal abundance. The sample with [Fe/H]> -1.0 shows a small velocity lag, with a relatively small amount of scatter about the least-square fit. The intermediate and low abundance samples show much larger lag velocities with the lowest abundance sample consistent with zero rotation. Columns 3 and 4 of Table 5.1 summarize the results for the solid body rotation model, where σ_{los} is the line of sight velocity dispersion characterized by the 1σ scatter about the least squares fit. This is also a very important parameter because it gives information on the form of dynamical support to the given sample. The high metallicity sample has both a high rotational velocity and a low σ_{los} indicating rotational support, whereas the lowest abundance sample has a zero rotational velocity and large dispersion suggesting dynamical pressure support. It is interesting to note that the intermediate metallicity sample shows a significant pro-grade rotation.

This non-zero result could be due to inclusion of normal thick disk stars with erroneous metallicities. This, however, seems unlikely since the abundance determinations are relatively accurate at [Fe/H] ~ -1.0. A second possibility is an increase in rotation velocity due to spin-up in an ELS-type collapse. Finally, this higher rotation could arise through mixing of halo and metal-weak thick disk components. If such mixing has occurred then it is expected that stars with small vertical distances should rotate more rapidly since this is the spatial region which is inhabited

Table 5.1. Kinematic Solutions for FHB Sample

N (1)	[Fe/H] (2)	Z (3)	R (4)	SB V_{rot} (5)	SB σ_{los} (6)	FW V_{rot} (7)	FW σ_{los} (8)	σ_r (9)	Woolley σ_ϕ (10)	Woolley σ_θ (11)
525	ALL	ALL	ALL	62 ± 14	103	54 ± 10	102 ± 3	138 ± 24	135 ± 27	67 ± 19
73	>-1.0	ALL	ALL	177 ± 22	64	133 ± 16	66 ± 5	92 ± 28	86 ± 30	35 ± 22
180	<-1.0,>-1.6	ALL	ALL	92 ± 24	101	79 ± 17	101 ± 5	152 ± 31	103 ± 34	59 ± 24
272	<-1.6	ALL	ALL	11 ± 20	109	10 ± 16	109 ± 5	129 ± 29	167 ± 34	74 ± 22
92	<-1.0,>-1.6	≤3	ALL	114 ± 37	111	112 ± 26	108 ± 8	153 ± 37	137 ± 46	45 ± 34
88	<-1.0,>-1.6	>3	ALL	67 ± 31	89	43 ± 22	90 ± 7	159 ± 38	53 ± 37	56 ± 26
131	<-1.6	≤3	ALL	13 ± 29	109	13 ± 22	110 ± 7	134 ± 34	161 ± 41	75 ± 27
141	<-1.6	>3	ALL	10 ± 27	110	8 ± 22	109 ± 6	121 ± 36	173 ± 41	74 ± 26
121	<-1.0,>-1.6	ALL	≤8	121 ± 31	98	85 ± 19	97 ± 6	149 ± 33	108 ± 35	61 ± 25
59	<-1.0,>-1.6	ALL	>8	52 ± 39	106	53 ± 40	105 ± 9	165 ± 46	66 ± 55	43 ± 36
155	<-1.6	ALL	≤8	68 ± 30	108	28 ± 18	109 ± 6	142 ± 35	176 ± 39	54 ± 25
117	<-1.6	ALL	>8	-32 ± 27	109	-33 ± 29	109 ± 7	106 ± 37	170 ± 45	93 ± 28

by the thick and possibly metal-weak thick disks. This effect is less likely to be present in an ELS collapse since abundance and rotational velocity are expected to be correlated with vertical height. To investigate these possibilities, figure 5.5a and 5.5b shows the intermediate and low metallicity samples further split at the vertical height of $|Z| = 3$ kpc. The open circles and dotted lines represent the stars below this vertical cut. There appears to be a small difference in lag velocity in the intermediate abundance plot, however, as shown in Table 5.1 this difference is not significant at the 1σ level. There is virtually no difference in the low abundance sample.

As a final characterization using the solid body assumption we split the FHB stars into an inner and outer halo sample cut at the solar Galactocentric distance of R = 8 kpc. Figures 5.5c-d are plots of the same metal abundance cuts but with the open circles and dotted lines representing the FHB stars interior to R = 8 kpc, while the filled circles and solid lines are exterior. The results for the solid body model are presented again in Table 5.1. It can be seen that the inner halo sample at both the intermediate and low metal abundances is in substantial rotation ($V_{rot} = 121 \pm 31$, 68 ± 30, respectively) while the outer halo in both cases has smaller systemic rotation ($V_{rot} = 52 \pm 39$, $V_{rot} = -32 \pm 27$, respectively). This result is in keeping with the past findings for the globular clusters (Zinn 1985) and the field RR Lyrae stars (Hartwick 1987).

5.3.2 V_{rot} Assuming Constant Rotational Velocity

As already suggested, the constant angular velocity assumption (solid body rotation) is probably not a physically meaningful interpretation for the halo of the Galaxy. This is immediately evident when one considers the enormous velocities which would result at large distances from the Galactic center. If the halo is instead

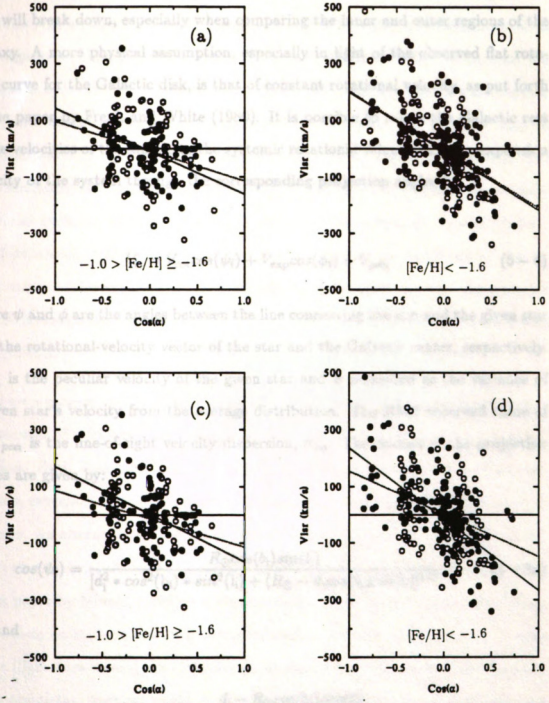

Fig 5.5: FHB sample split in Galactic distances $|Z|$ and R. Open and filled circles in plots (a) and (b) represent sub-samples with $|Z| > 3$ and $|Z| < 3$ kpc, respectfully. In plots (c) and (d) open and filled circles represent R> 8 and R< 8 kpc. In all plots the solid and dotted lines are the least-square fits to the filled and open data.

differentially rotating, it is expected that to some degree the solid body approximation will break down, especially when comparing the inner and outer regions of the Galaxy. A more physical assumption, especially in light of the observed flat rotation curve for the Galactic disk, is that of constant rotational velocity, as put forth in the paper by Frenk and White (1980). It is possible to relate the Galactic rest frame velocities of the sample to the systemic rotational velocity and the expansion velocity of the system through the corresponding projection angles by:

$$V_{s_i} = V_{rot} cos(\psi_i) + V_{exp} cos(\phi_i) + V_{pec_i} \qquad (5-4)$$

where ψ and ϕ are the angles between the line connecting the sun and the given star and the rotational-velocity vector of the star and the Galactic center, respectively. V_{pec_i} is the peculiar velocity of the given star and is measured as the variance of a given star's velocity from the average distribution. The RMS observed value of all V_{pec_i} is the line-of-sight velocity dispersion, σ_{los}. The cosines of the projection angles are given by:

$$cos(\psi_i) = \frac{R_\odot cos(b_i) sin(l_i)}{[d_i^2 * cos^2(b_i) * sin^2(l_i) + (R_\odot - d_i cos(b_i) cos(l_i))]^{1/2}} \qquad (5-5a)$$

and

$$cos(\phi_i) = \frac{d_i - R_\odot cos(b_i) cos(l_i)}{(d_i^2 + R_\odot^2 - 2 d_i R_\odot cos(b_i) cos(l_i))^{1/2}} \qquad (5-5b)$$

where d_i is the Solar distance to the star, and $R_\odot$ is the Galactocentric distance of the Sun.

Before calculating the various rotational velocities we will check the importance of the expansion velocity term in equation 5-4. It is expected, as found in previous investigations of the globular clusters (Zinn 1985, Frenk & White 1980), that the expansion term will be small enough to ignore. We explicitly test this assumption using the method of least squares to simultaneously solve for V_{rot} and V_{exp} in equation 5-4. The V_{exp} results for the entire sample, as well as, the sample split into the 3 abundance subsets are $V_{exp} = 3\pm9, 19\pm15, 19\pm14, -14\pm13$ km/s, respectively. With the exclusion of the lowest metal abundance sample there appears to be a small expansion velocity present. The 19 km/s results are significant at the 1σ level only, but interesting in that a similar effect has been seen in the globular cluster investigations of Clube and Watson (1979), Frenk and White (1980) and Zinn (1985).

If we constrain the [Fe/H]≥ -1.0 sample to R$<$ 8 kpc then the expansion velocity becomes 48 ± 25 km/s which is virtually identical to $V_{exp} = 42 \pm 19$ km/s found by Zinn. Both Zinn and Frenk and White doubted the true existence of this expansion, especially since it appeared to depend on the assumed solar Galactocentric distance. An alternate explanation of this expansion might be the breakdown of the constant rotational velocity assumption in fields nearer the Galactic center. In a recent paper by Minniti (1995) it is suggested that because the bulge of the Galaxy is an oblate isotropic rotator, it is better represented by solid body rotation. If some of the FHB stars toward the Galactic center are actually members of the Galactic bulge population then we might expect an increase in the expansion velocity and a large difference between the velocity dispersion of the halo and bulge members. We can test this assumption by further constraining the FHB sample in the R direction. To increase the sample size, stars with [Fe/H]> -1.6 were examined. For

the stars with R> 8 kpc the expansion and rotational velocities were found to be $V_{exp} = 33 \pm 19$ and $V_{rot} = 89 \pm 14$ km/s. We must constrain the sample to R> 5.5 kpc before the expansion velocity drops to a non-significant level ($V_{exp} = 13 \pm 22$ km/s). This is well beyond the accepted range of the bulge population (R$\sim$ 3 kpc) and may indicate that our assumption is not valid. It does appear, however, that a significant expansion velocity is only found in the inner most portion of the sample. It is interesting to note that in the following sections it is shown that a large velocity dispersion exists in the radial directions for the most metal-rich stars and may be associated with the expansion results.

The systemic rotational velocities for the entire sample and the various subsets were calculated using the Frenk and White method with the velocity of expansion approximated to be zero. This approximation appears valid since removal of the expansion term changes the rotation results by only a few km/s. The results for V_{rot} and σ_{los} are listed in columns 5 and 6 of Table 5.1. In general we see that the assumption of constant angular velocity is in agreement with the results from the solid-body calculations. Figures 5.6a-d and 5.7a-d are the corresponding plots for the constant angular velocity solutions with the same splits as in figures 5.4 and 5.5. As before, we see the unexpectedly high V_{rot} values in the intermediate abundance sample, especially when it is constrained to a vertical height of $|Z| < 3$ kpc. There is also the potentially interesting result that the lowest abundance sample in the outer halo (R> 8 kpc) is appears in counter-rotation. As we precede with the analysis of the FHB sample we will see that these two areas of interest will offer promising advances in the understanding of the halo field properties.

5.3.3 The Velocity Ellipsoid

It has been briefly mentioned that the line-of-sight velocity dispersion is an

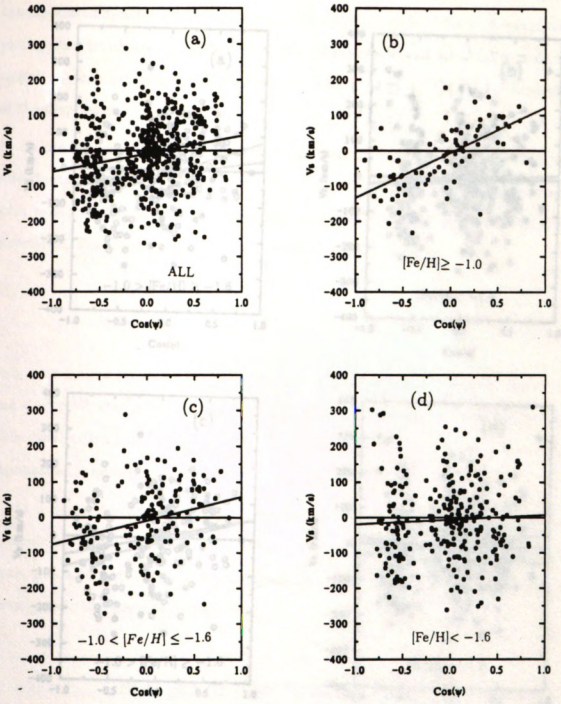

Fig 5.6 Rotational velocities for FHB subsamples split in [Fe/H] and assuming constant rotational velocity.

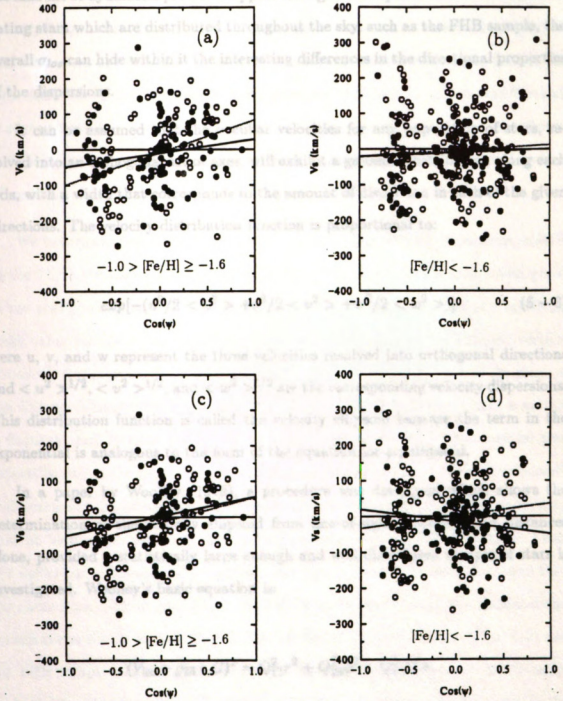

Fig 5.7: FHB sample split in Galactic distances $|Z|$ and R. Open and filled circles in plots (a) and (b) represent sub-samples with $|Z| > 3$ and $|Z| < 3$ kpc, respectfully. In plots (c) and (d) open and filled circles represent R> 8 and R< 8 kpc. In all plots the solid and dotted lines are the least-square fits to the filled and open data.

important kinematic property because the size of the dispersion offers insights into the amount of dynamical pressure support for a given sample of stars. When investigating stars which are distributed throughout the sky, such as the FHB sample, the overall σ_{los} can hide within it the interesting differences in the directional properties of the dispersions.

It can be assumed that the peculiar velocities for any population of stars, resolved into an orthogonal set of axes, will exhibit a gaussian distribution along each axis, with a width that corresponds to the amount of dispersion in each of the given directions. The velocity distribution function is proportional to:

$$exp[-(u^2/2 < u^2 > + v^2/2 < v^2 > + w^2/2 < w^2 >)] \qquad (5-6)$$

were u, v, and w represent the three velocities resolved into orthogonal directions and $< u^2 >^{1/2}$, $< v^2 >^{1/2}$, and $< w^2 >^{1/2}$ are the corresponding velocity dispersions. This distribution function is called the velocity ellipsoid because the term in the exponential is analogous to the form of the equation for an ellipsoid.

In a paper by Woolley (1978), a procedure was developed which allows the determination of the velocity ellipsoid from line-of-sight velocities and distances alone, provided a statistically large enough and well distributed sample of stars is investigated. Woolley's basic equation is:

$$(V_{lsr} + g_{23} * C)^2 = Q_{13}^2 r^2 + Q_{23}^2 \phi^2 + Q_{33}^2 \theta^2 +$$

$$2Q_{13}Q_{23} r\phi + 2Q_{23}Q_{33}\phi\theta + 2Q_{33}Q_{13}\theta r \qquad (5-7)$$

where V_{lsr} is the V_{los} relative to the LSR, C is the mean motion of the group

and g_{23}, Q_{13}, Q_{23}, and Q_{33} are trigonometric terms which project the velocities into the corresponding orthogonal directions. In this model it is assumed that the velocity ellipsoid is aligned with spherical polar coordinates. The variables r, ϕ, and θ are then the velocity dispersions in spherical coordinates, where R is in the direction of the Galactic center, Φ in the direction of Galactic rotation, and Θ which is perpendicular to the other two. The conditions of a large and well distributed sample allows the crossterms to be neglected making a solution in terms of each of the velocity dispersions possible.

We have used the Woolley formalism to calculate the velocity dispersions relative to the 3 Galactic directions. Table 5.1 list these results for the samples investigated in the previous sections. A general feature in nearly all the samples is a relatively small value for the θ dispersion. For those stars which are not at extreme vertical distances, θ is approximately a measure of the velocity dispersion out of the plane of the Galaxy. Therefore, a small dispersion in this direction indicates that a sample is flattened and at least partially supported by rotation. This effect can be seen especially well in the thick disk sample where σ_θ is only 41 km/s. A relatively small θ dispersion is also present in the intermediate metal abundance sample, suggesting that at least a portion of these stars also exhibit disklike characteristics. From the metal-poor sample it also appears that the inner halo is more flattened then the outer halo. This suggests that the FHB sample may consist of a flattened and spherical component as indicated in the RR Lyrae analysis of Hartwick (1987) and the FHB sample of Kinman *et al.* (1994). An important feature previously noted by both Pier (1983) and Sommer-Larsen and Zhen (1990), is the anisotropy in the radial velocity dispersion for the stars located in the inner halo. This has important ramifications for models of Galactic formation because highly radial orbits suggest

that the inner halo stars formed before the bulk of the matter in the inner Galaxy had collapsed. There is some evidence of this effect present in our FHB sample, especially for the metal-poor inner halo sample. For the most part, however, the high dispersion in the ϕ direction of the metal-poor sample masks this result. The high ϕ dispersions are likely to be the result of mixing of two populations that exhibit quite different rotational velocities. In the coming sections we examine more closely this assumption and its important ramifications.

5.3.4 Comparison to Other Published Results

Table 5.2 lists the systemic rotational velocity and velocity ellipsoid solutions for the halo from various surveys in the past 15 years. These results come from both kinematically-biased, proper motion surveys and from non-kinematiclly-biased tracer surveys. Generally, these surveys are confined to the local solar neighborhood or to within a few kiloparsecs of the sun.

The systemic rotational velocity agreement between nearly all surveys is quite good. The general consensus is that the halo of the Galaxy has a slightly significant pro-grade or zero velocity rotation. It is interesting that our FHB sample with [Fe/H]< -1.6 is consistent with zero rotation, while the intermediate metallicity sample shows a significant rotation. This suggests, as has been reported in other investigations, that to secure a true halo sample it is necessary to select stars with [Fe/H]< -1.6. Of all the surveys, only Pier (1984), Majewski (1992) and Zinn (1993) show significant counter-rotation in a halo sample. In all three cases the samples extend to distances greater than 3 kpc from the sun. This suggests that systemic counter-rotation in the halo can only be seen at larger distances from the Galactic plane. This result is still controversial, however, since neither the Pier (virtually no stars in the rotation directions) nor the Zinn (very few globular clusters)

Table 5.2. Previously Published Halo Kinematic Results.

Class (1)	N (2)	V_{rot} (3)	σ_r (4)	σ_ϕ (5)	σ_θ (6)	Reference (7)
Globular Cluster	66	50 ± 30	117 ± 14	159 ± 21	80 ± 60	Frenk and White (1980)
RR Lyrae	77	34 ± 17	168 ± 76	115 ± 52	89 ± 40	Hawley *et al.* (1985)
FHB	150	-52 ± 41	124 ± 16	75 ± 60	86 ± 12	Pier (1984)
FHB	21	48 ± 40	...	...	...	Sommer-Larson *et al.* (1985)
CH stars	27	-13 ± 39	71 ± 38	80 ± 38	114 ± 47	Hartwick and Cowley (1985)
Giant, Subdwarf	65	38 ± 20	125 ± 11	96 ± 9	88 ± 7	Norris *et al.* (1985)
Field Dwarfs	202	-2 ± 9	...	...	...	Carney and Latham (1985)
Red Giants	174	14 ± 23	154 ± 18	102 ± 27	107 ± 15	Carney and Latham (1985)
Complete	...	-47 ± 9	...	...	...	Majewski (1992)
RR Lyrae	...	12 ± 14	...	...	...	Layden (1993)
Old Globulars	46	70 ± 22	...	...	...	Zinn (1993)
Young Globulars	19	-64 ± 74	...	...	...	Zinn (1993)
Metal-poor stars	887	-16 ± 18	153 ± 10	93 ± 18	107 ± 7	Beers and Sommer-Larsen (1995)

results are firmly established.

The general trends for the velocity ellipsoid solutions show similarities to each other, but with greater variations and less certainty. In general most agree that the radial velocity dispersion is $\sim$ 125 km/s and is larger than the other two dispersions. This agrees well with the σ_r values found for our FHB stars. The ϕ velocity dispersion shows a much larger range of values extending from as low as 75 km/s to as high as 159 km/s. For the most part, our FHB sample shows a very large dispersion, especially in the most metal-poor sample. It is interesting that the Frenk and White value of $\sigma_\phi = 159 \pm 21$ km/s comes from the relatively distant globular clusters and is the only sample which is in close agreement with our FHB sample. As will be shown in the next section, the peak in σ_ϕ for the FHB stars appears to occur at [Fe/H] = -1.9, and is expected to be the result of mixing from two populations with very different rotational velocities. This effect is not expected to be seen in the samples closer to the solar neighborhood, where the prograde rotating halo dominates the results. Finally, there appears to be a split decision on the θ velocity dispersions. The results indicate either $\sigma_\theta \sim 80$ km/s, or $\sigma_\theta =\sim 110$ km/s. A currently popular model by Hartwick (1987) suggests that the halo consists of two components, a flattened inner component with a smaller σ_θ dispersion and an outer spherical component with a larger σ_θ dispersion. This model appears to be consistent with the split in the previously published data, as well as the σ_θ values from our various FHB samples.

5.4 The Binned Data Results

In order to see trends in the kinematic data as a function of one of the other non-kinematic parameters (e.g. [Fe/H], $|Z|$, R, etc.), it is a very useful exercise to bin the data. This allows individual stars with nearly the same non-kinematic

parameters to be grouped and therefore aid in the recognition of a kinematic functional dependency. The negative aspects of binning the data are a loss of individual properties of the stars, because the results are the mean from the binned sample, and a dependence on bin size and placement, since shifting the bin boundaries necessarily changes the derived result. Since the kinematic analysis of the FHB sample is, by necessity, statistical, there is no way to overcome the need to bin the data in some fashion. Some of the effects of relative bin size can be rectified, however, by forcing all bins to be the same size and allowing the bins to overlap. By passing a given number of stars through each bin it is possible to identify extra-ordinary results that are due only to the particular bin placement in a finite data set.

Figures 5.8a-c and 5.9a-c are plots of the rotational velocity and various velocity dispersions as a function of [Fe/H] from a Frenk and White and Woolley-type analysis. The bins each contain 150 stars with an overlap of 130 stars between consecutive bins. In figure 5.8a we see that the binned rotational velocity decreases as a function of metal abundance. The first data bins, which have a $V_{rot} \sim 120$ km/sec, are probably dominated by thick disk stars. We find zero rotational velocity for [Fe/H]< -1.9, with significant pro-grade rotation at slightly higher metallicities. The non-zero result for the stars with $-1.0 >$ [Fe/H] > -1.9 could be due to either mixing of the halo and metal-weak thick disk populations, or to the presence of a significantly pro-grade rotation halo. An important note of interest is the apparent discontinuity in rotational velocity at [Fe/H] = -1.9. Although in this analysis the discontinuity is not significant at the 1σ level, further analysis will show that this is not a statistical fluctuation but rather an actual difference in kinematic properties.

Figures 5.8b and c are the derived dependency of σ_{los} and V_{rot}/σ_{los} on [Fe/H]. σ_{los} shows a slight increase from the highest abundances and levels off in the

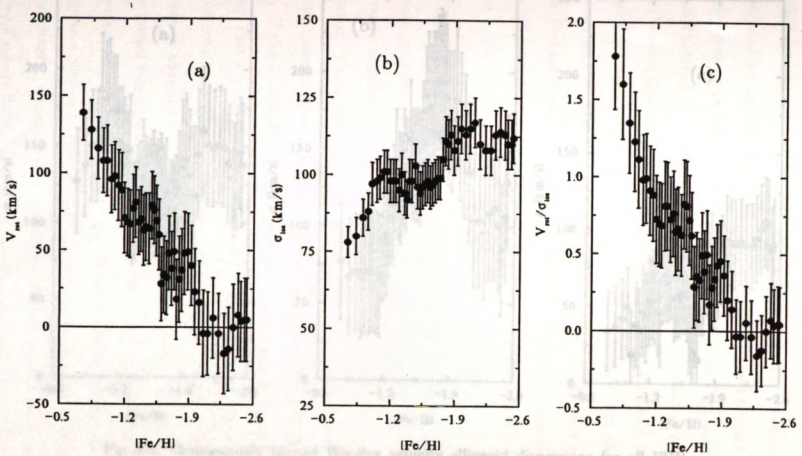

Fig 5.8: Continuously binned Frenk and White solutions for all FHB stars. Each bin size is 150 stars with an overlap of 130 stars between consecutive bins.

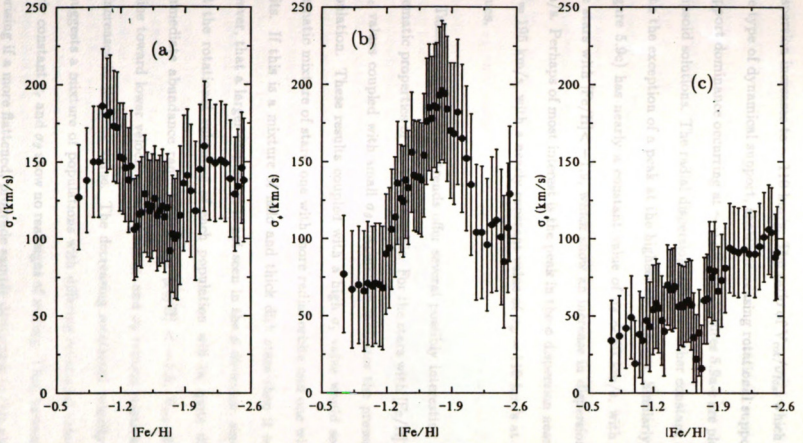

Fig 5.9: Continuously binned Woolley velocity ellipsoid dispersions for all FHB stars. Each bin size is 150 stars with an overlap of 130 stars between consecutive bins.

intermediate range of $-1.0 >$ [Fe/H] > -1.9. For the metallicities below -1.9 the dispersion increases to $\sim$ 110 km/s. The ratio of V_{rot}/σ_{los}, which is an indicator of the type of dynamical support, shows decreasing rotational support with pressure-support dominance occurring at ~ -1.9 dex. Figures 5.9a-c are plots of the velocity ellipsoid solutions. The radial dispersion appears rather constant at $\sigma_r \sim 130$ km/s with the exception of a peak at the highest abundances. Similarly, the θ dispersion (figure 5.9c) has nearly a constant value of $\sigma_\theta \sim 50$ km/s, with the exception of the stars with [Fe/H]< -1.9, which show an increase in dispersion up to $\sigma_\theta = 100$ km/s. Perhaps of most interest is the peak in the ϕ dispersion near [Fe/H] = -1.8 of $\sigma_\phi = 195$ km/s, with a nearly constant value of $\sigma_\phi = 110$ km/s at lower metallicity values.

Taken together, these trends offer several possibly interesting insights into the kinematic properties of the FHB sample. For the stars with [Fe/H]> -1.0, the high V_{rot} values coupled with small σ_θ dispersions indicates the presence of a disklike population. These results coupled with a high σ_r value would seem to suggest a kinematic mixture of stars, one with more radial orbits and one with more circular orbits. If this is a mixture of halo and thick disk stars then it seems surprising, however, that a larger dispersion is not seen in the ϕ direction, since it is expected that the rotational velocities of each population will be quite different. In the intermediate abundance range of $-1.0 <$ [Fe/H] < -1.8, V_{rot} shows a constant decline toward lower velocities while the σ_r and σ_θ remain relatively constant and σ_ϕ increases to its peak value. The decreasing rotational velocity and increasing σ_ϕ suggests a mixture of populations with differing rotational velocities, while the nearly constant σ_r and σ_θ show no real signs of mixing. This, however, might not be surprising if a more flattened, prograde sample dominates in this abundance range.

In the following sections it will be shown that the large ϕ dispersion is driven by a counter-rotating halo component, mixed with a prograde component. Since this counter-rotation is quite large the ϕ dispersion also becomes large. Though there are differences in the other dispersions the relative differences between these components are not as great and therefore vary much less. Finally, at the lowest abundances, [Fe/H] < -1.9, the rotational velocity drops to zero, with an increasing σ_θ and decreasing σ_ϕ. These effects will be shown shortly to be caused by the decreasing dominance of the prograde halo component and the increasing dominance of the counter-rotating halo.

5.5 The Vertical Velocity Distribution

Using only radial velocity data in our kinematic analysis it is generally not possible to directly measure the velocity components without some form of model assumptions. This is, however, not the case for stars which lie in directions that are perpendicular to the plane of the Galaxy ($|b| \sim 90$ deg). For such a sample of stars the line-of-sight velocity directly measures the velocity component W, which is defined to be positive directed into the plane from the north Galactic pole. Although the FHB sample does not contain a large number of stars exactly in the polar direction, there are 132 FHB stars which lie in the polar cap region ($|b| > 65$ deg) where 90% of the line-of-sight velocity is in the W velocity direction.

Figure 5.10a and b are plots of the estimated W velocity, W_{est}, as a function of $|Z|$ and [Fe/H]. In both figures there is obviously an excess of stars with small W velocities. By splitting the sample into our customary abundance ranges as in figures 5.11a-c we see that both the higher and intermediate abundances show small dispersions that extend to nearly 6 kpcs above the plane. In the metal-poor sample the dispersion is notably larger. Figure 5.12 a-h are histograms of the W_{est}

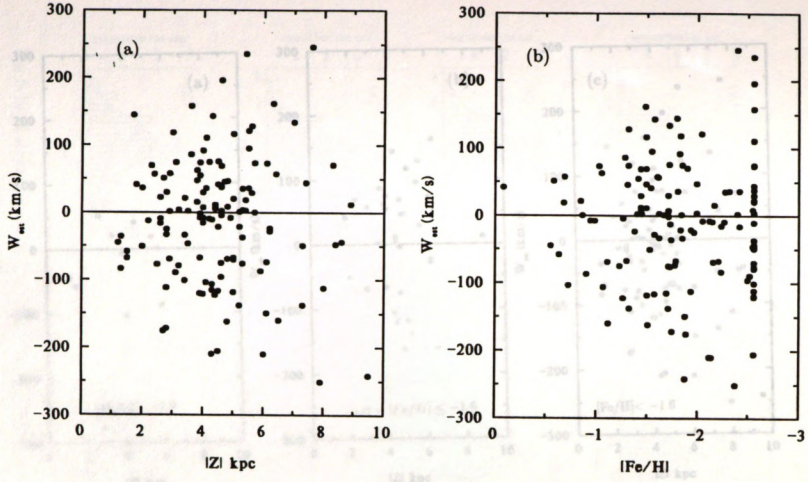

Fig 5.10 Plots of the estimated W velocities as a function of $|Z|$ and [Fe/H]. Polar cap regions are defined to have $|b| > 65$

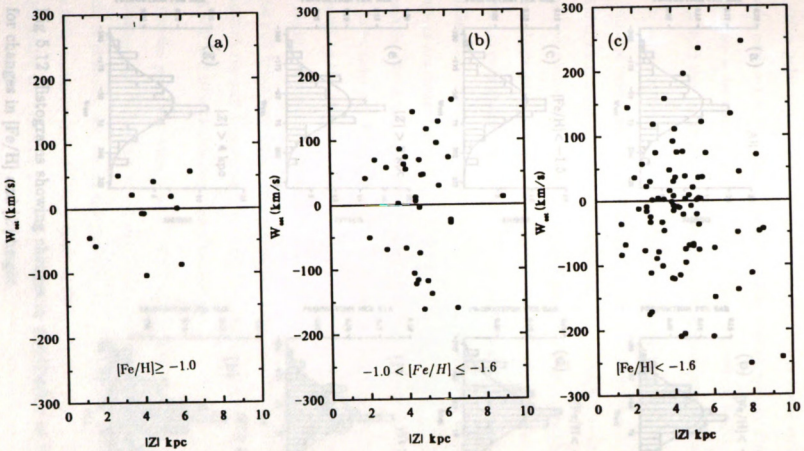

Fig 5.11 Plots of the three abundance sub-samples showing an increase in W velocity dispersion as metallicity decreases.

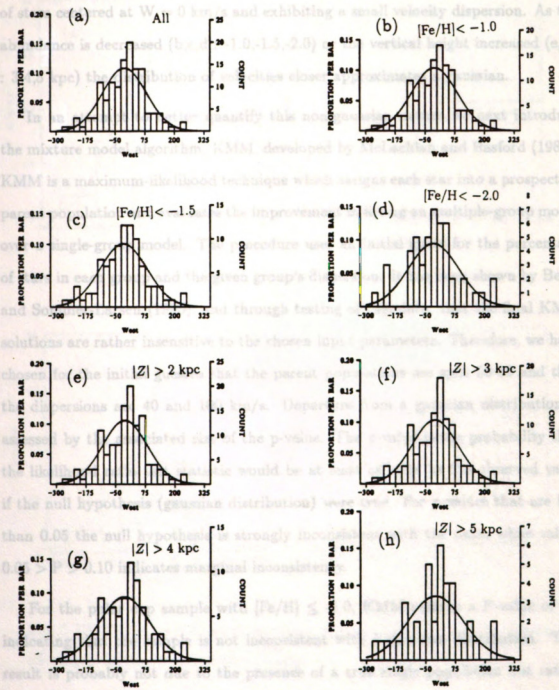

Fig 5.12 Histograms showing changes in distribution of W velocities for changes in [Fe/H] and $|Z|$ height.

velocities split at various abundances and $|Z|$ heights. Figure 5.12a which shows the entire polar cap sample is decidedly non-gaussian in shape with a large excess of stars centered at W = 0 km/s and exhibiting a small velocity dispersion. As the abundance is decreased (b,c,d : -1.0,-1.5,-2.0) or the vertical height increased (e,f,g : 3,4,5 kpc) the distribution of velocities closer approximates a gaussian.

In an attempt to better quantify this non-gaussian nature we next introduce the mixture model algorithm, KMM, developed by McLachlan and Basford (1988). KMM is a maximum-likelihood technique which assigns each star into a prospective parent population and evaluates the improvement in fitting an multiple-group model over a single-group model. The procedure uses an initial guess for the percentage of stars in each group and the given group's dispersion. It has been shown by Beers and Sommer-Larsen (1995), and through testing of this data, that the final KMM solutions are rather insensitive to the chosen input parameters. Therefore, we have chosen for the initial guesses that the parent populations are split 50-50 and that the dispersions are 40 and 100 km/s. Departure from a gaussian distribution is assessed by the associated size of the p-value. The p-value is the probability that the likelihood ratio test statistic would be at least as large as the observed value if the null hypothesis (gaussian distribution) were true. For p-values that are less than 0.05 the null hypothesis is strongly inconsistent with the data, while values $0.05 > P > 0.10$ indicates marginal inconsistency.

For the polar cap sample with [Fe/H] $\leq$ -1.0, KMM returns a P-value of 0.3 indicating that the sample is not inconsistent with a gaussian distribution. This result is probably not due to the presence of a true single population but rather due to insensitivity in KMM for a small number of stars in the second component which shares the dominate component's average velocity.

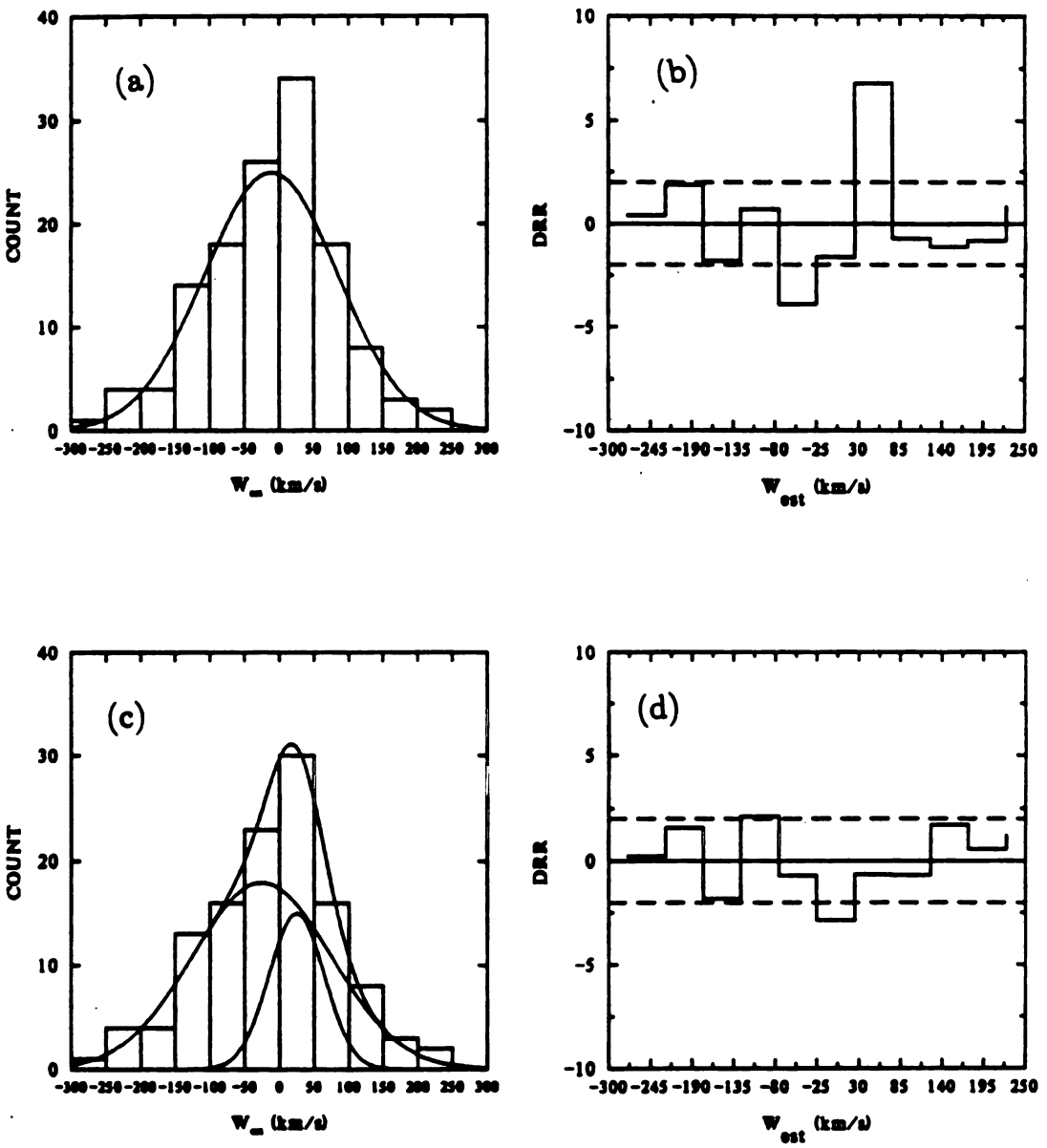

Fig 5.13 Single and Double gaussian fits for [Fe/H]< −1.0. Corresponding DRR plots are also shown

To further test for non-gaussian behavior Figures 5.13a-b show the histograms of W_{est} velocities for the polar cap region with the associated Double Root Residual (DRR). The DRR plot is a display of the differences between the observed and fitted bin frequencies, stabilized by a square-root transformation which has the property of equalizing variations to a scale roughly independent of bin population. For models which are close to the observations the DRR's are equivalent to normal deviants. (Gebhardt and Beers 1991). From the DRR plot we immediately see that a normal distribution does not satisfactorily fit the data. Figures 5.13c-d show the polar cap region fit with a double gaussian. The double gaussian was constrained by assuming a dispersion of σ_1 = 100 km/s and σ_2 = 40 km/s, the former consistent with published values for the halo, the latter consistent with the thick disk. This improved fit was achieved by assigning 90 stars to the halo and 30 stars to the thick disk, with an average velocity of W_{est} = -25 and 25 km/s respectively. It is possible that this smaller dispersion population represents the metal-weak tail of the thick disk. If so, the halo FHB stars outnumber the MWTD stars by a factor of 3. This is in stark contrast to findings of Morrison (1993) for the halo field giants towards the Galactic center where the MWTD stars outnumber the halo by a factor of 4.

5.6 The Halo Kinematics

We begin the investigation of the halo kinematics of the FHB stars by returning to the polar cap sample. As seen in figure 5.11b and c, the low dispersion population appears to lose dominance at $\sim$ 5 kpc above the plane. This is in agreement with the findings of Majewski (1992) for the cutoff of the flattened halo component. By simply assuming the solar Galactocentric distance of 8 kpc and a flattened halo cutoff between 5 and 6 kpc the minor-to-major axis ratio in the solar neighborhood is 0.63 to 0.75.

It is possible to more stringently approach this question using the dispersion models developed by White (1989). Starting with the assumption of a spherical isothermal potential, White showed that for an axisymmetric population the global dispersion tensor will have two independent principal values, along and perpendicular to the symmetry axis. These dispersions are then related to the minor-to-major axis ratio, b/a, to allow halo flattening to be determined from the velocity dispersions. Using the White formalism we calculate for the FHB sample with [Fe/H]< -1.6 an axial ratio of ~ 0.5. This relatively large amount of flattening is probably in part due to the uncertainty in the velocity ellipsoid values, since using the extremes of the 1σ deviation in the dispersion results gives b/a = 0.95. If we instead adopt the polar cap result from the double gaussian fit, σ = 100 km/s, then the axial ratio becomes b/a $\sim$ 0.65. In either case it is difficult, though not impossible, to reconcile the observed low vertical velocity dispersion in the FHB sample with a spherically distributed halo. We therefore conclude that a flattened halo component is present in this sample.

Figures 5.14a-d are plots of the halo Galactocentric velocities as a function of $\cos(\psi)$ for the FHB sample constrained by [Fe/H]< -1.6. The V_{rot} and dispersion results are listed in Table 5.3. The total sample with [Fe/H]< -1.6 has a V_{rot} which is consistent with zero rotation and a somewhat low dispersion in the θ direction. We now split the metal-poor sample at a vertical height of $|Z|$ = 5 kpc, in accord with the apparent population transition. The sample below 5 kpc (figure 5.14a) has a significant prograde rotation of $V_{rot} = 31 \pm 16$ km/sec with a rather large ϕ and small θ dispersion of 165 ± 34 km/s and 68 ± 23 km/s, respectively. The sample above 5 kpc shows a substantial counter-rotation of -118 +- 47 km/s. The sample size is small (N=49), however, and the velocity ellipsoid solutions are quite

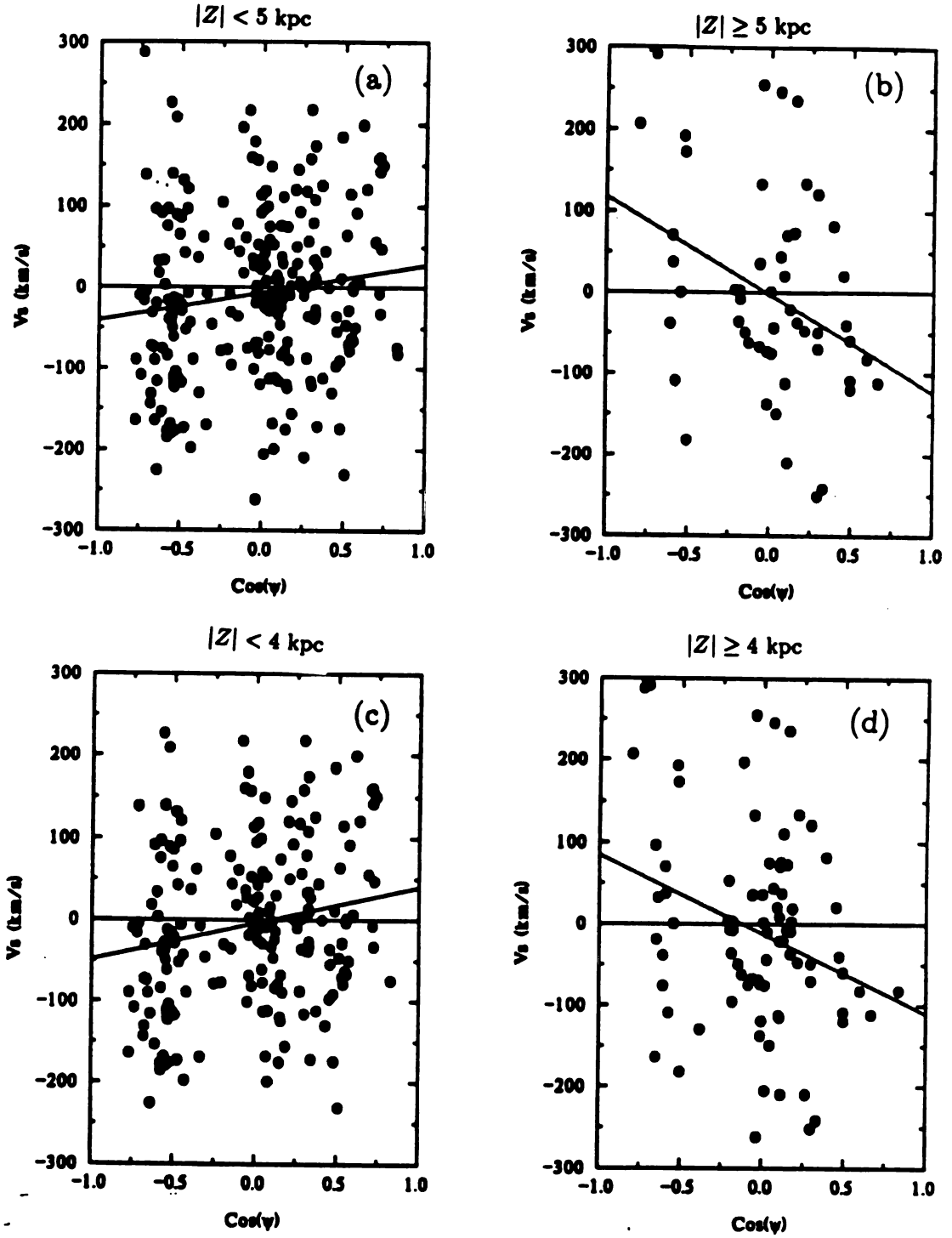

Fig 5.14 Change in systemic rotational velocity between low and high $|Z|$ samples.

uncertain. To increase the sample size we relax the vertical height criteria by making the cutoff at $|Z| = 4$ kpc. The resultant rotation value is still in substantial counter-rotation with $V_{rot} = -93 \pm 36$ km/s. The velocity ellipsoid dispersions have relatively large uncertainties but appear to be more isotropic then the sample below $|Z| = 5$ kpc. It is especially interesting that the theta dispersion has increased by a significant amount to $\sigma_\theta = 122 \pm 33$ km/sec.

If the counter-rotating result at large vertical heights is correct then it has strong implications for Galactic halo formation. Although statistically the result is significant at the 2.6σ level, the small number of stars in the rotation directions still leave room for some scepticism. It is possible that some of these stars are on highly radial, plunging, orbits which is in fact responsible for the V_{los} observed. Without proper motions for the FHB stars it is not possible at this time to completely remove this ambiguity. We can, however, estimate the number of these stars that are not consistent with purely radial orbits. If we assume that all the stars in the counter-rotation sample are actually on radial orbits, then we can project their Galactic rest frame velocities into the radial direction defined by the angle ϕ. If the calculated velocity in the radial direction is greater than the Galactic escape velocity than it is impossible to reverse the sign of the star's orbit. If the velocity is below the escape velocity then the orbital sign cannot be determined unambiguously. The star with the largest space velocity ever observed in the Galaxy is G166-37 with a velocity of 430 km/sec. If this star is assumed to be a member of the Galaxy then this is a lower limit on the velocity of escape. Figure 5.15a is a plot of V_s as a function of $\cos(\psi)$ for the counter-rotating sample. The "X" indicates those stars for which the orbital direction cannot be flipped. The open circles indicate the stars which have velocity in the radial direction greater than 220 km/sec, which is the circular

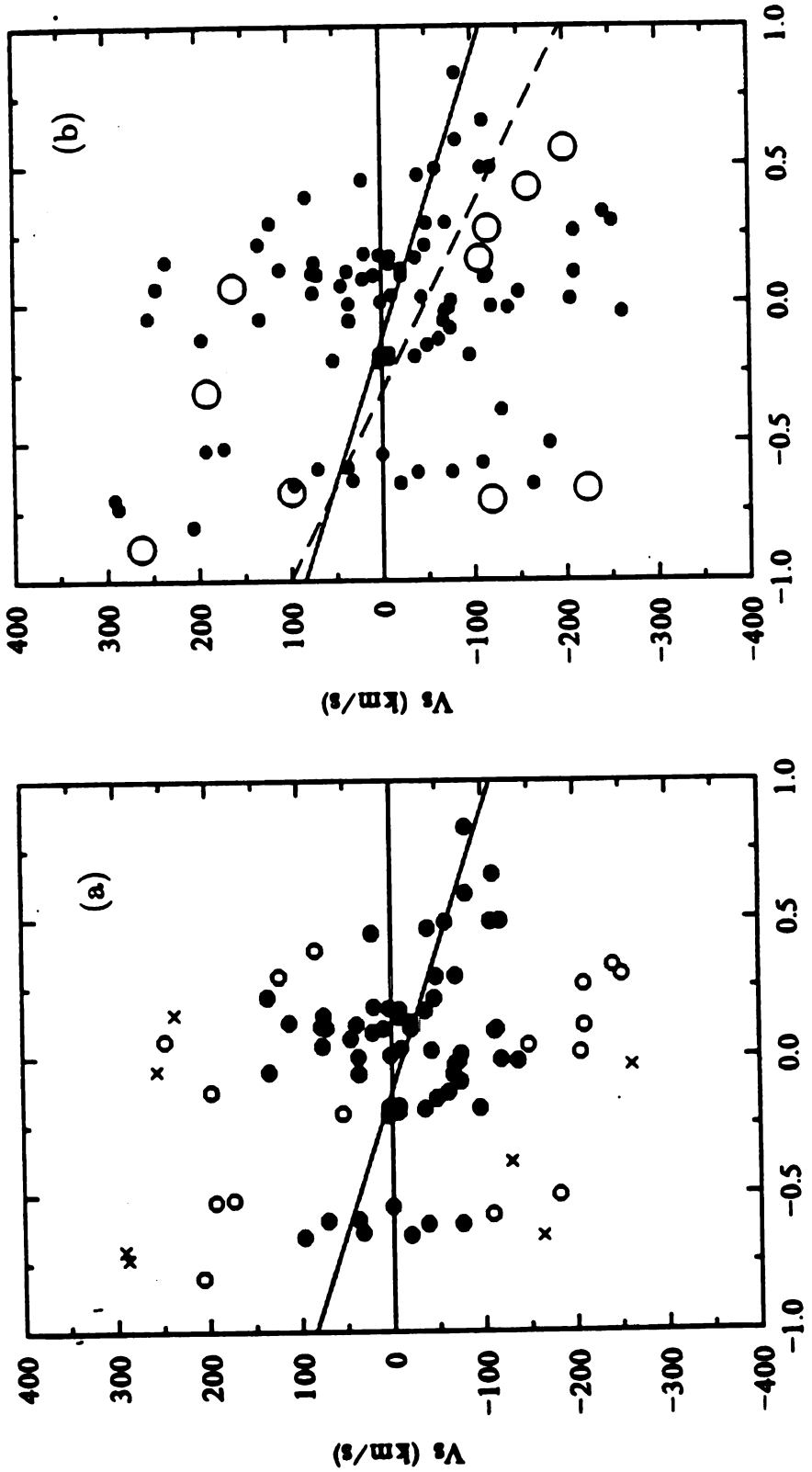

Fig 5.15 Plot (a) indicates stars which are unambigously in counter-rotation. Plot (b) is a comparison of $|Z| > 4$ kpc and [Fe/H]< -1.6 FHB sample with local young globular clusters.

velocity in the disk. Filled circles indicate stars with velocities less than 220 km/sec. It is clear from this plot that only two stars in the rotation direction can unambiguously be identified with true retrograde orbits. The assumed velocities in the radial direction is in excess of 1000 km/sec for both. Until proper motions for the other stars in the sample are determined this question will remain uncertain.

The results of this investigation appear to confirm a dual halo model, with one component being flattened (b/a $\sim$ 0.65) and in prograde rotation, the other more spherical and in counter-rotation. Similar counter-rotating halo results, though few, are not without precedence. Majewski (1992) finds retro-grade rotation of $V_{rot} = -47 \pm 9$ km/s in his sample of north Galactic pole stars with Z > 5 kpc. Zinn (1993) has found retro-grade rotation in his sample of young halo globular clusters of $V_{rot} = -67 \pm 74$ km/s, albeit not inconsistent with $V_{rot} = 0$ km/s. Figure 5.14b is again a plot of the counter-rotating sample including the 10 Zinn young halo clusters which have $R_{gal} < 12$ kpc represented as large open circles. Both the slope and distribution of the two samples appear very similar. It is clearly not beyond the scope of possibilities that a common accretion event is responsible for both the counter-rotating globular clusters and the FHB stars. Norris and Ryan (1989) have identified a secondary peak with retro-grade rotation in the distribution of rotational velocities in their proper motion sample. They speculate that this asymmetry in the gaussian distribution is evidence for an accretion event from a longer-lived counter-rotating companion of the Galaxy. This argument is strengthened by the evidence for a similar secondary peak in the Carney *et al.* sample.

Although several other surveys are suggestive of a counter-rotating halo component, in samples constrained to large $|Z|$ heights (Reid (1990), Carney *et al.* (1990a), Norris and Ryan (1986), Ryan and Norris (1991)) on average Vrot is found

to be ~ -20 km/s with only marginal significance. The seeming discrepancy between the various pro-grade and retro-grade results from different halo surveys is most likely due to differences in vertical height of the various samples. In general, the non-kinematic surveys that extend to only a few kpc above the plane and which have identified halo members by virtue of metallicity alone generally find $V_{rot} \sim 30$ km/sec while the kinematically selected solar neighborhood surveys find a slightly prograde or zero rotation halo. This is consistent with the derived V_{rot} results from the FHB stars with [Fe/H]< -1.6 and $|Z| < 5$ kpc. It is not, however, consistent with the findings of Zinn (1993) for the old halo clusters where $V_{rot} = 70 \pm 22$ km/s. This discrepancy could be driven by the fact that Zinn was able to separate the globular clusters by age, as opposed to the less revealing $|Z|$ height constraint. It is expected that the halo stars below $|Z| = 5$ kpc still suffer from contamination of the counter-rotating sample which could act to drive the resultant V_{rot} values lower.

We examine this possibility by first plotting histograms of the stars in the rotation directions. Figures 5.16a-c are histograms for the rotation sample chosen with the criteria $|cos(\psi)| > 0.5$ with the additional constraint that $20 < l < 100$ and $260 < l < 340$. To increase the number of stars in the sample we have folded the rotation and anti-rotation samples together. The axis then represents prograde rotation as positive and retro-grade rotation as negative. In both the entire sample and the [Fe/H]< -1.6 sample, there appears to be departure from a gaussian distribution. The two most prominent peaks appear to be centered on $V_s \sim -100$ and $V_s \sim 75$ km/sec. The sample with [Fe/H]> -1.6 shows a more gaussian distribution with a peak only at $V_s \sim 75$ km/sec. We now quantify the non-gaussian behavior by again employing the KMM mixture-modeling procedure. The results are listed

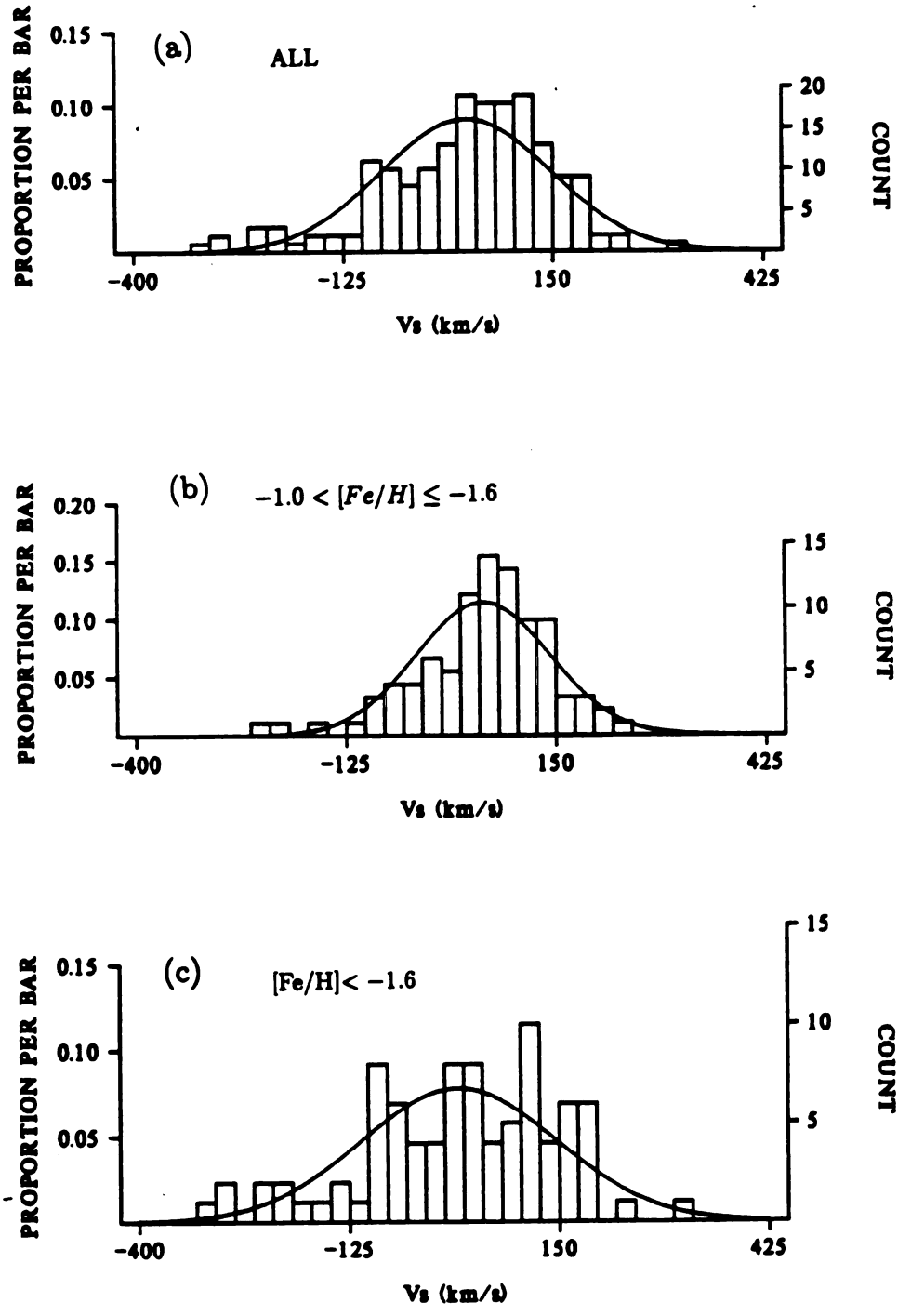

Fig 5.16 Histograms of rotation direction sample, split in [Fe/H].

Table 5.3. Halo Kinematics

N (1)	[Fe/H] (2)	Z (3)	V_{rot} (4)	σ_{los} (5)	σ_r (6)	σ_ϕ (7)	σ_θ (8)
286	<-1.6	ALL	10 ± 16	109 ± 5	129 ± 29	167 ± 34	74 ± 22
237	<-1.6	<5	31 ± 16	104 ± 5	124 ± 32	165 ± 34	68 ± 23
49	<-1.6	≥5	-118 ± 47	120 ± 12	92 ± 50	117 ± 68	137 ± 42
201	<-1.6	<4	40 ± 17	103 ± 5	124 ± 32	163 ± 35	62 ± 23
85	<-1.6	≥4	-93 ± 36	116 ± 9	86 ± 43	146 ± 54	122 ± 33
73	<-1.0	≥5	-65 ± 37	112 ± 9	100 ± 40	122 ± 58	115 ± 35
138	<-1.0	≥4	-35 ± 25	108 ± 6	117 ± 37	112 ± 43	100 ± 27

Table 5.4. KMM Analysis for Rotation Direction

Sample (1)	N (2)	Group 1 (3)	Group 2 (4)	$< V_{s1} >$ (5)	$< V_{s2} >$ (6)	σ_1 (7)	σ_2 (8)	p-value (9)
All	178	51	125	-42	72	126	67	.001
[Fe/H]≥ −1.6 All Z	91	15	76	-40	73	97	60	.034
[Fe/H]≥ −1.6 $Z < 4$	71	19	52	-35	91	97	55	.029

in Table 5.4 and clearly show the sample to be consistent with a two component model. The dominant component (Group 2) has a prograde rotation and low velocity dispersion, while the other component (Group 1) has a larger dispersion and is in counter-rotation. It is interesting to note that the results for the entire rotation sample and the [Fe/H]< -1.0 sample both give V_{rot} results for group 2 that are consistent with Zinn's old halo globular clusters. Also the percentage of young halo globular clusters, 29%, is the same as the percentage of stars in group 1.

Finally, it is evident from the samples cut at [Fe/H] = -1.6, that the percentage of counter-rotation stars mixed in the sample depends on abundance. This might be expected if these stars share a common origin, such as a single accretion event. It should be noted, however, that the sample with [Fe/H]< -1.6 does not appear to be consistent with a two-component model. This is probably due to the reduction in the number of stars with large V_s values. If this sample is truly from a single parent population then the velocity dispersion is quite large. It seems more likely that the small number of stars in each group is responsible for the null result. With the splits from mixture modeling we are nearly in a position to discuss the systemic rotation properties of each Galactic component. First, however, we will investigate evidence for the MWTD.

5.7 The Metal-Weak Thick Disk (MWTD)

The existence of the MWTD is still controversial. The great difficulty in unambiguously identifying this Galactic component arises from the fact that the halo and MWTD overlap spatially and in metallicity. This problem is compounded by the possible existence of a flattened pro-grade rotating halo component, which is similar to the MWTD in spatial distribution and vertical velocity dispersion. From the findings of Beers and Sommer-Larson (1995), it would be expected that the

MWTD comprises approximately 30% of the metal-weak stars in the solar neighborhood. This large fraction would be expected to have a profound effect on the kinematics of an assumed single population halo sample.

We begin the MWTD investigation by returning to the systemic rotation results for the FHB sample with $-1.0 >$ [Fe/H] > -1.6 and split at $|Z| = 3$ kpc. The sample with $|Z| < 3$ kpc. is in significantly higher rotation then the sample above 3 kpc. This result is probably not due to contamination of the normal thick disk since the sample, constrained to $-1.4 <$ [Fe/H] < -1.6, still shows consistency with the above result ($V_{rot} = 137 \pm 32$ km/s). At lower abundances the systemic rotation is consistent with zero rotation in both vertical samples. Figures 5.17a-c show the binned results for the two samples split at $|Z| = 3$ kpc, where the filled circles represent the $|Z| > 3$ kpc sample. Again, it is apparent that both the systemic rotation and disk-like properties are different for the two samples.

A straight forward method for identifying the MWTD component is to search for an excess of stars with low velocity dispersion in the abundance range of $-1.0 >$ [Fe/H] > -1.6. Unfortunately, the small number of program stars in this abundance range and toward the Galactic center and polar cap regions, force an analysis of all stars in these directions with [Fe/H]< -1.0. Figures 5.18 a and c are histograms of V_s in the direction of the Galactic center, defined by cos(l)> 0.98 and $|b| < 45$. The solid lines in the two figures are the best fit single and double gaussians, respectively. The corresponding DRR plots are shown in figures 5.17b and c. It appears that neither distribution can completely describe the observed velocities. The double gaussian is a better fit, however, to the center of the distribution and only fails near the positive outer tail, where outliers could affect the outcome. The two gaussian distributions used are $N_1 = 72$, $N_2 = 20$, $\sigma_1 = 125$ km/s, and $\sigma_2 = 40$ km/s. This

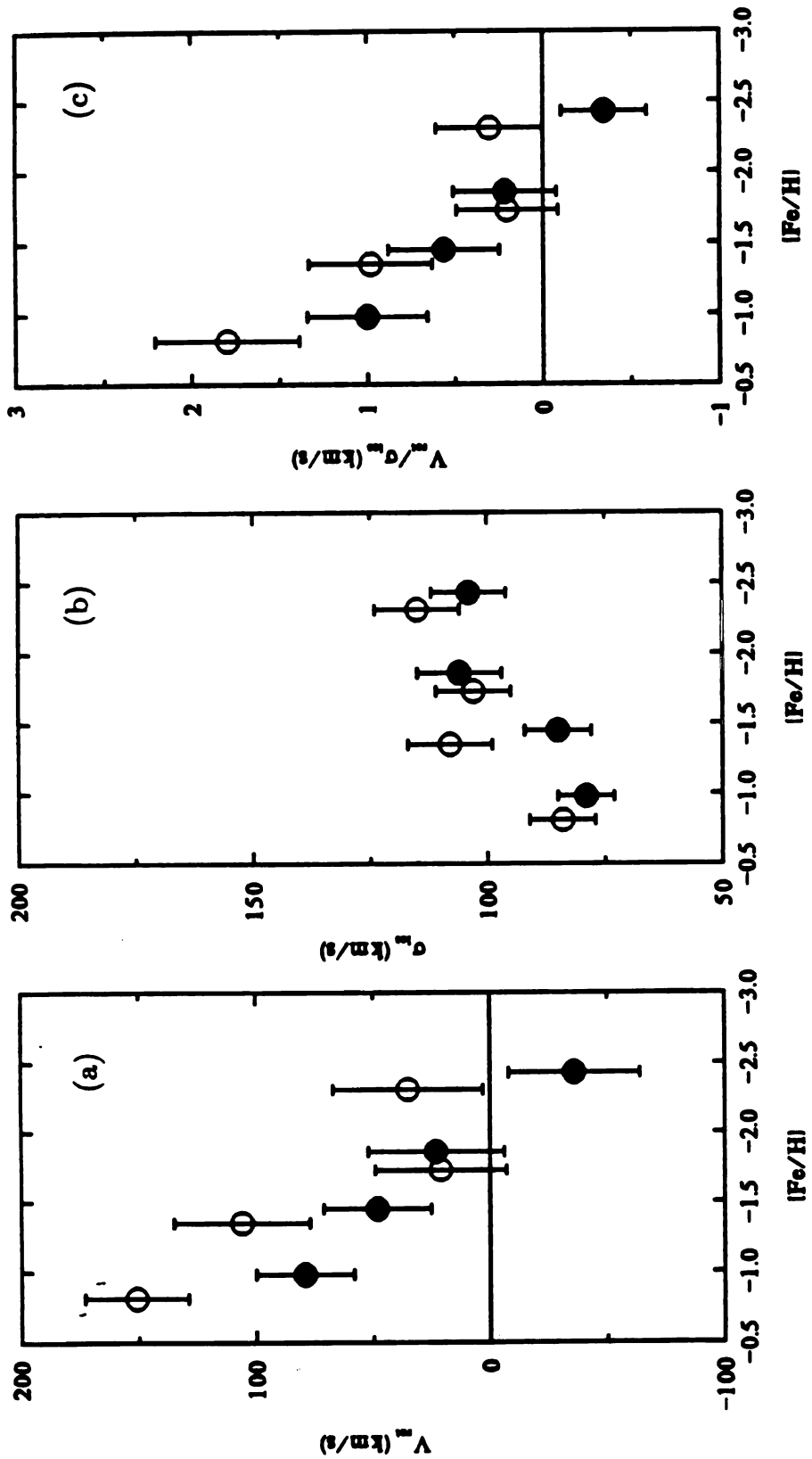

Fig 5.17: Systemic rotational characteristics of the FHB sample. Open and closed symbols represent $|Z| > 3$ and $|Z| \leq 3$ kpc.

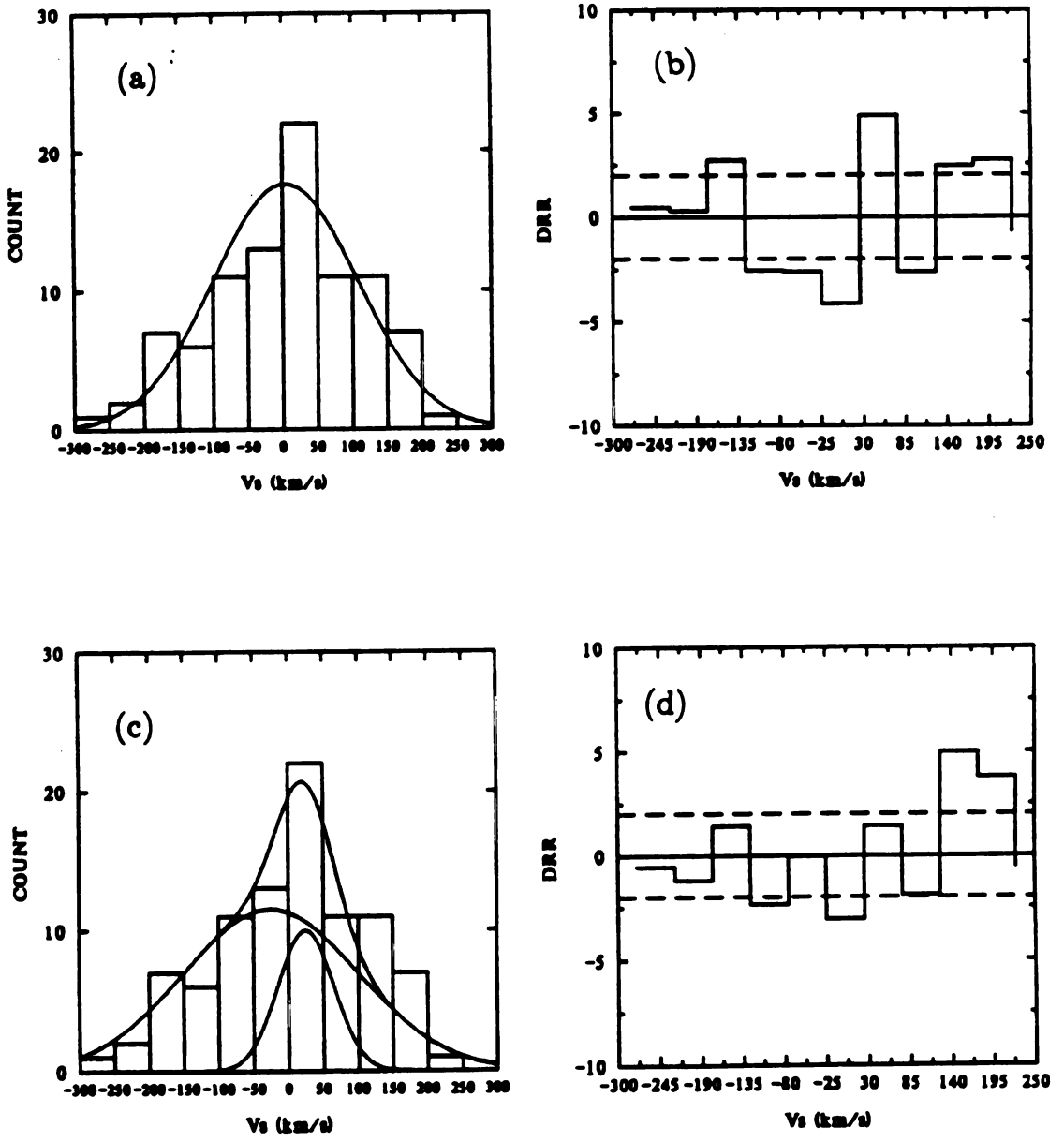

Fig 5.18 Single and double gaussian fit for Galactic center direction. Corresponding DRR plots are shown.

model then predicts that 28% of the FHB stars in the Galactic center direction are in the low dispersion population. A similar analysis has already been carried out for the stars in the polar cap regions (see section 5.5). The result indicates that $\sim$ 33% of the FHB stars are associated with the low dispersion population. If we assume that this is evidence of the MWTD then approximately one-third of the FHB stars are members of the MWTD. This value could be too low, if the halo does indeed have two components with the spherical component incorporating 29% of the stars. The final value of flattened halo FHB stars to MWTD stars would then be in a ratio of 1:1.

A second method which can be employed is presented in figures 5.19 a-c. These plots show the sample of stars in the rotation direction, where V_s has been folded to include both rotation directions and then projected into a ϕ velocity by assuming that the entire V_s velocity is in the rotation direction (hereafter V_{sp}). The rotational direction is defined as $|cos(\psi)| > 0.5$, and $0 < cos(l) < 0.93$. By making such assumptions there is clearly scatter introduced by those stars which actually have strongly radial orbits. Figure 5.19a is a plot of the projected V_s velocity as a function of metallicity for the entire rotation sample. The solid lines indicate V_s = 220 km/s (thin disk rotation) and 0 km/s. It is apparent from this plot that the stars with [Fe/H]> -1.0 are consistent with thick disk rotation. Figures 5.19 b-c are the same plots but with the sample cut at $|Z| = 3$ kpc. In the $|Z| < 3$ kpc sample there appears to be an excess of stars with $-1.0 >$ [Fe/H] > -1.6, with high rotational velocities that are not present in the $|Z| > 3$ kpc sample. It is difficult, however, to separate the halo and MWTD stars in this sample. Clearly, we do not find the large number of MWTD stars as found by Morrison (1993) in her giant star sample (4 MWTD for every 1 halo star). If the findings of Beers

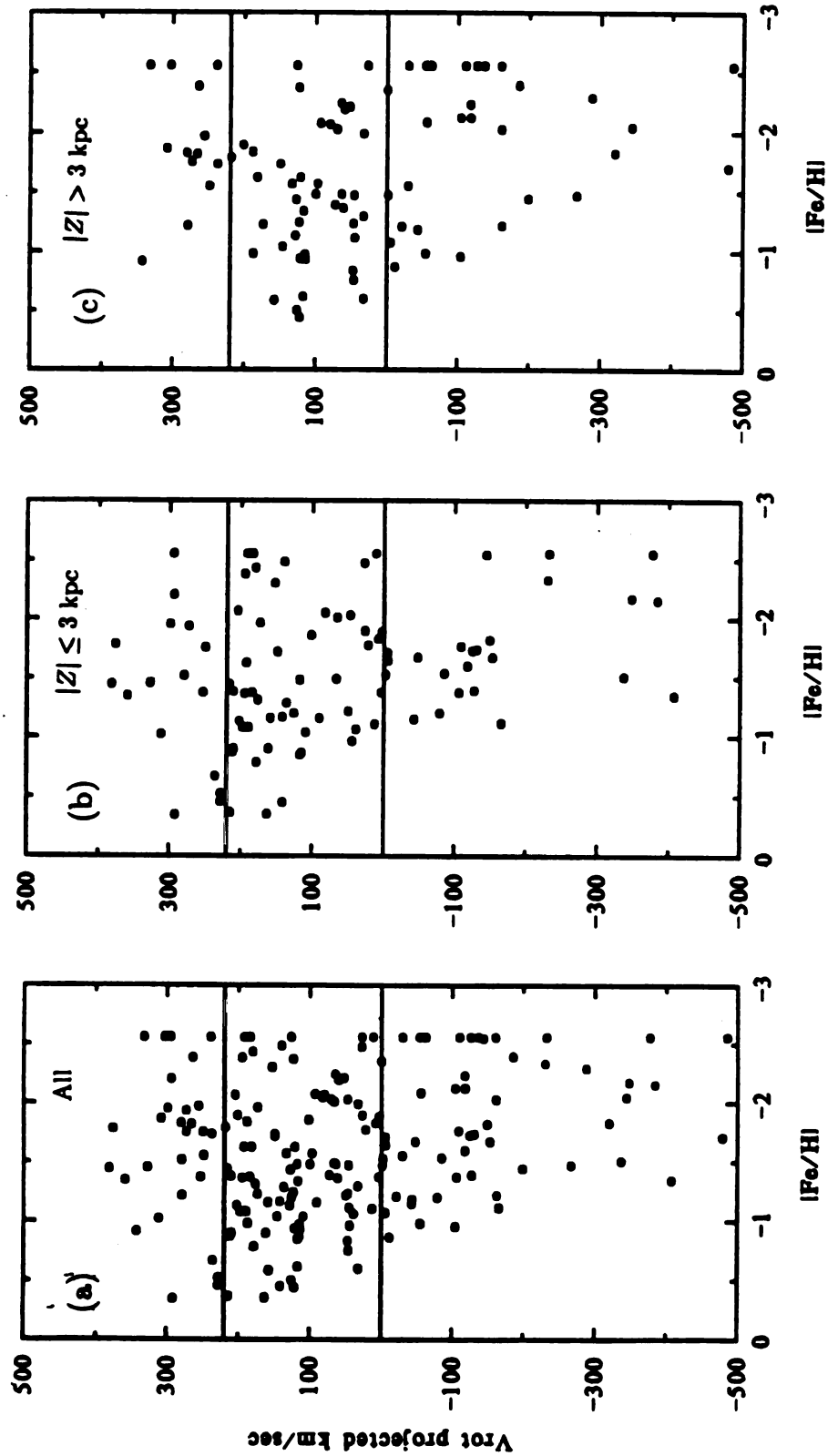

Fig 5.19 Projected velocities for FHB stars in the rotation directions.

and Sommer-Larson (1995) that the MWTD is predominately constrained to low vertical heights, ($|Z| < 2$ kpc) is correct, then it is not surprising that the number of MWTD stars in the FHB sample is small, considering that the program objects mostly sample stars above $|Z| = 2$ kpc.

Figures 5.20a-f are histograms of the various splits in the rotation sample. If we assume the prograde portion of the plot is comprised of two components, one the flattened halo, and the other the MWTD, then there is little or no evidence that a dominant component exists. In the plots we have trimmed the extreme velocity data points to keep them from pulling the tails of the fit. In the histogram of the entire sample and the splits in abundance (figures 5.20 a-c) there is little sign of departure from a normal distribution, with a peak which is consistent with group 2 from the mixture-model results. The splits in vertical height appear to be less consistent with a normal distribution. In the $|Z| < 3$ sample there appear to be separate peaks at $V_{sp} = 25$ km/s and 175 km/s. In contrast, the plot of $|Z| > 3$ kpc shows very few stars with $V_{sp} > 150$ km/s. There instead appears to be an excess of stars near $V_{sp} = 100$ km/s. As before, we find no dominating MWTD component with thick-disk-like rotation, and especially not in a 4 to 1 ratio with the halo stars. In fact, it is debatable whether or not the sample is drawn from a single population. In the following section on systemic rotational properties it will be shown that the flattened halo to MWTD ratio is also in a 1:1 correspondence for the rotation directions. It should be noted that along with the small sample size, the results are confused by the application of liberal directional constraints required to increase the number of stars.

There are several general conclusions that can be reached from this investigation. We do not see an excessively large number of MWTD stars in any of the samples

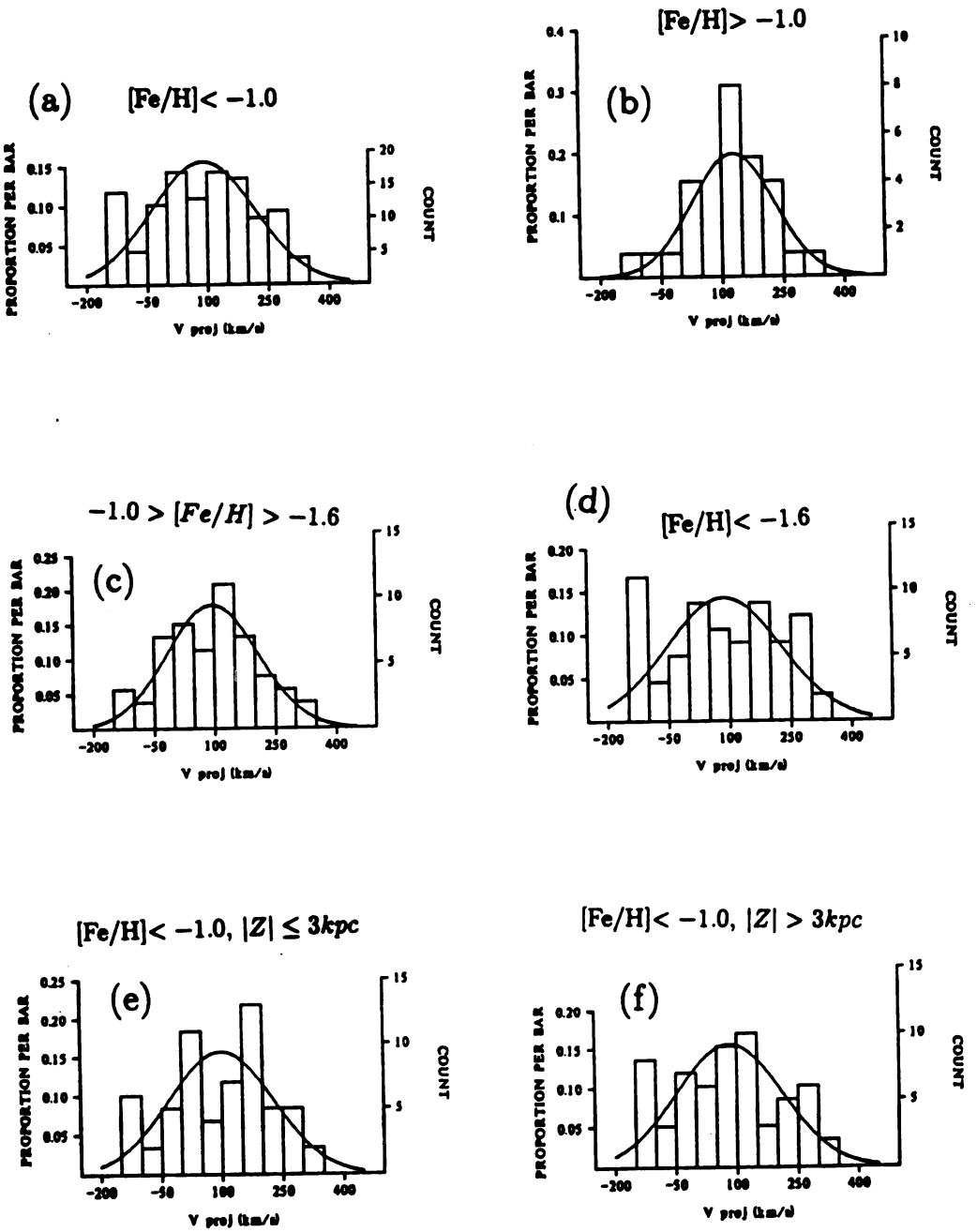

Fig 5.20: Histograms of the projected velocity in the rotation directions and with various splits in [Fe/H] and $|Z|$

which were searched. The rotation sample split on $|Z|$ height seems to indicate that the MWTD at $|Z| > 3$ kpc has either a smaller percentage of MWTD stars then the lower vertical height sample, or V_{sp} has decreased to less than 150 km/sec. If the lower sample does indeed contain a MWTD component then its ratio to flattened halo stars is probably not larger than 1. Finally, the evidence is only marginal that group 2 (prograde halo), identified from the mixture models, is not drawn from a single population.

5.8 Systemic Rotational Properties (revisited)

In the discussion by Norris (1994) on the duality of the Galactic halo, the need for multiple discrete components to explain the results from various tracer and proper motion surveys (3 disk and 2 halo components) is superseded by economy of hypothesis, which suggests that the same results can be explained through a combination of contracted (ELS-type) and accreted (SZ-type) components. This is what has been previously termed the ELS/SZ hybrid model. Both discrete and continuous models can adequately describe the present data since adjusting the mixing parameters correctly for the discrete component model can give the same results as a continuous component. As noted by Norris, however, the difference between competing models is more than a simple question of semantics since the discrete components may arise out of entirely separate formation events. Without a present understanding of our FHB sample completeness we remain seriously handicapped in our ability to fully model the kinematic properties. Through the use of several assumptions, we can however, attempt to better constrain the possible properties of the halo components.

We begin with an examination of figure 5.17a-c, which shows the V_{rot}, σ, and V_{rot}/σ solutions for the binned data cut at $|Z| = 3$ kpc. The V_{rot} plot shows a

marked difference between the two bins at $< [Fe/H] > \sim -1.4$, where the significantly higher rotation at lower $|Z|$ height is assumed to be due to the presences of a metal-thick disk component. It is interesting that the lower $|Z|$ height bin shows a large velocity dispersion in figure 5.17b. This is what would be expected from mixing of two components with very different rotational velocities. There is also a stark difference in the bins at lowest abundance, where the highest vertical bin is in counter-rotation. The two cuts agree at the $< [Fe/H] > \sim -1.8$ bin, where $V_{rot} = 22$ km/s. The fact that the lowest abundance bin in the low $|Z|$ height cut is also consistent with the other two, suggest that a $V_{rot} \sim 22$ km/sec is a good estimate for the systemic rotation of the flattened halo component. With this assumption, we begin by exploring the mixture of MWTD and flattened halo stars.

First we employ a very simple model that only depends on the average velocity and number ratio for each population. This is obviously only an approximation because the dispersion in each population is important in assessing the contribution that one population has on the other's average velocity. The model is, however, approximately valid, as long as the spread in average velocities is large compared to the dispersion. The model can be expressed as:

$$(N)V_{rot} = (N_1)V_{rot1} + (N_2)V_{rot2} \qquad (5-8)$$

where N_1, N_2, V_{rot1}, and V_{rot2} are the number of stars and rotational velocity for each component, while N and V_{rot} are the total number of stars and rotational velocity for the entire sample. To investigate the MWTD stars we begin by exploiting the differences in the second abundance bins. Because the value of N_1/N_2 is unclear in our current sample we will estimate this ratio by assuming a rotational value for

the MWTD. Beers and Sommer-Larsen (1995) find V_{rot} = 195 km/s for the thick disk of the Galaxy. If we use this value for the MWTD and the value of V_{rot} = 106 km/s for the total sample of 76 stars in the low $|Z|$ height cut, then the ratio of MWTD:flattened halo stars is 1:1. Using a lower value of V_{rot}MWTD = 150 km/s gives a ratio of 2:1. The first value is consistent with our previous estimate for the number ratio. If we next consider the high $|Z|$ cut, with V_{rot} = 48 km/s we find a ratio of 1:6 and 1:4 using the input 195 and 150 km/s, respectively. If, then, the rotational velocity remains constant for the MWTD the number of such stars decreases by a factor of $\sim$ 7 in going from $|Z|$ = 2 kpc to $|Z|$ = 4.5 kpc. This amount of change indicates a scale height for the MWTD of h_z = 1.3 kpc, which is consistent with the findings of Morrison, Flynn, and Freeman (1990). If, on the other hand, we assume that the number ratio of stars remains constant from $|Z|$ = 2 to 4.5 kpc. then we find that the rotational velocity decreases to 74 km/s and 62 km/s, depending on the assumed V_{rot} value. This implies the existence of a $|Z|$ gradient in V_{rot} of -48 to -35 km/s/kpc, in the range from $2 < |Z| < 4.5$. These values are consistent with the findings of Murray (1986), Hanson (1989), Spaenhauer (1989) and Majewski (1992a) for the $|Z|$ gradient in the thick disk stars.

Based on the assumptions for the number ratio estimate, incompleteness in the sample, and beginning assumption for the flattened halo rotation, it is not possible using this simple model to exclude either the constant V_{rot} or the constant number ratio solutions. Physically, it would not be expected that the ratio of MWTD:halo stars should remain constant from $|Z|$ = 2 Kpc. to 4.5 Kpc., unless the MWTD has a very large scale height and completely dominates the flattened halo component. As previously mentioned this does not appear to be the case. By necessity we have neglected any possible $|Z|$-gradient in the flattened halo component, which

could exist even if the MWTD and halo are discrete. Such a gradient would serve to reduce the number of MWTD stars. Finally, it should be mentioned that a dominant counter-rotating halo above $|Z| = 3$ kpc could also serve to reduce the V_{rot} value in the second metallicity bin. This appears, however, not be the case since the mixing of a counter-rotating population with a large prograde-rotation population should result in a large σ_ϕ dispersion. The actual ϕ dispersion is smaller in the higher $|Z|$ bin, suggesting instead that less mixing is taking place.

In an attempt to better quantify the rotational properties of the MWTD component, we next examine the departure from a normal distribution by displaying the DRR plots, figures 5.21a-c, for the sample with [Fe/H]< -1.0, and [Fe/H]< -1.0 split at $|Z| = 3$ kpcs as displayed in figures 5.20 a,e and f. To assist in this investigation, the stars assumed to be members of the counter-rotating population have been excluded to prevent them from giving undue weight to the tail of the distribution. We see that in all three cases the DRR indicate that a single population does not adequately describe the distribution of velocities. We next attempt to fit the distributions, split at $|Z| = 3$ kpc, with a double gaussian. The DRR plots are found in figures 5.22 a and b. The fit is improved in both cases although there are still some departures in the DRR plot. In both cases the best fit is found when $N_{flathalo}/N_{MWTD} = 1$, $\sigma_{halo} = 75$ km/s, and $\sigma_{MWTD} = 55$ km/sec. The average velocity for the halo component is 20 and 10 km/sec for $|Z| < 3$ kpc and $|Z| > 3$ kpc, respectively. We find that in this case the velocity for the MWTD decreases from 170 km/s to 110 km/s between the low and high $|Z|$ samples, corresponding to a vertical gradient of -24 km/s/kpc. Great caution must be used, however, in interpreting this result. The double gaussian fit is unable to satisfactorily describe the stars with velocities$>$ 220 km/s. It is expected that their existence is not due

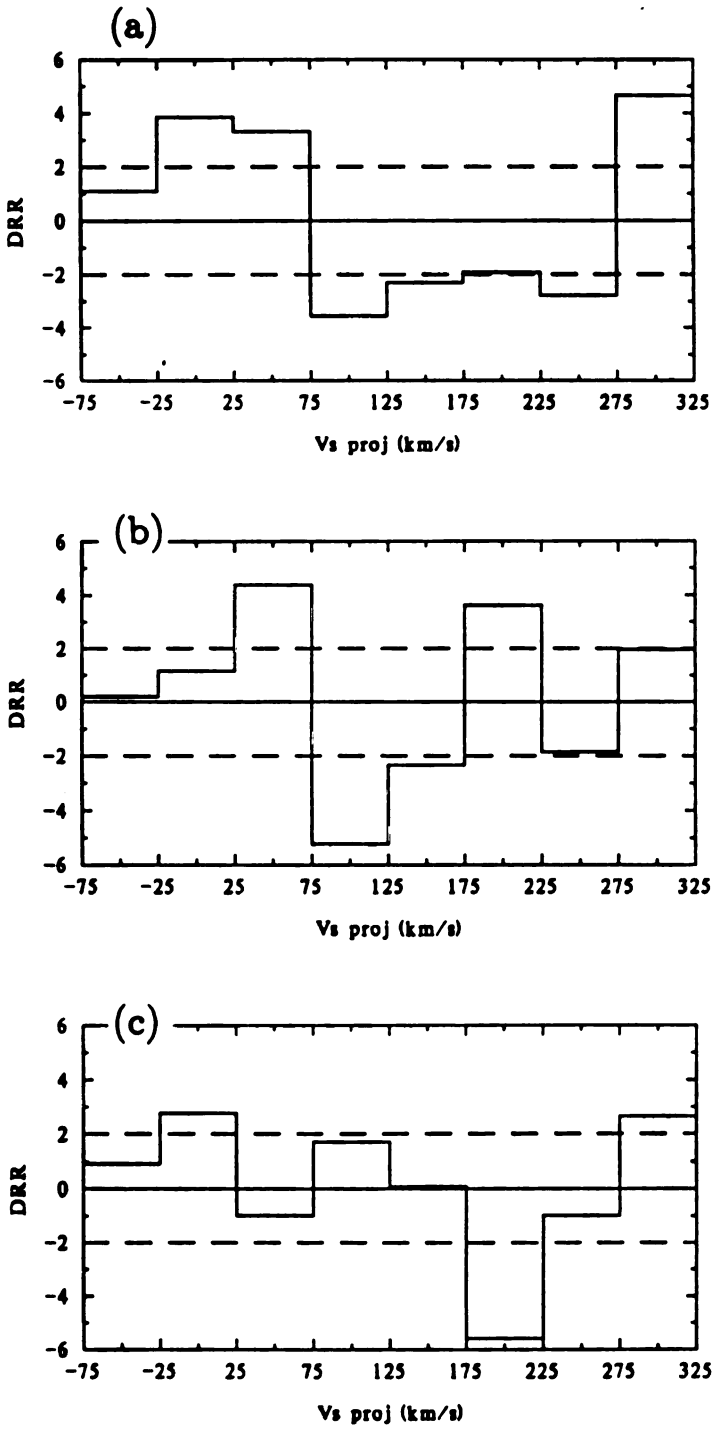

Fig 5.21: DRR plots for single Gaussian fit of (a) [Fe/H]< -1.0, (b) [Fe/H]$< -1.0, |Z| \leq 3$ kpc and (c) [Fe/H]$< -1.0, |Z| > 3$ kpc

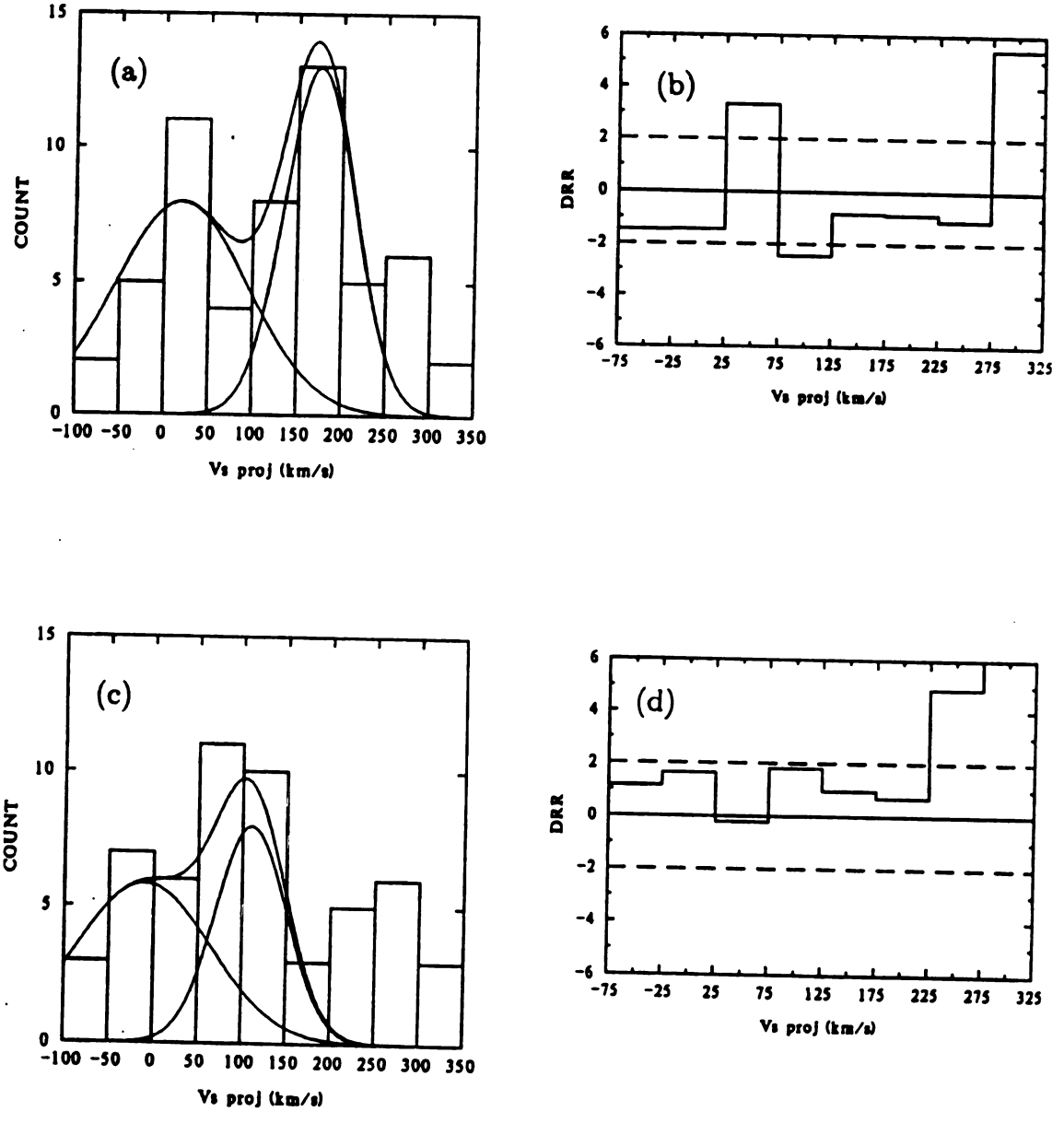

Fig 5.22 Double gaussian fits to projected Vs velocities split at $|Z| = 3$ kpc. Plots (a,b) correspond to $|Z| \leq 3$ kpc, (c,d) are for $|Z| > 3$ kpc. Both plots are for [Fe/H]< -1.0.

to a large rotational velocity, but rather a large radial velocity component which is present because of our liberal directional constraints. This same effect is undoubtedly present in the lower velocity sample and may even be responsible for the original non-gaussian distribution. Therefore, until the number of stars in the rotation sample increases, we can only conclude that there is marginal evidence for a velocity gradient in the MWTD.

We conclude from this line of analysis that there are probably four kinematically-distinct components present in the FHB sample. At the highest abundances it is expected the large rotational velocities are due to the presence of members of the "normal" thick disk. From the KMM mixture modeling of the rotation directions and the kinematic analysis of the low metallicity stars above $|Z| = 4$ kpc, it appears that there is a halo component in counter-rotation with $V_{rot} \sim -90$ km/s. Though somewhat less compelling, there is evidence for the existence of a MWTD component with a possible rotational dependence on $|Z|$ height and an average V_{rot} of ~ 140 km/s. Finally, there is the dominant halo component which appears to be flattened and has a mildly prograde rotation of $V_{rot} \sim 15$ km/s.

5.9 Concluding Remarks

From the systemic rotational and velocity dispersion results, there is strong evidence for a change in the kinematic properties of the FHB sample at a $|Z|$ height of ~ 5 kpc. The change in the velocity ellipsoid solution is particular intriguing because it suggests a fundamental departure from a flattened distribution to a more spherical one (change in σ_θ) with a corresponding peak in the rotational dispersion, σ_ϕ. The fact that at the same $|Z|$ height, the FHB sample exhibits a possible systemic rotation which is in counter-rotation is compelling evidence that the inner and outer halo formed under quite different circumstances. The consistency between

the kinematics of most of our FHB sample and other previously-published surveys is encouraging. The fact that departures, such as a high σ_ϕ dispersion, exist is suggestive, not of problems with our FHB sample, but rather of shortcomings in the previous surveys which are constrained to the local solar neighborhood. The fact that we find rather good consistency with the more distant halo surveys strengthens this argument.

Evidence for the MWTD is far less compelling. The fact that we do not see a strong kinematic signal from the MWTD may be due, in part to our metallicity bias and in part to the restricted vertical height of this population of stars. It is also possible that the MWTD is a younger population and is therefore present in giant star samples (such as Morrison *et al.*) but too red to be considered in the FHB sample. Currently, however, there is mounting evidence that the MWTD may not exist at all, and that the stars so identified by Morrison *et al.* are actually normal thick disk stars with derived abundances that are systematically too low (Ryan and Lambert 1995). While the verdict is still out on those particular stars, we must add that there does seem to be good evidence for a low dispersion population in our FHB sample. It is certainly possible that disk contamination from various A-type stars, and from the BMP's is present in our FHB sample. Especially worrisome is the possible presence of A-giants (Green 1995). The low velocity dispersion detected at [Fe/H]< -1.0 should, however, exclude many of the A-giants and suggests that their significance to the low dispersion result is minimal.

CHAPTER 6

KINEMATICS OF THE A-STAR SAMPLE

We now begin the investigation of the program stars which were identified as having surface gravities larger then those consistent with the horizontal branch. From previous studies of Rodgers *et al.* (1981), Lance (1988), and Preston *et al.* (1994), it is expected that this sample contains a mix of main-sequence stars associated with the thin disk, metal-weak Pop. I, and blue metal-poor Pop. II stars. At lower surface gravities, Log g $\sim$ 3.5, there is also expected to be some percentage of misidentified FHB stars, especially RR lyrae variables, subgiants, and spectral type A III giants, whose progenitors are A and F-type stars. Initially, the sample also contains a number of stars with (B-V) colors redward of 0.35, which are expected to include stars from the halo main sequence turn-off.

6.1 The Sample Properties

Distances were determined for the A-star sample using the color-absolute magnitude relation from Preston *et al* (1991):

$$M_v = 0.602 + 11.07(B-V) - 15.843(B-V)^2 \qquad (6-1)$$

Using the calculated distances and Galactic coordinates for each star the Galactocentric distance, Z height, V_{lsr} and V_s were calculated as before. Figure 6.1a is a plot of vertical height as a function of Galactocentric distance for the entire sample

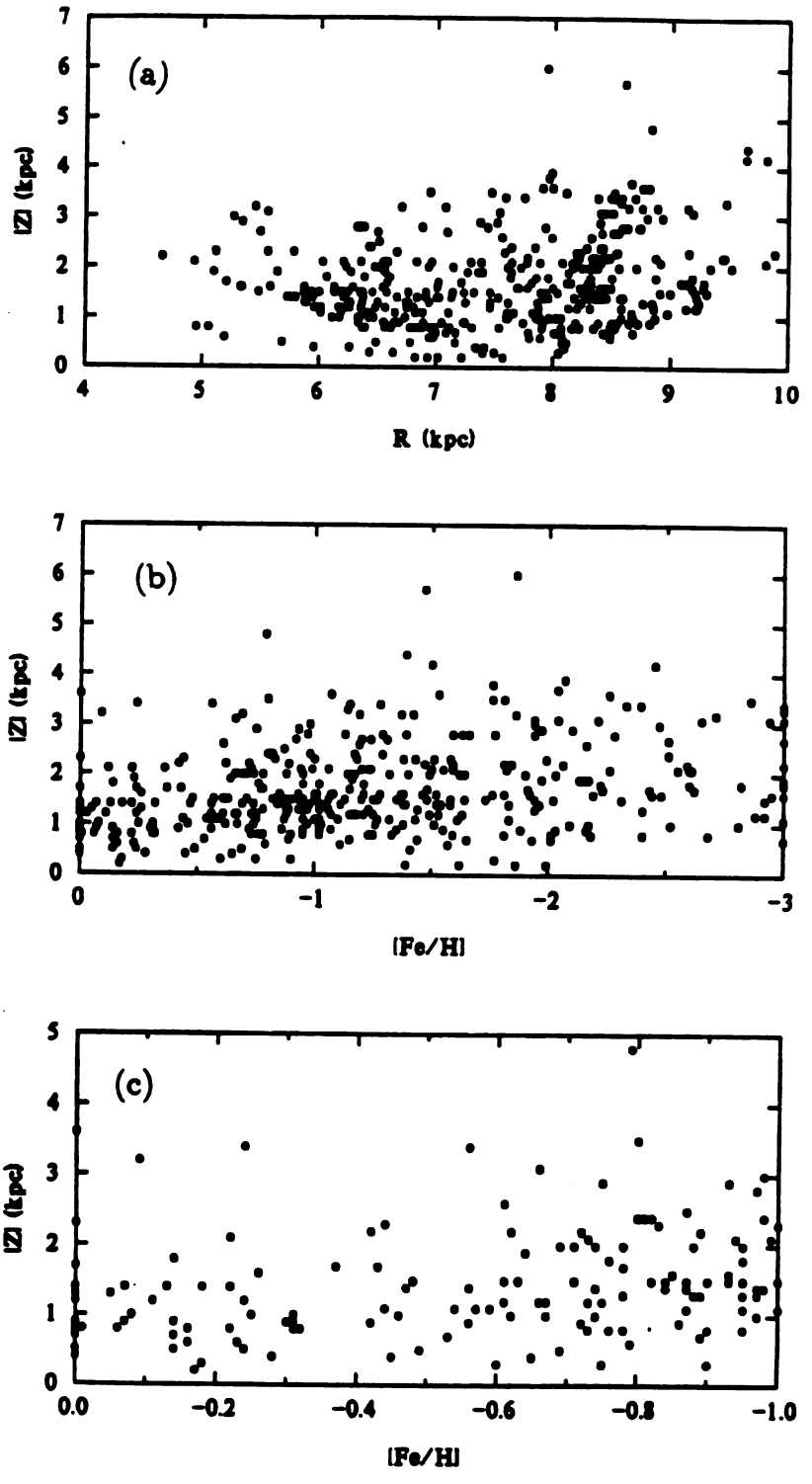

Fig 6.1 Spatial and abundance characteristics of the A-star sample.

of 448 A-type stars. It is immediately obvious that the spatial extent of the sample is considerably less then the FHB sample owing to the intrinsically lower luminosity of the main-sequence A-type stars. The bulk of the sample lies in the range of $5 < R < 10$ kpc and $0 < |Z| < 3$ kpc. Before beginning a detailed study of the A-type stars, the sample has been "cleaned" to remove the 45 stars redward of (B-V) = 0.35, along with the stars which show the largest deviation on the Teff-(B-V) plot as indicated in section 4.1.3.2. The resultant sample has thus been reduced to 360 stars and will serve hereafter as the A-star sample.

Figure 6.1b is a plot of $|Z|$ height as a function of [Fe/H] for the A stars. Again we see the majority of the stars at $|Z| < 3$ kpc with the bulk of the sample below $|Z| = 2$ kpc. In a similar plot by Lance (1988) for a sample of SGP stars, she identifies a distinct separation between her Pop I and Pop II stars characterized by a gap in the abundance distribution near [Ca/H] = -0.6. This transition is also suggested in our A-star sample near [Fe/H] = -0.6 but is probably less dramatic due to the bias against metal-rich stars in our sample. For clarity, figure 6.1c is the same plot constrained to [Fe/H]≥ -1.0. Again there appears to be a change in the distribution at abundances higher than [Fe/H] = -0.6.

Histograms of [Fe/H] for the A-star and FHB samples, binned in 0.2 dex intervals for better resolution, are shown in figures 6.2a-b. It is now more apparent that a distinct change in the A-star distribution has occurred near [Fe/H] = -0.6. It is expected that this change coincides with the transition from Pop I to Pop II as found by Lance. It is encouraging to note that the abundance distribution is significantly different from the FHB sample, which peaks near [Fe/H] = -2.0, and has a much larger number of stars with [Fe/H]< -2.2. Because of this difference, however, care must be taken in interpreting the results for the A-stars with [Fe/H]< -2 since even

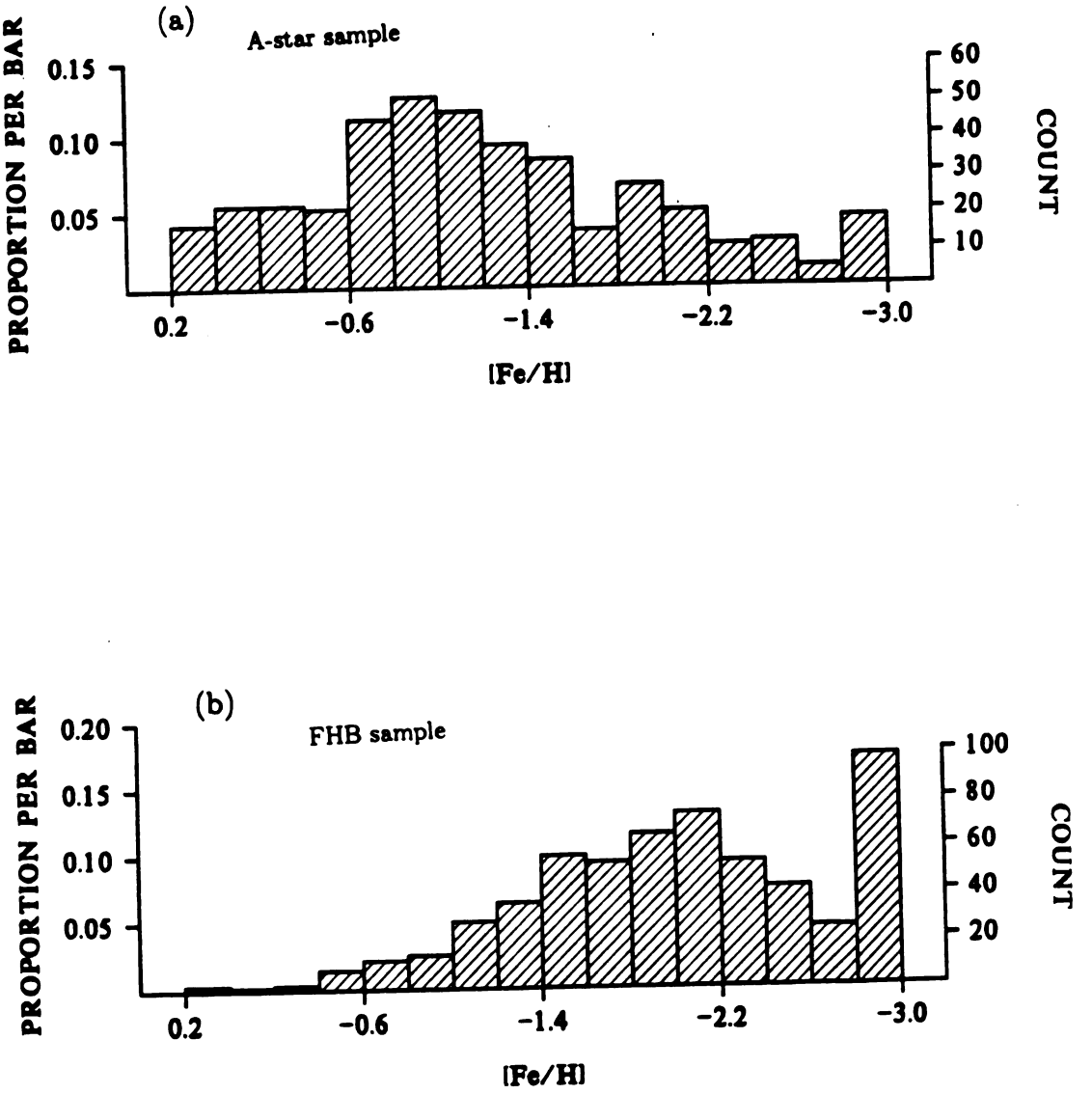

Fig 6.2: Comparison of the metallicity distribution for the A-star and FHB samples.

a small fraction of misidentified FHB stars will amount to a large percentage in the A-star sample.

To further examine the distinction between Pop. I and Pop. II in the A-star sample, we next plot the V_{lsr} for each star as a function of [Fe/H] and $|Z|$. Figure 6.3a indicates the existence of a very low dispersion population which begins to increase near [Fe/H] = -0.5, and becomes quite large for [Fe/H]< -1.0. Likewise, in figure 6.3b, there is a low dispersion for $|Z| < 800$ pc, with a large increase above $|Z| = 1$ kpc. Taken together with the abundance distribution evidence it is strongly suggestive that a change in population occurs in the range of $-0.6 >$ [Fe/H] > -1.0. In the following section on the A-star kinematics, we will further investigate the population boundary as well as possible effects from non-A star contaminants.

6.2 A-star kinematics

6.2.1 Binned Solutions

As with the FHB sample we have continuously binned the A-star sample to examine the V_{rot} and σ_{los} properties as a function of [Fe/H]. The size of each bin is 75 stars with an overlap of 15 stars between bins. Figure 6.4a-c are plots of the V_{rot}, σ_{los} and V_{rot}/σ_{los} results, respectively. It is clear that at the highest abundance the systemic rotation is close to the value for the thin disk of the Galaxy. The somewhat constant V_{rot} values in the next 3 bins are expected to reflect the mixture of systemic rotations for the Pop I and Pop II stars, while the bin at $-1.0 >$ [Fe/H] > -2.0 is consistent with the systemic rotation and velocity dispersion values found by Preston *et al.* for the BMP stars. The most curious feature of these plots is the near zero rotation and high dispersion found in the bin with [Fe/H]< -2.0. Such a result could be due to a relatively small number of BMP stars and consequently larger percentage of FHB contaminates, or possibly a different population of stars

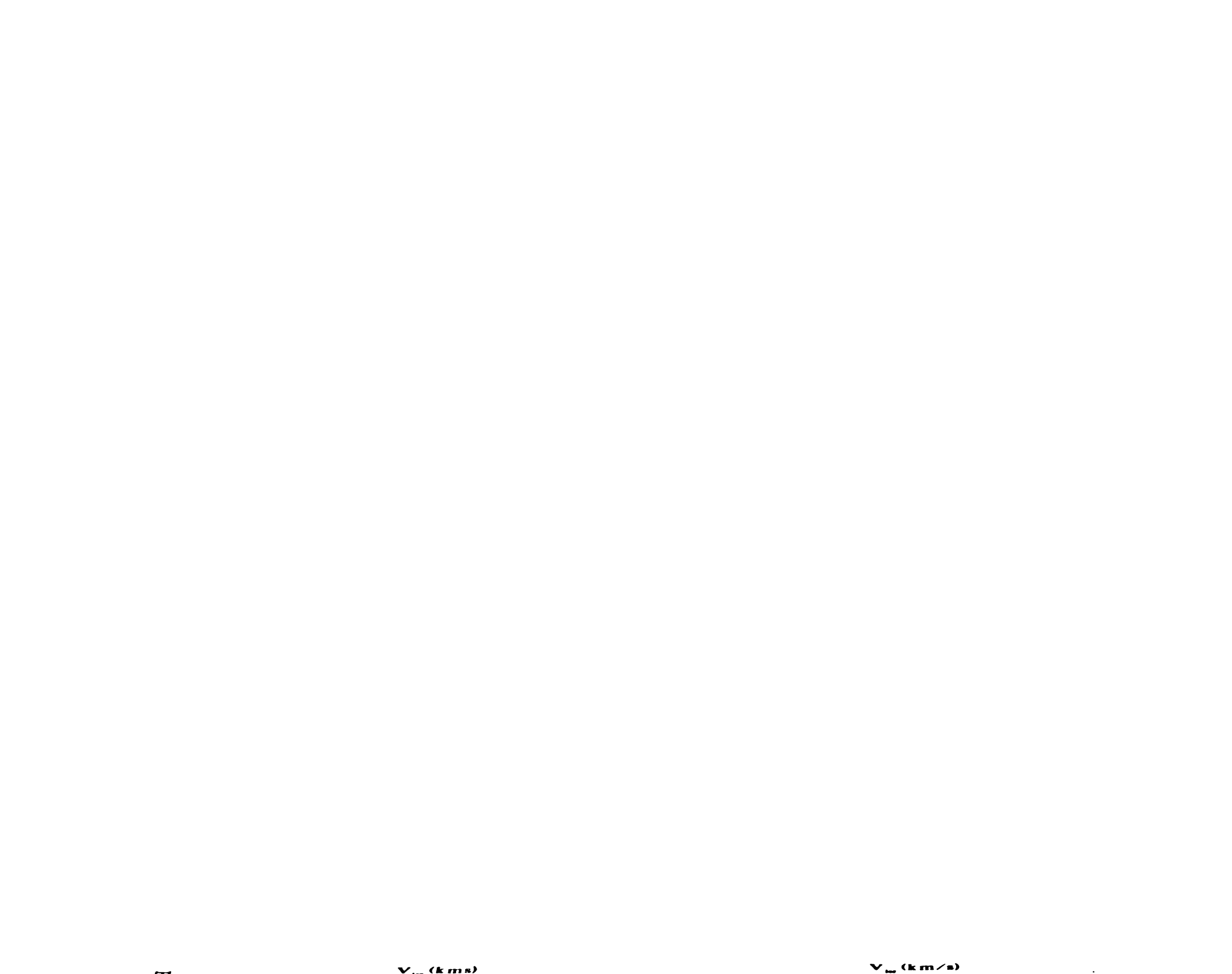

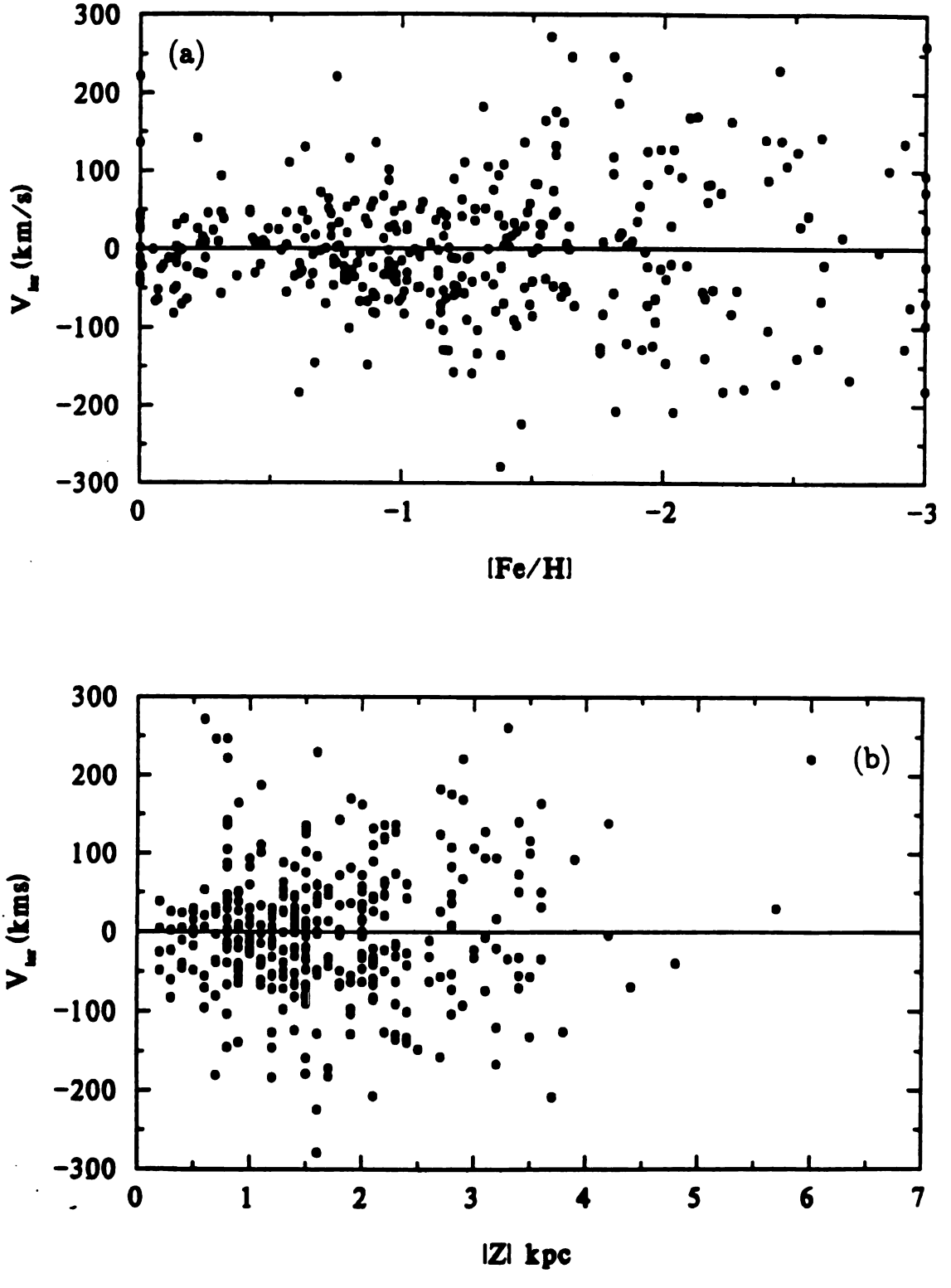

Fig 6.3 V_{lsr} as a function of [Fe/H] and $|Z|$ for all A-stars.

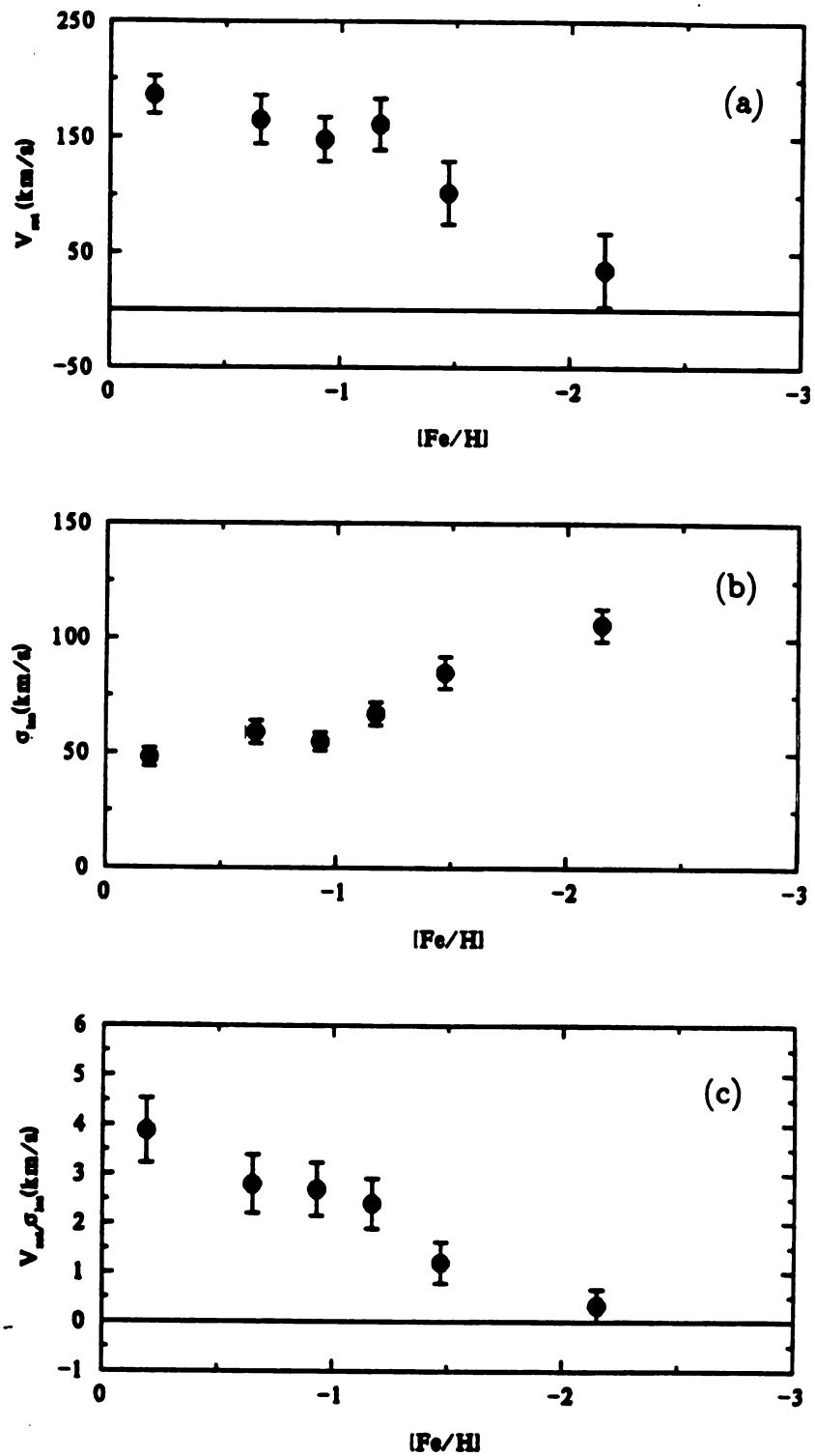

Fig 6.4: Continuously binned systemic rotation solutions for the A-star sample. Bin size is 75 stars with an over lap of 15 stars between consecutive bins.

altogether. We will examine both possibilities in the upcoming sections.

It remains unclear in figure 6.4 at what abundance the Pop II stars begin to dominate the sample. This may be due to overlap in the abundances between the two populations or may be an artifact of the continuous binning procedure. Therefore, we next analyze the kinematics of the sample with bin sizes of 100 stars each and no overlap between bins. The results for both the rotational properties and the velocity ellipsoid solutions are displayed in figures 6.5 a-f. The rotational velocity results indicate a significant difference for both the highest and lowest metallicity bins compared to the intermediate bins. This seems to be an indication that the Pop II sample begins to dominate at [Fe/H]~ -0.6 dex. This does not, however, agree with the results for σ_{los}, V_{rot}/σ_{los}, or σ_W, which all indicate that the transition from disk to more spherical dispersions occurs at abundances lower than -1.0 dex. The large σ_V values for [Fe/H]> -1.0, as will be shown shortly, is not due to population mixing, but rather a few extremely deviant outliers. Finally, it is interesting to contrast the σ_U value for the A-stars to that of the FHB sample. The A-star sample exhibits a constant $\sigma_U \sim 75$ km/s, whereas the FHB stars are significantly higher ($\sigma_r \sim 125$ km/s), hinting at a different origin for the two samples.

6.2.2 The Vertical Velocity Dispersion

We next consider the various A-star populations by investigating the velocity dispersions in the direction of the Galactic polar caps ($|b| > 65$). Figures 6.6a-f are histograms of W_{est} for various cuts in metallicity. The entire sample (figure 6.6a) appears non-gaussian with an excess of low velocity stars and a dispersion of $\sigma = 82$ km/s. This excess is undoubtedly due, in part, to the inclusion of stars with thin-disk kinematics. Figure 6.6b shows that the sample with [Fe/H]> -0.6 has a

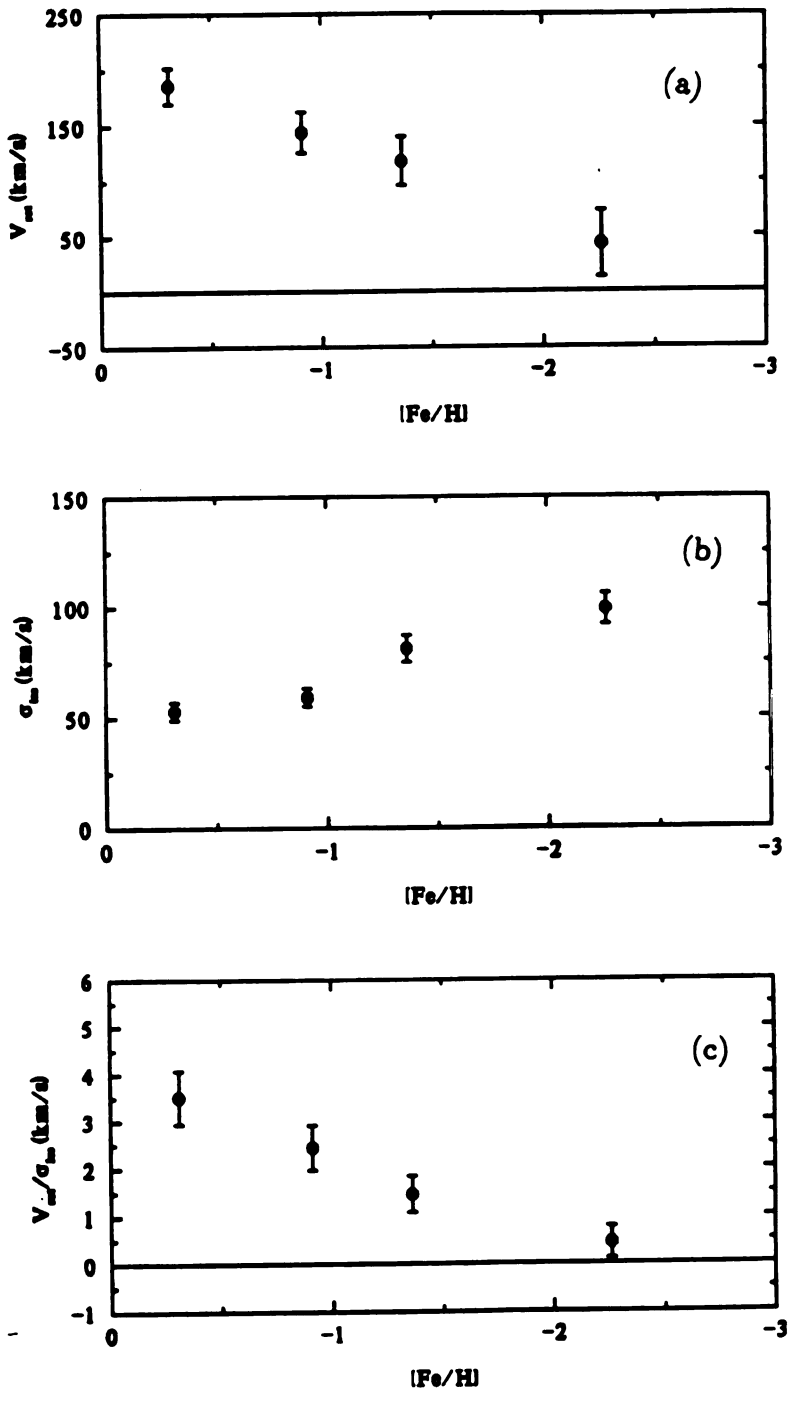

Fig 6.5: Systemic rotation solutions without continuous binning. Bin size is 100 stars.

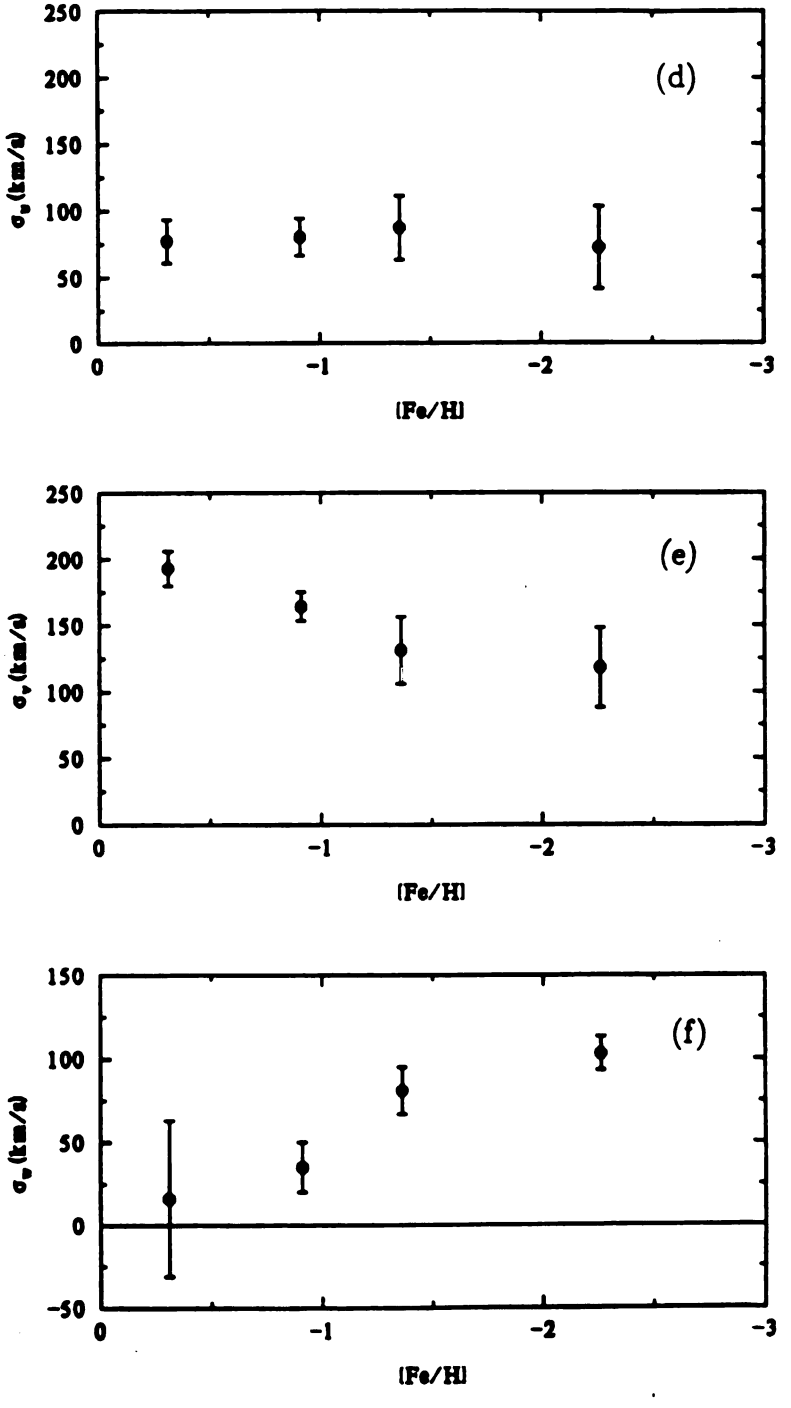

Fig 6.5B: Woolley velocity ellipsoid dispersions without continuous binning. Bin size is 100 stars.

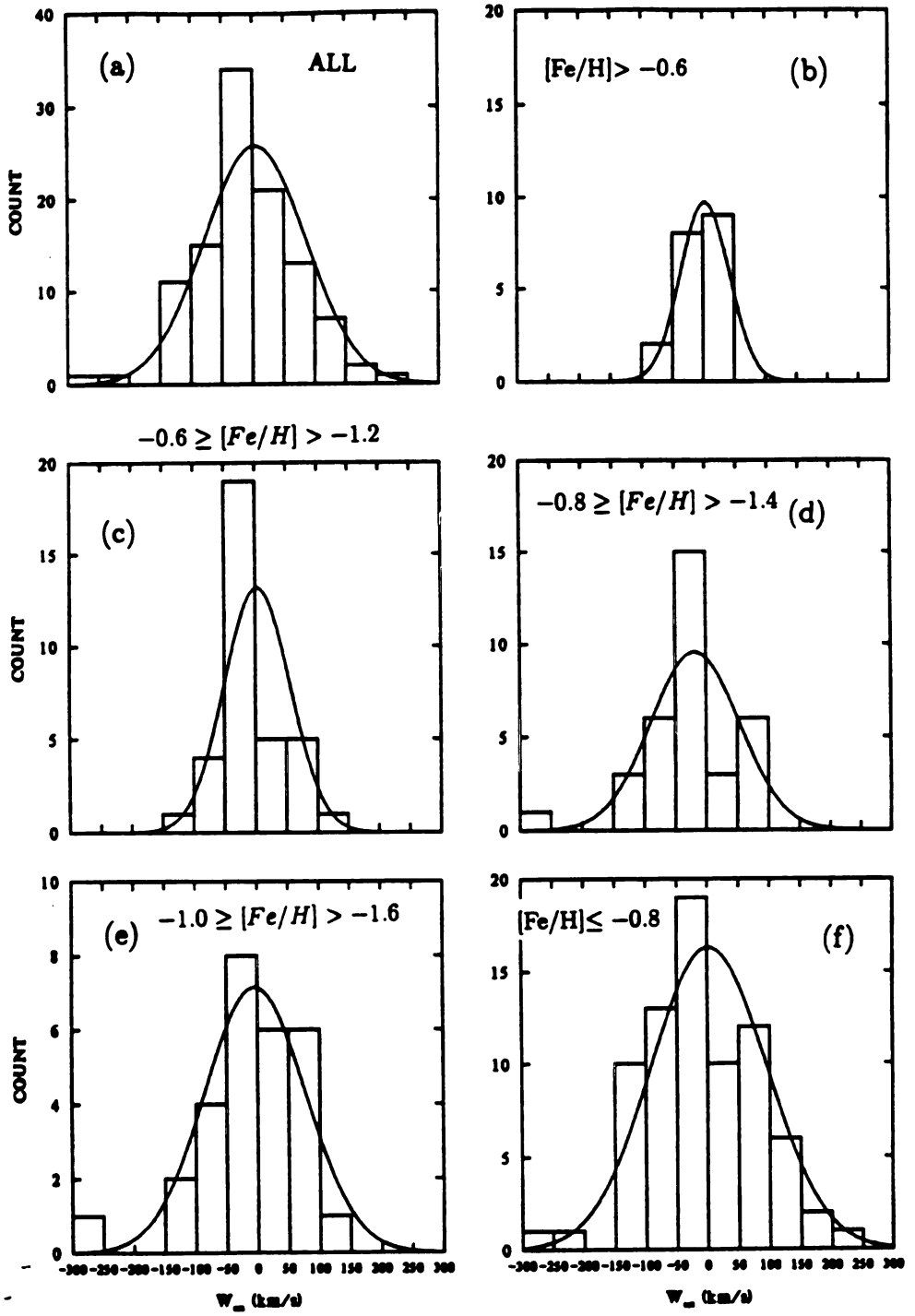

Fig 6.6: Estimated W velocities for the polar cap regions with splits in [Fe/H] indicating metallicity transition from Pop I to BMP stars.

very small dispersion, σ = 35 km/s, consistent with the thin disk of the Galaxy. Figures 6.6c-e are plots of the suspected transition region between Pop. I and Pop. II. The cuts in abundance are $-0.6 \leq$ [Fe/H] < -1.2, $-0.8 \leq$ [Fe/H] < -1.4, and $-1.0 \leq$ [Fe/H] < -1.6, respectively. It is clear that the number of excess stars is decreasing as the abundance window shifts to lower [Fe/H] values. Likewise, the dispersion is progressively increasing with σ_W = 50, 68, and 80 km/s. If we assume a dispersion of σ_W = 90 for the BMP stars, as found by Preston *et al*, then it appears a pure BMP sample begins at [Fe/H]~ -1.0. For comparison purposes, figure 6.6f is a histogram of all polar stars with [Fe/H]≤ -0.8. The best gaussian fit for this distribution is σ_W = 93 km/s.

6.3 Population I Kinematics

It is expected from the previous spatial and metal abundance plots, as well from inspection of the vertical velocity dispersions, that a reasonably pure Pop. I sample can be obtained for [Fe/H]> -0.6. This is also in close agreement with the findings of Lance. To minimize the overlap with Pop II stars, we will adopt an abundance cutoff of [Fe/H] = -0.5. The Pop I sample is expected to be dominated by stars belonging to the thin disk of the Galaxy at $|Z| < 1$ kpc, (due to the small scale height of $\sim$ 350 pc) and metal-weak (Lance-type) A stars at higher vertical heights. Table 6.1 lists the rotational values for the metal-rich populations split at $|Z| = 1$ kpc and $|Z|$ = 600 pc, respectively. The candidate thin disk stars show virtually no difference in systemic rotation between the sample cut at $|Z| = 1$ and $|Z| = 0.6$ kpc. The line-of-sight velocity dispersion for $|Z| < 0.6$ kpc appears, however, to be more consistent with the expected thin disk dispersion. Likewise, the best solution for the metal-weak A-star sample appears to be for those stars with $|Z| > 0.6$ kpc. Because the number of metal-richer stars in the sample is small the uncertainties in

Table 6.1. Pop I Systemic Rotation

[Fe/II] (1)	Z (2)	N (3)	V_{rot} (4)	σ_{los} (5)
> -0.75	< 1	46	192 ± 22	53 ± 6
> -0.75	> 1	63	186 ± 23	52 ± 5
> -0.75	< 0.6	15	213 ± 22	34 ± 6
> -0.75	> 0.6	97	184 ± 18	55 ± 4

the systemic rotational values are large and the difference between the thin disk and metal-weak A-star solutions are not significant at the 1σ level. It is interesting that the apparent lag of $\sim$ 25 km/s for the metal-rich sample is similar to the findings of Rodgers and Roberts (1993).

Owing to the small number of stars with [Fe/H]> -0.5 we do not wish to explore the specific kinematic properties of the Pop I stars further, since any solution will remain rather uncertain. We can, however, still use these stars to help constrain the transition region in metallicity where the Pop II stars begin to dominate the sample kinematics.

6.4 The BMP Sample

The kinematic results for the recently-identified blue, metal-poor, main sequence stars (hereafter, BMP) from Preston *et al.* (hereafter, PBS) indicate that the sample of A-type stars with [Fe/H]< -1.0 have a unique systemic rotation, $V_{rot} = 128 \pm 30$ km/s, and isotropic velocity ellipsoid of $\sim$ 90 km/s. Our sample includes 64 of the previously identified BMP stars by PBS. Because the new calibration grid was used in determining the stellar physical parameters, we will begin by investigating the calculated metallicity for the PBS subsample. Figure 6.7a is a histogram of the calculated abundance binned in 0.5 dex intervals. We see that over 80% of the BMP stars fall in the abundance range of $-0.75 >$ [Fe/H] > -2.25. Approximately 11% of the BMP stars have [Fe/H]> -0.75, and only 9% have [Fe/H]< -2.25. The latter result will be studied in much greater detail in the following sections. For comparison, figure 6.7b shows a metallicity distribution that is quite similar for the entire metal-poor A-star sample.

Our spectroscopic abundances are expected to be a large improvement over the photometric estimates used by PBS. It therefore appears that a small percentage of

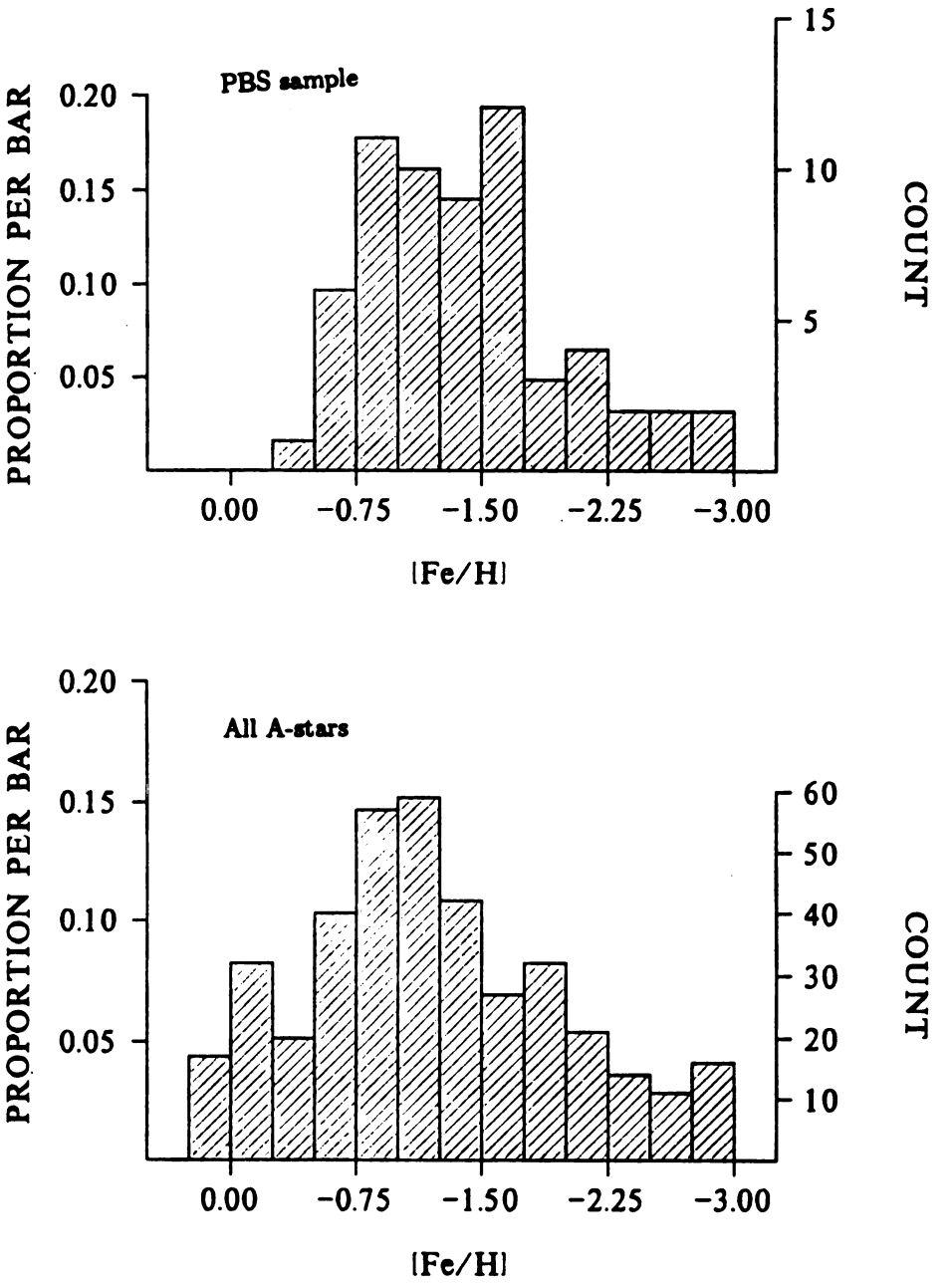

Fig 6.7: Comparison of metallicity distribution for stars in common with the Preston *et al* sample.

the stars which we have regarded as Pop I have been included in the PBS sample. To check the significance of this inclusion on the derived kinematics of the metal-poor sample, we will carry out our analysis using both an [Fe/H] = -0.75 and -1.0 cut-off.

6.4.1 BMP Kinematics

Table 6.2 lists the results for the systemic rotation and velocity dispersions at various cuts in [Fe/H]. The velocity dispersions in the cardinal directions were calculated using the same Galactic coordinate limits as that of PBS. The σ_W dispersion is confined to the Galactic polar regions with $|b| > 79$. σ_U is calculated from the stars in the Galactic center and anti-center directions, constrained by ± 11 degrees from $l = 0$ and 180 and $|b| < 60$, while σ_V is the combined dispersion from the rotation and anti-rotation directions, constrained by $30 < l < 91$, $271 < l < 330$, and $|b| < 60$. The number of stars in each of these directions is listed in parenthesis and constitutes approximately a factor of 2 increase over the PBS sample. The results indicate virtually no kinematic difference between the sample with a high metallicity cut of [Fe/H] = -0.75 and [Fe/H] = -1.0, the former of which is consistent with the PBS.

The value of $V_{rot} = 90 \pm 15$ km/s for our sample of 268 stars is not significantly different from the $V_{rot} = 128 \pm 30$ km/s reported in PBS. There is, however, clearly a metal-poor component present in the sample which is responsible for the somewhat lower rotational value. In Table 6.2 we see a very low value for V_{rot} in the samples with [Fe/H]< -2.0 and [Fe/H]< -2.2. Because of the small number of star with [Fe/H]< -2.0, however, it is impossible to meaningfully examine differences in the velocity ellipsoid solutions, which are presently in keeping with the BMP sample. By constraining the BMP sample to $-0.75 >$ [Fe/H] > -2.2, we see the rotational

Table 6.2. Kinematic Solutions for BMP Sample

N	[Fe/H]	V_{rot}	σ_{los}	σ_U N_U	σ_V N_V	σ_W N_W
(1)	(2)	(3)	(4)	(5)	(6)	(7)
268	≤ -0.75	90 ± 15	84 ± 3	74 ± 5 (50)	100 ± 7 (52)	81 ± 6 (41)
211	≤ -1.0	85 ± 18	90 ± 3	82 ± 7 (37)	98 ± 8 (41)	93 ± 84 (30)
55	≤ -2.0	39 ± 34	100 ± 7	... ...	... ...	... ...
36	≤ -2.2	4 ± 33	87 ± 7	... ...	... ...	... ...
232	$\leq -0.75, \geq -2.2$	115 ± 16	82 ± 3	71 ± 5 (49)	109 ± 9 (36)	82 ± 7 (36)
175	$\leq -1.0, \geq -2.2$	117 ± 21	88 ± 3	82 ± 7 (36)	110 ± 11 (25)	96 ± 10 (25)

value has increased to $V_{rot} = 115 \pm 16$ km/s. The velocity dispersion both in the cardinal directions and from a Woolley analysis have changed very little and remain consistent with the PBS findings of an isotropic velocity ellipsoid of $\sim$ 90 km/s. This is an important result since the number of stars in the cardinal directions have increased by a factor of more than 2 over the original PBS sample. The only possible point of departure is the high velocity dispersion result for σ_V from the Woolley calculation. The value of $\sigma_V = 153 \pm 19$ is now significantly different from that of the isotropic value of 90 km/s. It is expected that this high value, however, is due in part to the inclusion of rapidly rotating Lance-type stars at the high abundance end and a near zero-rotation component at more metal-poor abundances.

Because of the importance of an apparent metal-poor cut-off to the BMP sample, we now examine the previous results in greater detail. Figures 6.8a-d are plots of V_s as a function of $\cos(\psi)$ for the sample with [Fe/H]> -0.75, [Fe/H]< -0.75, $-0.75 >$ [Fe/H] > -2.2, and [Fe/H]< -2.2, respectively. From these plots it is clear that the substantial number of more rapidly rotating stars present at intermediate metallicities are all but non-existent in the most metal-poor sample. This alone appears to rule out a mixture of populations being responsible for the anomalously low rotational value below [Fe/H] = -2.2. Following the methodology employed in the FHB analysis we fold the rotation directions together and examine the histograms of the velocity for the intermediate and metal-poor sample. Figure 6.9a-b shows the marked difference between the two samples, with the intermediate sample peaking near $V_s = 150$ km/s with a long tail toward lower velocities and the metal-poor sample with an average value of $V_s \sim 0$ km/s and much more gaussian in shape. Presently the number of stars in the rotation direction is too small to employ KMM mixture modeling, as was done with the FHB sample. We can, however, explore

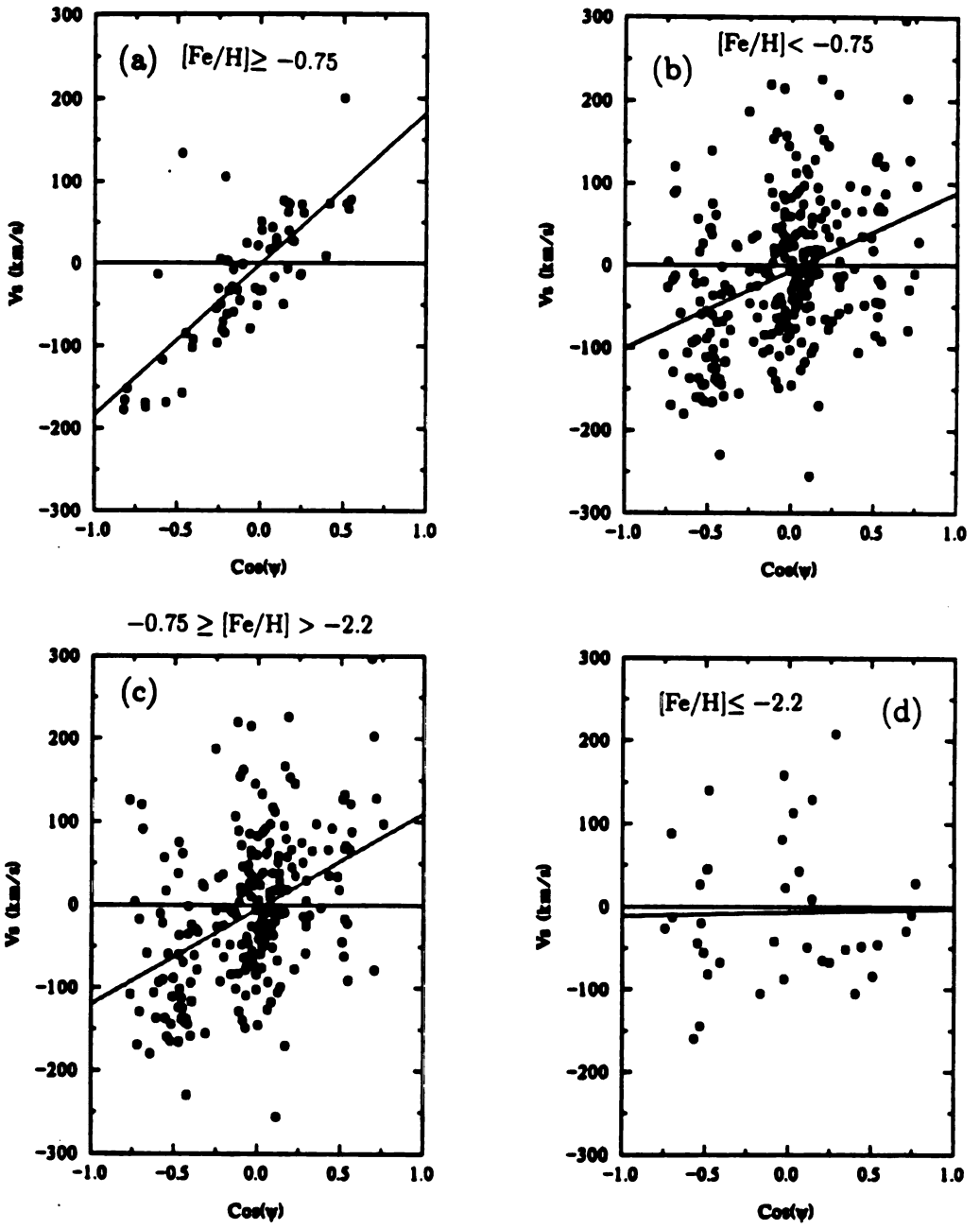

Fig 6.8 Systemic rotational velocities for the A-star sample, split into 3 abundance ranges.

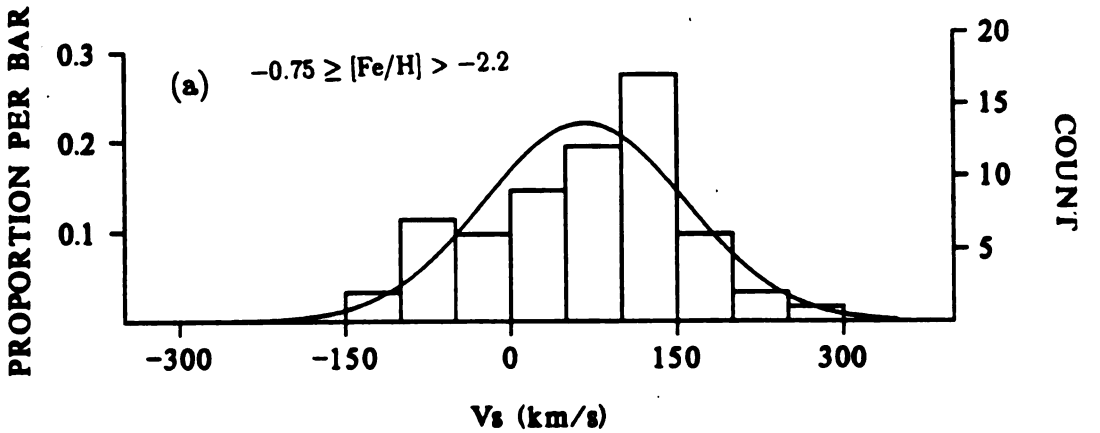

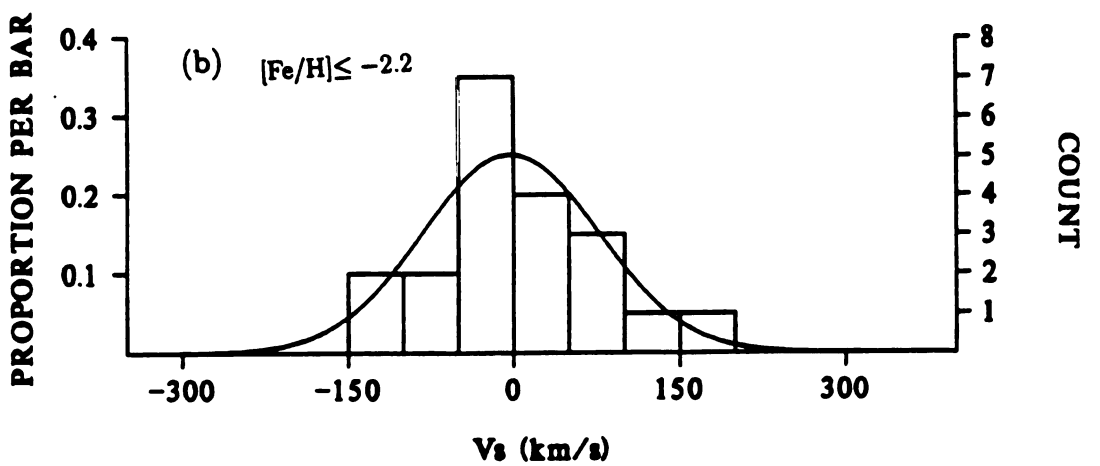

Fig 6.9 Histograms of the velocities in the rotation directions for intermediate and low metallicity A-stars.

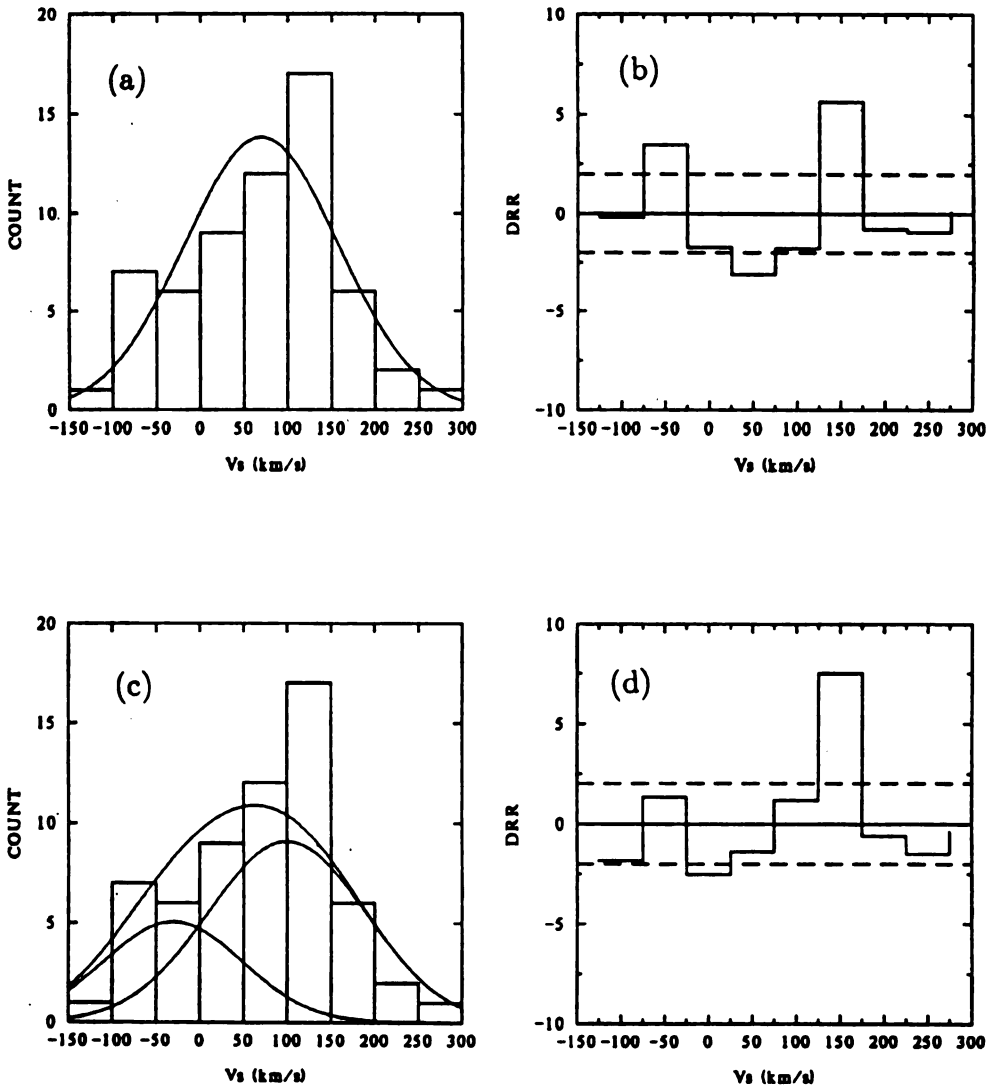

Fig 6.10 Single and double gaussian fit to rotation direction stars with $-0.75 > [Fe/H] > -2.2$. Also shown are the corresponding DRR plots.

the mixture proportions once again using the Double Root Residual plots.

6.4.2 Mixture Analysis

Figures 6.10a and c are histograms fit with a single and double gaussian for the abundance range, $-0.75 >$ [Fe/H] > -2.2. Also shown are each of the corresponding DRR plots. It is immediately apparent that neither fit can adequately describe the entire distribution. The primary departure occurs near the V_s = 125 km/s bin, which coincides with the expected V_{rot} for the BMPs. It is possible that the excess in this bin is due to the inclusion of metal-weak, Pop I stars.

We can test this possibility by limiting the sample to $-1.0 \leq$ [Fe/H] > -2.2. Figures 6.11a-d show that by so restricting the abundance the excess has gone away. This indicates that a relatively pure BMP sample can be achieved only by isolating those stars more metal-poor than [Fe/H] = -1.0. The DRR plots show that overall the best double gaussian fit is only marginally better than a normal distribution. The double gaussian was constructed using $\sigma_1 = \sigma_2 = 80$ km/s, $N_1 = 32$, $N_2 = 15$, $< V_1 >= 115$ km/s and $< V_2 >= 0$ km/s. If this subsample is drawn from two separate populations then it appears that $\sim$ 33% of the stars have zero systemic rotation.

Before considering the ramifications of such a result we next investigate the distribution for all stars with [Fe/H]≤ -1.0 and in the rotation directions. Figures 6.12a-d again shows the gaussian fits using the same σ and $< V_s >$ for the double gaussian, but $N_1 = 34$, and $N_2 = 33$. There is now virtually no evidence that a double gaussian is a better fit to the data than a normal distribution. If two separate populations exist then only about 50% of the stars below [Fe/H] = -1.0 have rotational velocities that can be considered BMP-like. This seems very unlikely since the V_{rot} values for the entire sample are consistent with the findings of PBS.

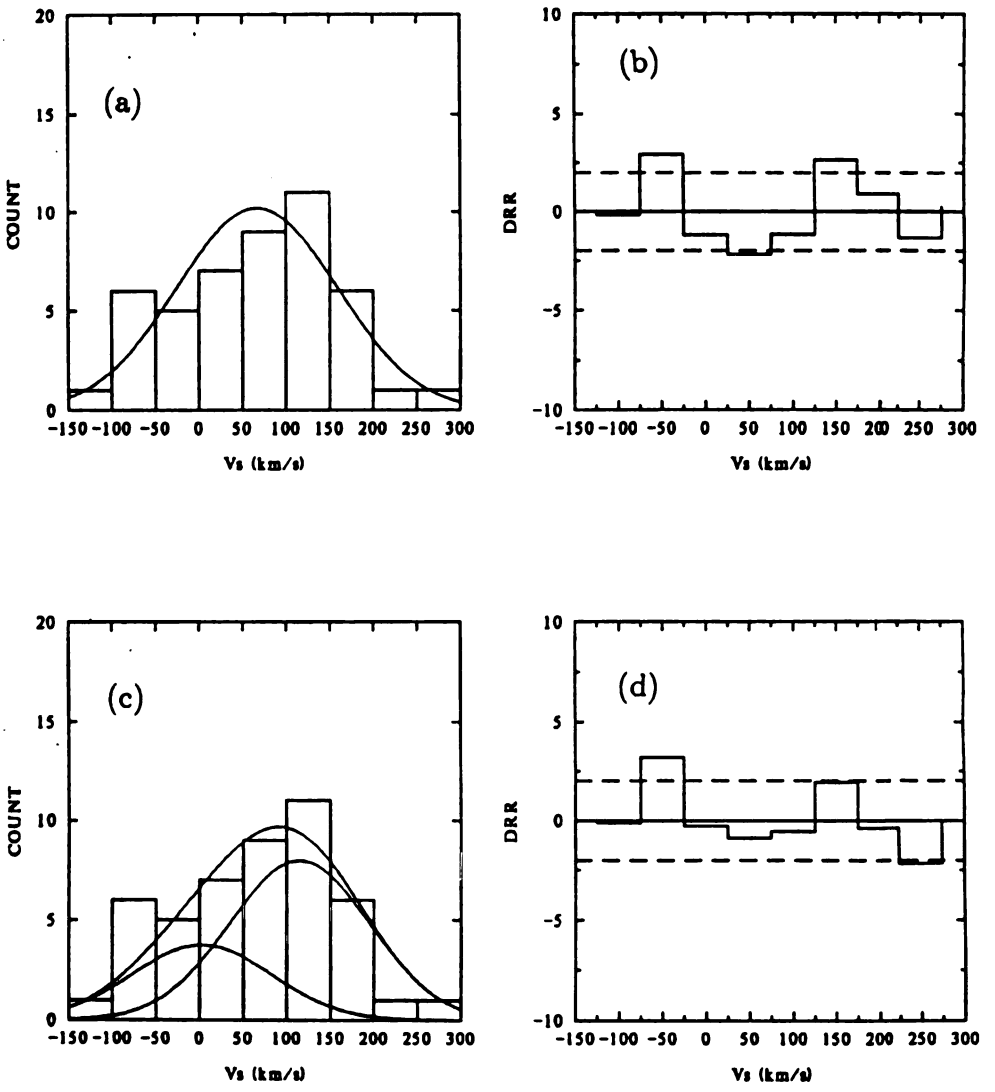

Fig 6.11 Single and double gaussian fit to rotation direction stars with $-1.0 > [Fe/H] > -2.2$. Also shown are the corresponding DRR plots.

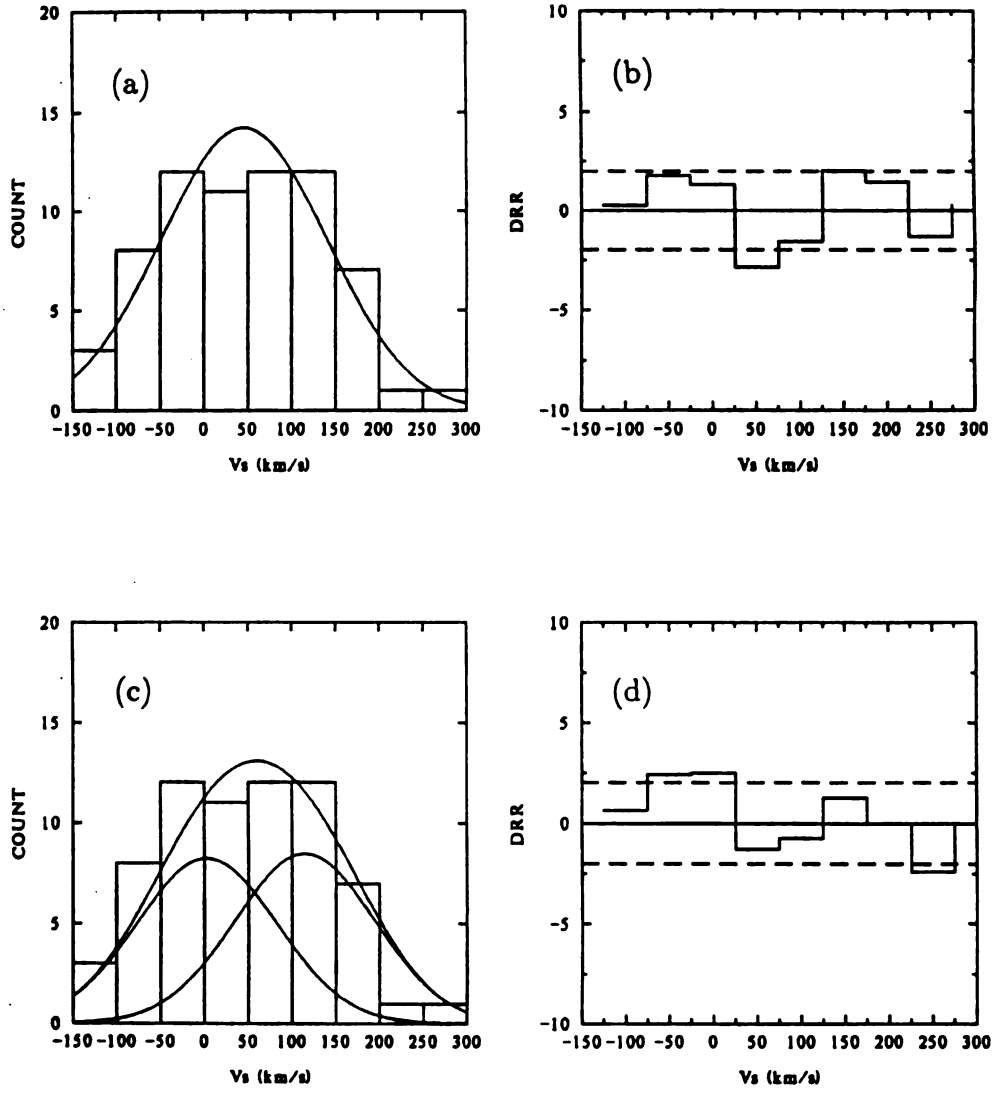

Fig 6.12 Single and double gaussian fit to rotation direction stars with $-1.0 >$ [Fe/H]. Also shown are the corresponding DRR plots.

If, on the other hand, we choose to believe there is a single population present for [Fe/H]≤ -1.0, then we must conclude that V_{rot} is a function of metallicity. For the moment we will assume that the stars with [Fe/H]< -2.2 are not members of the BMP population.

6.4.3 The Low Metallicity, Zero Rotation Sample

The two most likely candidates for non-rotating, non-BMP stars are misidentified FHB stars and "true" halo blue stragglers. As was mentioned in the discussion of the metallicity distribution function, there is a stark contrast between the number of FHB stars and main sequence A stars at the metal-poor end. This large difference means the modest number of FHB stars which are misidentifed as main sequence A-stars can amount to a large percentage of the metal-poor BMP sample. If we assume a misidentification of 8% for the 220 metal-poor FHB stars then it would be expected that around 18 FHB stars have wound up in the total of 36 BMP stars which have been identified. It would be expected, however, that the majority of these misidentified stars would have surface gravities near Log g = 3.5. For stars with Log g = 3.75 the FHB identification is approximately 3σ away, meaning only 3 FHB stars should have crept into the sample with Log g$>$ 3.75. Figure 6.13 is a plot of Log g as a function of T_{eff} for the metal-poor BMP sample. We find that only 9 of the 36 stars have Log g$<$ 3.75. Reanalysis of metal-poor BMP sample including only stars with Log g$>$ 3.75 returns $V_{rot} = -5 \pm 39$ km/s, consistent with the previous determination. It is therefore expected that contamination from FHB stars is not a significant source of the non-rotating sample at low metallicities.

Alternatively, the nonrotating sample could be a separate population from either the BMP or FHB stars. If the BMP sample is a separate population from the stars that would be considered "true" halo blue stragglers (BS), then it would be

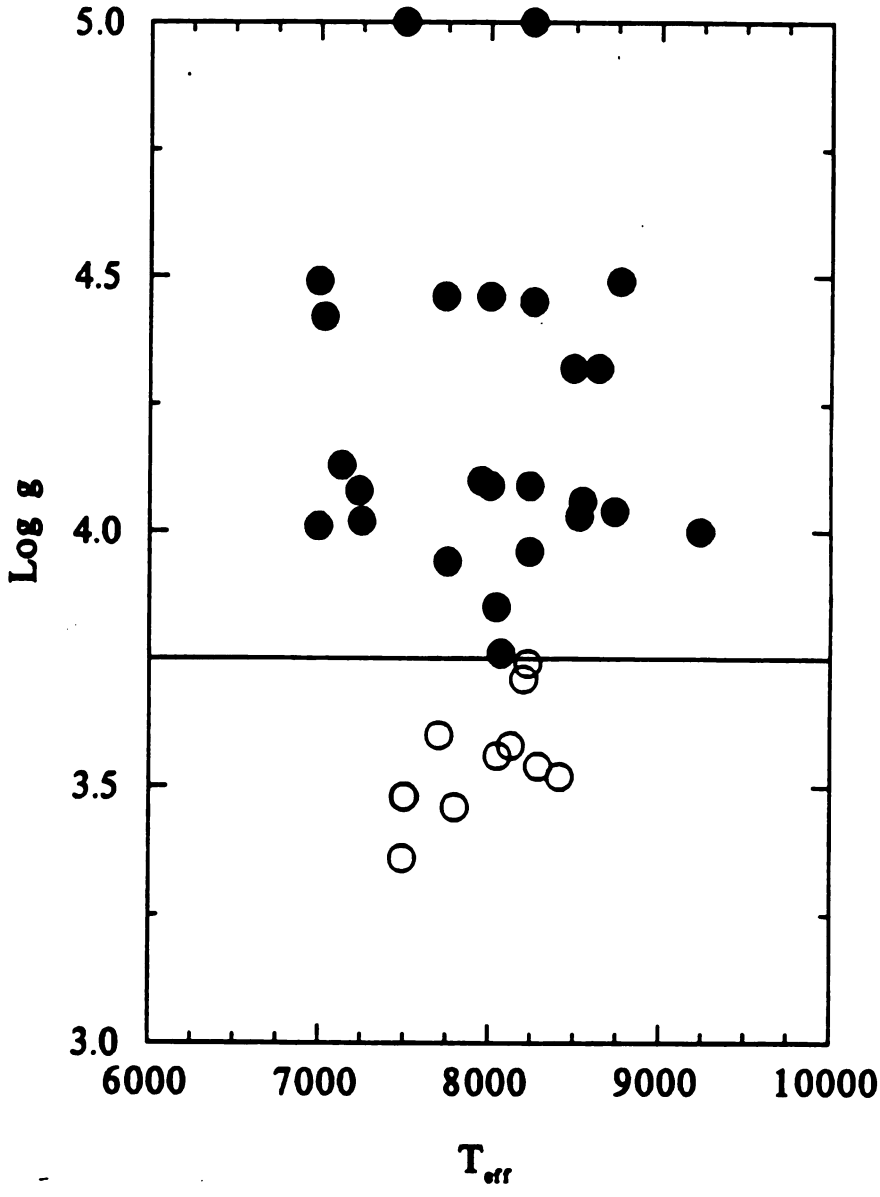

Fig 6.13: Log g - T_{eff} plot for A-stars with [Fe/H]≤ -2.2. Solid line indicates 3σ uncertainty in log g.

expected that the total sample of stars with [Fe/H]< -1.0 should include some percentage of BS. Also, the halo turn-off stars appear to cover the full range of metal abundance, so there should not be a shortage of such stars at the metal-poor end of the distribution. Finally, in the investigation of Beers and Sommer-Larsen (1995) for the metal-poor stars with [Fe/H]< -1.6 and $|Z| > 2$ kpc the sample was found to have $V_{rot} \sim 0$ km/s.

If halo BS are present in the BMP sample, we can attempt to estimate their significance by first assuming that the 25 stars with [Fe/H]< -2.2, and Log g> 3.75 are indeed halo BS and that the BMP population does not extend to this low metallicity. Then, the number of BS that fall in the range of $-0.75 >$ [Fe/H] > -2.2 will be 25 * 2.3 = 58, where the multiplication factor of 2.3 is the estimated increase in the factor of stars across this abundance range, taking into account the peak in the MDF near [Fe/H] = -1.6, (Laird *et al.* (1993)). From this number we expect the ratio of BMP to BS to be 3 to 1. This is almost a factor of 3 greater than would be expected from the ratio of BMP to globular BS estimated by PBS to be 9:1. Of course it should be noted that the FHB contamination may be somewhat larger than our above estimate and that the metallicity bias in our sample would probably cause the multiplication factor of 2.3 to be an overestimate. Therefore, the ratio of 3:1 should be considered a lower limit on the number of BMP to BS in the sample. By using our earlier estimates of 8% misidentification for the FHB stars and lowering the multiplication factor to 1.3, which is probably less than would be expected, we regain the 9:1 ratio as found in the PBS globular cluster analysis.

It should be noted that neither the FHB nor BS explanations are consistent with the mixture proportions for a double gaussian distribution, which suggests a one-to-one ratio between BMP and the non-rotating component. This ratio can be

reached only if we combine the 3:1 ratio of BMP:BS with an 8% misidentification for the FHB stars. This argument, of course, hinges on the assumption that the two component model describes the distribution of velocities better than a normal distribution. As mentioned in section 6.4.2, the single gaussian fit seems to describe the data equally well.

If all the A-stars with [Fe/H]< -1.0 constitute a single population then we must try to address the functional dependency of V_{rot} on [Fe/H]. Following from the accretion origin for the BMP as argued by PBS, it is possible that the functional dependency of V_{rot} could arise from a single accretion event of a Magellanic Cloud-like galaxy. As put forth by Quinn *et al.* (1993) a galaxy that begins on a somewhat inclined orbit will first decrease its orbital inclination, collide with the Galactic disk, and finally spiral radially into the Galactic center. Depending on the mass of the satellite and the initial orbital inclination, the accretion process could take place over a period of several orbits. It is expected that on each close encounter, the satellite galaxy will lose a portion of its loosely bound outer stars. Finally, as orbital inclination decreases the majority of the satellite will be disrupted by the disk, leaving the remaining stars in a lower inclination orbit. It would be expected, then, that the outer stars which were initially stripped would have a smaller rotational velocity but larger radial and vertical velocity than the stars that are bound to the satellite at final breakup. If the satellite galaxy had an internal abundance gradient it would also be expected that these outer stars would be more metal-poor then the more tightly bound stars. Such a scenario could then give rise to the dependency of V_{rot} on abundance.

To test this hypothesis, it should be possible to search for differences in the velocity ellipsoid solutions as a function of metallicity. At the moment the metal-

poor BMP sample has only 36 stars making such a comparison very uncertain. It should be noted, however, that the BMP sample with [Fe/H]< -2.2 has a σ_U value from a Woolley analysis, of 102 ± 33 km/s compared to the intermediate sample with $\sigma_U = 71 \pm 21$ km/s. Unfortunately, such a difference in σ_U would also be expected if FHB contamination is important.

PBS have also speculated that in a scenario where the BMP stars originate from multiple mergers of smaller dwarf spheroidal galaxies, a large vertical velocity dispersion can arise when loosely bound stars are stripped from satellites on very high inclination orbits. Quinn *et al.* have shown that such satellites will not merge with the galaxy in a Hubble time but the stripped stars would exhibit halo-like configurations. For this explanation to be applicable in this case, it is necessary that the low inclination satellites have abundances larger than -2.2 dex, while the high inclination galaxies have the full range in abundance to preserve the necessary large σ_W dispersions. This constraint may not be unreasonable considering that virtually none of the currently known dwarf spheroidals have metallicities below [Fe/H] = -2.0. If only a small number of low-abundance dwarfs with intermediate age main sequences existed in the past, then it is possible that none happened to have low enough inclination orbits to give high rotational velocities to the very low metallicity BMP stars.

6.4.4 Contaminants (revisited)

Before finishing the BMP discussion we will examine the possibility of FHB and Am contamination as described in sections 4.1.3.1 - 4.1.3.4 of chapter 4. By first splitting the BMP sample at $T_{eff} = 7750$ we can simultaneously explore possible RR Lyrae and Am contamination. Since the Am stars are associated with the thin disk of the Galaxy, and are expected to be present in the BMP sample at $T_{eff} > 7750$ K,

their presence in the sample is should cause an anomalously large value of V_{rot} to be found. In contrast, the presence of halo RR Lyrae stars should return a smaller V_{rot} for $T_{eff} < 7750$. The values found for each subsample is $V_{rot} = 118 \pm 20$ and 110 ± 28 for $T_{eff} < 7750$ and $T_{eff} > 7750$, respectively. The consistency in the two results indicate that these two contaminants either, do not constitute a large fraction of the BMP sample or else their presence has little effect on the systemic rotation.

We next test the effects of FHB contamination, in general, by constraining the sample to Log g> 3.75. The calculated $V_{rot} = 138 \pm 22$ is slightly, though not significantly, higher than the previous value of $V_{rot} = 115 \pm 21$ km/s. The velocity dispersions in the cardinal directions also remain virtually identical to that previously found for the entire BMP sample. These results suggest that contamination of the BMP sample by the various misidentified stellar types has little or no significance on the kinematic determination of the BMP stars.

6.4.5 Conclusions for BMP Sample

We conclude by summarizing the findings for the BMP stars. From systemic rotation arguments, the BMP sample appears to be constrained to the metallicity range of $-1.0 < [Fe/H] < -2.2$. Using this constraint, the systemic rotational value is $V_{rot} = 117 \pm 21$ km/s with a line-of-sight velocity dispersion of sigma = 88 km/s. The dispersions from both the cardinal directions and the Woolley analysis is consistent with an isotropic velocity dispersion of $\sim$ 90 km/s. These results, obtained from a sample which is larger by a factor of 2, are still agreement with the dispersions found by PBS. The subsample with [Fe/H]< -2.2 remains an enigma, with a systemic rotation which is consistent with zero. From modeling of the rotation directions it remains unclear if one or two components best describes

the velocity distribution for those stars with [Fe/H]< -1.0. It appears that even liberal estimates of the FHB contamination are unable to completely account for the number of stars found. The explanation that these stars are "true" halo BS still merits consideration. By assuming that all the stars below this abundance are BS, we estimate that the ratio of BMP:BS is at least 3:1. Considering the effects of FHB contamination and metallicity bias, this ratio is more likely to be 6:1.

The current sample with [Fe/H]< -1.0 appears to be drawn from a single distribution of stars. If further BMP observations confirm this, then the systemic rotation of the BMP is a function of metal abundance. This helps to place stronger constraints on the accretion processes that resulted in this functional dependency. With a greater number of stars, especially at the lowest abundances, it should be possible to probe the velocity ellipsoid to see if changes in the radial and vertical dispersions are consistent with that expected for a merger event by a higher inclination satellite.

CHAPTER 7

CONCLUSION

In the past decade the wealth of information on the spatial and kinematic properties of the halo of the Galaxy has been rapidly increasing. Global halo studies, mainly connected to the globular cluster system, along with large field surveys, have begun to unveil complexities which could not have been foreseen when ELS published their landmark paper in 1962. By the close of the next decade even greater advances and surprises are expected, as the number of observed halo objects moves from the realm of thousands and tens of thousands to millions. This current research has been an attempt to bridge the gap of time, by offering insights into the global halo kinematics, through the use of an unprecedented number of tracers which extend beyond the bounds of the local solar environment. Results from this thesis are summarized in the next section. Section 7.2 examinations the possible scenarios for the formation and early evolution of the Milky Way Galaxy, which are consistent with the findings from this work. The final section sets forth a path of future research for the FHB/A star sample.

7.1 Summary of Results

The primary goals of this project which were set forth in the Introduction have been realized. The new spectral calibration technique is quite effective in separating the FHB and main-sequence stars. Also the precision with which metal abundances can be assigned is a vast improvement over previous techniques employed for mod-

erate resolution FHB/A research. Using the assigned class identifications we are able reproduce most of the previously published results for the halo kinematics as a whole. In conjunction with this, the greater extent of the FHB sample has allowed us to probe the transition region between the inner and outer halo and confirm its apparent two-component nature. Also, doubling the previous sample size of BMP stars has not altered their unique kinematic signature.

The following is a summary of the most important results from this investigation.

1. Using the new spectral calibration technique it is possible to assign physical parameters to the FHB/A stars with an uncertainty of $\sigma T_{eff} = \pm 250$ K, σlogg = ± 0.25, and σ[Fe/H] = ± 0.30.

2. Even at low-S/N values the misidentification of FHB and main sequence A-stars is expected to be no more than $\sim$ 10%.

3. The newly developed template comparison technique appears to be very successful in identifying Am stars even at low-S/N values.

4. It appears that the [Ca/Fe] ratios for both the standard and program FHB stars are $\sim$ 0 and therefore significantly different then the metal-poor main sequence stars. This may be due to diffusion effects operating in the FHB samples.

5. There is marginal evidence of a mild abundance gradient as a function of Galactocentric distance in the inner halo. Also there appears to be a spread in age among the FHB stars with decreasing age as a function of Galactocentric distance.

6. The FHB kinematic results confirm the presence of a two-component halo. The dominant component has a mild pro-grade rotation of $\sim$ 20 km/s and is flattened with a vertical velocity dispersion of $\sim$ 70 km/s. The second component begins to

dominate the sample at vertical distances greater than 4-5 kpc, has a more isotropic velocity ellipsoid, and is in systemic counter-rotation with $V_{rot} =\sim -90$ km/s.

7. The evidence for FHB members of the MWTD is marginal, with best estimates for the ratio of MWTD:Halo being 1:3. Though this value is uncertain there is no evidence of a large dominating MWTD as has been previously reported in other surveys.

8. The BMP sample appears to be kinematically distinct from either the halo or thick disk populations, with a systemic rotation ~ 90 km/s and an isotropic velocity ellipsoid of ~ 90 km/s.

9. There is evidence that either the BMP sample does not include a large number of stars with [Fe/H]< -2.2 or else the sample's rotational velocity is a function of metal abundance.

7.2 A Possible Scenarios For Galactic Formation

The earliest stages of Galactic formation undoubtedly took place in the presence of some kind of centrally potential. The most crucial question yet to be answered is under what set of circumstances the Galaxy grew in the presence of this potential. In a bottom-up picture the largest locally-distinct mass fragment grew through gravitational interactions with other nearby smaller fragments. For a top-down picture, a Galaxy-size fragment, collapsing under its own self-gravity, gave rise to other smaller fragments which went on to form stars and clusters. In terms of the formation history of the Galaxy, it is often difficult to contrast the relevant physical difference between these two pictures with that of mere semantics. The difficulty arises because a proto-galaxy composed of gravitationally bound smaller fragments can also be interpreted as a clumpy galaxy-size fragment. This is the old "chicken or the egg" question, set to Galactic proportions. The resolution of

this question, however, extends to cosmological significance, since it ultimately sets the mass amplitude scale of the initial density perturbations in the early universe. At the current level of observational understanding it is not possible to distinguish which of the top-down or bottom-up pictures is the correct one. We can, however, investigate whether fragmentation arose completely (ELS) or partially (ELS/SZ) as a direct consequence of the cooling flow of a monolithic, galaxy-size fragment.

The kinematics of the FHB sample appears to confirm the existence of a two component halo. The dominant, inner component is flattened and in pro-grade rotation while the outer component is more spherical and in counter-rotation. Coupled with this is the somewhat less compelling evidence of a mild abundance gradient in the inner halo FHB sample, as well as, shifts in color which are consistent with a decline in age as a function of increasing galactocentric distance. Taken as a whole, this evidence appears to favor the ELS/SZ hybrid formation model. The inner galaxy (R< 8kpc) formed first in an ELS-type collapse. The initial prograde rotation was enhanced as a result of angular momentum conservation and dissipation processes. The stars that formed during the collapse had an increase in metallicity due to subsequent enrichment of the halo medium from the earliest supernova. It is not possible to change the direction of the angular momentum vector for any type of monolithic collapse and therefore, the outer halo (which has at least some stars in counter-rotation) did not participate in this initial collapse but instead formed stars more slowly from smaller self-gravitating fragments. These fragments, must have had a wide range of orbital inclinations, became disrupted through tidal interactions, leaving a halo that is much more isotropic in its velocity dispersions.

One problem with this scenario is that its characteristics are not unique. It is possible to imagine two larger fragments merging with their orbital angular momen-

tum being transferred into rotational angular momentum of the resulting system. Depending on the impact parameters in this merger, a flattened disk-like distribution of gas and stars could result. It is expected that disruption of other fragments will occur, preferentially, for those which move in the same direction as this initial disk. This is the case because decay of the fragment's orbit is a function of the time spent in the dissipational potential. This time is greater for fragments moving in a prograde direction. Therefore, the prograde orbits quickly decay into the initial disk, where the fragment is disrupted and finally merges with the newly forming Galaxy. In such a scenario it is not surprising that the inner halo is flattened and in prograde rotation.

Ultimately, the process which formed the inner halo may be directly linked to the existence and properties of the thick disk and MWTD. In the ELS/SZ model, the flattened halo, MWTD, and thick disk are seen as a continuous distribution of stars that reflect the properties of a dissipational collapse. Indeed, if the halo and thick disk are considered as a continuous entity, then there is a rather strong metallicity gradient with Z height, a systemic rotation that increases as a function of decreasing Z height, and a decrease in the velocity dispersion perpendicular to the plane with deceasing distance in Z. The second parameter analysis for the FHB stars is also suggestive of a thick disk which is of similar age as the old halo. The problem with this picture is that the kinematics of the flattened halo and thick disk are very different. The question then arises, could the MWTD serve as a transition population?

The FHB sample shows only marginal evidence that the MWTD exists at all. If we consider that possibly 8% of the FHB sample are actually misidentified main-sequence A-stars, and that scatter in the derived abundances could lead to inclusion

of "normal" thick disk stars in the sample with [Fe/H]< -1.0, then it becomes even more difficult to make strong claims of the presence of the MWTD. As mentioned in Chapter 5, high-dispersion analysis of giant stars claimed to MWTD are beginning to suggest that these stars are actually "normal" thick disk stars with systematic errors in their previous abundance determinations. If we assume for the moment that the MWTD does exist in significantly large numbers then we must wonder why they are not seen in the FHB sample. One explanation could be that the MWTD does not extend to large scale heights. This has been suggested by the work of Beers and Sommer-Larsen using a large number of metal-poor stars. Although these authors find a significantly large number of disk-like stars with arbitrarily low abundances, they also find a rapid drop off in MWTD numbers above $|Z| = 1$ kpc, suggesting a scale height similar to that of the thick disk. In such a case we would expect to find very few MWTD stars in our sample since the bright magnitude limit for the FHB stars places nearly all of them above $|Z| = 2$ kpc. A second possibility is that the MWTD is composed of much younger stars than the halo. As previously discussed, young FHB stars are constrained to the red side of the instability strip. Therefore, the MWTD giant stars would still be detected but very few of the FHB stars would be found in our sample.

Neither of these explanations promote the MWTD as a transition population between the halo and thick disk. It would appear to be more likely that the old halo and thick disk formed separately, but at the same epoch of rapid accretion. It is possible in fact that the thick disk formed as a result of dynamical heating when a large fragment merged with the initial (old) thin disk. If the MWTD is old then we might expect that the "normal" thick disk represents the stellar component of the initial disk, while the MWTD is composed of the stellar remnant of the

accreted fragment. In such a formation scheme, the possible rotational gradient with $|Z|$ height, suggested in Chapter 5, could be due to tidal stripping of the fragment as its orbit underwent tidal decay. Some evidence for this picture may ultimately come from further analysis of the inner halo globular clusters. The oldest globular clusters would be expected to be the only self-gravitating systems to have survived the fragment disruptions. This means that the old halo cluster system is composed of many separate cluster groups with a small fraction originating as a part of the initial galaxy. The disk clusters formed as a result of the merger event that subsequently created the thick disk, explaining the strong similarities in kinematics, metallicity, and age.

An accretion origin for the inner halo would be far less tantalizing if not for the strong evidence that such processes have taken place throughout the Galaxy's existence. The evidence for an accretion origin of the outer halo has recently become very strong. In fact it is from this mounting evidence that the ELS/SZ hybrid model arose. The global nature of the FHB sample has allowed us to show that a large departure in kinematics occurs as the distance above the Galactic plane is increased above $|Z| = 5$ kpc. The systemic counter-rotation of this sample helps to secure an accretion origin and also fuels further speculation.

On first thought it is difficult to believe that the outer halo of the Galaxy is in systemic counter-rotation. It is, of course, possible that this result is not truly global, but rather the signature of a counter-rotating disruption that occurred in our vicinity of the Galaxy. It is difficult, however, to explain why a local effect is seen in the young globular clusters, at the north galactic pole and in both galactic rotation directions. If we instead concede that the outer halo is globally in counter-rotation, we must explain how this can occur from what we know of tidal disruptions.

As mentioned earlier tidal decay preferentially selects those systems on prograde orbits. It might, therefore, be suspected that the prograde rotating systems have already decayed down to the galactic plane, where they rapidly sink to the center of the Galaxy. Since the retro-grade orbits are more resilient to decay, it would be expected that remnants of disrupted systems still exist as the counter-rotating stars seen today. This argument is strengthened by the fact that most of the currently surviving satellites of the Galaxy appear to be confined to nearly polar orbits, which are suspected to be the most resistant to orbital decay.

There is equally compelling evidence for accretion having occurred in the past 3-10 Gyrs. The large space densities, unique kinematics, and young age of the BMP stars strongly suggest an accretion origin. If the BMPs are remnants of such a process, then we might expect to see other evidence of this event. For the sake of argument, let us suppose that the BMP originated from the single disruption of a Magellanic Cloud-size satellite. As the merger takes place, the Galactic disk becomes dynamically heated with cloud-cloud collisions resulting in a rapid star forming phase. The stars that form during such a collision will probably have metallicities less than solar, since the metal-rich gas will be mixed with the more metal-poor gas of the satellite, along with resultant velocities that take them out of the plane of the Galaxy causing a rotational lag with the thin disk. Two very strong candidates for this effect are the Lance metal-weak A-stars and the old open clusters, since both share kinematics, metallicities and ages that are virtually identical.

7.3 Future Work

It is clear that the FHB stars are a powerful diagnostic tool with which to probe the workings of the Galaxy on a global scale. With the new spectral calibration for the FHB/A stars it should be possible, for the first time, to achieve the sufficient

purity of sample and accuracy in metal abundance needed to make the kinematic analysis both practical and believable. Armed with the calibration technique and insights gained from this kinematic research the future applications for the FHB and BMP stars are many.

In the immediate future, detailed modeling of the velocity ellipsoid for the FHB sample will be carried out with the collaborative help of Jesper Sommer-Larson. This modeling should allow a more rigorous analysis of the changes in kinematics of the FHB stars as a function of position in the Galaxy. Also, we have recently acquired 15 new objective-prism plates which are primarily in the rotation directions. Follow-up observations of the FHB/A candidates should help to rectify our current problem of undersampling in this crucial area of the Galaxy. By adding a significant number of FHB stars to the rotation directions it is expected that stronger constraints can be placed on the properties of the MWTD and the counter-rotation sample. The increase to the BMP sample will further help in characterizing the possible cut-off in metallicity at [Fe/H] = -2.2. We will also be able to drive down the somewhat large uncertainties present in the rotational velocity dispersion for both the FHB and BMP stars. This will be a great help in identifying large dispersions caused by a mixture of populations.

A new aspect of the FHB/A research will be the inclusion of a large number of stars with proper motions. Recently, Dr. Alexey Rastorguev from Moscow State University, has contributed several thousand proper motions for the candidates in the north and south galactic surveys. This addition will be a tremendous advance since we will now be able to calculate full space motions for a large number of the FHB/A stars. The observational goal will be to continue follow-up observations of these candidates with special emphasis on the polar cap region. Using both the

radial and tangential velocities in this direction it will be possible to investigate the kinematics of the MWTD, flattened halo and spherical halo without the ambiguity that results from a purely statistical analysis. It will be especially interesting to search for possible counter-rotating stars, evidence for moving groups or streams, and possible changes in the kinematics of the BMP stars as a function of vertical height.

APPENDICES

APPENDIX A

Table A.1. Spectral Calibration Grid.

T_{eff} (1)	Log g (2)	[Fe/H] (3)	(B-V) (4)	(U-B) (5)	W_k (6)	WHδ (7)	WHγ (8)	H$\delta D_{0.2}$ (9)	H$\gamma D_{0.2}$ (10)
6000	2.0	0.0	0.59	0.22	16.03	3.26	4.63	4.10	5.56
6000	2.0	-0.5	0.53	0.11	11.27	3.50	4.55	3.89	5.52
6000	2.0	-1.0	0.49	0.04	9.41	3.79	4.37	4.11	5.16
6000	2.0	-1.5	0.46	-0.01	6.79	3.94	4.25	4.35	4.98
6000	2.0	-2.0	0.45	-0.04	4.47	4.03	4.11	4.53	4.72
6000	2.0	-2.5	0.44	-0.06	2.93	4.07	4.02	4.62	4.58
6000	2.0	-3.0	0.44	-0.08	1.77	4.09	3.99	4.67	4.53
6000	2.5	0.0	0.59	0.17	13.85	3.22	4.35	3.26	5.10
6000	2.5	-0.5	0.53	0.06	10.32	3.40	4.29	3.87	5.10
6000	2.5	-1.0	0.49	-0.01	8.84	3.62	4.13	3.96	4.79
6000	2.5	-1.5	0.47	-0.06	6.43	3.75	4.03	4.12	4.64
6000	2.5	-2.0	0.46	-0.09	4.24	3.80	3.88	4.23	4.41
6000	2.5	-2.5	0.45	-0.11	2.78	3.82	3.79	4.28	4.28
6000	2.5	-3.0	0.44	-0.13	1.67	3.82	3.75	4.30	4.24
6000	3.0	0.0	0.60	0.14	12.60	3.16	4.10	3.20	4.69
6000	3.0	-0.5	0.54	0.01	9.84	3.29	3.97	3.90	4.51
6000	3.0	-1.0	0.50	-0.06	8.68	3.46	3.89	3.86	4.42
6000	3.0	-1.5	0.48	-0.11	6.39	3.54	3.78	3.92	4.27
6000	3.0	-2.0	0.46	-0.14	4.24	3.59	3.68	3.98	4.15
6000	3.0	-2.5	0.46	-0.16	2.80	3.59	3.61	4.01	4.07
6000	3.0	-3.0	0.45	-0.17	1.70	3.59	3.57	4.02	4.04
6000	3.5	0.0	0.60	0.11	12.03	3.16	3.36	3.19	4.70
6000	3.5	-0.5	0.54	-0.02	9.82	3.19	3.75	3.96	4.16
6000	3.5	-1.0	0.51	-0.10	8.89	3.31	3.68	3.84	4.11
6000	3.5	-1.5	0.48	-0.15	6.66	3.38	3.60	3.82	4.04
6000	3.5	-2.0	0.47	-0.18	4.48	3.41	3.53	3.84	3.98
6000	3.5	-2.5	0.47	-0.20	2.99	3.40	3.46	3.84	3.94
6000	3.5	-3.0	0.46	-0.22	1.82	3.39	3.42	3.84	3.93
6000	4.0	0.0	0.60	0.09	11.98	3.15	3.06	3.21	4.60
6000	4.0	-0.5	0.55	-0.05	10.14	3.10	3.44	3.25	3.97
6000	4.0	-1.0	0.52	-0.13	9.37	3.18	3.52	3.34	3.92
6000	4.0	-1.5	0.49	-0.18	7.16	3.26	3.48	3.81	3.90
6000	4.0	-2.0	0.48	-0.22	5.11	3.27	3.43	3.79	3.90
6000	4.0	-2.5	0.47	-0.24	3.34	3.26	3.38	3.78	3.64
6000	4.0	-3.0	0.47	-0.25	2.05	3.26	3.34	3.77	3.57

Table A.1. (continued)

T_{eff} (1)	Log g (2)	[Fe/H] (3)	(B-V) (4)	(U-B) (5)	W_k (6)	WHδ (7)	WHγ (8)	H$\delta D_{0.2}$ (9)	H$\gamma D_{0.2}$ (10)
6000	4.5	0.0	0.61	0.08	12.24	3.09	2.98	3.19	4.44
6000	4.5	-0.5	0.56	-0.06	10.73	3.01	3.04	3.20	4.09
6000	4.5	-1.0	0.52	-0.15	10.07	3.08	3.38	3.27	3.81
6000	4.5	-1.5	0.50	-0.20	7.78	3.13	3.40	3.32	3.85
6000	4.5	-2.0	0.49	-0.24	5.66	3.17	3.37	3.36	3.87
6000	4.5	-2.5	0.48	-0.26	3.77	3.16	3.33	3.36	3.56
6000	4.5	-3.0	0.48	-0.28	2.34	3.15	3.30	3.36	3.50
6000	5.0	0.0	0.61	0.08	12.63	3.03	3.44	3.19	3.76
6000	5.0	-1.0	0.54	-0.16	10.98	2.97	3.20	3.21	3.79
6000	5.0	-1.5	0.51	-0.22	8.44	3.02	3.35	3.23	3.83
6000	5.0	-2.0	0.50	-0.26	6.23	3.05	3.35	3.26	3.59
6000	5.0	-2.5	0.49	-0.28	4.32	3.06	3.32	3.26	3.52
6000	5.0	-3.0	0.49	-0.30	2.64	3.06	3.30	3.25	3.48
6250	2.0	0.0	0.51	0.17	13.25	4.37	5.73	4.81	7.04
6250	2.0	-0.5	0.45	0.09	9.86	4.60	5.54	5.31	6.81
6250	2.0	-1.0	0.42	0.03	8.24	4.85	5.37	5.69	6.59
6250	2.0	-1.5	0.40	-0.01	5.83	5.02	5.22	5.98	6.39
6250	2.0	-2.0	0.39	-0.03	3.76	5.11	5.05	6.16	6.12
6250	2.0	-2.5	0.38	-0.05	2.42	5.14	4.98	6.24	6.00
6250	2.0	-3.0	0.38	-0.06	1.44	5.16	4.95	6.28	5.96
6250	2.5	0.0	0.51	0.13	11.79	4.29	5.47	4.74	6.69
6250	2.5	-0.5	0.46	0.04	9.02	4.47	5.30	5.08	6.50
6250	2.5	-1.0	0.43	-0.02	7.65	4.66	5.13	5.48	6.30
6250	2.5	-1.5	0.41	-0.06	5.18	4.79	4.97	5.70	6.05
6250	2.5	-2.0	0.40	-0.08	3.49	4.84	4.81	5.81	5.79
6250	2.5	-2.5	0.40	-0.10	2.24	5.01	4.73	6.32	5.67
6250	2.5	-3.0	0.39	-0.11	1.34	4.87	4.71	5.89	5.63
6250	3.0	0.0	0.52	0.09	10.86	4.22	5.21	4.64	6.34
6250	3.0	-0.5	0.47	-0.01	8.58	4.32	5.03	4.85	6.14
6250	3.0	-1.0	0.44	-0.07	7.40	4.44	4.87	5.12	5.91
6250	3.0	-1.5	0.42	-0.11	5.04	4.53	4.70	5.39	5.66
6250	3.0	-2.0	0.41	-0.13	3.40	4.57	4.57	5.46	5.46
6250	3.0	-2.5	0.41	-0.15	2.20	4.57	4.49	5.49	5.35
6250	3.0	-3.0	0.40	-0.16	1.32	4.57	4.46	5.50	5.30

Table A.1. (continued)

T_{eff} (1)	Log g (2)	[Fe/H] (3)	(B-V) (4)	(U-B) (5)	W_k (6)	WHδ (7)	WHγ (8)	H$\delta D_{0.2}$ (9)	H$\gamma D_{0.2}$ (10)
6250	3.5	0.0	0.52	0.05	10.45	4.25	4.95	4.84	5.99
6250	3.5	-0.5	0.48	-0.05	8.53	4.16	4.77	4.60	5.76
6250	3.5	-1.0	0.45	-0.11	7.50	4.26	4.62	4.83	5.56
6250	3.5	-1.5	0.43	-0.15	5.40	4.30	4.48	4.95	5.37
6250	3.5	-2.0	0.42	-0.18	3.54	4.32	4.35	5.02	5.11
6250	3.5	-2.5	0.42	-0.20	2.30	4.31	4.28	5.03	4.99
6250	3.5	-3.0	0.41	-0.21	1.39	4.30	4.23	5.03	4.93
6250	4.0	0.0	0.53	0.02	10.51	4.11	4.87	4.47	5.96
6250	4.0	-0.5	0.49	-0.08	8.80	4.07	4.56	4.47	5.41
6250	4.0	-1.0	0.46	-0.15	7.91	4.10	4.42	4.58	5.20
6250	4.0	-1.5	0.44	-0.19	5.79	4.12	4.30	4.65	5.01
6250	4.0	-2.0	0.43	-0.22	3.85	4.12	4.20	4.69	4.86
6250	4.0	-2.5	0.43	-0.24	2.54	4.10	4.13	4.69	4.75
6250	4.0	-3.0	0.42	-0.25	1.54	4.09	4.09	4.68	4.69
6250	4.5	0.0	0.54	0.00	10.92	4.09	4.57	4.45	5.38
6250	4.5	-0.5	0.50	-0.11	9.31	4.00	4.39	4.35	5.11
6250	4.5	-1.0	0.47	-0.18	8.53	4.00	4.29	4.42	4.97
6250	4.5	-1.5	0.45	-0.23	6.37	4.00	4.20	4.47	4.84
6250	4.5	-2.0	0.44	-0.26	4.31	3.98	4.11	4.47	4.72
6250	4.5	-2.5	0.43	-0.28	2.88	3.96	4.05	4.46	4.61
6250	4.5	-3.0	0.43	-0.29	1.76	3.94	4.01	4.45	4.56
6250	5.0	0.0	0.55	-0.01	11.52	4.03	4.36	4.36	5.14
6250	5.0	-0.5	0.50	-0.13	10.02	3.94	4.31	4.27	5.00
6250	5.0	-1.0	0.47	-0.20	9.30	3.91	4.19	4.29	4.79
6250	5.0	-1.5	0.46	-0.25	7.02	3.90	4.14	4.32	4.73
6250	5.0	-2.0	0.45	-0.29	5.00	3.87	4.06	4.31	4.62
6250	5.0	-2.5	0.44	-0.31	3.29	3.85	4.01	4.30	4.54
6250	5.0	-3.0	0.44	-0.32	2.02	3.83	3.97	4.28	4.49
6500	2.0	0.0	0.40	0.22	11.85	7.15	8.58	8.79	11.08
6500	2.0	-0.5	0.35	0.15	9.23	7.44	8.42	9.22	10.90
6500	2.0	-1.0	0.32	0.10	7.75	7.78	8.25	9.77	10.70
6500	2.0	-1.5	0.34	0.01	4.86	6.54	6.55	8.17	8.29
6500	2.0	-2.0	0.29	0.04	3.49	7.83	7.91	9.87	10.23
6500	2.0	-2.5	0.28	0.03	2.23	8.11	7.87	10.40	10.19
6500	2.0	-3.0	0.32	-0.03	1.20	6.62	6.32	8.40	7.99

Table A.1. (continued)

T_{eff} (1)	Log g (2)	[Fe/H] (3)	(B-V) (4)	(U-B) (5)	W_k (6)	WHδ (7)	WHγ (8)	H$\delta D_{0.2}$ (9)	H$\gamma D_{0.2}$ (10)
6500	2.5	0.0	0.44	0.11	10.30	5.48	6.70	6.52	8.51
6500	2.5	-0.5	0.40	0.04	7.94	5.68	6.45	6.85	8.20
6500	2.5	-1.0	0.37	-0.01	6.62	5.90	6.23	7.23	7.89
6500	2.5	-1.5	0.36	-0.05	4.39	6.01	6.06	7.46	7.63
6500	2.5	-2.0	0.35	-0.07	2.87	6.07	5.91	7.59	7.39
6500	2.5	-2.5	0.35	-0.08	1.83	5.83	5.84	7.17	7.30
6500	2.5	-3.0	0.34	-0.09	1.08	6.08	5.81	7.65	7.28
6500	3.0	0.0	0.45	0.06	9.48	5.68	6.42	7.30	8.14
6500	3.0	-0.5	0.41	-0.01	7.51	5.50	6.21	6.61	7.85
6500	3.0	-1.0	0.38	-0.06	6.30	5.64	5.97	6.87	7.50
6500	3.0	-1.5	0.37	-0.10	4.19	5.72	5.60	7.05	6.93
6500	3.0	-2.0	0.36	-0.12	2.75	5.75	5.63	7.12	7.00
6500	3.0	-2.5	0.36	-0.13	1.75	5.75	5.56	7.15	6.90
6500	3.0	-3.0	0.36	-0.14	1.04	5.74	5.53	7.15	6.87
6500	3.5	0.0	0.46	0.02	9.13	5.21	6.17	6.14	7.75
6500	3.5	-0.5	0.42	-0.06	7.41	5.28	5.92	6.30	7.40
6500	3.5	-1.0	0.40	-0.11	6.28	5.38	5.69	6.52	7.07
6500	3.5	-1.5	0.38	-0.15	4.22	5.43	5.50	6.63	6.81
6500	3.5	-2.0	0.38	-0.17	2.79	5.43	5.36	6.66	6.62
6500	3.5	-2.5	0.37	-0.18	1.79	5.42	5.29	6.66	6.50
6500	3.5	-3.0	0.37	-0.19	1.07	5.40	5.24	6.65	6.44
6500	4.0	0.0	0.47	-0.02	9.18	5.12	5.90	6.01	7.31
6500	4.0	-0.5	0.43	-0.10	7.61	5.10	5.67	6.02	7.00
6500	4.0	-1.0	0.41	-0.16	6.58	5.16	5.44	6.18	6.69
6500	4.0	-1.5	0.39	-0.19	4.47	5.16	5.26	6.23	6.45
6500	4.0	-2.0	0.39	-0.22	3.01	5.14	5.14	6.23	6.25
6500	4.0	-2.5	0.38	-0.23	1.95	5.12	5.06	6.22	6.13
6500	4.0	-3.0	0.38	-0.24	1.17	5.10	5.01	6.20	6.06
6500	4.5	0.0	0.48	-0.05	9.54	5.05	5.70	5.91	7.00
6500	4.5	-0.5	0.44	-0.14	8.05	4.97	5.45	5.83	6.67
6500	4.5	-1.0	0.42	-0.20	7.12	4.98	5.26	5.90	6.44
6500	4.5	-1.5	0.40	-0.24	5.13	4.97	5.11	5.93	6.20
6500	4.5	-2.0	0.40	-0.26	3.38	4.94	4.99	5.92	6.02
6500	4.5	-2.5	0.39	-0.28	2.21	4.91	4.92	5.90	5.90
6500	4.5	-3.0	0.39	-0.29	1.33	4.89	4.88	5.88	5.84

Table A.1. (continued)

T_{eff} (1)	Log g (2)	[Fe/H] (3)	(B-V) (4)	(U-B) (5)	W_k (6)	WHδ (7)	WHγ (8)	H$\delta D_{0.2}$ (9)	H$\gamma D_{0.2}$ (10)
6500	5.0	0.0	0.49	-0.07	10.15	4.97	8.97	5.79	12.52
6500	5.0	-0.5	0.45	-0.17	8.66	4.88	5.28	5.70	6.43
6500	5.0	-1.0	0.43	-0.23	7.81	4.85	5.12	5.71	6.21
6500	5.0	-1.5	0.41	-0.27	5.73	4.82	5.00	5.71	6.02
6500	5.0	-2.0	0.40	-0.30	3.84	4.78	4.90	5.69	5.86
6500	5.0	-2.5	0.40	-0.31	2.54	4.75	4.83	5.67	5.76
6500	5.0	-3.0	0.40	-0.33	1.54	4.73	4.79	5.64	5.70
6750	2.0	0.0	0.33	0.22	10.59	8.69	10.86	10.96	14.95
6750	2.0	-0.5	0.28	0.16	8.23	8.98	9.82	11.41	12.89
6750	2.0	-1.0	0.26	0.11	6.83	9.34	9.66	11.97	12.71
6750	2.0	-1.5	0.24	0.09	4.53	9.54	9.52	12.31	12.51
6750	2.0	-2.0	0.23	0.07	2.95	9.58	9.38	12.40	12.32
6750	2.0	-2.5	0.23	0.06	1.86	9.60	9.34	12.46	12.27
6750	2.0	-3.0	0.23	0.05	1.09	9.62	9.33	12.51	12.28
6750	2.5	0.0	0.34	0.17	9.59	8.69	9.96	11.12	13.23
6750	2.5	-0.5	0.30	0.11	7.50	8.96	9.75	11.54	12.96
6750	2.5	-1.0	0.28	0.07	6.21	9.22	9.17	11.96	11.99
6750	2.5	-1.5	0.30	-0.02	3.76	7.71	7.57	9.93	9.82
6750	2.5	-2.0	0.26	0.02	2.66	9.43	9.22	12.35	12.24
6750	2.5	-2.5	0.25	0.01	1.68	9.44	9.16	12.38	12.17
6750	2.5	-3.0	0.29	-0.05	0.89	7.75	7.38	10.12	9.62
6750	3.0	0.0	0.39	0.06	8.39	6.75	7.79	8.40	10.13
6750	3.0	-0.5	0.35	-0.01	6.57	6.90	7.49	8.68	9.70
6750	3.0	-1.0	0.34	-0.05	5.18	7.05	7.22	8.98	9.33
6750	3.0	-1.5	0.32	-0.08	3.48	7.13	7.02	9.12	9.04
6750	3.0	-2.0	0.32	-0.09	2.23	6.74	6.89	8.46	8.87
6750	3.0	-2.5	0.31	-0.11	1.41	7.13	6.83	9.18	8.79
6750	3.0	-3.0	0.31	-0.11	0.83	7.11	6.80	9.17	8.75
6750	3.5	0.0	0.40	0.01	8.02	6.51	7.48	8.10	9.70
6750	3.5	-0.5	0.37	-0.06	6.39	6.63	7.20	8.31	9.30
6750	3.5	-1.0	0.35	-0.10	5.07	6.74	6.92	8.52	8.93
6750	3.5	-1.5	0.34	-0.13	3.43	6.77	6.35	8.61	7.96
6750	3.5	-2.0	0.33	-0.15	2.22	6.76	6.58	8.64	8.40
6750	3.5	-2.5	0.33	-0.16	1.41	6.74	6.50	8.62	8.30
6750	3.5	-3.0	0.33	-0.17	0.83	6.71	6.46	8.60	8.25

Table A.1. (continued)

T_{eff} (1)	Log g (2)	[Fe/H] (3)	(B-V) (4)	(U-B) (5)	W_k (6)	WHδ (7)	WHγ (8)	H$\delta D_{0.2}$ (9)	H$\gamma D_{0.2}$ (10)
6750	4.0	0.0	0.41	-0.04	8.03	6.33	7.22	7.84	9.31
6750	4.0	-0.5	0.38	-0.10	6.51	6.37	6.91	7.93	8.88
6750	4.0	-1.0	0.36	-0.15	5.22	6.80	6.61	8.96	8.44
6750	4.0	-1.5	0.35	-0.18	3.60	6.41	6.40	8.09	8.14
6750	4.0	-2.0	0.35	-0.20	2.36	6.38	6.27	8.08	7.95
6750	4.0	-2.5	0.34	-0.22	1.51	6.35	6.19	8.05	7.84
6750	4.0	-3.0	0.34	-0.22	0.89	6.32	6.14	8.01	7.78
6750	4.5	0.0	0.42	-0.08	8.33	6.21	6.95	7.65	8.91
6750	4.5	-0.5	0.39	-0.15	6.88	6.14	6.62	7.56	8.43
6750	4.5	-1.0	0.37	-0.20	5.86	6.16	6.36	7.64	8.07
6750	4.5	-1.5	0.36	-0.23	3.96	6.12	6.18	7.62	7.80
6750	4.5	-2.0	0.36	-0.25	2.64	6.09	6.05	7.59	7.60
6750	4.5	-2.5	0.35	-0.27	1.70	6.05	5.97	7.56	7.48
6750	4.5	-3.0	0.35	-0.28	1.01	6.02	5.92	7.52	7.41
6750	5.0	0.0	0.43	-0.11	8.87	6.07	6.73	7.40	8.57
6750	5.0	-0.5	0.40	-0.19	7.45	5.99	6.42	7.32	8.13
6750	5.0	-1.0	0.38	-0.24	6.48	5.95	6.18	7.31	7.79
6750	5.0	-1.5	0.37	-0.28	4.44	5.88	6.00	7.24	7.51
6750	5.0	-2.0	0.37	-0.30	3.02	5.84	5.87	7.21	7.32
6750	5.0	-2.5	0.36	-0.31	1.97	5.81	5.80	7.16	7.20
6750	5.0	-3.0	0.36	-0.32	1.17	5.78	5.75	7.13	7.14
7000	2.0	0.0	0.25	0.22	9.40	10.64	11.65	13.81	15.52
7000	2.0	-0.5	0.22	0.17	7.32	10.83	11.38	14.06	15.14
7000	2.0	-1.0	0.20	0.13	5.74	11.03	11.13	14.38	14.79
7000	2.0	-1.5	0.19	0.11	3.88	11.17	10.99	14.60	14.61
7000	2.0	-2.0	0.18	0.10	2.48	10.75	10.37	13.90	13.65
7000	2.0	-2.5	0.17	0.09	1.55	11.21	10.88	14.73	14.48
7000	2.0	-3.0	0.17	0.09	0.90	10.81	10.88	14.04	14.50
7000	2.5	0.0	0.28	0.18	8.55	10.39	11.53	13.56	15.52
7000	2.5	-0.5	0.25	0.12	6.66	10.62	11.28	13.92	15.19
7000	2.5	-1.0	0.23	0.09	5.22	11.35	11.08	15.40	14.93
7000	2.5	-1.5	0.22	0.07	3.48	11.03	10.93	14.60	14.71
7000	2.5	-2.0	0.21	0.05	2.22	11.05	10.81	14.66	14.56
7000	2.5	-2.5	0.21	0.05	1.39	11.06	10.77	14.69	14.52
7000	2.5	-3.0	0.21	0.04	0.73	11.07	10.76	14.73	14.53

Table A.1. (continued)

T_{eff} (1)	Log g (2)	[Fe/H] (3)	(B-V) (4)	(U-B) (5)	W_k (6)	WHδ (7)	WHγ (8)	H$\delta D_{0.2}$ (9)	H$\gamma D_{0.2}$ (10)
7000	3.0	0.0	0.31	0.13	7.89	10.29	11.47	13.58	15.63
7000	3.0	-0.5	0.27	0.08	6.03	10.52	11.15	13.94	15.19
7000	3.0	-1.0	0.25	0.04	4.85	10.72	10.91	14.28	14.86
7000	3.0	-1.5	0.24	0.01	3.22	10.79	10.69	14.41	14.53
7000	3.0	-2.0	0.24	0.00	2.06	10.76	10.08	14.39	13.57
7000	3.0	-2.5	0.23	-0.01	1.29	10.80	10.06	14.50	13.56
7000	3.0	-3.0	0.27	-0.08	0.60	8.93	8.49	11.91	11.34
7000	3.5	0.0	0.35	0.01	7.11	8.10	9.02	10.46	12.01
7000	3.5	-0.5	0.32	-0.04	5.41	8.21	8.64	10.68	11.49
7000	3.5	-1.0	0.31	-0.08	4.26	8.30	8.34	10.84	11.03
7000	3.5	-1.5	0.30	-0.10	2.80	8.32	8.12	10.91	10.71
7000	3.5	-2.0	0.29	-0.12	1.79	8.30	8.00	10.91	10.57
7000	3.5	-2.5	0.29	-0.13	1.12	8.26	7.93	10.88	10.47
7000	3.5	-3.0	0.29	-0.14	0.59	8.25	7.90	10.88	10.43
7000	4.0	0.0	0.36	-0.04	7.03	7.82	8.68	10.06	11.57
7000	4.0	-0.5	0.34	-0.10	5.42	7.86	8.75	10.16	12.52
7000	4.0	-1.0	0.32	-0.14	4.33	7.89	7.96	10.25	10.50
7000	4.0	-1.5	0.31	-0.16	2.89	7.87	7.75	10.26	10.17
7000	4.0	-2.0	0.31	-0.18	1.86	7.83	7.62	10.23	9.98
7000	4.0	-2.5	0.31	-0.19	1.18	7.79	7.54	10.19	9.87
7000	4.0	-3.0	0.31	-0.20	0.62	7.76	7.49	10.15	9.81
7000	4.5	0.0	0.37	-0.09	7.25	7.57	8.36	9.69	11.08
7000	4.5	-0.5	0.35	-0.15	5.64	7.55	7.98	9.68	10.52
7000	4.5	-1.0	0.33	-0.19	4.63	7.54	7.68	9.70	10.05
7000	4.5	-1.5	0.32	-0.22	3.16	7.49	7.45	9.66	9.71
7000	4.5	-2.0	0.32	-0.23	2.07	7.45	7.31	9.61	9.51
7000	4.5	-2.5	0.32	-0.25	1.32	7.39	7.22	9.56	9.39
7000	4.5	-3.0	0.32	-0.25	0.77	7.36	7.17	9.51	9.31
7000	5.0	0.0	0.38	-0.13	7.71	7.36	8.09	9.36	10.68
7000	5.0	-0.5	0.36	-0.20	6.31	7.29	7.70	9.28	10.08
7000	5.0	-1.0	0.34	-0.24	5.09	7.24	7.41	9.25	9.64
7000	5.0	-1.5	0.34	-0.27	3.57	7.16	7.19	9.16	9.31
7000	5.0	-2.0	0.33	-0.29	2.37	7.09	7.03	9.08	9.09
7000	5.0	-2.5	0.33	-0.30	1.52	7.04	6.94	9.03	8.95
7000	5.0	-3.0	0.33	-0.31	0.89	7.01	6.89	8.99	8.88

Table A.1. (continued)

T_{eff} (1)	Log g (2)	[Fe/H] (3)	(B-V) (4)	(U-B) (5)	W_k (6)	WHδ (7)	WHγ (8)	H$\delta D_{0.2}$ (9)	H$\gamma D_{0.2}$ (10)
7250	2.0	0.0	0.18	0.21	8.38	12.43	13.11	16.36	17.62
7250	2.0	-0.5	0.15	0.17	6.25	12.71	12.87	16.77	17.31
7250	2.0	-1.0	0.13	0.14	4.99	12.95	12.08	17.16	16.09
7250	2.0	-1.5	0.12	0.13	3.27	13.06	12.01	17.35	16.02
7250	2.0	-2.0	0.12	0.12	2.07	13.10	12.55	17.44	16.90
7250	2.0	-2.5	0.12	0.11	1.27	13.10	12.53	17.47	16.91
7250	2.0	-3.0	0.11	0.11	0.67	13.11	12.53	17.50	16.92
7250	2.5	0.0	0.22	0.18	7.60	12.41	13.25	16.54	18.09
7250	2.5	-0.5	0.19	0.14	5.74	12.54	12.91	16.71	17.60
7250	2.5	-1.0	0.18	0.11	4.51	12.71	12.68	16.99	17.27
7250	2.5	-1.5	0.17	0.10	2.93	12.78	11.87	17.12	16.00
7250	2.5	-2.0	0.16	0.09	1.85	12.80	12.47	17.18	17.00
7250	2.5	-2.5	0.16	0.08	1.14	12.79	12.43	17.19	16.96
7250	2.5	-3.0	0.16	0.07	0.60	12.20	12.42	16.16	16.97
7250	3.0	0.0	0.25	0.14	7.05	12.15	13.15	16.32	18.15
7250	3.0	-0.5	0.22	0.10	5.32	12.32	12.82	16.58	17.68
7250	3.0	-1.0	0.21	0.07	4.14	12.50	12.58	16.87	17.35
7250	3.0	-1.5	0.20	0.05	2.69	12.56	12.41	17.01	17.11
7250	3.0	-2.0	0.20	0.04	1.70	12.57	12.32	17.05	17.00
7250	3.0	-2.5	0.19	0.03	1.05	12.56	12.27	17.06	16.94
7250	3.0	-3.0	0.19	0.02	0.55	12.57	12.26	17.10	16.95
7250	3.5	0.0	0.28	0.09	6.51	11.94	13.01	16.17	18.15
7250	3.5	-0.5	0.25	0.04	5.05	12.08	12.61	16.40	17.57
7250	3.5	-1.0	0.26	-0.05	3.59	10.25	10.13	13.79	13.76
7250	3.5	-1.5	0.23	-0.01	2.58	12.27	11.56	16.76	15.94
7250	3.5	-2.0	0.22	-0.03	1.64	11.62	12.00	15.77	16.70
7250	3.5	-2.5	0.22	-0.03	1.02	12.20	11.93	16.73	16.61
7250	3.5	-3.0	0.25	-0.10	0.48	10.15	9.68	13.80	13.19
7250	4.0	0.0	0.31	-0.03	6.13	10.58	10.32	15.65	14.10
7250	4.0	-0.5	0.29	-0.08	4.58	9.58	9.87	12.77	13.40
7250	4.0	-1.0	0.28	-0.11	3.57	9.58	9.52	12.81	12.87
7250	4.0	-1.5	0.28	-0.13	2.33	9.55	9.31	12.80	12.55
7250	4.0	-2.0	0.27	-0.15	1.48	9.50	9.19	12.74	12.38
7250	4.0	-2.5	0.27	-0.16	0.93	9.46	8.46	12.70	11.11
7250	4.0	-3.0	0.27	-0.16	0.49	9.44	9.08	12.68	12.24

Table A.1. (continued)

T_{eff} (1)	Log g (2)	[Fe/H] (3)	(B-V) (4)	(U-B) (5)	W_k (6)	WHδ (7)	WHγ (8)	H$\delta D_{0.2}$ (9)	H$\gamma D_{0.2}$ (10)
7250	4.5	0.0	0.33	-0.09	6.22	9.22	9.99	12.20	13.61
7250	4.5	-0.5	0.31	-0.14	4.76	9.16	9.49	12.14	12.85
7250	4.5	-1.0	0.30	-0.17	3.80	9.13	9.16	12.12	12.33
7250	4.5	-1.5	0.29	-0.19	2.52	9.08	8.93	12.06	11.98
7250	4.5	-2.0	0.29	-0.21	1.62	9.01	8.78	11.99	11.79
7250	4.5	-2.5	0.29	-0.22	1.02	8.96	8.69	11.92	11.65
7250	4.5	-3.0	0.29	-0.22	0.54	8.36	8.05	10.85	10.50
7250	5.0	0.0	0.34	-0.14	6.67	8.87	9.59	11.68	13.01
7250	5.0	-0.5	0.32	-0.19	5.13	8.80	9.14	11.61	12.30
7250	5.0	-1.0	0.31	-0.23	4.20	8.73	8.81	11.53	11.82
7250	5.0	-1.5	0.30	-0.25	2.85	8.63	8.57	11.40	11.44
7250	5.0	-2.0	0.30	-0.27	1.85	8.55	8.41	11.30	11.19
7250	5.0	-2.5	0.30	-0.28	1.17	8.48	8.31	11.21	11.04
7250	5.0	-3.0	0.30	-0.29	0.62	8.02	8.27	10.41	10.98
7500	2.0	0.0	0.12	0.19	7.42	13.09	13.60	17.10	18.17
7500	2.0	-0.5	0.10	0.16	5.45	13.46	13.52	17.69	18.12
7500	2.0	-1.0	0.09	0.14	4.19	13.76	13.50	18.18	18.14
7500	2.0	-1.5	0.08	0.13	2.69	13.90	13.49	18.41	18.16
7500	2.0	-2.0	0.07	0.12	1.68	13.97	13.48	18.55	18.17
7500	2.0	-2.5	0.07	0.12	1.03	14.00	13.49	18.62	18.20
7500	2.0	-3.0	0.07	0.11	0.54	14.01	13.86	18.65	19.07
7500	2.5	0.0	0.15	0.18	6.57	14.59	14.98	19.79	20.72
7500	2.5	-0.5	0.13	0.15	4.99	14.57	14.54	19.74	20.05
7500	2.5	-1.0	0.12	0.13	3.81	14.74	13.58	20.02	18.50
7500	2.5	-1.5	0.11	0.12	2.43	14.79	14.26	20.13	19.68
7500	2.5	-2.0	0.11	0.11	1.52	14.38	14.21	19.54	19.64
7500	2.5	-2.5	0.11	0.10	0.85	14.35	13.53	19.50	18.47
7500	2.5	-3.0	0.11	0.10	0.49	14.77	14.17	20.17	19.59
7500	3.0	0.0	0.19	0.15	6.19	14.23	14.91	19.43	20.83
7500	3.0	-0.5	0.17	0.12	4.58	14.30	14.55	19.52	20.31
7500	3.0	-1.0	0.16	0.09	3.50	14.42	14.32	19.74	19.99
7500	3.0	-1.5	0.16	0.08	2.23	13.84	14.19	18.73	19.82
7500	3.0	-2.0	0.15	0.07	1.40	14.43	13.28	19.81	18.27
7500	3.0	-2.5	0.15	0.06	0.79	14.39	13.36	19.77	18.42
7500	3.0	-3.0	0.15	0.06	0.46	14.40	14.05	19.80	19.65

Table A.1. (continued)

T_{eff} (1)	Log g (2)	[Fe/H] (3)	(B-V) (4)	(U-B) (5)	W_k (6)	WHδ (7)	WHγ (8)	H$\delta D_{0.2}$ (9)	H$\gamma D_{0.2}$ (10)
7500	3.5	0.0	0.23	0.10	5.90	13.89	14.78	19.12	20.87
7500	3.5	-0.5	0.21	0.06	4.32	14.02	14.42	19.31	20.35
7500	3.5	-1.0	0.20	0.04	3.31	14.16	14.19	19.56	20.03
7500	3.5	-1.5	0.19	0.02	2.12	14.17	13.15	19.63	18.31
7500	3.5	-2.0	0.19	0.01	1.33	13.53	13.02	18.54	18.16
7500	3.5	-2.5	0.19	0.01	0.76	14.12	13.84	19.60	19.56
7500	3.5	-3.0	0.18	0.00	0.44	14.11	13.82	19.61	19.53
7500	4.0	0.0	0.26	0.04	5.77	13.65	14.62	18.93	20.86
7500	4.0	-0.5	0.24	0.00	4.25	13.67	14.12	18.98	20.09
7500	4.0	-1.0	0.24	-0.08	2.96	11.56	11.37	15.84	15.75
7500	4.0	-1.5	0.24	-0.10	1.89	10.60	11.15	14.15	15.44
7500	4.0	-2.0	0.23	-0.11	1.21	11.52	11.12	15.82	15.38
7500	4.0	-2.5	0.23	-0.12	0.68	11.43	11.00	15.71	15.21
7500	4.0	-3.0	0.23	-0.12	0.40	11.39	10.06	15.65	13.52
7500	4.5	0.0	0.29	-0.08	5.41	11.01	10.80	14.99	14.62
7500	4.5	-0.5	0.27	-0.12	3.96	10.98	11.21	14.96	15.56
7500	4.5	-1.0	0.26	-0.15	3.09	10.94	10.84	14.91	14.97
7500	4.5	-1.5	0.26	-0.17	2.01	10.85	10.60	14.81	14.61
7500	4.5	-2.0	0.26	-0.18	1.28	10.78	10.45	14.72	14.40
7500	4.5	-2.5	0.26	-0.19	0.73	10.72	10.37	14.64	14.28
7500	4.5	-3.0	0.25	-0.19	0.43	10.70	10.35	14.61	14.24
7500	5.0	0.0	0.31	-0.13	5.65	10.59	11.28	14.35	15.71
7500	5.0	-0.5	0.29	-0.18	4.28	10.46	10.72	14.18	14.80
7500	5.0	-1.0	0.28	-0.21	3.41	10.38	10.37	14.08	14.26
7500	5.0	-1.5	0.28	-0.23	2.26	10.28	10.12	13.94	13.88
7500	5.0	-2.0	0.27	-0.24	1.45	10.19	9.96	13.83	13.63
7500	5.0	-2.5	0.27	-0.25	0.83	10.13	9.87	13.74	13.49
7500	5.0	-3.0	0.27	-0.26	0.49	10.11	9.84	13.72	13.45
7750	2.0	0.0	0.08	0.15	6.22	13.14	13.50	16.95	17.81
7750	2.0	-0.5	0.06	0.13	4.47	13.50	13.54	17.53	17.94
7750	2.0	-1.0	0.05	0.12	3.37	13.76	13.58	17.96	18.05
7750	2.0	-1.5	0.04	0.11	2.13	13.88	13.28	18.18	17.56
7750	2.0	-2.0	0.04	0.11	1.32	13.94	13.61	18.28	18.16
7750	2.0	-2.5	0.04	0.10	0.80	13.95	13.62	18.33	18.19
7750	2.0	-3.0	0.04	0.10	0.43	13.95	13.61	18.34	18.20

Table A.1. (continued)

T_{eff} (1)	Log g (2)	[Fe/H] (3)	(B-V) (4)	(U-B) (5)	W_k (6)	WHδ (7)	WHγ (8)	H$\delta D_{0.2}$ (9)	H$\gamma D_{0.2}$ (10)
7750	2.5	0.0	0.10	0.17	5.88	15.14	15.37	20.40	21.10
7750	2.5	-0.5	0.09	0.14	4.18	15.45	15.32	20.89	21.10
7750	2.5	-1.0	0.08	0.13	3.14	15.68	15.31	21.29	21.14
7750	2.5	-1.5	0.07	0.12	1.99	15.79	15.28	21.50	21.14
7750	2.5	-2.0	0.07	0.11	1.22	15.53	15.27	21.13	21.16
7750	2.5	-2.5	0.06	0.11	0.69	15.43	15.27	21.04	21.17
7750	2.5	-3.0	0.06	0.11	0.41	15.84	15.27	21.65	21.18
7750	3.0	0.0	0.14	0.16	5.46	16.57	16.75	23.06	23.74
7750	3.0	-0.5	0.12	0.13	3.85	16.43	16.27	22.81	22.99
7750	3.0	-1.0	0.11	0.11	2.90	16.52	15.14	22.98	21.03
7750	3.0	-1.5	0.11	0.10	1.83	16.51	15.97	22.99	22.58
7750	3.0	-2.0	0.11	0.09	1.12	16.48	15.88	22.96	22.46
7750	3.0	-2.5	0.10	0.09	0.64	16.43	15.84	22.91	22.42
7750	3.0	-3.0	0.10	0.09	0.38	16.43	15.84	22.92	22.42
7750	3.5	0.0	0.18	0.12	5.14	17.38	17.53	24.75	25.42
7750	3.5	-0.5	0.17	0.09	3.63	16.06	16.24	22.44	23.21
7750	3.5	-1.0	0.16	0.07	2.75	16.18	16.03	22.67	22.91
7750	3.5	-1.5	0.15	0.05	1.74	16.10	15.86	22.57	22.66
7750	3.5	-2.0	0.15	0.05	1.08	16.05	14.90	22.53	20.95
7750	3.5	-2.5	0.15	0.04	0.61	15.69	15.69	21.95	22.43
7750	3.5	-3.0	0.15	0.04	0.37	16.04	15.72	22.55	22.50
7750	4.0	0.0	0.22	0.06	4.99	15.69	16.49	22.10	23.84
7750	4.0	-0.5	0.20	0.03	3.55	15.76	16.10	22.22	23.25
7750	4.0	-1.0	0.19	0.01	2.71	15.80	15.78	22.32	22.78
7750	4.0	-1.5	0.19	-0.01	1.73	14.88	15.58	20.70	22.48
7750	4.0	-2.0	0.18	-0.02	1.08	15.69	15.44	22.20	22.27
7750	4.0	-2.5	0.18	-0.02	0.62	15.63	15.36	22.14	22.16
7750	4.0	-3.0	0.18	-0.03	0.37	14.86	14.55	20.78	20.68
7750	4.5	0.0	0.24	0.00	4.62	13.05	13.56	18.18	19.29
7750	4.5	-0.5	0.24	-0.09	3.34	12.42	13.22	16.95	18.69
7750	4.5	-1.0	0.23	-0.12	2.54	12.97	11.84	18.08	16.34
7750	4.5	-1.5	0.23	-0.14	1.62	12.83	12.48	17.89	17.58
7750	4.5	-2.0	0.23	-0.15	0.95	11.76	12.31	16.01	17.33
7750	4.5	-2.5	0.22	-0.15	0.58	12.66	12.23	17.66	17.20
7750	4.5	-3.0	0.22	-0.16	0.35	12.63	12.20	17.62	17.17

Table A.1. (continued)

T_{eff} (1)	Log g (2)	[Fe/H] (3)	(B-V) (4)	(U-B) (5)	W_k (6)	WHδ (7)	WHγ (8)	H$\delta D_{0.2}$ (9)	H$\gamma D_{0.2}$ (10)
7750	5.0	0.0	0.27	-0.12	4.85	12.48	13.08	17.33	18.60
7750	5.0	-0.5	0.26	-0.16	3.53	12.36	12.53	17.15	17.72
7750	5.0	-1.0	0.25	-0.19	2.76	12.25	12.15	17.00	17.10
7750	5.0	-1.5	0.25	-0.20	1.80	12.12	11.88	16.82	16.68
7750	5.0	-2.0	0.25	-0.22	1.14	12.02	11.71	16.69	16.43
7750	5.0	-2.5	0.25	-0.22	0.65	11.96	11.62	16.61	16.30
7750	5.0	-3.0	0.24	-0.23	0.38	11.93	11.60	16.57	16.27
8000	2.0	0.0	0.04	0.11	5.00	12.70	12.95	16.10	16.81
8000	2.0	-0.5	0.03	0.09	3.46	13.02	13.06	16.63	17.02
8000	2.0	-1.0	0.02	0.09	2.59	13.23	13.14	16.98	17.20
8000	2.0	-1.5	0.01	0.08	1.62	13.33	13.19	17.17	17.33
8000	2.0	-2.0	0.01	0.08	0.99	13.39	13.22	17.27	17.40
8000	2.0	-2.5	0.01	0.08	0.56	13.30	13.21	17.23	17.40
8000	2.0	-3.0	0.01	0.08	0.34	13.39	13.22	17.32	17.43
8000	2.5	0.0	0.06	0.14	4.86	15.22	15.35	20.29	20.88
8000	2.5	-0.5	0.05	0.12	3.36	15.53	15.40	20.82	21.03
8000	2.5	-1.0	0.04	0.11	2.51	15.74	15.46	21.18	21.19
8000	2.5	-1.5	0.04	0.10	1.57	15.83	15.47	21.36	21.24
8000	2.5	-2.0	0.04	0.10	0.96	15.88	15.07	21.46	20.69
8000	2.5	-2.5	0.04	0.10	0.54	15.87	15.46	21.48	21.29
8000	2.5	-3.0	0.03	0.10	0.34	15.89	15.48	21.52	21.34
8000	3.0	0.0	0.09	0.14	4.59	17.19	17.27	23.81	24.38
8000	3.0	-0.5	0.08	0.12	3.17	17.48	17.23	24.30	24.40
8000	3.0	-1.0	0.07	0.11	2.37	18.28	17.20	26.12	24.41
8000	3.0	-1.5	0.07	0.11	1.48	18.31	17.15	26.19	24.36
8000	3.0	-2.0	0.07	0.10	0.84	17.76	16.62	24.87	23.57
8000	3.0	-2.5	0.07	0.10	0.52	17.73	16.61	24.85	23.54
8000	3.0	-3.0	0.07	0.10	0.32	17.75	16.64	24.89	23.60
8000	3.5	0.0	0.13	0.12	4.34	18.07	18.27	25.61	26.44
8000	3.5	-0.5	0.12	0.10	2.99	18.23	18.00	25.88	26.05
8000	3.5	-1.0	0.11	0.09	2.24	17.53	17.78	24.69	25.71
8000	3.5	-1.5	0.11	0.08	1.40	18.12	18.03	25.77	26.87
8000	3.5	-2.0	0.11	0.07	0.81	18.08	17.54	25.73	25.38
8000	3.5	-2.5	0.11	0.07	0.50	18.02	18.02	25.66	26.59
8000	3.5	-3.0	0.11	0.06	0.31	18.02	17.50	25.67	25.34

Table A.1. (continued)

T_{eff} (1)	Log g (2)	[Fe/H] (3)	(B-V) (4)	(U-B) (5)	W_k (6)	WHδ (7)	WHγ (8)	H$\delta D_{0.2}$ (9)	H$\gamma D_{0.2}$ (10)
8000	4.0	0.0	0.18	0.08	4.21	17.79	18.24	25.43	26.67
8000	4.0	-0.5	0.16	0.05	2.94	17.79	17.92	25.43	26.19
8000	4.0	-1.0	0.16	0.03	2.23	17.76	16.79	25.41	24.27
8000	4.0	-1.5	0.15	0.02	1.40	17.70	16.65	25.34	24.06
8000	4.0	-2.0	0.15	0.01	0.82	18.11	17.35	26.53	25.34
8000	4.0	-2.5	0.15	0.01	0.50	17.58	17.30	25.19	25.28
8000	4.0	-3.0	0.15	0.01	0.31	17.58	17.29	25.20	25.28
8000	4.5	0.0	0.21	0.01	4.24	17.39	18.06	25.02	26.67
8000	4.5	-0.5	0.20	-0.01	3.01	17.39	17.64	25.03	26.00
8000	4.5	-1.0	0.19	-0.03	2.31	17.35	17.33	25.02	25.53
8000	4.5	-1.5	0.18	-0.05	1.47	17.24	17.07	24.87	25.13
8000	4.5	-2.0	0.18	-0.06	0.87	17.17	16.95	24.78	24.95
8000	4.5	-2.5	0.18	-0.06	0.53	17.09	16.88	24.67	24.85
8000	4.5	-3.0	0.18	-0.06	0.33	17.09	16.86	24.68	24.83
8000	5.0	0.0	0.24	-0.11	4.08	14.54	15.02	20.60	21.75
8000	5.0	-0.5	0.23	-0.14	2.90	14.36	14.42	20.35	20.78
8000	5.0	-1.0	0.22	-0.16	2.23	14.20	14.01	20.12	20.13
8000	5.0	-1.5	0.22	-0.18	1.43	14.06	13.72	19.92	19.68
8000	5.0	-2.0	0.22	-0.19	0.84	13.96	12.45	19.78	17.38
8000	5.0	-2.5	0.22	-0.19	0.51	13.88	12.42	19.67	17.34
8000	5.0	-3.0	0.22	-0.20	0.31	12.96	12.40	18.03	17.31
8250	2.0	0.0	0.01	0.06	3.74	11.85	12.05	14.70	15.32
8250	2.0	-0.5	0.00	0.05	2.55	12.12	12.19	15.17	15.58
8250	2.0	-1.0	-0.01	0.04	1.89	12.30	12.33	15.49	15.91
8250	2.0	-1.5	-0.01	0.04	1.18	12.39	12.37	15.66	15.96
8250	2.0	-2.0	-0.01	0.04	0.72	12.41	12.37	15.72	15.98
8250	2.0	-2.5	-0.01	0.04	0.41	12.42	12.38	15.76	16.02
8250	2.0	-3.0	-0.01	0.03	0.27	12.42	12.38	15.77	16.05
8250	2.5	0.0	0.03	0.10	3.80	14.77	14.93	19.42	20.26
8250	2.5	-0.5	0.02	0.09	2.60	15.08	15.01	19.94	20.27
8250	2.5	-1.0	0.01	0.08	1.94	15.26	15.07	20.27	20.43
8250	2.5	-1.5	0.01	0.08	1.21	15.36	15.13	20.48	20.57
8250	2.5	-2.0	0.01	0.08	0.68	15.30	15.12	20.48	20.59
8250	2.5	-2.5	0.01	0.07	0.43	15.39	15.14	20.58	20.63
8250	2.5	-3.0	0.01	0.07	0.28	15.40	15.15	20.62	20.68

Table A.1. (continued)

T_{eff} (1)	Log g (2)	[Fe/H] (3)	(B-V) (4)	(U-B) (5)	W_k (6)	WHδ (7)	WHγ (8)	H$\delta D_{0.2}$ (9)	H$\gamma D_{0.2}$ (10)
8250	3.0	0.0	0.06	0.12	3.71	17.36	17.92	23.88	25.78
8250	3.0	-0.5	0.05	0.11	2.53	17.66	17.43	24.40	24.56
8250	3.0	-1.0	0.04	0.10	1.89	17.83	17.45	24.72	24.65
8250	3.0	-1.5	0.04	0.09	1.17	17.92	17.46	24.92	24.72
8250	3.0	-2.0	0.04	0.09	0.67	17.92	17.44	24.95	24.71
8250	3.0	-2.5	0.04	0.09	0.42	18.15	17.44	25.51	24.75
8250	3.0	-3.0	0.04	0.09	0.28	17.95	17.47	25.04	24.81
8250	3.5	0.0	0.09	0.12	3.58	19.34	19.23	27.55	27.92
8250	3.5	-0.5	0.08	0.10	2.43	19.55	19.17	27.94	27.91
8250	3.5	-1.0	0.08	0.09	1.82	19.64	19.67	28.14	29.22
8250	3.5	-1.5	0.07	0.09	1.07	19.69	19.02	28.25	27.75
8250	3.5	-2.0	0.07	0.08	0.65	19.63	18.96	28.19	27.68
8250	3.5	-2.5	0.07	0.08	0.41	19.64	18.96	28.23	27.71
8250	3.5	-3.0	0.07	0.08	0.27	19.64	18.97	28.23	27.74
8250	4.0	0.0	0.13	0.09	3.49	19.93	19.93	28.93	29.49
8250	4.0	-0.5	0.12	0.07	2.39	19.87	18.60	28.83	27.10
8250	4.0	-1.0	0.12	0.05	1.80	19.81	19.41	28.75	28.71
8250	4.0	-1.5	0.12	0.05	1.08	19.69	19.27	28.59	28.49
8250	4.0	-2.0	0.12	0.04	0.66	19.61	19.18	28.46	28.36
8250	4.0	-2.5	0.12	0.04	0.41	20.34	19.16	30.14	28.35
8250	4.0	-3.0	0.12	0.04	0.27	20.34	19.16	30.10	28.37
8250	4.5	0.0	0.17	0.03	3.54	19.47	18.69	28.41	27.41
8250	4.5	-0.5	0.17	0.01	2.46	19.41	19.50	28.33	29.10
8250	4.5	-1.0	0.16	-0.01	1.87	19.35	19.23	28.26	28.69
8250	4.5	-1.5	0.16	-0.02	1.14	19.27	19.07	28.18	28.44
8250	4.5	-2.0	0.16	-0.02	0.70	19.19	18.34	28.06	27.24
8250	4.5	-2.5	0.15	-0.03	0.43	18.67	18.93	27.21	28.25
8250	4.5	-3.0	0.15	-0.03	0.28	19.18	18.35	28.07	27.25
8250	5.0	0.0	0.21	-0.04	3.71	19.03	19.68	27.97	29.66
8250	5.0	-0.5	0.19	-0.07	2.64	18.94	19.16	27.83	28.82
8250	5.0	-1.0	0.19	-0.09	2.03	18.76	17.70	27.56	26.18
8250	5.0	-1.5	0.19	-0.14	1.11	15.24	15.83	21.60	23.17
8250	5.0	-2.0	0.19	-0.12	0.76	17.76	16.53	25.88	24.17
8250	5.0	-2.5	0.19	-0.16	0.42	15.95	15.54	23.01	22.70
8250	5.0	-3.0	0.19	-0.16	0.27	15.93	15.51	22.99	22.68

Table A.1. (continued)

T_{eff} (1)	Log g (2)	[Fe/H] (3)	(B-V) (4)	(U-B) (5)	W_k (6)	WHδ (7)	WHγ (8)	H$\delta D_{0.2}$ (9)	H$\gamma D_{0.2}$ (10)
8500	2.0	0.0	-0.02	0.00	2.67	10.60	10.98	12.86	13.64
8500	2.0	-0.5	-0.02	0.00	1.82	10.88	11.12	13.30	13.92
8500	2.0	-1.0	-0.02	0.00	1.34	11.08	11.25	13.63	14.16
8500	2.0	-1.5	-0.02	-0.01	0.82	11.16	11.27	13.78	14.25
8500	2.0	-2.0	-0.02	-0.01	0.46	11.18	11.28	13.86	14.30
8500	2.0	-2.5	-0.02	-0.01	0.31	11.19	11.28	13.89	14.33
8500	2.0	-3.0	-0.02	-0.01	0.22	11.19	11.28	13.91	14.36
8500	2.5	0.0	0.00	0.05	2.86	13.95	14.03	18.06	18.57
8500	2.5	-0.5	-0.01	0.05	1.95	14.22	14.20	18.52	18.90
8500	2.5	-1.0	-0.01	0.04	1.46	14.41	14.39	18.87	19.32
8500	2.5	-1.5	-0.01	0.04	0.90	14.48	14.37	19.01	19.27
8500	2.5	-2.0	-0.01	0.04	0.51	14.50	14.39	19.09	19.34
8500	2.5	-2.5	-0.01	0.04	0.33	14.52	14.40	19.14	19.39
8500	2.5	-3.0	-0.01	0.04	0.23	14.53	14.41	19.17	19.43
8500	3.0	0.0	0.03	0.08	2.90	16.98	16.97	23.12	23.61
8500	3.0	-0.5	0.02	0.08	1.98	17.27	17.34	23.65	24.71
8500	3.0	-1.0	0.02	0.07	1.48	17.49	17.22	24.04	24.15
8500	3.0	-1.5	0.01	0.07	0.85	17.57	17.25	24.21	24.25
8500	3.0	-2.0	0.01	0.07	0.52	17.58	17.25	24.26	24.28
8500	3.0	-2.5	0.01	0.07	0.34	17.61	17.28	24.33	24.36
8500	3.0	-3.0	0.01	0.07	0.24	17.62	17.30	24.36	24.41
8500	3.5	0.0	0.06	0.09	2.87	19.62	19.45	27.85	28.17
8500	3.5	-0.5	0.05	0.09	1.95	19.85	19.51	28.27	28.35
8500	3.5	-1.0	0.05	0.08	1.46	20.04	19.54	28.65	28.45
8500	3.5	-1.5	0.05	0.08	0.86	20.10	19.54	28.79	28.50
8500	3.5	-2.0	0.05	0.07	0.52	20.08	19.51	28.79	28.48
8500	3.5	-2.5	0.05	0.07	0.34	20.11	19.53	28.85	28.53
8500	3.5	-3.0	0.05	0.07	0.24	20.12	19.92	28.89	29.63
8500	4.0	0.0	0.09	0.08	2.84	21.37	21.12	31.25	31.48
8500	4.0	-0.5	0.09	0.07	1.92	21.49	20.99	31.52	31.35
8500	4.0	-1.0	0.09	0.06	1.45	21.52	20.84	31.61	31.15
8500	4.0	-1.5	0.08	0.06	0.87	21.48	20.79	31.57	31.09
8500	4.0	-2.0	0.08	0.05	0.53	21.76	20.71	32.62	30.98
8500	4.0	-2.5	0.08	0.05	0.35	21.39	20.70	31.46	30.98
8500	4.0	-3.0	0.08	0.05	0.23	21.74	20.71	32.56	31.01

Table A.1. (continued)

T_{eff} (1)	Log g (2)	[Fe/H] (3)	(B-V) (4)	(U-B) (5)	W_k (6)	WHδ (7)	WHγ (8)	H$\delta D_{0.2}$ (9)	H$\gamma D_{0.2}$ (10)
8500	4.5	0.0	0.14	0.04	2.89	22.24	21.54	33.88	32.58
8500	4.5	-0.5	0.13	0.02	1.99	21.39	21.23	31.68	32.09
8500	4.5	-1.0	0.13	0.01	1.51	22.04	20.98	33.24	31.70
8500	4.5	-1.5	0.13	0.00	0.91	21.17	20.84	31.34	31.49
8500	4.5	-2.0	0.13	0.00	0.56	21.09	20.77	31.23	31.38
8500	4.5	-2.5	0.13	0.00	0.36	21.06	20.75	31.18	31.36
8500	4.5	-3.0	0.13	0.00	0.24	21.06	20.74	31.19	31.36
8500	5.0	0.0	0.18	-0.03	3.07	21.05	21.41	31.35	32.65
8500	5.0	-0.5	0.17	-0.04	2.15	21.01	21.64	31.33	33.58
8500	5.0	-1.0	0.17	-0.06	1.64	20.97	20.82	31.31	31.75
8500	5.0	-1.5	0.16	-0.07	1.00	21.52	20.54	32.76	31.29
8500	5.0	-2.0	0.16	-0.07	0.61	20.64	20.46	30.78	31.17
8500	5.0	-2.5	0.16	-0.08	0.39	20.60	20.40	30.73	31.09
8500	5.0	-3.0	0.16	-0.08	0.25	20.61	20.40	30.74	31.10
8750	2.0	0.0	-0.03	-0.05	1.50	9.42	9.66	11.18	11.74
8750	2.0	-0.5	-0.03	-0.05	1.06	9.64	9.93	11.53	12.15
8750	2.0	-1.0	-0.03	-0.06	0.81	9.77	10.05	11.76	12.37
8750	2.0	-1.5	-0.03	-0.06	0.51	9.82	10.10	11.87	12.50
8750	2.0	-2.0	-0.03	-0.06	0.34	9.82	10.11	11.92	12.55
8750	2.0	-2.5	-0.03	-0.07	0.24	9.84	10.11	11.96	12.59
8750	2.0	-3.0	-0.03	-0.07	0.19	9.85	10.12	11.99	12.62
8750	2.5	0.0	-0.02	0.00	2.10	12.95	13.01	16.48	16.91
8750	2.5	-0.5	-0.03	0.00	1.25	13.21	13.21	16.91	17.29
8750	2.5	-1.0	-0.03	0.00	1.06	13.37	13.36	17.21	17.67
8750	2.5	-1.5	-0.03	0.00	0.60	13.39	13.36	17.29	17.64
8750	2.5	-2.0	-0.03	-0.01	0.38	13.40	13.37	17.36	17.71
8750	2.5	-2.5	-0.03	-0.01	0.26	13.42	13.39	17.41	17.77
8750	2.5	-3.0	-0.03	-0.01	0.20	13.43	13.40	17.45	17.81
8750	3.0	0.0	0.00	0.04	2.21	16.24	16.17	21.85	22.22
8750	3.0	-0.5	0.00	0.04	1.52	16.54	16.42	22.39	22.70
8750	3.0	-1.0	-0.01	0.04	1.13	16.75	16.58	22.77	23.01
8750	3.0	-1.5	-0.01	0.04	0.65	16.78	16.76	22.86	23.53
8750	3.0	-2.0	-0.01	0.04	0.41	16.82	16.62	22.97	23.17
8750	3.0	-2.5	-0.01	0.03	0.28	16.84	16.65	23.03	23.25
8750	3.0	-3.0	-0.01	0.03	0.21	16.86	16.66	23.08	23.30

Table A.1. (continued)

T_{eff} (1)	Log g (2)	[Fe/H] (3)	(B-V) (4)	(U-B) (5)	W_k (6)	WHδ (7)	WHγ (8)	H$\delta D_{0.2}$ (9)	H$\gamma D_{0.2}$ (10)
8750	3.5	0.0	0.03	0.06	2.26	19.39	19.22	27.34	27.67
8750	3.5	-0.5	0.03	0.06	1.55	19.66	19.35	27.84	27.97
8750	3.5	-1.0	0.02	0.06	1.16	19.86	19.45	28.22	28.17
8750	3.5	-1.5	0.02	0.06	0.68	19.88	19.79	28.30	29.08
8750	3.5	-2.0	0.02	0.05	0.43	19.92	19.75	28.40	29.10
8750	3.5	-2.5	0.02	0.05	0.29	19.95	19.53	28.47	28.44
8750	3.5	-3.0	0.02	0.05	0.21	19.97	19.56	28.52	28.51
8750	4.0	0.0	0.06	0.06	2.28	21.91	21.59	32.05	32.22
8750	4.0	-0.5	0.06	0.06	1.55	22.10	21.57	32.44	32.26
8750	4.0	-1.0	0.06	0.06	1.13	22.19	21.56	32.66	32.30
8750	4.0	-1.5	0.06	0.05	0.70	22.16	21.52	32.64	32.27
8750	4.0	-2.0	0.06	0.05	0.44	22.18	21.52	32.70	32.31
8750	4.0	-2.5	0.06	0.05	0.29	22.24	21.55	33.11	32.38
8750	4.0	-3.0	0.06	0.05	0.21	22.20	21.58	32.78	32.45
8750	4.5	0.0	0.10	0.04	2.34	23.23	22.82	34.85	34.86
8750	4.5	-0.5	0.10	0.03	1.60	23.21	22.62	34.86	34.59
8750	4.5	-1.0	0.10	0.02	1.19	23.08	22.45	34.66	34.33
8750	4.5	-1.5	0.10	0.02	0.73	22.94	22.92	34.43	35.56
8750	4.5	-2.0	0.10	0.01	0.46	22.87	22.27	34.33	34.06
8750	4.5	-2.5	0.10	0.01	0.31	23.05	22.27	34.95	34.07
8750	4.5	-3.0	0.10	0.01	0.21	22.81	22.86	34.24	35.48
8750	5.0	0.0	0.15	-0.02	2.51	22.96	22.92	34.70	35.37
8750	5.0	-0.5	0.14	-0.03	1.73	23.55	22.69	36.17	35.02
8750	5.0	-1.0	0.14	-0.04	1.32	22.76	22.52	34.39	34.76
8750	5.0	-1.5	0.14	-0.05	0.81	22.63	22.39	34.19	34.55
8750	5.0	-2.0	0.14	-0.05	0.50	22.58	22.30	34.12	34.41
8750	5.0	-2.5	0.14	-0.05	0.33	22.75	22.29	34.69	34.42
8750	5.0	-3.0	0.14	-0.05	0.22	22.54	22.73	34.08	35.69
9000	2.0	0.0	-0.04	-0.10	1.02	8.45	8.64	9.83	10.32
9000	2.0	-0.5	-0.04	-0.11	0.72	8.61	8.84	10.12	10.61
9000	2.0	-1.0	-0.04	-0.11	0.56	8.71	8.95	10.32	10.81
9000	2.0	-1.5	-0.04	-0.11	0.37	8.74	8.98	10.42	10.92
9000	2.0	-2.0	-0.04	-0.12	0.26	8.76	9.00	10.49	10.99
9000	2.0	-2.5	-0.04	-0.12	0.20	8.78	9.02	10.54	11.04
9000	2.0	-3.0	-0.04	-0.12	0.17	8.79	9.03	10.57	11.07

Table A.1. (continued)

T_{eff} (1)	Log g (2)	[Fe/H] (3)	(B-V) (4)	(U-B) (5)	W_k (6)	WHδ (7)	WHγ (8)	H$\delta D_{0.2}$ (9)	H$\gamma D_{0.2}$ (10)
9000	2.5	0.0	-0.04	-0.04	1.27	11.95	12.00	14.94	15.35
9000	2.5	-0.5	-0.04	-0.05	0.90	12.14	12.18	15.30	15.68
9000	2.5	-1.0	-0.04	-0.05	0.69	12.23	12.25	15.50	15.86
9000	2.5	-1.5	-0.04	-0.05	0.44	12.26	12.28	15.61	15.97
9000	2.5	-2.0	-0.04	-0.05	0.29	12.28	12.30	15.68	16.05
9000	2.5	-2.5	-0.04	-0.05	0.22	12.31	12.32	15.75	16.12
9000	2.5	-3.0	-0.04	-0.05	0.18	12.33	12.34	15.78	16.17
9000	3.0	0.0	-0.02	0.00	1.45	15.34	15.28	20.38	20.73
9000	3.0	-0.5	-0.02	0.00	1.03	15.61	15.54	20.86	21.21
9000	3.0	-1.0	-0.02	0.00	0.78	15.73	15.64	21.11	21.45
9000	3.0	-1.5	-0.02	0.00	0.49	15.79	15.69	21.25	21.59
9000	3.0	-2.0	-0.02	0.00	0.32	15.77	15.72	21.29	21.69
9000	3.0	-2.5	-0.02	0.00	0.24	15.75	15.75	21.32	21.78
9000	3.0	-3.0	-0.02	0.00	0.19	15.88	15.66	21.49	21.70
9000	3.5	0.0	0.00	0.03	1.77	18.78	18.61	26.24	26.57
9000	3.5	-0.5	0.00	0.03	1.13	19.10	19.07	26.81	27.58
9000	3.5	-1.0	0.00	0.03	0.85	19.26	18.97	27.15	27.30
9000	3.5	-1.5	0.00	0.03	0.53	19.23	19.03	27.23	27.44
9000	3.5	-2.0	0.00	0.03	0.35	19.36	19.07	27.39	27.57
9000	3.5	-2.5	0.00	0.03	0.25	19.38	19.11	27.47	27.68
9000	3.5	-3.0	0.00	0.03	0.19	19.41	19.14	27.52	27.75
9000	4.0	0.0	0.04	0.04	1.83	21.88	21.55	31.90	32.08
9000	4.0	-0.5	0.04	0.04	1.25	22.17	21.69	32.45	32.39
9000	4.0	-1.0	0.04	0.04	0.91	22.30	21.78	32.74	32.59
9000	4.0	-1.5	0.04	0.04	0.56	22.30	21.77	32.78	32.62
9000	4.0	-2.0	0.04	0.04	0.37	22.34	21.81	32.87	32.73
9000	4.0	-2.5	0.04	0.04	0.25	22.24	21.84	32.85	32.82
9000	4.0	-3.0	0.04	0.04	0.19	22.37	21.89	32.97	32.92
9000	4.5	0.0	0.08	0.03	1.89	24.38	23.53	37.43	36.11
9000	4.5	-0.5	0.07	0.02	1.29	24.48	23.51	37.39	36.16
9000	4.5	-1.0	0.07	0.02	0.97	24.26	23.52	36.72	36.23
9000	4.5	-1.5	0.07	0.02	0.60	24.23	23.49	36.68	36.22
9000	4.5	-2.0	0.07	0.02	0.39	24.24	23.65	36.72	36.80
9000	4.5	-2.5	0.07	0.02	0.26	24.24	23.51	36.75	36.33
9000	4.5	-3.0	0.07	0.02	0.19	24.46	23.57	37.53	36.44

Table A.1. (continued)

T_{eff} (1)	Log g (2)	[Fe/H] (3)	(B-V) (4)	(U-B) (5)	W_k (6)	WHδ (7)	WHγ (8)	H$\delta D_{0.2}$ (9)	H$\gamma D_{0.2}$ (10)
9000	5.0	0.0	0.12	-0.01	2.02	25.10	24.42	38.69	38.24
9000	5.0	-0.5	0.11	-0.01	1.38	25.04	24.26	38.65	38.06
9000	5.0	-1.0	0.11	-0.02	1.06	25.00	24.18	38.62	37.99
9000	5.0	-1.5	0.11	-0.02	0.65	24.91	24.09	38.47	37.86
9000	5.0	-2.0	0.11	-0.03	0.42	24.87	24.06	38.42	37.83
9000	5.0	-2.5	0.11	-0.03	0.28	24.85	24.22	38.40	38.67
9000	5.0	-3.0	0.11	-0.03	0.19	24.83	24.10	38.38	37.96
9250	2.0	0.0	-0.05	-0.15	0.74	7.67	7.83	8.83	9.21
9250	2.0	-0.5	-0.05	-0.16	0.52	7.81	8.00	9.05	9.46
9250	2.0	-1.0	-0.04	-0.16	0.40	7.89	8.09	9.20	9.64
9250	2.0	-1.5	-0.04	-0.16	0.28	7.93	8.13	9.31	9.76
9250	2.0	-2.0	-0.04	-0.16	0.22	7.96	8.17	9.39	9.85
9250	2.0	-2.5	-0.04	-0.16	0.18	7.99	8.19	9.44	9.91
9250	2.0	-3.0	-0.04	-0.16	0.16	8.00	8.20	9.47	9.94
9250	2.5	0.0	-0.05	-0.09	0.91	10.95	11.05	13.49	13.90
9250	2.5	-0.5	-0.05	-0.09	0.64	11.08	11.19	13.75	14.19
9250	2.5	-1.0	-0.05	-0.09	0.50	11.17	11.25	13.96	14.37
9250	2.5	-1.5	-0.05	-0.10	0.33	11.20	11.27	14.06	14.47
9250	2.5	-2.0	-0.05	-0.10	0.24	11.23	11.31	14.14	14.57
9250	2.5	-2.5	-0.05	-0.10	0.19	11.27	11.35	14.21	14.66
9250	2.5	-3.0	-0.05	-0.10	0.16	11.28	11.37	14.25	14.70
9250	3.0	0.0	-0.04	-0.04	1.08	14.36	14.33	18.83	19.20
9250	3.0	-0.5	-0.04	-0.04	0.77	14.59	14.55	19.23	19.62
9250	3.0	-1.0	-0.04	-0.04	0.59	14.67	14.63	19.44	19.82
9250	3.0	-1.5	-0.04	-0.04	0.38	14.71	14.67	19.56	19.96
9250	3.0	-2.0	-0.04	-0.05	0.26	14.76	14.71	19.69	20.09
9250	3.0	-2.5	-0.04	-0.04	0.21	14.81	14.76	19.79	20.20
9250	3.0	-3.0	-0.04	-0.04	0.17	14.84	14.79	19.85	20.26
9250	3.5	0.0	-0.02	-0.01	1.23	17.97	17.84	24.85	25.23
9250	3.5	-0.5	-0.02	0.00	0.87	18.26	18.21	25.40	25.99
9250	3.5	-1.0	-0.01	0.00	0.66	18.39	18.20	25.67	25.95
9250	3.5	-1.5	-0.01	0.00	0.42	18.46	18.27	25.84	26.15
9250	3.5	-2.0	-0.01	-0.01	0.29	18.51	18.33	25.97	26.30
9250	3.5	-2.5	-0.01	0.00	0.22	18.55	18.38	26.07	26.42
9250	3.5	-3.0	-0.01	0.00	0.17	18.58	18.42	26.13	26.51

Table A.1. (continued)

T_{eff} (1)	Log g (2)	[Fe/H] (3)	(B-V) (4)	(U-B) (5)	W_k (6)	WHδ (7)	WHγ (8)	H$\delta D_{0.2}$ (9)	H$\gamma D_{0.2}$ (10)
9250	4.0	0.0	0.01	0.01	1.36	21.59	21.17	31.47	31.34
9250	4.0	-0.5	0.01	0.01	0.96	21.79	21.42	31.72	31.83
9250	4.0	-1.0	0.02	0.01	0.73	21.90	21.49	31.95	32.01
9250	4.0	-1.5	0.02	0.01	0.46	21.97	21.56	32.12	32.19
9250	4.0	-2.0	0.02	0.01	0.31	22.01	21.62	32.25	32.35
9250	4.0	-2.5	0.02	0.01	0.22	22.05	21.67	32.34	32.47
9250	4.0	-3.0	0.02	0.01	0.17	21.88	21.71	32.11	32.57
9250	4.5	0.0	0.05	0.01	1.54	24.61	23.75	37.44	36.46
9250	4.5	-0.5	0.05	0.01	1.05	24.49	23.86	36.98	36.72
9250	4.5	-1.0	0.05	0.01	0.79	24.51	23.89	37.23	36.81
9250	4.5	-1.5	0.05	0.01	0.50	24.58	24.01	37.21	37.39
9250	4.5	-2.0	0.05	0.01	0.33	24.59	23.98	37.27	37.08
9250	4.5	-2.5	0.05	0.01	0.23	24.61	24.03	37.32	37.49
9250	4.5	-3.0	0.05	0.01	0.17	24.61	24.05	37.34	37.26
9250	5.0	0.0	0.09	-0.02	1.65	25.81	25.46	40.54	40.60
9250	5.0	-0.5	0.09	-0.02	1.15	25.91	25.14	40.17	39.67
9250	5.0	-1.0	0.09	-0.02	0.87	25.89	25.11	40.16	39.66
9250	5.0	-1.5	0.09	-0.02	0.55	25.87	25.09	40.15	39.67
9250	5.0	-2.0	0.09	-0.03	0.36	26.05	25.22	40.75	40.34
9250	5.0	-2.5	0.09	-0.03	0.24	25.84	25.14	40.14	39.84
9250	5.0	-3.0	0.09	-0.03	0.17	25.84	25.19	40.14	39.95
9500	2.0	0.0	-0.05	-0.20	0.55	7.07	7.20	8.06	8.34
9500	2.0	-0.5	-0.05	-0.20	0.40	7.19	7.35	8.27	8.60
9500	2.0	-1.0	-0.05	-0.20	0.32	7.27	7.44	8.43	8.78
9500	2.0	-1.5	-0.05	-0.20	0.24	7.32	7.50	8.54	8.92
9500	2.0	-2.0	-0.05	-0.20	0.19	7.36	7.54	8.63	9.02
9500	2.0	-2.5	-0.05	-0.20	0.17	7.38	7.56	8.68	9.08
9500	2.0	-3.0	-0.04	-0.20	0.14	7.40	7.57	8.72	9.12
9500	2.5	0.0	-0.06	-0.13	0.68	10.10	10.21	12.29	12.69
9500	2.5	-0.5	-0.06	-0.14	0.48	10.22	10.32	12.54	12.94
9500	2.5	-1.0	-0.06	-0.14	0.38	10.28	10.37	12.71	13.09
9500	2.5	-1.5	-0.05	-0.14	0.27	10.32	10.42	12.83	13.23
9500	2.5	-2.0	-0.05	-0.14	0.21	10.37	10.47	12.94	13.35
9500	2.5	-2.5	-0.05	-0.14	0.18	10.40	10.51	13.01	13.44
9500	2.5	-3.0	-0.05	-0.14	0.15	10.42	10.53	13.05	13.49

Table A.1. (continued)

T_{eff} (1)	Log g (2)	[Fe/H] (3)	(B-V) (4)	(U-B) (5)	W_k (6)	WHδ (7)	WHγ (8)	H$\delta D_{0.2}$ (9)	H$\gamma D_{0.2}$ (10)
9500	3.0	0.0	-0.06	-0.08	0.80	13.41	13.37	17.37	17.69
9500	3.0	-0.5	-0.05	-0.08	0.57	13.56	13.54	17.68	18.04
9500	3.0	-1.0	-0.05	-0.08	0.44	13.64	13.62	17.89	18.25
9500	3.0	-1.5	-0.05	-0.09	0.30	13.69	13.67	18.04	18.42
9500	3.0	-2.0	-0.05	-0.09	0.23	13.77	13.74	18.19	18.58
9500	3.0	-2.5	-0.05	-0.08	0.19	13.82	13.80	18.30	18.70
9500	3.0	-3.0	-0.05	-0.08	0.16	13.85	13.83	18.34	18.76
9500	3.5	0.0	-0.04	-0.04	0.95	17.05	16.93	23.33	23.69
9500	3.5	-0.5	-0.03	-0.04	0.67	17.26	17.15	23.75	24.12
9500	3.5	-1.0	-0.03	-0.04	0.51	17.38	17.26	24.03	24.40
9500	3.5	-1.5	-0.03	-0.04	0.34	17.46	17.33	24.22	24.60
9500	3.5	-2.0	-0.03	-0.04	0.25	17.54	17.42	24.39	24.80
9500	3.5	-2.5	-0.03	-0.04	0.19	17.60	17.56	24.51	25.14
9500	3.5	-3.0	-0.03	-0.04	0.16	17.47	17.52	24.29	25.01
9500	4.0	0.0	0.00	-0.02	1.08	20.83	20.72	29.97	30.65
9500	4.0	-0.5	0.00	-0.01	0.76	21.15	20.87	30.58	30.95
9500	4.0	-1.0	0.00	-0.01	0.58	21.24	20.93	30.79	31.00
9500	4.0	-1.5	0.00	-0.01	0.38	21.31	21.01	30.99	31.23
9500	4.0	-2.0	0.00	-0.01	0.26	21.38	21.09	31.14	31.43
9500	4.0	-2.5	0.00	-0.01	0.20	21.23	21.15	30.97	31.57
9500	4.0	-3.0	0.00	-0.01	0.16	21.46	21.19	31.32	31.65
9500	4.5	0.0	0.03	-0.01	1.21	24.20	23.68	36.54	36.27
9500	4.5	-0.5	0.03	-0.01	0.85	24.30	23.94	36.73	36.94
9500	4.5	-1.0	0.03	-0.01	0.64	24.49	23.93	36.96	36.85
9500	4.5	-1.5	0.03	-0.01	0.42	24.56	24.00	37.12	37.03
9500	4.5	-2.0	0.03	-0.01	0.28	24.59	24.05	37.22	37.17
9500	4.5	-2.5	0.03	-0.01	0.20	24.61	24.12	37.29	37.35
9500	4.5	-3.0	0.03	-0.01	0.16	24.62	24.16	37.32	37.43
9500	5.0	0.0	0.07	-0.03	1.35	26.75	25.65	41.94	40.51
9500	5.0	-0.5	0.07	-0.03	0.95	26.53	25.74	41.26	40.76
9500	5.0	-1.0	0.07	-0.03	0.71	26.52	25.78	41.26	40.87
9500	5.0	-1.5	0.07	-0.03	0.46	26.53	25.78	41.30	40.92
9500	5.0	-2.0	0.07	-0.03	0.31	26.53	25.80	41.33	41.00
9500	5.0	-2.5	0.07	-0.03	0.21	26.53	25.88	41.36	41.19
9500	5.0	-3.0	0.07	-0.03	0.16	26.52	25.92	41.35	41.27

Table A.1. (continued)

T_{eff} (1)	Log g (2)	[Fe/H] (3)	(B-V) (4)	(U-B) (5)	W_k (6)	WHδ (7)	WHγ (8)	H$\delta D_{0.2}$ (9)	H$\gamma D_{0.2}$ (10)
9750	2.0	0.0	-0.06	-0.25	0.43	6.59	6.70	7.42	7.73
9750	2.0	-0.5	-0.05	-0.25	0.32	6.70	6.84	7.65	7.94
9750	2.0	-1.0	-0.05	-0.24	0.27	6.79	6.94	7.87	8.12
9750	2.0	-1.5	-0.05	-0.24	0.21	6.84	7.01	7.97	8.26
9750	2.0	-2.0	-0.05	-0.24	0.18	6.89	7.05	8.05	8.36
9750	2.0	-2.5	-0.05	-0.24	0.16	6.91	7.08	8.10	8.41
9750	2.0	-3.0	-0.05	-0.24	0.14	6.93	7.09	8.13	8.45
9750	2.5	0.0	-0.07	-0.18	0.53	9.43	9.49	11.38	11.68
9750	2.5	-0.5	-0.07	-0.18	0.38	9.52	9.61	11.58	11.95
9750	2.5	-1.0	-0.06	-0.18	0.31	9.59	9.66	11.75	12.09
9750	2.5	-1.5	-0.06	-0.18	0.23	9.65	9.73	11.89	12.26
9750	2.5	-2.0	-0.05	-0.18	0.19	9.69	9.79	11.99	12.39
9750	2.5	-2.5	-0.06	-0.17	0.16	9.73	9.82	12.06	12.47
9750	2.5	-3.0	-0.06	-0.17	0.14	9.75	9.85	12.10	12.51
9750	3.0	0.0	-0.07	-0.12	0.62	12.53	12.50	16.07	16.35
9750	3.0	-0.5	-0.06	-0.12	0.45	12.65	12.63	16.34	16.66
9750	3.0	-1.0	-0.06	-0.12	0.35	12.73	12.90	16.55	17.31
9750	3.0	-1.5	-0.06	-0.12	0.25	12.81	12.79	16.71	17.08
9750	3.0	-2.0	-0.06	-0.12	0.20	12.89	12.87	16.86	17.25
9750	3.0	-2.5	-0.06	-0.12	0.17	12.94	12.93	16.97	17.37
9750	3.0	-3.0	-0.05	-0.12	0.15	12.97	12.96	17.03	17.43
9750	3.5	0.0	-0.05	-0.08	0.73	16.43	15.99	22.50	22.14
9750	3.5	-0.5	-0.05	-0.08	0.52	16.26	16.17	22.16	22.54
9750	3.5	-1.0	-0.04	-0.08	0.40	16.36	16.28	22.42	22.82
9750	3.5	-1.5	-0.04	-0.08	0.28	16.40	16.37	22.55	23.05
9750	3.5	-2.0	-0.04	-0.08	0.21	16.56	16.47	22.84	23.26
9750	3.5	-2.5	-0.04	-0.08	0.18	16.63	16.55	22.97	23.41
9750	3.5	-3.0	-0.04	-0.08	0.15	16.67	16.59	23.04	23.49
9750	4.0	0.0	-0.02	-0.05	0.86	19.99	19.79	28.52	28.86
9750	4.0	-0.5	-0.02	-0.05	0.60	20.22	19.99	28.99	29.30
9750	4.0	-1.0	-0.02	-0.05	0.46	20.36	20.13	29.31	29.63
9750	4.0	-1.5	-0.02	-0.05	0.31	20.41	20.20	29.54	29.92
9750	4.0	-2.0	-0.02	-0.05	0.23	20.55	20.33	29.74	30.12
9750	4.0	-2.5	-0.01	-0.05	0.18	20.62	20.42	29.87	30.29
9750	4.0	-3.0	-0.01	-0.04	0.15	20.65	20.32	29.94	30.18

Table A.1. (continued)

T_{eff} (1)	Log g (2)	[Fe/H] (3)	(B-V) (4)	(U-B) (5)	W_k (6)	WHδ (7)	WHγ (8)	H$\delta D_{0.2}$ (9)	H$\gamma D_{0.2}$ (10)
9750	4.5	0.0	0.01	-0.04	0.99	23.77	23.31	35.52	35.55
9750	4.5	-0.5	0.01	-0.03	0.69	23.98	23.50	35.95	35.97
9750	4.5	-1.0	0.01	-0.03	0.53	24.11	23.63	36.25	36.27
9750	4.5	-1.5	0.02	-0.03	0.35	24.19	23.72	36.45	36.52
9750	4.5	-2.0	0.02	-0.03	0.24	23.87	23.79	35.96	36.71
9750	4.5	-2.5	0.02	-0.03	0.19	24.29	23.87	36.68	36.88
9750	4.5	-3.0	0.02	-0.03	0.15	23.90	23.92	36.02	36.97
9750	5.0	0.0	0.05	-0.05	1.12	26.50	25.84	41.33	40.83
9750	5.0	-0.5	0.05	-0.05	0.78	26.80	26.01	41.69	41.23
9750	5.0	-1.0	0.05	-0.04	0.60	26.80	26.05	41.72	41.35
9750	5.0	-1.5	0.05	-0.04	0.39	26.82	25.90	41.80	41.32
9750	5.0	-2.0	0.05	-0.04	0.26	26.85	26.18	41.88	41.72
9750	5.0	-2.5	0.05	-0.04	0.19	26.36	26.24	41.06	41.85
9750	5.0	-3.0	0.05	-0.04	0.15	26.86	26.27	41.94	41.93
10000	2.0	0.0	-0.06	-0.29	0.35	6.19	6.29	6.92	7.18
10000	2.0	-0.5	-0.06	-0.28	0.27	6.30	6.43	7.14	7.42
10000	2.0	-1.0	-0.06	-0.28	0.23	6.40	6.54	7.32	7.66
10000	2.0	-1.5	-0.05	-0.28	0.19	6.46	6.61	7.45	7.78
10000	2.0	-2.0	-0.05	-0.28	0.17	6.51	6.66	7.55	7.86
10000	2.0	-2.5	-0.05	-0.27	0.15	6.53	6.68	7.60	7.92
10000	2.0	-3.0	-0.05	-0.27	0.13	6.55	6.69	7.64	7.95
10000	2.5	0.0	-0.08	-0.22	0.42	8.88	8.90	10.65	10.85
10000	2.5	-0.5	-0.07	-0.22	0.32	8.97	9.00	10.85	11.09
10000	2.5	-1.0	-0.07	-0.22	0.26	9.04	9.08	11.04	11.31
10000	2.5	-1.5	-0.07	-0.21	0.21	9.11	9.16	11.18	11.49
10000	2.5	-2.0	-0.07	-0.21	0.17	9.16	9.23	11.28	11.61
10000	2.5	-2.5	-0.06	-0.21	0.15	9.19	9.27	11.35	11.70
10000	2.5	-3.0	-0.06	-0.21	0.13	9.21	9.28	11.39	11.75
10000	3.0	0.0	-0.08	-0.16	0.50	11.77	11.72	14.98	15.20
10000	3.0	-0.5	-0.07	-0.16	0.36	11.88	11.84	15.23	15.50
10000	3.0	-1.0	-0.07	-0.16	0.29	11.96	11.93	15.45	15.74
10000	3.0	-1.5	-0.06	-0.16	0.22	12.05	12.04	15.64	15.97
10000	3.0	-2.0	-0.06	-0.16	0.18	12.14	12.13	15.79	16.14
10000	3.0	-2.5	-0.06	-0.16	0.16	12.19	12.18	15.89	16.24
10000	3.0	-3.0	-0.06	-0.16	0.14	12.22	12.21	15.94	16.30

Table A.1. (continued)

T_{eff} (1)	Log g (2)	[Fe/H] (3)	(B-V) (4)	(U-B) (5)	W_k (6)	WHδ (7)	WHγ (8)	H$\delta D_{0.2}$ (9)	H$\gamma D_{0.2}$ (10)
10000	3.5	0.0	-0.06	-0.12	0.58	15.17	14.98	20.38	20.60
10000	3.5	-0.5	-0.06	-0.12	0.42	15.31	15.23	20.71	21.04
10000	3.5	-1.0	-0.05	-0.12	0.33	15.78	15.34	21.69	21.34
10000	3.5	-1.5	-0.05	-0.12	0.24	15.53	15.47	21.21	21.62
10000	3.5	-2.0	-0.05	-0.11	0.19	15.65	15.58	21.42	21.85
10000	3.5	-2.5	-0.05	-0.11	0.16	15.72	15.66	21.55	21.98
10000	3.5	-3.0	-0.05	-0.11	0.14	15.75	15.70	21.62	22.06
10000	4.0	0.0	-0.04	-0.08	0.67	19.09	18.91	27.00	27.34
10000	4.0	-0.5	-0.03	-0.08	0.49	19.27	19.09	27.41	27.77
10000	4.0	-1.0	-0.03	-0.08	0.38	19.41	19.23	27.74	28.11
10000	4.0	-1.5	-0.03	-0.08	0.27	19.53	19.36	28.02	28.43
10000	4.0	-2.0	-0.03	-0.08	0.20	19.65	19.49	28.23	28.69
10000	4.0	-2.5	-0.03	-0.08	0.17	19.72	19.58	28.37	28.86
10000	4.0	-3.0	-0.03	-0.08	0.14	19.56	19.63	28.13	28.95
10000	4.5	0.0	-0.01	-0.07	0.80	23.14	22.72	34.36	34.46
10000	4.5	-0.5	0.00	-0.06	0.56	23.34	22.93	34.80	34.93
10000	4.5	-1.0	0.00	-0.06	0.44	23.47	23.08	35.12	35.29
10000	4.5	-1.5	0.00	-0.06	0.30	23.57	23.20	35.37	35.60
10000	4.5	-2.0	0.00	-0.06	0.22	23.49	22.90	35.32	35.20
10000	4.5	-2.5	0.00	-0.06	0.17	23.50	23.19	35.35	35.73
10000	4.5	-3.0	0.00	-0.06	0.14	23.75	23.44	35.72	36.12
10000	5.0	0.0	0.03	-0.07	0.93	26.50	25.49	41.04	40.19
10000	5.0	-0.5	0.04	-0.06	0.65	26.65	25.93	41.37	41.05
10000	5.0	-1.0	0.04	-0.06	0.50	26.75	26.05	41.62	41.34
10000	5.0	-1.5	0.04	-0.06	0.33	26.21	26.16	40.70	41.64
10000	5.0	-2.0	0.04	-0.06	0.23	26.26	26.25	40.75	41.86
10000	5.0	-2.5	0.04	-0.06	0.17	26.27	26.33	40.78	42.03
10000	5.0	-3.0	0.04	-0.06	0.14	26.87	26.35	41.95	42.08

Table A.2 Observable Weightings

T_{eff} (1)	Log g (2)	B-V(T_{eff}) (3)	B-V(Log g) (4)	U-B(T_{eff}) (5)	U-B(Log g) (6)	$D_{0.2}$(T_{eff}) (7)	$D_{0.2}$(Log g) (8)
6000	2.0	0.29	0.00	0.07	0.21	0.36	0.07
6000	2.5	0.29	0.00	0.07	0.21	0.36	0.07
6000	3.0	0.29	0.00	0.07	0.21	0.36	0.07
6000	3.5	0.23	0.00	0.08	0.23	0.38	0.08
6000	4.0	0.23	0.00	0.08	0.23	0.38	0.08
6000	4.5	0.23	0.00	0.08	0.23	0.38	0.08
6000	5.0	0.23	0.00	0.08	0.23	0.38	0.08
6250	2.0	0.29	0.00	0.07	0.21	0.36	0.07
6250	2.5	0.29	0.00	0.07	0.21	0.36	0.07
6250	3.0	0.29	0.00	0.07	0.21	0.36	0.07
6250	3.5	0.23	0.00	0.08	0.23	0.38	0.08
6250	4.0	0.23	0.00	0.08	0.23	0.38	0.08
6250	4.5	0.23	0.00	0.08	0.23	0.38	0.08
6250	5.0	0.23	0.00	0.08	0.23	0.38	0.08
6500	2.0	0.22	0.11	0.17	0.17	0.28	0.06
6500	2.5	0.22	0.11	0.17	0.17	0.28	0.06
6500	3.0	0.22	0.11	0.17	0.17	0.28	0.06
6500	3.5	0.20	0.13	0.07	0.20	0.33	0.07
6500	4.0	0.20	0.13	0.07	0.20	0.33	0.07
6500	4.5	0.20	0.13	0.07	0.20	0.33	0.07
6500	5.0	0.20	0.13	0.07	0.20	0.33	0.07
6750	2.0	0.21	0.11	0.16	0.21	0.26	0.05
6750	2.5	0.21	0.11	0.16	0.21	0.26	0.05
6750	3.0	0.21	0.11	0.16	0.21	0.26	0.05
6750	3.5	0.17	0.11	0.17	0.22	0.28	0.06
6750	4.0	0.17	0.11	0.17	0.22	0.28	0.06
6750	4.5	0.19	0.13	0.06	0.25	0.31	0.06
6750	5.0	0.19	0.13	0.06	0.25	0.31	0.06
7000	2.0	0.21	0.11	0.16	0.21	0.26	0.05
7000	2.5	0.21	0.11	0.16	0.21	0.26	0.05
7000	3.0	0.21	0.11	0.16	0.21	0.26	0.05
7000	3.5	0.17	0.11	0.17	0.22	0.28	0.06
7000	4.0	0.17	0.11	0.17	0.22	0.28	0.06
7000	4.5	0.19	0.13	0.06	0.25	0.31	0.06
7000	5.0	0.19	0.13	0.06	0.25	0.31	0.06

Table A.2 (continued)

T_{eff} (1)	Log g (2)	B-V(T_{eff}) (3)	B-V(Log g) (4)	U-B(T_{eff}) (5)	U-B(Log g) (6)	$D_{0.2}$(T_{eff}) (7)	$D_{0.2}$(Log g) (8)
7250	2.0	0.21	0.11	0.16	0.21	0.26	0.05
7250	2.5	0.21	0.11	0.16	0.21	0.26	0.05
7250	3.0	0.21	0.11	0.16	0.21	0.26	0.05
7250	3.5	0.17	0.11	0.17	0.22	0.28	0.06
7250	4.0	0.17	0.11	0.17	0.22	0.28	0.06
7250	4.5	0.17	0.11	0.17	0.22	0.28	0.06
7250	5.0	0.17	0.11	0.17	0.22	0.28	0.06
7500	2.0	0.31	0.15	0.08	0.31	0.08	0.08
7500	2.5	0.31	0.15	0.08	0.31	0.08	0.08
7500	3.0	0.31	0.15	0.08	0.31	0.08	0.08
7500	3.5	0.17	0.11	0.17	0.22	0.28	0.06
7500	4.0	0.17	0.11	0.17	0.22	0.28	0.06
7500	4.5	0.17	0.11	0.17	0.22	0.28	0.06
7500	5.0	0.17	0.11	0.17	0.22	0.28	0.06
7750	2.0	0.31	0.15	0.08	0.31	0.08	0.08
7750	2.5	0.31	0.15	0.08	0.31	0.08	0.08
7750	3.0	0.31	0.15	0.08	0.31	0.08	0.08
7750	3.5	0.17	0.11	0.17	0.22	0.28	0.06
7750	4.0	0.17	0.11	0.17	0.22	0.28	0.06
7750	4.5	0.17	0.11	0.17	0.22	0.28	0.06
7750	5.0	0.17	0.11	0.17	0.22	0.28	0.06
8000	2.0	0.33	0.17	0.08	0.17	0.08	0.17
8000	2.5	0.33	0.17	0.08	0.17	0.08	0.17
8000	3.0	0.33	0.17	0.08	0.17	0.08	0.17
8000	3.5	0.20	0.13	0.07	0.13	0.33	0.13
8000	4.0	0.20	0.13	0.07	0.13	0.33	0.13
8000	4.5	0.18	0.12	0.18	0.12	0.29	0.12
8000	5.0	0.18	0.12	0.18	0.12	0.29	0.12
8250	2.0	0.31	0.15	0.15	0.15	0.08	0.15
8250	2.5	0.31	0.15	0.15	0.15	0.08	0.15
8250	3.0	0.31	0.15	0.15	0.15	0.08	0.15
8250	3.5	0.20	0.13	0.07	0.13	0.33	0.13
8250	4.0	0.20	0.13	0.07	0.13	0.33	0.13
8250	4.5	0.18	0.12	0.18	0.12	0.29	0.12
8250	5.0	0.18	0.12	0.18	0.12	0.29	0.12

Table A.2 (continued)

T_{eff} (1)	Log g (2)	B-V(T_{eff}) (3)	B-V(Log g) (4)	U-B(T_{eff}) (5)	U-B(Log g) (6)	$D_{0.2}$(T_{eff}) (7)	$D_{0.2}$(Log g) (8)
8500	2.0	0.24	0.12	0.12	0.12	0.18	0.24
8500	2.5	0.24	0.12	0.12	0.12	0.18	0.24
8500	3.0	0.24	0.12	0.12	0.12	0.18	0.24
8500	3.5	0.18	0.12	0.06	0.12	0.29	0.24
8500	4.0	0.18	0.12	0.06	0.12	0.29	0.24
8500	4.5	0.16	0.11	0.16	0.11	0.26	0.21
8500	5.0	0.16	0.11	0.16	0.11	0.26	0.21
8750	2.0	0.25	0.13	0.13	0.06	0.19	0.25
8750	2.5	0.25	0.13	0.13	0.06	0.19	0.25
8750	3.0	0.25	0.13	0.13	0.06	0.19	0.25
8750	3.5	0.18	0.12	0.12	0.06	0.29	0.24
8750	4.0	0.18	0.12	0.12	0.06	0.29	0.24
8750	4.5	0.19	0.13	0.06	0.06	0.31	0.25
8750	5.0	0.19	0.13	0.06	0.06	0.31	0.25
9000	2.0	0.25	0.13	0.13	0.06	0.19	0.25
9000	2.5	0.25	0.13	0.13	0.06	0.19	0.25
9000	3.0	0.25	0.13	0.13	0.06	0.19	0.25
9000	3.5	0.18	0.12	0.12	0.06	0.29	0.24
9000	4.0	0.18	0.12	0.12	0.06	0.29	0.24
9000	4.5	0.19	0.13	0.06	0.06	0.31	0.25
9000	5.0	0.19	0.13	0.06	0.06	0.31	0.25
9250	2.0	0.25	0.13	0.13	0.06	0.19	0.25
9250	2.5	0.25	0.13	0.13	0.06	0.19	0.25
9250	3.0	0.25	0.13	0.13	0.06	0.19	0.25
9250	3.5	0.23	0.15	0.15	0.08	0.08	0.31
9250	4.0	0.23	0.15	0.15	0.08	0.08	0.31
9250	4.5	0.23	0.15	0.15	0.08	0.08	0.31
9250	5.0	0.23	0.15	0.15	0.08	0.08	0.31
9500	2.0	0.25	0.13	0.13	0.06	0.19	0.25
9500	2.5	0.25	0.13	0.13	0.06	0.19	0.25
9500	3.0	0.25	0.13	0.13	0.06	0.19	0.25
9500	3.5	0.23	0.15	0.15	0.08	0.08	0.31
9500	4.0	0.23	0.15	0.15	0.08	0.08	0.31
9500	4.5	0.23	0.15	0.15	0.08	0.08	0.31
9500	5.0	0.23	0.15	0.15	0.08	0.08	0.31

Table A.2 (continued)

T_{eff} (1)	Log g (2)	B-V(T_{eff}) (3)	B-V(Log g) (4)	U-B(T_{eff}) (5)	U-B(Log g) (6)	$D_{0.2}$(T_{eff}) (7)	$D_{0.2}$(Log g) (8)
9750	2.0	0.25	0.13	0.13	0.06	0.19	0.25
9750	2.5	0.25	0.13	0.13	0.06	0.19	0.25
9750	3.0	0.25	0.13	0.13	0.06	0.19	0.25
9750	3.5	0.23	0.15	0.15	0.08	0.08	0.31
9750	4.0	0.23	0.15	0.15	0.08	0.08	0.31
9750	4.5	0.23	0.15	0.15	0.08	0.08	0.31
9750	5.0	0.23	0.15	0.15	0.08	0.08	0.31
10000	2.0	0.25	0.13	0.13	0.06	0.19	0.25
10000	2.5	0.25	0.13	0.13	0.06	0.19	0.25
10000	3.0	0.25	0.13	0.13	0.06	0.19	0.25
10000	3.5	0.23	0.15	0.15	0.08	0.08	0.31
10000	4.0	0.23	0.15	0.15	0.08	0.08	0.31
10000	4.5	0.23	0.15	0.15	0.08	0.08	0.31
10000	5.0	0.23	0.15	0.15	0.08	0.08	0.31

APPENDIX B

Table B.1. The FHB Sample.

Star (1)	RA (1950) (2)	Dec (3)	l (4)	b (5)	V (6)	$(B-V)_o$ (7)	$(U-B)_o$ (8)	W_λ (9)	Hδ $D_{0.2}$ (10)	Hγ $D_{0.2}$ (11)	T_{eff} (12)	Log g (13)	[Fe/H] (14)	V_{hel} (15)	Dist (16)	Z (17)	Class (18)	Obs (19)
BS 15621-9	10 25 13.4	+27 47 58	203.8	58.3	13.93	0.28	0.02	3.6	16.8	15.1	7016	3.0	-1.5	29	4.6	3.9	FHB	KL
BS 15621-15	10 23 33.6	+23 45 53	211.0	57.1	12.27	0.14	0.15	1.6	21.6	20.3	7668	2.7	-2.2	167	2.1	1.8	FHB	KL
BS 15621-22	10 19 7.1	+24 6 6	210.0	56.2	12.88	0.29	0.00	4.4	17.1	15.4	7187	3.1	-1.1	-5	2.9	2.4	FHB	K
BS 15621-25	10 18 31.0	+24 6 52	209.9	56.1	15.17	0.04	0.06	...	25.4	21.7	8400	3.0	-2.0	40	7.2	6.0	FHB	L
BS 15621-31	10 16 50.7	+26 38 11	205.3	56.2	14.49	0.27	0.11	...	18.0	13.8	7169	2.7	-1.9	-148	6.0	5.0	FHB	L
BS 15621-37	10 13 17.5	+24 59 15	207.9	55.1	11.69	0.20	0.02	2.1	19.2	15.8	7481	3.2	-1.5	255	1.7	1.4	FHB	EL
BS 15621-39	10 11 2.6	+25 33 18	206.8	54.8	13.60	0.06	0.13	...	21.7	21.4	9750	2.0	0.0	131	3.6	2.9	FHB	L
BS 15621-43	10 6 38.9	+25 4 50	207.2	53.7	14.41	0.05	0.07	...	22.9	23.7	8692	3.0	-3.0	67	5.1	4.1	FHB	L
BS 15621-51	10 14 32.8	+23 18 16	210.9	55.0	13.97	0.45	0.09	4.4	9.1	9.2	6712	2.6	-1.3	368	4.7	3.9	FHB	K
BS 15621-54	10 21 4.3	+24 10 40	210.1	56.7	13.80	0.36	-0.04	0.0	7.4	6.1	6546	3.0	-1.1	9	4.4	3.6	FHB	E
BS 15623-1	14 6 11.8	+23 35 2	24.9	72.2	13.75	0.14	0.19	...	21.5	19.3	7738	2.9	-3.0	-159	4.1	3.9	FHB	L
BS 15625-7	11 46 12.3	+26 12 2	214.3	75.9	14.55	0.01	0.17	...	26.3	23.0	8332	3.0	-1.9	-77	5.1	5.0	FHB	L
BS 15625-13	11 54 23.9	+27 39 29	208.6	77.9	14.00	0.15	0.12	2.2	18.8	19.7	7378	2.6	-1.9	-47	4.7	4.6	FHB	EL
BS 15625-16	11 54 0.8	+25 10 16	220.1	77.5	14.41	0.00	0.07	...	25.7	20.0	8575	3.0	-3.0	238	4.7	4.6	FHB	L
BS 15625-26	11 49 14.9	+26 38 37	212.8	76.7	11.03	0.28	0.07	5.4	17.2	15.5	7248	3.2	-0.5	-5	1.2	1.2	FHB	EK
BS 15625-27	11 53 7.6	+23 16 39	228.0	76.7	11.51	0.28	0.04	5.2	14.2	12.9	7019	2.9	-0.9	-8	1.5	1.5	FHB	EK
BS 16026-8	12 15 35.0	+30 34 4	187.6	82.0	14.71	0.09	0.15	...	25.4	25.2	8045	3.1	-1.8	-61	6.2	6.1	FHB	LL
BS 16026-11	12 14 18.8	+29 12 43	197.6	82.2	13.46	0.10	0.13	1.4	23.0	23.3	7807	2.9	-1.8	19	3.5	3.5	FHB	KLL
BS 16026-26	12 19 32.9	+28 20 36	203.0	83.4	13.96	0.03	-0.05	...	21.9	23.5	8887	3.0	-1.9	23	4.1	4.0	FHB	LL
BS 16026-28	12 20 32.4	+27 43 53	208.3	83.7	13.65	0.01	0.06	...	23.6	22.5	8735	3.0	-3.0	-81	3.4	3.4	FHB	L
BS 16026-41	12 28 42.4	+31 8 1	171.6	84.2	14.02	0.10	0.12	...	24.8	24.3	8015	3.0	-3.0	-205	4.5	4.5	FHB	L
BS 16026-69	12 34 5.7	+32 20 2	155.3	84.1	14.45	0.21	-0.03	...	17.6	15.4	7255	3.0	-1.2	-95	5.9	5.9	FHB	L
BS 16027-1	13 3 52.2	+32 58 21	93.9	83.6	12.81	0.34	-0.01	5.2	12.3	13.0	6757	2.6	-0.8	19	2.8	2.7	FHB	K
BS 16027-24	13 6 55.3	+28 37 59	51.4	85.9	14.54	0.55	0.05	7.0	3.9	3.3	6000	2.5	-1.4	52	6.1	6.1	FHB	K
BS 16027-34	13 6 10.0	+32 59 37	90.5	83.3	14.03	0.12	0.16	...	23.8	23.1	7815	3.0	-3.0	4	4.6	4.6	FHB	L
BS 16027-38	13 8 28.2	+32 44 11	85.9	83.2	11.74	-0.01	0.06	...	24.2	23.9	8700	3.0	-2.7	-118	1.4	1.3	FHB	L
BS 16027-41	13 9 8.7	+32 3 1	81.0	83.6	14.70	0.08	0.14	...	21.8	18.5	7770	2.5	-2.6	-243	6.1	6.0	FHB	L
BS 16027-49	13 10 5.2	+30 37 10	69.2	84.4	13.40	0.41	0.03	3.9	8.1	7.7	6493	2.4	-1.6	57	3.6	3.6	FHB	K
BS 16027-50	13 10 48.9	+31 0 53	71.5	84.0	14.20	0.03	0.11	...	70.6	23.3	8271	3.1	-2.3	-52	4.5	4.5	FHB	L
BS 16027-51	13 10 40.6	+31 17 21	73.8	83.9	15.20	0.23	0.08	...	16.7	16.8	7253	3.0	-2.3	39	8.3	8.3	FHB	L
BS 16027-57	13 13 53.3	+32 12 41	76.2	82.8	14.60	0.01	0.05	...	21.9	23.7	8878	3.0	-2.4	-57	5.3	5.2	FHB	L

Table B.1. (continued)

Star (1)	RA (1950) (2)	Dec (3)	l (4)	b (5)	V (6)	$(B-V)_o$ (7)	$(U-B)_o$ (8)	W_k (9)	Hδ $D_{0.2}$ (10)	Hγ $D_{0.2}$ (11)	T_{eff} (12)	Log g (13)	[Fe/H] (14)	V_{los} (15)	Dist. (16)	Z (17)	Class (18)	Obs (19)
BS 16032-7	12 35 31.3	+30 14 48	168.2	85.9	14.67	0.32	0.09	...	15.3	13.7	7011	2.6	-1.5	-160	6.5	6.5	FHB	L
BS 16032-8	12 36 50.9	+29 54 21	169.1	86.3	13.70	0.07	0.16	...	27.0	22.3	8195	3.2	-2.4	48	3.8	3.8	FHB	L
BS 16032-19	12 42 16.5	+32 46 19	137.7	84.4	12.72	0.17	0.09	...	20.7	17.5	7510	3.0	-2.6	-25	2.6	2.6	FHB	L
CS 22166-5	0 50 13.8	-11 17 35	124.1	-73.9	14.26	-0.02	-0.13	0.4	26.3	26.3	8656	3.0	-3.0	-20	4.2	-4.0	FHB	K
CS 22166-32	1 5 4.2	-12 27 2	137.9	-74.6	13.25	0.12	0.15	0.8	23.3	22.6	7781	3.0	-3.0	-128	3.2	-3.1	FHB	K
CS 22167-1	3 9 14.5	-6 35 16	187.5	-50.8	15.00	0.02	0.11	...	24.3	22.6	8491	3.0	-2.2	155	6.5	-5.0	FHB	L
CS 22167-3	3 8 33.6	-4 33 60	184.8	-49.7	12.99	0.21	0.09	...	16.5	21.4	7257	3.0	-0.6	48	3.0	-2.3	FHB	L
CS 22167-5	3 9 27.3	-3 59 42	184.3	-49.2	13.95	0.37	0.03	...	7.8	8.7	6725	3.1	-1.1	-120	4.7	-3.5	FHB	L
CS 22167 6	3 11 0.2	-5 57 3	187.1	-50.0	12.50	0.17	0.12	...	18.4	19.9	7499	3.0	-1.4	176	2.4	-1.8	FHB	L
CS 22167-8	3 14 0.9	-7 17 46	189.5	-50.2	15.41	-0.02	-0.21	0.8	15.2	16.7	9264	2.5	-0.6	14	7.1	-5.5	FHB	K
CS 22167-17	3 16 15.3	-3 49 43	185.7	-47.7	13.49	0.00	0.06	0.5	25.4	24.3	8647	3.1	-2.8	198	3.1	-2.3	FHB	K
CS 22167-30	3 21 58.3	-3 37 33	186.8	-46.5	14.77	-0.02	0.02	1.8	21.4	27.7	8925	3.0	-3.0	50	5.3	-3.9	FHB	K
CS 22169-25	4 13 47.5	-14 41 26	208.9	-40.9	14.15	0.32	0.08	2.9	10.6	9.5	6500	2.0	-2.1	10	5.1	-3.4	FHB	H
CS 22170-2	0 32 6.0	-10 45 22	108.8	-72.9	14.05	0.08	0.15	...	25.1	26.6	8053	3.0	-2.6	-270	4.5	-4.3	FHB	L
CS 22170-3	0 30 14.0	-10 3 1	107.8	-72.1	13.68	-0.05	-0.11	...	19.2	18.0	9516	3.0	-2.3	-62	3.0	-2.9	FHB	L
CS 22170 9	0 38 21.3	-10 35 58	114.0	-73.0	13.97	0.03	0.12	...	25.0	25.6	8304	3.0	-1.7	-125	4.1	-3.9	FHB	L
CS 22170-13	0 38 49.1	-8 39 46	115.2	-71.1	13.18	-0.03	-0.10	...	19.6	21.6	9327	3.0	-2.0	-7	2.5	-2.4	FHB	L
CS 22170-15	0 40 29.7	-8 31 36	116.5	-71.0	13.97	0.30	0.11	...	13.6	12.2	7019	2.9	-0.1	-22	4.7	-4.5	FHB	L
CS 22170-24	0 41 16.1	-11 38 40	116.1	-74.1	15.03	0.11	0.18	...	20.8	23.1	7731	2.5	-2.1	81	7.3	-7.0	FHB	L
CS 22170-32	0 45 23.5	-10 32 44	119.9	-73.1	15.51	0.08	0.20	...	20.9	27.8	7823	2.5	-3.0	-102	8.8	-8.4	FHB	L
CS 22171-5	1 54 11.6	-11 48 21	170.6	-68.2	13.73	0.26	0.02	3.4	16.6	14.6	7148	3.1	-1.2	-21	4.2	-3.9	FHB	H
CS 22171-22	2 0 42.9	-8 27 34	168.2	-64.6	12.85	0.07	0.19	0.6	23.5	24.1	8137	3.0	-2.7	-210	2.6	-2.3	FHB	EK
CS 22172-14	3 18 59.1	-11 26 16	196.1	-51.4	14.63	0.34	0.01	3.7	14.3	12.6	7000	3.0	-1.4	17	6.4	-6.0	FHB	H
CS 22172-26	3 27 40.4	-11 23 26	197.6	-49.5	14.71	0.33	0.09	1.4	16.8	14.8	7073	2.5	-2.3	-14	6.6	-6.0	FHB	H
CS 22173-17	4 6 11.7	-17 9 40	211.0	-43.5	12.68	0.25	0.14	1.9	17.7	15.5	7212	2.5	-2.1	44	2.6	-1.8	FHB	H
CS 22173-36	4 11 42.6	-18 6 11	212.9	-42.7	13.58	0.22	0.14	1.5	23.5	20.4	7715	3.2	-1.8	7	3.9	-2.7	FHB	H
CS 22174-34	1 22 54.9	-9 51 54	149.1	-70.7	13.40	0.07	0.19	0.5	25.2	22.8	8167	3.0	-3.0	37	3.3	-3.1	FHB	K

Table B.1. (continued)

Star (1)	RA (1950) (2)	Dec (3)	l (4)	b (5)	V (6)	$(B-V)_o$ (7)	$(U-B)_o$ (8)	W_k (9)	$H\delta$ $D_{0.2}$ (10)	$H\gamma$ $D_{0.2}$ (11)	T_{eff} (12)	Log g (13)	[Fe/H] (14)	V_{los} (15)	Dist. (16)	Z (17)	Class (18)	Obs (19)
CS 22174-42	1 27 50.0	-10 0 25	152.6	-70.3	12.43	-0.01	-0.02	0.3	21.2	22.4	9005	3.0	-1.9	7	1.9	-1.8	FHB	K
CS 22175-1	2 11 3.9	-11 51 36	178.1	-65.3	12.85	0.06	0.15	1.2	25.8	22.2	8169	3.0	-1.9	67	2.5	-2.3	FHB	E
CS 22175-3	2 13 5.4	-10 54 23	177.2	-64.3	13.67	0.11	0.15	1.9	21.0	23.5	7748	2.5	-1.6	16	3.9	-3.5	FHB	E
CS 22175-12	2 17 39.9	-8 21 57	174.9	-61.7	12.71	0.22	0.04	2.5	16.7	21.0	7238	3.1	-1.8	-10	2.6	-2.3	FHB	E
CS 22175-24	2 26 51.9	-10 37 49	181.7	-61.5	14.35	0.11	0.15	0.8	24.9	22.5	7977	3.2	-2.4	-115	5.3	-4.7	FHB	E
CS 22176-8	3 36 15.5	-7 58 48	194.9	-46.0	11.93	0.09	0.12	0.4	26.0	25.1	8098	3.1	-3.0	123	1.7	-1.2	FHB	E
CS 22179-6	0 32 40.4	-4 31 29	112.6	-66.8	13.04	0.23	0.08	...	15.6	12.5	7021	2.5	-2.2	-252	3.1	-2.8	FHB	L
CS 22179-11	0 37 3.3	-4 52 8	115.3	-67.3	13.00	0.21	0.13	...	16.2	1.1	7212	2.6	-2.0	-110	3.0	-2.8	FHB	L
CS 22179-13	0 36 23.5	-6 5 48	114.4	-68.5	14.75	0.01	0.08	...	22.5	24.3	8739	3.0	-1.7	-211	5.6	-5.2	FHB	L
CS 22179-14	0 35 18.2	-6 54 20	113.4	-69.2	14.45	0.16	0.16	...	22.3	6.7	7723	3.0	-0.9	-53	5.8	-5.4	FHB	L
CS 22179-19	0 40 1.6	-5 16 54	117.1	-67.8	13.77	0.14	0.18	...	22.8	19.7	7749	3.0	-1.7	0	4.2	-3.9	FHB	L
CS 22179-20	0 41 56.9	-4 40 12	118.5	-67.2	13.89	0.13	0.15	...	19.9	91.3	7505	2.5	-3.0	-196	4.4	-4.0	FHB	L
CS 22179-21	0 39 12.6	-3 16 54	117.0	-65.8	14.31	0.11	0.16	...	14.6	11.2	7250	2.0	-1.9	-34	5.2	-4.8	FHB	L
CS 22179-22	0 40 29.6	-3 20 60	117.8	-65.9	15.22	0.12	0.13	...	21.0	18.1	7563	2.5	-3.0	-129	8.0	-7.3	FHB	L
CS 22180-3	1 28 17.2	-10 41 21	153.8	-70.9	13.91	0.10	0.16	0.6	22.4	22.9	7753	2.6	-3.0	79	4.3	-4.1	FHB	E
CS 22180-6	1 32 50.8	-10 48 39	157.0	-70.5	14.14	0.09	0.17	1.1	22.8	22.3	7860	2.8	-2.1	47	4.7	-4.5	FHB	E
CS 22180-17	1 34 22.0	-12 16 9	160.3	-71.5	13.19	0.10	0.16	1.5	22.2	19.1	7755	2.6	-2.0	34	3.1	-2.9	FHB	E
CS 22181-12	2 58 49.3	-11 11 29	191.4	-55.5	13.46	0.33	0.06	2.1	17.2	13.7	7212	2.9	-2.0	-31	3.7	-3.1	FHB	E
CS 22183-10	0 47 56.6	-3 23 36	122.4	-66.0	13.61	0.05	0.14	0.8	26.6	27.9	8221	3.1	-2.4	-72	3.6	-3.2	FHB	E
CS 22183-11	0 50 23.2	-3 8 59	123.8	-65.7	12.42	0.09	0.15	1.9	22.4	22.5	7769	2.6	-1.9	-126	2.2	-2.0	FHB	E
CS 22183-14	0 57 42.3	-2 33 38	128.2	-65.1	14.08	-0.01	0.05	0.0	23.1	22.5	8781	3.0	-3.0	85	4.0	-3.6	FHB	E
CS 22183-24	1 0 21.0	-5 0 60	130.4	-67.5	11.80	0.01	0.03	0.4	24.3	24.2	8701	3.0	-2.2	-100	1.4	-1.3	FHB	E
CS 22183-28	0 59 36.1	-7 18 41	130.6	-69.8	13.87	0.10	0.17	1.5	21.6	26.3	7760	2.5	-2.1	-50	4.2	-4.0	FHB	E
CS 22184-19	2 38 17.8	-12 3 54	187.5	-60.2	13.87	0.14	0.15	4.7	11.7	12.8	7000	2.0	-1.1	110	4.4	-3.8	FHB	E
CS 22184-33	2 40 56.9	-12 18 4	188.6	-59.8	13.72	0.30	-0.01	3.7	13.6	12.1	7002	3.0	-1.4	-135	4.2	-3.6	FHB	H
CS 22185-14	3 20 9.5	-13 25 27	199.1	-52.1	14.63	-0.04	-0.08	0.6	20.1	23.6	9270	3.0	-2.1	13	4.7	-3.7	FHB	E
CS 22185-20	3 25 26.7	-14 17 8	201.3	-51.4	12.50	0.15	0.15	1.8	20.2	19.8	7503	2.7	-2.1	24	2.3	-1.8	FHB	E

Table B.1. (continued)

Star (1)	RA (1950) (2)	Dec (3)	l (4)	b (5)	V (6)	$(B-V)_o$ (7)	$(U-B)_o$ (8)	W_k (9)	$H\delta$ $D_{0.2}$ (10)	$H\gamma$ $D_{0.2}$ (11)	T_{eff} (12)	Log g (13)	[Fe/H] (14)	V_{los} (15)	Dist. (16)	Z (17)	Class (18)	Obs (19)
CS 22186-34	4 21 56.6	-33 34 19	234.4	-44.2	14.10	0.34	-0.04	3.1	13.1	11.6	6707	2.7	-1.5	-135	5.0	-3.5	FHB	H
CS 22189-5	2 30 6.2	-14 44 60	189.9	-63.3	14.12	0.29	0.06	2.5	17.3	15.2	7213	3.1	-1.5	-120	5.1	-4.5	FHB	H
CS 22189-24	2 44 21.5	-15 38 32	195.2	-60.8	11.72	0.11	0.14	1.0	22.4	17.7	7766	3.0	-2.3	48	1.6	-1.4	FHB	H
CS 22871-3	14 31 7.4	-20 59 50	332.7	35.7	14.24	0.03	0.11	1.3	23.7	23.6	8500	3.0	-1.8	78	4.6	2.7	FHB	E
CS 22871-5	14 31 41.3	-20 37 49	333.0	35.9	15.04	0.06	0.14	1.3	23.6	25.1	8270	3.0	-1.5	105	7.0	4.1	FHB	K
CS 22871-8	14 29 14.4	-20 21 4	332.6	36.4	14.53	-0.03	0.02	2.0	21.9	23.1	8789	3.0	-2.1	83	4.7	2.8	FHB	K
CS 22871-10	14 31 26.0	-19 57 42	333.4	36.5	13.01	0.29	0.10	5.0	14.6	12.8	7019	2.9	-0.9	-20	3.0	1.8	FHB	H
CS 22871-11	14 28 53.3	-19 37 21	332.9	37.1	14.80	0.03	0.12	0.6	25.7	24.5	8317	3.0	-2.8	4	5.9	3.6	FHB	K
CS 22871-12	14 32 1.2	-19 29 10	333.8	36.9	14.85	0.33	0.04	2.7	11.0	9.8	6747	2.5	-2.1	363	7.1	4.3	FHB	H
CS 22871-13	14 31 26.0	-19 24 18	333.7	37.0	14.63	0.08	-9.99	...	21.2	23.7	8800	3.1	-2.2	-14	5.9	3.5	FHB	L
CS 22871-17	14 29 39.9	-19 12 37	333.4	37.4	13.92	-0.04	-0.05	0.4	21.5	20.8	9052	3.0	-2.0	-108	3.4	2.1	FHB	E
CS 22871-22	14 31 29.9	-17 36 3	334.8	38.6	13.97	0.12	0.14	1.2	22.4	19.1	7762	3.0	-2.2	181	4.5	2.8	FHB	H
CS 22871-31	14 35 59.5	-18 41 6	335.3	37.1	14.24	0.07	0.16	0.2	26.1	24.8	8204	3.1	-3.0	210	4.8	2.9	FHB	E
CS 22871-32	14 35 18.1	-18 58 23	335.0	37.0	13.91	-0.02	-0.04	0.0	23.1	20.1	8799	2.9	-3.0	203	3.6	2.2	FHB	E
CS 22871-33	14 34 16.6	-18 59 56	334.7	37.1	13.44	0.06	0.14	0.3	24.4	23.9	8221	3.0	-3.0	115	3.3	2.0	FHB	E
CS 22871-34	14 36 31.6	-19 3 19	335.2	36.7	15.21	0.16	0.14	2.3	23.7	20.3	7749	3.1	-1.6	84	8.2	4.9	FHB	K
CS 22871-36	14 33 53.4	-19 50 43	334.1	36.4	15.11	0.39	0.06	3.5	11.7	10.4	6714	2.5	-1.5	-2	8.0	4.7	FHB	H
CS 22871-42	14 37 9.8	-21 7 19	334.1	34.9	12.68	0.08	0.16	0.5	25.2	25.8	8094	3.1	-3.0	70	2.4	1.4	FHB	E
CS 22871-44	14 35 31.1	-21 22 34	333.6	34.8	13.51	0.18	0.19	4.3	23.4	20.4	7748	3.1	-0.5	-97	3.8	2.2	FHB	H
CS 22871-45	14 35 21.7	-21 32 51	333.4	34.7	14.20	0.00	-0.01	0.3	22.6	23.5	8807	3.0	-2.9	-6	4.3	2.4	FHB	E
CS 22871-47	14 33 39.5	-21 48 36	332.9	34.7	13.51	0.25	0.13	3.4	12.4	11.0	6750	2.0	-1.8	144	3.8	2.2	FHB	H
CS 22871-52	14 40 1.7	-22 11 46	334.2	33.6	13.70	-0.03	-0.01	0.2	20.3	23.8	9031	3.0	-1.9	79	3.2	1.8	FHB	E
CS 22871-62	14 39 15.7	-20 25 58	335.1	35.2	14.68	0.06	-9.99	...	22.2	24.7	8781	3.0	-1.9	35	5.9	3.4	FHB	L
CS 22871-63	14 40 10.6	-20 30 10	335.2	35.1	13.48	0.14	0.18	1.0	22.4	23.9	7760	3.0	-3.0	159	3.6	2.1	FHB	E
CS 22871-64	14 39 32.6	-20 18 16	335.2	35.3	14.39	0.17	0.14	1.8	19.5	17.1	7493	2.6	-1.8	192	5.7	3.3	FHB	E
CS 22871-68	14 38 45.4	-19 44 56	335.4	35.9	15.49	0.37	0.12	1.4	15.4	13.6	7043	2.4	-2.5	278	9.5	5.6	FHB	H
CS 22871-75	14 38 34.1	-18 6 52	336.4	37.3	13.02	0.09	0.16	0.5	25.4	24.7	8052	3.1	-2.5	-22	2.8	1.7	FHB	E
CS 22871-77	14 38 29.7	-17 50 37	336.5	37.6	15.13	0.00	0.06	...	20.4	20.8	8335	2.5	-1.8	-10	6.5	4.0	FHB	L
CS 22871-85	14 41 3.2	-18 30 38	336.7	36.7	14.10	0.05	0.17	1.1	24.7	22.2	8225	3.0	-2.0	203	4.5	2.7	FHB	EL
CS 22871-87	14 42 28.2	-18 45 58	336.9	36.3	13.99	-0.01	0.09	0.6	25.5	26.6	8516	3.0	-2.3	-107	3.8	2.3	FHB	E
CS 22871-88	14 41 37.1	-19 7 46	336.5	36.1	14.18	0.01	0.08	0.9	23.9	23.1	8635	3.0	-1.6	115	4.4	2.6	FHB	E
CS 22871-92	14 43 18.4	-20 17 39	336.1	34.9	14.09	0.05	0.10	1.0	21.9	24.1	8155	2.6	-2.2	57	4.4	2.5	FHB	E
CS 22871-96	14 45 11.7	-21 20 24	335.9	33.7	13.45	0.03	0.10	1.2	23.9	24.8	8498	3.0	-1.7	-40	3.2	1.8	FHB	E

Table B.1. (continued)

Star (1)	RA (1950) (2)	Dec (3)	l (4)	b (5)	V (6)	$(B-V)_o$ (7)	$(U-B)_o$ (8)	W_k (9)	$H\delta$ $D_{0.2}$ (10)	$H\gamma$ $D_{0.2}$ (11)	T_{eff} (12)	Log g (13)	[Fe/H] (14)	V_{RS} (15)	Dist. (16)	Z (17)	Class (18)	Obs (19)
CS 22871-99	14 47 32.6	-21 30 48	336.4	33.3	14.73	-0.01	0.05	...	24.9	26.1	8658	3.0	-2.1	162	5.3	2.9	FHB	L
CS 22871-103	14 48 2.1	-20 40 56	337.0	34.0	15.02	0.28	0.05	...	15.8	12.5	7045	2.9	-1.2	75	7.7	4.3	FHB	L
CS 22871-109	14 45 53.5	-18 35 32	337.9	36.0	14.20	0.00	0.02	...	21.7	23.7	8926	3.0	-2.1	-54	4.3	2.5	FHB	L
CS 22871-113	14 48 36.9	-19 19 29	338.1	35.0	14.59	0.07	0.18	...	26.7	21.2	8190	3.1	-2.5	97	5.7	3.3	FHB	L
CS 22871-115	14 45 47.4	-17 24 55	338.6	37.0	13.86	0.03	0.12	1.7	24.5	25.7	8404	3.0	-2.8	23	3.8	2.3	FHB	EL
CS 22872-1	16 17 26.1	-5 57 40	7.6	29.6	14.76	0.02	-0.01	...	19.9	23.3	9192	3.0	-3.0	-154	5.8	2.9	FHB	L
CS 22872-2	16 17 37.2	-5 11 53	8.3	30.1	14.84	0.20	0.13	...	17.3	17.4	7250	2.6	-2.7	-95	7.0	3.5	FHB	L
CS 22872-5	16 13 33.6	-4 55 29	7.9	31.0	12.79	0.30	0.02	2.4	14.5	16.3	6894	2.6	-1.8	54	2.7	1.4	FHB	EH
CS 22872-7	16 17 46.1	-4 58 56	8.5	30.1	12.96	0.08	0.15	1.4	22.8	20.3	8081	2.8	-1.8	86	2.7	1.4	FHB	EL
CS 22872-9	16 15 3.1	-4 40 50	8.4	30.9	13.21	0.13	0.17	2.9	14.6	12.9	7000	2.0	-1.9	117	3.2	1.6	FHB	H
CS 22872-10	16 15 9.2	-4 33 24	8.5	30.9	14.08	0.35	0.03	2.2	10.3	9.1	6500	2.0	-2.1	77	5.0	2.6	FHB	K
CS 22872-12	16 16 22.1	-4 1 38	9.2	31.0	14.38	0.16	0.16	3.6	19.0	18.5	7479	2.6	-1.3	151	5.6	2.9	FHB	E
CS 22872-18	16 14 17.5	-2 51 28	10.0	32.1	13.40	0.10	0.15	1.4	22.2	25.1	7750	2.6	-2.1	47	3.4	1.8	FHB	E
CS 22872-21	16 16 37.3	-2 50 26	10.4	31.6	14.48	0.02	0.15	0.5	25.6	22.2	8271	3.0	-2.6	-13	5.1	2.7	FHB	H
CS 22872-25	16 14 26.3	-2 0 53	10.8	32.5	14.26	0.05	0.16	1.0	20.3	21.7	7840	2.5	-2.4	31	4.8	2.6	FHB	E
CS 22872-26	16 16 52.5	-2 1 28	11.2	32.0	13.84	-0.03	0.00	...	22.5	21.8	8804	3.0	-2.1	-60	3.4	1.8	FHB	L
CS 22872-34	16 19 25.1	-1 57 25	11.7	31.5	13.95	0.02	0.12	...	24.9	22.2	8419	3.0	-1.5	83	4.0	2.1	FHB	L
CS 22872-35	16 18 24.8	-2 5 35	11.4	31.7	14.45	0.05	0.15	...	21.6	30.1	7987	2.5	-1.6	67	5.2	2.7	FHB	L
CS 22872-40	16 19 6.7	-3 0 58	10.6	31.0	13.67	0.21	0.10	...	16.4	15.5	7259	2.9	-1.4	-65	4.1	2.1	FHB	L
CS 22872-41	16 20 3.1	-3 17 40	10.5	30.7	11.64	0.05	0.10	0.8	25.2	26.0	8421	3.1	-2.1	-215	1.4	0.7	FHB	EL
CS 22872-42	16 17 38.5	-3 20 25	10.1	31.1	14.12	0.02	0.05	...	23.9	20.3	8702	3.0	-2.8	-134	4.3	2.2	FHB	L
CS 22872-45	16 20 37.4	-3 40 49	10.2	30.3	14.55	-0.01	-0.09	0.4	17.3	15.2	9525	3.0	-1.2	41	4.9	2.5	FHB	H
CS 22872-50	16 19 47.7	-4 12 39	9.6	30.2	12.63	0.20	0.14	...	17.6	18.9	7266	2.4	-2.2	75	2.6	1.3	FHB	L
CS 22872-51	16 20 41.1	-4 14 47	9.7	30.0	13.96	-0.05	-0.14	0.3	20.0	20.2	9671	3.1	-1.4	-69	3.4	1.7	FHB	K
CS 22872-52	16 20 46.6	-4 20 22	9.6	29.9	15.26	-0.01	0.00	...	23.3	22.3	8752	3.0	-3.0	-34	6.8	3.4	FHB	L
CS 22872-57	16 22 9.9	-5 15 26	9.0	29.1	14.36	0.11	0.16	0.8	23.7	21.7	7806	3.0	-2.5	-82	5.4	2.6	FHB	K
CS 22872-60	16 24 34.3	-4 44 28	9.9	28.9	14.94	0.06	0.14	1.0	25.2	23.7	8213	3.0	-2.9	-221	6.6	3.2	FHB	K
CS 22872-61	16 25 28.3	-4 26 53	10.3	28.9	14.33	0.03	0.07	0.5	25.4	24.5	8457	3.0	-2.5	60	4.8	2.3	FHB	K
CS 22872-62	16 23 58.4	-4 26 13	10.1	29.2	13.51	0.24	0.07	...	17.0	17.7	7252	3.2	-0.6	91	3.8	1.9	FHB	L
CS 22872-63	16 23 4.5	-4 26 45	9.9	29.4	11.61	0.21	0.17	...	22.9	18.8	7689	3.1	0.0	21	1.6	0.8	FHB	L
CS 22872-65	16 25 24.1	-4 2 48	10.7	29.1	14.04	0.13	0.18	0.7	22.2	25.5	7751	3.0	-2.2	-36	4.7	2.3	FHB	K
CS 22872-66	16 22 13.7	-3 56 11	10.3	29.8	15.22	0.23	0.07	...	...	18.9	7953	3.0	-3.0	-999	8.4	4.2	FHB	L
CS 22872-67	16 23 13.9	-3 32 14	10.8	29.9	14.12	0.07	0.14	...	24.4	22.9	8138	3.0	-2.3	-16	4.6	2.3	FHB	L
CS 22872-69	16 23 7.1	-3 21 42	11.0	30.0	14.47	0.24	0.14	...	35.1	17.2	7760	3.1	-1.4	-36	5.9	3.0	FHB	L

Table B.1. (continued)

Star (1)	RA (1950) (2)	Dec (3)	l (4)	b (5)	V (6)	$(B-V)_o$ (7)	$(U-B)_o$ (8)	W_λ (9)	$H\delta$ $D_{0.2}$ (10)	$H\gamma$ $D_{0.2}$ (11)	T_{eff} (12)	Log g (13)	[Fe/H] (14)	V_{rad} (15)	Dist. (16)	Z (17)	Class (18)	Obs (19)
CS 22872-70	16 23 44.8	-3 12 42	11.2	29.9	14.98	0.09	0.17	...	12.3	19.6	8041	3.2	-2.2	-101	7.0	3.5	FHB	L
CS 22872-71	16 23 3.5	-2 50 32	11.4	30.3	14.15	0.17	0.20	...	21.0	22.5	7475	2.7	-3.0	74	5.1	2.6	FHB	L
CS 22872-72	16 21 50.3	-2 42 32	11.4	30.6	13.71	-0.08	-0.41	...	16.9	14.2	9779	2.9	-3.0	-51	2.7	1.4	FHB	L
CS 22872-77	16 23 17.8	-1 55 58	12.4	30.8	14.48	-0.06	-0.01	...	22.4	22.6	9023	3.0	-2.0	-82	4.2	2.1	FHB	L
CS 22872-81	16 22 53.2	-1 20 4	12.9	31.2	13.95	0.04	0.12	...	26.3	21.7	8260	3.0	-2.2	-46	4.1	2.1	FHB	L
CS 22872-82	16 22 19.7	-1 15 0	12.9	31.3	14.28	0.11	0.10	...	15.1	14.5	7156	2.5	-1.2	96	5.2	2.7	FHB	L
CS 22872-85	16 26 12.6	-1 6 56	13.6	30.6	15.02	-0.05	0.02	...	21.8	25.0	8889	3.0	-2.1	-156	5.5	2.8	FHB	L
CS 22872-87	16 26 33.6	-1 22 44	13.4	30.4	13.50	0.08	0.10	2.4	23.6	19.6	8348	3.0	-1.2	-237	3.5	1.8	FHB	K
CS 22872-91	16 28 33.3	-1 27 59	13.6	29.9	13.85	0.02	0.13	...	23.7	23.9	8500	3.0	-1.7	-51	3.8	1.9	FHB	L
CS 22872-96	16 26 47.8	-2 25 2	12.4	29.8	13.45	0.09	0.17	2.9	25.6	23.8	8041	3.1	-3.0	163	3.5	1.7	FHB	K
CS 22872-98	16 27 47.1	-2 28 28	12.5	29.5	15.22	0.07	0.10	...	22.4	23.1	7959	2.6	-3.0	-63	7.6	3.7	FHB	L
CS 22872-101	16 27 11.4	-2 49 33	12.1	29.4	13.57	0.37	0.14	...	16.6	14.3	7104	2.5	-0.6	15	3.9	1.9	FHB	L
CS 22872-103	16 28 44.5	-3 22 51	11.8	28.8	14.33	0.07	0.13	...	24.9	22.3	8243	3.0	-3.0	-9	5.1	2.5	FHB	L
CS 22872-109	16 29 47.1	-4 47 33	10.7	27.8	14.61	0.22	0.24	...	17.0	12.2	7179	2.6	-2.6	135	6.3	3.0	FHB	L
CS 22872-112	16 27 38.4	-5 31 42	9.7	27.8	12.75	0.14	0.12	1.0	24.0	20.9	7767	3.0	-2.0	4	2.6	1.2	FHB	H
CS 22872-114	16 30 19.3	-5 30 17	10.1	27.3	14.55	0.15	0.06	...	18.9	20.2	7489	3.0	-3.0	-178	6.0	2.8	FHB	L
CS 22872-119	16 31 36.0	-4 22 27	11.4	27.7	14.47	0.07	0.13	...	25.6	26.1	8234	3.0	-2.6	-53	5.4	2.5	FHB	L
CS 22872-122	16 33 13.9	-3 29 40	12.4	27.8	13.03	0.52	0.07	4.6	7.8	7.1	6567	2.5	-0.5	3	3.1	1.4	FHB	E
CS 22872-127	16 29 52.8	-2 45 17	12.6	28.9	14.84	0.02	-0.03	...	23.3	20.4	8769	3.0	-1.8	105	6.0	2.9	FHB	L
CS 22872-128	16 32 21.6	-2 16 48	13.5	28.7	14.44	0.23	0.28	1.3	18.4	16.1	7214	2.5	-2.6	-106	5.9	2.8	FHB	H
CS 22872-137	16 32 37.7	-1 41 8	14.1	28.9	13.56	0.05	0.13	0.7	26.9	25.5	8236	3.1	-2.3	-34	3.5	1.7	FHB	K
CS 22872-139	16 29 11.8	-1 26 4	13.8	29.8	14.04	-0.06	-0.02	...	21.9	24.7	8927	3.0	-3.0	114	3.4	1.7	FHB	L
CS 22873-165	20 15 32.0	-61 50 9	335.0	-34.1	14.70	0.29	-0.01	3.8	15.5	13.6	7019	2.9	-1.3	138	6.6	-3.7	FHB	H
CS 22874-3	14 31 15.0	-27 20 0	329.3	30.0	13.68	0.02	0.13	1.0	26.8	23.1	8516	3.2	-1.7	-106	3.5	1.7	FHB	EE
CS 22874-4	14 29 43.9	-27 9 58	329.0	30.3	14.02	0.12	0.16	2.8	21.5	22.1	7728	2.6	-1.4	74	4.6	2.3	FHB	E
CS 22874-9	14 31 29.1	-26 4 30	330.0	31.1	13.29	0.25	-0.02	4.4	16.8	13.9	7220	3.1	-0.7	-42	3.5	1.8	FHB	EE
CS 22874-12	14 27 28.1	-25 16 0	329.4	32.2	14.84	0.00	0.09	1.4	22.3	24.7	8742	3.0	-0.9	-973	5.8	3.1	FHB	E
CS 22874-15	14 30 7.1	-24 55 48	330.3	32.3	13.38	-0.06	-0.15	0.7	18.6	19.8	9678	3.0	-2.5	-32	2.5	1.3	FHB	E
CS 22874-17	14 30 56.5	-24 36 58	330.6	32.5	14.83	0.01	0.05	0.9	17.9	20.4	8590	2.5	-1.6	62	5.8	3.1	FHB	E
CS 22874-20	14 29 0.3	-24 18 35	330.3	32.9	15.23	0.12	0.15	5.0	18.2	28.1	7672	2.6	-2.0	179	8.1	4.4	FHB	E
CS 22874-21	14 30 24.8	-24 19 36	330.7	32.8	13.60	0.00	0.08	0.6	25.5	26.7	8510	3.0	-2.5	71	3.3	1.8	FHB	EE
CS 22874-25	14 27 33.1	-23 46 53	330.2	33.6	13.04	0.03	0.11	0.7	24.9	26.1	8478	3.1	-2.2	-21	2.7	1.5	FHB	EE
CS 22874-29	14 29 8.0	-23 20 24	330.9	33.8	14.80	0.09	0.16	2.2	21.2	20.3	7769	2.5	-1.7	68	6.4	3.6	FHB	E

Table B.1. (continued)

Star (1)	RA (1950) (2)	Dec (3)	l (4)	b (5)	V (6)	$(B-V)_o$ (7)	$(U-B)_o$ (8)	W_k (9)	$H\delta$ $D_{0.2}$ (10)	$H\gamma$ $D_{0.2}$ (11)	T_{eff} (12)	Log g (13)	[Fe/H] (14)	V_{gsr} (15)	Dist. (16)	Z (17)	Class (18)	Obs (19)
CS 22874-31	14 30 14.5	-23 37 8	331.0	33.4	13.85	0.31	0.15	1.5	20.5	17.9	7473	2.6	-2.0	-28	4.5	2.5	FHB	H
CS 22874-33	14 34 17.8	-22 43 19	332.5	33.8	13.66	0.26	-0.04	4.2	13.0	11.5	6933	3.0	-1.4	17	4.1	2.3	FHB	H
CS 22874-40	14 36 23.5	-24 26 15	332.0	32.1	14.79	0.40	0.04	3.0	11.0	9.8	6695	2.5	-1.6	12	6.9	3.7	FHB	H
CS 22874-47	14 34 18.4	-25 14 17	331.1	31.6	13.34	0.01	0.13	0.7	24.4	24.1	8475	3.0	-2.5	61	3.0	1.5	FHB	E
CS 22874-53	14 32 43.0	-26 18 11	330.1	30.8	13.29	-0.07	-0.16	0.6	18.6	15.4	9682	3.0	-1.4	-94	2.3	1.2	FHB	E
CS 22874-60	14 37 55.4	-26 42 0	331.1	29.9	13.79	0.34	0.07	3.8	7.9	7.2	6528	2.4	-1.9	51	4.3	2.2	FHB	H
CS 22874-106	14 41 19.9	-26 27 36	332.0	29.7	12.84	0.16	0.14	2.0	21.6	21.5	7733	3.2	-1.8	-64	2.7	1.4	FHB	E
CS 22874-120	14 48 58.5	-24 55 12	334.6	30.2	13.24	0.27	0.05	4.5	14.5	12.8	7009	3.0	-1.1	-28	3.4	1.7	FHB	H
CS 22874-135	14 41 28.5	-26 4 36	332.3	30.1	12.69	0.39	0.17	1.9	9.9	8.9	6510	2.7	-2.7	-90	2.6	1.3	FHB	H
CS 22876-10	23 51 17.0	-34 8 33	0.9	-75.9	14.47	0.12	0.15	0.7	21.0	20.4	7631	2.6	-2.0	96	5.7	-5.5	FHB	E
CS 22876-11	23 48 26.9	-34 20 41	1.1	-75.3	14.24	0.13	0.16	1.3	23.6	21.6	7797	3.0	-1.9	117	5.1	-5.0	FHB	E
CS 22876-19	23 56 46.0	-33 33 46	1.1	-77.2	14.28	0.17	0.13	1.2	19.2	14.5	7470	2.6	-2.1	2	5.4	-5.2	FHB	E
CS 22876-22	23 55 32.1	-34 1 53	359.7	-76.7	13.78	0.16	0.15	1.0	19.1	20.0	7469	2.6	-2.2	38	4.2	-4.1	FHB	E
CS 22876-23	23 55 7.2	-34 17 54	358.8	-76.6	14.39	0.20	0.08	1.8	20.8	18.4	7498	3.0	-1.7	131	5.8	-5.6	FHB	E
CS 22876-29	23 59 24.0	-36 57 28	347.5	-75.8	14.28	0.31	-0.01	1.2	9.0	10.0	6729	2.6	-2.7	48	5.4	-5.3	FHB	E
CS 22876-30	0 3 3.7	-36 58 10	345.5	-76.4	12.96	-0.06	-0.22	0.2	23.7	22.3	8833	3.1	-2.8	50	2.1	-2.0	FHB	E
CS 22876-31	0 5 53.4	-36 25 57	345.6	-77.2	14.15	0.26	0.07	2.3	10.8	11.6	6780	2.4	-2.2	-54	5.1	-5.0	FHB	E
CS 22876-34	0 3 48.0	-35 33 56	349.9	-77.4	13.70	0.39	0.04	5.7	10.6	11.1	6744	3.0	-1.0	-94	4.2	-4.1	FHB	E
CS 22876-38	0 7 12.7	-34 55 56	350.3	-78.3	14.16	0.13	0.15	1.7	23.0	19.7	7759	3.0	-1.9	-153	4.9	-4.8	FHB	E
CS 22876-41	0 7 11.5	-34 15 60	353.0	-78.7	14.07	0.20	0.03	1.1	17.8	14.3	7253	3.0	-2.6	-62	4.9	-4.8	FHB	E
CS 22877-2	13 12 17.1	-11 52 40	311.9	50.3	14.34	-0.05	-0.12	...	19.5	21.1	9402	3.0	-2.3	-76	4.0	3.1	FHB	L
CS 22877-5	13 12 50.5	-11 9 41	312.3	51.0	14.78	0.05	0.11	...	26.8	24.2	8236	3.2	-3.0	31	6.1	4.7	FHB	L
CS 22877-8	13 10 12.4	-10 16 37	311.5	52.0	14.39	0.04	0.11	0.5	25.5	26.0	8402	3.0	-3.0	90	5.0	4.0	FHB	E
CS 22877-12	13 10 55.7	-9 19 25	312.0	52.9	13.50	0.13	0.17	0.8	24.8	21.5	7958	3.2	-2.6	312	3.7	2.9	FHB	E
CS 22877-14	13 9 49.3	-9 3 58	311.6	53.2	13.54	0.08	0.16	0.7	25.6	24.9	8220	3.0	-2.4	-1	3.5	2.8	FHB	E
CS 22877-20	13 15 56.1	-7 33 31	314.5	54.4	13.83	0.12	0.17	0.9	23.6	23.9	7812	3.0	-2.3	-18	4.2	3.4	FHB	E
CS 22877-26	13 18 18.1	-8 23 6	315.2	53.5	13.49	0.21	0.12	2.3	11.8	10.5	6750	2.0	-2.2	161	3.8	3.0	FHB	H
CS 22877-27	13 15 33.6	-8 35 19	314.1	53.4	14.99	0.05	-9.99	...	25.8	21.5	8233	3.0	-2.0	-11	6.7	5.4	FHB	L
CS 22877-28	13 14 27.2	-8 42 20	313.6	53.4	15.13	0.27	0.12	1.9	18.7	16.4	7226	2.6	-1.7	29	8.1	6.5	FHB	H
CS 22877-30	13 15 48.8	-8 51 26	314.1	53.2	15.23	0.09	-9.99	...	24.3	22.9	8028	3.0	-3.0	136	7.8	6.3	FHB	L
CS 22877-31	13 14 31.1	-9 24 37	313.4	52.7	14.11	0.10	0.18	0.7	23.1	21.9	7857	3.0	-2.6	65	4.7	3.8	FHB	E
CS 22877-34	13 19 8.9	-10 6 34	315.0	51.8	12.59	0.06	0.15	0.8	24.9	26.4	8206	3.0	-2.3	71	2.2	1.8	FHB	E
CS 22877-36	13 15 1.4	-11 2 46	313.2	51.0	14.29	0.04	0.14	0.7	25.4	21.4	8229	3.0	-2.5	202	4.8	3.7	FHB	E

Table B.1. (continued)

Star (1)	RA (1950) (2)	Dec (3)	l (4)	b (5)	V (6)	$(B-V)_o$ (7)	$(U-B)_o$ (8)	W_λ (9)	Hδ $D_{0.2}$ (10)	Hγ $D_{0.2}$ (11)	T_{eff} (12)	Log g (13)	[Fe/H] (14)	V_{lsr} (15)	Dist (16)	Z (17)	Class (18)	Obs (19)
CS 22877-38	13 15 23.6	-11 42 59	313.2	50.4	13.52	0.01	0.09	0.6	26.3	25.5	8407	3.1	-2.5	57	3.2	2.5	FHB	E
CS 22877-45	13 18 56.9	-11 13 34	314.6	50.7	13.28	0.27	0.14	1.4	17.6	16.6	7279	2.6	-2.3	42	3.4	2.7	FHB	E
CS 22877-46	13 19 45.7	-11 1 47	315.0	50.9	14.02	0.06	0.16	0.7	23.9	22.1	8101	3.0	-2.5	60	4.3	3.4	FHB	E
CS 22877-49	13 20 13.6	-11 42 58	315.0	50.2	13.67	0.00	0.04	0.4	24.4	22.9	8695	3.0	-3.0	-7	3.3	2.6	FHB	E
CS 22877-52	13 24 0.6	-12 17 19	316.2	49.4	14.26	0.03	0.09	0.4	26.0	25.1	8446	3.0	-3.0	178	4.7	3.5	FHB	E
CS 22878-19	16 30 48.5	+11 36 45	27.6	35.9	14.88	0.03	-9.99	...	24.5	25.5	8489	3.0	-2.8	59	6.2	3.6	FHB	L
CS 22878-20	16 30 40.4	+12 0 43	28.0	36.1	14.06	-0.02	0.09	1.3	25.2	22.8	8467	3.0	-1.6	-25	3.8	2.3	FHB	K
CS 22878-24	16 34 29.8	+10 53 5	27.2	34.7	14.02	-0.02	-9.99	...	25.6	23.1	8433	3.0	-2.3	-98	3.8	2.1	FHB	L
CS 22878-34	16 36 12.1	+ 9 14 4	25.7	33.6	14.19	0.06	0.14	1.4	25.8	25.5	8177	3.0	-1.7	-341	4.7	2.6	FHB	K
CS 22878-57	16 40 54.5	+ 9 9 41	26.2	32.6	13.04	-0.02	-0.05	0.4	23.0	20.5	8875	2.9	-1.9	-19	2.4	1.3	FHB	K
CS 22878-58	16 39 18.4	+ 9 10 51	26.0	32.9	14.35	-0.05	0.27	0.4	23.6	23.9	8664	3.0	-2.8	-6	4.1	2.2	FHB	K
CS 22878-60	16 37 24.4	+ 9 19 41	25.9	33.4	13.10	0.00	0.05	0.4	23.5	26.1	8742	3.0	-3.0	-188	2.6	1.4	FHB	K
CS 22878-88	16 43 38.0	+10 5 24	27.6	32.4	13.51	0.04	0.10	0.7	24.2	24.2	8493	3.0	-1.5	-18	3.3	1.8	FHB	K
CS 22878-97	16 44 38.6	+ 8 44 19	26.3	31.5	14.85	0.15	-9.99	...	16.2	15.6	7243	2.5	-1.3	-133	6.9	3.6	FHB	L
CS 22878-105	16 47 39.9	+ 8 16 21	26.2	30.7	13.40	0.05	0.07	0.6	26.3	25.2	8268	3.1	-2.2	-179	3.2	1.6	FHB	K
CS 22878-111	16 46 5.2	+ 9 21 47	27.1	31.5	14.09	-0.01	0.09	...	24.5	23.5	8546	3.0	-3.0	-96	4.0	2.1	FHB	L
CS 22878-122	16 45 25.4	+11 49 50	29.6	32.7	15.62	0.05	-9.99	...	25.4	22.8	8240	3.0	-3.0	-191	9.0	4.8	FHB	L
CS 22879-63	20 41 50.2	-41 24 56	0.3	-38.3	14.44	0.29	0.02	4.3	12.8	11.3	6998	3.0	-1.5	9	5.9	-3.6	FHB	H
CS 22879-101	20 43 32.8	-38 29 31	4.1	-38.3	15.30	0 41	0.08	4.3	12.8	11.3	6861	2.3	-1.5	62	8.7	-6.4	FHB	H
CS 22879-153	20 55 57.7	-37 46 44	5.3	-40.6	13.93	0.30	-0.01	3.6	13.4	11.8	7003	3.0	-1.8	18	4.6	-3.0	FHB	H
CS 22880-54	20 41 37.8	-20 59 47	25.0	-33.8	14.74	0.05	0.15	0.6	26.1	22.7	8220	3.0	-2.5	-31	6.0	-3.3	FHB	H
CS 22880-57	20 39 38.6	-21 38 54	24.1	-33.6	13.98	0.01	0.08	0.6	24.9	21.7	8500	3.0	-2.1	-113	4.0	-2.2	FHB	H
CS 22880-59	20 41 17.0	-21 48 10	24.1	-34.0	14.58	0.05	0.11	0.5	22.9	19.9	8513	3.0	-2.3	37	5.5	-3.1	FHB	H
CS 22880-61	20 38 34.6	-21 57 57	23.6	-33.4	14.65	-0.05	0.00	0.4	19.6	17.1	8543	2.5	-1.9	-134	4.7	-2.6	FHB	H
CS 22880-64	20 42 14.9	-22 28 7	23.4	-34.4	14.87	-0.03	0.03	0.2	23.5	20.4	8742	3.0	-3.0	118	5.4	-3.1	FHB	H
CS 22880-66	20 45 58.1	-22 14 32	24.0	-35.1	14.07	0.10	0.19	1.0	24.1	20.9	7968	3.0	-2.1	-86	4.6	-2.7	FHB	H
CS 22880-68	20 46 26.1	-21 43 25	24.6	-35.1	13.97	0.05	0.07	0.5	23.2	20.2	7694	2.3	-3.0	31	4.2	-2.4	FHB	H
CS 22880-89	20 45 27.4	-18 41 21	28.0	-33.8	14.48	0.23	0.00	1.5	14.9	13.1	6998	2.5	-2.5	-48	6.0	-3.3	FHB	H
CS 22880-114	20 49 22.0	-19 43 45	27.2	-35.1	13.93	0.38	0.15	4.1	12.3	10.9	6750	2.0	-1.7	-10	4.6	-2.7	FHB	H
CS 22882-23	0 33 36.5	-30 32 42	349.0	-85.4	14.92	0.32	0.10	2.8	12.5	11.1	6782	2.3	-2.1	-132	7.3	-7.3	FHB	H

Table B.1. (continued)

Star (1)	RA (1950) (2)	Dec (3)	l (4)	b (5)	V (6)	$(B-V)_o$ (7)	$(U-B)_o$ (8)	W_k (9)	$H\delta\ D_{0.2}$ (10)	$H\gamma\ D_{0.2}$ (11)	T_{eff} (12)	Log g (13)	[Fe/H] (14)	V_{los} (15)	Dist (16)	Z (17)	Class (18)	Obs (19)
CS 22883-7	14 13 7.6	+10 35 38	356.7	64.0	12.38	0.07	0.20	...	25.1	22.4	8143	3.0	-2.5	51	2.1	1.9	FHB	L
CS 22883-11	14 11 8.9	+12 7 32	358.6	65.4	13.07	0.09	0.19	...	25.8	22.6	8013	3.2	-3.0	17	2.9	2.6	FHB	L
CS 22883-18	14 16 0.9	+10 6 17	357.0	63.2	14.64	0.03	0.15	...	24.9	23.0	8270	3.0	-2.7	-264	5.5	4.9	FHB	L
CS 22883-26	14 21 13.0	+ 8 12 13	356.0	61.0	13.65	0.03	0.12	...	26.6	23.7	8271	3.0	-2.6	-19	3.5	3.1	FHB	L
CS 22883-27	14 19 58.1	+ 9 0 24	356.7	61.7	15.09	0.15	-9.99	...	21.0	19.7	7565	2.8	-2.4	253	7.7	6.8	FHB	L
CS 22883-28	14 18 19.7	+ 9 28 53	356.9	62.4	13.55	0.03	0.14	0.3	24.5	24.1	8435	3.0	-3.0	-1	3.4	3.0	FHB	K
CS 22883-39	14 23 40.5	+10 52 12	1.0	62.3	13.75	0.02	0.09	...	24.1	21.5	8521	3.0	-1.8	-72	3.6	3.2	FHB	L
CS 22883-50	14 26 41.3	+10 15 28	1.0	61.3	14.30	0.24	0.08	3.5	18.1	15.9	7262	3.0	-1.4	-61	5.5	4.8	FHB	H
CS 22883-51	14 26 18.9	+10 39 3	1.5	61.7	15.03	0.18	-9.99	...	20.8	20.1	7505	3.0	-1.9	95	7.7	6.7	FHB	L
CS 22884-2	15 31 41.9	-12 2 47	353.4	34.2	12.35	0.16	0.19	1.9	23.3	24.3	7753	3.2	-1.7	160	2.2	1.2	FHB	K
CS 22884-6	15 32 29.2	-11 30 57	354.1	34.5	14.32	-0.11	-0.53	2.6	11.8	10.3	7052	2.8	-3.0	34	3.2	1.8	FHB	E
CS 22884-15	15 29 4.4	-9 18 23	355.2	36.6	12.78	-0.01	0.13	0.7	25.7	22.6	8272	3.0	-2.5	223	2.2	1.3	FHB	K
CS 22884-21	15 32 3.5	-8 6 41	357.0	36.9	13.94	0.00	0.08	1.3	23.7	25.5	8705	3.0	-1.2	-59	3.8	2.3	FHB	K
CS 22884-23	15 34 18.3	-8 4 19	357.5	36.5	13.73	0.04	0.12	1.4	24.7	22.9	8448	3.0	-1.5	-219	3.7	2.2	FHB	K
CS 22884-36	15 34 53.8	-11 20 50	354.7	34.2	12.95	0.06	0.12	0.8	25.2	23.0	8238	3.0	-2.1	69	2.7	1.5	FHB	K
CS 22885-92	20 22 41.9	-40 54 24	0.4	-34.6	14.32	0.27	0.11	2.0	15.8	13.9	7019	2.5	-2.2	36	5.5	-3.1	FHB	H
CS 22885-125	20 23 37.7	-38 7 31	3.8	-34.4	14.05	0.24	0.10	2.8	14.6	12.9	7001	2.5	-2.0	-175	4.9	-2.8	FHB	H
CS 22885-174	20 30 41.2	-39 22 27	2.5	-35.9	12.88	0.31	-0.01	4.3	11.6	10.3	6744	2.5	-1.4	-9	2.9	-1.7	FHB	H
CS 22885-179	20 30 25.1	-38 52 43	3.1	-35.8	14.54	0.29	0.01	3.3	11.9	10.6	6989	3.0	-1.6	-28	6.1	-3.6	FHB	H
CS 22889-10	13 28 55.9	-8 38 57	319.4	52.7	14.37	-0.06	-9.99	...	21.1	22.2	8975	3.0	-3.0	68	4.0	3.2	FHB	L
CS 22889-13	13 33 54.5	-7 59 58	321.7	53.0	13.61	0.13	0.14	2.0	15.0	14.8	7304	2.3	-2.0	32	3.8	3.1	FHB	E
CS 22889-23	13 35 35.2	-11 54 11	320.6	49.1	14.45	-0.01	-0.02	0.6	18.9	19.5	8683	2.5	-2.3	-75	4.7	3.6	FHB	E
CS 22889-52	13 43 28.9	-10 11 48	324.2	50.2	13.63	-0.30	-0.97	0.0	14.4	14.7	9635	2.6	-3.0	-71	0.5	0.4	FHB	E
CS 22889-53	13 45 2.0	-11 59 25	323.9	48.3	14.12	0.31	-9.99	...	16.7	19.8	7052	2.9	-1.1	59	5.1	3.8	FHB	L
CS 22889-57	13 49 41.5	-10 53 7	326.1	49.0	14.05	0.26	0.02	4.9	12.7	14.4	7013	3.0	-1.2	8	4.9	3.7	FHB	E
CS 22889-58	13 48 33.7	-10 48 42	325.7	49.2	13.45	-0.14	-0.44	0.3	15.0	14.7	7013	3.0	-3.0	65	1.9	1.4	FHB	E
CS 22889-60	13 46 34.6	-10 7 28	325.4	50.0	12.97	-0.04	-0.07	0.4	20.4	21.2	9301	3.0	-1.5	-107	2.2	1.7	FHB	E
CS 22890-1	15 10 49.6	-1 11 4	358.9	45.5	14.08	0.37	0.23	4.5	17.4	15.2	7123	2.5	-1.1	-10	5.0	3.5	FHB	H
CS 22890-9	15 7 0.4	+ 2 0 25	1.4	48.4	12.60	0.11	0.18	...	23.5	21.5	7900	3.1	-2.2	-5	2.4	1.8	FHB	L
CS 22890-15	15 13 38.4	+ 2 20 17	3.4	47.3	12.40	0.12	0.15	0.5	20.8	20.7	7544	2.5	-3.0	129	2.2	1.6	FHB	K
CS 22890-17	15 14 52.3	+ 2 15 23	3.6	47.0	13.55	0.08	0.17	4.4	19.5	9.6	7895	2.5	-0.6	39	3.6	2.6	FHB	K

Table B.1. (continued)

Star (1)	RA (1950) (2)	Dec (3)	l (4)	b (5)	V (6)	$(B-V)_o$ (7)	$(U-B)_o$ (8)	W_k (9)	$H\delta$ $D_{0.2}$ (10)	$H\gamma$ $D_{0.2}$ (11)	T_{eff} (12)	Log g (13)	[Fe/H] (14)	V_{los} (15)	Dist. (16)	Z (17)	Class (18)	Obs (19)
CS 22890-19	15 13 50.1	+1 26 9	2.4	46.7	13.36	0.13	0.16	0.8	23.2	22.1	7779	3.0	-2.6	42	3.4	2.5	FHB	K
CS 22890-26	15 11 55.5	-0 17 32	0.1	45.9	13.91	0.04	0.08	5.0	23.8	22.5	8603	3.0	-2.5	85	4.0	2.9	FHB	K
CS 22890-32	15 16 41.0	-0 18 53	1.2	45.0	14.03	0.34	0.10	2.9	12.9	11.5	6750	2.0	-2.0	-10	4.9	3.4	FHB	H
CS 22890-38	15 17 22.4	+0 27 4	2.2	45.4	15.20	0.19	0.17	1.8	20.5	17.9	7486	2.9	-1.9	-55	8.3	5.9	FHB	H
CS 22890-41	15 18 24.9	+0 59 3	3.0	45.5	12.55	0.33	0.15	2.3	14.3	12.6	6922	2.7	-1.9	-55	2.5	1.8	FHB	H
CS 22890-42	15 16 20.8	+0 56 44	2.5	45.9	12.68	0.17	0.16	1.6	20.3	19.5	7528	2.9	-2.0	-78	2.6	1.8	FHB	K
CS 22890-43	15 17 49.6	+1 27 6	3.4	45.9	14.18	0.02	0.11	0.7	25.5	24.3	8408	3.0	-2.3	33	4.4	3.2	FHB	K
CS 22890-68	15 21 33.9	+3 20 13	6.3	46.4	14.04	0.06	0.22	0.8	24.7	23.9	8214	3.1	-2.1	-43	4.4	3.2	FHB	K
CS 22890-81	15 24 16.9	-0 32 35	2.7	43.4	13.21	0.03	-0.04	0.6	17.5	19.1	8750	2.5	-2.4	-131	2.9	2.0	FHB	K
CS 22890-82	15 23 58.2	+0 22 13	3.6	44.1	14.07	0.26	0.16	1.3	16.1	14.1	7044	2.4	-2.8	-11	4.9	3.4	FHB	H
CS 22891-93	19 7 17.6	-62 1 54	334.4	-26.1	14.11	0.00	0.06	0.8	25.1	23.5	8662	3.0	-1.6	54	4.1	-1.8	FHB	E
CS 22891-94	19 11 59.0	-62 15 59	334.2	-26.7	13.32	0.11	0.16	2.4	19.5	17.7	7500	2.0	-1.9	-84	3.3	-1.5	FHB	E
CS 22891-144	19 18 28.8	-57 46 45	339.3	-26.7	13.53	-0.01	0.04	0.3	23.2	21.1	8768	3.0	-3.0	188	3.1	-1.4	FHB	E
CS 22891-161	19 22 8.5	-58 36 19	338.5	-27.4	14.71	0.11	0.14	0.5	26.5	23.0	7996	3.2	-2.8	59	6.3	-2.9	FHB	H
CS 22891-181	19 27 11.1	-60 31 5	336.4	-28.2	13.63	0.17	0.12	0.3	21.2	16.8	7521	2.7	-3.0	302	4.0	-1.9	FHB	E
CS 22891-211	19 36 19.4	-60 53 35	336.1	-29.4	13.48	0.22	0.11	1.4	16.4	14.4	7187	2.7	-2.4	-104	3.8	-1.8	FHB	H
CS 22891-216	19 33 52.9	-60 14 8	336.8	-29.0	14.55	0.21	0.12	3.2	14.9	13.1	7027	2.3	-1.8	150	6.2	-3.0	FHB	H
CS 22891-217	19 29 57.5	-60 8 24	336.9	-28.5	14.12	0.42	0.06	2.5	11.3	10.1	6751	2.4	-1.9	3	5.1	-2.4	FHB	H
CS 22892-11	22 0 19.9	-15 16 13	41.4	-49.1	14.07	0.34	0.10	3.0	14.3	12.6	6980	2.5	-1.8	-65	4.9	-3.7	FHB	H
CS 22892-48	22 11 14.4	-15 1 47	43.4	-51.4	14.07	0.33	0.00	1.0	9.9	8.9	6734	2.5	-3.0	-166	4.9	-3.9	FHB	H
CS 22893-29	23 1 27.9	-7 53 43	65.4	-57.9	14.37	0.36	-0.02	1.6	15.5	13.6	7020	2.9	-2.0	-30	5.7	-4.8	FHB	H
CS 22894-27	23 41 4.5	-1 41 59	87.8	-59.6	15.16	0.07	0.17	...	24.5	22.5	8142	3.0	-2.9	-154	7.4	-6.4	FHB	L
CS 22894-30	23 37 24.6	-1 5 13	86.9	-58.6	14.59	0.39	0.06	3.4	11.7	10.4	6715	2.5	-1.5	-71	6.3	-5.4	FHB	H
CS 22894-33	23 37 31.6	-0 35 58	87.4	-58.2	14.93	0.11	0.15	...	25.4	22.2	8010	3.1	-3.0	-178	6.9	-5.9	FHB	L
CS 22894-34	23 39 3.5	-0 15 14	88.4	-58.1	14.70	0.17	0.12	...	18.3	16.5	7317	2.4	-2.4	-228	6.5	-5.5	FHB	L
CS 22894-36	23 39 33.6	+0 16 14	89.1	-57.7	14.70	0.26	0.06	1.2	13.7	12.1	6837	2.4	-2.6	-240	6.6	-5.6	FHB	H
CS 22894-48	23 42 55.6	-2 14 7	88.0	-60.3	15.31	0.00	0.02	...	23.2	22.9	8792	3.0	-1.9	-135	7.1	-6.2	FHB	L
CS 22894-53	23 45 24.1	-0 23 43	90.9	-59.0	13.76	0.14	0.16	...	24.4	17.1	7777	3.0	-1.7	6	4.1	-3.6	FHB	L
CS 22896-41	19 25 26.4	-53 0 19	344.8	-26.9	13.10	0.09	0.11	1.1	24.1	20.9	8039	3.1	-3.0	-122	2.9	-1.3	FHB	E
CS 22896-43	19 23 44.2	-53 27 12	344.2	-26.7	14.06	0.05	0.14	1.2	26.1	19.3	8179	3.0	-1.8	-92	4.4	-2.0	FHB	E

Table B.1. (continued)

Star (1)	RA (1950) (2)	Dec (3)	l (4)	b (5)	V (6)	$(B-V)_o$ (7)	$(U-B)_o$ (8)	W_k (9)	$H\delta$ $D_{0.2}$ (10)	$H\gamma$ $D_{0.2}$ (11)	T_{eff} (12)	Log g (13)	[Fe/H] (14)	V_{los} (15)	Dist (16)	Z (17)	Class (18)	Obs (19)
CS 22896-59	19 25 32.5	-54 39 20	342.9	-27.2	13.21	-0.01	0.02	0.6	22.8	20.5	8765	3.0	-2.4	116	2.7	-1.2	FHB	E
CS 22896-86	19 32 36.0	-57 25 41	340.0	-28.6	13.45	-0.07	-0.26	0.6	17.7	14.9	9697	2.9	-1.0	-169	2.5	-1.2	FHB	E
CS 22896-91	19 32 40.7	-56 19 1	341.3	-28.4	12.77	0.07	0.14	1.2	27.4	22.1	8075	3.0	-1.6	-82	2.5	-1.2	FHB	E
CS 22896-92	19 32 38.6	-56 12 11	341.4	-28.4	14.58	0.40	0.10	2.3	18.3	16.0	7176	2.6	-2.0	-14	6.3	-3.0	FHB	H
CS 22896-97	19 32 40.1	-55 25 52	342.3	-28.3	13.75	0.16	0.13	1.1	20.3	16.1	7499	2.6	-2.8	152	4.2	-2.0	FHB	E
CS 22896-100	19 30 6.2	-55 20 35	342.3	-27.9	14.36	0.31	0.03	4.9	15.4	13.5	7014	2.9	-1.1	-24	5.6	-2.6	FHB	H
CS 22896-120	19 35 19.1	-52 49 23	345.3	-28.3	13.02	0.05	0.11	1.5	26.4	24.7	8216	3.1	-1.6	-60	2.7	-1.3	FHB	E
CS 22896-122	19 33 55.0	-53 16 6	344.7	-28.2	12.49	0.09	0.15	1.4	27.0	23.0	8021	3.1	-1.7	136	2.2	-1.0	FHB	E
CS 22896-123	19 34 27.3	-53 17 33	344.7	-28.3	15.24	0.22	0.14	2.6	17.0	14.9	7236	2.5	-1.9	95	8.5	-4.0	FHB	H
CS 22896-141	19 40 24.9	-55 9 47	342.7	-29.4	12.42	0.15	0.10	1.4	20.3	17.7	7511	3.0	-2.8	46	2.3	-1.1	FHB	E
CS 22896-169	19 43 42.0	-55 58 8	341.9	-29.9	13.59	0.15	0.16	3.8	21.0	19.4	7529	2.5	-1.3	-172	3.9	-1.9	FHB	E
CS 22896-174	19 45 59.0	-55 41 33	342.2	-30.2	13.53	0.22	0.09	1.2	11.6	8.4	6750	2.0	-3.0	-143	3.9	-1.9	FHB	E
CS 22896-184	19 43 24.3	-54 38 53	343.4	-29.7	13.44	0.25	0.08	2.5	11.4	8.9	6750	2.0	-2.2	88	3.7	-1.8	FHB	E
CS 22897-7	20 59 46.6	-65 27 22	329.4	-38.2	14.39	0.43	0.08	2.2	15.8	13.9	6943	2.5	-2.0	15	5.7	-3.5	FHB	H
CS 22897-58	21 16 21.7	-65 36 00	328.5	-39.7	13.43	0.03	0.11	2.0	26.0	23.2	8449	3.1	-1.5	114	3.2	-2.0	FHB	E
CS 22897-65	21 20 53.1	-64 55 28	329.0	-40.4	14.21	0.01	0.05	0.3	23.3	20.7	8743	3.0	-3.0	-91	4.4	-2.9	FHB	E
CS 22897-93	21 29 43.5	-64 48 55	328.6	-41.3	14.37	0.17	0.15	0.8	19.7	19.4	7491	2.7	-3.0	104	5.6	-3.7	FHB	E
CS 22897-96	21 24 32.7	-65 31 35	328.1	-40.5	14.99	0.19	0.17	1.7	21.8	19.0	7511	3.0	-2.0	-61	7.5	-4.9	FHB	H
CS 22897-103	21 29 41.5	-66 42 23	326.4	-40.5	13.43	0.32	0.12	4.2	19.0	13.8	7262	2.8	-1.4	-21	3.7	-2.4	FHB	E
CS 22897-106	21 25 18.7	-67 29 51	325.7	-39.7	14.37	0.13	0.12	1.8	22.9	20.8	7756	3.0	-1.6	-72	5.5	-3.5	FHB	E
CS 22897-116	21 36 9.9	-65 41 55	327.2	-41.5	13.92	0.38	-0.04	4.9	9.8	8.8	6710	3.0	-1.2	21	4.6	-3.1	FHB	H
CS 22897-120	21 35 12.3	-64 55 19	328.2	-41.8	15.32	0.34	-0.02	3.8	16.1	14.2	6989	3.0	-0.8	16	8.8	-5.9	FHB	H
CS 22937-58	21 11 47.1	-40 13 46	2.3	-43.8	14.39	0.30	0.04	4.1	15.5	13.6	7016	2.9	-1.4	-7	5.7	-4.0	FHB	H
CS 22937-65	21 11 25.0	-38 34 24	4.6	-43.7	14.28	0.31	0.04	4.7	13.7	12.1	7002	3.0	-1.1	-9	5.4	-3.8	FHB	H
CS 22937-74	21 15 58.6	-37 32 39	6.1	-44.6	14.69	0.49	-0.15	0.9	22.6	19.7	6347	2.9	-3.0	-3	6.6	-4.6	FHB	H
CS 22937-86	21 17 55.8	-40 50 13	1.4	-45.0	13.80	0.33	-0.03	4.3	10.7	9.6	6734	2.5	-1.4	-76	4.4	-3.1	FHB	H
CS 22938-4	22 30 11.6	-65 43 44	322.7	-46.0	14.54	0.38	-0.02	5.4	10.7	9.6	6727	3.1	-0.8	74	6.1	-4.4	FHB	H
CS 22938-16	22 43 4.3	-63 45 47	323.3	-48.4	14.09	0.35	-0.04	3.6	11.9	10.6	6720	2.6	-1.5	61	5.0	-3.7	FHB	H
CS 22938-19	22 46 30.5	-65 15 24	321.4	-47.5	14.26	0.40	0.05	2.5	12.2	10.9	6732	2.5	-1.8	50	5.4	-4.0	FHB	H
CS 22938-21	22 45 53.2	-66 46 37	320.0	-46.4	14.56	0.34	0.02	1.3	16.1	14.1	6949	2.6	-2.4	79	6.2	-4.5	FHB	H
CS 22939-58	19 19 20.7	-28 14 56	10.2	-18.7	14.48	0.22	0.09	2.4	11.0	7.0	6913	2.5	-2.2	17	6.0	-1.9	FHB	E
CS 22939-115	19 23 21.0	-31 4 8	7.8	-20.6	13.76	-0.04	-0.22	0.6	19.7	17.1	9673	3.0	-0.3	-52	3.2	-1.1	FHB	E

Table B.1. (continued)

Star (1)	RA (1950) (2)	Dec (3)	l (4)	b (5)	V (6)	$(B-V)_o$ (7)	$(U-B)_o$ (8)	W_λ (9)	$H\delta$ $D_{0.2}$ (10)	$H\gamma$ $D_{0.2}$ (11)	T_{eff} (12)	Log g (13)	[Fe/H] (14)	V_{los} (15)	Dist (16)	Z (17)	Class (18)	Obs (19)
CS 22939-164	19 29 23.9	-28 47 48	10.5	-21.0	13.03	0.06	0.06	3.0	21.5	19.0	8041	2.5	-2.0	-264	2.8	-1.0	FHB	E
CS 22939-167	19 25 35.8	-28 56 38	10.1	-20.3	13.21	0.12	0.14	1.8	26.6	24.1	7993	3.1	-1.8	-32	3.2	-1.1	FHB	E
CS 22940-63	20 38 51.5	-62 11 43	334.1	-36.7	14.43	0.33	0.04	4.1	11.6	10.3	6750	2.5	-1.2	-130	5.8	-3.5	FHB	H
CS 22940-105	20 48 24.4	-62 23 25	333.6	-37.8	13.86	0.26	0.02	3.6	16.0	14.1	7065	2.9	-1.2	-51	4.5	-2.8	FHB	H
CS 22941-2	23 25 44.2	-36 12 36	1.3	-70.3	14.44	0.12	0.13	1.0	22.4	21.5	7762	3.0	-2.2	-77	5.6	-5.3	FHB	E
CS 22941-8	23 26 0.1	-34 11 54	7.0	-71.0	12.88	0.10	0.13	0.5	22.5	21.1	7756	2.7	-3.0	-85	2.7	-2.5	FHB	E
CS 22941-19	23 29 2.0	-34 56 26	4.2	-71.4	14.69	-0.06	-0.14	0.1	20.4	19.6	9670	3.1	-3.0	-15	4.5	-4.3	FHB	E
CS 22941-22	23 30 32.0	-35 38 38	1.8	-71.4	14.77	0.14	0.08	1.5	23.6	21.7	7762	3.2	-1.8	-25	6.6	-6.2	FHB	E
CS 22941-28	23 32 40.2	-37 5 1	357.2	-71.2	14.31	0.02	0.10	1.5	23.7	26.3	8469	3.0	-1.8	10	4.7	-4.4	FHB	H
CS 22941-30	23 37 51.2	-36 56 17	356.1	-72.2	14.00	0.30	0.07	2.6	16.0	14.1	7064	2.8	-1.6	1	4.8	-4.6	FHB	H
CS 22941-37	23 36 15.8	-35 33 15	0.7	-72.5	13.22	0.06	0.12	0.8	26.0	23.5	8231	3.0	-1.5	-69	3.0	-2.9	FHB	E
CS 22941-64	23 41 26.2	-33 18 14	6.8	-74.3	14.70	0.13	0.13	1.3	21.4	18.6	7739	2.9	-2.3	-155	6.4	-6.1	FHB	E
CS 22943-45	20 10 5.5	-43 58 27	356.4	-32.7	14.64	0.32	0.08	3.9	16.8	14.8	7169	2.9	-1.1	10	6.4	-3.5	FHB	H
CS 22943-58	20 17 24.3	-43 27 31	357.2	-34.0	15.10	0.31	0.10	2.9	18.3	16.0	7243	2.8	-1.2	22	7.9	-4.4	FHB	H
CS 22943-68	20 15 39.6	-44 46 15	355.6	-33.8	15.49	0.04	-0.14	0.0	19.1	16.7	9686	3.0	-3.0	29	8.3	-4.6	FHB	H
CS 22943-70	20 13 5.7	-45 3 10	355.2	-33.4	15.11	0.21	0.12	1.5	18.3	16.0	7239	2.6	-2.5	-120	8.0	-4.4	FHB	H
CS 22943-75	20 16 27.4	-45 16 53	355.0	-34.0	14.42	0.38	0.07	2.5	15.4	13.5	6975	2.6	-1.9	-39	5.8	-3.2	FHB	H
CS 22943-108	20 19 4.6	-46 3 37	354.1	-34.6	14.53	0.23	0.15	1.9	21.4	18.6	7474	3.0	-1.9	-38	6.1	-3.5	FHB	H
CS 22943-150	20 25 4.9	-44 11 55	356.5	-35.4	14.98	0.22	0.16	1.5	19.8	17.3	7443	2.9	-2.1	59	7.5	-4.4	FHB	H
CS 22945-20	23 33 38.0	-63 26 59	316.5	-61.9	14.00	0.39	0.02	4.2	12.4	11.1	6675	2.6	-1.0	67	4.8	-3.8	FHB	H
CS 22947-36	19 0 5.0	-49 47 10	347.2	-22.3	13.11	0.26	0.02	3.3	16.8	14.8	7177	3.2	-1.3	-38	3.2	-1.2	FHB	H
CS 22947-47	19 3 26.3	-48 52 39	348.3	-22.5	12.56	0.25	0.12	2.7	21.1	18.4	7459	3.1	-1.0	-68	2.5	-0.9	FHB	H
CS 22947-79	19 8 27.8	-47 58 30	349.5	-23.1	13.91	0.32	0.03	5.4	12.4	11.0	6741	2.5	-1.3	-62	4.6	-1.8	FHB	H
CS 22947-84	19 10 5.5	-48 14 59	349.3	-23.4	13.54	0.31	-0.01	5.6	12.4	11.0	6747	2.5	-1.0	-29	3.9	-1.5	FHB	H
CS 22947-100	19 10 18.2	-48 45 10	348.8	-23.6	12.95	0.16	0.16	3.3	13.2	11.7	7000	2.0	-1.6	134	2.9	-1.2	FHB	H
CS 22947-301	19 28 10.7	-49 31 22	348.7	-26.6	14.02	0.29	0.09	4.1	18.3	16.0	7206	3.0	-0.7	-28	4.8	-2.2	FHB	H
CS 22948-2	21 30 41.5	-41 6 59	1.0	-47.4	14.83	0.16	0.18	1.5	23.8	20.7	7747	3.2	-1.8	-66	6.9	-5.1	FHB	H
CS 22948-25	21 32 13.2	-39 32 26	3.3	-47.8	13.03	0.29	0.06	3.2	13.1	11.6	7017	2.9	-1.5	-78	3.1	-2.3	FHB	H
CS 22948-101	21 51 46.9	-39 10 14	3.6	-51.6	14.43	0.29	0.00	2.8	16.1	14.1	7054	2.9	-1.5	-5	5.8	-4.6	FHB	H

Table B.1. (continued)

Star (1)	RA (1950) (2)	Dec (3)	l (4)	b (5)	V (6)	$(B-V)_o$ (7)	$(U-B)_o$ (8)	W_k (9)	$H\delta\ D_{0.2}$ (10)	$H\gamma\ D_{0.2}$ (11)	T_{eff} (12)	Log g (13)	[Fe/H] (14)	V_{los} (15)	Dist (16)	Z (17)	Class (18)	Obs (19)
CS 22949-4	23 9 50.9	-6 32 35	70.0	-58.6	13.06	0.23	0.17	...	20.8	20.9	7509	3.0	-0.5	-13	3.1	-2.6	FHB	L
CS 22949-6	23 13 39.1	-5 1 46	73.3	-58.1	13.93	0.04	0.09	...	21.4	23.9	8193	2.5	-2.7	-185	4.1	-3.4	FHB	L
CS 22949-11	23 15 21.7	-2 34 56	76.9	-56.6	14.77	0.28	0.05	3.2	16.1	14.1	7040	2.9	-1.4	-125	6.8	-5.7	FHB	H
CS 22949-12	23 16 38.6	-2 32 17	77.4	-56.7	14.11	0.02	0.07	...	21.9	22.1	8762	3.0	-2.6	-184	4.3	-3.6	FHB	L
CS 22949-20	23 17 3.3	-7 3 57	71.8	-60.2	15.04	0.43	0.05	3.3	12.6	11.2	6756	2.5	-1.7	-3	7.7	-6.7	FHB	H
CS 22949-41	23 23 56.2	-4 31 43	77.7	-59.4	13.47	-0.04	-0.03	...	15.0	15.6	8983	2.5	-2.6	-343	2.8	-2.4	FHB	L
CS 22950-3	20 17 50.6	-16 30 21	27.5	-26.9	14.84	0.23	0.13	2.7	9.3	8.4	6750	2.0	-2.0	208	7.0	-3.2	FHB	H
CS 22950-8	20 15 35.8	-16 10 41	27.6	-26.3	12.76	0.33	0.08	4.0	15.6	13.7	7037	2.8	-1.2	-6	2.7	-1.2	FHB	H
CS 22950-14	20 13 52.8	-15 53 10	27.7	-25.8	14.05	0.38	0.00	6.0	10.5	9.4	6722	3.0	-0.6	-19	4.9	-2.1	FHB	H
CS 22950-23	20 13 32.5	-14 42 55	28.9	-25.2	11.11	0.20	0.14	3.7	14.4	12.8	7000	2.0	-1.5	-13	1.3	-0.5	FHB	H
CS 22950-38	20 20 29.9	-13 6 41	31.3	-26.1	14.09	0.26	0.12	2.4	17.5	15.3	7204	2.6	-1.8	15	5.0	-2.2	FHB	H
CS 22950-64	20 18 8.6	-15 19 50	28.7	-26.5	13.97	0.27	0.12	3.3	13.7	12.1	7004	2.5	-1.5	-52	4.7	-2.1	FHB	H
CS 22950-136	20 26 41.3	-13 35 17	31.5	-27.7	14.45	0.20	0.07	1.8	16.1	14.2	7252	2.8	-2.2	-188	5.9	-2.8	FHB	H
CS 22950-175	20 32 6.1	-15 45 18	29.8	-29.8	15.20	0.16	0.10	2.0	21.0	18.3	7516	2.9	-1.9	-107	8.1	-4.0	FHB	H
CS 22952-17	23 38 52.4	-5 49 8	82.1	-62.7	14.57	0.25	0.12	1.5	16.6	14.6	7154	2.6	-2.3	-81	6.2	-5.5	FHB	H
CS 22953-8	1 0 56.2	-61 6 58	300.4	-56.2	14.32	0.25	0.10	3.1	11.9	10.6	6750	2.0	-1.9	80	5.5	-4.6	FHB	H
CS 22955-12	20 21 28.9	-26 39 60	16.9	-31.2	13.77	0.15	0.13	2.0	21.4	18.6	7579	2.8	-1.8	-135	4.2	-2.2	FHB	H
CS 22955-15	20 21 15.7	-26 26 5	17.2	-31.1	13.86	0.19	0.10	2.0	15.4	13.5	7192	2.5	-2.1	-101	4.5	-2.3	FHB	H
CS 22955-18	20 19 56.9	-26 10 20	17.3	-30.7	14.65	0.09	0.12	1.3	24.2	21.0	8139	3.0	-1.8	-142	6.0	-3.1	FHB	H
CS 22955-25	20 19 20.5	-25 23 24	18.2	-30.4	13.28	0.31	0.00	5.4	15.4	13.5	7014	2.9	-0.9	32	3.4	-1.7	FHB	H
CS 22955-39	20 20 42.2	-23 19 24	20.5	-30.0	14.00	0.32	0.05	3.3	18.3	16.0	7157	3.1	-0.9	-57	4.8	-2.4	FHB	H
CS 22955-61	20 24 44.5	-24 20 40	19.8	-31.2	14.77	0.41	0.04	1.9	18.3	16.0	7261	3.0	-2.1	-106	6.8	-3.5	FHB	H
CS 22955-99	20 29 47.0	-26 43 38	17.5	-33.0	12.06	0.18	0.12	3.2	12.4	11.1	7000	2.0	-1.6	-101	2.0	-1.1	FHB	H
CS 22955-103	20 28 54.6	-26 17 3	17.9	-32.7	15.99	0.34	0.01	2.2	12.5	11.1	6759	2.5	-2.2	-148	12.0	-6.5	FHB	H
CS 22955-104	20 28 35.6	-26 1 32	18.2	-32.5	15.18	0.02	0.09	0.9	25.0	21.8	8470	3.0	-1.7	-122	7.0	-3.7	FHB	H
CS 22955-129	20 27 35.4	-23 7 30	21.4	-31.4	13.62	0.29	0.06	3.4	16.1	14.2	7054	2.8	-1.3	-15	4.0	-2.1	FHB	H
CS 22955-132	20 30 32.3	-22 45 57	22.0	-31.9	14.18	0.38	0.07	3.4	15.4	13.5	6997	2.7	-1.4	39	5.2	-2.7	FHB	H
CS 22955-146	20 35 48.3	-25 32 37	19.3	-33.9	14.30	0.28	-0.07	4.3	11.0	9.8	6998	3.0	-1.5	-31	5.5	-3.1	FHB	H
CS 22955-147	20 35 36.8	-25 58 40	18.8	-34.0	14.04	0.15	0.14	1.5	22.0	19.1	7705	3.1	-1.8	10	4.7	-2.7	FHB	H
CS 22955-163	20 37 35.2	-25 51 10	19.1	-34.4	12.92	0.33	0.04	1.1	16.9	14.9	7155	3.2	-2.4	-180	2.9	-1.6	FHB	H

Table B.1. (continued)

Star (1)	RA (1950) (2)	Dec (3)	l (4)	b (5)	V (6)	$(B-V)_o$ (7)	$(U-B)_o$ (8)	W_k (9)	$H\delta\ I_{0.2}$ (10)	$H\gamma\ D_{0.2}$ (11)	T_{eff} (12)	Log g (13)	[Fe/H] (14)	V_{tan} (15)	Dist. (16)	Z (17)	Class (18)	Obs (19)
CS 22956-26	21 45 44.6	-63 48 44	328.8	-43.3	14.33	0.06	0.19	1.2	26.3	25.1	8191	3.2	-1.9	243	5.0	-3.4	FHB	E
CS 22956-33	21 47 45.4	-62 23 39	330.4	-44.2	14.82	0.17	0.11	0.6	20.2	17.7	7503	2.9	-3.0	110	6.9	-4.8	FHB	H
CS 22956-39	21 51 0.8	-63 46 54	328.4	-43.8	14.74	0.28	0.13	2.2	14.1	12.5	6970	2.3	-2.2	-81	6.7	-4.7	FHB	H
CS 22956-43	21 49 8.8	-64 23 37	327.8	-43.4	14.92	0.25	0.09	2.9	11.6	10.3	6750	2.0	-2.0	103	7.3	-5.0	FHB	H
CS 22956-44	21 47 57.8	-64 32 55	327.7	-43.2	15.03	0.33	0.08	1.0	11.6	10.3	6785	2.4	-3.0	377	7.7	-5.3	FHB	H
CS 22956-58	22 3 15.1	-67 4 7	323.7	-43.1	13.35	0.31	0.16	2.5	17.3	15.2	7190	2.5	-1.8	-15	3.5	-2.4	FHB	H
CS 22956-60	21 58 58.0	-66 30 19	324.6	-43.1	13.36	-0.04	-0.22	0.5	18.1	16.7	9607	2.9	-1.5	86	2.6	-1.8	FHB	E
CS 22956-64	21 58 34.5	-66 4 27	325.2	-43.3	14.44	0.03	0.01	0.7	23.3	23.0	8731	3.0	-2.4	-62	5.0	-3.4	FHB	E
CS 22956-70	21 57 32.8	-65 20 48	326.1	-43.6	13.13	0.08	0.16	1.7	25.2	25.1	8227	3.0	-1.2	20	2.9	-2.0	FHB	E
CS 22956-78	21 59 44.6	-64 23 9	327.0	-44.3	13.88	-0.02	-0.08	1.7	19.0	19.0	9342	3.0	-2.3	70	3.5	-2.5	FHB	E
CS 22958-1	1 49 1.7	-57 37 46	287.8	-68.0	14.79	0.28	-0.03	3.1	12.7	11.2	6758	2.4	-2.0	55	6.9	-5.8	FHB	H
CS 22959-22	18 40 24.6	-66 0 38	329.4	-24.0	12.89	0.00	0.04	0.6	24.1	23.6	8740	3.0	-1.9	304	2.3	-1.0	FHB	E
CS 22959-66	18 48 33.7	-63 4 49	332.8	-24.2	14.48	0.33	0.03	4.2	12.3	10.9	6750	2.5	-1.5	-31	6.0	-2.4	FHB	H
CS 22959-126	18 53 58.1	-64 49 48	331.0	-25.1	13.22	0.48	0.12	3.2	12.3	10.9	6541	2.4	-1.9	-101	3.3	-1.4	FHB	H
CS 22959-134	18 53 22.4	-63 45 32	332.2	-24.9	15.34	0.06	-0.13	0.1	13.7	12.1	9508	2.5	-3.0	-30	8.0	-3.4	FHB	H
CS 22959-189	19 5 48.7	-66 38 10	329.3	-26.6	13.09	0.04	0.11	1.2	26.1	24.7	8407	3.1	-1.8	-129	2.8	-1.2	FHB	E
CS 22959-210	19 17 17.2	-66 7 44	330.0	-27.7	13.34	0.18	0.14	1.4	20.6	18.0	7500	2.8	-2.2	-129	3.5	-1.6	FHB	H
CS 22959-215	19 14 54.9	-65 57 56	330.1	-27.5	14.91	-0.04	-0.62	0.1	13.8	12.2	7500	2.8	0.4	-187	5.5	-2.5	FHB	H
CS 22959-236	18 30 48.9	-66 20 12	328.8	-23.2	14.71	0.36	-0.05	4.7	9.8	8.8	6737	3.0	-1.3	78	6.6	-2.6	FHB	H
CS 22960-50	22 15 33.7	-45 4 4	352.6	-54.8	14.93	0.16	0.10	0.8	22.9	19.9	7727	3.2	-2.4	-35	7.2	-5.9	FHB	H
CS 22960-70	22 19 50.1	-44 2 6	353.9	-55.9	15.46	0.30	0.05	3.7	13.0	11.5	7004	3.0	-1.6	-68	9.4	-7.8	FHB	H
CS 22960-84	22 22 24.1	-46 25 47	349.6	-55.5	14.58	0.19	0.09	0.5	20.0	17.5	7497	3.0	-3.0	13	6.3	-5.2	FHB	H
CS 22964-79	19 48 12.2	-40 31 41	359.4	-28.1	14.78	0.31	-0.01	4.8	11.7	10.4	6740	2.5	-1.3	-33	6.9	-3.2	FHB	H
CS 22964-89	19 51 10.5	-41 21 7	358.7	-28.9	15.10	0.19	0.15	1.1	20.5	17.9	7494	2.9	-2.4	42	7.9	-3.8	FHB	H
CS 22964-121	19 51 44.3	-39 29 11	0.8	-28.5	12.16	0.00	-0.12	0.8	19.7	18.9	9252	3.0	-1.5	-175	1.7	-0.8	FHB	E
CS 22964-151	19 54 43.8	-37 24 36	3.2	-28.6	14.49	0.34	0.02	4.8	13.2	11.7	6758	2.5	-1.4	19	6.0	-2.9	FHB	H
CS 22964-198	20 2 17.1	-41 34 30	358.9	-30.9	14.10	0.33	-0.01	5.6	10.1	9.1	6751	3.0	-1.0	-7	5.0	-2.6	FHB	H
CS 22964-209	20 2 51.2	-40 20 53	0.3	-30.8	15.21	-0.04	-0.72	0.1	15.5	13.6	9686	2.8	-3.0	-33	6.2	-3.2	FHB	H
CS 22964-219	20 3 9.2	-39 12 20	1.6	-30.6	14.16	0.30	0.06	4.9	15.4	13.5	7019	2.9	-1.1	19	5.2	-2.6	FHB	H
CS 22966-4	23 33 39.2	-32 1 22	12.7	-73.0	15.53	0.13	0.15	1.2	24.7	23.6	7976	3.1	-1.8	-1	9.3	-8.9	FHB	E

Table B.1. (continued)

Star (1)	RA (1950) (2)	Dec (3)	l (4)	b (5)	V (6)	$(B-V)_o$ (7)	$(U-B)_o$ (8)	W_k (9)	$H\delta$ $D_{0.2}$ (10)	$H\gamma$ $D_{0.2}$ (11)	T_{eff} (12)	Log g (13)	[Fe/H] (14)	V_{hel} (15)	Dist. (16)	Z (17)	Class (18)	Obs (19)
CS 22966-29	23 38 38.7	-30 40 38	16.8	-74.3	13.69	0.12	0.19	1.1	21.0	23.6	7659	2.7	-2.6	0	4.0	-3.8	FHB	E
CS 22966-42	23 41 52.7	-28 36 1	24.4	-75.1	13.15	0.04	0.11	0.7	25.6	23.8	8342	3.0	-2.4	-46	2.8	-2.8	FHB	E
CS 22966-59	23 47 23.4	-30 12 52	17.6	-76.2	15.44	0.05	0.14	0.8	24.3	20.3	8184	3.0	-2.4	-126	8.3	-8.0	FHB	E
CS 22966-61	23 44 12.4	-30 17 9	17.7	-75.5	14.01	0.14	0.14	2.5	12.3	16.6	7000	2.0	-2.0	-131	4.7	-4.5	FHB	E
CS 22966-65	23 48 41.3	-31 47 15	10.9	-76.2	15.36	0.04	0.16	1.6	26.0	25.6	8210	3.1	-2.8	238	7.8	-7.6	FHB	E
CS 22966-69	23 52 24.0	-31 22 35	11.7	-77.1	13.83	0.17	0.17	2.0	19.6	20.3	7477	2.7	-1.4	-114	4.4	-4.3	FHB	E
CS 22966-71	23 53 13.6	-30 52 25	13.7	-77.3	15.37	0.02	0.11	0.3	25.6	24.5	8428	3.0	-3.0	35	7.6	-7.4	FHB	E
CS 22968-3	2 56 0.1	-65 4 56	272.1	-54.0	13.24	0.27	0.11	2.8	16.1	14.2	7033	2.5	-1.8	7	3.4	-2.7	FHB	H
CS 22968-11	3 1 47.7	-53 42 57	269.4	-54.2	14.62	0.20	0.11	1.9	14.7	13.0	7015	2.4	-2.3	325	6.4	-5.2	FHB	H
CS 22968-13	3 5 41.9	-54 38 16	270.2	-53.2	13.66	0.15	0.12	2.0	23.6	17.7	7745	3.1	-1.6	32	4.0	-3.2	FHB	E
CS 22968-23	3 20 16.5	-56 31 50	271.0	-50.4	15.40	0.22	0.17	1.0	16.3	14.3	7148	2.7	-2.7	318	9.1	-7.0	FHB	H
CS 22968-35	3 19 54.6	-64 4 27	267.6	-51.7	15.45	0.09	0.18	0.3	26.3	22.9	8029	3.2	-3.0	-41	8.7	-6.8	FHB	H
CS 29493-9	21 36 46.1	-31 7 16	15.9	-48.2	13.36	0.38	0.12	3.8	13.3	11.8	6750	2.0	-1.6	1	3.6	-2.7	FHB	H
CS 29493-12	21 38 24.1	-30 7 19	17.5	-48.4	14.41	0.31	0.12	2.6	15.4	13.6	7022	2.5	-1.9	-175	5.8	-4.3	FHB	H
CS 29493-33	21 41 7.9	-31 14 9	15.9	-49.2	14.88	0.21	0.14	1.1	21.3	18.6	7475	2.9	-2.4	38	7.2	-5.4	FHB	H
CS 29496-25	23 44 30.1	-30 19 29	17.5	-75.6	14.67	-0.02	-0.42	0.1	22.2	19.3	8785	2.8	-3.0	6	5.1	-5.0	FHB	H
CS 29497-9	0 26 31.5	-23 56 36	66.1	-83.9	14.02	0.06	0.13	0.9	24.8	23.7	8240	3.0	-2.1	-131	4.3	-4.3	FHB	E
CS 29497-13	0 28 45.8	-23 31 52	72.2	-84.0	14.57	-0.02	0.00	0.6	23.9	25.7	8738	3.0	-3.0	-8	4.9	-4.8	FHB	E
CS 29497-22	0 29 2.1	-25 11 8	58.2	-85.0	13.39	-0.03	-0.06	0.2	20.7	22.5	9238	3.0	-3.0	-122	2.8	-2.8	FHB	E
CS 29497-31	0 36 13.1	-24 43 25	75.3	-86.1	13.92	0.03	0.13	0.6	25.8	28.1	8241	3.0	-2.7	-24	4.0	-4.0	FHB	E
CS 29497-33	0 38 40.4	-26 12 58	59.6	-87.4	13.83	0.12	0.17	1.3	20.8	19.6	7666	2.6	-2.3	73	4.2	-4.2	FHB	E
CS 29497-38	0 41 19.6	-27 0 15	45.6	-88.2	15.42	0.10	0.17	0.4	25.8	21.2	8014	3.1	-3.0	-42	8.6	-8.6	FHB	E
CS 29499-1	23 36 42.4	-27 41 15	27.8	-74.0	14.72	0.01	0.11	0.1	22.6	27.0	8677	3.0	-3.0	209	5.6	-5.4	FHB	E
CS 29499-19	23 36 26.5	-23 29 14	42.4	-73.2	14.78	0.12	0.16	1.5	21.6	22.2	7699	2.7	-2.0	-69	6.5	-6.2	FHB	E
CS 29499-22	23 36 8.3	-22 47 57	44.6	-72.9	12.08	0.05	0.15	0.7	27.2	23.0	8275	3.2	-2.2	101	1.7	-1.7	FHB	E
CS 29499-31	23 40 3.5	-26 31 30	32.3	-74.6	13.36	0.29	0.04	3.8	17.0	14.9	7112	2.9	-1.1	-8	3.6	-3.4	FHB	H
CS 29499-35	23 40 35.5	-26 55 26	30.9	-74.8	12.90	0.15	0.13	1.3	21.8	18.0	7709	3.2	-2.3	-203	2.8	-2.7	FHB	E
CS 29499-36	23 44 16.0	-27 4 48	30.5	-75.6	14.79	0.03	0.14	0.4	26.0	21.7	8255	3.0	-3.0	48	5.9	-5.7	FHB	E
CS 29499-37	23 46 47.1	-26 52 24	31.6	-76.2	13.43	0.06	0.13	0.5	26.1	29.2	8214	3.0	-3.0	-104	3.3	-3.2	FHB	E
CS 29499-38	23 47 4.6	-26 48 17	31.9	-76.2	14.31	0.07	0.17	0.7	26.6	23.9	8208	3.1	-2.6	-33	5.0	-4.9	FHB	E

Table B.1. (continued)

Star (1)	RA (1950) (2)	Dec (3)	l (4)	b (5)	V (6)	$(B-V)_o$ (7)	$(U-B)_o$ (8)	W_λ (9)	$H\delta$ $D_{0.2}$ (10)	$H\gamma$ $D_{0.2}$ (11)	T_{eff} (12)	Log g (13)	[Fe/H] (14)	V_{rad} (15)	Dist. (16)	Z (17)	Class (18)	Obs (19)
CS 29499-40	23 43 38.8	-26 1 47	34.6	-75.4	14.50	0.07	0.16	1.0	24.5	25.2	8199	3.0	-3.0	-66	5.5	-5.3	FHB	E
CS 29499-42	23 44 59.3	-25 11 49	38.1	-75.5	13.98	0.23	0.14	2.3	14.3	13.1	7000	2.0	-2.1	-29	4.7	-4.6	FHB	E
CS 29501-10	20 58 48.2	-36 23 47	7.2	-41.0	15.09	0.35	0.07	2.9	18.4	16.1	7252	2.9	-1.6	80	7.9	-5.2	FHB	H
CS 29501-23	21 5 5.9	-32 56 50	12.0	-41.8	13.53	0.35	0.13	2.3	17.6	15.4	7214	2.5	-2.0	-30	3.9	-2.6	FHB	H
CS 29501-36	21 4 8.4	-36 18 51	7.5	-42.1	13.66	0.18	0.17	1.6	21.4	18.7	7502	3.0	-2.0	-151	4.1	-2.7	FHB	H
CS 29501-57	21 13 8.4	-35 21 43	9.0	-43.8	14.01	0.41	0.09	2.7	15.4	13.6	7025	2.5	-1.8	-98	4.8	-3.3	FHB	H
CS 29503-8	0 3 29.1	-24 53 51	44.2	-79.5	14.32	0.02	0.10	1.0	24.3	24.1	8493	3.0	-1.8	45	4.7	-4.6	FHB	E
CS 29503-14	0 3 41.0	-23 5 40	53.3	-78.9	14.60	0.07	0.15	1.2	26.1	24.4	8166	3.1	-1.8	-1	5.7	-5.6	FHB	E
CS 29503-24	0 7 36.0	-25 50 22	40.2	-80.6	14.63	0.17	0.14	2.6	17.7	15.5	7269	2.4	-1.9	143	6.3	-6.3	FHB	H
CS 29503-29	0 8 46.8	-26 43 20	35.0	-81.0	13.56	0.05	0.13	0.6	26.0	23.8	8241	3.0	-2.3	-49	3.5	-3.4	FHB	E
CS 29504-4	1 28 47.5	-36 54 0	264.0	-77.3	14.31	0.16	0.12	0.9	21.4	20.0	7624	3.0	-2.6	45	5.4	-5.3	FHB	EE
CS 29504-28	1 33 56.8	-34 21 25	251.6	-78.1	14.08	0.12	0.15	0.8	21.0	23.9	7579	2.5	-2.9	-56	4.7	-4.6	FHB	E
CS 29504-35	1 38 36.5	-33 40 45	246.5	-77.6	14.67	0.02	0.11	1.4	25.0	24.2	8458	3.0	-2.0	43	5.5	-5.4	FHB	E
CS 29504-45	1 45 17.1	-34 22 19	246.5	-76.1	13.89	0.15	0.16	1.3	19.3	19.8	7479	2.7	-2.0	189	4.4	-4.3	FHB	E
CS 29506-45	21 18 54.5	-21 59 16	27.4	-42.3	14.12	0.35	0.01	3.9	15.4	13.6	6998	3.0	-0.8	12	5.1	-3.4	FHB	H
CS 29506-78	21 28 41.2	-20 2 20	30.9	-43.9	14.54	0.33	0.05	3.5	16.2	14.2	7048	2.9	-1.3	-20	6.1	-4.3	FHB	H
CS 29506-100	21 31 4.2	-21 7 34	29.7	-44.7	13.67	0.34	0.00	4.4	14.6	12.9	6983	3.0	-1.1	-61	4.1	-2.9	FHB	H
CS 29509-39	0 52 16.0	-28 30 9	270.0	-88.7	13.60	0.17	0.14	1.6	23.7	18.5	7751	3.1	-1.8	54	3.9	-3.9	FHB	E
CS 29512-68	22 19 43.3	-12 15 51	48.9	-52.0	14.20	0.39	0.01	5.8	11.1	9.9	6744	2.9	-0.7	-32	5.2	-4.1	FHB	H
CS 29513-17	23 16 33.7	-37 57 13	358.6	-68.0	13.77	0.19	0.14	1.8	15.5	13.6	7221	2.5	-2.2	94	4.3	-4.0	FHB	H
CS 29514-8	1 3 17.2	-24 14 43	169.3	-85.5	13.37	0.01	-0.01	0.7	21.7	20.3	8844	3.0	-2.3	113	3.0	-3.0	FHB	E
CS 29514-11	1 10 2.0	-23 4 58	171.9	-83.6	12.49	0.09	0.15	1.0	25.2	24.5	8053	3.0	-2.2	-18	2.2	-2.2	FHB	E
CS 29514-16	1 8 6.8	-26 20 46	200.2	-85.6	13.16	0.00	0.03	0.4	24.8	22.3	8716	3.0	-2.9	-15	2.6	-2.6	FHB	E
CS 29514-30	1 16 48.8	-23 9 58	180.6	-82.4	14.37	-0.02	0.04	0.3	22.3	20.5	8810	3.0	-1.9	9	4.5	-4.4	FHB	E
CS 29514-38	1 20 31.4	-26 33 14	207.9	-82.9	13.98	0.38	0.04	3.8	8.5	7.9	6532	2.4	-1.7	54	4.7	-4.7	FHB	E
CS 29516-11	22 26 5.3	+6 5 48	71.7	-41.9	12.23	0.00	0.07	0.4	21.9	21.2	8792	3.0	-2.2	-14	1.7	-1.2	FHB	K
CS 29516-17	22 25 26.8	+3 44 8	69.3	-43.5	12.46	0.04	0.08	0.8	24.4	23.6	8493	3.0	-2.0	-228	2.1	-1.4	FHB	K
CS 29516-21	22 26 17.0	+1 50 49	67.6	-44.9	13.82	-0.04	-0.19	0.6	20.0	18.6	9713	3.0	-1.7	-46	3.3	-2.3	FHB	K

Table B.1. (continued)

Star (1)	RA (1950) (2)	Dec (3)	l (4)	b (5)	V (6)	$(B-V)_o$ (7)	$(U-B)_o$ (8)	W_k (9)	$H\delta$ $D_{0.2}$ (10)	$H\gamma$ $D_{0.2}$ (11)	T_{eff} (12)	Log g (13)	[Fe/H] (14)	V_{los} (15)	Dist. (16)	Z (17)	Class (18)	Obs (19)
CS 29516-25	22 24 5.2	+ 2 37 50	67.9	-44.0	14.63	0.03	-0.05	0.4	19.0	17.9	9262	3.0	-2.2	5	5.5	-3.8	FHB	K
CS 29517-2	23 44 29.3	-16 57 41	64.7	-71.8	13.63	0.19	0.14	...	12.0	12.6	7000	2.0	-1.4	2	4.0	-3.8	FHB	L
CS 29517-7	23 45 17.9	-15 4 40	69.5	-70.7	15.75	0.10	0.16	...	23.3	22.4	7912	3.0	-2.3	-309	10.0	-9.5	FHB	L
CS 29517-31	23 59 36.1	-14 25 37	79.0	-72.7	15.39	0.08	0.17	...	26.1	20.7	8192	3.1	-2.8	-314	8.3	-7.9	FHB	L
CS 29517-44	0 0 34.8	-14 41 7	79.0	-73.0	14.66	0.04	0.16	...	25.1	22.8	8231	3.0	-2.5	60	5.7	-5.5	FHB	L
CS 29517-46	0 2 13.0	-14 19 20	80.9	-73.0	14.73	-0.02	-0.41	0.1	24.1	21.0	8988	2.8	-3.0	-132	5.2	-5.0	FHB	H
CS 29518-35	1 14 36.0	-28 1 45	220.8	-84.3	14.58	0.05	0.16	0.5	26.4	24.1	8234	3.1	-2.9	45	5.6	-5.5	FHB	E
CS 29520-2	4 18 53.0	-62 26 1	273.8	-41.2	14.62	0.05	0.15	0.7	23.0	26.1	7941	2.6	-3.0	29	5.7	-3.7	FHB	E
CS 29520-9	4 25 28.6	-61 2 30	271.7	-40.9	16.13	0.01	0.09	0.4	25.5	20.8	8490	3.0	-2.8	174	10.5	-6.9	FHB	E
CS 29520-19	4 25 37.9	-59 12 49	269.4	-41.4	14.34	-0.25	-0.99	0.0	15.5	15.5	7243	2.5	-3.0	4	1.2	-0.8	FHB	E
CS 29520-28	4 34 50.6	-57 56 35	267.4	-40.6	14.46	0.01	0.03	0.7	22.3	20.4	8817	3.0	-1.9	115	4.9	-3.2	FHB	E
CS 29520-36	4 34 51.1	-60 42 39	270.9	-39.9	14.56	0.00	0.05	0.9	21.2	26.4	8967	3.0	-1.6	274	5.0	-3.2	FHB	E
CS 29520-41	4 28 8.4	-62 7 21	273.0	-40.3	14.64	0.11	0.20	0.9	22.5	27.2	7819	2.8	-2.7	144	6.1	-3.9	FHB	E
CS 29520-42	4 27 8.3	-62 9 28	273.1	-40.4	13.84	0.20	0.11	2.0	16.5	15.4	7248	2.5	-2.3	170	4.5	-2.9	FHB	E
CS 29520-46	4 32 6.8	-62 56 22	273.8	-39.6	13.64	-0.04	-0.19	1.6	8.2	8.3	9500	2.0	-1.5	276	3.1	-1.9	FHB	E
CS 29520-53	4 36 34.6	-61 14 54	271.5	-39.5	14.82	0.13	0.21	1.0	20.7	19.1	7584	2.6	-3.0	274	6.7	-4.3	FHB	E
CS 29520-59	4 36 15.2	-59 42 42	269.6	-40.0	15.46	0.01	0.09	3.0	23.8	22.6	8534	3.0	-2.7	138	7.9	-5.1	FHB	E
CS 29520-74	4 46 15.3	-59 34 2	269.0	-38.8	14.07	0.01	0.09	0.6	25.2	23.2	8505	3.0	-2.8	318	4.1	-2.6	FHB	E
CS 29520-78	4 45 3.9	-60 56 4	270.8	-38.6	13.79	0.03	0.07	0.4	23.5	22.5	8709	3.0	-2.9	72	3.7	-2.3	FHB	E
CS 29527-16	0 25 22.9	-19 14 19	88.2	-80.2	13.95	0.06	0.16	0.7	25.5	21.7	8215	3.0	-2.7	-43	4.2	-4.2	FHB	E
CS 29527-22	0 29 46.6	-19 42 33	92.2	-81.1	11.85	0.01	0.07	0.5	24.7	24.2	8633	3.0	-2.7	-98	1.5	-1.5	FHB	E
CS 29527-26	0 30 34.9	-21 27 46	86.8	-82.7	14.00	0.08	0.16	1.2	23.0	24.8	7754	2.7	-1.6	-146	4.4	-4.4	FHB	E
CS 29527-31	0 34 9.7	-22 42 14	86.6	-84.2	13.66	0.14	0.16	1.2	21.6	18.3	7725	3.0	-2.1	-19	4.0	-3.9	FHB	E
CS 29527-35	0 32 53.3	-21 17 18	91.2	-82.9	13.14	0.03	0.09	0.3	26.0	24.1	8499	3.0	-2.4	-7	2.8	-2.8	FHB	EE
CS 29527-39	0 34 23.9	-20 13 21	97.3	-82.1	14.52	0.12	0.17	2.4	23.9	21.5	7787	3.0	-1.1	-26	5.8	-5.7	FHB	E
CS 29527-61	0 41 19.6	-21 2 6	107.2	-83.4	13.74	0.01	0.01	0.1	22.5	20.5	8754	3.0	-3.0	-67	3.5	-3.5	FHB	E
CS 29529-53	3 56 7.9	-62 26 23	275.3	-43.6	14.18	0.22	0.14	2.1	15.4	12.3	7000	2.0	-2.2	34	5.2	-3.6	FHB	E
CS 29529-55	3 59 0.2	-62 19 47	274.9	-43.3	14.86	0.40	-0.02	5.9	12.4	11.0	6746	2.9	-0.6	93	7.1	-4.9	FHB	H
CS 29529-94	4 13 32.7	-61 39 19	273.2	-42.0	15.39	0.11	0.16	1.0	22.6	23.0	7824	2.8	-2.6	241	8.6	-5.7	FHB	E

Table B.1. (continued)

Star (1)	RA (1950) (2)	Dec (3)	l (4)	b (5)	V (6)	$(B-V)_o$ (7)	$(U-B)_o$ (8)	W_k (9)	$H\delta$ $D_{0.2}$ (10)	$H\gamma$ $D_{0.2}$ (11)	T_{eff} (12)	Log g (13)	[Fe/H] (14)	V_{los} (15)	Dist. (16)	Z (17)	Class (18)	Obs (19)
CS 30312-1	15 30 2.6	-2 31 43	1.9	41.0	12.63	0.38	0.14	3.3	19.6	17.1	7406	2.7	-1.4	-14	2.5	1.7	FHB	H
CS 30312-18	15 27 17.4	+0 36 17	4.5	43.6	11.35	0.27	0.06	2.4	17.0	14.9	7221	3.0	-1.7	-2	1.4	1.0	FHB	H
CS 30312-38	15 31 59.3	+1 17 23	6.3	43.1	13.54	0.28	0.02	5.5	14.5	12.8	7009	3.0	-0.7	-21	3.9	2.6	FHB	H
CS 30312-45	15 34 56.3	+0 38 5	6.2	42.1	13.47	0.28	0.00	3.8	17.0	14.9	7178	3.1	-1.0	-58	3.7	2.5	FHB	H
CS 30312-70	15 38 9.7	-2 25 56	3.7	39.5	13.06	0.37	0.14	2.8	15.5	13.7	7050	2.4	-1.8	-22	3.1	2.0	FHB	H
CS 30321-35	18 24 24.3	-35 31 18	358.5	-11.0	14.59	0.03	0.10	2.2	23.3	22.5	8502	3.0	-0.8	39	5.4	-1.0	FHB	E
CS 30321-106	18 29 1.9	-32 31 34	1.7	-10.5	14.33	0.05	0.04	2.1	24.7	23.2	8509	3.0	-1.0	1	4.9	-0.9	FHB	E
CS 30321-151	18 26 33.4	-35 21 14	358.9	-11.3	14.52	0.02	0.11	0.7	26.4	23.0	8441	3.1	-1.8	52	5.1	-1.0	FHB	E
CS 30321-152	18 27 37.1	-35 34 39	358.7	-11.6	14.87	0.03	0.13	0.9	25.7	23.9	8250	3.0	-1.9	-7	6.2	-1.2	FHB	E
CS 30321-168	18 26 20.2	-36 5 58	358.2	-11.6	13.56	0.00	0.05	1.0	23.1	26.7	8735	3.0	-1.6	-62	3.2	-0.6	FHB	E
CS 30321-169	18 26 9.6	-36 9 43	358.1	-11.6	14.18	-0.03	-0.01	0.6	20.3	21.8	9240	3.0	-1.8	-138	4.0	-0.8	FHB	E
CS 30321-189	18 29 1.1	-36 47 40	357.7	-12.3	13.76	0.03	0.09	0.9	26.0	22.6	8351	3.0	-2.7	160	3.7	-0.8	FHB	E
CS 30321-243	18 29 5.8	-33 56 55	0.4	-11.1	14.05	0.11	0.13	0.6	24.7	24.4	8012	3.0	-2.9	17	4.6	-0.9	FHB	E
CS 30321-279	18 31 25.8	-32 20 46	2.1	-10.9	13.94	0.03	0.06	0.9	24.1	22.6	8579	3.0	-1.9	-195	4.0	-0.8	FHB	E
CS 30321-322	18 31 52.1	-34 33 6	0.1	-11.9	14.29	0.10	0.20	1.9	24.1	24.8	8063	3.1	-1.4	158	5.1	-1.1	FHB	E
CS 30321-345	18 33 7.6	-35 40 15	359.1	-12.6	14.31	0.09	0.19	1.1	25.7	24.3	8053	3.1	-2.1	-74	5.1	-1.1	FHB	E
CS 30321-347	18 32 35.5	-35 50 44	358.9	-12.6	13.47	0.17	0.16	8.9	14.7	14.5	7275	2.7	-2.6	152	3.7	-0.8	FHB	E
CS 30321-423	18 35 38.5	-34 38 1	0.3	-12.6	13.78	0.03	0.07	1.1	25.2	23.8	8504	3.0	-2.4	-23	3.7	-0.8	FHB	E
CS 30321-1046	18 37 47.6	-35 29 52	359.7	-13.4	14.05	0.15	0.13	1.3	22.9	19.0	7746	3.0	-2.1	106	4.8	-1.1	FHB	E
CS 30321-1101	18 37 19.7	-32 35 59	2.4	-12.1	13.67	0.08	0.16	1.7	25.8	20.8	8043	3.1	-1.5	-287	3.8	-0.8	FHB	E
CS 30321-1179	18 38 41.5	-35 28 30	359.8	-13.6	13.74	0.07	0.15	1.1	26.6	18.2	8090	3.0	-2.0	16	3.9	-0.9	FHB	E
CS 30321-1196	18 40 49.0	-36 19 47	358.0	-12.2	13.93	0.12	0.17	1.3	24.1	19.8	8526	3.0	-1.5	-86	6.1	-1.3	FHB	E
CS 30321-1265	18 42 50.9	-34 42 20	0.9	-14.0	13.82	0.04	0.12	0.7	24.5	23.1	8434	3.0	-2.9	87	3.9	-0.9	FHB	E
CS 30321-1270	18 42 11.9	-34 28 55	1.0	-13.8	13.97	0.02	0.06	1.0	23.1	24.7	8742	3.0	-1.6	-79	4.0	-1.0	FHB	E
CS 30321-1284	18 42 12.1	-33 41 6	1.8	-13.5	14.09	0.07	0.14	0.7	25.0	24.5	8181	3.0	-3.0	-184	4.5	-1.1	FHB	E
CS 30321-1431	18 46 6.1	-36 37 32	359.3	-15.4	14.04	0.01	0.08	0.7	23.5	22.5	8714	3.0	-2.1	-87	4.1	-1.1	FHB	E
CS 30321-1493	18 47 19.7	-33 0 16	2.9	-14.2	14.96	0.01	0.10	1.9	23.2	21.5	8544	3.0	-1.6	-52	6.2	-1.5	FHB	E
CS 30332-25	22 43 45.0	+7 35 45	77.5	-43.7	12.77	-0.02	-0.27	0.7	18.0	17.5	9406	2.9	-1.2	-37	2.1	-1.5	FHB	E
CS 30332-30	22 45 10.5	+9 0 20	79.1	-42.8	14.12	0.05	0.15	0.9	26.6	25.7	8226	3.1	-2.2	-24	4.5	-3.1	FHB	E
CS 30332-82	22 36 18.0	+9 37 28	77.4	-41.0	15.30	0.07	0.10	1.7	23.3	21.8	8351	3.0	-2.8	-282	8.0	-6.2	FHB	E
CS 30492-15	21 0 28.9	-40 35 24	1.7	-41.7	13.97	0.22	0.13	1.0	20.3	17.7	7476	2.9	-2.5	-39	4.7	-3.1	FHB	H
CS 30492-53	21 5 19.9	-39 48 7	2.8	-42.6	13.39	0.25	0.14	1.7	21.7	18.9	7492	2.7	-1.6	23	3.6	-2.4	FHB	H

Table B.1. (continued)

Star (1)	RA (1950) (2)	Dec (3)	l (4)	b (5)	V (6)	$(B-V)_o$ (7)	$(U-B)_o$ (8)	W_λ (9)	$H\delta$ $D_{0.2}$ (10)	$H\gamma$ $D_{0.2}$ (11)	T_{eff} (12)	Log g (13)	[Fe/H] (14)	V_{hel} (15)	Dist (16)	Z (17)	Class (18)	Obs (19)
CS 30492-63	21 5 19.7	-40 59 38	1.2	-42.6	15.70	-0.03	-0.47	0.6	16.3	14.3	9696	2.9	-0.2	15	7.9	-5.4	FHB	H
CS 30492-112	21 16 31.0	-38 48 51	4.3	-44.7	14.49	0.32	0.10	3.7	18.4	16.1	7114	2.5	-1.3	-25	6.0	-4.2	FHB	H
CS 30492-117	21 17 1.2	-40 17 48	2.2	-44.8	14.23	0.32	0.09	3.4	21.3	18.6	7464	3.1	-1.2	-50	5.3	-3.7	FHB	H
CS 30493-48	23 8 6.5	-37 27 11	1.2	-66.6	14.83	0.29	0.06	4.4	16.7	14.7	7115	2.9	-0.9	55	7.0	-6.4	FHB	H
CS 31072-11	5 38 20.7	-59 27 31	268.1	-32.2	13.60	0.31	0.10	1.2	16.9	16.6	7220	2.6	-2.4	32	4.0	-2.1	FHB	E
CS 31072-40	5 32 46.0	-58 25 26	266.9	-32.9	13.50	0.10	0.18	1.0	24.4	21.5	7998	3.0	-2.1	105	3.6	-1.9	FHB	E
CS 31072-61	5 26 27.6	-59 7 42	267.7	-33.7	12.69	-0.02	-0.01	1.6	18.1	18.2	9246	3.0	-0.5	64	2.1	-1.1	FHB	E
CS 31072-68	5 28 47.8	-61 18 43	270.3	-33.4	11.71	0.18	0.17	1.3	19.2	15.8	7477	2.8	-2.3	495	1.7	-0.9	FHB	E
CS 31072-95	5 15 34.6	-61 0 49	270.1	-35.0	14.82	-0.17	-0.94	0.0	12.6	13.0	7018	2.9	-3.0	2	2.9	-1.7	FHB	E
CS 31072-122	5 7 42.0	-58 41 39	267.4	-36.2	13.40	0.10	0.19	2.0	22.1	22.4	7739	2.6	-1.1	116	3.4	-2.0	FHB	E
CS 31072-131	5 2 37.3	-57 53 23	266.5	-36.9	13.43	0.33	0.00	5.1	14.0	11.8	6998	3.0	-0.9	43	3.7	-2.2	FHB	E
CS 31075-42	3 30 16.6	-66 48 25	282.4	-43.6	13.18	0.08	0.15	1.0	16.5	28.0	7500	2.0	-2.9	145	3.0	-2.1	FHB	E
CS 31075-62	3 20 43.0	-66 28 49	282.9	-44.5	14.24	0.30	0.00	3.7	15.3	16.4	7035	2.9	-1.4	71	5.3	-3.7	FHB	E
CS 31075-81	3 10 30.7	-67 17 8	284.7	-44.8	15.10	-0.05	-0.06	0.6	17.5	20.4	9534	3.0	-1.3	44	5.8	-4.1	FHB	E
CS 31080-104	4 41 28.2	-46 15 18	251.9	-41.0	12.28	-0.04	-0.17	0.5	19.4	19.4	9541	2.9	-1.7	292	1.6	-1.0	FHB	E

Table B.2. The A-star Sample.

Star (1)	RA (1950) (2)	Dec (3)	l (4)	b (5)	V (6)	$(B-V)_o$ (7)	$(U-B)_o$ (8)	W_λ (9)	Hδ $D_{0.2}$ (10)	Hγ $D_{0.2}$ (11)	T_{eff} (12)	Log g (13)	[Fe/H] (14)	V_{los} (15)	Dist. (16)	Z (17)	Class (18)	Obs (19)
BS 15621-2	10 26 24.4	+26 14 18	206.8	58.3	11.84	0.14	0.11	1.6	32.2	26.7	8534	4.3	-1.0	-18	1.0	0.9	A	KL
BS 15621-3	10 27 40.3	+24 45 53	209.6	58.3	12.76	0.45	-0.08	7.0	6.4	6.5	6510	3.9	-0.5	-8	1.2	1.0	A	KK
BS 15621-5	10 26 40.6	+23 19 47	212.2	57.7	12.86	0.23	0.11	4.3	21.5	19.4	7753	3.9	-0.5	19	1.3	1.1	A	KL
BS 15621-6	10 26 12.0	+23 17 51	212.2	57.6	13.36	0.46	-0.21	5.4	6.7	5.5	6502	4.4	-1.2	-25	1.6	1.3	A	K
BS 15621-12	10 24 30.4	+25 37 33	207.8	57.7	12.27	0.22	0.09	3.5	21.7	20.8	7763	3.9	-0.9	102	1.0	0.8	A	K
BS 15621-17	10 22 10.0	+27 55 06	203.4	57.6	11.09	0.09	0.09	2.3	30.1	29.1	8588	3.8	-1.5	47	0.8	0.7	A	KL
BS 15621-24	10 19 21.2	+25 42 08	207.2	56.6	14.64	0.42	-0.21	5.0	6.4	7.8	6505	4.2	-1.6	185	2.7	2.3	A	K
BS 15621-35	10 14 24.9	+25 40 23	206.8	55.5	14.59	0.40	-0.09	...	11.6	7.8	6957	4.0	-0.5	104	2.6	2.2	A	L
BS 15621-40	10 09 42.1	+27 32 30	203.3	54.8	13.81	0.20	-0.03	2.0	21.5	19.5	7767	4.0	-1.2	66	2.1	1.7	A	EL
BS 15621-41	10 08 39.5	+23 13 56	210.4	53.7	12.60	0.22	0.05	4.0	24.8	22.4	8007	4.5	-0.4	11	1.2	0.9	A	EL
BS 15621-48	10 14 18.0	+24 30 50	208.8	55.2	12.20	0.26	0.08	5.4	19.2	19.2	7507	4.0	0.0	-21	0.9	0.7	A	E
BS 15621-52	10 14 47.1	+23 13 33	211.1	55.0	13.42	0.44	-0.11	7.8	6.6	6.2	6542	4.1	-1.1	297	1.6	1.3	A	K
BS 15621-54	10 21 04.3	+24 10 40	210.1	56.7	13.80	0.36	-0.04	0.0	7.4	6.1	6742	3.5	-0.6	9	1.8	1.5	A	E
BS 15621-55	10 23 04.5	+24 11 01	210.2	57.1	13.28	0.42	-0.11	6.5	7.3	6.3	6546	3.7	-0.8	21	1.5	1.2	A	K
BS 15621-57	10 26 14.6	+23 37 08	211.6	57.7	13.16	0.41	-0.09	7.3	7.7	7.6	6769	4.4	-0.2	44	1.4	1.2	A	K
BS 15621-58	10 26 50.6	+23 40 02	211.6	57.8	14.39	0.31	-0.04	1.9	14.5	10.8	7124	4.0	-1.7	51	2.4	2.0	A	EL
BS 15621-59	10 27 11.2	+23 57 46	211.1	58.0	13.24	0.22	0.11	3.6	26.0	20.7	7987	4.0	-0.9	62	1.6	1.3	A	EL
BS 15621-65	10 25 11.3	+26 31 42	206.1	58.1	14.17	0.35	-0.10	6.2	8.5	8.9	6963	4.1	-1.0	102	2.1	1.8	A	E
BS 15621-70	10 19 07.9	+27 26 28	204.1	56.9	12.61	0.36	-0.07	2.4	10.9	9.8	6950	3.6	-0.9	35	1.0	0.9	A	E
BS 15621-71	10 12 44.2	+27 15 19	204.0	55.4	13.03	0.41	-0.03	...	6.8	7.5	6732	4.0	-0.1	37	1.3	1.1	A	L
BS 15621-72	10 14 29.2	+26 05 13	206.1	55.6	12.83	0.29	0.07	5.0	20.2	18.9	7521	3.9	-0.1	-11	1.2	1.0	A	E
BS 15621-73	10 10 30.5	+24 19 59	208.8	54.4	13.53	0.42	-0.21	3.5	7.0	6.4	6517	4.0	-1.8	106	1.6	1.3	A	K
BS 15621-75	10 08 43.0	+26 22 42	205.2	54.4	13.69	0.46	-0.15	6.0	6.3	5.9	6000	5.0	-1.7	162	1.9	1.5	A	K
BS 15621-77	10 10 11.7	+25 04 42	207.5	54.5	13.87	0.43	-0.17	3.0	7.7	7.5	6654	4.1	-1.9	131	1.9	1.6	A	K
BS 15625-3	11 38 20.7	+24 31 40	219.3	73.9	13.32	0.29	0.00	4.3	19.3	15.4	7514	3.9	-0.4	18	1.5	1.4	A	EL
BS 15625-17	11 53 50.0	+24 44 53	222.0	77.3	12.83	0.63	0.02	...	3.0	4.6	6000	4.5	0.0	41	2.0	2.0	A	L
BS 15625-18	11 57 11.4	+25 22 46	219.9	78.2	13.73	0.49	-0.15	...	6.1	4.7	6515	4.6	-0.1	20	2.0	2.0	A	L
BS 15625-22	11 38 27.9	+26 43 58	211.4	74.3	12.04	0.31	0.00	6.5	14.5	15.4	7246	3.5	-0.2	10	0.8	0.8	A	E
BS 15625-25	11 49 47.1	+24 40 38	221.2	76.4	13.33	0.43	-0.10	6.6	7.9	6.8	6714	3.9	-0.6	24	1.5	1.5	A	K
BS 15625-29	11 55 57.4	+25 33 05	218.8	78.0	13.03	0.38	-0.07	7.6	8.3	7.6	6980	4.5	0.0	-3	1.3	1.2	A	K
BS 15625-938	11 54 06.8	+23 52 16	225.9	77.1	12.26	0.33	-0.09	4.8	9.7	11.3	6964	3.7	-1.1	-37	0.9	0.9	A	E
BS 16026-6	12 14 26.5	+30 59 24	185.5	81.7	14.32	0.35	-0.22	1.8	8.7	8.3	6980	4.5	-2.3	127	2.3	2.3	A	KK
BS 16026-10	12 14 15.4	+29 51 49	193.0	82.0	10.06	0.32	-0.04	...	13.8	9.8	7227	4.1	-0.2	-16	0.3	0.3	A	L

Table B.2. (continued)

Star (1)	RA (1950) (2)	Dec (3)	l (4)	b (5)	V (6)	$(B-V)_o$ (7)	$(U-B)_o$ (8)	W_δ (9)	$H\delta$ $D_{0.2}$ (10)	$H\gamma$ $D_{0.2}$ (11)	T_{eff} (12)	Log g (13)	[Fe/H] (14)	V_{rot} (15)	Dist (16)	Z (17)	Class (18)	Obs (19)
BS 16026-14	12 13 55.6	+28 07 19	205.6	82.2	14.70	0.22	0.06	...	20.7	19.3	7514	3.5	-1.0	-24	3.1	3.0	A	L
BS 16026-18	12 17 38.6	+29 01 06	198.0	82.9	13.84	0.44	-0.22	5.6	5.4	5.6	6391	4.6	-1.5	50	1.9	1.9	A	K
BS 16026-23	12 19 27.4	+31 23 19	179.4	82.4	12.77	0.16	0.02	3.0	22.8	24.4	7765	3.6	-1.0	-25	1.4	1.4	A	K
BS 16026-35	12 24 55.9	+28 01 30	204.9	84.6	13.75	0.35	-0.12	...	9.9	8.1	7008	4.3	-0.8	27	1.7	1.7	A	L
BS 16026-37	12 26 43.8	+29 24 20	189.4	84.7	15.04	0.35	-0.20	...	12.4	11.3	7209	4.5	-1.2	155	3.2	3.2	A	L
BS 16026-38	12 27 04.2	+29 50 17	184.8	84.6	12.92	0.35	-0.06	...	9.5	7.7	6988	3.9	-0.6	-2	1.2	1.2	A	L
BS 16026-39	12 25 26.7	+31 48 47	170.8	83.2	14.76	0.43	-0.21	6.0	6.0	6.8	6514	4.4	-1.2	16	2.9	2.9	A	H
BS 16026-40	12 27 56.6	+31 11 22	172.2	84.0	13.34	0.39	-0.20	...	8.3	5.4	6732	4.2	-1.5	-54	1.5	1.5	A	L
BS 16026-56	12 31 45.1	+30 56 21	168.7	84.8	10.96	0.17	0.10	2.5	25.7	22.9	8023	3.8	-0.8	24	0.6	0.6	A	K
BS 16026-57	12 30 24.5	+31 18 35	167.9	84.4	14.37	0.42	-0.15	7.2	4.8	5.1	6000	5.0	-1.6	-59	2.4	2.4	A	K
BS 16026-61	12 32 54.2	+31 34 39	162.0	84.5	14.22	0.14	0.06	...	27.4	21.2	8048	3.6	-2.5	109	3.0	3.0	A	L
BS 16026-66	12 33 37.9	+27 56 49	203.0	86.6	14.09	0.36	-0.11	...	7.6	6.0	6803	4.0	-0.7	-17	2.0	2.0	A	L
BS 16026-68	12 34 11.4	+27 44 59	206.1	86.7	10.82	0.40	-0.22	4.1	6.8	6.9	6720	4.5	-1.6	-120	0.5	0.5	A	K
BS 16026-73	12 36 31.8	+30 59 14	159.4	85.5	13.35	0.32	-0.09	4.0	13.1	10.9	7243	4.0	-0.9	-31	1.5	1.5	A	KL
BS 16027-11	13 04 06.9	+31 02 42	81.8	85.1	14.70	0.39	-0.20	4.8	9.7	8.8	6973	4.6	-0.9	29	2.7	2.7	A	K
BS 16027-18	13 04 47.0	+30 02 33	71.3	85.6	15.00	0.38	-0.17	...	7.7	5.5	6731	4.0	-2.2	-8	3.1	3.1	A	L
BS 16027-22	13 04 03.8	+28 32 04	52.7	86.5	11.77	0.28	0.04	5.3	16.5	17.8	7280	3.5	-0.5	16	0.7	0.7	A	K
BS 16027-27	13 05 39.9	+29 06 27	58.9	86.0	14.61	0.34	-0.12	6.0	11.0	11.1	7250	5.0	-0.6	-40	2.6	2.6	A	K
BS 16027-28	13 06 44.3	+29 15 48	59.6	85.7	12.81	0.64	0.13	10.8	3.5	2.6	6000	4.0	-0.1	34	2.1	2.1	A	K
BS 16027-29	13 06 35.6	+29 32 23	63.0	85.6	15.21	0.36	-0.21	...	12.5	8.3	7199	4.5	-2.3	-17	3.4	3.4	A	L
BS 16027-33	13 06 01.1	+32 41 50	89.2	83.6	14.07	0.32	-0.04	...	13.0	11.0	7237	4.0	-0.8	-14	2.0	2.0	A	L
BS 16027-36	13 08 51.9	+33 14 32	88.0	82.8	15.27	0.30	-0.14	...	12.5	12.1	7246	4.1	-1.5	23	3.6	3.6	A	L
BS 16027-43	13 09 33.5	+29 05 02	54.6	85.2	14.95	0.39	-0.25	1.9	6.6	8.5	6520	4.0	-2.7	-16	3.1	3.1	A	K
BS 16027-45	13 11 45.4	+28 48 35	50.0	84.8	14.30	0.28	-0.04	...	19.6	18.3	7501	3.9	-0.8	-27	2.3	2.3	A	L
BS 16027-46	13 10 25.2	+28 57 33	52.5	85.0	14.92	0.44	-0.28	2.5	6.0	6.9	6446	4.6	-2.4	89	3.2	3.2	A	K
BS 16027-47	13 10 50.1	+29 11 07	54.7	84.9	13.97	0.35	-0.07	...	10.4	11.0	7013	4.1	-0.2	19	1.9	1.9	A	L
BS 16027-52	13 10 05.8	+31 28 38	75.9	83.9	14.97	0.24	-0.10	...	16.9	18.4	7727	4.5	-1.1	-43	3.3	3.3	A	L
BS 16027-58	13 13 18.5	+31 54 59	75.0	83.1	15.07	0.44	-0.21	4.1	8.2	7.7	6710	4.3	-1.4	10	3.4	3.4	A	K
BS 16027-59	13 12 22.1	+31 47 00	75.2	83.3	13.93	0.09	0.03	...	32.2	27.2	8734	4.0	-2.9	-83	3.1	3.1	A	L
BS 16027-63	13 12 21.4	+28 38 59	48.0	84.7	15.00	0.37	-0.20	3.1	7.4	6.5	6737	4.0	-1.9	-7	3.1	3.1	A	K
BS 16027-69	13 18 00.7	+31 13 44	65.9	82.6	14.83	0.29	-0.01	...	15.8	15.0	7269	3.5	-2.0	-102	3.0	2.9	A	L
BS 16027-70	13 17 21.9	+29 39 28	54.6	83.4	13.75	0.04	0.02	...	38.2	31.4	9214	4.5	-1.8	-66	3.5	3.5	A	L
BS 16027-74	13 17 06.4	+28 19 05	43.0	83.7	15.21	0.41	-0.21	6.4	6.7	6.0	6664	4.7	-1.2	-73	3.5	3.5	A	K

Table B.2. (continued)

Star (1)	RA (1950) (2)	Dec (3)	l (4)	b (5)	V (6)	$(B-V)_o$ (7)	$(U-B)_o$ (8)	W_δ (9)	Hδ $D_{0.2}$ (10)	Hγ $D_{0.2}$ (11)	T_{eff} (12)	Log g (13)	[Fe/H] (14)	V_{hel} (15)	Dist. (16)	Z (17)	Class (18)	Obs (19)
BS 16032-6	12 36 31.7	+30 59 08	159.5	85.5	13.42	0.34	-0.09	...	12.3	12.8	7182	4.1	-0.9	-80	1.5	1.5	A	L
CS 22166-4	00 49 40.8	-11 20 56	123.6	-73.9	13.08	0.16	0.08	1.8	24.4	27.8	7808	3.5	-1.8	-127	1.7	-1.6	A	K
CS 22166-12	00 53 50.4	-11 32 57	127.3	-74.1	14.73	0.19	0.10	3.4	30.1	25.2	8268	4.1	-0.1	-20	3.3	-3.2	A	K
CS 22166-30	01 02 58.2	-12 13 34	135.9	-74.5	13.58	0.42	-0.20	1.3	5.7	5.1	6308	3.3	-3.0	93	1.7	-1.6	A	K
CS 22166-34	01 05 33.8	-12 27 37	138.4	-74.6	14.47	0.15	0.16	1.1	21.0	19.5	7750	3.4	-2.0	128	3.2	-3.1	A	K
CS 22167-22	03 22 08.0	-06 31 07	190.3	-48.1	13.54	0.29	0.09	...	15.3	20.3	7263	3.5	0.0	30	1.6	-1.2	A	L
CS 22167-29	03 23 19.5	-04 16 25	187.8	-46.6	13.40	0.20	0.04	...	18.0	19.3	7764	4.5	0.0	50	1.7	-1.3	A	L
CS 22170-14	00 39 56.9	-08 04 43	116.3	-70.6	12.56	0.12	0.09	...	29.6	27.7	8309	3.9	-2.0	-123	1.5	-1.4	A	L
CS 22170-28	00 48 36.4	-11 24 45	122.7	-74.0	11.72	0.18	0.04	...	27.0	21.2	8224	4.5	-0.9	-15	0.8	-0.8	A	L
CS 22170-29	00 49 40.5	-11 20 52	123.6	-73.9	13.05	0.16	0.06	...	23.7	24.9	7782	3.5	-1.9	-127	1.6	-1.6	A	L
CS 22170-38	00 49 03.1	-08 30 39	123.0	-71.1	13.31	0.26	0.12	...	14.1	18.5	7293	3.4	0.0	2	1.5	-1.4	A	L
CS 22171-16	01 58 55.9	-11 55 46	173.1	-67.5	13.05	0.37	-0.21	1.7	8.5	6.5	6757	3.8	-2.9	139	1.3	-1.2	A	E
CS 22172-6	03 14 42.9	-09 00 41	191.9	-51.0	12.73	0.39	-0.07	...	16.2	12.2	7031	3.8	-0.4	-6	1.1	-0.9	A	L
CS 22172-27	03 26 51.8	-10 59 33	197.0	-49.5	13.16	0.36	-0.04	4.6	11.3	10.1	6967	3.6	-1.0	-14	1.3	-1.0	A	H
CS 22172-28	03 27 41.6	-10 48 23	196.9	-49.2	13.92	0.29	0.04	4.5	15.7	13.8	7257	3.5	-0.8	-1	1.9	-1.5	A	H
CS 22172-36	03 29 12.2	-09 20 05	195.2	-48.2	12.08	0.18	0.13	...	28.7	20.1	8232	4.0	-0.1	36	1.0	-0.7	A	L
CS 22172-37	03 29 51.5	-09 18 45	195.3	-48.0	12.51	0.17	0.10	...	26.4	24.9	8063	3.8	0.0	-15	1.2	-0.9	A	L
CS 22172-40	03 25 15.2	-08 10 04	193.0	-48.4	13.04	0.22	0.07	...	28.7	18.9	8218	4.4	-0.5	3	1.4	-1.1	A	L
CS 22173-9	03 56 08.3	-18 08 35	211.1	-46.1	13.39	0.34	-0.06	4.7	11.0	9.8	6995	3.5	-0.9	108	1.5	-1.1	A	H
CS 22174-2	01 10 37.2	-12 09 14	142.4	-73.9	12.98	0.08	0.08	1.2	31.2	30.7	8622	4.0	-1.5	56	2.1	-2.0	A	K
CS 22174-40	01 26 10.3	-07 39 36	148.8	-68.4	13.15	0.21	-0.01	1.5	21.6	22.8	7758	4.0	-1.8	16	1.5	-1.4	A	K
CS 22175-11	02 16 40.6	-07 59 35	174.0	-61.6	14.04	0.17	0.04	2.8	27.5	23.5	8246	4.4	-0.6	49	2.5	-2.2	A	E
CS 22175-13	02 17 03.5	-07 46 05	173.8	-61.4	12.83	0.34	-0.24	2.0	7.9	6.1	6807	4.3	-2.1	-20	1.1	-1.0	A	E
CS 22175-19	02 27 03.9	-08 46 01	178.8	-60.3	11.91	0.19	0.13	4.1	23.8	22.2	7782	3.5	-0.3	40	0.9	-0.8	A	E
CS 22175-30	02 21 17.3	-10 44 18	179.9	-62.7	13.66	0.38	-0.19	3.8	6.4	5.6	6536	4.0	-1.7	-14	1.7	-1.5	A	E
CS 22175-33	02 18 15.4	-10 45 14	178.9	-63.2	14.66	0.30	-0.01	1.9	27.7	23.0	8095	4.2	-1.9	108	2.7	-2.4	A	K
CS 22175-34	02 17 54.9	-10 51 53	179.0	-63.4	12.50	0.34	-0.11	5.6	9.7	11.3	7058	4.4	-0.4	50	1.0	-0.9	A	K

Table B.2. (continued)

Star (1)	RA (1950) (2)	Dec (3)	l (4)	b (5)	V (6)	$(B-V)_o$ (7)	$(U-B)_o$ (8)	W_λ (9)	Hδ $D_{0.2}$ (10)	Hγ $D_{0.2}$ (11)	T_{eff} (12)	$\log g$ (13)	[Fe/H] (14)	V_{los} (15)	Dist (16)	Z (17)	Class (18)	Obs (19)
CS 22176-20	03 43 25.7	-10 32 31	199.3	-45.7	13.50	0.23	0.11	2.7	25.6	26.9	8021	3.8	-1.2	-6	1.7	-1.2	A	KL
CS 22176-32	03 45 18.5	-09 55 20	198.9	-45.0	13.59	0.27	0.10	...	23.2	19.5	7737	3.9	-0.1	-5	1.7	-1.2	A	L
CS 22179-7	00 30 30.8	-04 29 26	111.3	-66.7	13.93	0.22	0.04	...	21.0	20.3	7753	4.0	-1.2	16	2.1	-2.0	A	L
CS 22179-18	00 41 57.6	-06 34 29	118.1	-69.1	15.77	0.29	0.15	...	20.1	17.4	7492	3.4	-2.5	139	4.5	-4.2	A	L
CS 22180-2	01 29 13.5	-10 20 55	154.0	-70.5	12.97	0.17	0.17	3.6	25.5	25.1	7997	3.6	-0.1	-82	1.5	-1.4	A	E
CS 22180-4	01 30 43.0	-10 44 43	155.5	-70.7	14.01	0.23	0.08	3.1	23.2	21.5	7770	3.9	-0.7	45	2.2	-2.1	A	E
CS 22180-26	01 47 38.8	-09 52 24	164.0	-67.7	12.20	0.02	0.01	1.3	29.6	27.8	9434	4.0	-0.1	3	1.9	-1.8	A	E
CS 22180-40	01 43 22.4	-08 20 01	159.5	-67.0	14.46	0.31	-0.18	3.8	9.5	8.5	7014	4.4	-1.4	-135	2.4	-2.3	A	H
CS 22181-2	02 54 25.4	-11 23 47	190.6	-56.5	13.96	0.18	0.01	3.1	24.8	24.8	7991	4.1	-0.7	75	2.4	-2.0	A	E
CS 22181-3	02 54 35.6	-11 48 22	191.3	-56.7	11.11	0.03	0.01	1.2	30.8	30.5	9252	4.0	-0.9	41	1.1	-0.9	A	E
CS 22181-14	03 00 17.2	-11 32 04	192.2	-55.4	12.28	0.10	0.11	1.6	28.1	27.5	8278	3.5	-1.2	33	1.4	-1.2	A	E
CS 22181-15	03 00 29.8	-12 11 32	193.3	-55.7	12.64	0.07	0.02	1.4	35.3	31.8	8909	4.3	-1.0	-51	1.9	-1.6	A	E
CS 22181-32	02 59 07.9	-09 07 51	188.5	-54.3	14.04	0.14	0.17	1.9	25.4	23.8	8012	3.5	-1.2	-126	2.8	-2.3	A	E
CS 22183-29	01 04 48.8	-06 02 38	133.7	-68.3	13.74	0.15	0.23	0.9	22.1	25.7	7799	3.5	-2.6	-126	2.3	-2.2	A	E
CS 22183-38	00 59 17.1	-06 34 54	130.2	-69.0	10.72	0.27	0.23	4.4	29.5	28.4	8264	4.1	0.0	29	0.5	-0.4	A	E
CS 22184-27	02 36 43.1	-09 27 02	182.9	-58.9	11.86	0.09	0.07	2.2	30.6	31.8	8619	4.0	-1.0	32	1.2	-1.0	A	E
CS 22185-13	03 18 05.9	-13 15 12	198.5	-52.5	13.61	0.09	0.03	1.1	34.2	32.4	8775	4.4	-1.5	-37	2.7	-2.1	A	E
CS 22185-22	03 27 17.5	-15 11 56	202.9	-51.4	13.61	0.22	0.05	3.3	29.7	23.2	8239	4.5	-0.2	-26	1.9	-1.4	A	E
CS 22185-23	03 28 40.9	-15 35 15	203.7	-51.2	11.96	0.28	0.07	4.7	15.1	18.5	7260	3.5	-0.2	11	0.8	-0.6	A	E
CS 22185-25	03 29 36.7	-16 31 57	205.2	-51.4	14.02	0.37	-0.25	1.5	7.7	10.8	6819	4.3	-3.0	-71	2.0	-1.6	A	E
CS 22186-43	04 32 26.1	-33 59 27	235.4	-42.1	14.22	0.28	0.04	2.4	17.5	15.4	7282	3.3	-1.4	84	2.3	-1.5	A	H
CS 22189-8	02 37 01.1	-12 48 37	188.4	-60.9	13.24	0.28	-0.02	3.9	15.8	13.9	7469	4.1	-0.8	-21	1.4	-1.3	A	H
CS 22189-38	02 46 30.0	-14 15 51	193.3	-59.7	13.68	0.22	0.01	2.0	21.9	18.8	7757	4.0	-1.5	49	1.9	-1.7	A	E
CS 22189-39	02 46 51.3	-15 18 05	195.2	-60.1	14.30	0.22	0.00	1.9	19.5	22.8	7507	3.5	-1.8	120	2.5	-2.2	A	E
CS 22871-6	14 32 50.7	-20 34 33	333.4	35.8	13.00	0.28	0.11	4.6	20.8	23.6	7733	4.0	0.0	-24	1.3	0.8	A	E
CS 22871-38	14 36 21.5	-20 23 04	334.4	35.6	14.49	0.26	0.05	3.6	17.5	15.4	7511	3.9	-0.7	-72	2.6	1.5	A	H

Table B.2. (continued)

Star (1)	RA (1950) (2)	Dec (3)	l (4)	b (5)	V (6)	$(B-V)_o$ (7)	$(U-B)_o$ (8)	W_δ (9)	Hδ $D_{0.2}$ (10)	Hγ $D_{0.2}$ (11)	T_{eff} (12)	Log g (13)	[Fe/H] (14)	V_{los} (15)	Dist. (16)	Z (17)	Class (18)	Obs (19)
CS 22871-40	14 36 30.2	-20 37 38	334.3	35.4	12.46	0.18	0.03	0.9	24.3	23.6	7991	4.0	-2.0	-41	1.2	0.7	A	E
CS 22871-55	14 39 31.7	-21 20 07	334.6	34.4	12.95	0.25	0.08	3.3	20.5	17.9	7509	3.4	-1.1	-83	1.3	0.7	A	H
CS 22871-56	14 39 05.9	-21 02 25	334.7	34.7	13.98	0.09	0.01	0.9	27.0	33.3	8236	4.1	-2.8	-7	3.1	1.8	A	E
CS 22871-65	14 40 12.5	-20 14 00	335.4	35.3	14.53	0.32	-0.04	4.3	14.0	12.4	7240	3.8	-0.9	-69	2.5	1.5	A	H
CS 22871-78	14 36 38.9	-17 44 45	336.1	37.9	14.49	0.14	0.18	1.9	25.0	18.6	7990	3.5	-1.6	129	3.4	2.1	A	E
CS 22871-80	14 39 17.7	-17 19 03	337.1	37.9	15.05	0.10	0.18	0.8	30.7	29.4	8546	4.1	-3.0	91	5.0	3.1	A	K
CS 22871-82	14 42 22.9	-17 32 28	337.7	37.3	14.48	0.24	0.13	2.2	22.7	19.7	7710	3.5	-1.4	39	2.7	1.6	A	H
CS 22871-100	14 47 12.9	-21 10 26	336.5	33.6	13.83	0.18	0.04	2.0	22.7	19.7	7725	3.6	-1.6	-74	2.2	1.2	A	H
CS 22871-102	14 49 39.2	-20 48 32	337.3	33.6	13.13	0.24	-0.51	3.3	12.4	11.0	7280	4.4	-1.2	38	1.4	0.8	A	H
CS 22871-104	14 48 02.1	-20 36 12	337.1	34.0	14.65	0.34	-0.14	3.8	13.0	9.6	7223	4.3	-1.8	-161	2.6	1.5	A	KL
CS 22871-106	14 46 56.9	-20 15 17	337.1	34.5	14.73	0.05	0.10	...	30.6	26.9	8488	3.5	-1.9	-26	5.3	3.0	A	L
CS 22871-107	14 47 35.0	-20 08 48	337.3	34.5	13.76	0.38	-0.20	...	8.9	7.1	6758	3.9	-2.8	2	1.8	1.0	A	L
CS 22871-108	14 46 05.1	-19 55 24	337.1	34.8	14.18	0.28	0.06	3.2	19.8	17.3	7498	3.5	-0.9	-27	2.2	1.3	A	H
CS 22872-6	16 16 21.1	-04 58 31	8.3	30.4	10.35	0.09	0.00	1.5	30.7	28.7	8667	3.9	-0.8	-15	0.6	0.3	A	EL
CS 22872-8	16 17 18.4	-04 42 03	8.7	30.4	14.36	0.26	-0.06	...	15.4	14.5	7488	4.0	-1.1	-23	2.5	1.2	A	L
CS 22872-13	16 15 44.7	-03 45 12	9.4	31.3	13.10	0.15	0.12	...	24.7	20.2	7973	3.5	-0.3	-4	1.8	0.9	A	L
CS 22872-19	16 13 54.8	-02 46 42	10.0	32.2	13.09	0.23	0.00	2.7	18.3	16.0	7473	3.5	-1.6	34	1.4	0.8	A	H
CS 22872-29	16 16 20.6	-01 13 05	11.9	32.6	12.34	0.09	0.01	0.7	25.7	24.8	8044	3.9	-2.4	-112	1.5	0.8	A	EL
CS 22872-32	16 20 03.9	-01 37 30	12.1	31.6	14.55	0.26	-0.13	...	11.9	11.5	7353	4.6	-0.1	-66	2.7	1.4	A	L
CS 22872-43	16 18 28.3	-03 24 12	10.1	30.9	11.78	0.26	0.10	...	19.7	15.6	7490	3.6	0.0	-53	0.8	0.4	A	L
CS 22872-46	16 19 37.1	-03 50 48	9.9	30.4	13.12	0.22	0.14	...	22.4	20.1	7733	3.7	0.0	26	1.5	0.8	A	L
CS 22872-56	16 20 34.0	-05 35 50	8.4	29.2	14.56	0.18	0.23	1.6	26.4	21.8	8028	3.9	-1.9	112	3.2	1.5	A	K
CS 22872-58	16 22 37.4	-05 06 57	9.2	29.1	14.85	0.10	0.21	1.0	27.3	25.5	8269	3.6	-1.8	7	4.6	2.2	A	K
CS 22872-64	16 22 27.1	-04 18 55	9.9	29.6	12.36	0.26	0.09	...	24.2	18.0	7749	3.9	0.0	16	1.0	0.5	A	L
CS 22872-68	16 22 19.2	-03 23 53	10.8	30.1	13.79	0.16	0.11	3.1	26.6	25.8	8018	3.6	-0.7	14	2.3	1.2	A	K
CS 22872-74	16 22 53.1	-02 17 08	11.9	30.6	14.65	0.19	0.05	...	20.8	22.9	7799	3.9	-1.3	22	3.2	1.6	A	L
CS 22872-86	16 27 19.5	-01 08 27	13.8	30.3	12.99	0.14	0.04	...	24.1	20.5	8032	4.3	0.0	12	1.7	0.9	A	L
CS 22872-94	16 28 17.0	-02 10 52	12.9	29.6	13.84	0.31	0.03	...	15.9	11.6	7234	3.7	-0.3	-71	1.8	0.9	A	L
CS 22872-100	16 27 05.0	-02 45 08	12.2	29.5	13.29	0.19	0.14	...	33.1	23.1	8487	4.4	-1.3	91	1.7	0.8	A	L
CS 22872-106	16 27 32.6	-04 13 33	10.9	28.6	13.23	0.33	0.10	4.9	24.4	24.8	7636	3.4	-0.4	-49	1.4	0.7	A	KL
CS 22872-107	16 29 03.5	-04 21 36	11.0	28.2	13.28	0.20	0.18	2.4	26.3	22.8	7955	4.1	-1.0	16	1.7	0.8	A	H
CS 22872-111	16 28 15.0	-04 56 05	10.3	28.0	10.84	0.21	0.20	...	26.7	24.7	8039	4.0	-0.2	25	0.5	0.2	A	L
CS 22872-113	16 27 00.7	-05 33 06	9.5	27.9	11.77	0.34	0.29	3.3	23.8	23.0	6669	3.7	-0.6	12	0.7	0.3	A	K
CS 22872-115	16 31 47.1	-05 46 42	10.1	26.8	11.32	0.42	0.29	3.5	23.1	22.2	6669	3.7	-1.3	-25	0.6	0.3	A	K

Table B.2. (continued)

Star (1)	RA (1950) (2)	Dec (3)	l (4)	b (5)	V (6)	$(B-V)_o$ (7)	$(U-B)_o$ (8)	W_λ (9)	$H\delta$ $D_{h/2}$ (10)	$H\gamma$ $D_{h/2}$ (11)	T_{eff} (12)	Log g (13)	[Fe/H] (14)	V_{los} (15)	Dist. (16)	Z (17)	Class (18)	Obs (19)
CS 22872-118	16 30 29.1	-05 07 22	10.5	27.5	13.85	0.25	0.17	1.4	24.0	20.9	7726	3.7	-1.9	-4	2.0	0.9	A	H
CS 22872-120	16 31 28.6	-04 19 19	11.4	27.7	14.83	0.20	0.20	...	28.0	20.7	8092	4.1	-2.2	-66	3.4	1.6	A	L
CS 22872-129	16 32 18.7	-02 13 52	13.5	28.7	14.76	0.13	0.21	...	28.0	25.2	8226	3.7	-3.0	-111	3.9	1.9	A	L
CS 22872-131	16 32 56.6	-02 01 45	13.8	28.7	14.36	0.21	0.08	...	23.1	25.7	7747	3.5	-1.9	-86	2.7	1.3	A	L
CS 22873-66	19 49 29.9	-60 50 23	336.3	-31.0	14.71	0.27	0.05	2.4	23.2	20.2	7758	3.9	-1.2	-92	2.9	-1.5	A	H
CS 22874-7	14 32 14.5	-26 38 59	329.9	30.5	14.92	0.05	0.15	2.2	31.1	20.9	8433	3.6	-0.8	220	5.7	2.9	A	E
CS 22874-16	14 31 01.5	-24 43 56	330.6	32.4	14.39	0.03	-0.01	0.8	32.6	28.4	9263	4.0	-1.3	181	5.0	2.7	A	E
CS 22874-22	14 30 20.7	-24 12 38	330.7	32.9	14.81	0.04	0.11	1.1	33.7	26.3	8818	4.0	-1.4	93	5.8	3.2	A	E
CS 22874-27	14 27 19.1	-23 44 53	330.2	33.6	15.00	0.16	0.13	2.2	29.6	26.1	8274	4.0	-1.0	-23	4.1	2.3	A	EE
CS 22874-37	14 32 36.5	-24 10 54	331.3	32.7	13.13	0.20	0.02	1.9	21.1	20.2	7757	4.0	-1.2	-14	1.5	0.8	A	E
CS 22874-42	14 35 08.5	-24 45 48	331.5	31.9	13.62	0.34	-0.22	4.1	8.2	6.4	6877	4.7	-1.5	163	1.6	0.9	A	E
CS 22874-43	14 34 36.2	-24 48 38	331.4	31.9	13.99	0.02	0.01	0.1	33.3	30.5	9116	4.0	-1.4	-92	4.4	2.3	A	E
CS 22874-72	14 38 18.9	-24 01 42	332.7	32.2	14.02	0.12	0.06	1.9	25.4	22.0	7998	3.7	-1.4	-81	2.9	1.5	A	H
CS 22874-74	14 37 17.0	-23 48 35	332.6	32.5	13.36	0.27	0.01	3.4	17.5	15.3	7500	4.0	-0.8	-41	1.5	0.8	A	H
CS 22874-81	14 41 27.3	-22 37 51	334.3	33.1	14.09	0.27	-0.07	4.1	10.4	9.3	6985	3.6	-1.2	-58	2.1	1.2	A	H
CS 22874-84	14 41 51.2	-23 27 56	333.9	32.3	11.97	0.32	0.08	5.4	18.4	17.2	7499	3.9	0.0	-13	0.8	0.4	A	E
CS 22874-107	14 44 40.2	-26 34 48	332.7	29.3	13.06	0.18	0.19	3.9	33.8	6.9	8542	4.5	0.0	326	1.6	0.8	A	E
CS 22876-12	23 47 11.5	-34 11 28	2.1	-75.1	14.76	0.15	0.09	4.0	28.9	29.5	8260	4.1	0.0	-33	3.7	-3.6	A	E
CS 22876-21	23 58 29.7	-34 04 56	358.3	-77.3	14.45	0.30	-0.09	4.3	10.4	10.0	7003	3.7	-0.8	-99	2.5	-2.4	A	E
CS 22876-25	23 57 22.4	-35 23 40	353.8	-76.4	15.19	0.24	-0.13	13.2	14.5	15.7	7500	5.0	-2.3	165	3.7	-3.6	A	E
CS 22876-26	23 55 51.6	-35 24 19	354.4	-76.1	14.00	0.23	0.01	1.2	22.1	15.7	7754	3.9	-2.3	-81	2.2	-2.1	A	E
CS 22876-27	23 57 00.5	-35 56 17	352.1	-76.0	14.33	0.38	-0.22	2.8	6.8	7.4	6735	4.5	-2.1	-120	2.3	-2.2	A	E
CS 22876-32	00 05 04.7	-35 47 57	348.3	-77.4	12.81	0.38	-0.26	1.0	6.6	6.4	6637	4.7	-3.0	-89	1.1	-1.1	A	E
CS 22876-33	00 06 58.9	-35 42 44	347.5	-77.8	13.34	0.04	0.01	1.5	30.0	24.8	9223	4.0	-1.1	38	2.9	-2.8	A	E
CS 22876-42	00 09 28.5	-34 16 30	351.5	-79.1	13.09	0.35	-0.22	2.8	7.2	8.7	6779	4.5	-1.9	39	1.3	-1.3	A	E
CS 22877-32	13 14 46.1	-09 42 10	313.4	52.4	14.42	0.22	0.04	...	18.9	17.9	7499	3.5	-2.5	46	2.7	2.1	A	L
CS 22879-37	20 39 58.2	-37 43 53	4.9	-37.5	14.47	0.30	-0.14	1.8	12.2	10.8	7242	4.0	-2.0	96	2.5	-1.5	A	H
CS 22879-142	20 58 08.6	-39 34 16	3.0	-41.2	14.28	0.29	-0.07	3.5	14.3	12.6	7292	4.0	-1.2	-52	2.3	-1.5	A	H
CS 22879-146	20 56 00.6	-39 07 37	3.6	-40.8	13.86	0.34	-0.04	5.8	12.5	11.1	7229	4.4	-0.2	1	1.8	-1.2	A	H

Table B.2. (continued)

Star (1)	RA (1950) (2)	Dec (3)	l (4)	b (5)	V (6)	$(B-V)_o$ (7)	$(U-B)_o$ (8)	W_λ (9)	Hδ $D_{0.2}$ (10)	Hγ $D_{0.2}$ (11)	T_{eff} (12)	Log g (13)	[Fe/H] (14)	V_{rad} (15)	Dist (16)	Z (17)	Class (18)	Obs (19)
CS 22880-50	20 40 48.7	-20 41 33	25.3	-33.5	13.38	0.13	0.03	0.3	27.6	24.0	8202	3.7	-2.9	-136	2.1	-1.2	A	H
CS 22880-73	20 45 17.9	-21 10 30	25.2	-34.6	13.76	0.22	-0.03	3.1	15.8	13.9	7510	4.0	-1.3	-51	2.0	-1.1	A	H
CS 22883-9	14 09 37.9	+11 04 40	356.2	65.0	15.32	0.06	-9.99	...	39.6	29.1	9267	4.6	-1.9	214	6.6	6.0	A	L
CS 22883-40	14 22 28.8	+10 14 15	359.5	62.1	15.33	0.35	-0.10	4.9	11.1	9.7	7015	4.0	-0.7	9	3.6	3.2	A	K
CS 22883-42	14 22 12.1	+09 30 50	358.3	61.7	14.31	0.15	-9.99	...	36.2	43.4	8236	4.0	-3.0	18	3.0	2.7	A	L
CS 22884-13	15 30 36.7	-09 34 51	355.3	36.2	13.88	0.19	0.03	2.8	22.6	19.7	7738	3.6	-1.1	-58	2.2	1.3	A	H
CS 22884-20	15 31 40.6	-08 23 41	356.6	36.8	14.50	0.32	-0.24	3.5	10.2	9.1	7009	4.5	-1.6	19	2.5	1.5	A	H
CS 22884-32	15 36 02.7	-09 44 32	356.3	35.1	13.73	0.15	0.12	1.3	26.3	20.4	7996	3.6	-1.4	-107	2.3	1.3	A	K
CS 22885-48	20 16 35.4	-39 06 05	2.3	-33.2	14.17	0.31	-0.09	2.5	12.5	11.1	6990	3.5	-1.6	-60	2.1	-1.2	A	H
CS 22885-162	20 32 08.7	-41 57 46	359.4	-36.5	12.99	0.30	-0.05	4.2	12.8	11.4	7245	4.0	-0.9	-86	1.3	-0.7	A	H
CS 22886-41	22 19 43.3	-10 53 24	50.8	-51.3	13.96	0.33	-0.10	4.4	12.5	11.1	7229	4.1	-0.8	-41	1.9	-1.5	A	H
CS 22886-73	22 26 06.8	-09 45 08	53.7	-52.0	13.17	0.28	0.07	4.4	18.3	16.0	7304	3.4	-0.6	-40	1.4	-1.1	A	H
CS 22887-12	22 33 41.5	-08 08 12	57.6	-52.7	13.31	0.35	-0.07	5.3	10.3	9.2	6995	4.0	-0.8	-49	1.4	-1.1	A	E
CS 22887-32	22 40 09.1	-10 40 28	55.6	-55.4	14.72	0.29	0.07	4.9	18.3	16.0	7285	3.4	-0.4	-35	2.8	-2.3	A	H
CS 22887-53	22 48 41.9	-11 37 50	56.3	-57.7	13.91	0.19	0.16	1.3	23.5	20.4	7747	3.4	-2.0	-67	2.3	-1.9	A	H
CS 22889-25	13 36 53.3	-12 11 48	320.9	48.7	14.85	0.16	-9.99	...	26.3	28.7	8250	5.0	-2.3	-51	3.8	2.8	A	L
CS 22889-44	13 41 49.2	-08 18 26	324.6	52.1	15.17	0.15	-9.99	...	26.2	25.6	8089	4.3	-0.8	117	4.5	3.5	A	L
CS 22890-69	15 21 41.6	+03 15 42	6.3	46.3	12.65	0.20	0.05	1.0	28.0	25.5	8251	4.4	-2.0	-31	1.2	0.9	A	K
CS 22890-78	15 20 17.6	-00 55 14	1.4	43.9	12.64	0.24	-0.61	2.9	11.0	9.8	6992	3.7	-1.6	-11	1.1	0.8	A	H
CS 22890-86	15 25 18.5	+00 58 26	4.5	44.2	14.05	0.29	-0.03	3.4	16.8	14.8	7644	4.6	-0.7	-31	2.1	1.4	A	H
CS 22891-5	19 01 03.5	-62 11 51	334.0	-25.4	13.16	0.03	0.00	1.3	30.6	32.8	9314	4.0	-1.1	-74	2.8	-1.2	A	E
CS 22891-119	19 17 50.8	-59 52 50	337.0	-27.0	14.45	0.32	-0.19	3.2	11.0	9.9	7195	4.6	-1.6	-63	2.4	-1.1	A	H
CS 22892-20	22 04 40.4	-14 19 16	43.4	-49.7	14.29	0.31	-0.22	1.9	10.1	9.1	7026	4.4	-2.2	-188	2.3	-1.7	A	H
CS 22892-27	22 05 21.9	-15 50 11	41.3	-50.5	12.68	0.30	-0.06	2.9	15.2	13.4	7466	4.3	-1.3	-6	1.1	-0.8	A	H
CS 22892-59	22 14 29.2	-14 14 23	45.1	-51.8	14.46	0.30	-0.05	4.2	15.0	13.2	7488	4.5	-0.6	31	2.5	-1.9	A	H

Table B.2. (continued)

Star (1)	RA (1950) (2)	Dec (3)	l (4)	b (5)	V (6)	$(B-V)_o$ (7)	$(U-B)_o$ (8)	W_δ (9)	$H\delta$ $D_{0.2}$ (10)	$H\gamma$ $D_{0.2}$ (11)	T_{eff} (12)	Log g (13)	[Fe/H] (14)	V_{hel} (15)	Dist. (16)	Z (17)	Class (18)	Obs (19)
CS 22894-7	23 29 36.4	-00 10 56	84.7	-56.8	13.57	0.17	0.15	...	29.2	20.7	8247	4.0	0.0	-46	2.0	-1.7	A	L
CS 22894-11	23 30 59.8	+01 11 24	86.6	-55.8	15.08	0.29	-0.06	...	15.9	11.6	7450	4.2	-1.2	-60	3.3	-2.7	A	L
CS 22894-14	23 33 13.2	+00 36 19	86.9	-56.6	14.47	0.10	0.13	...	29.5	22.5	8389	3.8	-2.7	-173	3.8	-3.2	A	LL
CS 22894-20	23 35 31.0	-00 41 51	86.5	-58.0	14.80	0.31	-0.06	...	12.6	10.0	7000	3.5	-1.3	-136	2.9	-2.4	A	L
CS 22894-22	23 36 43.4	-01 43 19	85.9	-59.0	14.78	0.22	0.03	...	30.2	17.4	8248	4.5	-1.2	-160	3.2	-2.7	A	L
CS 22894-23	23 34 44.4	-02 25 03	84.4	-59.3	13.69	0.38	-0.21	0.0	7.9	6.3	6752	4.4	-2.8	-332	1.7	-1.5	A	H
CS 22894-29	23 39 40.7	-01 08 12	87.8	-58.9	14.31	0.27	-0.07	2.3	16.6	14.6	7473	4.1	-1.4	11	2.4	-2.0	A	H
CS 22894-40	23 42 57.1	+01 03 14	91.2	-57.4	13.42	0.25	0.09	...	19.2	17.9	7494	3.6	-0.1	-55	1.6	-1.4	A	L
CS 22894-43	23 44 43.9	+00 27 56	91.4	-58.1	13.94	0.31	-0.06	3.5	13.4	11.8	7259	3.9	-1.2	-51	1.9	-1.6	A	H
CS 22896-52	19 23 04.4	-54 13 50	343.3	-26.8	15.26	0.25	-0.09	2.0	13.2	11.7	7322	4.0	-1.9	51	3.7	-1.7	A	H
CS 22896-56	19 26 43.4	-54 14 56	343.4	-27.3	14.53	0.20	0.09	2.8	21.2	18.5	7702	3.5	-1.4	-26	2.9	-1.4	A	H
CS 22896-75	19 23 03.4	-56 23 52	341.0	-27.1	14.81	0.17	0.09	2.7	24.9	21.6	7933	3.9	-0.9	-52	3.6	-1.6	A	H
CS 22896-77	19 25 06.6	-56 45 44	340.6	-27.5	14.61	0.22	0.14	1.9	22.7	19.7	7697	3.5	-1.5	27	2.9	-1.4	A	H
CS 22896-90	19 30 47.9	-56 38 34	340.9	-28.2	14.60	0.31	-0.06	3.2	15.4	13.5	7445	4.2	-1.2	-56	2.6	-1.2	A	H
CS 22896-99	19 27 44.4	-55 18 11	342.3	-27.6	12.97	0.23	0.11	2.4	24.8	23.8	7993	3.9	-1.1	-99	1.3	-0.6	A	E
CS 22896-105	19 28 01.1	-54 32 31	343.1	-27.5	14.62	0.27	-0.02	2.9	17.3	15.2	7708	4.5	-1.0	21	2.7	-1.3	A	H
CS 22896-133	19 35 32.1	-53 47 45	344.2	-28.5	15.31	0.19	0.07	1.7	27.0	23.5	8042	4.0	-1.5	-89	4.3	-2.1	A	H
CS 22896-147	19 36 57.7	-55 48 45	341.9	-29.0	14.67	0.27	0.05	2.8	20.9	18.2	7498	3.5	-1.0	-4	2.8	-1.4	A	H
CS 22896-173	19 49 03.1	-55 51 48	342.1	-30.7	14.00	0.31	-0.11	3.3	11.0	9.9	7012	3.8	-1.5	80	2.0	-1.0	A	H
CS 22896-178	19 42 44.9	-55 11 40	342.7	-29.7	13.01	0.06	0.03	1.4	35.1	32.7	8840	4.4	-0.7	-35	2.3	-1.2	A	E
CS 22896-182	19 45 40.7	-54 49 52	343.2	-30.1	13.81	0.14	0.10	2.6	28.9	26.2	8257	4.0	-0.6	-187	2.4	-1.2	A	E
CS 22897-47	21 11 09.0	-67 05 04	326.9	-38.7	14.41	0.14	0.14	0.6	32.8	20.3	8638	4.3	-2.6	-66	3.3	-2.1	A	E
CS 22897-101	21 24 33.3	-66 28 54	327.0	-40.1	14.23	0.17	0.00	0.9	23.9	25.6	7952	4.1	-2.2	72	2.7	-1.8	A	E
CS 22897-111	21 35 16.8	-66 09 41	326.7	-41.2	13.61	0.35	-0.01	4.5	10.8	9.6	6959	3.6	-1.1	-74	1.6	-1.1	A	H
CS 22897-117	21 32 58.7	-65 43 37	327.4	-41.2	14.85	0.32	-0.16	1.6	12.8	11.4	7244	4.4	-2.2	-55	2.9	-1.9	A	H
CS 22897-119	21 33 58.9	-64 52 54	328.3	-41.7	14.94	0.33	-0.16	4.5	10.1	9.1	6990	4.0	-1.1	-2	3.0	-2.0	A	H
CS 22897-121	21 38 45.6	-64 47 15	328.1	-42.2	14.29	0.14	-0.67	4.0	10.2	9.0	7111	4.4	-1.1	-100	3.1	-2.1	A	E
CS 22897-124	21 31 25.3	-64 17 46	329.2	-41.7	12.50	0.04	0.05	1.8	30.2	30.7	9321	4.0	-0.1	-1	1.9	-1.3	A	E
CS 22898-26	21 03 16.4	-18 45 10	29.8	-37.8	13.33	0.20	-0.53	2.9	9.9	8.9	6988	4.4	-1.9	-9	1.7	-1.0	A	H
CS 22936-242	18 54 04.9	-33 45 46	2.7	-15.8	13.94	0.42	-0.25	3.2	5.7	6.8	6497	4.4	-2.3	14	2.0	-0.5	A	E
CS 22936-262	18 56 40.1	-33 24 04	3.3	-16.1	12.34	0.12	0.32	0.7	22.1	23.3	7783	3.4	-2.8	2	1.3	-0.4	A	E

Table B.2. (continued)

Star (1)	RA (1950) (2)	Dec (3)	l (4)	b (5)	V (6)	$(B-V)_o$ (7)	$(U-B)_o$ (8)	W_λ (9)	Hδ $D_{0.2}$ (10)	Hγ $D_{0.2}$ (11)	T_{eff} (12)	Log g (13)	[Fe/H] (14)	V_{los} (15)	Dist. (16)	Z (17)	Class (18)	Obs (19)
CS 22936-306	18 58 10.4	-33 28 01	3.4	-16.5	12.50	0.09	0.06	0.9	31.2	30.1	8710	4.0	-1.4	-6	1.6	-0.5	A	E
CS 22937-17	20 59 05.9	-38 55 48	3.9	-41.3	13.59	0.31	-0.05	4.0	12.5	11.1	7240	4.0	-1.3	-40	1.6	-1.1	A	H
CS 22937-50	21 09 37.9	-41 06 08	1.1	-43.5	14.85	0.34	-0.08	4.0	15.2	13.4	7449	4.5	-0.7	-51	2.9	-2.0	A	H
CS 22937-56	21 11 45.3	-40 25 20	2.0	-43.8	14.64	0.33	0.01	4.6	13.7	12.1	7248	4.0	-0.8	29	2.6	-1.8	A	H
CS 22937-68	21 11 48.7	-38 22 04	4.9	-43.8	14.95	0.33	-0.12	3.2	11.3	10.1	7022	3.9	-1.5	-43	3.0	-2.1	A	H
CS 22938-15	22 43 39.8	-63 44 12	323.3	-48.4	13.98	0.38	-0.09	5.2	9.2	8.3	6743	3.5	-1.1	18	2.0	-1.5	A	H
CS 22938-71	23 09 34.7	-64 06 38	319.6	-50.0	14.04	0.32	-0.03	3.9	14.0	12.4	7217	3.6	-1.0	56	2.0	-1.5	A	H
CS 22940-3	20 24 57.3	-61 45 37	334.9	-35.2	14.31	0.24	-0.01	2.7	18.5	16.2	7459	3.5	-1.1	6	2.5	-1.4	A	H
CS 22941-1	23 26 01.1	-36 54 49	359.3	-70.1	14.88	0.18	0.02	3.5	29.0	20.5	8248	4.4	-0.2	-32	3.7	-3.4	A	E
CS 22941-5	23 27 12.3	-35 29 34	3.0	-70.8	14.51	0.24	-0.15	1.3	18.6	14.5	7731	4.5	-2.2	-62	2.7	-2.6	A	E
CS 22941-12	23 25 49.7	-33 05 13	10.3	-71.2	12.35	0.27	-0.18	1.4	12.9	11.5	7383	4.6	-2.2	-138	1.0	-0.9	A	E
CS 22941-13	23 31 25.0	-32 41 17	10.8	-72.4	13.94	0.20	0.01	2.9	19.5	20.7	7504	3.5	-1.2	-34	2.2	-2.1	A	E
CS 22941-32	23 34 34.0	-36 27 18	358.4	-71.8	14.13	0.33	-0.05	6.1	10.1	9.1	6971	3.6	-0.9	-3	2.1	-2.0	A	H
CS 22941-34	23 33 39.2	-36 25 45	358.8	-71.7	13.66	0.18	-0.01	1.3	23.0	19.0	7775	3.8	-2.0	30	2.1	-2.0	A	E
CS 22941-35	23 35 29.1	-36 09 33	359.1	-72.1	13.94	0.30	-0.11	4.1	12.2	10.8	7240	4.0	-0.9	-1	1.9	-1.8	A	H
CS 22941-38	23 36 59.7	-35 22 15	1.1	-72.7	14.31	0.23	0.03	3.0	20.5	17.9	7506	3.5	-1.0	-41	2.5	-2.4	A	H
CS 22941-40	23 33 06.5	-33 11 03	8.9	-72.7	14.90	0.19	0.01	2.6	18.4	16.7	7516	3.4	-1.3	52	3.6	-3.4	A	E
CS 22942-12	00 48 38.7	-25 47 57	120.1	-88.4	14.14	0.29	-0.06	2.9	14.3	12.6	7362	4.0	-1.5	-46	2.2	-2.2	A	H
CS 22943-34	20 06 56.5	-44 55 42	355.2	-32.3	14.23	0.32	0.04	3.8	18.3	16.0	7500	3.9	-0.7	-151	2.2	-1.2	A	H
CS 22943-38	20 11 31.9	-44 51 29	355.4	-33.1	14.51	0.23	0.13	2.5	26.4	22.9	7947	3.6	-0.9	-38	2.8	-1.5	A	H
CS 22943-113	20 22 04.0	-45 23 30	355.0	-35.0	14.64	0.18	0.17	0.9	25.6	22.2	7965	3.6	-2.1	165	3.3	-1.9	A	H
CS 22943-133	20 20 13.9	-42 50 40	358.0	-34.4	14.89	0.31	0.16	1.8	28.0	24.2	7963	4.0	-1.1	5	3.0	-1.7	A	H
CS 22943-172	20 29 13.6	-47 17 23	352.8	-36.4	14.63	0.32	0.02	3.0	21.3	18.6	7506	3.5	-0.9	9	2.6	-1.6	A	H
CS 22944-18	21 39 14.3	-14 15 33	39.6	-44.1	13.96	0.31	0.03	5.1	11.0	9.8	6999	3.5	-0.9	24	1.9	-1.4	A	H
CS 22945-1	23 27 38.0	-67 49 47	314.3	-47.8	14.67	0.31	-0.02	1.8	17.9	15.7	7289	3.4	-1.6	164	2.7	-2.0	A	H
CS 22947-15	19 02 50.1	-50 51 25	346.2	-23.0	13.23	0.33	-0.04	5.7	11.7	10.4	6989	3.5	-0.7	-7	1.4	-0.5	A	H

Table B.2. (continued)

Star (1)	RA (1950) (2)	Dec (3)	l (4)	b (5)	V (6)	$(B-V)_o$ (7)	$(U-B)_o$ (8)	W_λ (9)	Hδ $D_{0.2}$ (10)	Hγ $D_{0.2}$ (11)	T_{eff} (12)	Log g (13)	[Fe/H] (14)	V_{los} (15)	Dist. (16)	Z (17)	Class (18)	Obs (19)
CS 22947-206	19 19 22.1	-48 30 06	349.4	-25.0	13.91	0.33	-0.05	5.2	14.6	12.9	7466	4.5	-0.2	137	1.9	-0.8	A	H
CS 22947-216	19 23 03.0	-50 07 12	347.8	-25.9	13.90	0.35	-0.04	6.1	13.2	11.7	7185	4.2	-0.3	42	1.9	-0.8	A	H
CS 22947-287	19 27 18.4	-50 20 45	347.8	-26.7	13.68	0.17	0.06	2.4	26.4	22.9	8011	4.0	-1.0	-9	2.2	-1.0	A	H
CS 22948-8	21 27 37.3	-39 07 55	03.9	-46.9	14.71	0.35	-0.02	4.9	11.3	10.1	6968	3.6	-0.9	-37	2.7	-2.0	A	H
CS 22948-68	21 46 05.0	-37 41 52	06.0	-50.5	13.77	0.32	-0.14	2.8	13.1	11.6	7223	4.1	-1.5	79	1.8	-1.4	A	H
CS 22949-1	23 12 29.4	-07 11 33	70.0	-59.5	14.35	0.41	-0.19	...	8.3	8.8	6730	4.0	-2.3	-327	2.4	-2.0	A	L
CS 22949-7	23 13 23.6	-04 55 55	73.3	-58.0	13.64	0.42	-0.20	2.1	8.2	7.7	6721	4.0	-2.2	-340	1.7	-1.5	A	E
CS 22949-13	23 17 01.6	-02 34 44	77.5	-56.8	14.77	0.10	0.17	...	27.2	5.8	8255	3.5	-2.0	-212	4.4	-3.7	A	L
CS 22950-24	20 13 38.5	-14 12 26	29.4	-25.1	14.20	0.26	0.04	2.4	20.8	18.1	7479	3.5	-1.3	-22	2.3	-1.0	A	H
CS 22950-151	20 29 09.4	-15 47 14	29.4	-29.1	14.58	0.32	-0.03	4.8	11.7	10.4	7004	3.5	-0.9	16	2.6	-1.3	A	H
CS 22951-39	21 40 39.0	-44 44 07	355.3	-48.9	14.65	0.32	-0.12	3.6	12.8	11.4	7256	4.3	-1.2	-66	2.7	-2.0	A	H
CS 22951-43	21 45 42.2	-45 27 31	354.0	-49.6	15.04	0.33	-0.02	4.4	12.5	11.1	7002	3.5	-0.8	58	3.2	-2.4	A	H
CS 22951-51	21 48 30.1	-46 39 46	352.0	-49.9	15.30	0.28	-0.12	1.8	16.2	14.3	7548	4.4	-1.6	4	3.7	-2.8	A	H
CS 22951-58	21 48 30.0	-45 05 39	354.4	-50.2	15.31	0.31	-0.08	2.5	13.3	11.7	7262	4.0	-1.6	173	3.6	-2.8	A	H
CS 22951-78	21 51 12.1	-43 33 26	356.6	-50.9	15.26	0.28	-0.01	2.8	22.9	19.9	7699	4.0	-1.0	45	3.6	-2.8	A	H
CS 22955-27	20 19 45.4	-25 03 17	18.6	-30.3	13.54	0.24	0.10	3.0	26.4	22.9	7980	3.9	-0.7	42	1.7	-0.9	A	H
CS 22955-40	20 21 28.3	-22 43 27	21.3	-30.0	14.04	0.28	0.02	3.7	22.7	19.7	7735	4.0	-0.7	8	2.1	-1.0	A	H
CS 22955-50	20 25 51.5	-23 38 52	20.6	-31.2	14.81	0.31	0.05	4.8	18.3	16.0	7496	4.0	-0.5	-3	2.9	-1.5	A	H
CS 22955-60	20 23 47.6	-24 22 04	19.7	-31.0	14.50	0.06	0.05	3.3	29.3	25.3	8639	3.6	0.0	127	4.5	-2.3	A	H
CS 22955-83	20 24 08.8	-26 44 35	17.0	-31.8	14.14	0.29	-0.05	4.3	14.6	12.9	7229	3.6	-0.9	-76	2.1	-1.1	A	H
CS 22955-110	20 29 27.6	-25 18 38	19.1	-32.5	13.43	0.28	-0.15	4.1	14.6	12.9	7489	4.6	-0.8	-5	1.6	-0.8	A	H
CS 22955-115	20 30 29.0	-24 35 17	20.0	-32.5	14.36	0.24	-0.03	3.4	19.0	16.7	7479	3.6	-0.8	-76	2.5	-1.4	A	H
CS 22955-124	20 31 06.9	-23 51 32	20.8	-32.4	14.66	0.21	0.03	1.9	22.7	19.8	7682	3.6	-1.5	-9	3.1	-1.6	A	H
CS 22955-155	20 32 41.5	-27 12 14	17.2	-33.8	13.19	0.17	0.07	1.9	26.4	22.9	8018	3.9	-1.4	-33	1.7	-1.0	A	H
CS 22956-2	21 45 07.8	-66 54 35	325.2	-41.7	15.05	0.34	-0.07	4.1	11.6	10.3	6986	3.5	-1.2	111	3.2	-2.1	A	H
CS 22956-22	21 45 50.2	-64 07 14	328.4	-43.2	15.25	0.32	-0.06	3.8	15.2	13.4	7266	3.9	-0.8	-27	3.5	-2.4	A	H
CS 22956-28	21 40 59.6	-63 35 56	329.4	-43.0	12.98	0.34	-0.17	1.2	10.5	9.4	6995	4.0	-2.7	14	1.2	-0.8	A	H
CS 22956-53	21 52 58.7	-66 33 17	325.0	-42.6	12.95	0.21	0.09	3.7	29.1	25.2	8227	4.4	-0.1	-64	1.4	-0.9	A	E

Table B.2. (continued)

Star (1)	RA (1950) (2)	Dec (3)	l (4)	b (5)	V (6)	$(B-V)_o$ (7)	$(U-B)_o$ (8)	W_λ (9)	Hδ $D_{0.2}$ (10)	Hγ $D_{0.2}$ (11)	T_{eff} (12)	Log g (13)	[Fe/H] (14)	V_{tan} (15)	Dist (16)	Z (17)	Class (18)	Obs (19)
CS 22956-65	21 58 03.6	-65 54 09	325.4	-43.3	13.31	0.10	0.04	1.3	29.7	26.9	8492	4.3	-2.9	136	2.2	-1.5	A	E
CS 22956-83	22 03 15.5	-62 24 18	329.1	-45.7	15.34	0.29	-0.09	1.4	12.0	10.6	7233	4.1	-2.5	124	3.7	-2.7	A	H
CS 22956-98	22 08 42.0	-65 20 52	325.1	-44.6	13.72	0.20	0.17	2.2	22.4	19.5	7721	3.5	-1.4	30	2.0	-1.4	A	H
CS 22956-104	22 11 48.2	-65 54 20	324.2	-44.5	15.11	0.35	-0.17	3.5	9.1	8.2	6985	4.5	-1.5	-25	3.3	-2.3	A	H
CS 22956-120	22 23 56.9	-65 04 09	324.0	-46.0	14.07	0.25	-0.04	0.7	24.2	21.0	8001	4.5	-2.4	230	2.2	-1.6	A	H
CS 22958-13	01 39 45.2	-54 40 39	287.7	-61.2	13.68	0.35	-0.05	5.0	12.7	11.3	6987	3.5	-0.6	15	1.7	-1.5	A	H
CS 22958-16	01 52 09.1	-53 23 32	283.1	-61.5	14.79	0.41	-0.14	3.6	8.0	7.3	6533	3.5	-1.8	188	2.9	-2.6	A	H
CS 22958-22	01 47 15.6	-54 07 23	285.2	-61.2	13.52	0.31	-0.06	4.0	14.1	12.5	7257	4.0	-1.0	-20	1.6	-1.4	A	H
CS 22958-50	02 10 00.3	-57 23 50	283.1	-56.8	15.31	0.21	-0.01	0.1	27.2	23.6	8005	4.1	-3.0	76	4.1	-3.4	A	H
CS 22959-10	18 39 38.4	-67 16 49	328.0	-24.2	14.37	0.30	0.01	4.3	18.1	15.9	7496	4.0	-0.3	93	2.4	-1.0	A	H
CS 22959-26	18 33 44.0	-65 38 33	329.6	-23.3	13.88	0.29	-0.08	6.4	13.9	14.0	7481	4.6	-0.1	-67	1.9	-0.8	A	E
CS 22959-51	18 38 23.1	-64 17 53	331.2	-23.4	14.64	0.33	0.00	4.7	15.6	13.7	7240	3.5	-0.5	-21	2.6	-1.0	A	H
CS 22959-89	18 47 09.1	-66 11 44	329.4	-24.7	14.92	0.23	0.08	1.9	21.1	18.4	7545	3.4	-1.6	43	3.4	-1.4	A	H
CS 22959-142	18 54 22.8	-63 19 04	332.7	-24.9	14.68	0.27	-0.03	2.6	17.7	15.5	7715	4.5	-1.2	0	2.8	-1.2	A	H
CS 22959-216	19 17 22.0	-65 48 23	330.3	-27.7	14.17	0.25	0.08	3.9	21.4	18.6	7518	3.5	-0.6	110	2.3	-1.1	A	H
CS 22960-21	22 10 15.1	-42 32 08	357.2	-54.5	14.64	0.36	-0.13	4.8	10.2	9.1	6976	4.1	-1.1	61	2.6	-2.1	A	H
CS 22960-43	22 18 50.9	-46 12 09	350.4	-55.0	14.45	0.32	-0.07	4.7	13.4	11.9	7229	4.1	-0.7	-1	2.4	-2.0	A	H
CS 22960-54	22 14 38.9	-43 56 48	354.5	-55.0	14.14	0.39	-0.06	6.1	12.3	11.0	7180	4.4	-0.2	-12	2.1	-1.7	A	H
CS 22960-58	22 13 04.7	-42 41 43	356.7	-55.0	13.48	0.34	-0.22	1.6	10.2	9.1	6994	4.5	-2.4	86	1.5	-1.3	A	H
CS 22960-90	22 25 32.3	-47 02 14	348.3	-55.8	15.46	0.33	-0.13	3.5	10.5	9.4	7001	4.0	-1.4	15	3.9	-3.2	A	H
CS 22960-98	22 25 34.0	-45 03 11	351.6	-56.5	14.30	0.22	0.06	3.1	21.1	18.4	7519	3.5	-1.2	88	2.5	-2.1	A	H
CS 22964-96	19 47 52.3	-42 29 36	357.2	-28.5	13.56	0.28	0.05	4.0	19.0	16.6	7447	3.7	-0.7	10	1.7	-0.8	A	H
CS 22964-97	19 50 35.7	-42 16 18	357.6	-28.9	11.48	0.04	0.11	1.9	30.3	28.7	8580	3.6	-1.1	-62	1.2	-0.6	A	E
CS 22964-117	19 55 07.2	-40 01 12	0.3	-29.3	14.78	0.39	-0.02	6.3	10.2	9.1	6974	3.9	-0.3	47	2.8	-1.4	A	H
CS 22964-125	19 53 56.7	-39 09 22	1.2	-28.9	14.15	0.22	0.14	2.1	26.0	19.0	8022	4.3	-1.4	26	2.4	-1.1	A	E
CS 22965-30	21 55 25.2	-04 02 20	54.6	-42.5	14.28	0.39	-0.09	4.5	11.1	9.9	6867	3.5	-1.1	-90	2.3	-1.5	A	H
CS 22965-53	21 59 50.0	-02 38 04	57.0	-42.6	12.66	0.37	0.20	3.1	22.9	19.9	7531	3.5	-0.9	21	1.1	-0.7	A	H
CS 22965-69	22 04 36.5	-05 03 44	55.2	-45.0	15.44	0.25	0.14	1.1	24.2	21.1	7774	3.8	-2.1	161	4.1	-2.9	A	H
CS 22965-77	22 09 43.7	-06 37 56	54.3	-46.9	15.29	0.38	-0.06	6.7	16.2	14.3	7449	4.6	0.0	-40	3.6	-2.6	A	H

Table B.2. (continued)

Star (1)	RA (1950) (2)	Dec (3)	l (4)	b (5)	V (6)	$(B-V)_o$ (7)	$(U-B)_o$ (8)	W_λ (9)	Hδ $D_{0.2}$ (10)	Hγ $D_{0.2}$ (11)	T_{eff} (12)	Log g (13)	[Fe/H] (14)	V_{gsr} (15)	Dist. (16)	Z (17)	Class (18)	Obs (19)
CS 22966-18	23 34 58.9	-28 16 04	25.6	-73.6	14.41	0.09	0.17	1.2	27.5	22.3	8282	3.5	-1.8	-124	3.9	-3.8	A	E
CS 22966-23	23 35 19.7	-29 35 26	20.9	-73.7	15.28	0.09	0.18	1.3	28.9	23.1	8395	3.5	-1.5	31	5.9	-5.7	A	E
CS 22966-25	23 38 14.4	-29 55 02	19.6	-74.3	14.80	0.13	0.15	1.4	24.8	24.4	8010	3.5	-2.1	94	4.0	-3.9	A	E
CS 22966-37	23 41 01.4	-32 05 02	11.3	-74.5	14.00	0.26	-0.05	3.1	16.3	15.0	7487	4.0	-1.3	53	2.1	-2.0	A	E
CS 22966-43	23 41 17.8	-28 35 11	24.5	-75.0	13.56	0.26	-0.05	2.6	17.5	17.7	7739	4.5	-1.4	-277	1.7	-1.6	A	E
CS 22966-76	23 49 04.7	-29 26 57	20.6	-76.7	13.60	0.27	0.09	5.5	15.3	15.6	7270	3.4	-0.4	-32	1.7	-1.7	A	E
CS 22968-12	03 01 52.1	-54 12 01	270.1	-53.9	15.21	0.31	-0.07	2.5	15.5	13.6	7487	4.3	-1.4	112	3.5	-2.8	A	H
CS 22968-15	03 02 29.4	-54 57 19	271.0	-53.4	14.12	0.15	0.08	1.2	29.3	25.3	8245	4.0	-1.6	125	2.8	-2.2	A	H
CS 22968-17	03 11 07.1	-56 00 28	271.3	-51.8	14.28	0.21	0.02	1.7	24.1	21.0	7720	3.6	-1.6	4	2.6	-2.0	A	H
CS 22968-42	03 11 49.0	-53 29 51	267.8	-53.0	15.53	0.16	0.10	1.3	29.2	25.3	8247	4.0	-1.5	0	5.2	-4.2	A	H
CS 29496-20	23 33 53.0	-31 43 26	13.6	-73.1	13.56	0.31	-0.03	3.6	17.0	14.9	7242	3.5	-1.1	61	1.6	-1.6	A	H
CS 29497-7	00 22 49.5	-25 01 27	53.6	-83.7	14.82	0.19	0.03	3.9	19.4	18.2	7530	3.5	-1.1	-65	3.4	-3.4	A	E
CS 29497-17	00 28 55.8	-24 14 01	66.9	-84.5	14.13	0.25	-0.09	3.8	19.2	16.2	7731	4.5	-0.7	70	2.2	-2.2	A	E
CS 29497-30	00 38 19.3	-24 23 58	83.7	-86.2	12.62	0.31	-0.14	1.3	13.7	10.5	7250	4.0	-2.5	34	1.1	-1.0	A	E
CS 29497-41	00 43 46.1	-24 15 44	102.1	-86.6	14.62	0.14	0.06	1.9	28.5	27.5	8261	4.1	-1.1	55	3.6	-3.6	A	E
CS 29499-13	23 36 24.7	-24 37 25	38.6	-73.5	12.77	0.25	0.01	2.3	16.6	15.6	7267	3.5	-1.8	189	1.2	-1.1	A	E
CS 29499-28	23 40 31.1	-23 48 57	42.2	-74.2	12.13	0.16	0.10	3.4	28.5	22.6	8245	4.0	-0.2	-9	1.1	-1.0	A	E
CS 29499-57	23 48 57.0	-26 02 29	35.4	-76.5	13.85	0.20	-0.01	0.7	28.6	18.5	8254	4.4	-2.6	-18	2.2	-2.1	A	E
CS 29499-59	23 48 11.5	-26 24 40	33.7	-76.4	14.28	0.09	0.17	1.0	27.7	22.6	8286	3.5	-2.9	103	3.6	-3.5	A	E
CS 29499-66	23 52 55.6	-25 32 58	38.2	-77.3	13.90	-0.01	-0.03	0.2	20.4	20.3	8254	4.4	-3.0	151	4.9	-4.8	A	E
CS 29499-67	23 52 11.9	-25 27 13	38.5	-77.1	14.61	0.29	-0.01	3.1	16.2	12.8	7246	3.5	-1.2	-8	2.7	-2.6	A	E
CS 29499-74	23 53 18.1	-23 41 18	46.4	-76.9	11.60	0.12	0.11	1.1	35.2	27.9	8768	4.5	-1.4	-42	0.9	-0.9	A	E
CS 29501-26	21 06 43.8	-33 55 38	10.8	-42.3	13.76	0.36	-0.11	4.2	11.8	10.5	7053	3.8	-0.9	108	1.8	-1.2	A	H
CS 29501-102	21 22 55.2	-36 22 49	7.8	-45.9	14.38	0.28	0.06	3.4	23.6	20.5	7749	3.9	-0.8	-37	2.4	-1.7	A	H
CS 29503-11	00 03 24.8	-24 27 17	46.5	-79.3	13.85	-0.02	0.00	1.9	28.7	24.1	9658	4.0	-0.8	-36	4.9	-4.8	A	E
CS 29503-33	00 09 41.6	-24 10 22	50.8	-80.6	14.16	0.30	-0.01	3.0	17.7	15.5	7699	4.5	-0.9	-27	2.2	-2.1	A	H
CS 29503-34	00 08 29.7	-23 34 55	53.4	-80.1	13.55	0.35	-0.08	5.8	11.8	10.5	7231	4.5	-0.3	50	1.6	-1.6	A	H
CS 29503-46	00 13 25.2	-25 41 41	43.1	-81.9	12.02	0.16	0.14	4.2	26.0	21.6	7994	3.5	-0.2	14	1.0	-1.0	A	E
CS 29504-8	01 26 14.8	-35 46 09	261.9	-78.5	14.14	0.25	0.01	4.5	18.8	15.9	7507	4.0	-0.4	43	2.2	-2.2	A	E

Table B.2. (continued)

Star (1)	RA (1950) (2)	Dec (3)	l (4)	b (5)	V (6)	$(B-V)_o$ (7)	$(U-B)_o$ (8)	W_λ (9)	Hδ $D_{0.2}$ (10)	Hγ $D_{0.2}$ (11)	T_{eff} (12)	Log g (13)	[Fe/H] (14)	V_{rad} (15)	Dist. (16)	Z (17)	Class (18)	Obs (19)
CS 29504-17	01 29 19.0	-33 08 44	248.9	-79.6	13.69	0.25	-0.01	0.1	17.7	15.5	7738	4.5	-3.0	-72	1.8	-1.8	A	H
CS 29504-18	01 30 38.0	-33 10 48	248.3	-79.3	13.67	0.36	-0.23	2.2	8.3	6.6	6812	4.3	-2.6	-27	1.7	-1.7	A	E
CS 29504-39	01 42 31.6	-37 40 08	258.8	-74.8	14.10	0.25	0.05	4.4	20.6	18.0	7587	3.9	-0.2	24	2.2	-2.1	A	H
CS 29506-47	21 18 59.7	-22 18 42	26.9	-42.4	14.14	0.25	0.12	0.9	22.1	19.3	7705	3.6	-2.3	-186	2.2	-1.5	A	H
CS 29506-50	21 23 24.1	-22 31 33	27.1	-43.5	14.12	0.31	0.08	4.4	21.4	18.7	7600	3.8	-0.2	-71	2.1	-1.4	A	H
CS 29506-73	21 27 30.7	-19 06 26	32.0	-43.3	14.93	0.33	-0.08	3.3	14.7	13.0	7249	4.0	-1.0	-74	3.0	-2.1	A	H
CS 29506-85	21 26 00.1	-21 19 13	28.9	-43.7	14.00	0.36	-0.06	4.7	14.7	13.0	7170	4.1	-0.7	-25	2.0	-1.4	A	H
CS 29506-114	21 32 19.1	-18 40 13	33.1	-44.2	14.65	0.15	0.10	1.7	31.5	27.3	8492	4.0	-0.9	-155	3.6	-2.5	A	H
CS 29509-24	00 49 19.1	-32 10 24	302.2	-85.2	13.49	0.12	0.12	1.9	29.0	25.1	8297	3.6	-1.0	-65	2.3	-2.3	A	E
CS 29509-27	00 47 50.3	-31 16 17	306.7	-86.1	12.38	0.29	-0.14	1.1	12.0	11.2	7245	4.1	-2.2	58	1.0	-1.0	A	E
CS 29509-53	00 58 27.6	-28 21 39	238.2	-87.7	14.14	0.20	0.04	1.8	28.7	24.9	8235	4.4	-1.2	36	2.4	-2.4	A	E
CS 29512-35	22 13 10.5	-12 13 52	47.7	-50.6	13.55	0.36	-0.04	5.5	11.1	9.9	6979	3.6	-0.7	13	1.6	-1.2	A	H
CS 29512-49	22 17 33.8	-12 33 05	48.1	-51.6	13.68	0.35	-0.05	4.7	12.5	11.1	6994	3.6	-0.9	-20	1.7	-1.3	A	H
CS 29512-60	22 22 52.8	-09 19 34	53.6	-51.1	13.15	0.39	0.01	6.3	13.2	11.7	7062	3.9	0.0	-4	1.3	-1.0	A	H
CS 29512-64	22 20 30.7	-10 52 56	51.0	-51.4	14.41	0.34	-0.06	4.2	11.8	10.5	6997	3.5	-1.2	-134	2.4	-1.9	A	H
CS 29512-71	22 22 00.9	-13 12 58	48.0	-52.9	12.83	0.25	0.07	3.8	22.1	19.3	7745	4.0	-0.6	-33	1.2	-1.0	A	H
CS 29513-55	23 30 31.0	-39 26 59	351.5	-69.7	15.14	0.32	-0.07	4.1	14.8	13.0	7459	4.5	-0.7	-7	3.3	-3.1	A	H
CS 29513-58	23 27 42.0	-38 37 16	354.4	-69.7	14.98	0.31	-0.09	3.5	14.7	12.9	7252	4.0	-0.9	68	3.1	-2.9	A	H
CS 29514-6	01 04 24.5	-25 17 49	182.5	-86.0	14.17	0.30	0.00	5.7	11.7	10.0	7089	3.4	-0.9	57	2.2	-2.2	A	E
CS 29514-10	01 06 17.7	-22 52 56	164.8	-84.0	14.33	0.33	-0.19	2.6	11.2	10.2	7222	4.5	-2.0	126	2.3	-2.3	A	E
CS 29514-21	01 11 35.6	-26 41 04	206.2	-84.9	14.27	0.26	-0.05	1.5	22.1	19.3	7885	4.6	-1.6	69	2.4	-2.3	A	H
CS 29514-41	01 20 00.3	-23 51 48	187.9	-82.2	12.29	0.09	0.08	2.0	32.3	31.1	8767	4.0	-0.6	-22	1.5	-1.5	A	E
CS 29516-23	22 23 19.0	+02 13 15	67.3	-44.1	13.95	0.20	0.03	2.1	24.4	21.6	7987	4.0	-1.5	-232	2.3	-1.6	A	K
CS 29516-26	22 24 23.1	+02 48 08	68.1	-43.9	12.96	0.28	0.17	3.3	24.1	23.8	7989	3.9	-0.2	44	1.3	-0.9	A	K
CS 29516-37	22 22 55.8	+04 17 57	69.3	-42.6	12.32	0.18	0.23	0.7	26.2	24.3	8041	3.8	-3.0	-189	1.1	-0.7	A	K
CS 29516-44	22 19 28.3	+03 18 40	67.5	-42.7	11.55	0.13	0.09	2.8	31.1	29.6	8517	4.0	-0.8	45	0.9	-0.6	A	K
CS 29517-6	23 45 03.6	-15 16 19	69.0	-70.8	15.19	0.25	0.03	...	20.9	19.4	7650	4.0	-0.6	-54	3.6	-3.4	A	L
CS 29517-21	23 55 35.0	-15 08 28	74.9	-72.6	13.55	0.33	-0.08	3.9	12.5	11.1	7232	4.0	-1.0	-81	1.6	-1.5	A	H

Table B.2. (continued)

Star (1)	RA (1950) (2)	Dec (3)	l (4)	b (5)	V (6)	$(B-V)_o$ (7)	$(U-B)_o$ (8)	W_λ (9)	Hδ $D_{0.2}$ (10)	Hγ $D_{0.2}$ (11)	T_{eff} (12)	Log g (13)	[Fe/H] (14)	V_{hel} (15)	Dist. (16)	Z (17)	Class (18)	Obs (19)
CS 29517-32	23 58 37.1	-14 48 09	77.5	-72.8	14.05	0.25	0.03	2.9	19.9	17.4	7500	3.5	-1.2	-57	2.2	-2.1	A	H
CS 29518-6	01 03 44.2	-31 22 54	265.0	-84.9	14.79	0.21	0.02	1.6	22.2	17.8	7754	3.9	-1.9	-125	3.2	-3.2	A	E
CS 29518-12	01 04 34.7	-28 23 46	230.0	-86.4	13.21	0.21	0.05	1.8	23.5	17.9	7782	3.8	-1.8	90	1.6	-1.6	A	E
CS 29518-24	01 14 52.0	-32 42 47	258.1	-82.3	14.52	0.21	-0.05	1.5	24.2	18.6	8002	4.5	-1.7	-77	2.9	-2.8	A	E
CS 29518-26	01 14 22.5	-32 08 35	255.3	-82.7	11.85	0.22	0.04	1.7	22.1	18.3	7753	3.9	-1.8	242	0.8	-0.8	A	E
CS 29518-39	01 20 24.6	-28 40 11	225.2	-83.0	14.26	0.31	-0.17	0.6	12.6	9.7	7131	4.1	-3.0	-28	2.2	-2.2	A	E
CS 29518-47	01 22 56.0	-31 50 59	246.2	-81.4	13.93	0.21	0.02	1.7	29.5	21.6	8232	4.4	-1.5	132	2.2	-2.2	A	E
CS 29518-49	01 24 41.2	-29 57 22	233.2	-81.8	14.43	0.19	0.06	1.7	28.7	23.9	8224	4.1	-1.3	-108	2.9	-2.8	A	E
CS 29520-18	04 20 30.7	-59 25 0	269.9	-42.0	14.44	0.46	-0.19	5.9	7.3	4.5	6517	4.3	-1.5	224	2.6	-1.7	A	E
CS 29520-30	04 29 09.8	-59 12 58	269.3	-41.0	14.46	0.46	-0.30	3.0	5.5	5.0	6500	5.0	-2.0	277	2.7	-1.7	A	E
CS 29520-50	04 40 56.1	-61 14 36	271.3	-39.0	13.49	0.15	0.07	1.7	28.5	28.7	8246	4.1	-1.2	71	2.1	-1.3	A	E
CS 29520-61	04 39 19.0	-59 40 10	269.4	-39.6	14.48	0.22	0.00	1.0	20.8	18.3	7506	3.5	-2.6	151	2.8	-1.8	A	E
CS 29520-79	04 46 11.5	-61 20 30	271.2	-38.4	14.54	0.03	0.03	0.4	32.4	28.1	9236	4.0	-3.0	269	5.2	-3.3	A	E
CS 29520-89	04 58 07.3	-59 50 60	269.0	-37.3	14.64	0.37	-0.21	1.3	8.7	6.7	6501	3.5	-2.5	326	2.6	-1.6	A	E
CS 29521-8	22 50 29.5	+08 24 20	80.1	-44.1	14.83	0.34	0.05	2.9	18.8	15.4	7461	3.4	-1.1	-35	2.9	-2.0	A	E
CS 29521-17	22 52 20.4	+10 19 51	82.2	-42.9	14.43	0.48	-0.16	4.7	6.2	6.2	6324	3.5	-1.5	-128	2.7	-1.8	A	E
CS 29521-32	23 00 26.8	+09 31 47	83.8	-44.7	12.53	0.41	-0.06	8.1	11.3	9.9	6975	4.2	0.0	-10	1.0	-0.7	A	E
CS 29527-45	00 33 20.5	-18 13 38	100.7	-80.1	14.05	0.26	-0.16	1.9	15.7	13.7	7587	4.4	-1.8	-204	2.1	-2.1	A	E
CS 29527-55	00 42 53.8	-22 02 39	108.2	-84.5	12.27	0.14	0.08	1.6	31.8	27.2	8510	4.1	-1.5	22	1.2	-1.2	A	E
CS 29527-56	00 43 14.8	-21 46 08	109.6	-84.2	11.43	0.17	0.15	1.1	28.3	24.4	8229	4.0	-1.9	0	0.8	-0.7	A	E
CS 29527-67	00 43 10.4	-19 03 12	113.6	-81.5	14.59	0.24	-0.14	1.8	17.6	15.4	7733	4.5	-1.8	11	2.8	-2.8	A	E
CS 30312-20	15 30 29.8	+00 39 25	5.3	43.0	13.93	0.21	0.07	1.8	21.7	18.9	7556	3.4	-1.6	-59	2.2	1.5	A	H
CS 30312-32	15 32 40.2	+01 54 50	7.1	43.3	13.89	0.31	-0.06	4.7	11.9	10.6	7063	3.5	-1.0	-51	1.9	1.3	A	H
CS 30312-36	15 34 18.7	+01 25 37	6.9	42.7	13.20	0.33	-0.04	5.1	12.3	10.9	7221	4.1	-0.6	-7	1.4	0.9	A	H
CS 30321-13	18 23 50.7	-36 19 28	357.7	-11.2	13.85	0.09	0.08	3.0	30.6	27.7	8666	4.0	-0.2	-79	2.9	-0.6	A	E
CS 30321-33	18 24 55.2	-35 36 52	358.5	-11.1	11.86	0.06	0.04	1.3	33.3	31.4	8948	4.0	-0.9	-69	1.4	-0.3	A	E
CS 30321-65	18 24 36.2	-34 13 09	359.7	-10.4	13.15	0.20	0.23	1.3	30.1	24.2	8263	4.1	-1.8	-92	1.6	-0.3	A	E
CS 30321-94	18 25 25.8	-33 08 22	0.8	-10.1	14.46	0.13	0.18	1.2	27.4	24.2	8234	3.8	-2.7	-170	3.4	-0.6	A	E
CS 30321-96	18 24 13.8	-32 58 56	0.8	-9.8	12.26	0.23	0.07	1.8	27.3	24.4	8085	4.1	-2.0	-35	1.0	-0.2	A	E

Table B.2. (continued)

Star (1)	RA (1950) (2)	Dec (3)	l (4)	b (5)	V (6)	$(B-V)_o$ (7)	$(U-B)_o$ (8)	W_δ (9)	Hδ $D_{0.2}$ (10)	Hγ $D_{0.2}$ (11)	T_{eff} (12)	Log g (13)	[Fe/H] (14)	V_{los} (15)	Dist. (16)	Z (17)	Class (18)	Obs (19)
CS 30321-167	18 27 04.9	-36 03 46	358.3	-11.7	11.97	0.12	0.04	1.5	28.6	25.4	8275	4.0	-1.6	-57	1.1	-0.2	A	E
CS 30321-232	18 30 00.5	-34 30 21	360.0	-11.5	10.74	0.05	0.00	0.9	33.9	31.9	9143	4.1	-1.4	-5	0.8	-0.2	A	E
CS 30321-282	18 32 24.8	-32 27 03	2.1	-11.1	12.62	0.04	-0.01	1.1	29.4	28.5	9473	4.0	-0.6	-55	2.1	-0.4	A	E
CS 30321-344	18 33 04.2	-35 39 31	359.2	-12.6	13.63	0.12	0.09	2.4	33.4	27.8	8706	4.3	-0.1	-57	2.4	-0.5	A	E
CS 30321-408	18 34 55.7	-35 36 25	359.4	-12.9	12.92	0.11	0.07	2.5	29.6	28.1	8443	4.1	-0.3	15	1.8	-0.4	A	E
CS 30321-476	18 23 44.5	-33 22 50	0.4	-9.9	11.59	0.06	0.04	0.8	30.8	31.3	8542	4.3	-1.9	-5	1.2	-0.2	A	E
CS 30332-16	22 46 16.5	+10 35 55	80.8	-41.7	13.74	0.11	0.18	0.8	26.6	24.1	8126	3.6	-2.4	-180	2.6	-1.7	A	E
CS 30332-115	22 31 49.5	+09 00 48	75.8	-40.7	13.92	0.13	0.16	1.8	33.7	31.4	8703	4.4	-0.9	-73	2.7	-1.8	A	E
CS 30332-123	22 32 13.3	+11 30 05	78.0	-38.9	14.51	0.11	0.05	1.2	34.3	30.0	8764	4.5	-2.5	-148	3.8	-2.4	A	E
CS 30339-6	00 11 59.4	-36 21 51	341.9	-78.1	13.83	0.29	-0.02	3.4	13.4	11.9	7211	3.7	-1.2	-48	1.9	-1.8	A	H
CS 30339-13	00 12 28.5	-34 29 19	348.6	-79.4	12.95	0.32	-0.06	4.6	13.0	11.5	7232	4.1	-0.8	-16	1.2	-1.2	A	H
CS 30339-16	00 10 19.5	-33 17 02	355.4	-79.8	12.37	0.26	0.05	3.5	18.1	15.9	7517	3.9	-0.7	-11	1.0	-1.0	A	H
CS 30339-47	00 21 12.0	-36 32 11	334.0	-79.1	13.49	0.34	-0.09	4.9	12.7	11.2	7166	4.2	-0.6	131	1.6	-1.5	A	H
CS 30492-29	20 59 05.6	-38 55 50	3.9	-41.3	13.64	0.31	-0.06	3.8	15.9	14.0	7445	4.1	-1.0	-45	1.7	-1.1	A	H
CS 30492-59	21 07 51.5	-40 28 22	1.9	-43.1	13.97	0.34	-0.11	4.2	12.3	10.9	7169	4.1	-0.9	-61	1.9	-1.3	A	H
CS 30492-89	21 12 23.4	-39 31 37	3.3	-43.9	14.30	0.36	-0.08	4.6	9.8	8.8	6790	3.4	-1.0	-2	2.3	-1.6	A	H
CS 30492-92	21 09 19.0	-39 12 07	3.7	-43.3	14.73	0.33	-0.04	4.2	11.2	10.0	6990	3.5	-1.2	-108	2.8	-1.9	A	H
CS 30492-98	21 11 25.1	-38 34 23	4.6	-43.7	14.29	0.30	0.04	5.5	13.4	11.8	7236	3.6	-1.1	-8	2.3	-1.6	A	H
CS 30493-5	22 57 52.0	-36 56 12	3.8	-64.7	14.14	0.34	-0.18	2.0	10.9	9.7	6966	4.1	-2.2	81	2.1	-1.9	A	H
CS 30493-22	23 00 17.2	-33 49 48	10.9	-65.8	14.31	0.37	-0.05	5.4	14.5	12.8	7196	4.0	-0.4	-25	2.3	-2.1	A	H
CS 30493-34	23 04 04.6	-35 31 32	6.4	-66.3	13.31	0.27	0.03	3.9	18.1	15.8	7507	4.0	-0.6	46	1.5	-1.4	A	H
CS 30493-57	23 09 16.3	-33 42 44	10.4	-67.7	15.12	0.22	-0.04	1.1	28.7	24.8	8171	4.5	-1.8	-132	3.8	-3.5	A	H
CS 30493-66	23 13 17.3	-35 04 39	6.4	-68.2	14.84	0.28	-0.09	2.0	13.4	11.8	7281	4.0	-1.9	83	3.0	-2.8	A	H
CS 30493-76	23 20 56.6	-37 20 50	359.2	-69.0	13.24	0.39	-0.05	6.8	10.9	9.7	6949	3.7	-0.3	11	1.4	-1.3	A	H
CS 31064-37	03 08 56.1	-67 48 28	285.3	-44.5	11.74	0.21	0.06	2.4	20.8	19.8	7522	3.5	-1.6	277	0.8	-0.6	A	E
CS 31072-52	05 27 51.4	-56 54 34	265.1	-33.6	10.81	0.07	0.12	3.0	29.5	27.2	8511	3.6	-0.4	15	0.8	-0.4	A	E
CS 31072-83	05 22 40.0	-57 46 02	266.1	-34.3	12.41	0.34	-0.12	6.2	10.1	10.2	7073	4.5	-0.2	25	0.9	-0.5	A	E
CS 31072-123	05 08 29.1	-58 22 59	267.0	-36.1	11.26	0.13	0.10	3.4	27.9	26.6	8278	3.8	-0.5	35	0.8	-0.5	A	E

Table B.2. (continued)

Star (1)	RA (1950) (2)	Dec (3)	l (4)	b (5)	V (6)	$(B-V)_o$ (7)	$(U-B)_o$ (8)	W_δ (9)	$H\delta$ $D_{0,2}$ (10)	$H\gamma$ $D_{0,2}$ (11)	T_{eff} (12)	Log g (13)	[Fe/H] (14)	V_{hel} (15)	Dist. (16)	Z (17)	Class (18)	Obs (19)
CS 31075-36	03 35 09.6	-66 09 33	281.3	-43.6	13.52	0.41	-0.06	6.9	7.3	7.8	6609	3.4	-0.6	8	1.6	-1.1	A	E
CS 31075-59	03 21 10.4	-68 07 05	284.6	-43.4	13.21	0.22	0.06	3.2	19.7	22.1	7503	3.5	-1.0	-9	1.5	-1.1	A	E
CS 31075-63	03 22 02.4	-66 32 18	282.8	-44.4	14.84	0.08	0.15	0.7	29.0	21.5	8413	3.5	-2.4	146	4.9	-3.4	A	E
CS 31075-64	03 24 00.7	-66 29 47	282.6	-44.3	12.83	0.28	-0.04	4.5	14.4	12.0	7238	3.6	-0.9	142	1.2	-0.8	A	E
CS 31075-78	03 15 24.2	-66 45 14	283.6	-44.8	13.60	0.17	0.08	2.6	21.1	23.9	7724	3.5	-1.0	28	2.0	-1.4	A	E
CS 31080-106	04 41 30.7	-47 07 53	253.0	-41.0	12.46	0.14	0.10	2.7	28.9	28.1	8267	4.0	-0.1	-2	1.3	-0.9	A	E
CS 31080-111	04 38 36.3	-47 15 50	253.2	-41.5	12.85	0.25	0.06	5.1	21.2	20.8	7738	4.0	0.0	-8	1.2	-0.8	A	E
CS 30321-1094	18 38 28.0	-33 16 01	1.9	-12.6	13.70	0.02	0.10	0.7	28.6	25.0	8301	3.8	-2.5	-107	3.8	-0.8	A	E
CS 30321-1175	18 39 35.5	-35 19 55	0.0	-13.7	13.95	0.09	0.15	0.8	27.3	22.2	8275	3.5	-2.2	74	3.2	-0.8	A	E
CS 30321-1244	18 42 36.3	-35 33 59	0.1	-14.3	13.83	0.08	0.15	0.8	28.0	24.7	8331	3.5	-2.0	-154	3.1	-0.8	A	E

Table B.3. The FHB/A Sample.

Star (1)	RA (1950) (2)	Dec (3)	l (4)	b (5)	V (6)	$(B-V)_o$ (7)	$(U-B)_o$ (8)	W_λ (9)	Hδ $D_{0.2}$ (10)	Hγ $D_{0.2}$ (11)	T_{eff} (12)	Log g (13)	[Fe/H] (14)	V_{los} (15)	Dist. (16)	Z (17)	Class (18)	Obs (19)
BS 15621-8	10 24 50.4	+28 03 26	203.3	58.2	11.24	-0.02	-0.06	1.1	24.2	23.9	9522	3.5	-1.2	20	...	...	HB/A	K,L
BS 15621-10	10 25 19.1	+26 48 11	205.6	58.1	13.77	0.64	0.18	11.8	3.1	2.8	6000	3.0	0.0	46	...	...	HB/A	K
BS 15621-32	10 16 27.7	+26 42 31	205.2	56.2	14.86	0.04	0.13	...	27.9	23.9	8672	3.5	-2.2	140	...	...	HB/A	L
BS 15621-68	10 21 25.3	+23 05 13	212.0	56.5	10.31	0.39	-0.02	7.4	8.2	9.4	6731	3.2	-0.2	-29	...	...	HB/A	E
BS 15621-76	10 08 02.9	+26 28 26	205.0	54.3	12.92	0.44	-0.02	7.1	7.6	7.4	6540	3.1	-0.4	-24	...	...	HB/A	K
BS 16027-35	13 06 21.0	+33 08 08	90.9	83.2	11.69	0.01	0.04	...	26.6	23.1	9146	3.5	-0.8	-41	...	...	HB/A	L
BS 16027-77	13 19 52.4	+31 37 14	67.0	82.1	15.22	0.04	0.10	...	27.2	22.6	8729	3.5	-1.8	-126	...	...	HB/A	L
BS 16032-11	12 38 50.5	+29 25 46	170.1	87.0	13.83	0.03	0.09	...	26.9	25.0	8893	3.5	-1.6	-70	...	...	HB/A	L
BS 16032-15	12 39 41.4	+31 12 09	150.5	85.7	13.18	0.00	0.05	...	26.7	22.9	9072	3.5	-1.9	-18	...	...	HB/A	L
BS 16032-17	12 39 46.1	+32 13 13	145.0	84.8	11.76	0.12	0.15	...	25.0	18.8	8005	3.3	-1.3	3	...	...	HB/A	L
CS 22167-7	03 12 21.0	-06 53 06	188.6	-50.3	14.91	0.03	0.10	0.0	27.8	23.3	8729	3.5	-1.4	0	...	...	HB/A	K
CS 22175-22	02 26 24.6	-09 26 52	179.6	-60.9	12.43	-0.05	-0.09	0.9	23.6	21.8	9720	3.5	-1.3	38	...	...	HB/A	K
CS 22181-7	02 56 16.6	-12 14 41	192.4	-56.6	13.26	0.05	0.13	0.6	27.9	24.2	8410	3.5	-2.7	-16	...	...	HB/A	E
CS 22181-21	03 05 07.3	-11 56 01	193.9	-54.6	13.33	0.07	0.14	1.1	27.0	24.1	8309	3.3	-2.0	156	...	...	HB/A	E
CS 22183-17	00 57 22.8	-03 28 38	128.1	-66.0	14.14	0.03	0.11	0.0	28.0	25.5	8683	3.5	-3.0	93	...	...	HB/A	E
CS 22189-13	02 35 42.7	-15 42 13	193.2	-62.7	12.34	0.04	0.05	1.5	29.5	29.0	8753	3.6	-0.6	-18	...	...	HB/A	E
CS 22871-9	14 32 41.7	-20 14 49	333.5	36.1	11.66	-0.07	-0.22	0.6	24.1	24.1	9729	3.4	-1.6	-179	...	...	HB/A	E
CS 22871-15	14 28 36.8	-19 28 02	332.9	37.3	14.48	0.15	0.12	2.0	22.9	18.6	7770	3.3	-1.5	105	...	...	HB/A	E
CS 22871-39	14 34 09.1	-20 27 07	333.8	35.8	15.23	0.03	0.13	0.7	26.8	19.1	8912	3.5	-1.9	81	...	...	HB/A	K
CS 22871-49	14 32 39.1	-22 14 47	332.4	34.4	15.10	0.02	0.07	6.8	25.5	23.5	9003	3.5	-1.8	81	...	...	HB/A	K
CS 22871-53	14 39 08.8	-21 48 42	334.2	34.0	13.44	0.00	-0.05	0.9	25.5	22.3	9293	3.5	-1.5	-5	...	...	HB/A	E
CS 22871-57	14 40 19.6	-20 58 45	335.0	34.6	13.35	0.05	0.12	0.7	27.8	23.6	8363	3.4	-2.6	82	...	...	HB/A	E
CS 22871-110	14 46 49.9	-18 28 58	338.2	36.0	15.21	0.00	0.04	...	26.1	25.2	9231	3.5	-2.4	-136	...	...	HB/A	L
CS 22872-17	16 15 11.4	-02 56 19	10.0	31.9	14.24	-0.01	-0.03	...	26.2	19.3	9248	3.5	-2.3	111	...	...	HB/A	L
CS 22872-23	16 15 30.2	-02 20 32	10.7	32.1	14.39	-0.01	-9.99	...	24.9	22.9	9310	3.5	-2.4	89	...	...	HB/A	L
CS 22872-31	16 21 00.8	-01 28 07	12.4	31.5	14.74	0.00	0.07	0.6	28.3	25.6	8887	3.5	-1.5	-129	...	...	HB/A	K

Table B.3. The FHB/A Sample.

Star (1)	RA (1950) (2)	Dec (3)	l (4)	b (5)	V (6)	$(B-V)_o$ (7)	$(U-B)_o$ (8)	W_λ (9)	Hδ $D_{0.2}$ (10)	Hγ $D_{0.2}$ (11)	T_{eff} (12)	Log g (13)	[Fe/H] (14)	V_{los} (15)	Dist. (16)	Z (17)	Class (18)	Obs (19)
BS 15621-8	10 24 50.4	+28 03 26	203.3	58.2	11.24	-0.02	-0.06	1.1	24.2	23.9	9522	3.5	-1.2	20	...	...	HB/A	K,L
BS 15621-10	10 25 19.1	+26 48 11	205.6	58.1	13.77	0.64	0.18	11.8	3.1	2.8	6000	3.0	0.0	46	...	...	HB/A	K
BS 15621-32	10 16 27.7	+26 42 31	205.2	56.2	14.86	0.04	0.13	...	27.9	23.9	8672	3.5	-2.2	140	...	...	HB/A	L
BS 15621-68	10 21 25.3	+23 05 13	212.0	56.5	10.31	0.39	-0.02	7.4	8.2	9.4	6731	3.2	-0.2	-29	...	...	HB/A	E
BS 15621-76	10 08 02.9	+26 28 26	205.0	54.3	12.92	0.44	-0.02	7.1	7.6	7.4	6540	3.1	-0.4	-24	...	...	HB/A	K
BS 16027-35	13 06 21.0	+33 08 08	90.9	83.2	11.69	0.01	0.04	...	26.6	23.1	9146	3.5	-0.8	-41	...	...	HB/A	L
BS 16027-77	13 19 52.4	+31 37 14	67.0	82.1	15.22	0.04	0.10	...	27.2	22.6	8729	3.5	-1.8	-126	...	...	HB/A	L
BS 16032-11	12 38 50.5	+29 25 46	170.1	87.0	13.83	0.03	0.09	...	26.9	25.0	8893	3.5	-1.6	-70	...	...	HB/A	L
BS 16032-15	12 39 41.4	+31 12 09	150.5	85.7	13.18	0.00	0.05	...	26.7	22.9	9072	3.5	-1.9	-18	...	...	HB/A	L
BS 16032-17	12 39 46.1	+32 13 13	145.0	84.8	11.76	0.12	0.15	...	25.0	18.8	8005	3.3	-1.3	3	...	...	HB/A	L
CS 22167-7	03 12 21.0	-06 53 06	188.6	-50.3	14.91	0.03	0.10	0.0	27.8	23.3	8729	3.5	-1.4	0	...	...	HB/A	K
CS 22175-22	02 26 24.6	-09 26 52	179.6	-60.9	12.43	-0.05	-0.09	0.9	23.6	21.8	9720	3.5	-1.3	38	...	...	HB/A	K
CS 22181-7	02 56 16.6	-12 14 41	192.4	-56.6	13.26	0.05	0.13	0.6	27.9	24.2	8410	3.5	-2.7	-16	...	...	HB/A	E
CS 22181-21	03 05 07.3	-11 56 01	193.9	-54.6	13.33	0.07	0.14	1.1	27.0	24.1	8309	3.3	-2.0	156	...	...	HB/A	E
CS 22183-17	00 57 22.8	-03 28 38	128.1	-66.0	14.14	0.03	0.11	0.0	28.0	25.5	8683	3.5	-3.0	93	...	...	HB/A	E
CS 22189-13	02 35 42.7	-15 42 13	193.2	-62.7	12.34	0.04	0.05	1.5	29.5	29.0	8753	3.6	-0.6	-18	...	...	HB/A	E
CS 22871-9	14 32 41.7	-20 14 49	333.5	36.1	11.66	-0.07	-0.22	0.6	24.1	24.1	9729	3.4	-1.6	-179	...	...	HB/A	E
CS 22871-15	14 28 36.8	-19 28 02	332.9	37.3	14.48	0.15	0.12	2.0	22.9	18.6	7770	3.3	-1.5	105	...	...	HB/A	E
CS 22871-39	14 34 09.1	-20 27 07	333.8	35.8	15.23	0.03	0.13	0.7	26.8	19.1	8912	3.5	-1.9	81	...	...	HB/A	K
CS 22871-49	14 32 39.1	-22 14 47	332.4	34.4	15.10	0.02	0.07	6.8	25.5	23.5	9003	3.5	-1.8	81	...	...	HB/A	K
CS 22871-53	14 39 08.8	-21 48 42	334.2	34.0	13.44	0.00	-0.05	0.9	25.5	22.3	9293	3.5	-1.5	-5	...	...	HB/A	E
CS 22871-57	14 40 19.6	-20 58 45	335.0	34.6	13.35	0.05	0.12	0.7	27.8	23.6	8363	3.4	-2.6	82	...	...	HB/A	E
CS 22871-110	14 46 49.9	-18 28 58	338.2	36.0	15.21	0.00	0.04	...	26.1	25.2	9231	3.5	-2.4	-136	...	...	HB/A	L
CS 22872-17	16 15 11.4	-02 56 19	10.0	31.9	14.24	-0.01	-0.03	...	26.2	19.3	9248	3.5	-2.3	111	...	...	HB/A	L
CS 22872-23	16 15 30.2	-02 20 32	10.7	32.1	14.39	-0.01	-9.99	...	24.9	22.9	9310	3.5	-2.4	89	...	...	HB/A	L
CS 22872-31	16 21 00.8	-01 28 07	12.4	31.5	14.74	0.00	0.07	0.6	28.3	25.6	8887	3.5	-1.5	-129	...	...	HB/A	K

Table B.3. (Continued)

Star (1)	RA (1950) (2)	Dec (3)	l (4)	b (5)	V (6)	$(B-V)_o$ (7)	$(U-B)_o$ (8)	W_λ (9)	Hδ $D_{0.2}$ (10)	Hγ $D_{0.2}$ (11)	T_{eff} (12)	Log g (13)	[Fe/H] (14)	V_{hel} (15)	Dist. (16)	Z (17)	Class (18)	Obs (19)
CS 22872-47	16 18 19.2	-04 00 56	9.5	30.6	14.67	0.04	0.16	1.1	28.9	28.5	8554	3.5	-1.5	13	...	...	HB/A	K
CS 22872-48	16 18 57.9	-04 08 01	9.5	30.4	14.34	0.07	0.19	1.3	28.5	22.1	8435	3.5	-1.4	33	...	...	HB/A	K
CS 22872-55	16 21 00.9	-05 03 05	9.0	29.4	14.88	0.06	0.08	0.6	27.5	25.6	8672	3.5	-2.2	19	...	...	HB/A	K
CS 22872-88	16 25 10.9	-01 25 51	13.1	30.6	13.48	-0.01	0.09	0.7	25.6	24.4	9187	3.5	-1.6	7	...	...	HB/A	K,L
CS 22872-95	16 26 22.0	-02 11 28	12.6	30.0	14.61	0.06	0.14	...	28.4	22.3	8422	3.5	-2.5	-159	...	...	HB/A	L
CS 22872-97	16 28 25.8	-02 18 46	12.8	29.5	14.77	0.05	0.09	...	26.7	19.7	8891	3.5	-2.6	-5	...	...	HB/A	L
CS 22872-99	16 27 23.7	-02 45 21	12.2	29.4	12.60	0.08	0.14	...	27.8	23.5	8328	3.5	-3.0	-208	...	...	HB/A	L
CS 22872-133	16 31 16.1	-01 51 11	13.7	29.1	13.62	0.08	0.16	...	26.7	23.6	8241	3.4	-2.7	85	...	...	HB/A	L
CS 22874-3	14 31 15.0	-27 20 00	329.3	30.0	13.68	0.02	0.13	0.6	28.0	22.8	8723	3.5	-1.8	-119	...	...	HB/A	E
CS 22874-5	14 30 33.6	-26 45 58	329.4	30.6	14.44	-0.01	0.12	0.3	27.9	28.7	8741	3.5	-2.8	105	...	...	HB/A	E
CS 22874-10	14 29 55.8	-26 00 03	329.7	31.3	13.90	0.28	-0.48	5.6	6.9	6.1	6701	3.2	-0.9	54	...	...	HB/A	E
CS 22874-11	14 30 25.7	-25 27 16	330.1	31.8	15.35	-0.01	0.11	1.5	26.3	20.5	8967	3.5	-1.7	48	...	...	HB/A	E
CS 22874-19	14 30 19.1	-24 35 14	330.5	32.6	14.66	0.03	0.12	2.0	29.8	24.1	8539	3.5	-1.2	0	...	...	HB/A	E
CS 22874-32	14 30 12.3	-23 16 55	331.2	33.7	13.94	0.05	0.17	1.8	27.3	21.5	8645	3.5	-0.6	148	...	...	HB/A	E
CS 22874-36	14 32 05.2	-23 59 58	331.2	32.9	13.09	0.01	0.09	0.9	26.2	24.7	8957	3.5	-1.3	40	...	...	HB/A	E
CS 22874-56	14 34 08.2	-26 43 35	330.3	30.3	14.01	-0.02	0.02	0.5	26.7	20.1	9052	3.5	-2.0	-21	...	...	HB/A	E
CS 22876-6	23 49 43.6	-36 20 35	353.8	-74.6	14.01	0.02	0.09	0.4	26.6	25.7	8920	3.5	-2.8	-28	...	...	HB/A	E
CS 22877-21	13 21 10.2	-07 45 37	316.6	54.0	15.29	0.08	-9.99	...	26.9	21.8	8329	3.4	-1.2	106	...	...	HB/A	L
CS 22878-51	16 38 09.1	+08 29 17	25.1	32.9	13.47	0.12	0.10	0.5	24.8	23.2	8015	3.3	-3.0	-315	...	...	HB/A	K
CS 22878-74	16 36 09.7	+11 48 24	28.5	34.8	14.65	0.01	0.01	...	25.5	22.6	9229	3.5	-3.0	-58	...	...	HB/A	L
CS 22883-13	14 14 26.6	+12 27 15	0.4	65.0	14.44	0.17	0.18	...	22.5	18.8	7748	3.4	-2.9	-95	...	...	HB/A	L
CS 22883-14	14 15 35.2	+12 16 21	0.5	64.7	14.77	0.04	0.15	...	29.5	25.2	8562	3.5	-3.0	-76	...	...	HB/A	L
CS 22884-28	15 33 50.0	-09 03 35	356.5	36.0	13.67	-0.03	-0.08	1.5	22.9	22.2	9097	3.5	-1.4	-7	...	...	HB/A	K
CS 22884-47	15 38 42.9	-11 18 31	355.5	33.5	12.92	0.05	0.08	0.7	26.6	26.3	8641	3.5	-2.0	-90	...	...	HB/A	K
CS 22889-35	13 40 25.5	-09 19 58	323.5	51.2	14.85	-0.06	-9.99	...	25.8	29.6	9269	3.4	-2.3	-27	...	...	HB/A	L
CS 22889-37	13 37 36.3	-08 58 54	322.6	51.8	13.68	0.04	0.14	1.3	27.8	25.1	8669	3.5	-2.2	174	...	...	HB/A	E
CS 22889-40	13 40 16.2	-07 33 57	324.4	52.9	15.16	0.06	-9.99	...	28.1	22.2	8680	3.5	-2.6	-80	...	...	HB/A	L

Table B.3. (Continued)

Star (1)	RA (1950) (2)	Dec (3)	l (4)	b (5)	V (6)	$(B-V)_o$ (7)	$(U-B)_o$ (8)	W_λ (9)	Hδ $D_{0.2}$ (10)	Hγ $D_{0.2}$ (11)	T_{eff} (12)	Log g (13)	[Fe/H] (14)	V_{los} (15)	Dist (16)	Z (17)	Class (18)	Obs (19)
CS 22890-36	15 18 15.2	-00 05 27	1.8	44.9	14.56	0.19	0.12	1.9	24.6	21.4	7818	3.4	-1.5	15	...	...	HB/A	H
CS 22891-143	19 15 07.5	-57 50 13	339.2	-26.3	12.51	0.00	0.04	1.7	26.8	26.4	9039	3.5	-0.3	-76	...	...	HB/A	E
CS 22891-219	19 34 45.8	-59 50 12	337.3	-29.1	14.25	0.38	-0.03	6.0	10.1	9.1	6720	3.1	-0.6	121	...	...	HB/A	H
CS 22894-31	23 37 26.5	-00 47 16	87.2	-58.3	14.12	0.05	0.13	...	27.9	22.8	8362	3.4	-2.2	-216	...	...	HB/A	L
CS 22894-51	23 47 44.0	-01 33 17	90.8	-60.3	14.87	0.16	0.17	...	23.3	20.1	7794	3.4	-2.4	-330	...	...	HB/A	L
CS 22896-13	19 17 03.0	-55 50 27	341.4	-26.2	14.14	0.05	0.14	1.4	29.1	25.2	8527	3.5	-1.5	233	...	...	HB/A	E
CS 22896-14	19 18 25.4	-55 36 01	341.7	-26.4	14.03	-0.03	0.03	0.7	25.1	20.5	9289	3.5	-1.5	-12	...	...	HB/A	E
CS 22896-82	19 22 02.5	-57 07 47	340.1	-27.1	14.72	0.17	0.11	1.9	24.1	21.0	7829	3.3	-1.4	-82	...	...	HB/A	H
CS 22896-127	19 37 28.5	-52 44 53	345.4	-28.6	13.61	-0.02	...4	0.9	25.4	26.7	9261	3.5	-1.2	115	...	...	HB/A	E
CS 22896-181	19 44 42.8	-54 58 26	343.0	-30.0	13.10	0.09	0.18	1.0	26.4	24.5	8245	3.4	-2.0	120	...	...	HB/A	E
CS 22897-3	21 00 29.3	-65 50 45	328.9	-38.1	15.01	-0.04	0.00	1.9	23.7	24.1	9427	3.5	-1.3	67	...	...	HB/A	E
CS 22897-100	21 25 19.4	-66 18 36	327.1	-40.3	14.53	0.04	0.05	0.7	26.1	23.8	9045	3.5	-1.9	157	...	...	HB/A	E
CS 22939-87	19 22 38.7	-29 32 01	9.2	-19.9	13.20	-0.02	-0.02	0.3	23.3	22.3	9488	3.5	-2.6	-18	...	...	HB/A	E
CS 22939-148	19 25 04.9	-30 23 16	8.6	-20.7	13.42	0.06	0.09	0.8	27.0	25.6	8478	3.5	-1.8	90	...	...	HB/A	E
CS 22941-16	23 28 47.7	-34 13 36	6.4	-71.5	13.95	-0.06	-0.20	0.3	26.6	21.7	9729	3.3	-1.0	43	...	...	HB/A	E
CS 22941-50	23 43 51.3	-35 12 41	359.6	-74.1	14.17	0.00	0.05	0.6	24.9	24.7	9255	3.5	-1.6	58	...	...	HB/A	E
CS 22953-6	01 04 35.0	-61 37 15	299.7	-55.7	14.48	0.34	-0.07	4.0	9.5	8.6	6727	3.1	-1.5	7	...	...	HB/A	H
CS 22955-23	20 21 27.3	-25 25 32	18.3	-30.8	14.31	0.15	0.18	1.9	22.8	19.8	7751	3.3	-1.6	-80	...	...	HB/A	H
CS 22959-88	18 49 50.1	-66 04 44	329.6	-25.0	13.99	0.03	0.09	1.3	29.2	25.4	8582	3.5	-1.4	114	...	...	HB/A	E
CS 22959-183	19 07 38.2	-66 21 09	329.6	-26.8	14.97	0.04	0.14	1.0	28.5	23.0	8612	3.5	-1.9	59	...	...	HB/A	E
CS 22959-193	19 06 12.0	-66 51 40	329.0	-26.7	13.27	0.08	0.08	2.4	27.7	30.1	8625	3.5	-0.6	-24	...	...	HB/A	E
CS 22966-58	23 47 53.2	-29 56 48	18.6	-76.4	14.13	0.06	0.15	1.2	28.7	23.5	8472	3.5	-1.7	-34	...	...	HB/A	E
CS 22968-45	03 09 47.2	-52 50 30	267.1	-53.6	14.16	0.10	0.11	0.5	26.0	22.6	8061	3.3	-3.0	74	...	...	HB/A	E

Table B.3. (Continued)

Star (1)	RA (1950) (2)	Dec (3)	l (4)	b (5)	V (6)	$(B-V)_o$ (7)	$(U-B)_o$ (8)	W_λ (9)	Hδ $D_{0.3}$ (10)	Hγ $D_{0.3}$ (11)	T_{eff} (12)	Log g (13)	[Fe/H] (14)	V_{los} (15)	Dist (16)	Z (17)	Class (18)	Obs (19)
CS 29497-37	00 42 14.2	-27 27 20	30.5	-88.5	13.02	0.07	0.15	2.7	26.8	27.2	8353	3.3	-0.4	6	...	...	HB/A	E
CS 29499-25	23 40 54.2	-23 06 59	44.8	-74.0	13.40	0.05	0.14	0.5	28.7	23.8	8487	3.5	-3.0	-55	...	...	HB/A	E
CS 29499-26	23 40 55.6	-23 14 29	44.4	-74.1	14.32	0.00	...0	0.6	24.2	22.5	9352	3.5	-1.9	-73	...	...	HB/A	E
CS 29499-32	23 38 55.0	-26 31 23	32.2	-74.4	14.62	0.06	0.13	1.0	27.4	24.3	8373	3.4	-2.8	-56	...	...	HB/A	E
CS 29499-64	23 52 58.3	-25 49 34	37.0	-77.4	14.69	0.01	0.09	0.7	26.4	21.9	8972	3.5	-1.8	-48	...	...	HB/A	E
CS 29503-27	00 05 17.8	-26 47 38	34.1	-80.3	14.33	0.02	0.10	0.7	27.4	24.7	8888	3.5	-2.2	-136	...	...	HB/A	E
CS 29509-31	00 50 31.9	-30 10 55	296.2	-87.2	13.91	0.12	0.16	1.8	25.4	21.9	8018	3.4	-1.6	131	...	...	HB/A	E
CS 29514-13	01 08 07.2	-25 56 44	195.3	-85.5	14.27	0.00	0.08	0.4	27.0	25.8	8971	3.5	-2.7	-50	...	...	HB/A	E
CS 29514-20	01 14 09.1	-27 11 16	212.3	-84.4	14.74	0.05	0.14	0.3	27.9	22.8	8376	3.5	-3.0	-75	...	...	HB/A	E
CS 29516-54	22 17 26.8	+04 37 28	68.3	-41.4	11.92	0.19	0.16	3.0	23.8	22.6	7810	3.3	-1.1	56	...	...	HB/A	K
CS 29518-28	01 14 23.9	-31 20 46	250.0	-83.2	15.00	0.09	0.18	0.7	27.2	25.6	8295	3.5	-2.5	14	...	...	HB/A	E
CS 29520-7	04 22 20.4	-61 38 37	272.7	-41.1	16.05	0.07	0.14	1.5	29.0	20.7	8476	3.5	-2.7	117	...	...	HB/A	E
CS 29520-44	04 30 26.3	-62 41 02	273.6	-39.8	15.45	0.07	0.00	0.9	28.4	28.0	8732	3.5	-1.9	44	...	...	HB/A	E
CS 29520-83	04 47 13.5	-62 31 59	272.7	-38.0	11.95	0.07	0.16	0.5	27.9	24.4	8418	3.5	-2.8	129	...	...	HB/A	E
CS 29529-43	03 50 51.4	-60 52 12	273.7	-44.8	11.80	-0.01	-0.04	0.9	25.1	24.9	9408	3.5	-0.9	-20	...	...	HB/A	E
CS 29529-79	04 13 11.2	-58 05 33	268.6	-43.3	14.03	0.02	0.05	0.3	25.1	22.3	9211	3.5	-2.8	128	...	...	HB/A	E
CS 30321-21	18 24 04.1	-35 57 31	358.1	-11.1	14.00	0.04	0.09	0.8	27.8	23.7	8786	3.5	-1.7	327	...	...	HB/A	E
CS 30321-166	18 27 20.7	-35 59 57	358.3	-11.7	14.61	0.06	0.15	2.8	27.0	27.5	8487	3.5	-2.1	246	...	...	HB/A	E
CS 30321-294	18 33 16.9	-33 05 47	1.5	-11.6	12.94	0.00	-0.10	0.8	25.1	22.5	9425	3.5	-1.1	17	...	...	HB/A	E
CS 30321-424	18 34 06.8	-34 35 57	0.2	-12.3	13.55	-0.04	-0.05	0.9	22.6	21.4	9716	3.5	-0.6	-116	...	...	HB/A	E
CS 30332-68	22 38 14.8	+11 07 54	79.1	-40.1	13.81	0.04	0.11	0.8	27.9	23.9	8667	3.5	-1.8	-162	...	...	HB/A	E
CS 30332-122	22 32 32.4	+11 20 03	77.9	-39.1	14.73	0.01	0.04	14.5	25.7	26.2	9145	3.5	-0.1	-134	...	...	HB/A	E
CS 30332-124	22 31 18.4	+11 39 47	77.9	-38.6	12.96	0.13	0.13	1.4	26.3	21.0	8024	3.4	-1.8	82	...	...	HB/A	E
CS 31072-27	05 36 06.3	-60 45 01	269.6	-32.5	11.79	0.02	-0.03	0.5	28.0	25.2	9016	3.5	-2.3	23	...	...	HB/A	E

Table B.3. (Continued)

Star (1)	RA (1950) (2)	Dec (3)	l (4)	b (5)	V (6)	$(B-V)_o$ (7)	$(U-B)_o$ (8)	W_λ (9)	Hδ $D_{0.2}$ (10)	Hγ $D_{0.2}$ (11)	T_{eff} (12)	$Log\ g$ (13)	[Fe/H] (14)	V_{los} (15)	Dist. (16)	Z (17)	Class (18)	Obs (19)
CS 31072-133	05 04 44.9	-59 05 59	268.0	-36.5	14.53	-0.04	-0.17	0.9	26.1	22.5	9712	3.5	-1.1	90	...	...	HB/A	E
CS 31075-29	03 41 18.5	-63 28 24	277.7	-44.5	14.24	-0.01	0.06	0.6	28.1	25.7	8929	3.5	-1.8	152	...	...	HB/A	E
CS 30321-1014	18 36 21.4	-36 46 18	358.4	-13.7	13.40	-0.03	-0.05	0.9	23.6	24.5	9695	3.5	-1.6	-284	...	...	HB/A	E
CS 30321-1139	18 39 10.7	-33 31 49	1.7	-12.9	12.82	0.10	0.10	1.4	25.8	23.5	8040	3.3	-1.8	-136	...	...	HB/A	E
CS 30321-1163	18 39 44.1	-34 59 27	0.4	-13.6	13.09	0.05	0.14	1.1	27.9	27.9	8514	3.5	-1.5	-167	...	...	HB/A	E
CS 30321-1214	18 41 10.6	-37 09 00	358.4	-14.7	13.73	0.05	0.14	1.5	27.2	24.7	8559	3.4	-1.5	-21	...	...	HB/A	E
CS 30321-1287	18 42 12.9	-33 40 03	1.8	-13.5	12.78	0.01	0.06	2.3	29.4	27.7	8820	3.5	-0.4	-121	...	...	HB/A	E
CS 30321-1463	18 46 28.7	-34 50 09	1.1	-14.8	14.10	0.04	0.12	1.0	26.2	24.5	9250	3.5	-0.9	77	...	...	HB/A	E
CS 30321-1481	18 46 20.1	-33 57 12	1.9	-14.4	14.18	0.02	0.12	1.5	27.3	22.8	8900	3.5	-1.2	-78	...	...	HB/A	E

Table B.4. The Am Candidates.

Star (1)	RA (1950) (2)	Dec (3)	l (4)	b (5)	V (6)	$(B-V)_o$ (7)	$(U-B)_o$ (8)	W_k (9)	Hδ $D_{0.2}$ (10)	Hγ $D_{0.2}$ (11)	T_{eff} (12)	Log g (13)	[Fe/H] (14)	V_{los} (15)	Dist (16)	Z (17)	Class (18)	Obs (19)
BS 15621-19	10 23 07.7	+26 16 11	206.5	57.6	11.93	0.16	0.11	1.9	26.9	26.7	8136	3.9	-0.9	-7	1.0	0.8	Am	KL
BS 15621-21	10 22 22.0	+23 56 09	210.6	56.9	12.49	0.19	0.14	3.0	24.8	25.2	7938	3.3	-0.8	56	1.2	1.0	Am	KL
BS 15621-53	10 17 15.9	+23 09 05	211.4	55.6	13.59	0.25	0.04	2.4	17.5	17.7	7398	3.4	-1.7	-9	1.7	1.4	Am	EL
CS 22171-21	01 59 51.6	-09 17 50	169.1	-65.4	12.35	0.19	0.14	3.2	23.9	22.9	7827	3.3	-0.8	142	1.1	-1.0	Am	K
CS 22171-36	02 06 27.2	-09 26 42	172.2	-64.4	11.63	0.24	0.07	3.5	19.1	18.6	7501	3.5	-0.9	25	0.7	-0.6	Am	EK
CS 22174-27	01 24 03.7	-11 59 50	152.8	-72.5	12.74	0.20	0.09	1.5	26.4	26.0	8059	4.0	-1.6	40	1.3	-1.2	Am	K
CS 22175-10	02 14 30.3	-08 03 49	173.3	-62.0	11.89	0.08	0.08	1.3	31.1	26.6	8561	4.0	-1.5	-13	1.2	-1.1	Am	E
CS 22175-17	02 26 47.2	-08 32 55	178.4	-60.2	11.84	0.22	0.05	1.8	18.2	22.1	7498	3.5	-2.0	-22	0.8	-0.7	Am	E
CS 22176-1	03 29 12.4	-09 20 07	195.2	-48.2	12.06	0.18	0.13	2.0	26.4	24.1	8046	3.8	-1.2	54	1.0	-0.7	Am	E
CS 22176-16	03 36 12.8	-12 26 56	200.6	-48.2	13.04	0.29	0.12	3.7	21.4	24.4	7548	2.8	-0.7	-12	1.3	-1.0	Am	E
CS 22180-7	01 32 32.3	-11 02 59	157.1	-70.7	13.28	0.20	0.12	2.9	20.8	20.5	7513	2.9	-1.6	48	1.7	-1.6	Am	E
CS 22181-8	02 56 52.1	-12 37 15	193.1	-56.7	12.27	0.25	0.07	1.7	18.9	19.0	7497	3.5	-1.8	0	1.0	-0.8	Am	E
CS 22181-35	03 07 54.1	-08 16 11	189.4	-52.0	13.19	0.26	0.06	3.3	21.5	17.5	7535	3.5	-1.0	-5	1.4	-1.1	Am	E
CS 22184-6	02 32 27.4	-08 51 43	180.7	-59.3	13.07	0.25	0.06	3.5	21.1	22.8	7752	4.0	-0.6	19	1.4	-1.2	Am	E
CS 22184-21	02 36 49.5	-11 31 13	186.2	-60.1	11.75	0.25	0.09	2.3	16.8	16.8	7251	3.0	-1.6	8	0.7	-0.6	Am	EE
CS 22184-34	02 47 28.9	-12 01 38	189.9	-58.3	12.74	0.19	0.12	3.4	21.0	22.6	7514	3.0	-1.0	-14	1.3	-1.1	Am	E
CS 22185-8	03 12 48.2	-15 44 54	201.2	-54.7	11.30	0.25	0.07	3.4	17.2	18.3	7248	3.0	-1.5	43	0.6	-0.5	Am	E
CS 22185-23	03 28 40.9	-15 35 15	203.7	-51.2	11.96	0.28	0.07	4.7	15.1	18.5	7021	2.9	-1.1	-4	0.8	-0.6	Am	EE
CS 22185-28	03 32 48.6	-14 39 06	203.0	-49.9	11.82	0.31	0.09	3.4	15.8	18.8	7052	2.8	-1.1	51	0.7	-0.6	Am	E
CS 22189-12	02 36 44.1	-14 27 27	191.2	-61.8	13.40	0.26	0.05	2.1	19.1	18.0	7458	3.5	-1.6	10	1.6	-1.4	Am	E
CS 22189-17	02 40 22.2	-15 47 07	194.5	-61.7	12.70	0.22	0.06	3.6	18.5	20.0	7506	3.5	-0.9	-27	1.2	-1.1	Am	E
CS 22189-21	02 44 29.7	-17 02 31	197.8	-61.4	12.48	0.16	0.09	2.1	25.5	21.6	8012	3.9	-1.4	8	1.3	-1.1	Am	E
CS 22189-31	02 45 09.2	-13 51 03	192.3	-59.7	13.61	0.24	0.05	3.1	19.0	19.5	7501	3.5	-1.0	14	1.8	-1.6	Am	E
CS 22189-42	02 49 25.2	-17 24 39	199.6	-60.5	11.33	0.26	0.08	2.4	17.9	19.2	7254	3.0	-1.4	53	0.6	-0.5	Am	E
CS 22871-4	14 31 24.4	-20 36 35	333.0	36.0	13.89	0.23	0.12	2.3	20.7	18.5	7494	3.2	-1.5	-9	2.1	1.2	Am	K

Table B.4. (continued)

Star (1)	RA (1950) (2)	Dec (3)	l (4)	b (5)	V (6)	$(B-V)_o$ (7)	$(U-B)_o$ (8)	W_λ (9)	Hδ $D_{0.2}$ (10)	Hγ $D_{0.2}$ (11)	T_{eff} (12)	Log g (13)	[Fe/H] (14)	V_{tan} (15)	Dist. (16)	Z (17)	Class (18)	Obs (19)
CS 22871-28	14 36 09.9	-18 13 35	335.7	37.5	13.18	0.27	0.08	3.9	19.7	17.7	7500	3.5	-0.7	-78	1.4	0.9	Am	E
CS 22871-93	14 43 06.3	-20 24 23	336.0	34.8	13.16	0.35	0.14	3.7	10.6	15.5	6840	2.6	-1.9	-44	1.3	0.8	Am	KL
CS 22871-94	14 42 12.4	-21 13 38	335.3	34.2	12.39	0.25	0.13	2.4	17.5	22.3	7226	2.6	-1.8	-16	1.0	0.6	Am	E
CS 22871-97	14 44 24.6	-21 25 33	335.7	33.8	12.01	0.16	0.10	2.0	30.1	24.8	8286	4.0	-0.9	-48	1.0	0.6	Am	E
CS 22871-111	14 46 18.8	-18 27 47	338.1	36.0	12.94	0.26	0.09	2.2	12.8	23.7	6750	2.0	-2.4	35	1.3	0.7	Am	E
CS 22872-20	16 15 42.2	-3 01 25	10.0	31.7	12.70	0.00	0.04	0.7	26.4	25.2	9073	3.5	-1.8	-41	2.7	1.4	Am	E
CS 22872-116	16 31 30.4	-5 11 57	10.6	27.2	12.86	0.22	-0.19	3.0	22.9	18.2	8000	5.0	-0.6	-46	1.3	0.6	Am	K
CS 22874-26	14 27 16.7	-23 45 05	330.2	33.6	11.25	0.14	0.09	1.8	29.1	27.0	8280	4.0	-1.0	-19	0.8	0.4	Am	E
CS 22874-93	14 44 34.3	-24 23 14	334.0	31.2	11.47	0.18	0.11	3.0	23.2	25.5	7793	3.4	-1.1	-93	0.8	0.4	Am	E
CS 22874-95	14 45 00.7	-24 45 12	333.8	30.8	12.76	0.22	0.08	3.5	20.7	19.8	7528	3.5	-0.9	192	1.3	0.6	Am	E
CS 22876-15	23 49 39.8	-32 53 48	6.2	-76.1	12.40	0.04	0.01	1.1	32.7	31.4	9173	4.0	-0.9	17	1.9	-1.8	Am	E
CS 22896-62	19 22 36.4	-54 57 42	342.5	-26.8	12.90	0.22	0.11	2.4	22.2	22.9	7742	3.6	-1.2	-13	1.3	-0.6	Am	E
CS 22896-149	19 39 41.0	-56 17 20	341.4	-29.4	11.89	0.17	0.02	2.6	22.4	24.8	7762	3.5	-1.2	33	0.9	-0.5	Am	H
CS 22936-255	18 56 54.2	-32 53 50	3.8	-16.0	13.69	0.35	0.09	5.1	15.5	15.0	7046	2.9	-0.8	36	1.7	-0.5	Am	E
CS 22936-260	18 56 51.0	-33 21 44	3.4	-16.2	12.70	0.34	0.15	3.6	14.7	13.1	6999	2.4	-1.6	-24	1.1	-0.3	Am	E
CS 22936-341	19 00 45.4	-35 12 28	1.9	-17.6	11.32	0.07	0.04	1.7	34.7	32.2	8783	4.4	-0.6	22	1.0	-0.3	Am	E
CS 22939-106	19 23 28.3	-30 39 30	8.2	-20.4	13.12	0.13	0.08	1.3	24.9	30.3	7989	3.4	-2.0	-50	1.9	-0.6	Am	E
CS 22941-46	23 41 36.2	-35 02 03	0.9	-73.7	14.43	0.44	-0.16	4.7	3.8	6.5	6000	3.0	-2.0	-51	2.5	-2.4	Am	E
CS 22951-15	21 35 11.7	-45 49 52	353.9	-47.8	13.99	0.16	0.13	2.7	28.0	22.1	8224	3.8	-0.8	133	2.5	-1.9	Am	E
CS 22956-55	21 48 03.1	-66 34 45	325.4	-42.1	12.11	0.25	0.10	1.9	20.9	19.7	7506	3.0	-1.6	-30	0.9	-0.6	Am	E
CS 22964-50	19 50 05.5	-38 16 08	2.0	-27.9	12.06	0.08	0.08	1.9	33.8	30.3	8772	4.1	-0.7	-66	1.4	-0.6	Am	E
CS 22964-51	19 49 05.8	-38 13 40	2.0	-27.7	11.50	0.17	0.17	2.7	28.0	25.7	8232	4.0	-0.7	6	0.8	-0.4	Am	E
CS 29497-12	00 27 04.7	-23 27 38	70.3	-83.7	11.19	0.23	0.09	1.8	20.9	21.9	7579	3.3	-1.8	-8	0.6	-0.6	Am	E

Table B.4. (continued)

Star (1)	RA (1950) (2)	Dec (3)	l (4)	b (5)	V (6)	$(B-V)_o$ (7)	$(U-B)_o$ (8)	W_λ (9)	Hδ $D_{0.2}$ (10)	Hγ $D_{0.2}$ (11)	T_{eff} (12)	Log g (13)	[Fe/H] (14)	V_{tan} (15)	Dist. (16)	Z (17)	Class (18)	Obs (19)
CS 29499-6	23 34 31.6	-26 30 34	31.8	-73.4	12.09	0.16	0.09	1.9	32.4	28.0	8520	4.4	-0.8	-18	1.1	-1.0	Am	E
CS 29499-9	23 35 24.4	-25 39 28	34.9	-73.5	12.51	0.23	0.08	3.4	19.5	20.8	7508	3.5	-1.0	-9	1.1	-1.0	Am	E
CS 29499-23	23 42 23.4	-22 44 32	46.5	-74.2	13.40	0.28	0.09	1.7	22.6	20.5	7764	3.5	-1.6	3	1.5	-1.5	Am	E
CS 29499-45	23 45 20.2	-24 07 42	42.3	-75.3	11.91	0.21	0.12	3.4	24.5	29.5	7826	3.6	-0.7	-12	0.9	-0.8	Am	E
CS 29514-29	01 17 42.6	-22 45 33	179.0	-82.0	12.14	0.22	0.14	2.6	21.0	20.9	7770	3.8	-1.0	-4	0.9	-0.9	Am	E
CS 29516-9	22 26 15.8	+06 10 00	71.8	-41.9	12.56	0.19	0.14	2.6	27.7	25.0	8231	4.3	-0.7	23	1.2	-0.8	Am	K
CS 29518-29	01 11 33.0	-30 02 12	242.4	-84.4	12.25	0.15	0.05	1.8	33.3	22.2	8552	4.5	-0.9	51	1.2	-1.2	Am	E
CS 29518-53	01 22 08.1	-28 19 44	222.2	-82.6	12.31	0.25	0.10	2.2	19.0	14.7	7425	3.0	-1.8	-41	1.0	-1.0	Am	E
CS 29520-34	04 30 40.5	-60 09 06	270.4	-40.5	13.81	0.28	0.15	2.5	18.8	18.6	7500	3.1	-1.4	62	1.9	-1.2	Am	E
CS 29529-49	03 51 06.2	-62 15 02	275.4	-44.2	12.23	0.25	0.13	3.1	24.1	20.9	7830	3.6	-0.8	57	0.9	-0.6	Am	E
CS 30321-76	18 26 02.8	-33 55 06	0.1	-10.6	13.22	0.27	0.12	2.3	25.4	20.4	7953	3.6	-1.2	-62	1.4	-0.3	Am	E
CS 30321-178	18 26 39.5	-37 08 33	357.2	-12.1	11.88	0.17	0.09	3.4	22.9	23.7	7768	3.5	-0.7	-17	0.9	-0.2	Am	E
CS 30321-181	18 29 04.1	-37 11 42	357.4	-12.5	13.31	0.07	0.03	0.4	26.3	24.1	9126	3.6	-3.0	-23	2.6	-0.6	Am	E
CS 30321-203	18 30 12.5	-36 11 23	358.4	-12.3	13.59	0.24	0.11	3.0	19.5	20.0	7524	3.3	-1.1	-103	1.8	-0.4	Am	E
CS 30321-233	18 30 13.6	-34 28 52	360.0	-11.6	13.59	0.17	0.13	2.0	31.4	65.9	8449	4.1	-0.8	-97	2.0	-0.4	Am	E
CS 30321-256	18 29 15.3	-33 14 17	1.0	-10.9	12.98	0.18	0.15	2.9	24.2	24.2	8002	3.8	-0.8	-61	1.5	-0.3	Am	E
CS 30321-301	18 33 15.2	-33 37 12	1.1	-11.8	12.24	0.19	0.12	1.8	22.1	23.0	7758	3.5	-1.6	3	1.0	-0.2	Am	E
CS 30321-362	18 31 25.9	-36 18 33	358.4	-12.6	13.35	0.31	0.07	2.3	13.2	15.8	6793	2.4	-2.0	-18	1.5	-0.3	Am	E
CS 30321-375	18 33 03.0	-37 03 20	357.9	-13.2	13.42	0.17	0.10	2.1	25.0	23.7	7983	3.6	-1.1	-48	1.9	-0.4	Am	E
CS 30321-417	18 36 08.0	-35 10 33	359.9	-13.0	14.22	0.18	0.13	1.8	24.9	21.6	7959	3.5	-1.6	-44	2.7	-0.6	Am	E
CS 30332-20	22 45 48.8	+09 38 36	79.8	-42.4	12.43	0.05	0.04	1.6	28.4	26.8	8767	3.5	-0.9	35	1.8	-1.2	Am	E
CS 30332-44	22 42 23.2	+09 14 25	78.6	-42.2	13.58	0.24	0.12	2.4	22.4	21.0	7759	3.6	-1.1	-28	1.8	-1.2	Am	E
CS 30332-59	22 39 09.5	+11 58 50	80.1	-39.6	14.14	0.29	0.03	3.7	13.8	15.3	7011	3.0	-1.3	-79	2.1	-1.4	Am	E
CS 31072-20	05 38 23.6	-57 22 54	265.6	-32.2	12.75	0.31	0.09	4.7	14.6	14.3	7018	2.9	-1.0	5	1.1	-0.6	Am	E
CS 31072-34	05 33 47.3	-60 24 09	269.2	-32.8	11.85	0.35	0.09	3.3	19.0	21.8	7472	3.1	-1.0	-14	0.7	-0.4	Am	E
CS 31072-43	05 32 13.3	-57 41 26	266.0	-33.0	11.85	0.28	0.16	2.5	16.3	16.9	7170	2.6	-1.8	35	0.8	-0.4	Am	E

Table B.4. (continued)

Star (1)	RA (1950) (2)	Dec (3)	l (4)	b (5)	V (6)	$(B-V)_o$ (7)	$(U-B)_o$ (8)	W_δ (9)	$H\delta$ $D_{0.2}$ (10)	$H\gamma$ $D_{0.2}$ (11)	T_{eff} (12)	Log g (13)	[Fe/H] (14)	V_{los} (15)	Dist. (16)	Z (17)	Class (18)	Obs (19)
CS 31072-100	05 16 31.3	-59 02 59	267.7	-35.0	11.49	0.10	0.11	1.6	27.7	25.6	8279	3.5	-1.2	48	1.0	-0.6	Am	E
CS 31075-7	03 52 23.7	-65 57 20	279.7	-42.2	13.21	0.21	0.10	1.6	25.1	22.4	7940	3.7	-1.7	-2	1.6	-1.1	Am	E
CS 31075-15	03 45 44.5	-64 45 31	278.8	-43.5	12.34	0.27	0.06	3.8	15.0	16.1	7147	3.0	-1.0	22	1.0	-0.7	Am	E
CS 31075-41	03 31 33.5	-68 04 13	283.7	-42.7	11.77	0.17	0.08	1.7	24.1	22.8	7790	3.5	-1.6	-54	0.9	-0.6	Am	E
CS 31075-65	03 23 01.9	-66 02 12	282.2	-44.6	13.18	0.28	0.04	4.9	16.4	14.3	7260	3.5	-0.6	8	1.4	-1.0	Am	E
CS 31080-101	04 40 53.4	-44 16 09	249.2	-41.2	10.83	0.18	0.13	3.6	26.3	27.2	8003	3.5	-0.6	-21	0.6	-0.4	Am	E

BIBLIOGRAPHY

BIBLIOGRAPHY

Adelman, S. J., Philip A. G. D. 1992, MNRAS, 269, 579 & Philip

Alexander, S., 1852, AJ, 13, 95

Arnold, R., & Gilmore, G. 1992, MNRAS, 257, 225

Beers, T. C., Preston G. W., Shectman, S. A., Doinidis, S. P., & Griffin, K. E. 1992, AJ, 103, 267

Beers, T. C., Preston, G. W., Schectman, S. A., & Kage, J. A. 1990, AJ, 100, 84 9

Beers, T. C., Preston, G. W., Shectman, S. A. 1985, AJ, 90, 2089

Beers, T. C., Preston, G. W., Shectman, S. A. 1988, ApJS, 67, 461

Beers, T. C., Wilhelm, R., Doinidis, S. P. & Mattson C. J. 1995, preprint

Beers, T. C., & Sommer-Larsen, J. 1995, ApJS, 96, 175

Burstein, D. & Heiles, C. 1982, AJ, 87, 1165

Carney, B. W., Latham, D. W. 1985 in Stellar Radial Velocities, IAU Collq. 88, e d. A. G. D. Philip & D. W. Latham (Davis, Schenectady, NY), 139

Carney, B. W., Aguilar, L., Latham, D. W., & Laird, J. B. 1990, AJ, 99, 201

Carney, B. W., Laird, J. B., Latham, D. W., & Kurucz, R. L. 1987, AJ, 94, 1066

Carney, B. W., Latham, D. W. & Laird, J. B. 1990, AJ, 99, 572

Clube, S. V. M., & Watson, F. G. 1979, MNRAS, 187, 863

Cote, P., Welch, D. L, Fischer, P., & Irwin, M. J. 1993, preprint

Croswell, K., Latham, D. W., Carney, B. W., Schuster, W., & Aguilar, L. 1991, A J, 101, 2078

Doinidis, S. P., & Beers, T. C. 1990, PASP, 102, 1392

Doinidis, S. P., & Beers, T. C. 1989, ApJ, 340, L57

Eggen, O. J. 1987, in The Galaxy, NATO ASI, ed. G. Gilmore & B. Carswell (Dordr echt: Reidel), 211

Eggen, O. J., Lynden-Bell, D., & Sandage, A. R. 1962, ApJ, 136, 748

Flynn, C., & Sommer-Larsen, J. 1988, MNRAS, 235, 175

Frenk, C. S., & White, S. D. M. 1980, MNRAS, 193, 295

Gebhardt, K., & Beers, T. C. 1991, ApJ, 383, 72

Gilmore, G., & Reid, N. 1983, MNRAS, 202, 1025

Gray, R. O., & Corbally, C. J. 1995, private communication

Green, E. M. 1995, private communication

Green, E. M., & Morrison, H. L. 1993 in The Globular Cluster-Galaxy Connection, ed. G. H. Smith & J. P. Brodie (ASP Conf. Ser. 48), 318

Hanson, R. B. 1989, BAAS, 21, 1107

Hartwick, F. D. A. 1987 in The Galaxy, NATO ASI, ed. G. Gilmore & B. Carswell (Dordrecht: Reidel), 237

Hartwick, F. D. A., & Cowley, A. P. 1985, AJ, 90, 2244

Hawley, S. L., Jeffreys, W. H., Barnes III, T. G., & Lai, W. 1986, ApJ, 302, 626

Ibata, R. A., Gilmore, G., & Irwin, M. J. 1994, Nature, 370, 194

Kinman, T. D., Suntzeff, N. B., & Kraft, R. P. 1994, AJ, 108, 1722

Kodaira, K. & Philip, A. G. D. 1984, ApJ, 278, 201

Kurucz, R. L. 1992, private communication

Laird, J. B., Carney, B. W., Latham, D. W. 1993 in The Globular Cluster-Galaxy C onnection, ed. G. H. Smith & J. P. Brodie (ASP Conf. Ser. 48), 95

Lance, C. M. 1988, ApJS, 68, 463

Layden, A. C. 1993 in The Globular Cluster-Galaxy Connection, ed. G. H. Smith & J. P. Brodie (ASP Conf. Ser. 48), 326

Layden, A. C. 1995, private communication

Lee, Y-W. 1991 in ASP Symp., The Formation and Evolution of Star Clusters, ed. K. Janes (San Fransico: ASP), 205

Lee, Y-W. 1992, PASP, 104, 798

Lee, Y-W. 1993 in The Globular Cluster-Galaxy Connection, ed. G. H. Smith & J. P. Brodie (ASP Conf. Ser. 48), 142

Majewski, S. R. 1992, ApJS, 78, 87

Majewski, S. R., Munn, J. A. & Hawley, S. L, 1994, ApJ, 427, L37

Manduca, A., & Bell R. 1978, ApJ, 225, 908

McLachlan, G. J., & Basford, K. E. 1988 in Mixture Models (New York: Marcel Dek ker)

Michaud, G., Vauclair, G., Vauclair, S. 1983, ApJ, 267, 256

Minniti, D. 1995, AJ, 109, 1663

Morrison, H. L. 1993 in The Globular Cluster-Galaxy Connection, ed. G. H. Smith & J. P. Brodie (ASP Conf. Ser. 48), 334

Morrison, H. L. 1994, private communication

Morrison, H. L., Flynn, C., & Freeman, K. C. 1990, AJ, 100, 1191

Murray, C. A. 1986, MNRAS, 223, 649

Norris, J. E. 1986, ApJS, 61, 667

Norris, J. E. 1994, ApJ, 431, 645

Norris, J. E., Bessell, M. S., & Pickles, A. J. 1985, ApJS, 58, 463

Norris, J. E., & Ryan, S. G. 1989, ApJ, 380, 403

Pearson, E. S., & Stephens, M. A. 1964, Biometrika, 51, 484

Peterson, R. C. 1993, ApJ, 275, 737

Pier, J. R. 1983, ApJS, 53, 791

Pier, J. R. 1984, ApJ, 281, 260

Poveda, A., Allen, C., & Schuster, W. 1992, in IAU Symp. 149, The Stellar Populations of Galaxies, ed. B. Barbuy & A. Renzini (Dordrecht: Kluwer), 471

Preston, G. W., 1994, private communication

Preston, G. W., Beers, T. C., & Shectman, S. A. 1994, AJ, 108, 538

Preston, G. W., Shectman, S. A., & Beers T. C. 1991, ApJ, 375, 121

Preston, G. W., Shectman, S. A., & Beers T. C. 1991, ApJS, 76, 1001

Quinn, P. J., Hernquist, L., & Fullagar, D. P. 1993, ApJ, 403, 74

Reid, N. 1990, MNRAS, 247, 70

Rodgers, A. W., Harding, P., & Sadler, E. 1981, ApJ, 244, 912

Rodgers, A. W., & Paltoglou, G. 1984, ApJ, 283, L5

Ryan, S. G., & Lambert, D. L. 1995, AJ, 109, 2068

Ryan, S. G., & Norris, J. E. 1991, AJ, 101, 1835

Schneider, D. P., & Young, P. J. 1980, ApJ, 238, 946

Searle, L., & Zinn, R. 1978, ApJ, 225, 357

Smith, M. A. 1973, ApJS, 25, 277

Sommer-Larsen, J., Christensen, P., & Carter, D. 1989, MNRAS, 238, 225

Sommer-Larsen, J., & Christensen, P. R. 1987, MNRAS, 225, 499

Sommer-Larsen, J., & Zhen, C. 1990, MNRAS, 242, 10

Spaenhauser, A. 1989, Contri. Van Vleck Obs., 9, 45

Stetson, P. B. 1991, AJ, 102, 589

Suntzeff, N. B. 1993, in The Globular Cluster-Galaxy Connection, ed. G. H. Smith & J. P. Brodie (ASP Conf. Ser. 48), 167

Suntzeff, N. B., Kinman, T. D., & Kraft, R. P. 1991, ApJ, 367, 528

Sweigart, A. U. 1987, ApJS, 65, 95

Thogersen, E. N., Friel, E. D., Fallon, B. V. 1993, PASP, 105, 1253

Tonry, J., & Davis, M. 1979, AJ, 84, 1511

Wheeler, J. C., Sneden, C., and Truran, J. W. 1989, ARAA, 27, 279

White, S. D. M. 1989, MNRAS, 237, 51P

Woolley, R. 1978, MNRAS, 184, 311

Zinn, R. 1985, ApJ. 293, 424

Zinn, R. 1986 in Stellar Populations, ed. C. A. Norman, A. Renzini, & M. Tosi (Cambridge: Cambridge Univ. Press), 73

Zinn, R. 1993, in The Globular Cluster-Galaxy Connection, ed. G. H. Smith & J. P. Brodie (ASP Conf. Ser. 48), 38

MICHIGAN STATE UNI
31293014